Cytoplasmic Freezing

Exploring a Newly Discovered Extreme Immobilisation of the Cytoplasmic Content of the Fission Yeast *Schizosaccharomyces pombe*

Dissertation

zur
Erlangung der naturwissenschaftlichen Doktorwürde
(Dr. sc. nat.)

vorgelegt der
Mathematisch-naturwissenschaftlichen Fakultät
der
Universität Zürich

von
Maria Barbara Heimlicher

von
Neuhausen SH

Promotionskommission

Prof. Dr. Damian Brunner (Vorsitz, Leitung der Dissertation)
Prof. Dr. Lucas Pelkmans
Prof. Dr. Roland Wedlich-Söldner

Zürich, 2018

Table of Contents

Summary

Cell function and survival require a highly ordered, cell type-specific organization of the cellular content, the cytoplasm. It involves the asymmetric distribution of material, mediated by active transport of key regulatory components, which counteracts the entropic activity of diffusion. The maintenance of this complex, anisotropic cellular architecture and its remodelling according to environmental changes require a constant input of energy. However, organisms often experience energetically unfavourable conditions, such as nutrient limitation. In this context, a key question is whether, and if so how, an anisotropic cytoplasmic organization is maintained. Recent evidence suggests that the transition from a fluid-like to a protective solid-like state could be a general adaption response of the cytoplasm. This would serve to slow down diffusional processes and preserve intracellular architecture under low energy conditions.

During my PhD, I explored a newly discovered cytoplasmic solidification in the fission yeast *Schizosaccharomyces pombe*. We found that in advanced glucose starvation, the diffusive motion of lipid granules and other observable structures is completely restricted. We call this cytoplasmic state "cytoplasmic freezing" (CF), based on its reminiscence of a frozen cell.

I developed standardized methods to describe CF and the cytoplasmic state of cells in general. With these methods, I characterized the experimental parameters influencing the cytoplasmic state and thus the induction of CF. I investigated the behaviour of the cytoskeleton, and the general intracellular architecture upon CF. I found that F-actin undergoes a dramatic rearrangement during the starvation period, culminating in the disappearance of dynamic actin patches and the formation of stable, shoelace-like actin bundles that extend along the cell cortex in CF cells. Although I excluded a functional requirement for cytoskeletal elements to CF establishment, the F-Actin rearrangement together with the almost simultaneous completion of mitochondrial fragmentation and the reorganization of lipid droplet morphology and distribution indicate a global transition occurring in cells at the time of CF induction.

Importantly, I showed that the drastic immobilisation of intracellular structures in CF cells is accompanied with the ability to preserve cell shape in the absence of the cell wall, which is normally shape determining. This supports the idea that the cytoplasm of CF cells resembles a solid structure in which components such as lipid droplets no longer can rearrange.

In collaboration with another PhD student, I compared the CF state with newly published cytoplasmic solidification states that occur in budding yeast cells upon acute energy depletion.

First, we showed that the solidity of CF cells is significantly higher than that of cells under acute energy depletion. Further, we found no evidence for either of the molecular mechanisms that were proposed to cause cytoplasmic solidification in budding yeast, to operate in fission yeast and mediate CF. We hypothesize that CF might represent a complete protective solidification of the cytoplasm that cells preferably undergo if provided with sufficient adaptation time and energy.

In order to elucidate the molecular mechanism underlying the striking cytoplasmic immobilization in CF cells, I aimed to identify genes that are required for CF to occur. To that end, I developed a workflow to systematically investigate the capability of thousands of mutant strains of inducing CF. I applied this workflow on a gene deletion library, a strain collection harbouring fission yeast deletion mutants of all non-essential genes. I thereby identified 500 potential candidate genes that did not undergo CF in two independent experiments. After their careful evaluation and validation, these candidate genes will provide an invaluable entry point for elucidating the molecular mechanism mediating CF.

Zusammenfassung

Das Überleben und Funktionieren einer Zelle bedingt eine hochgeordnete, zelltypspezifische Organisation des zellulären Inhalts, des Zytoplasmas. Diese geht einher mit einer asymmetrischen Verteilung von Material mittels aktivem Transport von wichtigen regulatorischen Komponenten, was der entropischen Aktivität der Diffusion entgegenwirkt. Die Aufrechterhaltung dieser komplexen, anisotropen zellulären Architektur und bei Bedarf deren Umbau zur Anpassung an Veränderungen in den Umweltbedingungen benötigen eine konstante Energiezufuhr. Allerdings erfahren Lebewesen häufig energetisch ungünstige Bedingungen, zum Beispiel bei Nahrungsknappheit. Eine Schlüsselfrage ist nun, ob die anisotrope zytoplasmatische Organisation unter ungünstigen Bedingungen aufrechterhalten wird, und falls ja, wie. Neueste Anhaltspunkte legen nahe, dass der Übergang von einem flüssigen in einen festkörperartigen Zustand des Zytoplasmas dabei von Nutzen sein könnte, beispielsweise durch die damit einhergehende Verlangsamung der Diffusionsprozesse, oder um damit die intrazelluläre Architektur ganz zu fixieren.

In meiner Dissertation habe ich eine neu entdeckte Verfestigung des Zytoplasmas in Zellen der Spalthefe *Schizosaccharomyces pombe* erforscht. Wir haben beobachtet, dass die Diffusionsbewegung von Lipid-Tröpfchen und anderen sichtbaren zellulären Strukturen im fortgeschrittenen Stadium des Hungerns aufgrund von Glukosemangel zum Stillstand kommt. Wir nennen diesen zytoplasmatischen Zustand „cytoplasmic freezing“ (CF), aufgrund seiner Ähnlichkeit mit einer gefrorenen Zelle.

Ich habe standardisierte Methoden entwickelt, um CF und den zytoplasmatischen Zustand im Allgemeinen zu beschreiben. Mit diesen Methoden habe ich die experimentellen Parameter charakterisiert, die den zytoplasmatischen Zustand und folglich auch das Einsetzen des CF beeinflussen. Des Weiteren habe ich das Verhalten des Zytoskeletts und der allgemeinen intrazellulären Architektur von CF-Zellen untersucht. Dabei habe ich entdeckt, dass F-Aktin, welches zusammen mit den Mikrotubuli das Zytoskelett bildet, während der Hungerphase einen dramatischen Umbau erfährt. Dieser endet damit, dass in CF-Zellen keine dynamischen Aktinflecken mehr sichtbar sind, sich dafür aber lange, stabile, schuhbändelartige Aktinbündel gebildet haben, die sich entlang des Zellkortex winden. Die funktionelle Beteiligung des Zytoskeletts im Allgemeinen und der schuhbändelartigen Aktinbündel im Besonderen konnte ich mittels Experimenten ausschliessen. Jedoch ist es sehr interessant, dass zeitgleich mit dem Einsetzen von CF und dem Umbau des F-Aktin, auch die Fragmentierung der Mitochondrien abgeschlossen ist und sich die Morphologie und Verteilung der Lipidtröpfchen verändert hat.

Dies deutet darauf hin, dass zum Zeitpunkt der beobachteten zytoplasmatischen Verfestigung in den Zellen ein globaler Übergang stattfindet.

Zudem konnte ich zeigen, dass die dramatische Fixierung der intrazellulären Strukturen in CF-Zellen mit der Fähigkeit der Zellen einhergeht, ihre zylindrische Form unabhängig von der normalerweise formgebenden Zellwand zu erhalten. Dies unterstützt die Idee, wonach das Zytoplasma von CF-Zellen einem Festkörper gleicht, worin die einzelnen Komponenten, wie zum Beispiel die Lipid-Tröpfchen oder die Mitochondrien, sich nicht mehr neu anordnen können.

In Zusammenarbeit mit einer anderen Doktorandin habe ich den CF-Zustand mit kürzlich publizierten zytoplasmatischen Verfestigungen verglichen, die in der Bäckerhefe bei abruptem Energieverlust beobachtet wurden. Wir konnten zeigen, dass die Immobilisierung von zytoplasmatischen Komponenten in CF-Zellen signifikant höher ist als in Zellen, die einen abrupten Energieverlust erlitten hatten. Ausserdem haben wir keine Hinweise gefunden, die darauf hindeuten, dass einer der für die Verfestigung in der Bäckerhefe vorgeschlagenen molekularen Mechanismen auch in der Spalthefe stattfindet und CF herbeiführt.

Um dem molekularen Mechanismus, der hinter der verblüffenden zytoplasmatischen Fixierung in CF-Zellen steckt auf den Grund zu gehen, habe ich versucht Gene zu identifizieren die zur Entstehung von CF notwendig sind. Dafür habe ich einen experimentellen Ablauf entwickelt mit dem Ziel, systematisch tausende von mutanten Hefestämmen daraufhin zu testen, ob sie die Fähigkeit haben, CF zu erzeugen. Diesen Ablauf habe ich auf eine Sammlung von *S. pombe*-Stämmen angewendet, in der für jedes nicht-essentielle Gen ein Deletionsstamm enthalten ist. Dabei habe ich 500 potentielle Kandidatengene identifiziert, deren Deletionsstämme in zwei unabhängigen Experimenten kein CF gezeigt haben. Nach einer sorgfältigen Evaluierung und Validierung werden diese Kandidatengene einen ausserordentlich wertvollen Einstieg in die Ergründung des molekularen Mechanismus bieten, der zu CF führt.

Acknowledgements

First and foremost, I would like to thank Damian Brunner. I was indecisive as to whether or not I should pursue a PhD after my Master's degree. You were very enticing in introducing me to the novel phenomenon CF where so much was still unknown. I soon knew that this is was what I wanted to investigate. Going through the highs and lows, you were always supportive and optimistic. What I appreciated the most during all this time were our engaging scientific discussions. From the outside, it may have seemed like a serious argument, and it often was. But afterwards there were never bad feelings.

Aside from my primary supervisor, I would like to thank my PhD committee members Prof. Dr. Lucas Pelkmans, Prof. Dr. Roland Wedlich-Söldner, and Prof. Dr. Yves Barral. I immensely enjoyed our annual committee meetings, where we had great discussions and you shared your invaluable thoughts and advice with me. I always felt supported, strengthened and motivated after those meetings.

I would like to thank our collaborators Ernst-Ludwig Florin from Austin, Tx. and Andy Hoenger from Boulder, Co. for their discussions, advice and knowledge. I am grateful not only for the professors' contributions, but also for the PhD students working on CF from those two groups for sharing their experience and results: Chieze Ibeneche, Andrea Keidel and Aaron Foote from Austin and Minghua Liu from Boulder. Special thanks go to EL, Andrea and Aaron for having me in Austin for a short, but memorable research stay in 2014.

Next, I would like to thank all the present and former members of the Brunner lab: Laurynas, David, Adam, Michèle, Steve, Arina, Marisa, Erich, Werner, Martina, Wolfgang, Mandy, Magda, Dominica, Mirjam, Francesco, Arne, Meret, Daniel, Fiona, Kristian (like always from left to right). I always felt at home and accepted, and we had such good times in and out of the lab. My special thanks go to Adam Kijowski and Laurynas Pasakarnis. You were always there for me and were a significant part of my feeling at home. I will never forget the long evenings or even nights in the lab before deadlines or just for experiments, nor the fun nights out. Also, I would like to mention Michèle Gemünden, my desk neighbour after Adam left the lab. I really enjoyed our exchange regarding scientific and personal perspectives. I would like to thank my fellow Yeasties for your open experience transfer. Special thanks go to Mirjam Bächler. You are a talented scientist and I am very happy that you joined the CF project. I enjoyed working with you on the CF manuscript and am looking forward to your future findings. Also, I want to thank Stephen Huisman for introducing me to the fission yeast, and for your invaluable

experience and willingness to discuss problems. Thank you and Angela Lloyd for proofreading parts of this thesis. Thank you Werner Boll. Your technical support was extraordinary.
Last but not least, I would like to thank my family and my friends. You listened when necessary, and were kind enough not to ask at other times. My special gratitude goes to my man Michael, for your continuous love and support, and for sharing with me the joy and responsibility of raising our son, Melvin, and the little one on its way.

1 Introduction

1.1 Effect of environmental changes on cytoplasmic organization and fluidity

Cell function and survival require a highly ordered, cell type-specific organization of the cellular content, the cytoplasm. How cells generate, maintain, and reproduce this spatial organization is central to any understanding of the living state. It involves the asymmetric distribution of material, mediated by active transport of key regulatory components, which counteracts the entropic activity of diffusion. This occurs in a highly crowded and dynamic environment, with extremely disperse constituents ranging from small ions and metabolites via macromolecular complexes to large and complex structures like the cytoskeletal network and organelles.

Accordingly, it was shown that particles in the cytoplasm do not follow the principles of free diffusion in an aqueous solution, but rather perform sub diffusive motion influenced by macromolecular crowding, unspecific interactions, and polymer networks like the cytoskeleton (Luby-Phelps, Taylor, & Lanni, 1986; Tolić-Nørrelykke, Munteanu, Thon, Oddershede, & Berg-Sørensen, 2004; Weiss, Elsner, Kartberg, & Nilsson, 2004; Wirtz, 2009). Consequently, the cytoplasm was described as a complex viscoelastic fluid, a gel-like material (Fels, Orlov, & Grygorczyk, 2009; Grygorczyk, Boudreault, Platonova, & Orlov, 2015; Luby-Phelps et al., 1986; Mitchison, Charras, & Mahadevan, 2008; Moeendarbary et al., 2013; Tolić-Nørrelykke et al., 2004), or a colloidal liquid at the transition to a glass-like state (Miermont et al., 2013; Parry et al., 2014) rather than as a simple fluid containing solid particles.

The maintenance of the complex anisotropic cellular architecture, and its remodelling according to environmental changes, require a constant input of energy. However, organisms often experience unfavourable conditions such as nutrient limitation. Accordingly, organisms ranging from single cells to large mammals have evolved to deal with stress factors imposed by the local environment.

Under nutrient limitation, cells enter a quiescence state characterized by a reversible growth arrest (Coller, Sang, & Roberts, 2006). Cellular quiescence is a common life form for cells from many tissues and organisms (Lennon & Jones, 2011; Yanagida, 2009). Not only can most cell types execute such an environmentally induced dormancy program, but many organisms have even developed specialized cell types like spores and seeds, that can survive long periods of dormancy without any energy expenditure (Lennon & Jones, 2011). There have even been

reports of bacterial spores having survived millions of years in this state (Cano & Borucki, 1995; Vreeland, Rosenzweig, & Powers, 2000). Moreover, some animals are able to reorganize their whole body into a specialized state by down-regulating their metabolism and entering dormancy, like tardigrades or hibernating mammals.

This raises the question whether, and if so how, an anisotropic cytoplasmic organization is maintained under nutrient limited conditions. Known strategies for executing a dormancy program on the cellular level include lowering the water content, which leads to an increased cytoplasmic viscosity, or even a liquid-to-glass transition that can provide the physical conditions for low metabolism (Cowan, Koppel, Setlow, & Setlow, 2003; Dijksterhuis, Nijsse, Hoekstra, & Golovina, 2007; Sun & Leopold, 1997), the production of carbohydrates to prevent unfavourable fusion events by replacement of water, or by supporting cytoplasmic vitrification upon desiccation (Elbein, Pan, Pastuszak, & Carroll, 2003; Soto, Fernandez, Vicente-Soler, Cansado, & Gacto, 1999; Sun & Leopold, 1997).

Recent evidence suggests similar strategies are applied not only in specialized cell types, but by quiescent cells in general. It was shown that the cytoplasm of metabolically inactive bacteria displays glass-like properties which disproportionally constrains the motion of cytoplasmic components with increasing particle size (Parry et al., 2014). A similar liquid-to-solid-like transition was reported upon acute glucose starvation in S. cerevisiae (Joyner et al., 2016), (Munder et al., 2016). Moreover, the result from Joyner et al. suggest that molecular crowding due to water loss was responsible for the observed restriction in macromolecular mobility in *S. cerevisiae* as well as in bacteria (Joyner et al., 2016).

In addition to global adaptations like increased macromolecular crowding that impact all intracellular processes, more specific structural changes of the cytoplasm have been reported upon starvation-induced quiescence. It was shown that many proteins reversibly assemble into microscopically visible structures upon energy-depletion, among them several metabolic enzymes (Laporte, Salin, Daignan-Fornier, & Sagot, 2008; Narayanaswamy et al., 2009; Noree, Sato, Broyer, & Wilhelm, 2010; O'Connell, Zhao, Ellington, & Marcotte, 2012; Petrovska et al., 2014; Sagot, Pinson, Salin, & Daignan-Fornier, 2006). These structures were suggested to serve as storage depots for proteins or to inactivate enzymatic function.

Interestingly, it was recently proposed that such macromolecular assemblies serve an additional function as a collective. Munder et al. demonstrated that entry into dormancy is triggered by an influx of protons promoting a transition of the cytoplasm from a fluid- to a solid-like state through widespread assembly of proteins into higher-order structures (Munder et al., 2016).

Their results indicate that this solid-like cytoplasmic state is beneficial for the survival of the dormant cells (Munder et al., 2016).

Together, these results indicate that the transition from a fluid-like to a more solid-like state could be a rather general adaption response of the cytoplasm to nutrient-limited conditions. Solidification of the cytoplasm has been hypothesized to allow cells to down-regulate their metabolism by slowing down intracellular diffusion (Joyner et al., 2016; Munder et al., 2016). Furthermore, such a vitrified cytoplasmic state was suggested to help preserve cytoplasmic architecture during quiescence periods (Parry et al., 2014) or to save energy (Munder et al., 2016).

1.2 Fission yeast physiology

1.2.1 Introduction to fission yeast

The fission yeast *Schizosaccharomyces pombe* is a rod-shaped unicellular eukaryote of the Fungi kingdom (Hayles & Nurse, 2001). The first detailed description of the *S. pombe* dates to the early 1890s by Paul Lindner. He named it *Schizosaccharomyces* for its reproduction by fission in contrast to the budding behaviour of reproducing *S. cerevisiae*. *Pombe* means beer in Swahili, and was used to describe fission yeast, since the initial isolation came from contaminated millet beer from East Africa (Ian M Hagan, Carr, Grallert, & Nurse, 2016). Urs Leupold established fission yeast as a laboratory model organism in the 1940s. The strains that he used – and that are still commonly used in fission yeast laboratories – were not from the Lindner strain, but are thought to originate from a strain isolated from rancid wine in Wädenswil, Switzerland (Ian M Hagan et al., 2016).

Fission yeast has since become an invaluable model organism mainly in the fields of genetics and cell biology. Its greatest moment of fame came when Paul Nurse was awarded the Nobel Prize in Physiology or Medicine in 2001 for his discoveries regarding the regulation of the cell cycle using fission yeast.

S. pombe is readily amenable by classical and molecular genetics. Its genome was sequenced in 2002 as the fourth eukaryote to be sequenced (Wood et al., 2002). Around 5000 genes on 3 chromosomes are annotated in its 14Mb genome, of which 67% are conserved in humans (www.pombase.org). There is a genome-wide gene deletion collection (deletion library) covering almost all 5000 genes, of which 3600 are non-essential genes (Kim et al., 2010).

Fission yeast cells have a defined shape of 7-14 µm length and 4 µm width. They grow by tip-elongation and divide by medial fission. They have a typical eukaryotic cell cycle that takes around 3h, with the length of the cells reflecting cell cycle progression.
S. pombe is normally a haploid organism, but if nitrogen levels become limiting, cells of the opposite mating type conjugate and form a diploid zygote. The zygote can undergo meiosis to form four haploid spores, or it can re-enter vegetative growth as a diploid under appropriate conditions (Ian M Hagan et al., 2016).

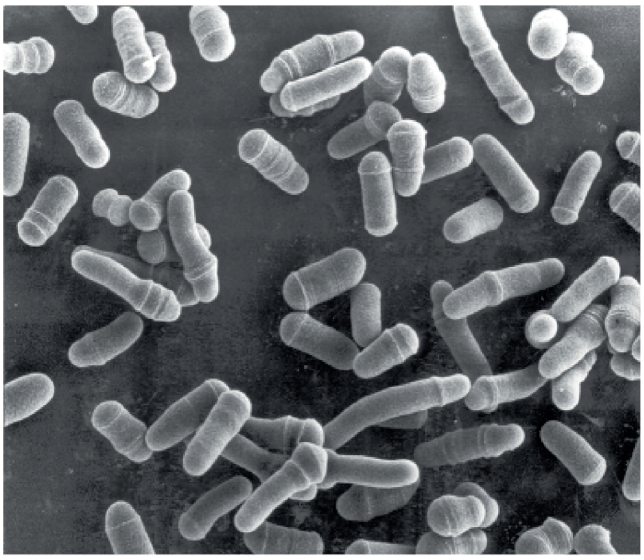

Figure 1. Scanning electron micrograph of fission yeast cells from (Hayles & Nurse, 2001).

1.2.2 Cell wall and turgor pressure

As many other unicellular organisms and plant cells, *S. pombe* cells have a rigid cell wall of about 200 nm thickness that is composed primarily of alpha, beta-glucans and galactomannans (Kopecká, Fleet, & Phaff, 1995; Manners & Meyer, 1977). The cell wall is crucial for the cylindrical shape. When the cell wall is digested away, the protoplast squeezes out of the wall as soon as there is a reasonable leak, and adopts a spherical shape (Chang, 2017). To re-establish a cylindrical shape, the generation of new cell wall material is required (Kobori, Yamada, Taki, & Osumi, 1989).
Additionally, internal turgor pressure influences the cell shape. Turgor pressure is the intracellular hydrostatic pressure that results from the osmotic potential across the membrane, which is balanced by mechanical stress in the cell wall (Rojas & Huang, 2017). Addition of an osmotic agent such as sorbitol into the medium causes a decrease in turgor pressure and shrinkage of the cell and its wall (Atilgan, Magidson, Khodjakov, & Chang, 2015). However,

experiments with sorbitol have their limitations, as on a time scale of 10-30 minutes the cells adapt to the new environmental osmolarity by inducing gpd1+, a NADH-dependent glycerol-3-phosphate dehydrogenase that is involved in glycerol synthesis (Aiba, Yamada, Ohmiya, & Mizuno, 1995; Minc, Boudaoud, & Chang, 2009). By increasing the intracellular glycerol, the intracellular solute concentration rises, so that the turgor pressure is restored. The relaxed state of the fission yeast cell wall, induced by cell lysis, was shown to be significantly smaller than the natural state, where the cell wall is inflated by turgor pressure (Atilgan et al., 2015). The external molarity required to shrink intact cells to the size of the relaxed cell wall, and thus match the turgor pressure, was found to be around 1.3 M Sorbitol (Atilgan et al., 2015).

1.2.3 Metabolism

Yeasts have been used for hundreds of years to produce alcohol as a by-product of growth. The majority of yeast species is facultatively fermentative, as is *S. pombe* (van Dijken, Weusthuis, & Pronk, 1993). They are thus able to generate ATP by substrate-level phosphorylation and do not depend on respiration and oxidative phosphorylation to drive energy-requiring reactions (van Dijken et al., 1993). However, only very few yeasts, among them *S. cerevisiae* but not *S. pombe*, are able to grow under strictly anaerobic conditions (Visser, Scheffers, Batenburg-van der Vegte, & van Dijken, 1990). This is not contradictory, since the physiological function of oxygen is not limited to its role as an electron acceptor for mitochondrial respiration, as the biosynthesis of crucial compounds also involves oxygenation reactions.

Like budding yeast, fission yeast fermentation dominates and mitochondrial respiration is repressed by excess of glucose. This regulatory system is called the Crabtree-effect (De Deken, 1966). Conversely, under glucose-limited conditions, oxygen is the key parameter determining the rate of alcoholic fermentation (van Dijken et al., 1993). Low oxygen conditions promote fermentation, while respiration is used in high oxygen conditions.

Fission yeast can grow on glycerol, a non-fermentable carbon source, but only in the presence of other carbon sources. While the glycerol metabolism is repressed in the presence of high glucose concentrations, it is derepressed during glucose starvation (Matsuzawa et al., 2010).

1.2.4 Quiescence induced by glucose starvation

Fission yeast has a proliferating and a quiescence state. Cellular quiescence is defined as a reversible arrest of growth and proliferation (Coller et al., 2006). It is a common life form for single celled organisms and for cells from many tissues and organisms (Yanagida, 2009). The

link between quiescence and proliferation must be tightly regulated since misregulation can lead to cell death, as well as to cancer and tissue degeneration in multicellular organisms.

Quiescence in fission yeast, as in most eukaryotic cells, can be induced by nutrient starvation. Most cell types enter quiescence through G1 phase of the cell cycle. This state is often referred to as G0 (Wei, Nurse, & Broek, 1993). Exceptionally, fission yeast cells can enter a quiescence state from either G1 or G2 (Costello, Rodgers, & Beach, 1986), depending on the nature of the starvation. Such quiescence cells become resistant to heat shock and are viable for long periods of time in the absence of nutrients (Wei et al., 1993).

Nitrogen-source deficiency arrests heterothallic cells in the absence of sexual partners after 2 cell cycles predominantly in a pre-replicative stage containing 1C DNA (Yanagida, 2009). These cells are small and have a very long chronological life span (Su, Tanaka, Samejima, Tanaka, & Yanagida, 1996).

Conversely, when cells run out of glucose, they enter quiescence through G2 phase (Costello et al., 1986). Upon a sudden and complete elimination of glucose from the growth medium, *S. pombe* cells arrest rapidly without further cell division (Yanagida, 2009). These cells are long and display large vacuoles, the movement of intracellular organelles is significantly reduced, and they lose viability within a day (Pluskal, Hayashi, Saitoh, Fujisawa, & Yanagida, 2011). However, when cells run out of glucose by reaching stationary phase, or when adapted to glucose limited conditions prior to fasting, their lifespan is dramatically prolonged (Pluskal et al., 2011; Roux et al., 2009). The way fission yeast cells enter such a stationary phase differs from budding yeast. After glucose exhaustion, budding yeast cells switch to a respiratory mode of energy production by metabolizing the ethanol produced during an earlier growth stage (Herman, 2002). This shift from glucose to ethanol as a carbon source – also referred to as "diauxic shift" – does not occur in *S. pombe*, since *S. pombe* lacks the glyoxylate enzymes required for the utilization of ethanol for growth (Flores, Rodríguez, Petit, & Gancedo, 2000; Heslot, Goffeau, & Louis, 1970).

Interestingly, the chronological lifespan of stationary phase cells depends on the initial glucose concentration of the medium (B.-R. Chen & Runge, 2009; Roux et al., 2009; Zuin et al., 2010). Similar to many organisms from budding yeast to mammals, glucose seems to act as a pro-aging factor (Kassi & Papavassiliou, 2008; Roux et al., 2009). The activity of nutrient-signalling pathways like PKA and TOR-SCH9 seem to promote aging by inhibiting both stress resistance and respiration (Barros, Bandy, Tahara, & Kowaltowski, 2004; Bonawitz, Chatenay-Lapointe, Pan, & Shadel, 2007; Dilova, Easlon, & Lin, 2007; Lin et al., 2002; Piper, Harris, & MacLean, 2006; Roux, Quissac, Chartrand, Ferbeyre, & Rokeach, 2006). Calorie restriction, or

inactivation of nutrient-dependent pathways, induces lifespan extension, and this effect is dependent on the activation of the stress-dependent Sty1 mitogen-activated protein (MAP) kinase (Zuin et al., 2010). It was suggested that the Sty1 MAP kinase activation might be induced by high respiratory rates stimulating the production of reactive oxygen species (ROS) (Zuin et al., 2010).

However, the effect of glucose levels on the lifespan of fission yeast is only apparent in rich medium (YE5S) and not in minimal medium (B.-R. Chen & Runge, 2009; Roux et al., 2009). This is in agreement with the report that the respiration rate is generally higher in cells grown in minimal medium than in rich medium (Zuin et al., 2008).

1.2.5 Autophagy

Macroautophagy (hereafter autophagy), or "self-eating", is a cellular degradation and recycling process that is conserved from yeast to humans (Yang & Klionsky, 2010). In contrast to the proteasome that is responsible for the degradation of most short-lived proteins, long-lived proteins, large protein complexes and organelles are degraded by autophagy (Wen & Klionsky, 2016). Too little or too much degradation from uncontrolled autophagy is harmful, and autophagy dysfunction is associated with various diseases such as cancer and neurodegeneration (Wirawan, Vanden Berghe, Lippens, Agostinis, & Vandenabeele, 2012). Autophagy can be selective or non-selective, depending on the type of cargo that is sequestered. Autophagy is induced upon starvation or other stress conditions and promotes the turnover of cytoplasmic materials that can be turned into proteins and other building blocks or energy required for cell survival, or removing superfluous or damaged organelles (Yang & Klionsky, 2010). The autophagic cargo is sequestered by the expanding phagophore, leading to the formation of the double-membrane autophagosome (Feng, Yao, & Klionsky, 2015). Subsequently, the outer membrane of the autophagosome fuses with the vacuole or the lysosome in non-yeasts. The inner membrane as well as the cargo are then degraded by resident hydrolases (Wen & Klionsky, 2016).

Whereas in budding yeast both nitrogen and carbon starvation induce autophagy (Takeshige, Baba, Tsuboi, Noda, & Ohsumi, 1992), autophagy in fission yeast was reported to be induced only under nitrogen starvation but not under glucose starvation , or depending on the carbon sensing pathway, cAMP-PKA (Kohda et al., 2007; Nakashima et al., 2006). Moreover, it was suggested that the major function of fission yeast autophagy is to provide a supply of nitrogen or amino acids, rather than to remove surplus proteins or organelles that would potentially interfere with crucial cellular activities (Kohda et al., 2007; Nakashima et al., 2006).

Autophagy occurs mainly under the control of a key regulator of cell homeostasis, the Ser/Thr kinase TOR (target of rapamycin), in yeast, or mTOR in mammals (Laplante & Sabatini, 2012). Fission yeast possess two Tor homologs, Tor1 and Tor2, which are the major components of the TOR complexes TORC2 and TORC1, respectively (Weisman, Roitburg, Schonbrun, Harari, & Kupiec, 2007). It has recently been shown that only TORC1 negatively regulates autophagy in fission yeast as in other eukaryotic organisms (Abada & Elazar, 2014; Otsubo, Nakashima, Yamamoto, & Yamashita, 2017).

1.3 Intracellular architecture of fission yeast cells

Cell function and survival require a highly ordered, cell type-specific spatial organization of the cellular content, the cytoplasm. In eukaryotic cells, membrane-enclosed organelles form distinct compartments with physical barriers, large macromolecular complexes form domains by protein-protein interactions and the cytoskeleton provides tracks for directed transport of cytoplasmic subunits to overcome the limits of Brownian motion.
In the next section, I will introduce the intracellular entities that are particularly important for my work in more detail.

1.3.1 The cytoskeleton

All cells organize themselves in space, as they need to rearrange their internal components as they grow, divide, and adapt to changing circumstances. For these spatial and mechanical functions, eukaryotic cells have developed a system of filaments called the cytoskeleton (Alberts, 2008). Unlike most cells, fission yeast has only 2 types of cytoskeletal filaments: the microtubules and actin filaments. Therefore, intermediate filaments are not present in this yeast.

1.3.1.1 Microtubules

Microtubules are hollow cylinders, with a diameter of 25nm, made from polymers of alpha and beta-tubulin dimers. They stochastically switch between growing and shrinking phases (Mitchison & Kirschner, 1984). The switch between growing and shrinking is termed catastrophe, while the reverse process is called rescue. During cell division microtubules form the mitotic spindle, which segregates the duplicated chromosomes in all eukaryotes. Interphase MT organization varies greatly between organisms and cell types. In fission yeast interphase cells, microtubules are organized in 2-6 antiparallel microtubule bundles that span the length of the cell (I M Hagan, 1998; Höög et al., 2007; Tran, Marsh, Doye, Inoué, & Chang, 2001). They are important for correct growth site positioning in interphase by positioning polarity

markers at the cell ends (Mata & Nurse, 1997), and for cytokinesis by centering the nucleus (Tran et al., 2001). Both processes require tight control of microtubule catastrophe events (Brunner & Nurse, 2000; Huisman & Brunner, 2011).

It was shown that upon entry into quiescence by carbon starvation, microtubules rearrange. Quiescent cells assemble one spindle-pole body-associated microtubule bundle composed of stable antiparallel microtubules (Laporte et al., 2015).

1.3.1.2 Actin filaments

Actin filaments (F-actin) are flexible, two-stranded helical polymers made from actin monomers with a diameter of 5-9 nm (Alberts, 2008). In fission yeast, actin filaments are organized into three distinct structures: actin patches, actin cables, and the contractile ring (Kovar, Sirotkin, & Lord, 2011). Actin patches are linked to endocytosis, the contractile ring drives cytokinesis, and actin cables are crucial for polarized transport by providing tracks for directed delivery of vesicles and organelles to the expanding cell tips (Kovar et al., 2011). While the patches are based on a branched network of Arp2/3-complex-mediated actin assembly, actin cables are formed by short unbranched parallel filaments assembled by the actin nucleation and elongation factor For3, which is part of the formin family (Kovar et al., 2011).

It was shown that upon entry into quiescence by carbon starvation, F-actin-based structures lose their polarity (Laporte et al., 2015; Makushok, Alves, Huisman, Kijowski, & Brunner, 2016), and were reported to rearrange into a big cytoplasmic structure (Laporte et al., 2015). This structure displayed all the characteristics described for similar actin structures in quiescent *S. cerevisiae* (Sagot et al., 2006), such as variable size and shape and resistance to Latrunculin A, an inhibitor of actin polymerisation (Spector, Shochet, Kashman, & Groweiss, 1983). Such actin bodies were proposed to serve as actin reserves that could immediately be made available for cells re-entering a proliferating cycle (Sagot et al., 2006). However, another study indicated that the occurrence of such actin bodies negatively correlated with the lifespan of cells, as in quiescence induced by calorie restriction, dynamic actin filaments dominated (Vasicova, Lejskova, Malcova, & Hasek, 2015).

1.3.1.3 Septins

Septins are a family of small GTPases that are highly conserved among eukaryotes. Due to their ability to form filaments, it has been suggested that they should be regarded as the fourth component of the cytoskeleton (Mostowy & Cossart, 2012). In fission yeast this would be the third component, since this organism does not seem to have intermediate filaments. Septins were first known for their localization to the cytokinetic ring where they play a role in

cytokinesis, but it became clear that they are involved in numerous processes such as the formation of lateral diffusion barriers and as scaffold proteins (Saarikangas & Barral, 2011).
In *S. pombe* there are seven septin genes (*spn1-spn7*) (Longtine et al., 1996; F. Pan, Malmberg, & Momany, 2007). Four of them (*spn1-spn4*) are expressed in mitotic cells where the gene products form a hetero-oligomeric complex that assembles during cytokinesis into a ring at the division site (An, Morrell, Jennings, Link, & Gould, 2004; Berlin, Paoletti, & Chang, 2003; Tasto, Morrell, & Gould, 2003). They are not essential, but the absence of any of them causes a septation defect, resulting in a chained cell phenotype (An et al., 2004; Berlin et al., 2003; Tasto et al., 2003). The other three septin genes (*spn5-spn7*) are expressed only during sporulation (Abe & Shimoda, 2000; Mata, Lyne, Burns, & Bähler, 2002; Onishi et al., 2010; Watanabe et al., 2001), where they are important for the orientation of the forespore membrane (Onishi et al., 2010).

1.3.2 Lipid droplets

Lipid droplets are best known as storage organelles for neutral lipids as energy reservoirs and key building blocks for formation of the cellular membrane system, (Walther & Farese, 2012). However, accumulating evidence suggests a broader role than mere fat storage. They seem actively involved in biosynthesis and in the breakdown of neutral lipids and thereby neutralization of potentially cytotoxic fatty acids (Walther & Farese, 2012). Additionally, they have been linked to protein storage and the immune system, as well as to viral replication (Walther & Farese, 2012; Welte, 2015). Their dysfunction has been linked to many diseases (Welte, 2015).
Lipid droplets are found in most cells from bacteria to humans (Walther & Farese, 2012). They are composed of a hydrophobic core consisting mostly of triacylglycerols and sterol esters, and are surrounded by a phospholipid monolayer containing a specific set of proteins (Walther & Farese, 2012). Biogenesis of lipid droplets in eukaryotes is believed to be mainly initiated through neutral lipid synthesis in the ER, leading to the accumulation of neutral lipids between the two leaflets of the ER lipid bilayer and subsequent budding of lipid droplets from the ER surface (Choudhary, Ojha, Golden, & Prinz, 2015; Martin & Parton, 2006; Schuldiner & Bohnert, 2017).
Whether the nascent lipid droplets completely separate from the ER is currently under debate, as it has been reported that in S. cerevisiae, all cellular lipid droplets are connected to the ER outer leaflet where the nascent lipid droplet formed (Jacquier et al., 2011). These continuities between the phospholipid monolayer bordering the LD and the outer leaflet of the phospholipid

bilayer of the ER, so called “lipidic bridges” were thought to be remnants of the biogenesis route (Schuldiner & Bohnert, 2017). However, similar “lipidic bridges” have been described between lipid droplets and peroxisomes as well as between distinct lipid droplets (Binns et al., 2006; Thazar-Poulot, Miquel, Fobis-Loisy, & Gaude, 2015). It has also been shown that such bridges can form de novo between previously separated lipid droplets and the ER (Wilfling et al., 2014). Together, these results indicate that lipidic connections might represent a type of contact site unique to lipid droplets with their phospholipid monolayer, rather than just remainders of lipid droplet biogenesis (Schuldiner & Bohnert, 2017). Additionally, in fission yeast, lipid droplets can form independent of the ER via fission, suggesting that at least part of the lipid droplets are separated from the ER (Long et al., 2012).

1.3.3 Mitochondria

The main function of mitochondria is the production of ATP via oxidative phosphorylation in a cell’s aerobic metabolism. Additionally, they play a role in diverse processes such as metabolite homeostasis, and stress response like autophagy and apoptosis. It is therefore not surprising that their malfunction is correlated with many diseases, for example neurodegenerative and metabolic disorders (Nunnari & Suomalainen, 2012).

In contrast to textbook mitochondria with the characteristic kidney shaped ovals containing cristae, actual mitochondria in living cells are of tubular shape. They are dynamic structures that undergo fission and fusion and translocation. The fission and fusion need to be tightly controlled, since an imbalance in one of the processes influences not only their morphology but also their proper function (H. Chen & Chan, 2005). The fission of mitochondria is regulated by a dynamin-related protein called DRP1 in mammals or dnm1 in yeast (Otsuga et al., 1998; Smirnova, Griparic, Shurland, & van der Bliek, 2001).

Their distribution throughout the cell is dependent on the cytoskeleton, but different organisms and cell types rely on different mechanisms. For example, the budding yeast *S. cerevisiae* and plants depend mainly on the actin cytoskeleton for transport (Boldogh & Pon, 2006), while Drosophila and mammalian neurons employ motors such as kinesin and dynein for microtubule-dependent dislocation (Hollenbeck & Saxton, 2005; Russo et al., 2009). Fission yeast uses a microtubule-dependent, but motor-independent mechanism for positioning of its mitochondria (Yaffe et al., 1996; Yaffe, Stuurman, & Vale, 2003).

1.3.4 Membraneless compartments

In the classical view, organelles that function to provide a distinct environment for chemical reactions are surrounded by membranes, such as mitochondria or the endoplasmic reticulum (ER). However, many cellular compartments where specific reactions take place are not surrounded by membranes. Examples are the centrosomes (Mahen & Venkitaraman, 2012) which nucleate microtubules, the nucleoli which make ribosomes inside the nucleus (Boisvert, van Koningsbruggen, Navascués, & Lamond, 2007), or stress granules (Buchan & Parker, 2009; Decker & Parker, 2012) forming under stress conditions.

How cells organize such membrane-less organelles has recently become the focus of intense research. It has been suggested that the best way to think of them is as liquid drops that coexist with the cytoplasm (Banani, Lee, Hyman, & Rosen, 2017; Hyman, Weber, & Jülicher, 2014). The first example where such a compartment had been described as a phase-separated liquid, were the P granules from *Caenorhabditis elegans* embryos that segregate with the germ line of *C. elegans* embryos (Brangwynne et al., 2009). It was shown that these granules behave like liquids; they fuse, exchange components rapidly with the cytoplasm, are easily deformed by flows, and have a viscosity similar to runny honey (Brangwynne et al., 2009; Hyman et al., 2014).

Such membrane-less compartments are thought to be formed by phase separation through liquid-liquid demixing (Hyman et al., 2014). Such a phase transition occurs, when the components of the de-mixed compartment have a higher affinity to each other than to the rest of the cytoplasmic molecules, similar to oil drops separating from the vinegar in a salad dressing. This is counterbalanced by the entropy-driven tendency of all components to mix (Hyman et al., 2014). There is increasing evidence that membrane-less compartments, like phase separation in general, are very sensitive to fluctuating intracellular conditions such as changes in temperature, concentration or affinities of macromolecules (Alberti & Hyman, 2016; Hyman et al., 2014; P. Li et al., 2012; Nott et al., 2015; S. C. Weber & Brangwynne, 2015).

The molecular mechanisms behind phase separation are only beginning to unravel, but it seems that intrinsically disordered proteins (IDPs), also called prion-like proteins, are an important class of proteins, that drive phase separation (Alberti & Hyman, 2016; Han et al., 2012; Kato et al., 2012; Molliex et al., 2015; Nott et al., 2015; Patel et al., 2015; Toretsky & Wright, 2014). When expressed in vitro, these IDPs form liquid-like droplets. However, unlike liquid-like compartments studied in vivo, these liquid-like droplets quickly convert into more solid-like structures with different physical properties and structural organization, such as hydrogels and highly ordered fibrils (Han et al., 2012; Kato et al., 2012; Molliex et al., 2015; Murakami et al.,

2015; Patel et al., 2015). This suggests that a liquid drop is a metastable state, which will quickly convert into a gel or solid-like state if not regulated otherwise (Alberti & Hyman, 2016). The driving force for the solidification is so far unknown.

Such solid-like states have not only been implicated in diseases such as ALS (Han et al., 2012; Kato et al., 2012; Murakami et al., 2015; Patel et al., 2015), but have also been shown to be used by cells to inactivate or store cytoplasmic content. It was shown that quiescent oocytes of Xenopus use an amyloid-like mechanism to form a super-organelle called the Balbiani body, which stores mRNA and organelles such as mitochondria (Boke et al., 2016). These physiological amyloids are formed by a prion-like protein, and are proposed to serve as a stable matrix in which the organelles are embedded (Boke et al., 2016).

1.4 Previous work on cytoplasmic freezing in fission yeast

A while ago, Prof. Damian Brunner and Prof. Ernst-Ludwig Florin performed optical tweezer experiments on endogenous lipid droplets in fission yeast. An optical tweezer – also called an optical trap – is formed by tightly focusing a laser beam with a high numerical aperture (NA) objective lens. The focused laser light creates a gradient in the electric field. A dielectric particle near the focus will experience a gradient force that pulls it in the direction of the focus. For small displacements, the optical trap acts as a spring whose stiffness is proportional to the light intensity (Neuman & Block, 2004). In most cells, lipid droplets were easily movable through the cell, the cytoplasm containing them seemed liquid-like as expected. However, in some cells the lipid droplets could not be moved at all by these optical tweezers, the cytoplasm in those cells seemed frozen. After trial and error, they found that they could reproduce this frozen state of the cytoplasm by starving fission yeast cells for glucose for several days. They termed this phenomenon cytoplasmic freezing (CF) based on its resemblance to a frozen cell (see Figure 2).

Very intrigued by this phase transition, they speculated that the observed cytoplasmic solidification was an adaptation strategy of cells to unfavourable conditions, rather than a passive consequence of another adaptive process. Such solidification could serve to preserve the anisotropic intracellular architecture at low cost, or to protect cytoplasmic structures from damage in nutrient scarce times. They hypothesized that pure macromolecular crowding would not be strong enough to explain CF, as even in a highly viscous fluid, components can rearrange albeit on a larger time scale, and thus an external force like the optical tweezers should be able to move a lipid droplet. Therefore, they hypothesized that CF involved the formation of a dense, cross-linked network that would trap and immobilized the cytoplasmic content. They decided

to study CF in more detail, as to gain insight into its purpose and molecular mechanism. They followed a collaborative approach between the Florin lab with their biophysical expertise, the Brunner lab with the strong molecular biology background and the Hoenger lab as electron microscopy experts. Chieze Ibeneche, a PhD student in the Florin lab, started the project during her time as a PhD candidate.

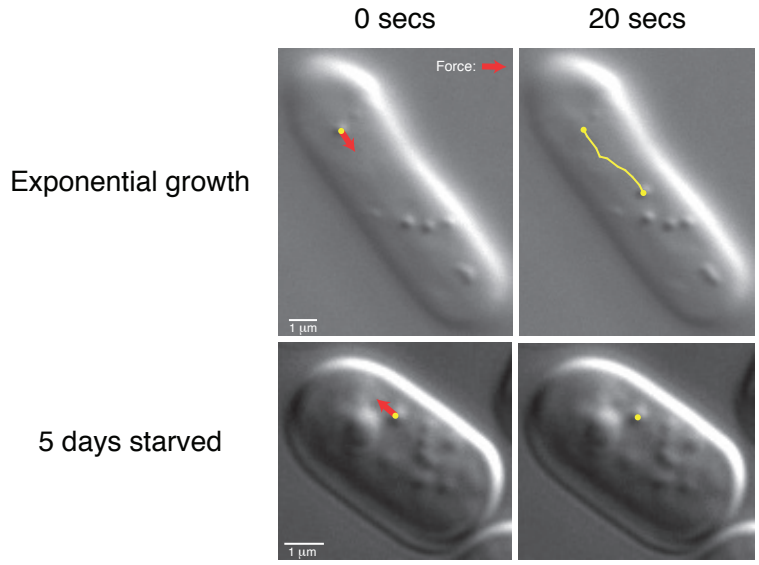

Figure 2. Cytoplasmic freezing in fission yeast characterized by the inability to move endogenous lipid granules by optical tweezers.

DIC images showing optical tweezer manipulations of lipid granules for exponentially growing and starved cells. Red arrow indicates direction of applied force, yellow line indicates granule trajectory. Figure from (Ibeneche, 2011).

While performing optical tweezer experiments on CF cells it became obvious that not only could the lipid droplets no longer be moved, but they themselves did not display any visible diffusive motion. To quantify this, Chieze performed single particle tracking (SPT) with very high spatial and time resolution on lipid droplets. From this, she calculated the mean square displacement (MSD) by averaging the square of displacement over all pairs of points of a given time interval (time lag). The diffusive motion of lipid droplets was described by anomalous subdiffusion, where $MSD = 4Dt^{\alpha}$ (see Figure 3A, (Ibeneche, 2011; M. J. Saxton & Jacobson, 1997; Tolić-Nørrelykke et al., 2004)). Each MSD vs time lag trajectory could thus be described by the characteristic scaling exponent, α (α value) and generalized diffusion coefficient, D. These two values were determined by a linear fit applied to the logarithm of the MSD vs time lag trajectory.

When Chieze analysed the lipid droplet motion in SD5-8 cells, the α value and the MSD for a given time lag were significantly lower compared to exponentially growing cells (see Figure

3B, (Ibeneche, 2011)). This showed that not only could lipid droplets in CF cells no longer be moved by external force, but they themselves significantly increased their anomalous diffusion and decreased the space they explored in a given time.

CF was induced by culturing cells in EMM medium with low glucose concentration (EMMLG: 0.5% glucose instead of 2% glucose for EMM2) where they reached stationary phase after 2 days of culturing (starvation day 2) and induced CF around starvation day 5. In order to find out, whether CF could be induced earlier by lowering the initial glucose concentration, Chieze tested the motion of lipid droplets cultured under glucose concentrations from 0%-0.5%. Interestingly, the motion of lipid droplets became gradually more anomalous with time of starvation until around starvation day 5 the α value reached a plateau, where it stayed up to starvation day 8 for all glucose concentrations between 0.1-0.5%. Only the α value from cells cultured without glucose did not decrease over time but stayed constantly high (see Figure 3C, (Ibeneche, 2011)). From this they concluded, that CF could not be induced significantly earlier by lowering the glucose concentration, and that CF induction required energy.

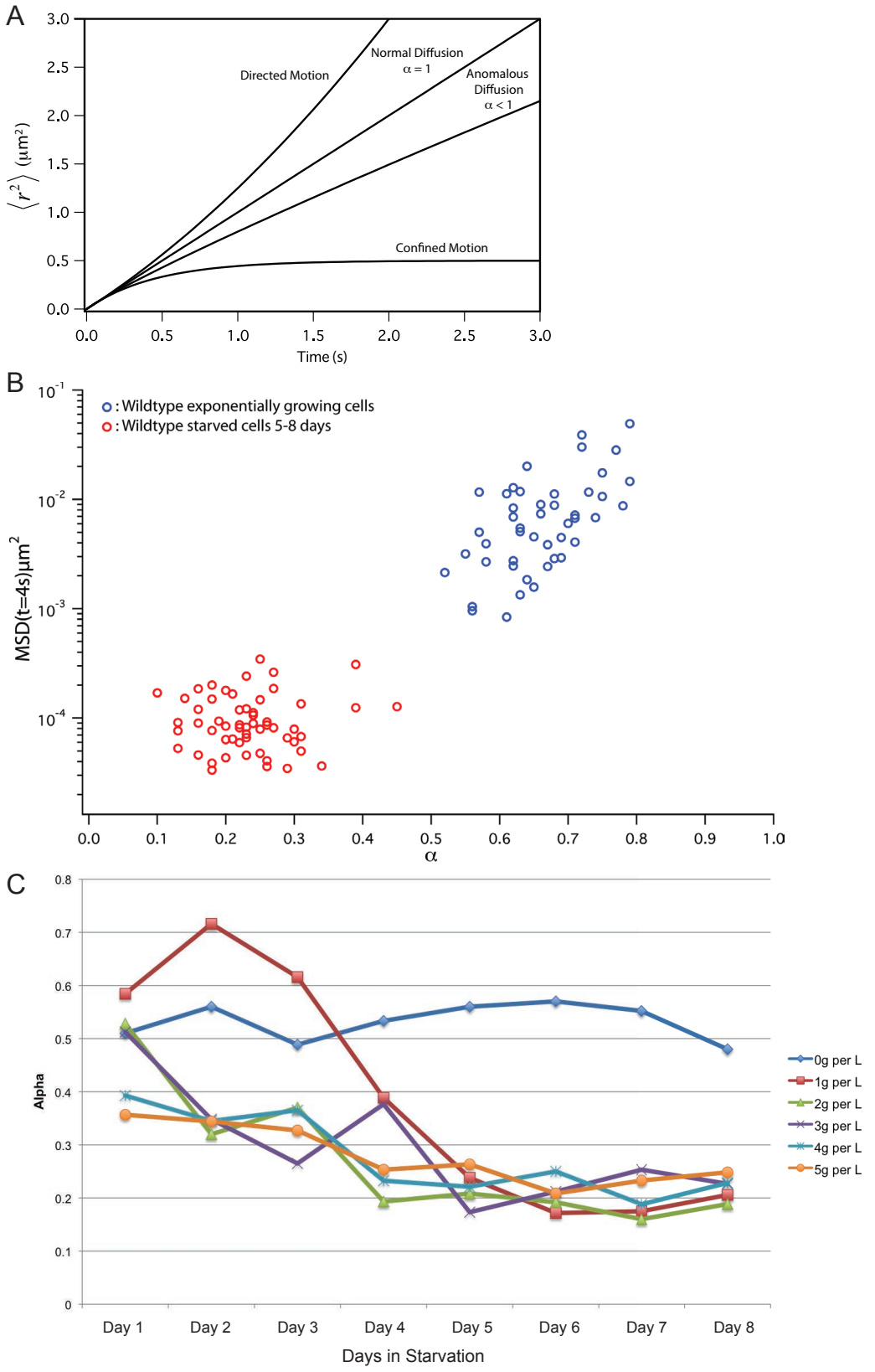

Figure 3. Single particle tracking and MSD analysis of fission yeast lipid droplets during starvation.

(**A**) The mean squared displacement $\langle r^2 \rangle$ as a function of time characterizes the various modes of motion. (**B**) Semi-log plot of MSD vs. α for wildtype exponentially growing cells and cells starved for glucose for 5-8 days. (**C**) Plot showing α values of lipid droplets from cells of starvation days 1-8 cultured in EMM medium with different initial glucose concentrations. (A) and (B) are from (Ibeneche, 2011) and (C) courtesy of Chieze Ibeneche.

After having characterized the CF state by the disability to move the endogenous lipid droplets by optical tweezers and by their stark drop in diffusive motion, the researchers sought out to understand the molecular mechanism underlying CF. They hypothesized that a dense filamentous network forming throughout the cell could be responsible for the observed motion drop of intracellular objects.

The most likely candidates for forming such a network were members of the cytoskeleton. Chieze excluded actin and microtubules by their sparse presence in deep starvation. There are no intermediate filaments in fission yeast, but in recent years the septins have been proposed as the fourth component of the cytoskeleton due to their filament forming ability (Mostowy & Cossart, 2012). As stated above, septins are a family of small GTPases that are highly conserved among eukaryotes. In fission yeast there are 7 septins, 4 of which are expressed during interphase (An et al., 2004).

By analysis of GFP-tagged septins, Chieze found that the septins 1-3 showed strong homogeneous cytoplasmic signal in deep starvation (see Figure 4A). Further, she found that the α value as a readout for the cytoplasmic state was significantly higher in spn1-3 deletion mutants in deep starvation compared to wildtype cells (see Figure 4B and C).

Together, these results led to the conclusion that septin1-3 were likely the filament formers of the hypothesized polymer network responsible for the immobilization of lipid droplets in CF cells.

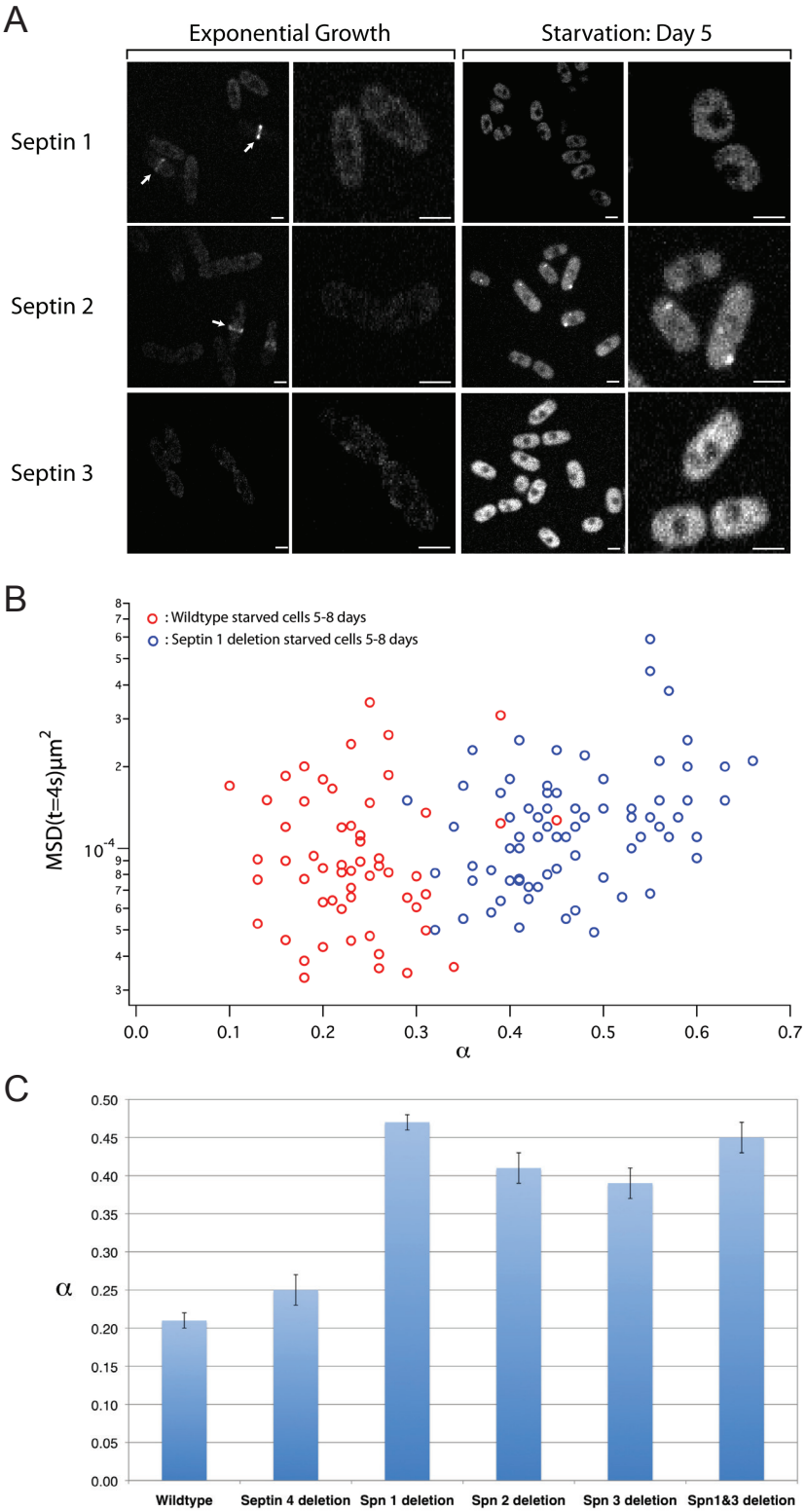

Figure 4. The role of septins in CF

(**A**) Images show GFP-tagged septins 1-3 in exponentially growing and starved cells. Arrows indicate the septa where septins localize in exponential growth. Scale bars are 3µm. (**B**) Semi-log plot of MSD vs. alpha for wildtype and septin1Δ starved for 5-8 days. (**C**) Bar plot showing the anomalous exponent alpha for wildtype and septin-deletion mutants in exponential growth and starvation. Error bars indicate SEM. From (Ibeneche, 2011)

1.5 Aims of the thesis

Recent evidence suggests that the transition from a fluid-like to a more solid-like state could be a general adaption response of the cytoplasm to nutrient-limited conditions. Solidification of the cytoplasm has been hypothesized to allow cells to down-regulate their metabolism by slowing down intracellular diffusion (Joyner et al., 2016; Munder et al., 2016). Furthermore, such a vitrified cytoplasmic state was suggested to help preserving cytoplasmic architecture during quiescence periods (Parry et al., 2014) or to save energy (Munder et al., 2016).

We found a novel cytoplasmic solidification in fission yeast cells under advanced glucose starvation conditions. The diffusive motion of lipid granules and other observable structures is thereby completely restricted. We call this cytoplasmic state "cytoplasmic freezing" (CF), according to its reminiscence of a frozen cell. We show that the cytoplasmic solidity in CF cells is significantly higher as compared to other known solid-like cytoplasmic states. Further, we found no evidence for CF induction by either of the molecular mechanisms proposed to cause the already known cytoplasmic solidification. We hypothesize that CF might represent a complete protective solidification of the cytoplasm that cells preferably undergo if provided with enough adaptation time and energy.

The aim of my work comprised a detailed characterization of CF. This involved the development of standardized methods to describe the cytoplasmic state of cells in general and of CF cells in particular. With these methods, I characterized the experimental parameters influencing the cytoplasmic state in cells under glucose starvation and thus the induction of CF. Further, I set out to explore the intracellular architecture during glucose starvation to identify changes therein. I challenged the observed changes for their functional requirement for CF induction. Moreover, I established an independent method to assay the fluidity of the cytoplasm and accordingly the solidity of the CF cytoplasm, by exploring the shape-preserving ability of cells without cell wall. Finally, I aimed to tackle the molecular mechanism underlying CF by identifying genes essential for CF. Our strategy hereby was to screen a gene deletion library – a strain collection harbouring deletion mutants of all non-essential *S. pombe* genes – for candidates that were not able to undergo CF.

2 Results – Part 1: Manuscripts for Publication

2.1 Cytoplasmic freezing: Selective immobilisation of the fission yeast cytoplasm content in deep starvation

Authors: **Maria B. Heimlicher**, Mirjam Bächler, Chieze C. Ibeneche-Nnewihe, Ernst-Ludwig Florin, Andreas Hoenger and Damian Brunner

Journal: to be submitted to Elife

Contribution: My contribution includes the experimental design, performance and analysis of most main and supplementary figures concerning CF as well as the writing of the manuscript together with Damian Brunner. Mirjam Bächler performed the acute starvation experiments in Figure 2 and Figure 3, and the whole Figure 4, the FLIP experiments in Figure 6 and the atg-deletion mutant experiments in Figure 7.

Cytoplasmic freezing: Selective immobilisation of the fission yeast cytoplasm content in deep starvation

Maria B. Heimlicher[1], Mirjam Bächler[1], Chieze Ibeneche-Nnewihe[2], Ernst-Ludwig Florin[2], Andreas Hoenger[3] and Damian Brunner[1‡]

‡ corresponding author

1: University of Zurich, Institute of Molecular Life Sciences, Winterthurerstrasse 190, 8057 Zurich, Switzerland

2: University of Texas at Austin, Center for Nonlinear Dynamics and Department of Physics, Austin, TX 78712, USA

3: University of Colorado at Boulder, Dept. of Molecular, Cellular and Developmental Biology, UCB-0347, Boulder CO, 80309, USA

Abstract

Cells depend on a highly ordered organization of their content, the maintenance of which accounts for much of their energy consumption. To survive energy depletion during periods of nutrient shortage, cells have developed various strategies. One of them, shown to be used by bacteria and yeast cell, is a reversible solidification of the cytoplasm, which maintains the anisotropic distribution of organelles by restricting their freedom of movement. Here we describe a type of cytoplasm solidification that relies on a mechanism providing much more profound and more robust immobilisation of the cellular content than what was previously described mainly for cells experiencing acute energy depletion. It occurs in fission yeast cells that have naturally run out of nutrients after multiple days of culturing. We find good evidence that cells need time and energy to build up competence for inducing this state, which we call cytoplasmic freezing. We find that cellular components are fixed in place in a size-dependent manner suggesting the presence of a matrix with a certain mesh size. Cytoplasmic freezing may provide a means to protect cellular architecture in dormant cells, without the need for energy consumption.

Introduction

Cell function and survival require a highly ordered, cell type-specific organization of the cellular content, the cytoplasm. How cells generate, maintain, and reproduce their spatial organization is central to any understanding of the living state. It involves the asymmetric distribution of material, mediated by active transport of key regulatory components, which counteracts the entropic activity of diffusion. This occurs in a highly crowded and dynamic environment, with extremely dispersed constituents ranging from small ions and metabolites over macromolecular complexes to large, complex structures like the cytoskeletal network and organelles. Accordingly, it was shown, that free particles in the cytoplasm do not follow the principles of free diffusion in an aqueous solution, but rather perform sub-diffusive motion, being influenced by macromolecular crowding, specific and unspecific interactions and the polymer networks of the cytoskeleton (Luby-Phelps, Taylor, & Lanni, 1986; Tolić-Nørrelykke, Munteanu, Thon, Oddershede, & Berg-Sørensen, 2004; Weiss, Elsner, Kartberg, & Nilsson, 2004; Wirtz, 2009). Consequently, rather than being a simple fluid containing solid particles, the cytoplasm was described as a complex viscoelastic fluid, a gel-like material (Fels, Orlov, & Grygorczyk, 2009; Grygorczyk, Boudreault, Platonova, & Orlov, 2015; Luby-Phelps et al.,

1986; Mitchison, Charras, & Mahadevan, 2008; Moeendarbary et al., 2013; Tolić-Nørrelykke et al., 2004) or a colloidal liquid at the transition to a glass-like state (Miermont et al., 2013; Parry et al., 2014).

The maintenance of the complex, anisotropic cellular architecture and its remodelling according to environmental changes require a constant input of energy. To deal with energetically limiting conditions such as shortage of specific nutrients, organisms have adopted a variety of strategies. Growing and dividing cells, such as stem cells, can exit the growth and division cycle and enter a state of quiescence, as do differentiating cells (Coller, Sang, & Roberts, 2006). Usually, nutrient starvation-induced quiescence is reversible (Lennon & Jones, 2011; Yanagida, 2009). In extreme cases of energy shortage, cells can enter a dormant state with no or hardly any energy consumption (Lennon & Jones, 2011). Mostly, this involves the formation of specialized cell types such as spores and seeds, some of which can survive centuries. Similarly, some animal species, such as tardigrades or hibernating mammals, manage to adopt dormant states with extremely low energy consumption by massively downregulating cellular metabolism. In many cases, it is not known whether such dormant cells still maintain anisotropic cytoplasmic organization with low energy consumption, or whether they re-organise their content *de novo* when nutrients become available again. Both options have been described. For example, quiescent fission yeast cells were shown to rebuild sub-cellular architecture and to polarise *de novo* when exiting glucose starvation (Makushok, Alves, Huisman, Kijowski, & Brunner, 2016). In contrast, a strategy to preserve anisotropic cellular architecture during an extended dormancy period is to reduce water content. This increases macromolecular crowding and can trigger a transition into a glass-like state of the cytoplasm that constrains the motion of cytoplasmic components (Cowan, Koppel, Setlow, & Setlow, 2003; Dijksterhuis, Nijsse, Hoekstra, & Golovina, 2007; Sun & Leopold, 1997). This mechanism was shown to operate in metabolically inactive bacteria and in budding yeast cells (Joyner et al., 2016; Munder et al., 2016; Parry et al., 2014).

As an alternative strategy, cells replace water with high amounts of carbohydrates which can prevent unfavourable fusion events and support cytoplasmic vitrification (Elbein, Pan, Pastuszak, & Carroll, 2003; Soto, Fernandez, Vicente-Soler, Cansado, & Gacto, 1999; Sun & Leopold, 1997).

Furthermore, specific structural changes of the cytoplasm have been reported upon starvation induced quiescence. Upon energy-depletion, many metabolic enzymes and other proteins reversibly form assemblies (Laporte, Salin, Daignan-Fornier, & Sagot, 2008; Narayanaswamy et al., 2009; Noree, Sato, Broyer, & Wilhelm, 2010; O'Connell, Zhao,

Ellington, & Marcotte, 2012; Petrovska et al., 2014; Sagot, Pinson, Salin, & Daignan-Fornier, 2006). These were suggested to inactivate enzymatic function and to serve as storage depots. As a collective, they were proposed to form higher-order structures that mediate a solid-like state of the cytoplasm (Munder et al., 2016).

When nutrients become limiting to cells of the fission yeast *Schizosaccharomyces pombe*, these will mate and produce dormant spores. A subset of cells however, enter a quiescent state as do heterothallic cells of the same mating type. Most research on fission yeast has focussed on the physiology of nitrogen starved cells or cells acutely depleted of glucose (Joyner et al., 2016; Oda et al., 2015; Saitoh & Yanagida, 2014; van Werven & Amon, 2011; Yanagida, Ikai, Shimanuki, & Sajiki, 2011). Here we describe a cytoplasmic solidification of fission yeast cells that occurs when cells have naturally run out of nutrients after several days of culturing. In this state, which we termed "cytoplasmic freezing" (CF), the diffusive motion of lipid droplets and other observable structures is completely restricted. This restriction is much more profound than in the previously described solid-like cytoplasmic states induced by acute energy depletion (Joyner et al., 2016; Munder et al., 2016). Consistently, the latter cells lacking a cell wall cannot maintain their cylindrical shape in a hypotonic solution, while shape preservation is extremely robust for CF cells. We find no evidence for CF being caused by increased macromolecular crowding due to fluid loss or by widespread macromolecular assemblies. In contrast to other known liquid- to solid-like transitions cells need several days to prepare for CF. This time may be required for *de novo* synthesis of critical components, since eliminating autophagy, a cytoplasmic recycling process that cell autonomously delivers energy, significantly delays CF onset. Our data provide evidence that CF may be caused by some sort of global cellular matrix with a certain mesh size that stably traps the bigger cytoplasmic components whereas small molecules are still able to freely diffuse.

Results

Starved cells have 2 intracellular immobilisation states

It is known that after 2 days of culturing, cells suffer of glucose starvation (GS), arrest growth and enter a quiescent state (Costello, Rodgers, & Beach, 1986; Makushok et al., 2016). When imaging fission yeast cells in GS after several additional days of culturing, we noticed a striking immobilisation of subcellular structures (Movie 1; Methods [yeast culturing]). To further describe this cellular state, we tracked the motion of lipid droplets (LDs), which are clearly distinguishable when imaging cells in DIC, at different days of culturing (Methods[Trajectories from DIC movies]; (Daemen, van Zandvoort, Parekh, & Hesselink, 2016; Lyn et al., 2010). In our experiments, we refer to culturing day 2 as starvation day 2 (SD2), to culturing day 3 as starvation day 3 (SD3) etc. In exponentially growing cells the lipid droplets are dispersed throughout the cell and dynamically explore the intracellular space (Figure 1A, Movie 1). At SD2 the cell size was reduced, a typical feature of quiescent cells caused by cells arresting growth right after cell division. At this stage, LDs frequently accumulated in 1-2 grape-like structures (Figure 1 – Figure supplement 1A) that displayed visible motion, although their overall position within cells stayed fairly constant. Cells at SD3-SD4 showed similar LD dynamicity, but the LD distribution changed and cells increasingly ended up with few, relatively big LDs suggesting that within the grape-like structures LDs had fused (Figure 1 – Figure supplement 1A). By SD 5 and SD6 this LD phenotype was prominent in a large fraction of cells. But strikingly, we observed a complete absence of LD motion, which persisted throughout the following starvation days (Figure 1A, Movie 1). This mobility restriction was similar for all LDs, independent of their size, sub-cellular location, or aggregation state (Figure 1 – Figure supplement 1B).

To quantify this drastic mobility change of LDs, we selectively labelled these with the lipophilic dye Bodipy (Listenberger & Brown, 2007; Long et al., 2012), and developed a procedure for automated quantification of their motion (Methods [microscopy and CC quantification of lipid droplet motion]). Simultaneous Phloxine B treatment enabled automatic exclusion of dead cells from analysis (Figure 1 – Figure supplement 2A; Methods[microscopy]). Phototoxicity prevented prolonged imaging, which is necessary to determine LD mean square displacement. Instead, we segmented the imaged cells and determined the Pearson Correlation Coefficient (CC) for each cell between two consecutive time points. This statistic is commonly used to quantify the co-localisation of two fluorescent markers, whereas we used it to quantify the co-localisation of a fluorescent marker with itself

within a given time interval (Methods [CC quantification of lipid droplet motion]). While a CC of 1 describes a completely static distribution of fluorescence intensity, increased mobility of fluorescent structures will decrease the CC accordingly. In exponentially growing cells, we measured an average median CC of 0.56, 95%CI [0.49, 0.64] (mean of 4 medians, 95% CI [lower limit, upper limit]), which reflects the strong, seemingly erratic motion and occasional jumps of LDs that occurred throughout the cell volume (Figure 1B; Movie 1). After cells had entered a quiescent state at around SD2, LD mobility was reduced and LDs mainly wobbled in a given location but showed no major translocations (Movie 1). Accordingly, the median CC increased to 0.70, 95%CI [0.67, 0.72] (Figure 1B). The CC stayed very similar with a mean of medians CC of 0.68, 95%CI [0.65, 0.71] on SD3 (Figure 1B). During the following starvation days SD4 and SD5 the CC started to rise, with a mean of medians CC of 0.75, 95%CI [0.73, 0.76] on SD4 and 0.84, 95%CI [0.83, 0.85] on SD5 (Figure 1B). On SD6 the median CC reached a very high 0.966, 95%CI [0.961, 0.970], consistent with the apparent, complete immobilisation of LDs (Figure 1B). The CC remained high during the following culturing days (SD7: and 0.95, 95%CI [0.94, 0.96]; SD8: and 0.95, 95%CI [0.94, 0.96]).

Remarkably, observing individual cell cultures suggested that the mobility reduction occurring between SD4 and SD6 was abrupt and coordinated as the vast majority of cells showed a nearly simultaneous transition mostly at SD5 or SD6 (Figure 1C). Accordingly, the median CC of individual cell cultures at SD5 either remained close to the CC measured at SD4, or it increased to that measured at SD6 (Figure 1D). Occasionally, cells of an entire culture did not undergo this transition to near complete immobilisation and accordingly LD mobility remained at the level of cells at SD3-SD4 (Figure 1 – Figure supplement 1C). Since such cell populations were clearly distinct, we excluded them from all our analysis.

Altogether, our LD mobility measurements indicate the presence of two starvation phases, which we termed early starvation and deep starvation. Due to the apparently global "freezing" of lipid droplet motion throughout the cytoplasm of cells in deep starvation, we termed this state "cytoplasmic freezing" (CF).

To see how cells regained LD mobility when exiting starvation, we supplied cells that had transitioned to CF at SD5 with fresh growth medium (Methods [yeast culturing and microscopy]). Many cells regained visible LD mobility within no more than 5 minutes showing that the release occurs in a switch-like manner (Figure 1E; Movie 2). During the following hour, the LD mobility increased, which led to a broadening of the CC distribution (Figure 1F). Some cells remained in the CF state during our 1 hour observation period (Figure 1G, white arrows; Movie 2). The number of cells able to undergo release from CF varied between different

experiments. Extending the starvation period prior to inducing starvation exit, increasingly affected the penetrance of CF release.

CF differs from other solid-like cytoplasmic states

Two recent studies reported on a solidification of the cytoplasm in budding yeast cells that were acutely depleted of energy either by acute glucose depletion (AGD) or by "drug-induced energy depletion" (DED) (Joyner et al., 2016; Munder et al., 2016). Both studies showed some evidence for conservation in fission yeast. Since these cellular states were much reminiscent of CF, we compared fission yeast cells exposed to both means of acute energy depletion with cells in deep starvation (Methods). Unlike in CF cells, LD motion was evident in AGD and DED cells when imaged with DIC microscopy (Figure 2A; Movie 3). Quantification with our Bodipy-labelling approach confirmed a clear difference (Figure 2B). Next, we compared CF with acute energy depletion states in protoplasts, which is cells lacking the cell wall that normally preserves their cylindrical cell shape. For DED cells we tested two protocols using 30min and 2hours drug exposure (Methods). When applying the standard protocol for cell wall digestion, exponentially growing cells exiting the cell wall shell adopt a spherical shape (Figure 2C, Movie 4; (Methods [cell wall digestion]). AGD or DED cells however, were shown to remain cylindrical (Figure 2C; Movie 4; (Joyner et al., 2016; Munder et al., 2016)). Likewise, cell wall-depleted CF cells remained cylindrical, indicating a solid-like cytoplasm similar to that of AGD or DED cells (Figure 2C; Movie 4). To investigate the robustness of shape preservation, we extended the observation period of cells in the continued presence of the digestive enzymes (Methods [prolonged cell wall digest]). This revealed that the initially cylindrical shape of AGD cells lacking a cell wall was unstable as the majority of cells completely rounded up within 3 hours (Figure 2C). In contrast, CF and DED cells remained cylindrical even after 3hours (Figure 2C). After three days of incubation, approximately 80% of the DED cells with 30min drug treatment had rounded up (Figure 2D). DED cells with 2 hours drug treatment showed an intermediate phenotype with 20% of the cells rounding up (Figure 2D). In contrast, CF cells at SD6 remained cylindrical even after three days of incubation (Figure 2D). Taken together, these results indicate that the content of AGD and DED cells but not CF cells can still rearrange, raising the possibility that the cytoplasmic state of CF cells differs from that of cells with acute energy depletion.

To prevent cell rupturing, the standard cell wall digestion protocol is performed in a hypertonic solution (1.2M Sorbitol), which acutely dehydrates cells and consequently increases macromolecular crowding (Atilgan, Magidson, Khodjakov, & Chang, 2015). It is possible, that

this additional dehydration contributes to the observed initial shape preservation of AGD, DED and CF protoplasts. Consistently, the surfaces of cell wall depleted cells appeared shrivelled, suggesting cell volume shrinkage (Figure 2C). To test to what extent AGD, DED and CF cells are able to lose fluid, we placed them in a hypertonic solution containing 1.2M Sorbitol and measured the changes in cell length and width. In particular the reduction in cell width is a good indicator of fission yeast cell volume loss. We found that under these conditions AGD and DED cells considerably reduced their volume (Figure 3A and 3B). In contrast, cell length and width of CF cells decreased little (Figure 2E).

A possible explanation for this difference is that CF cells are already dehydrated and cannot shrink much further. To test this possibility, we measured the development of cell length and width with daily measurements from SD3-SD7. Cells in starvation are generally shorter than exponentially growing cells, as they usually arrest growth right after the last cell division at SD2, when they are shortest. During SD3-7 the length and width of cells did not change any further (Figure 2F). This indicates that CF is not accompanied by significant fluid loss and speaks against a fluid loss-based increase in macromolecular crowding as causing CF. Electron microscopy pictures support this view, showing no evidence for a global crowding of cellular content (Figure 6D).

To compare the contribution of fluid loss to shape preservation of cells lacking a cell wall, we removed the cell walls of AGD, DED and CF cells in a solution containing 0.5M Sorbitol only (Methods [cell wall digestion 0.5M Sorbitol.]). Under these conditions all exponentially growing cells rapidly lysed and no protoplasts formed suggesting that this solution is hypertonic (Figure 3A, Movie 5). Similarly, most DED cells lysed independent of drug incubation times, although with 2h drug treatment the approximately 15% surviving cells remained roughly cylindrical (Figure 3A). Movies showed that these cells had only partially squeezed out of the cell wall shells (Figure 3B, Movie 5). Of the AGD cells, approximately 50% immediately lysed as soon as cell walls were sufficiently perturbed (Figure 3A, Movie 5). The remaining cells adopted a spherical shape, squeezing out of the cell wall shell very much like exponentially growing cells in the hypertonic digestion solution (Figure 3B, Movie 5, Movie 4). This was different for CF cells, which exited the cell wall shell as solid cylinders also in the hypotonic solution (Figure 3A and 3B; Movie 5). In contrast to the shrivelled and indented surfaces of the cylindrical protoplasts generated in the hypertonic solution, these protoplasts had a taut surface (compare Figure 2C and 3A). This suggests that CF cells do respond to changes in osmolality of the environment with fluid loss or uptake. The shape of the protoplast produced in a hypotonic solution remained cylindrical after an additional incubation day showing robustness

also under these conditions (Figure 3F). Altogether, our cell wall digestion experiments show that unlike cells with acute energy depletion, the shape preservation of CF cells stably fixes the entire cellular content and is insensitive to osmotic stress, which makes increased macromolecular crowding an unlikely cause. From this we conclude that the mechanism generating CF differs from the mechanisms that solidify the cytoplasm in response to acute energy depletion.

Starved fission yeast lack extensive protein assemblies

In budding yeast, DED caused a large number of proteins to phase separate in a pH dependent manner, whereby each protein formed multiple macromolecular assemblies. Together, these assemblies were proposed to be responsible for the solidification of the cytoplasm. To check for a similar behaviour of fission yeast proteins in DED cells, we analysed fission yeast homologs tagged with GFP or mCherry. Only one of eight tested proteins formed a few DED-specific assemblies that were reminiscent of those seen in budding yeast (Figure 4A). Another two proteins formed assemblies already in exponentially growing cells, which did not change after DED (Figure 4B). Intriguingly however, both proteins did not form assemblies at all if tagged with mCherry instead of GFP suggesting that these assemblies are GFP-dependent (Figure 4C). All other proteins did not change their localisation much (Figure 4D). This was also the case after prolonged drug incubation (Figure 4 – Figure supplement 1B). These results suggest that unlike in budding yeast, DED in fission yeast cells does not appear to induce significant macromolecular protein assemblies.

The absence of macromolecular protein assemblies in DED cells does not exclude their formation in CF. Therefore, we checked the behaviour of all eight proteins also in CF cells. When imaging control cells not expressing any markers with a 488nm excitation laser and the appropriate GFP filter set, we noticed the gradual appearance of multiple autofluorescent particles (Figure 6 – Figure supplement 1A, (Liu et al., n.d.)). At SD6 this autofluorescence had reached a significant level such that it had to be considered when imaging GFP-tagged proteins. Indeed, at SD6 the signal of most of the GFP-tagged proteins dropped below the autofluorescence level, suggesting that protein levels were significantly reduced (Figure 4E). Importantly, no obvious aggregates formed and pre-existing aggregates disappeared as well (Figure 4D). In contrast, when proteins were tagged with mCherry, fluorescence mostly accumulated in large globular structures (Figure 4F). Co-expressing a vacuolar marker showed that the globular structures represented the vacuolar lumen (Figure 4 – Figure supplement 1A). The most likely explanation is that the mCherry tag accumulates in vacuoles after degradation

of the attached proteins. In one case, bright nuclear fluorescence accompanied the vacuolar labelling (Figure 4F). Supporting a complete absence of macromolecular assemblies in CF cells, electron microscopy pictures of CF cells showed no evidence of regions revealing protein aggregates as found in electron microscopy pictures of budding yeast cells (Figure 6D; (Petrovska et al., 2014). These results indicate that macromolecular protein assemblies are not the cause of CF.

CF occurs independent of the cytoskeleton

Having found no evidence for increased macromolecular crowding or protein assemblies causing the restriction of lipid droplet motion in CF cells, we investigated the possibility of structural fixation by a mesh-like protein network that might form throughout the cells. Tubulin and actin, which form the filaments of the cytoskeleton, are obvious candidates. Confirming previous results, we found that the multiple, dynamic microtubule arrangements typical for growing cells remained active during SD2-4 but disappeared in deep starvation (Figure 5 – Figure supplement 1A; (Laporte et al., 2015; Makushok et al., 2016)). If ever, only a single, very short microtubule stump remained that often could barely be discriminated from the autofluorescence signal. Since our electron microscopy images of CF cells also did not show any evidence of cytoplasmic microtubules (Figure 6D), we conclude that microtubules do not contribute to the CF state.

To test for a role of actin, we used cells expressing the F-actin marker Lifeact-GFP (Huang et al., 2012; Riedl et al., 2008). In exponentially growing cells, Lifeact-GFP labels thin actin filament bundles that align parallel to the long cell axis and dynamic actin particles that concentrate at growing cell poles. At SD2-SD4, the actin particles rapidly disappeared except for a few remaining dynamic patches that were distributed throughout the cells. The thin interphase filaments were replaced by thick and dynamic F-actin bundles (Figure 5A; Movie 6). These extended along the cell periphery and often curled around the cell ends or curled up inside the cells. At SD6 all actin patches had disappeared and the F-actin bundles had evolved into extremely prominent, very long F-actin bands (Figure 5A). These bands were completely immobile and extended along the cell circumference while curling around both cell ends to form a structure often reminiscent of a shoelace (Figure 5A; Movie 6). The strong signal of these actin bands indicates that it is likely to contain much of the actin protein pool normally present in cells. Yet, we could not exclude that the cells in addition would harbour a global F-actin network, as single actin filaments cannot be detected by fluorescence imaging or electron microscopy as applied here. To exclude the presence of such filaments, we treated cells with

LatrunculinB (LatB), a drug that interferes with F-actin polymerization (Methods [latB treatment];(Spector, Shochet, Kashman, & Groweiss, 1983)). Adding LatB to exponentially growing cells resulted in a fast depletion of all visible F-actin structures (Figure 5 – Figure supplement 1B). Adding LatB to cells at SD6 however, did not affect the F-actin shoelace structures (Figure 5 – Figure supplement 1B). This suggest that either these structures are no longer dynamic, or LatB cannot enter CF cells. Since this did not allow any conclusion about the involvement of actin in CF, we applied the drug prior to the induction of CF at SD3 (Methods [latB treatment]). This visibly decreased the dynamicity of the F-actin structures but did not deplete them (Figure 5 – Figure supplement 1B). Interference with actin cable formation only occurred when incubating such cells in the continued presence of the drug until SD6 when many cells ended up with a dispersed Lifeact-GFP signal (Figure 5B). Although in some cells, the marker still labelled short stumps and ring-like structures, it is conceivable, that such extended drug exposure blocks the formation of a putative global network of invisible, single actin filaments. Nevertheless, these cells showed CF at SD6 similar to DMSO-treated control cells (Figure 5C and 5D, Movie 7). We conclude that F-actin is unlikely to mediate CF.

Septins represent another protein family that is known to assemble into filaments and therefore are good candidates for forming a global network in CF cells (Mostowy & Cossart, 2012). Fission yeast has seven non-essential septin genes (*spn1-spn7*) (Longtine et al., 1996; F. Pan, Malmberg, & Momany, 2007). Of these, spn5p-7p are exclusively expressed during meiosis (Abe & Shimoda, 2000), (Watanabe et al., 2001), (Mata, Lyne, Burns, & Bähler, 2002), (Onishi et al., 2010). To ensure that they are not additionally expressed in deep starvation, we checked the signal of GFP-tagged spn5-spn7 cells at SD6. We found no signal above the autofluorescent signal from the mitochondria (Figure 5 – Figure supplement 2B) and therefore carried on with the non-meiotic septins spn1-spn4 (An, Morrell, Jennings, Link, & Gould, 2004; Berlin, Paoletti, & Chang, 2003; Tasto, Morrell, & Gould, 2003). When imaging fluorescently labelled strains of these 4 septins, we found that they all formed aggregates in deep starvation (Figure 5E). However, the aggregates were rather sparse to form a network that could immobilize global cytoplasmic content. Next, we tested cells carrying a deletion of any of the four septins *spn1-spn4.* All septin deletion mutants showed CF at SD6 (Figure 5F and 5G). Taken together, these results make septins an unlikely candidate for mediating CF.

Subcellular architecture changes in starvation

Since CF coincides with cytoskeleton rearrangements and appears to affect the entire cell, we initiated a general investigation of sub-cellular structures in deep starvation. For this we

expressed various proteins tagged with GFP or mCherry that are known to mark cellular organelles and compared their localisation in exponentially growing cells with that of cells at SD6 (Table 1, strains used in this study). As described before, cells expressing mCherry-tagged proteins at SD6 ended up brightly staining the vacuoles (Figure 4F). At the same time, the organelle signal was no longer detectable. Similarly, the usual signal of most of the GFP-tagged protein markers often vanished below the level of autofluorescence. Only GFP-tagged nucleoporin nup85, GFP-tagged cnx1, a marker of the endoplasmatic reticulum and nuclear membrane lumen, and a GFP-tagged marker of the vacuoles showed a very similar distribution in exponentially growing cells and in cells at SD6 (Figure 6A). This suggests that the position and distribution of these organelles did not change significantly in deep starvation.

A striking change we observed only with GFP-tagged cox4p (cox4p-GFP), which marks the tubular mitochondria of exponentially growing cells (Figure 6B) (Yaffe, Stuurman, & Vale, 2003). At SD3 cox4p-GFP labelled shortened mitochondrial tubes and multiple dynamic globular structures of uniform size, suggesting that the mitochondria were fragmenting (Figure 6B; Movie 8; (Liu et al., n.d.)). At SD6, fragmentation was complete and only globular mitochondria of uniform size were present usually near the cell poles (Figure 6B). Similar to LDs, the motion of these globular mitochondria had arrested (Movie 8). Since cox4p-GFP fluorescence was sufficiently bright and stable, we could produce movie sequences that allowed determining the mitochondria MSD (Methods [MSD of mitochondria]). We found an MSD close to zero in cells at SD6, confirming a nearly complete freezing of motion (Figure 6C). To further explore sub-cellular architecture of CF cells, we performed electron microscopy on plastic sections of cells collected at SD7 (Methods [electron microscopy]). Compared to exponentially growing cells, we found a clear difference in distribution and appearance of cellular organelles (Figure 6D). In CF cells, we could not detect any rough ER or Golgi structures, which are clearly visible in wild type cells. Also, we found no evidence for any kind of filamentous assemblies. Confirming our fluorescence images, organelles such as LDs and vacuoles had the tendency to cluster around the nucleus in the cell centre while mitochondria were more prominent in polar regions near the cell periphery (compare Figure 1 – Figure supplement 1A, 6B and 6D). The almost spherical mitochondria had an approximate diameter of 250-350nm. As reported elsewhere, they were completely coated with ribosomes (Figure 6D; (Liu et al., n.d.)). In between these organelles, cells had major regions bare of any distinct structures, except for the typical electron dense spots representing ribosomes. These data suggest that the sub-cellular architecture of cells in deep starvation differs from that of growing cells and cells in early starvation.

Small proteins freely diffuse in CF cells

Having shown that fragmented mitochondria and LDs, both roughly ranging from 250µm - 350µm in size, were immobilized in CF cells, we wondered whether this also applies to components as small as individual proteins. The aforementioned Lifeact-GFP is a mainly globular, 29kDa protein of 4.5x2.5nm, which binds to F-actin with a high turnover rate and otherwise seems to be biochemically inert (Riedl et al., 2008; F. Yang, Moss, & Phillips, 1996). To test the mobility of the free, cytoplasmic Lifeact-GFP pool we used the "fluorescence loss in photobleaching" (FLIP) method (Bancaud, Huet, Rabut, & Ellenberg, 2010). FLIP involves repetitive bleaching of a defined small sub-cellular region. The kinetics of fluorescence loss in the unbleached cell areas provides a good measure of fluorescent particle motion into the bleached regions thereby revealing information about the diffusive behaviour of the particle. In CF cells at SD6, Lifeact-GFP depleted fast in the unbleached regions (Figure 6E). These data indicate a rapid diffusion of the fluorescent protein that is comparable to the diffusion rate in exponentially growing cells (Figure 6A).

Autophagy contributes to CF establishment

To further investigate the molecular nature of CF, we used our automated quantification of LD motion to screen for gene deletions that would prevent CF in cells in deep starvation, using a library of 3400 fission yeast strains each carrying a deletion of a non-essential gene (Kim et al., 2010). Amongst the roughly 500 deletions that did not show CF in deep starvation we noticed a clear accumulation of mutants affecting autophagy. Autophagy is an evolutionarily conserved mechanism used by cells to remove damaged organelles and to recycle cellular components (Z. Yang & Klionsky, 2010). We further tested the contribution of autophagy to CF by taking a prolonged look at two strains carrying a deletion of *atg1* (*atg1*Δ) or *atg8* (*atg8*Δ), which encode essential components of the autophagy pathway. We found that both mutants arrested LD motion after all, but only at SD8-SD9 (Figure 7A, 7B). This suggests that CF is not prevented, but merely delayed in autophagy mutants. To be sure that the mutant cells had entered a true CF state at SD9, we again performed protoplast experiments in a hypotonic environment. Protoplasts of *atg1*Δ and *atg8*Δ mutants robustly stayed cylindrical under these conditions, suggesting that autophagy is not part of the machinery causing CF but rather contributes to its establishment.

Discussion

Here we describe cytoplasmic freezing (CF), a solid-like state of the cytoplasmic content that fission yeast cells reach after 4-5 days of quiescence in nutrient starvation. CF is different from the cytoplasm solidification previously reported to occur in starved bacteria and in budding yeast cells that were acutely depleted of energy production (Joyner et al., 2016; Munder et al., 2016; Parry et al., 2014). There, the proposed cause was largely assigned to increased macromolecular crowding, which in bacteria is caused by the loss of metabolic activity and in budding yeast by fluid loss and/or the formation of numerous protein assemblies. Several observations suggest that the cause for CF is fundamentally different. First, we do not find any evidence for fluid loss, which should measurably reduce cell volume. Second, in contrast to cells with acute energy depletion, CF cells very robustly maintain their cylindrical shape after cell wall removal under hypotonic conditions, while cells under acute energy depletion lyse or adopt a spherical shape. Finally, while we can still detect clear lipid droplet motion in cells with acute energy depletion, we cannot in CF cells. Altogether, this suggests a global and strict fixation of cellular content in CF cells.

Importantly, small proteins such as Lifeact-GFP are exempt from such fixation as they continue to diffuse almost freely. This is compatible with the presence of some sort of a matrix with a minimal grid size that allows small proteins to move while embedding larger structures and holding them in place. Our electron microscopy pictures do not reveal any structures reminiscent of a matrix but it may well not may not be visible. In budding yeast cells, drug induced energy depletion was proposed to result in widespread macromolecular assembly of proteins, which was suggested to mediate solidification of the cytoplasm (Munder et al., 2016). This mechanism does not contribute to CF as testing a selection of the fission yeast homologs of some of the most prominently assembling budding yeast proteins, did not reveal any evidence of such behaviour in CF cells. Also, such protein assemblies, if present, should have been detectable in our electron microscopy pictures (Petrovska et al., 2014). Notably, we also find no evidence for macromolecular protein assemblies in fission yeast cells with DED. This stresses that predicting fission yeast behaviour based on budding yeast studies is inapt.

In a given cell population, CF occurs with tremendous synchrony in a time window of several hours, either at SD5 or SD6. This suggests that cells need the 2-3 preceding days to build up the competence for switching into the CF state. In support of this, we find that the absence of autophagy, a conserved mechanism for cell autonomous energy production, delays the onset of CF by 2 days. Obviously, alternative internal energy sources contribute to driving the process. The need for energy consumption to generate the CF state too, is compatible with

the hypothesis of a global matrix forming. This could involve crosslinked filamentous networks such as produced by F-actin. However, our LatB experiments strongly argue against a role for actin. Similarly, we find no evidence for a role of microtubules or the filament forming septins. Instead, the coordinated switch-like transition to CF that occurs with variable timing between cell populations raise the possibility that the entire cytoplasm undergoes a phase transition and turns into a hydrogel, once the production of relevant components has reached a critical concentration. Such a phase transition was described to occur during Balbiani body formation and in other processes and also can be mediated by a global phase transition of mRNAs (Boke et al., 2016; Brangwynne et al., 2009; Han et al., 2012; A. Jain & Vale, 2017; Kato et al., 2012; Patel et al., 2015). A further observation speaking in favour of a hydrogel-like state of the cytoplasm in CF cells is their ability to retain fluid in hypertonic conditions, which is a typical property of hydrogels. However, at this point we cannot exclude other mechanisms.

Whatever the mechanism mediating CF, clear is that following nutrient addition it can revert fast as some cells can exit this state within 5 minutes or even less. The following reestablishment of standard subcellular architecture and metabolism with tubular mitochondria and polar growth then happens in the range of 1-2 hours as previously described (Makushok et al., 2016). The high variability in the onset of CF exit most likely is due to variable reaction times in nutrient sensing as the actual release from CF seems to be switch-like in all cells independent of when it occurs.

Currently we cannot provide experimental evidence for a cytoprotective role of CF in deep starvation. It is likely though to occur, considering that CF provides a means to preserve cellular architecture. It seems obvious that during an extended starvation period the CF state will counteract entropy and provide resistance to various stresses without the need for metabolic activity. Unfortunately, our starvation conditions, which rely on standard fission yeast liquid culturing, are not optimal for investigating the role of CF in cell survival. The problem is that mortality rates increase fast over time, which is most likely due to the fact that under these conditions cells enter starvation in their own, toxic waste. We will thus now need to establish more natural starvation conditions that avoid liquid culturing. For comparison, we will need to durably interfere with CF establishment, a tool which should be provided by some of the isolated deletion strains.

Methods

Yeast culturing

Cells were grown at 25°C in EMM2 as described in (Moreno, Klar, & Nurse, 1991). For CF analysis, cells were cultured in Erlenmeyer flasks on a shaker (New Brunswick scientific innova 4230; 220rpm) for up to 8 days. Thereby, cells were first grown to mid exponential phase, and then diluted down to OD 0.02 (spectrophotometer Genesys 10S Vis, Thermo Fisher Scientific, Waltham, Massachusetts) to EMM with low glucose (0.5% glucose; EMMLG, SD0) plus supplements as required. The culture volume did not exceed 1/10 of the total volume of the flask. All strains used are listed in Supplemental Table 1. Gene tagging was done as published previously (Bähler et al., 1998) using the primers listed in Supplemental Table 2.

For bulk starvation exit experiments used for CC quantification (Figure 1 F), starvation cultures were incubated with fresh EMM2 (1:4) in an erlenmeyer flask on the shaker at 25°C.

AGD for fission yeast was done as described in {Joyner et al 2016}. DED was done as described in ({Munder et al 2016.}; Antimycin A from Streptomyces sp., Merck, Darmstadt, Germany, A8674; 2-Deoxy-D-glucose, Merck, D8375). Incubation time for DED was 30 min (personal communication) unless stated otherwise.

Microscopy

Live imaging was performed at room temperature on a spinning disc microscope (Zeiss Axio Observer Z1, Yokogawa CSU-X) using 63x and 100x NA 1.4 oil plan apo objectives, Andor iQ2.9 software and Andor Neo sCMOS and iXon3 EMMCCD cameras (Andor Technology, Belfast, UK) using 488nm and 561nm laser excitation and 525/50 BP and 568 LP emission filter sets. For standard fluorescence, z stacks with 0.5µm steps were acquired, unless stated otherwise.

DIC imaging of starved cells was done on poly-L-lysine (2mg/ml, Merck, P1399) coated glass bottom dishes (Bioswisstec, Schaffhausen, Switzerland; 5160). A chamber was constructed by adding a cover slip on top of parafilm spacers that simultaneously acted as glue when shortly heated. This chamber was filled with cell culture (~30µl). For DIC movies made to extract LD trajectories, cells were centrifuged at low speed (100 rpm with Multifuge 1S-R centrifuge from Thermo Fisher Scientific) and imaged immediately (5-15 min after mounting) as prolonged residence in the chamber could cause artefacts. 100 frames at 4fps were acquired.

For DIC imaging of starvation exit (Figure 1 E), the cells were followed during starvation exit on a lectin (griffonia (bandeiraea) simplicifolia lectin 1; Vector laboratories, Burlingame, California; L-1100) coated imaging dish. The first timepoint before glucose addition was acquired with EMM0G, then 2% glucose was added and the cells were imaged 5min and 60min later.

Live cell imaging for Bodipy Phloxine B time lapse movies for CC quantification was done on lectin coated glass bottom 8 well slides (ibidi, Martinsried, Germany; 80827) or 10 well slides (Greiner Bio-One, Kremsmünster, Austria; 543079). Bodipy (BODIPY 493/503; Thermo Fisher Scientific; D3922) was dissolved in DMSO (1mg/ml) and used at a final concentration of 4µg/ml in EMM0G (EMM without glucose). Phloxine B (Merck, P4030) was dissolved in water to 5mg/ml, diluted to 100µg/ml in water, and used at a final concentration of 10µg/ml. When imaging, we first acquired one red fluorescent Phloxine B single focal plane image followed by 3 green fluorescent Bodipy single focal plane images with a time interval of 45s.

The movies for cox4p particle tracking were made of 300 frames taken at 4fps.

Cell wall digestion

1.2M sorbitol buffer

For protoplast generation, approx. 0.3 OD units of cells were transferred to a 2ml Eppendorf tube for a final cell wall digestion volume of 500µl. Cells were washed twice in E buffer + sorbitol (50 mM sodium citrate, 100 mM sodium phosphate buffer, +1.2 M Sorbitol, pH 5.6; (Kelly & Nurse, 2011)). Cells were resuspended in E buffer + sorbitol plus cell wall digesting enzymes (final concentration 5mg/ml Zymolyase 20-T (MP Biomedicals, Santa Ana, California; 320921) plus 5mg/ml lysing enzymes from Trichoderma Harzianum (Merck; L1412)) and incubated for 1h on a rotor at 25°C unless stated otherwise. Protoplasts were washed once with E buffer + sorbitol, with centrifugation at minimum speed for 5min.

For DED, protoplasts were generated in continued presence of 20 mM 2-deoxyglucose and 10 mM antimycin A in E buffer as described in {Munder et al 2016.}

0.5M Sorbitol

Approx. 0.2 OD units of cells were washed with 500µl 0.5M sorbitol solution (2:3 E buffer + 1.2M sorbitol to EMM0G). The pellet was resuspended in 30µl EMM0G, 10µl of each enzyme stock solution (Zymolyase 20-T (MP Biomedicals, 320921) and lysing enzymes from Trichoderma Harzianum (sigma-aldrich, L1412); stock concentration 25mg/ml in E buffer +1.2MSorbitol) and immediately put into an imaging chamber, sealed off with VALAP (Vaseline, Lanoline, Parafilm; 1:1:1) and imaged.

FLIP acquisition and analysis

Fluorescence loss in photobleaching (FLIP) experiments were performed on cells mounted to an imaging chamber that was sealed with VALAP (Vaseline, Lanoline, Parafilm; 1:1:1) to prevent dehydration. Imaging was done at room temperature on a spinning disc microscope (Nikon Eclipse Ti, VisiScope system, Yokogawa W1) using a 60x water objective, VisiView software and an Andor EMCCD camera. A z stack of 3 planes at a 1µm step size was acquired every second for 100 seconds, and a small region near one cell pole was bleached every 5 seconds. The mean fluorescence intensity loss of a region at the opposite pole (reference region) was then measured using Fiji. The analysis was done using Matlab, as described in (Bancaud et al., 2010). For background subtraction, the mean signal of a background region close to the bleached cell was selected. The acquisition photobleaching was estimated by fitting an exponential function to the signal of a neighbouring cell, and dividing the background subtracted signal of the reference region by the exponential function. The signal was normalized to the last pre-bleach timepoint. For each condition, 10 cells were analysed.

Electron microscopy

Cells were directly high pressure frozen as a solution (reviewed in (McDonald et al., 2010)). Both specimens were high pressure frozen using a Wohlwend Compact-2 high-pressure freezer (Martin Wohlwend AG, Sennwald Switzerland). *S. pombe* samples destined for plastic section microtomy were freeze-substituted in 0.1% glutaraldehyde and 1% uranyl acetate in acetone for 48hrs and warmed from -90°C to -50°C in 8hrs (5°C per hour). Cells were then washed by acetone for 3 times and infiltrated in HM20 solution (25%, 33%, 50%, 67%, 75%, 100% in acetone) (Lowicryl HM20 Embedding Kit, Electron Microscopy Science, Hatfield, PA) over 5 days using Leica EMAFS (Leica, Vienna, Austria). Samples were then polymerized to blocks under Leica EMAFS UV light unit for 72hrs.

Plastic blocks were cut into ribbons of 80 (for single projection images) – 250 nm thick plastic sections (for tomographic reconstructions), depending on the questions asked, by Leica Ultracut microtome (Leica Inc., Vienna, Austria) using Diatome Ultra 45° (Diatome AG, Biel, Switzerland). Ribbons were collected on formvar-coated Cu-Rn grids (Electron Microscopy Science, Hatfield, PA) or Carbon Film Finder grids (Electron Microscopy Science, Hatfield, PA), immuno-labeled (optional), stained by uranyl acetate (2% uranyl acetate in 70% methanol) for ~4min and Reynold's lead citrate for ~2min (the staining time was adjusted based on the thickness of the sections).

Individual pictures of plastic sections, mostly used as a control, were acquired with a FEI Philips CM100 TEM and AMT 2Kx2K bottom-mount digital camera.

LatB treatment

LatB (Latrunculin B, Latrunculia magnifica, Merck; 428020) was added from a stock solution of 10mM in DMSO to a final concentration of 100µM (1% DMSO). Control cultures were treated with 1% DMSO. For the short-term effect of this latB concentration, the stock solution was diluted in EMM2 for exp. cells and EMM0G for SD3 and SD6 cells. For 3-day latB incubations, starved cultures were split in half at SD3. One half was supplemented with latB, the other with DMSO to serve as control. Both cultures were incubated at 25°C on the shaker for another 3 days.

Image Analysis

Routine image processing was done using Fiji/ImageJ. Deconvolution was done using Huygens software (Scientific Volume Imaging) on image stacks acquired using Nyquist criteria. Plots were made using Matlab (MathWorks).

Trajectories from DIC movies

The DIC movies (100frames, 4fps) were stack registered (Fiji plugin "StackReg"). Lipid droplets were tracked with the Fiji plugin "Manual Tracking with TrackMate" (settings for semi-automated tracking: Quality threshold: 0.2, Distance tolerance: 0.1, Max nFrames: 0). The lipid droplets were manually seeded in the first time-frame, and the trajectory was considered if the particle could be tracked for more than 95/100 frames. The manually seeded first trajectory point was excluded from the final trajectory, such that all LD positions were automatically detected. The trajectories were plotted using Matlab.

Mean square displacement of mitochondria

Cox4-GFP labelled mitochondria were tracked using the Mosaic particle tracking plugin in Fiji (Mosaic Toolsuite, (Sbalzarini & Koumoutsakos, 2005); Settings: radius: 4, cutoff: 0, per/abs: 2, link: 3, displacement: 2). The subsequent analysis was done in Matlab (Mathworks). Only trajectories longer than 160 frames were considered, and the MSD up to a time lag of 40 frames was computed. The time-averaged MSD for each particle is plotted as a color-coded histogram, and additionally the ensemble-averaged mean is shown.

CC quantification of lipid droplet motion

For cell segmentation, first the signal from the image with the Phloxine B stain was log transformed and background subtracted in Fiji (Mosaic ToolSuite). Using pixel classification in ilastik the cell's inside was separated from the outline and the background. At the same time, the dead cells revealed by being filled with Phloxine B signal, were marked as a separate class and were excluded from the subsequent analysis. The insides were segmented in Cellprofiler and used as seeds for segmentation of all the alive cells (Figure 1 – figure supplement 2 A). Subsequently, the 3 Bodipy images, taken at a time interval of 45s (t1-t3), were stack registered using the StackReg plugin in Fiji. Since the signal intensity of Bodipy varied significantly within a population of cells in deep starvation (SD6, SD7, SD8; Figure 1 – figure supplement 2B, white arrows) as well as throughout starvation, with particularly low signal at SD2 and SD3 (Figure 1 – figure supplement 2 B), we included additional procedures. In addition, the Bodipy signal increased over the 3 timepoints, with the major increase between t1 and t2 (Figure 1 – figure supplement 2 C). During SD2 and SD3 more LDs were detectable at t2 and t3 than at t1, which is why we decided to use only t2 and t3. Because signal intensities do not matter when extracting LD dynamics, we equalized them by performing a log transform and background subtraction (Moasaic ToolSuite) on the fluorescent images. The signals were further equalised by pixel classification using ilastik. This procedure resulted in pseudoimages with pixel values representing the probability to belong to a lipid droplet instead of the actual fluorescence intensities (Figure 1 – figure supplement 2 D). From the pseudoimages we computed the Pearson's correlation coefficient (CC) between t2 and t3 for the pixels of individual cells in Cellprofiler. In the absence of LD motion during the 45s separating t2 and t3, the colocalization was very high leading to a CC close to 1. For cells with high LD motion, the colocalization was low, leading to a lower CC accordingly. A CC close to 0, or even below was rarely obtained, showing that a situation where all LDs of a cell completely changed their localization within the 45s time interval was unusual. We present CC values as dot plots showing individual CC values using the function plotSpread from the MathWorks File Exchange (Jonas Dorn, https://ch.mathworks.com/matlabcentral/fileexchange/37105-plot-spread-points--beeswarm-plot-). We overlay a boxplot indicating the median and the 25th to 75th percentile of the values. Where several experiments were pooled, the mean of the medians of the single experiments was plotted in blue. As a measure for the variance between individual experiments, blue error bars indicate the 95% confidence interval (95% CI) of the medians. This variance does not describe the variance of the individual medians, and might thus underestimate the true variance of the median.

Cell size measurements

For comparison of cell size in standard and high sorbitol medium (Figure 2 E, Figure 2 – figure supplement 1 C), cell length and width were measured manually from DIC images using Fiji. Subsequently, we extracted the means of the mean cell length measured independently in 3 experiments each for cells grown in standard and high sorbitol medium. We then divided the mean of EMM cells by the mean of high Sorbitol cells (EMMLength1 + EMMLength2 + EMMLength3) / (SorbLength1 + SorbLength2 + SorbLength3) to define the amount of shrinkage upon transfer to 1.2M sorbitol. To estimate the variance of this ratio, bootstrapping was performed (999x resampling of each individual experiment), leading to 999 fractions from bootstrapped samples. The mean and 95% CI of these normally distributed fractions are shown in Figure 2E.

Measurements of cell length and width throughout starvation were done in an automated fashion using Phloxine B signal, as described above.

Table 1: Strains used in this study

Strains	Genotype	Source
DB404	h- Sec63-GFP::KanMX6 ura4-D18, leu-32	(Vjestica, Tang, & Oliferenko, 2008)
DB558	h- wild-type	Laboratory collection
DB933	h- nup85-GFP::kanMX6 ade6-M216, leu1	This study
DB2003	h+ cnx1-linkerGFP::kanMX6 ura4-D18 leu1-32 ade6-M216	This study
DB2057	h- SV40p-GFP-atb2::LEU2 leu1-32	(Pardo & Nurse, 2005)
DB2400	h+ anp1-GFP::ura4+ ade6-216 ura4-D18 leu1-32	(Vjestica et al., 2008)
DB2401	h+ sec72-GFP::ura4+ ade6-216 ura4-D18 leu1-32	(Vjestica et al., 2008)
DB2402	h+ anp1- mCherry::ura4+ ade6-216 leu1-32 ura4-D18	(Vjestica et al., 2008)
DB2403	h+ uch2-mCherry::ura4+ ade6-216 leu1-32 ura4-D18	(Vjestica et al., 2008)
DB2404	h- ost1::GFP-ura4+ ura4-D18 leu1-32	(Vjestica et al., 2008)
DB2405	h+ ost1-mCherry::ura4+ ade6-210 leu1-32 ura4-D18	(Vjestica et al., 2008)
DB3287	h- spn1Δ::kanMX6	(Wu, Ye, Wang, Pollard, & Pringle, 2010)
DB3293	h- spn2Δ::ura4+ ura4D18	(An et al., 2004)
DB3297	h+ spn2-GFP::kanMX6 *	(An et al., 2004)
DB3310	h+ spn3-GFP::kanMX6 *	(An et al., 2004)
DB3324	h- spn4-Δ1::kanMX6 *	(Wu et al., 2010)
DB3326	h+ spn5-GFP::kanMX6	This study
DB3340	h+ spn6-GFP::kanMX6	This study
DB3410	h- leu1-32::pAct1-Lifeact-GFP::leu1+ *	(Huang et al., 2012)
DB3422	h- spn1-GFP::kanMX6 *	(Wu et al., 2010)
DB3426	h+ spn3-Δ::ura4+ ura4-D18	(An et al., 2004)
DB3455	h+ spn7-GFP::kanMX6 *	(Onishi et al., 2010)
DB3587	h- spn4-tagRFP::kanMX6	This study
DB3623	h- Pbip1-GFP-AHDL::leu1+ ura4-D18 leu1-32 ade6	(Zhang, Vjestica, & Oliferenko, 2010)
DB3624	h- Pbip1-mCherry-AHDL::leu1+	(Zhang et al., 2010)
DB3726	h- cox4-GFP::LEU2 leu1-32 *	(Fu, Jain, Costa, Velve-Casquillas, & Tran, 2011)
DB3856	h- hsp104-mCherry::kanMX	(Coelho et al., 2013)
DB4192	h- GMA12-GFP::ura4+ ura4-D18 *	(H. Wang et al., 2002)
DB4672	h+ Pnmt1-Tts-2TM(1-83aa)-linker-mCherry::leu+	(Zhang, Vjestica, & Oliferenko, 2012)
DB5013	h- atg8Δ::kanMX *	Bioneer M-4030H-U5, (Kim et al., 2010)
DB5018	h- atg1Δ::kanMX *	Bioneer M-4030H-U5, (Kim et al., 2010)
DB5160	h- cts1-GFP::kanMX	This study

DB5162	h- pre6-mGFP::kanMX6	This study
DB5209	h+ suc22-GFP	(Vejrup-Hansen et al., 2014)
DB5310	h- gln1-mCherry::natR	(Coelho, Lade, Alberti, Gross, & Tolić, 2014)
DB5315	h+ dis2-NEGFP::ura4 ura4-D18*	(Alvarez-Tabarés, Grallert, Ortiz, & Hagan, 2007)
DB5320	h+ adh1-GFP::kanMX*	(Sigova, Rhind, & Zamore, 2004)
DB5380	h+ cts1-mCherry::kanMX*	(Coelho et al., 2014)
DB5381	h- hsp104-GFP::kanMX*	(Coelho et al., 2013)
DB5470	h- tif221-GFP::kanMX	This study
DB5730	h? nmt1:GFP-spac11D3.06::kanMX gln1-mCherry::natR	This study
	* the auxotrophic alleles were crossed out from the original strain	

Table 2: Primers used in this study

DB3340	DPE872	CTGAATATCACGAAAGGATCCGTGCTTTGGAGACCCAAA TTGAAAGTTTGAAAAGTTACAAGGGCCGCGGTCATAAAA AAATCCTTGGAGCTCCTTCAGGA
	DPE873	AATTGCAAATTTAGTAAGAAAAAGCCATCAGATGAGCAA ATAAAAGGAGATGGAAAAGTTAAAAGTTTGACTTGAGAC TT GAATTCGAGCTCGTTTAAAC
DB933	DPE 275	GTCAACTGTAAAGGACCAGCAGCTTTTACTATCCATTCAT GAGCGTCTTTCTTCTGCGATATCATGGTATTTTCTTCACTT AAAAAAAATCCTTGGAGCTCCTTCAGGA
	DPE 274	GTATCTTAATAAAAACATGTATGAAGCTTCTATGTTACAG AAAGATTAAAATGTCAAGTAACAGAAATAGCCTAATTTA AATCCCgaattcgagctcgtttaaac
DB2003	DPE739	TAAGCAAGAGACTGAGACTGAGAAGATAGACGTTTCTTA CGCTCCCGAAACTGAATCACCAACTGCGAAGAATGAAGA CATCCTTGGAGCTCCTTCAGGA
	DPE740	GATAGTACTACCCACGATTTATAAATTCATAGTCTATTTA TTGATATTACTCATAATAAGAACTAGAGAAAACAGAATT CGAGCTCGTTTAAAC
DB5160	DPE1495	ATTTTAACGCTGAATCTGCCTTAGCTGACATGAATGACTC TGTTGAAGTTACTGAAGAAGCCACTGTCGTCACCATCAG T ATCCTTGGAGCTCCTTCAGG
	DPE1496	CACCCCAGAACCCAATTTTTCCTATAGATAAAGAAAAAC ACACCAACAAACACACATTATTTCCTAATTCCCGGAATC CC GAATTCGAGCTCGTTTAAAC
DB5162	DPE1450	AAGATGAGAAAGAAGCTGAAGCTGCTCGTAAAAAGAGT GGCCGTTCTGCCCCTGGAGTCTCTACAACTTCTACGATTC AA ATCCTTGGAGCTCCTTCAGG
	DPE1451	CAAAAGGGAAAAGACATATGAACCTTATAAACAAGAAA TTCTTAAGTCGGTTTGCATGTAATGAAATAAAAGAGGTA TCA GAATTCGAGCTCGTTTAAAC
DB5470	DPE1535	TTGTCTCAGGTCTCATTACCGATTTAGGGATCATTGATTC GAAGAGTGGGGTAAGCGAAGAGCTAATTAAATTGTATCT T ATCCTTGGAGCTCCTTCAGG
	DPE1536	AAGACTTATGAGAAATTTAAGTCAACTCAAAGTACAATC TATTCATATTTTATTTTTAAGATCAGGAGAATCTGATTG GAATTCGAGCTCGTTTAAACTG
DB5730	DPE1473	GGTTCCATCCGTTCAATCAATATGATAAAAGCTTAGTAA ACTTTTATTAAAGGAAAATTTGAACCTTCGGTGAACAGA CAgaattcgagctcgtttaaac
	DPE1474	GAGTTTTGCAAGGCATATCCAAGGATTACCGGAGCTGAA TTTATCAAAAGGTATTTCACCTCTGTAAGTGGTCTACCCA Taattaaccccgcaggtccac

Acknowledgements:

We would like to thank Craig Wang from the biostatistics group of Prof. Reinhard Furrer from the UZH for his statistical consulting. We thank Mohan Balasubramanian, Kathleen L. Gould, Ian M. Hagan, Olaf Nielsen, Paul Nurse, Snezhana Oliferenko, John Pringle, Iva M. Tolic-Nørrelykke, Phong T. Tran and Phillip D. Zamore for sharing strains.

This work was supported by the following grants: Human Frontier Science Programme RGP0007- 2010 (to D.B. (PI), A.H. and E.F. (co-PIs)). D.B. acknowledges financial support from the University of Zurich.

References

Abe, H., & Shimoda, C. (2000). Autoregulated expression of Schizosaccharomyces pombe meiosis-specific transcription factor Mei4 and a genome-wide search for its target genes. *Genetics*, *154*(4), 1497–1508.

Alvarez-Tabarés, I., Grallert, A., Ortiz, J.-M., & Hagan, I. M. (2007). Schizosaccharomyces pombe protein phosphatase 1 in mitosis, endocytosis and a partnership with Wsh3/Tea4 to control polarised growth. *Journal of Cell Science*, *120*(Pt 20), 3589–3601. http://doi.org/10.1242/jcs.007567

An, H., Morrell, J. L., Jennings, J. L., Link, A. J., & Gould, K. L. (2004). Requirements of fission yeast septins for complex formation, localization, and function. *Molecular Biology of the Cell*, *15*(12), 5551–5564. http://doi.org/10.1091/mbc.E04-07-0640

Atilgan, E., Magidson, V., Khodjakov, A., & Chang, F. (2015). Morphogenesis of the Fission Yeast Cell through Cell Wall Expansion. *Current Biology : CB*, *25*(16), 2150–2157. http://doi.org/10.1016/j.cub.2015.06.059

Bancaud, A., Huet, S., Rabut, G., & Ellenberg, J. (2010). Fluorescence perturbation techniques to study mobility and molecular dynamics of proteins in live cells: FRAP, photoactivation, photoconversion, and FLIP. *Cold Spring Harbor Protocols*, *2010*(12), pdb.top90–pdb.top90. http://doi.org/10.1101/pdb.top90

Bähler, J., Wu, J. Q., Longtine, M. S., Shah, N. G., McKenzie, A., Steever, A. B., et al. (1998). Heterologous modules for efficient and versatile PCR-based gene targeting in Schizosaccharomyces pombe. *Yeast (Chichester, England)*, *14*(10), 943–951. http://doi.org/10.1002/(SICI)1097-0061(199807)14:10<943::AID-YEA292>3.0.CO;2-Y

Berlin, A., Paoletti, A., & Chang, F. (2003). Mid2p stabilizes septin rings during cytokinesis in fission yeast. *The Journal of Cell Biology*, *160*(7), 1083–1092. http://doi.org/10.1083/jcb.200212016

Boke, E., Ruer, M., Wühr, M., Coughlin, M., Lemaitre, R., Gygi, S. P., et al. (2016). Amyloid-like Self-Assembly of a Cellular Compartment. *Cell*, *166*(3), 637–650. http://doi.org/10.1016/j.cell.2016.06.051

Brangwynne, C. P., Eckmann, C. R., Courson, D. S., Rybarska, A., Hoege, C., Gharakhani, J., et al. (2009). Germline P granules are liquid droplets that localize by controlled dissolution/condensation. *Science (New York, N.Y.)*, *324*(5935), 1729–1732. http://doi.org/10.1126/science.1172046

Coelho, M., Dereli, A., Haese, A., Kühn, S., Malinovska, L., DeSantis, M. E., et al. (2013). Fission yeast does not age under favorable conditions, but does so after stress. *Current Biology : CB*, *23*(19), 1844–1852. http://doi.org/10.1016/j.cub.2013.07.084

Coelho, M., Lade, S. J., Alberti, S., Gross, T., & Tolić, I. M. (2014). Fusion of protein aggregates facilitates asymmetric damage segregation. *PLoS Biology*, *12*(6), e1001886. http://doi.org/10.1371/journal.pbio.1001886

Coller, H. A., Sang, L., & Roberts, J. M. (2006). A new description of cellular quiescence. *PLoS Biology*, *4*(3), e83. http://doi.org/10.1371/journal.pbio.0040083

Costello, G., Rodgers, L., & Beach, D. (1986). Fission yeast enters the stationary phase G0 state from either mitotic G1 or G2. *Current Genetics*, 1–7.

Cowan, A. E., Koppel, D. E., Setlow, B., & Setlow, P. (2003). A soluble protein is immobile in dormant spores of Bacillus subtilis but is mobile in germinated spores: implications for spore dormancy. *Proceedings of the National Academy of Sciences of the United States of America*, *100*(7), 4209–4214. http://doi.org/10.1073/pnas.0636762100

Daemen, S., van Zandvoort, M. A. M. J., Parekh, S. H., & Hesselink, M. K. C. (2016). Microscopy tools for the investigation of intracellular lipid storage and dynamics. *Molecular Metabolism*, *5*(3), 153–163. http://doi.org/10.1016/j.molmet.2015.12.005

Dijksterhuis, J., Nijsse, J., Hoekstra, F. A., & Golovina, E. A. (2007). High viscosity and anisotropy characterize the cytoplasm of fungal dormant stress-resistant spores. *Eukaryotic Cell*, *6*(2), 157–170. http://doi.org/10.1128/EC.00247-06

Dynamics of lipid droplets induced by the hepatitis C virus core protein. (2010). Dynamics of lipid droplets induced by the hepatitis C virus core protein. *Biochemical and Biophysical Research Communications*, *399*(4), 518–524. http://doi.org/10.1016/j.bbrc.2010.07.101

Elbein, A. D., Pan, Y. T., Pastuszak, I., & Carroll, D. (2003). New insights on trehalose: a multifunctional molecule. *Glycobiology*, *13*(4), 17R–27R. http://doi.org/10.1093/glycob/cwg047

Fels, J., Orlov, S. N., & Grygorczyk, R. (2009). The hydrogel nature of mammalian cytoplasm contributes to osmosensing and extracellular pH sensing. *Biophysical Journal*, *96*(10), 4276–4285. http://doi.org/10.1016/j.bpj.2009.02.038

Fu, C., Jain, D., Costa, J., Velve-Casquillas, G., & Tran, P. T. (2011). mmb1p binds mitochondria to dynamic microtubules. *Current Biology : CB*, *21*(17), 1431–1439. http://doi.org/10.1016/j.cub.2011.07.013

Grygorczyk, R., Boudreault, F., Platonova, A., & Orlov, S. N. (2015). Salt and osmosensing: role of cytoplasmic hydrogel. *Pflugers Archiv : European Journal of Physiology*, *467*(3), 475–487. http://doi.org/10.1007/s00424-014-1680-2

Han, T. W., Kato, M., Xie, S., Wu, L. C., Mirzaei, H., Pei, J., et al. (2012). Cell-free formation of RNA granules: bound RNAs identify features and components of cellular assemblies. *Cell*, *149*(4), 768–779. http://doi.org/10.1016/j.cell.2012.04.016

Huang, J., Huang, Y., Yu, H., Subramanian, D., Padmanabhan, A., Thadani, R., et al. (2012). Nonmedially assembled F-actin cables incorporate into the actomyosin ring in fission yeast. *The Journal of Cell Biology*, *199*(5), 831–847. http://doi.org/10.1083/jcb.201209044

Jain, A., & Vale, R. D. (2017). RNA phase transitions in repeat expansion disorders. *Nature*, *546*(7657), 243–247. http://doi.org/10.1038/nature22386

Joyner, R. P., Tang, J. H., Helenius, J., Dultz, E., Brune, C., Holt, L. J., et al. (2016). A glucose-starvation response regulates the diffusion of macromolecules. *eLife*, *5*, 833. http://doi.org/10.7554/eLife.09376

Kato, M., Han, T. W., Xie, S., Shi, K., Du, X., Wu, L. C., et al. (2012). Cell-free formation of RNA granules: low complexity sequence domains form dynamic fibers within hydrogels. *Cell*, *149*(4), 753–767. http://doi.org/10.1016/j.cell.2012.04.017

Kelly, F. D., & Nurse, P. (2011). De novo growth zone formation from fission yeast spheroplasts. *PloS One*, *6*(12), e27977. http://doi.org/10.1371/journal.pone.0027977

Kim, D. U., Hayles, J., Kim, D., Wood, V., Park, H.-O., Won, M., et al. (2010). Analysis of a genome-wide set of gene deletions in the fission yeast Schizosaccharomyces pombe. *Nature Biotechnology*, *28*(6), 617–623. http://doi.org/10.1038/nbt.1628

Laporte, D., Courtout, F., Pinson, B., Dompierre, J., Salin, B., Brocard, L., & Sagot, I. (2015). A stable microtubule array drives fission yeast polarity reestablishment upon quiescence exit. *The Journal of Cell Biology*, *210*(1), 99–113. http://doi.org/10.1083/jcb.201502025

Laporte, D., Salin, B., Daignan-Fornier, B., & Sagot, I. (2008). Reversible cytoplasmic localization of the proteasome in quiescent yeast cells. *The Journal of Cell Biology*, *181*(5), 737–745. http://doi.org/10.1083/jcb.200711154

Lennon, J. T., & Jones, S. E. (2011). Microbial seed banks: the ecological and evolutionary implications of dormancy. *Nature Reviews. Microbiology*, *9*(2), 119–130. http://doi.org/10.1038/nrmicro2504

Listenberger, L. L., & Brown, D. A. (2007). Fluorescent detection of lipid droplets and associated proteins. *Current Protocols in Cell Biology*, *Chapter 24*, Unit 24.2–24.2.11. http://doi.org/10.1002/0471143030.cb2402s35

Liu, M., Heimlicher, M. B., Bächler, M., Florin, E.-L., Brunner, D., & Hoenger, A. (n.d.). Glucose starvation triggers mitochondrial fission and dense decoration of their outer membranes with ribosomes.

Long, A. P., Manneschmidt, A. K., VerBrugge, B., Dortch, M. R., Minkin, S. C., Prater, K. E., et al. (2012). Lipid droplet de novo formation and fission are linked to the cell cycle in fission yeast. *Traffic (Copenhagen, Denmark)*, *13*(5), 705–714. http://doi.org/10.1111/j.1600-0854.2012.01339.x

Longtine, M. S., DeMarini, D. J., Valencik, M. L., Al-Awar, O. S., Fares, H., De Virgilio, C., & Pringle, J. R. (1996). The septins: roles in cytokinesis and other processes. *Current Opinion in Cell Biology*, *8*(1), 106–119.

Luby-Phelps, K., Taylor, D. L., & Lanni, F. (1986). Probing the structure of cytoplasm. *The Journal of Cell Biology*, *102*(6), 2015–2022.

Makushok, T., Alves, P., Huisman, S. M., Kijowski, A. R., & Brunner, D. (2016). Sterol-Rich Membrane Domains Define Fission Yeast Cell Polarity. *Cell*, *165*(5), 1182–1196. http://doi.org/10.1016/j.cell.2016.04.037

Mata, J., Lyne, R., Burns, G., & Bähler, J. (2002). The transcriptional program of meiosis and sporulation in fission yeast. *Nature Genetics*, *32*(1), 143–147. http://doi.org/10.1038/ng951

McDonald, K., Schwarz, H., Müller-Reichert, T., Webb, R., Buser, C., & Morphew, M. (2010). "Tips and tricks" for high-pressure freezing of model systems. *Methods in Cell Biology*, *96*, 671–693. http://doi.org/10.1016/S0091-679X(10)96028-7

Miermont, A., Waharte, F., Hu, S., McClean, M. N., Bottani, S., Léon, S., & Hersen, P. (2013). Severe osmotic compression triggers a slowdown of intracellular signaling, which can be explained by molecular crowding. *Proceedings of the National Academy of Sciences of the United States of America*, *110*(14), 5725–5730. http://doi.org/10.1073/pnas.1215367110

Mitchison, T. J., Charras, G. T., & Mahadevan, L. (2008). Implications of a poroelastic cytoplasm for the dynamics of animal cell shape. *Seminars in Cell & Developmental Biology*, *19*(3), 215–223. http://doi.org/10.1016/j.semcdb.2008.01.008

Moeendarbary, E., Valon, L., Fritzsche, M., Harris, A. R., Moulding, D. A., Thrasher, A. J., et al. (2013). The cytoplasm of living cells behaves as a poroelastic material. *Nature Materials*, *12*(3), 253–261. http://doi.org/10.1038/nmat3517

Moreno, S., Klar, A., & Nurse, P. (1991). Molecular genetic analysis of fission yeast Schizosaccharomyces pombe. *Methods in Enzymology*, *194*, 795–823.

Mostowy, S., & Cossart, P. (2012). Septins: the fourth component of the cytoskeleton. *Nature Reviews. Molecular Cell Biology*, *13*(3), 183–194. http://doi.org/10.1038/nrm3284

Munder, M. C., Midtvedt, D., Franzmann, T., Nüske, E., Otto, O., Herbig, M., et al. (2016). A pH-driven transition of the cytoplasm from a fluid- to a solid-like state promotes entry into dormancy. *eLife*, *5*, 59. http://doi.org/10.7554/eLife.09347

Narayanaswamy, R., Levy, M., Tsechansky, M., Stovall, G. M., O'Connell, J. D., Mirrielees, J., et al. (2009). Widespread reorganization of metabolic enzymes into reversible assemblies upon nutrient starvation. *Proceedings of the National Academy of Sciences of the United States of America*, *106*(25), 10147–10152. http://doi.org/10.1073/pnas.0812771106

Noree, C., Sato, B. K., Broyer, R. M., & Wilhelm, J. E. (2010). Identification of novel filament-forming proteins in Saccharomyces cerevisiae and Drosophila melanogaster. *The Journal of Cell Biology*, *190*(4), 541–551. http://doi.org/10.1083/jcb.201003001

O'Connell, J. D., Zhao, A., Ellington, A. D., & Marcotte, E. M. (2012). Dynamic reorganization of metabolic enzymes into intracellular bodies. *Annual Review of Cell and Developmental Biology*, *28*(1), 89–111. http://doi.org/10.1146/annurev-cellbio-101011-155841

Oda, A., Takemata, N., Hirata, Y., Miyoshi, T., Suzuki, Y., Sugano, S., & Ohta, K. (2015). Dynamic transition of transcription and chromatin landscape during fission yeast adaptation to glucose starvation. *Genes to Cells : Devoted to Molecular & Cellular Mechanisms*, *20*(5), 392–407. http://doi.org/10.1111/gtc.12229

Onishi, M., Koga, T., Hirata, A., Nakamura, T., Asakawa, H., Shimoda, C., et al. (2010). Role of septins in the orientation of forespore membrane extension during sporulation in fission yeast. *Molecular and Cellular Biology*, *30*(8), 2057–2074. http://doi.org/10.1128/MCB.01529-09

Pan, F., Malmberg, R. L., & Momany, M. (2007). Analysis of septins across kingdoms reveals orthology and new motifs. *BMC Evolutionary Biology*, *7*(1), 103. http://doi.org/10.1186/1471-2148-7-103

Pardo, M., & Nurse, P. (2005). The nuclear rim protein Amo1 is required for proper microtubule cytoskeleton organisation in fission yeast. *Journal of Cell Science*, *118*(Pt 8), 1705–1714. http://doi.org/10.1242/jcs.02305

Parry, B. R., Surovtsev, I. V., Cabeen, M. T., O'Hern, C. S., Dufresne, E. R., & Jacobs-Wagner, C. (2014). The Bacterial Cytoplasm Has Glass-like Properties and Is Fluidized by Metabolic Activity. *Cell*, *156*(1-2), 183–194. http://doi.org/10.1016/j.cell.2013.11.028

Patel, A., Lee, H. O., Jawerth, L., Maharana, S., Jahnel, M., Hein, M. Y., et al. (2015). A Liquid-to-Solid Phase Transition of the ALS Protein FUS Accelerated by Disease Mutation. *Cell*, *162*(5), 1066–1077. http://doi.org/10.1016/j.cell.2015.07.047

Petrovska, I., Nüske, E., Munder, M. C., Kulasegaran, G., Malinovska, L., Kroschwald, S., et al. (2014). Filament formation by metabolic enzymes is a specific adaptation to an advanced state of cellular starvation. *eLife*, *3*, 6063. http://doi.org/10.7554/eLife.02409

Riedl, J., Crevenna, A. H., Kessenbrock, K., Yu, J. H., Neukirchen, D., Bista, M., et al. (2008). Lifeact: a versatile marker to visualize F-actin. *Nature Methods*, *5*(7), 605–607. http://doi.org/10.1038/nmeth.1220

Sagot, I., Pinson, B., Salin, B., & Daignan-Fornier, B. (2006). Actin bodies in yeast quiescent cells: an immediately available actin reserve? *Molecular Biology of the Cell*, *17*(11), 4645–4655. http://doi.org/10.1091/mbc.E06-04-0282

Saitoh, S., & Yanagida, M. (2014). Does a shift to limited glucose activate checkpoint control in fission yeast? *FEBS Letters*, *588*(15), 2373–2378. http://doi.org/10.1016/j.febslet.2014.04.047

Sbalzarini, I. F., & Koumoutsakos, P. (2005). Feature point tracking and trajectory analysis for video imaging in cell biology. *Journal of Structural Biology*, *151*(2), 182–195. http://doi.org/10.1016/j.jsb.2005.06.002

Sigova, A., Rhind, N., & Zamore, P. D. (2004). A single Argonaute protein mediates both transcriptional and posttranscriptional silencing in Schizosaccharomyces pombe. *Genes & Development*, *18*(19), 2359–2367. http://doi.org/10.1101/gad.1218004

Soto, T., Fernandez, J., Vicente-Soler, J., Cansado, J., & Gacto, M. (1999). Accumulation of trehalose by overexpression of tps1, coding for trehalose-6-phosphate synthase, causes increased resistance to multiple stresses in the fission yeast schizosaccharomyces pombe. *Applied and Environmental Microbiology*, *65*(5), 2020–2024.

Spector, I., Shochet, N. R., Kashman, Y., & Groweiss, A. (1983). Latrunculins: novel marine toxins that disrupt microfilament organization in cultured cells. *Science (New York, N.Y.)*, *219*(4584), 493–495.

Sun, W. Q., & Leopold, A. C. (1997). Cytoplasmic Vitrification and Survival of Anhydrobiotic Organisms. *Comparative Biochemistry and Physiology Part a Physiology*, *117*(3), 327–333. http://doi.org/https://doi.org/10.1016/S0300-9629(96)00271-X

Tasto, J. J., Morrell, J. L., & Gould, K. L. (2003). An anillin homologue, Mid2p, acts during fission yeast cytokinesis to organize the septin ring and promote cell separation. *The Journal of Cell Biology*, *160*(7), 1093–1103. http://doi.org/10.1083/jcb.200211126

Tolić-Nørrelykke, I. M., Munteanu, E. L., Thon, G., Oddershede, L., & Berg-Sørensen, K. (2004). Anomalous diffusion in living yeast cells. *Physical Review Letters*, *93*(7), 078102. http://doi.org/10.1103/PhysRevLett.93.078102

van Werven, F. J., & Amon, A. (2011). Regulation of entry into gametogenesis. *Philosophical Transactions of the Royal Society of London. Series B, Biological Sciences*, *366*(1584), 3521–3531. http://doi.org/10.1098/rstb.2011.0081

Vejrup-Hansen, R., Fleck, O., Landvad, K., Fahnøe, U., Broendum, S. S., Schreurs, A.-S., et al. (2014). Spd2 assists Spd1 in the modulation of ribonucleotide reductase architecture but does not regulate deoxynucleotide pools. *Journal of Cell Science*, *127*(Pt 11), 2460–2470. http://doi.org/10.1242/jcs.139816

Vjestica, A., Tang, X.-Z., & Oliferenko, S. (2008). The actomyosin ring recruits early secretory compartments to the division site in fission yeast. *Molecular Biology of the Cell*, *19*(3), 1125–1138. http://doi.org/10.1091/mbc.E07-07-0663

Wang, H., Tang, X., Liu, J., Trautmann, S., Balasundaram, D., McCollum, D., & Balasubramanian, M. K. (2002). The multiprotein exocyst complex is essential for cell separation in Schizosaccharomyces pombe. *Molecular Biology of the Cell*, *13*(2), 515–529. http://doi.org/10.1091/mbc.01-11-0542

Watanabe, T., Miyashita, K., Saito, T. T., Yoneki, T., Kakihara, Y., Nabeshima, K., et al. (2001). Comprehensive isolation of meiosis-specific genes identifies novel proteins and unusual non-coding transcripts in Schizosaccharomyces pombe. *Nucleic Acids Research*, *29*(11), 2327–2337.

Weiss, M., Elsner, M., Kartberg, F., & Nilsson, T. (2004). Anomalous subdiffusion is a measure for cytoplasmic crowding in living cells. *Biophysical Journal*, *87*(5), 3518–3524. http://doi.org/10.1529/biophysj.104.044263

Wirtz, D. (2009). Particle-tracking microrheology of living cells: principles and applications. *Annual Review of Biophysics*, *38*(1), 301–326. http://doi.org/10.1146/annurev.biophys.050708.133724

Wu, J.-Q., Ye, Y., Wang, N., Pollard, T. D., & Pringle, J. R. (2010). Cooperation between the septins and the actomyosin ring and role of a cell-integrity pathway during cell division in fission yeast. *Genetics*, *186*(3), 897–915. http://doi.org/10.1534/genetics.110.119842

Yaffe, M. P., Stuurman, N., & Vale, R. D. (2003). Mitochondrial positioning in fission yeast is driven by association with dynamic microtubules and mitotic spindle poles. *Proceedings of the National Academy of Sciences of the United States of America*, *100*(20), 11424–11428. http://doi.org/10.1073/pnas.1534703100

Yanagida, M. (2009). Cellular quiescence: are controlling genes conserved? *Trends in Cell Biology*, *19*(12), 705–715. http://doi.org/10.1016/j.tcb.2009.09.006

Yanagida, M., Ikai, N., Shimanuki, M., & Sajiki, K. (2011). Nutrient limitations alter cell division control and chromosome segregation through growth-related kinases and phosphatases. *Philosophical Transactions of the Royal Society of London. Series B, Biological Sciences*, *366*(1584), 3508–3520. http://doi.org/10.1098/rstb.2011.0124

Yang, F., Moss, L. G., & Phillips, G. N. (1996). The molecular structure of green fluorescent protein. *Nature Biotechnology*, *14*(10), 1246–1251. http://doi.org/10.1038/nbt1096-1246

Yang, Z., & Klionsky, D. J. (2010). Eaten alive: a history of macroautophagy. *Nature Cell Biology*, *12*(9), 814–822. http://doi.org/10.1038/ncb0910-814

Zhang, D., Vjestica, A., & Oliferenko, S. (2010). The cortical ER network limits the permissive zone for actomyosin ring assembly. *Current Biology : CB*, *20*(11), 1029–1034. http://doi.org/10.1016/j.cub.2010.04.017

Zhang, D., Vjestica, A., & Oliferenko, S. (2012). Plasma membrane tethering of the cortical ER necessitates its finely reticulated architecture. *Current Biology : CB*, *22*(21), 2048–2052. http://doi.org/10.1016/j.cub.2012.08.047

Figure legends

Figure 1. Motion arrest of lipid droplets in deep starvation.

(**A**) Lipid droplet trajectories extracted from 25sec movies (4frames/sec, droplets depicted in lower DIC images) of cells during exponential growth (EG) and starvation days 2-8 (SD2-8) (Methods). (**B**) Dot plots (one dot represents one cell; 4 independent experiments) showing correlation coefficient-based (CC) quantification of Bodipy-labelled lipid droplet dynamics (Methods). Overlain boxes represent the 25-75 percentile. The blue line represents the mean of all 4 experimental medians with error bars showing the 95% confidence interval. (**C**) Dot plot representing CC of Bodipy-labelled lipid droplets in 2 cell populations (left and right panel), revealing differing timing of transition to motion arrest (SD4-5 and SD5-6 respectively). Overlain are standard box plots. (**D**) Dot plot as in (C) showing lipid droplet dynamics at SD5 in 8 independent cell populations. (**E**) Lipid droplet trajectories as in (A) of cells at SD5, before and 5min or 60min after glucose addition (methods). (**F**) Dot plot representation as in (B) showing quantification of lipid droplet dynamics in samples of cells taken at defined time points during starvation exit (blue lines represent the mean of the medians of 3 individual experiments). (**G**) Lipid droplet trajectories as in (A) in cells at SD5 before and 60minutes after glucose addition, showing lipid droplets remaining immobilized in two of the cells (white arrows). Scale bars in all panels: 5μm.

Figure 1 - figure supplement 1. Lipid droplet morphology and dynamics in starvation.

(**A**) Lipid droplet composition changes from evenly distributed droplets in exponentially growing cells to grape-like lipid droplets (white arrows) in cells at starvation day 2 (SD2). From SD3 to SD5 yet another type of lipid droplet morphology starts to dominate, with fewer, bigger lipid droplets. (**B**) Lipid droplet trajectories as in Figure 1 (A) of cells with many grape-like lipid droplets (white arrows; orange trajectories) and cells with fewer, bigger lipid droplets (blue trajectories) before the lipid droplet motion arrest (SD4; upper panel) and after (SD6; lower panel). (**C**) Lipid droplet trajectories as in Figure 1 (A) of a cell population where no motion arrest occurred up to SD8. Scale bars in all panels: 5μm.

Figure 1- figure supplement 2. Quantification of lipid droplet dynamics by correlation coefficient.

(**A**) Images show Phloxine-labelled cell outlines (upper panel) that were used to segment the cells (methods). The outlines of the segmented cells are overlain in green (lower panel). Dead cells identified by internalized Phloxine (white arrow) were not segmented and thus excluded from the subsequent analysis. (**B**) Images show Bodipy signal from cells (for location of cells see DIC images in lower panel) in exponential growth, at starvation day 3 (SD3) and SD6 (upper panel). White arrows indicate cells from the same population showing very different Bodipy signal intensity. (**C**) 3 consecutive images of Bodipy-labelled cells from SD3 imaged every 45s (t1-t3). (**D**) The Bodipy image pixels (upper panel; t2) were classified with ilastik before computing the correlation coefficient. This resulted in pseudoimages showing the probability of pixels to belong to lipid droplets (lower panel). Scale bars in all panels: 5µm.

Figure 2. CF differs from other solid-like states and is unlikely to be caused by fluid loss.

(**A**) Lipid droplet trajectories extracted from 25sec movies (4frames/sec, droplets depicted in lower DIC images) of cells in cytoplasmic freezing (CF) at starvation day 6 (SD6) compared to acute glucose depletion (AGD; (Joyner et al., 2016)) and drug-induced energy depletion (DED; (Munder et al., 2016)). (**B**) Dot plots (one dot represents one cell; 3 independent experiments) showing correlation coefficient-based (CC) quantification of Bodipy-labelled lipid droplet dynamics (Methods) of CF, AGD and DED cells. Overlain boxes represent the 25-75 percentile. The blue line represents the mean of all 3 experimental medians with error bars showing the 95% confidence interval. (**C**) Protoplasts from cells incubated with cell wall digesting enzymes in 1.2M Sorbitol containing buffer for 1h (upper panel) and for 3h (lower panel). (**D**) SD6 protoplasts from cells incubated for 3 days with cell wall digesting enzymes in 1.2M Sorbitol. (**E**) Ratio of length (blue) or width (red) from cells in standard medium and 1.2M Sorbitol containing buffer. Dots represent the mean of 1000 ratios, where 1 ratio results from manually measured cells (ratio of means of cells from 3 experiments, see Figure 2 - figure supplement 1 (C)) and the other 999 ratios result from means of bootstrapped values (methods). The error bars show the 95% confidence interval of the 1000 ratios. (**F**) Dot plots showing the cell length (left) and cell width (right) during starvation from SD3 to SD7. Overlain boxes represent the 25-75 percentile. The blue line represents the mean of 3 experimental means with error bars showing the 95% confidence interval. Measurements result from automated cell segmentation based on Phloxine B signal (methods). Scale bar is 5µm in all panels.

Figure 2 – figure supplement 1. Cell wall evasion of an exponentially growing cell.

Cell wall digestion in 1.2M Sorbitol. Total duration 5min. Scale bar is 5µm.

Figure 2 – figure supplement 2. Cell size in normal medium and high sorbitol buffer.

Cell length and width of CF, AGD and DED cells in standard culturing medium (-S) or in 1.2M Sorbitol containing buffer (+S) from 3 experiments each, measured manually from DIC images. The blue line represents the mean of 3 experimental means with error bars showing the 95% confidence interval.

Figure 3. Protoplast generation under hypotonic conditions.

(**A**) Protoplasts or cell remnants from cells incubated with cell wall digesting enzymes in 0.5M Sorbitol for the indicated times. (**B**) Live imaging of protoplast evasion from cell wall (white arrow) under 0.5M sorbitol conditions. (**C**) CF protoplasts after 1 day of incubation with digesting enzymes in 0.5M Sorbitol. Scale bar is 5µm in all panels.

Figure 4. No obvious widespread macromolecular assembly of proteins in fission yeast.

(**A**)-(**D**): Images show fluorescence signal of the indicated fusion proteins in exponentially growing cells (upper panels) and DED cells (lower panels). (**E**)-(**F**): Images show fluorescence signal of the indicated fusion proteins in exponentially growing cells (upper panels) and SD6 cells (lower panels). The unspecific signal portion can be estimated from comparison to the autofluorescence from a SD6 wildtype cell without fluorescent tag with the same imaging and contrast settings (small inlet). Images are maximum intensity projections in all panels except (G) which are single focal plane images. Scale bar is 5µm in all panels.

Figure 4. No assemblies of Gln1 formed in DED cells after prolonged drug incubation.

(**A**) Single focal plane images showing double labelling of Gln1-mCherry and the vacuolar marker spac11D3.06-GFP. (**B**) Images show Gln1-mCherry in exponentially growing cells (upper panels) and DED cells incubated for 2h prior to imaging (lower panels). Images are maximum intensity projections. Scale bar is 5µm.

Figure 5. Cytoskeletal structures unlikely to be functionally relevant for CF.

(**A**) Lifeact-GFP visualizing F-actin during starvation. (**B**) Lifeact-GFP from cells at SD6 that were incubated with latB or DMSO from SD3 onwards. (**C**) Lipid droplet trajectories extracted from 25sec movies (4frames/sec, droplets depicted in lower DIC images) of wildtype cells at SD6 incubated with DMSO or latB from SD3 onwards. (**D**) Dot plots (one dot represents one cell; 3 independent experiments) showing correlation coefficient-based (CC) quantification

of Bodipy-labelled lipid droplet dynamics (Methods) of wildtype cells at SD6 incubated with DMSO or latB from SD3 onwards. Overlain boxes represent the 25-75 percentile. The blue line represents the mean of all 3 experimental medians with error bars showing the 95% confidence interval. (**E**) Fluorescently labelled septins 1-4p in deep starvation at SD6. The unspecific signal portion can be estimated from comparison to the autofluorescence from a SD6 wildtype cell without fluorescent tag with the same imaging and contrast settings (small inlet) (**F**) Lipid droplet trajectories as in (C) of cells with spn1-spn4-deletions at SD6. (**G**) Dot plot representation as in (D) showing quantification of lipid droplet dynamics in cells with spn1-spn4-deletions at SD6. Images represent maximum intensity projections. Scale bar is 5µm in all panels.

Figure 5 – figure supplement 1. Microtubules during starvation and acute effect of latB.

(**A**) Microtubules visualized by GFP-atb2 during starvation. (**B**) Effect of 100µM latB/DMSO on F-actin in exponential cells (upper panel), SD3 cells (middle panel; white arrows indicate cells with reduced F-actin dynamics), SD6 cells (lower panel). Images represent maximum intensity projections. Scale bar is 5µm in all panels.

Figure 5 – figure supplement 2. Localization of septins.

(**A**) Spn1p-spn4p localization in exponential cells. (**B**) GFP-tagged spn5p, spn6p, spn7p in exponential growth (left; corresponding DIC images show cell location) and at SD6 (middle). The unspecific signal portion can be estimated from comparison to the autofluorescence from a SD6 wildtype cell without fluorescent tag with the same imaging and contrast settings (to the right of dashed line). Images represent maximum intensity projections. Scale bar is 5µm in all panels.

Figure 6. Subcellular architecture in deep starvation.

(**A**) Nucleus (nup85-GFP), vacuoles (spac11D3.06-GFP) and ER (GFP-AHDL) at starvation day 6 (SD6) compared to exponential growth. The cytoplasmic dots in SD6 nup85-GFP cells represent autofluroescence rather than nup85-specific signal, see Figure 6 – Figure supplement 1. Images show single planes, deconvolved where indicated. (**B**) Mitochondria visualized by maximum intensity projections of cox4-GFP during starvation. The fragmented mitochondria at SD6 are often polarized (white arrows) and mostly cortical, as seen in the single planes of a z stack (lower panel; cell marked by the dotted square in upper panel) (**C**) Mean squared displacement (MSD) of spherical mitochondria particles at SD 3 and SD6. Timelapse: 300

frames with 4fps time interval. MSD from trajectories with minimum length of 160 frames, shown up to a timelag of 40 frames. 6 experiments pooled. Plot shows colour coded histogram of each particle's time-averaged MSD; in blue the ensemble- and time-averaged MSD's. 2nd plot of SD6 with magnified y axis. (**D**) Electron micrographs of freeze-substituted, plastic-embedded and sectioned cells during exponential growth (left) and at SD7 (right). Starvation produces fragmented mitochondria, visible as small spheres marked (m in right panel), and remarkably different from regular, tube-like shapes (m in left panel). Vacuoles are marked (v) and low density areas are labelled with (ld). Scalebar is 1µm. (**E**) Fluorescence loss in photobleaching (FLIP) experiments on Lifeact-GFP in exponential growth (upper panel) and at SD6 (lower panel). Images show maximum intensity projections of 3 planes. Repeated bleaching at the orange square every 5s. Plot shows bleach corrected and normalized mean signal intensity of white square. Thick lines: mean of 10 cells; error bars: 95% CI of the mean; dotted lines: normalized signal of single cells. Scale bar is 5µm in all panels except for (D).

Figure 6 – figure supplement 1.

(**A**) Autofluorescence (excitation 488nm, emission 525/50) of wildtype strain in exponentially growing cells, at SD3 and SD6. Images show maximum intensity projections. (**B**) Images show fluorescence of markers for the indicated subcellular structures in exponentially growing cells and at SD6. The unspecific signal portion can be estimated from comparison to the autofluorescence from a SD6 wildtype cell without fluorescent tag with the same imaging and contrast settings (to the right of dashed line). All images are maximum intensity projections. Scale bar is 5µm in all panels.

Figure 7. CF is delayed without autophagy.

(**A**) Lipid droplet trajectories extracted from 25sec movies (4frames/sec, droplets depicted in lower DIC images) of atg1Δ and atg8Δ cells at SD6 (left) and SD9 (right). (**B**) Dot plots (one dot represents one cell; 4 independent experiments) showing correlation coefficient-based (CC) quantification of Bodipy-labelled lipid droplet dynamics (Methods). Shown are 3 single experiments for wildtype, atg1Δ and atg8Δ cells. Overlain boxes indicate the 25-75 percentile. (**C**) Protoplasts of atg1Δ and atg8Δ at SD6 (left), SD8 (middle) and SD9 (right). Cell wall digestion for 4h in 0.5M Sorbitol. Scale bar is 5µm in all panels.

Figure 1

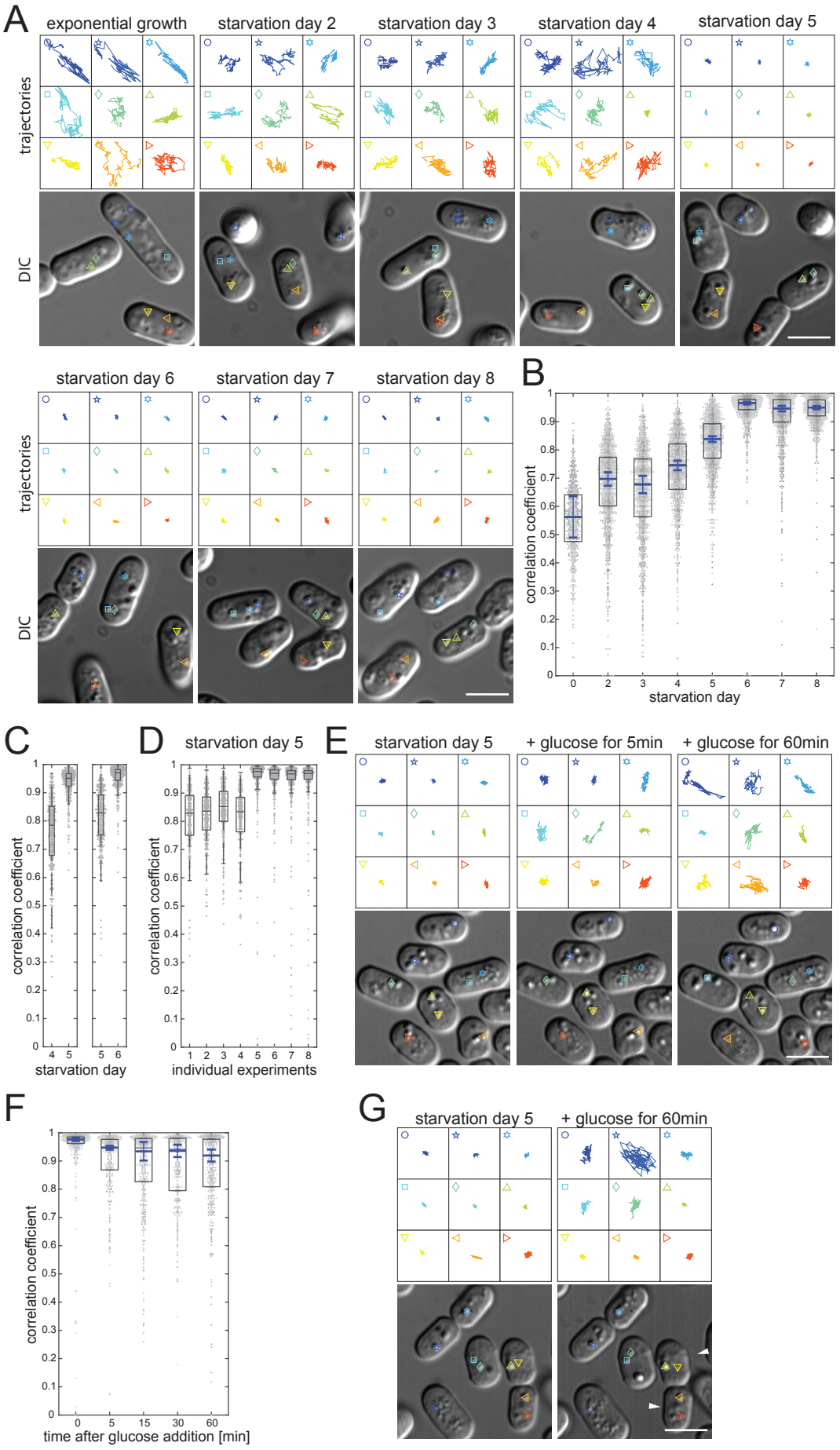
A
exponential growth
starvation day 2
starvation day 3
starvation day 4
starvation day 5
trajectories
DIC
starvation day 6
starvation day 7
starvation day 8
B
correlation coefficient
starvation day
C
correlation coefficient
starvation day
D
starvation day 5
correlation coefficient
individual experiments
E
starvation day 5
+ glucose for 5min
+ glucose for 60min
F
correlation coefficient
time after glucose addition [min]
G
starvation day 5
+ glucose for 60min

Figure 1 – Figure supplement 1

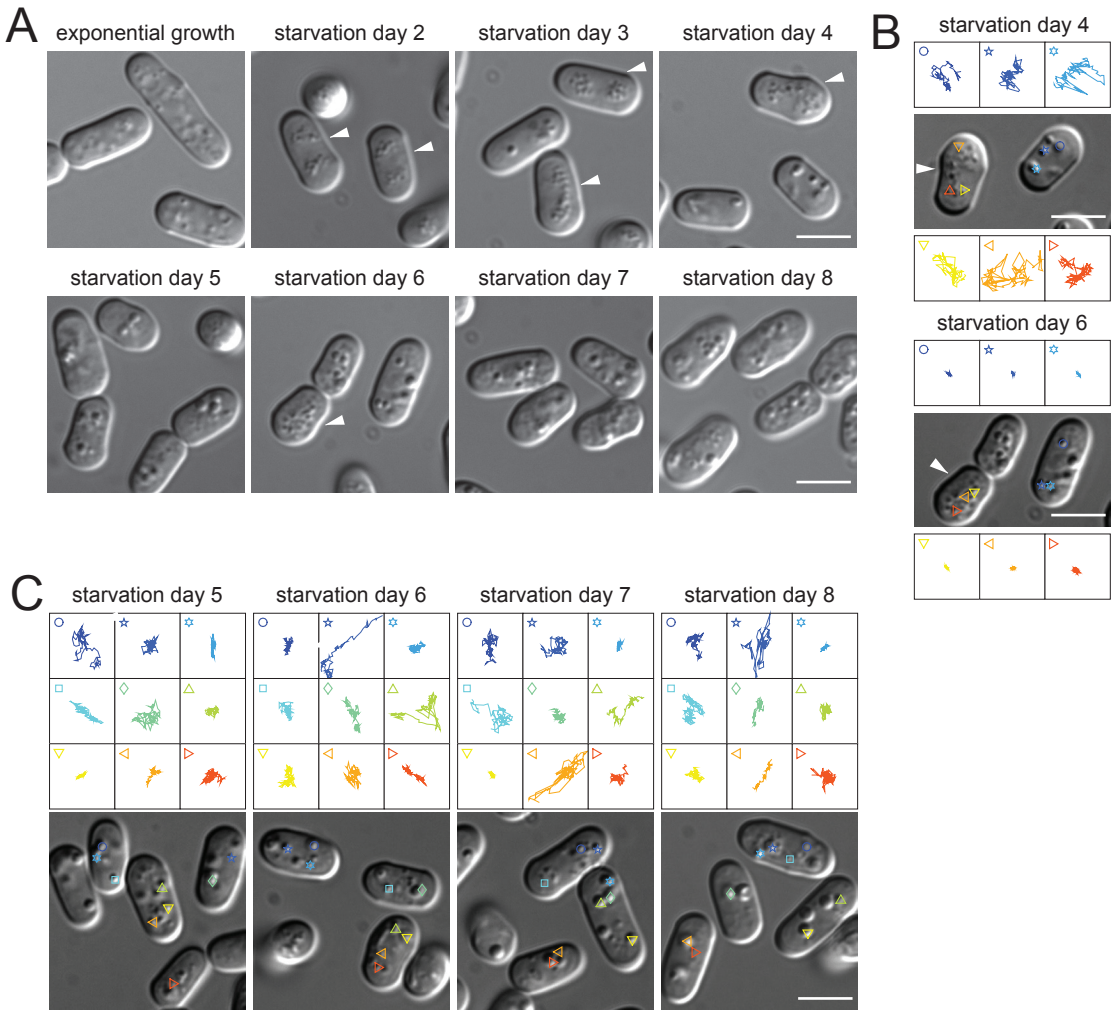

Figure 1 – Figure supplement 2

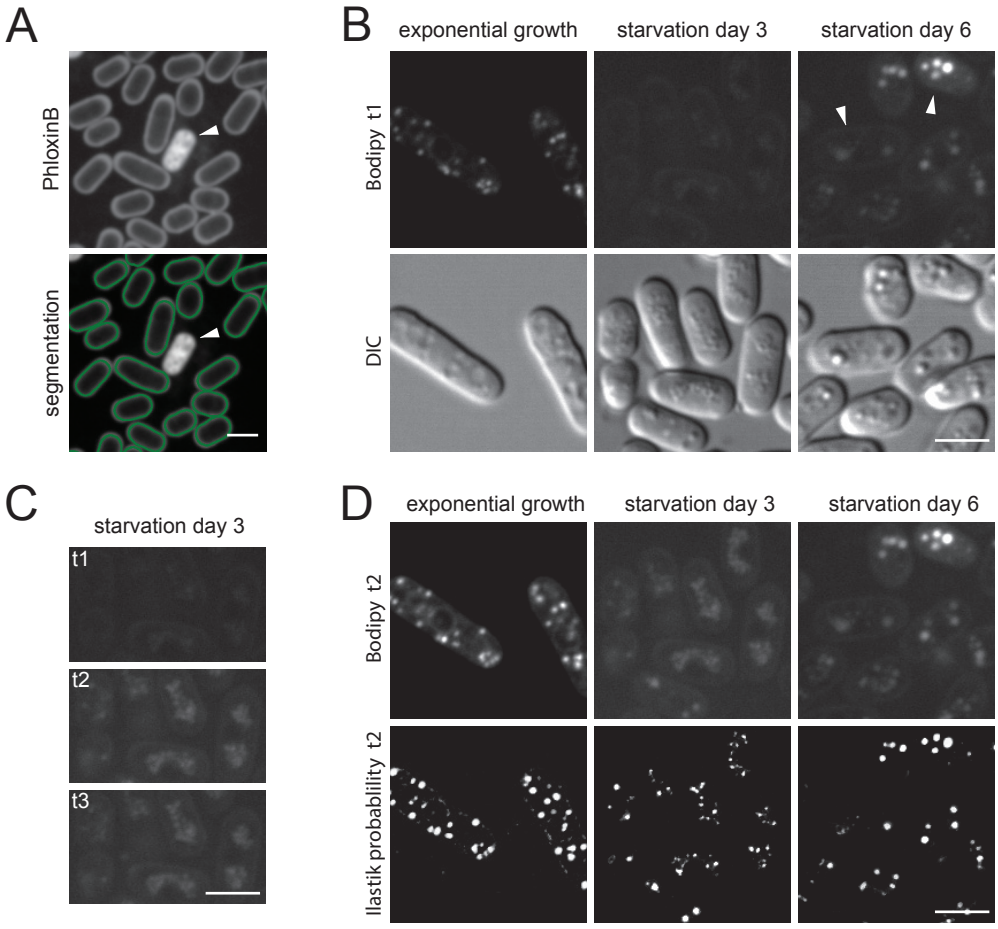

Figure 2

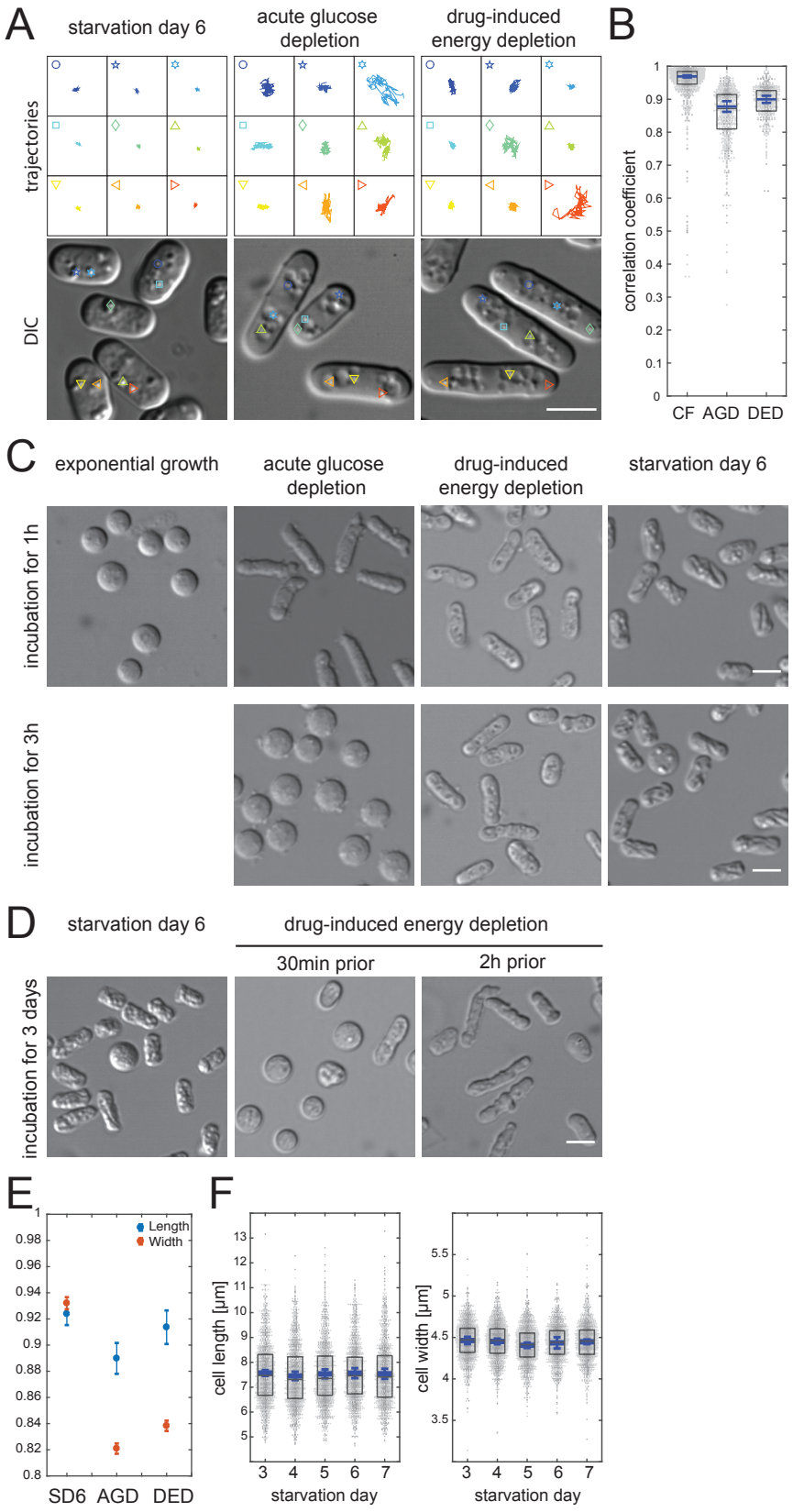
A
starvation day 6
acute glucose depletion
drug-induced energy depletion
trajectories
DIC
B
correlation coefficient
CF AGD DED
C
exponential growth
acute glucose depletion
drug-induced energy depletion
starvation day 6
incubation for 1h
incubation for 3h
D
starvation day 6
drug-induced energy depletion
30min prior
2h prior
incubation for 3 days
E
Length
Width
SD6 AGD DED
F
cell length [µm]
cell width [µm]
starvation day
starvation day

Figure 2 – Figure supplement 1

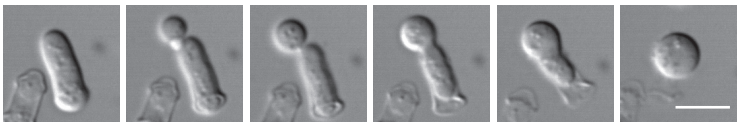

Figure 2 – Figure supplement 2

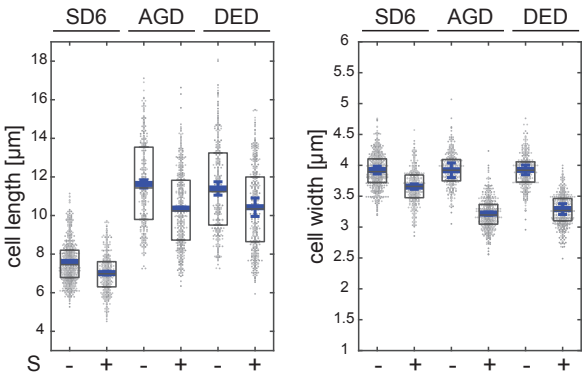

Figure 3

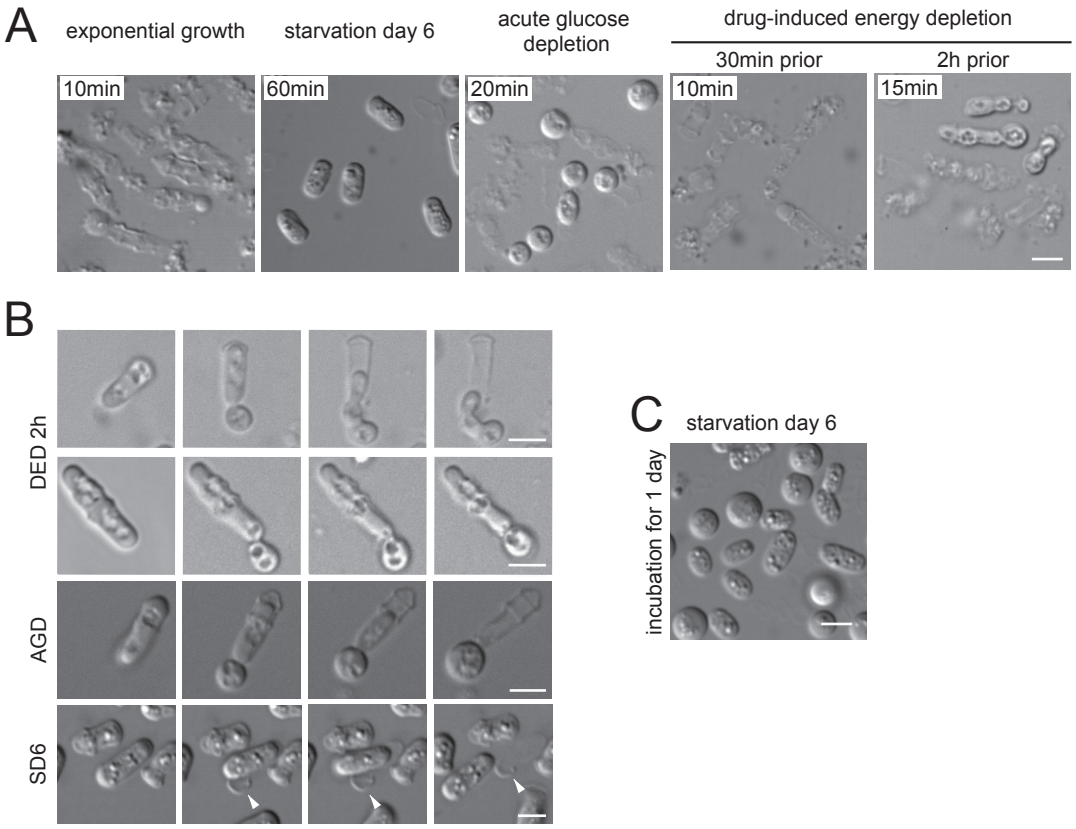
A
exponential growth
starvation day 6
acute glucose depletion
drug-induced energy depletion
30min prior
2h prior
10min
60min
20min
10min
15min
B
DED 2h
AGD
SD6
C
starvation day 6
incubation for 1 day

Figure 4

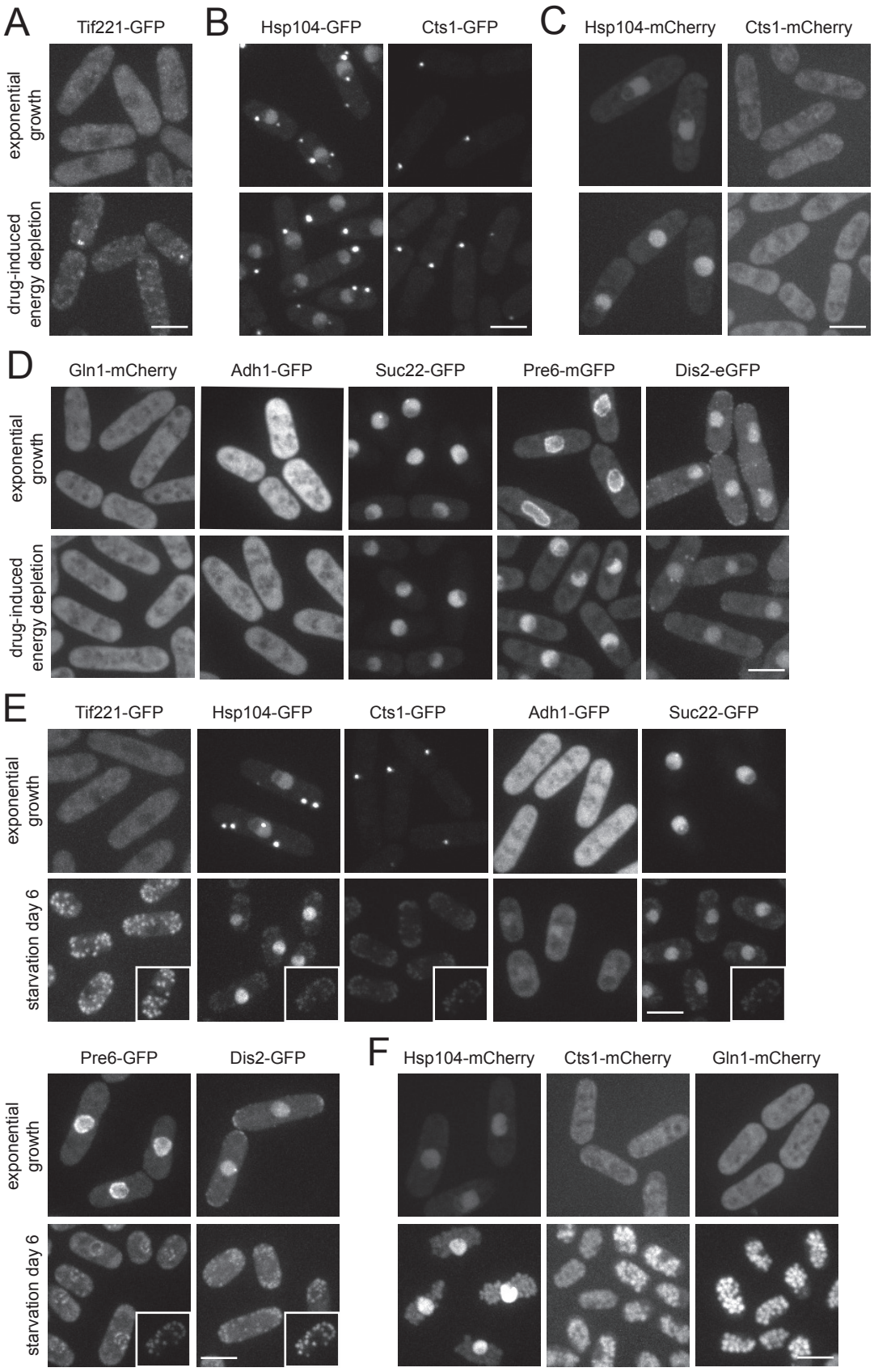
A
Tif221-GFP
B
Hsp104-GFP
Cts1-GFP
C
Hsp104-mCherry
Cts1-mCherry
exponential growth
drug-induced energy depletion
D
Gln1-mCherry
Adh1-GFP
Suc22-GFP
Pre6-mGFP
Dis2-eGFP
exponential growth
drug-induced energy depletion
E
Tif221-GFP
Hsp104-GFP
Cts1-GFP
Adh1-GFP
Suc22-GFP
exponential growth
starvation day 6
Pre6-GFP
Dis2-GFP
F
Hsp104-mCherry
Cts1-mCherry
Gln1-mCherry
exponential growth
starvation day 6

Figure 4 – Figure supplement 1

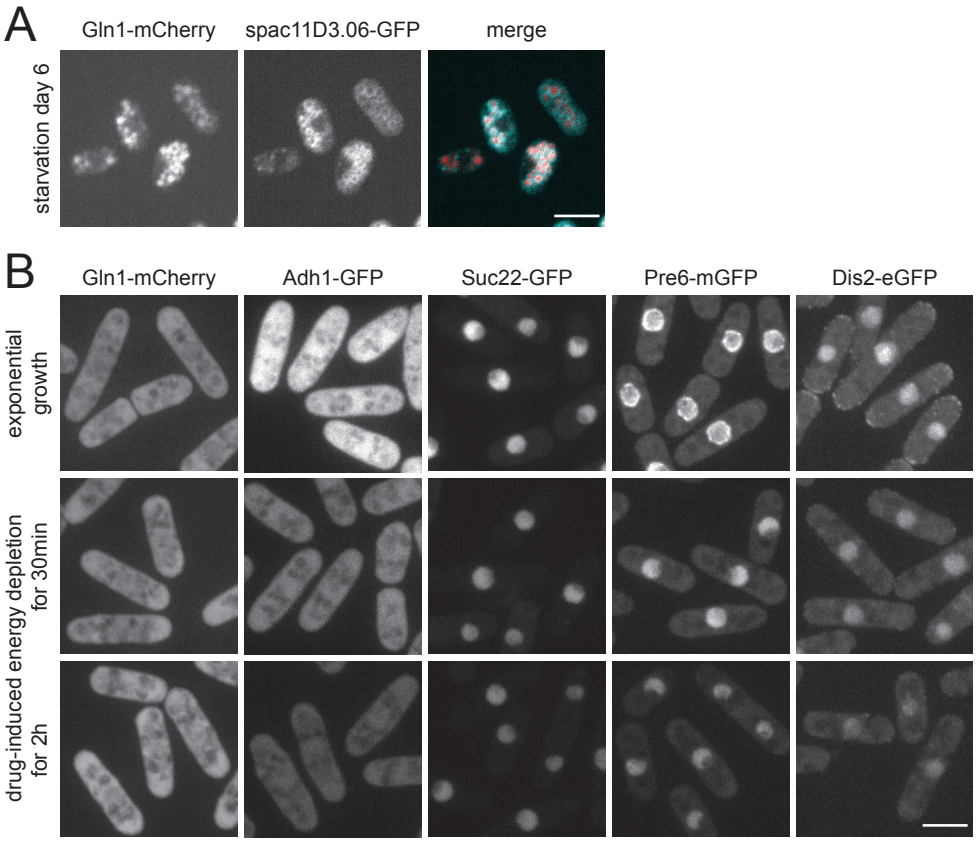

Figure 5

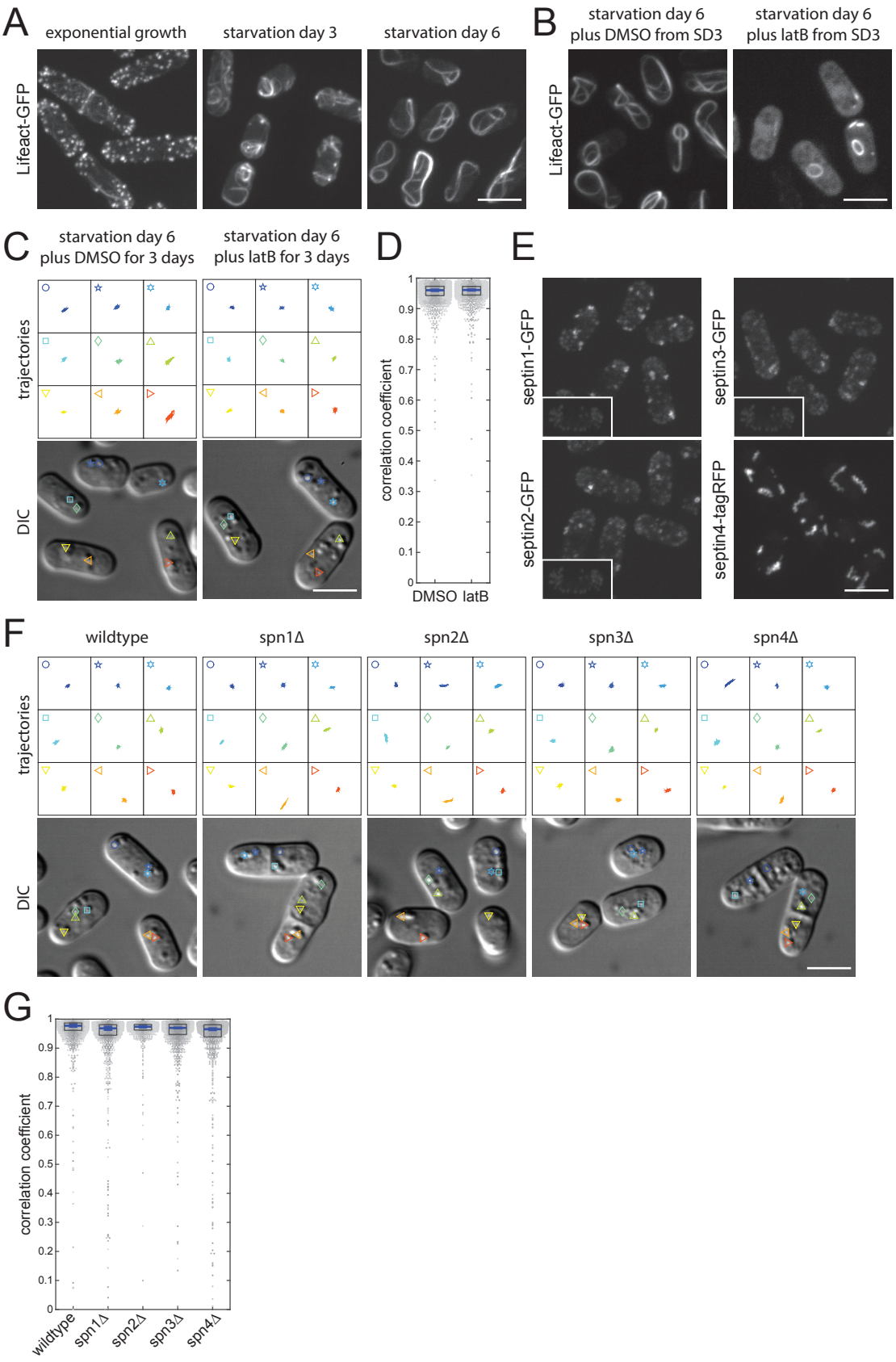
A
exponential growth
starvation day 3
starvation day 6
Lifeact-GFP
B
starvation day 6 plus DMSO from SD3
starvation day 6 plus latB from SD3
Lifeact-GFP
C
starvation day 6 plus DMSO for 3 days
starvation day 6 plus latB for 3 days
trajectories
DIC
D
correlation coefficient
DMSO latB
E
septin1-GFP
septin3-GFP
septin2-GFP
septin4-tagRFP
F
wildtype
spn1Δ
spn2Δ
spn3Δ
spn4Δ
trajectories
DIC
G
correlation coefficient
wildtype
spn1Δ
spn2Δ
spn3Δ
spn4Δ

Figure 5 – Figure supplement 1

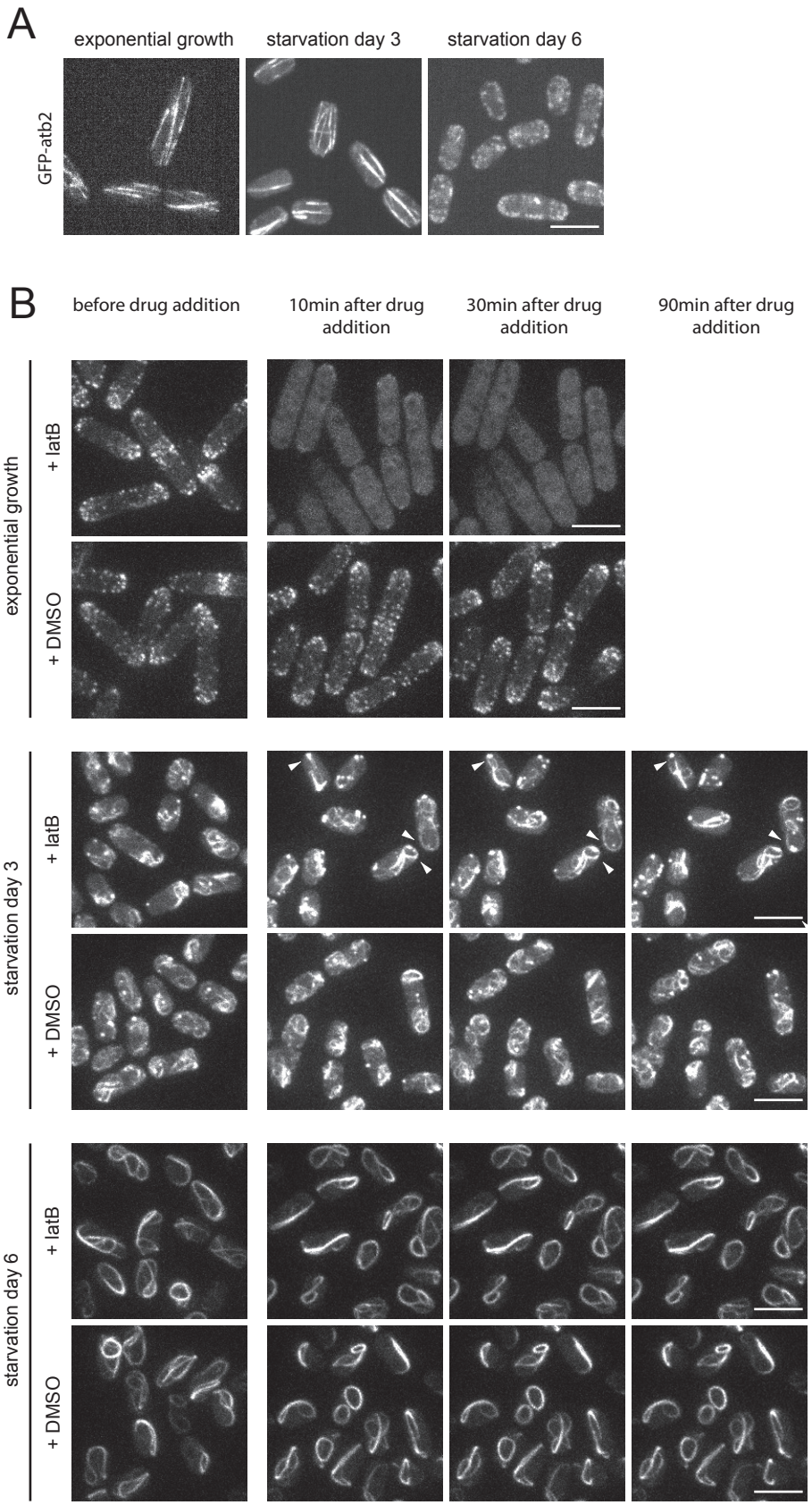

Figure 5 – Figure supplement 2

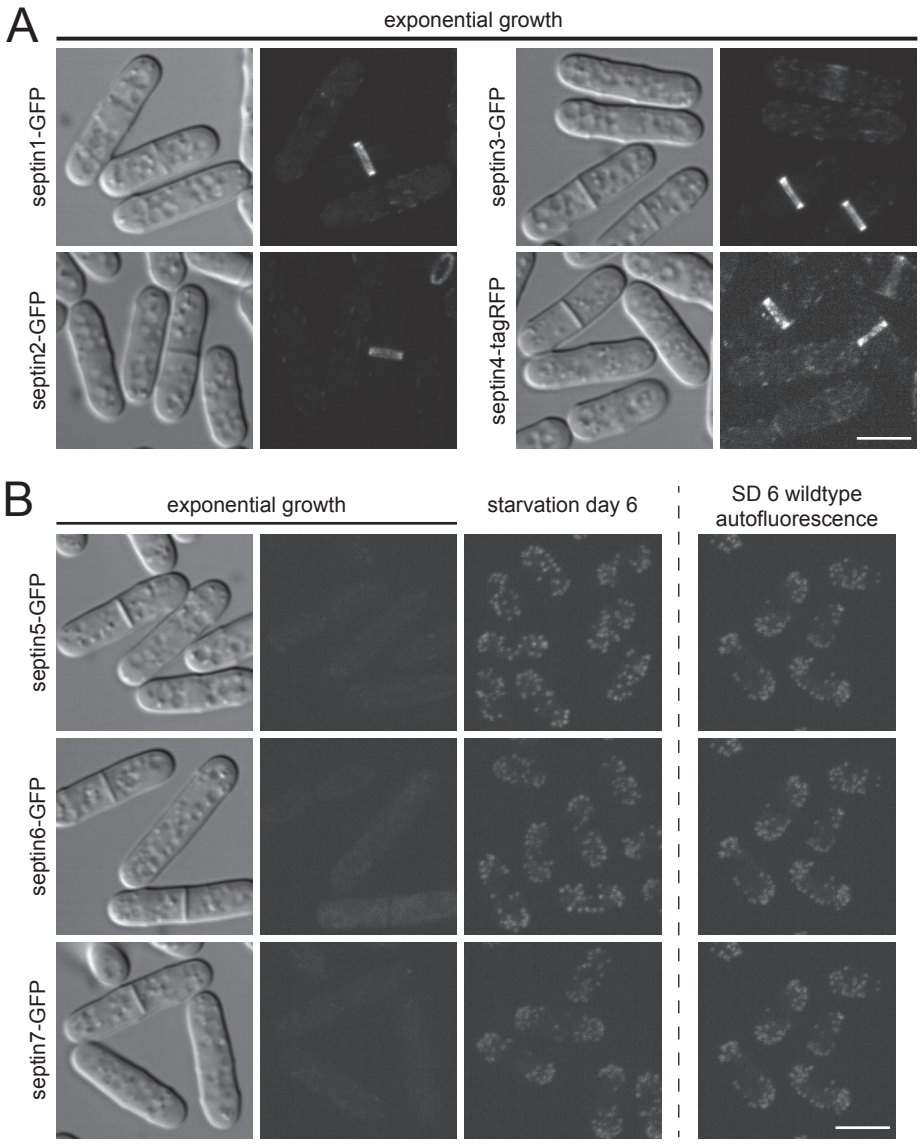

Figure 6

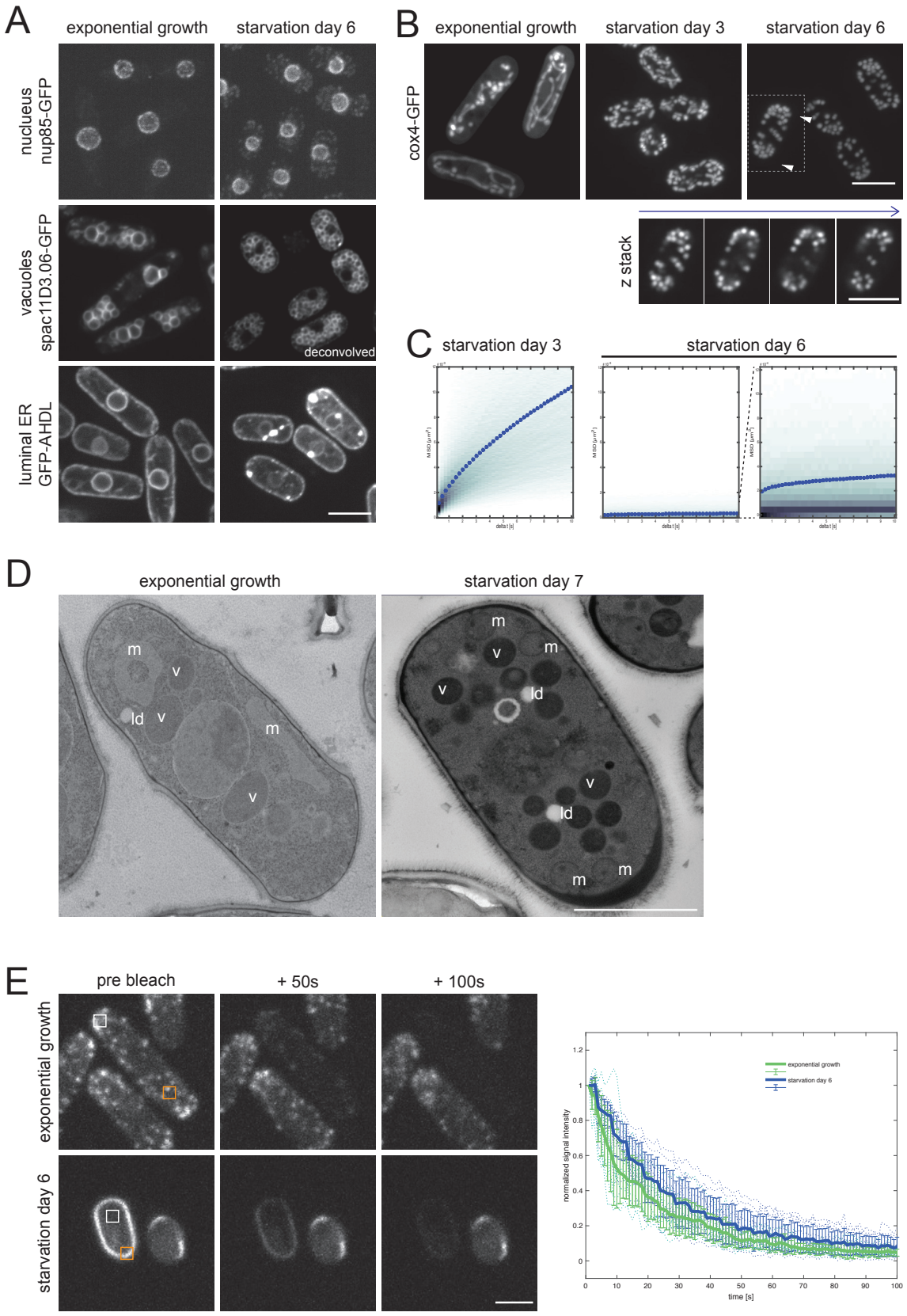
A
exponential growth
starvation day 6
nucleus nup85-GFP
vacuoles spac11D3.06-GFP
deconvolved
luminal ER GFP-AHDL
B
exponential growth
starvation day 3
starvation day 6
cox4-GFP
z stack
C
starvation day 3
starvation day 6
D
exponential growth
starvation day 7
m
v
ld
E
pre bleach
+ 50s
+ 100s
exponential growth
starvation day 6
normalized signal intensity
time [s]

Figure 7

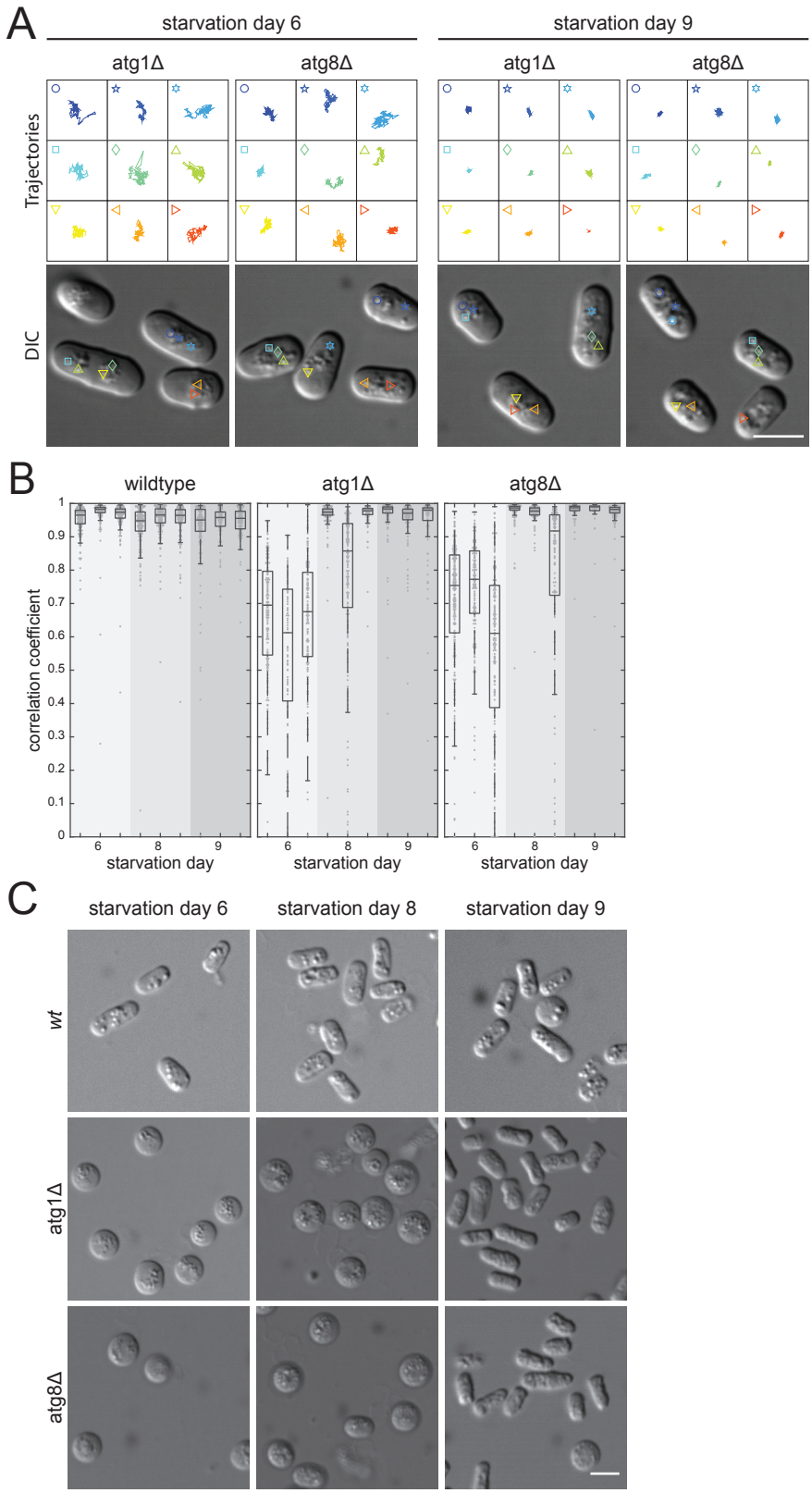
A
starvation day 6
starvation day 9
atg1Δ
atg8Δ
atg1Δ
atg8Δ
Trajectories
DIC
B
wildtype
atg1Δ
atg8Δ
correlation coefficient
starvation day
starvation day
starvation day
C
starvation day 6
starvation day 8
starvation day 9
wt
atg1Δ
atg8Δ

2.2 Glucose starvation triggers filamentous septin assemblies in an *S. pombe* septin 2 deletion mutant

Authors: Minghua Liu, **Maria B. Heimlicher**, Chieze C. Ibeneche-Nnewihe, Ernst-Ludwig Florin, Damian Brunner and Andreas Hoenger

Journal: revised manuscript submitted to PLOS ONE

Contribution: I performed the experiments for Figure 1 and Figure 6.

Glucose Starvation triggers filamentous Septin Assemblies in an *S. pombe* Septin 2 deletion Mutant

Minghua Liu[1], Maria B. Heimlicher[2], Chieze C. Ibeneche-Nnewihe[3], Ernst-Ludwig Florin[3],
Damian Brunner[2], & Andreas Hoenger[1@]

1: University of Colorado at Boulder, Dept. of Molecular, Cellular and Developmental Biology, UCB-0347, Boulder CO, 80309, USA

2: University of Zürich, Department of Molecular Life Sciences, Winterthurerstrasse 190, 8057 Zurich, Switzerland

3: University of Texas at Austin, Center for Nonlinear Dynamics and Department of Physics, Austin, TX 78712, USA

@: Corresponding Author

Keywords:

- Conventional and cryo-electron microscopy
- Vitrified sectioning
- Correlative light and electron microscopy
- Septins
- Filamentous Septin assemblies
- Glucose starvation in *S. pombe*

Abbreviations Used

EM:	electron microscopy	Cryo-EM:	cryo-electron microscopy
ET:	electron tomography	Cryo-ET:	cryo-electron tomography
LM:	light microscopy	Confocal-LM:	confocal light microscopy
EMM:	Edinburgh Minimal Media	LG-EMM:	low glucose EMM

CLEM: correlative light and electron microscopy

Abstract:

Little is known about the sub-cellular changes that occur in cells of the fission yeast *Schizosaccharomyces pombe* when they enter a quiescent state. We therefore studied the intracellular organization of glucose-starved fission yeast cells with regards to the localization of septin proteins throughout the cytoplasm. Thereby, we made an intriguing observation that we explored here in more detail by correlative light and electron microscopy (CLEM): In cells carrying a deletion of the gene encoding septin-2 (*spn2*Δ), starvation causes a GFP-tagged version of septin-3 (spn3p-GFP), to assemble into a single, prominent filamentous structure. It was previously shown that during exponential growth, *spn2*Δ cells form septin-3 polymers (1). However, the polymers we observed during exponential growth are different from the spn3p-GFP structure we observed in starved cells. Using CLEM, in combination with anti-GFP immuno-labeling on plastic-sections, we could unambiguously locate spn3p-GFP in filaments we have found in EM pictures. Besides septin-3, these filamentous assemblies most likely also contain septin-1 as a GFP-tagged version of this protein forms a very similar structure in starved *spn2*Δ cells. Our data correlate phase-contrast and fluorescence microscopy with electron micrographs of plastic-embedded cells, and further on with detailed views of tomographic 3-D reconstructions. Cryo-electron microscopy of *spn2*Δ cells in vitrified sections revealed a very distinct overall morphology of the spn3p-GFP assembly. The fine-structured, regular density pattern suggests the presence of assembled septin-3 filaments that are clearly different from F-actin bundles.

Introduction

Most cellular systems and organisms have an emergency plan that allows them to adapt their metabolism to stressful situations such as nutrient starvation. When yeast cells run out of glucose (reviewed in: 2) or nitrogen (3), they enter a quiescent state, which allows them to survive for some time until nutrients become available again. Thereby, a key goal is to reduce energy consumption while preserving a certain level of cellular organization and maintenance. It has been shown previously that cells entering quiescence reorganize their cytoplasm. A number of publications have analyzed this reorganization for *Saccharomyces cerevisiae* (*S. cerevisiae*, or budding yeast; e.g. see: 2, 4). However, for the fission yeast *Schizosaccharomyces pombe* (*S. pombe*), much less is known about the processes accompanying starvation. Besides arresting growth and its associated functions such as membrane trafficking, fission yeast cells also lose all known signs of cell polarization (5). Similar to budding yeast, actin in *S. pombe* reorganizes first into a number of globular assemblies that randomly move through the cells (6). In contrast, microtubule based traffic continuously slows down and microtubules eventually seem to disappear or cluster into a small hyper-stable bundle (7, 8). How these changes in cytoskeleton organization affect the position and organization of other cellular structures, such as the Golgi, mitochondria or the endoplasmic reticulum, is not known.

To better describe sub-cellular organization of starved *S. pombe* cells, we have analyzed the localization of various proteins in wild type cells and in cells carrying genetic modifications. Amongst these were cells with deletions of septin genes. Septins are conserved GTP-binding proteins that associate with cellular membranes as well as the actin and microtubule cytoskeletons (9). They were first discovered in *S. cerevisiae* where they form a collar ring at the bud neck (10, 11). It is believed that this septin collar provides a physical barrier for proteins and RNAs and serves as a scaffold for the recruitment of other proteins (12). Septins localize throughout the cytoplasm in non-dividing cells (9, 13; see also Fig. 1). They are involved in multiple processes including cell morphogenesis, membrane shaping and cytoskeleton dynamics (14). A recent study in human cells also demonstrated that septins build a cage-like structure to entrap intracytosolic bacteria (15). Septins have been linked to several human diseases such as neurological disorders and oncogenesis (16, 17). They may form various polymers that assemble into filamentous structures forming meshworks, fibers or rings (1, 12). In *S. pombe*, septins are not essential (18). Septin-1 (spn1p), septin-2 (spn2p), septin-3 (spn3p) and septin-4 (spn4p) are all expressed in vegetatively growing cells where they form hetero-

octamer septin rods, which can further assemble into larger septin filaments (1, 14). In exponentially growing cells performing cytokinesis, septins 1-4 form a ring structure in the cell center. The septin ring contributes to the assembly of the contractile actin/myosin-II ring that constricts to separate the cytoplasm of the two daughter cells similar to mammalian cells (19). Thereby, spn1p and spn4p are present during septin ring formation, while either spn2p or spn3p, although required for proper septum function, are often absent. However, there is no indication that any septins are required for ring formation (19). Septin-5, septin-6 and septin-7 are only expressed during meiosis and sporulation (10, 20, 21; see also Fig. 6). Near atomic X-ray crystal structures of septin polymers are now available from *S. cerevisiae* (22), and mammals (23).

Here we describe a prominent filamentous spn3p assembly that formed in glucose-starved cells carrying a deletion of the *spn2* gene (*spn2*Δ). Filamentous spn3p assemblies were identified in electron microscopy pictures with correlative light and electron microscopy (CLEM) and with immuno-labeling. The structural appearance of the spn3p-GFP assemblies suggests that they represent assembled spn3p filaments. It is most likely that the filaments contain spn1p as well, which forms similar assemblies in glucose-starved *spn2*Δ cells (1). The filamentous spn3p assemblies we observed are different in structure from the metabolic enzyme polymers as reported previously for glucose-starved *S. cerevisiae* cells (24). Control experiments designed to test the distribution and macromolecular assembly form of actin within these strains were performed with LifeAct®-mCherry as well as Phalloidin-Rhodamin labeling and showed convincingly that septin-GFP polymers do not coincide with actin polymers, or F-actin bundles. (see: Figs. 3-5). Here we are focusing on a comparison of spn3p-GFP in wild type and *spn2*Δ mutants, which formed distinct fluorescent structures that were further investigated by EM, both, by tomographic 3-D reconstruction on thin-sections of plastic-embedded specimens (Figs. 2-4), as well as on thin-sections of frozen-hydrated, vitrified cells (Fig. 5; reviewed in 25, 26).

Results and Discussion

Distribution of spn3p-GFP and spn1p-RFP in wild type cells:

We induced glucose starvation to *S. pombe* by culturing cells in low-glucose Edinburgh Minimal Media (LG-EMM: see Materials and Methods). The cultures stopped growing within about two days of glucose starvation but sub-cellular reorganizations proceeded up to day seven of culturing (Fig.1B1-B3, & D1-D2). After that, cells remain static or started to die. Therefore, we focused our analysis on cells at day seven (Materials and Methods, 5).

In a first set of experiments we have analyzed the structure and dynamics of spn3p-GFP and spn1p-RFP in exponentially growing (Fig. 1, A1-A3, & B1-B3 (*spn*2Δ), and in glucose starved cells (Fig. 1, C1-C3, & D1-D2 (*spn*2Δ) by confocal fluorescence, and differential interference contrast (DIC) microscopy (Fig. 1). In addition, we performed Western blotting to show the expression levels of all septins present (septins 1-7), both, in wild type and mutants during exponential growth and starvation (Fig. 6). Generally, septins 1-4 are expressed in both conditions, while septins 5-7 are mostly absent. Septins 1-4 seem about equally expressed at both conditions, while septins 1, 3, and 4 appear more fragmented under starvation. Under standard exponential growth conditions cells expressing both, spn3p-GFP and spn1p-RFP showed normal growth and division. The expression and cytosolic localization of both tagged proteins was visualized by fluorescence microscopy and is illustrated in figure 1, A1-A2, and overlaid with a DIC image in figure 1, A3. We find both, spn3p-GFP and spn1p-RFP often, but not always co-localizing to multiple, tiny clusters scattered throughout the cytosol. In some cells, under specific conditions the proteins formed large assemblies. In dividing cells, both proteins localized to the typical location at the cell periphery where the septin ring forms. At the same time the cytosolic signal decreased, suggesting a reduced cytosolic concentration (Fig. 1A1-A3).

Seven days of glucose starvation abolished any cell division or growth and reduced the distribution of most of the spn3p-GFP (Fig. 1, C1) and spn1p-RFP (Fig. 1, C2) to one single clump that often accumulates both proteins together (see overlay in Fig. 1, C3). However, residual amounts of both proteins can still be detected in the background, but any precise quantitative analyses by the fluorescence microscopy methods used here are not reliable enough

for these kinds of interpretations. Also, several of the protein aggregates do not seem to contain both septins, or very different amounts of it (arrows in Fig. 1, C1-C3).

Distribution of spn3p-GFP and spn1p-RFP in wild *spn2*Δcells:

The overall distribution and accumulation of spn3p-GFP and spn1p-RFP expressing cells was very different when the *spn2* gene was deleted (*spn*2Δ Fig. 1, B1-B3 & D1-D3). At exponential growth conditions (Fig. 1, B1-B3), spn3p-GFP was mostly found in small polymers and at the septa of dividing cells (arrows: Fig. 1, B1). Unlike spn3p-GFP, and spn1p-RFP in wild type cells, *spn*2Δcells do not seem to incorporate spn1p-RFP into the septa, although these cells continued dividing, grew normally, and still accumulate spn3p-GFP at the septa (arrows in Fig. 1B1 - B3 (overlay with DIC)). This differs from earlier findings based on GFP-tagged spn1p, which formed a ring during cytokinesis in the absence of spn2p. Furthermore, this result challenges the previous hypothesis, which states that spn1p is essential for the other septins to form a ring (19).

Similar to wild type cells, after 2-3 days of culturing *spn*2Δcells result in a complete growth arrest. Figure 1, D1 to D3 shows *spn*2Δcells and the distribution of spn3p-GFP and spn1p-RFP after seven days of starvation. Interestingly, in such starved cells both, spn3p-GFP and spn1p-RFP co-localized into what appears to be large, straight filamentous assemblies, or bundles, consuming almost all protein and leaving only trace amounts still visible throughout the cytosol. Consistently, each cell contained only one single filamentous assembly (Fig. 1F). However, similar to the roundish spn1p-RFP/spn3p-GFP particles formed in exponentially growing cells, not all of these filamentous spn1p-RFP assemblies contain spn3p-GFP (arrows: Fig. 1, D1-D3). These assemblies were also very well visible by EM and electron tomography (ET), which initiated a brief study of spn3p-GFP assembly morphology that conveniently served to establish a correlative light and electron microscopy (CLEM) approach. (exemplified in Fig. 2).

Correlating septin bundles from light to electron microscopy:

Today, fluorescence LM in its multiple forms, employing super-resolution methods and genetically encoded fluorophores such as GFP and mCherry allows imaging large macromolecular complexes and organelles within a cellular context and in a fully hydrated *in vivo* state (reviewed in: 27). This is obviously a significant advantage over EM. Despite some recent efforts in viewing hydrated biological specimens in a fluid chamber by EM (reviewed

in: 28), examination of active, living cells in the electron microscope is still very difficult and far from a routine application. On the other hand, the light-microscopy community achieved spectacular progress in super-resolution light microscopy. Nevertheless, detailed structural investigations *in vitro* and *in situ* on macromolecular complexes and sub-components thereof are still the domain of EM simply because EMs feature superior resolution and independence of labeling tools, which, however, could be both, a blessing or a curse. Whether in its classical specimen preparation forms such as chemical-fixation, or freeze-substitution and plastic-embedding (Figs. 2-4), or by new emerging techniques that is vitrification, vitrified sectioning, and imaging in a frozen-hydrated state (Fig. 5), the spatial resolution of an EM is still unmatched by any LM approaches, but the absence of anything comparable to fluorescent labels sometimes interferes with an unambiguous identification of structures, especially in an intact cell, which is a very significant difference between fluorescence and electron microscopy.

Since the detectable signals with fluorescence-based microscopy mostly come from distinct proteins labeled with fluorochromes, there is little else that obscures the images. In contrast, electron microscopy, in particular of unstained, frozen hydrated specimens, typically produces 2-D projections that includes all electron scattering structures such as proteins, lipids, glycosylation, and whatever else is there, often with very low contrast (29, 30, 31). Hence, while fluorescence LM is ideal for the identification of specifically labeled targets, in the EM we have to deal with large arrays of superimposed densities, and most of them cannot be directly identified. On the other hand, EM reveals these structures with finer molecular detail and within their larger context that is usually not visible by fluorescence microscopy due to the limits of how many structures can be fluorescently labeled within the same preparation. This may all not be much of a problem in an *in vitro* approach where only few components are present, but it may be a huge problem within the complex environment and the vast amounts of different densities within an intact cell. Addressing these issues, CLEM methods are in great demand and by now have produced some exciting results (e.g. see: 32, 33). The demand for CLEM on cryo-specimens initiated the development of novel cryo-light microscopy stages to pre-examine cryo-EM specimens in a light microscope (e.g. see 34 (our own work), 35).

To verify the nature of the filamentous septin assemblies observed by EM we engaged in a straightforward CLEM approach. To this end we correlated a phase contrast image (Fig. 2A) a fluorescence image (Fig. 2B), an overview EM micrograph (Fig. 2C), and a thin computational slice through a tomographic 3-D reconstruction (Fig. 2D), all recorded from the very same

specimen. By this CLEM method we have investigated the spn3p-GFP containing septin assemblies in intact, starved *spn2*Δcells in a 250-nm thick plastic section (Fig. 2A-C), as well as a tomographic 3-D reconstruction thereof (Fig. 2D). We achieved an unambiguous correlation of the spn3p-GFP fluorescence with the dense assemblies observed in plastic or vitrified sections. In the figures, blue arrows connect identical elements such as entire cell outlines, or the large piece of dense and highly fluorescent material. Likewise, two dense granules seen by electron microscopy in Fig. 2C are connected by blue arrows to the 40-nm tomographic slice in Fig. 2D. The filamentous spn3p-GFP containing assembly itself (connected by green arrows) is not visible by phase contrast, but shows up well by fluorescence microscopy and can be seen as an elongated density in the overview image (Fig. 2C). Finally, our analysis reveals more molecular details about the assembly's filamentous supra-molecular nature within a thin slice of the tomographic 3-D reconstruction (Fig. 2D). Seven days of glucose starvation significantly enhanced spn3p-GFP bundling in *spn2*Δ mutants (Fig. 1, D1-D3; Fig. 3A) as compared to the wild type (Fig. 1, C1-C3; Fig. 5A). These filamentous assemblies appeared to be quite straight (Fig. 2D).

Immuno-labeling of spn3p-GFP by anti-GFP primary, and gold-linked secondary antibodies:

To further confirm the presence of spn3p-GFP at a higher spatial resolution within the septa and filamentous assemblies that we had observed by EM in *spn2*Δspn3p-GFP cells (Fig. 2), we employed immuno-gold labeling using a gold-linked antibody system directed towards GFP (Fig. 3). Cellular preparations embedded in plastic often preserve antigens of epitopes such as the GFP tag used here. Hence, when these epitopes are accessible at the surface of a section they can be decorated by antibodies and observed in both, light as well as electron microscopes (reviewed in: 37). Typically, this method employs a primary antibody directed against an exposed epitope of interest and a gold-linked secondary antibody against the Fc domain of the primary antibody. In our case the secondary antibody was a generic anti-rabbit antibody, linked to a 15-nm gold particle (see: Materials and Methods). Immuno-labeling against GFP domains confirmed the presence of the spn3p-GFP protein within the dense filamentous assemblies formed in *spn2*Δspn3p-GFP cells after seven days of glucose starvation (see Fig. 3A, both examples are recorded at identical conditions). The insets show fluorescence labeling of actin and septin-3 with LifeAct-mCherry (upper inset)

In a control experiment, we examined septa in exponentially growing cells with anti-GFP immuno-labeling. In spn3p-GFP expressing cells we could detect the presence of GFP at the site of cytokinesis by EM, and consequently that of spn3p-GFP in 100 nm thick plastic sections (Fig. 3B). Fluorescence microscopy revealed a very obvious, dense GFP signal within the septa (Fig. 3B insets), and on plastic sections GFP-antibody immuno-labels find spn3p-GFP there as well. In both panels of figure 3, the lower fluorescence insets show projections of a thin slice through a confocal stack with actin labeled with Rhodamine-Phalloidin, overlaid with a phase-contrast image., the upper insets show projections through a full confocal 3-D stack that are slightly tilted and shows actin labeled with LifeAct-mCherry. The tilting reveals dividing cells and their septa (in B) from an oblique angle. This data illustrates that most of the spn3p-GFP (green) locate to the outer periphery of the septum, with some actin (red) more towards the center, which is in accordance with the immuno-gold labeling of spn3p-GFP.

Septin-actin interactions:

To further clarify the nature of the spn3p-GFP assemblies we tested whether actin may play a role in their formation. We visualized actin either with Rhodamine-Phalloidin (Fig. 3A, lower inset) or LifeAct®-mCherry (Figs. 3-5) to make sure actin cable formation was not triggered artificially by any of these stains. The Phalloidin-stained images (Fig. 3A, lower inset) are thin confocal sections, while the cells stained with LifeAct®-mCherry (Figs. 3A, upper inset, 4 & 5) are entire 3-D stacks that also allowed us to rotate them for a better view of septa (Fig. 3B). Both methods revealed clear, identical signals (36). Here we found that glucose starvation of *S. pombe* cells, independent of the presence or absence of septin-2, not only modifies septin aggregates, but also triggers the formation of long actin cables (inset panels in Fig. 3A & Fig. 4). Most importantly, under any conditions actin and spn3p-GFP do not co-localize, no matter whether spn3p-GFP accumulates into filamentous assemblies as found within *spn*2Δ cells (inset, Figs. 3A & 4A), or remain randomly distributed within small clusters of spn3-GFP expressing cells (insets, Figs. 3B & 4B).

Morphological differences between septin assemblies and actin bundles observed in vitrified sections:

In this study, we expanded our EM imaging with preparations of vitrified sections from frozen-hydrated cellular samples to avoid potential artifacts from chemical fixation or freeze-substitution (see Fig. 5). As of today, most ultra-structural research into intact cells is still

carried out by at least some mild chemical fixation, followed by freeze-substitution and embedding in plastic for cutting thin sections by a microtome. Due to effects of chemical fixation and/or freeze-substitution this technique produces image data of cellular structures to an interpretable resolution of approximately 4-5 nm, and rarely below (e.g. see: 38, 39). For molecular data beyond that samples have to be imaged in a frozen-hydrated, vitrified state. For EM studies vitrification is the only preparation method that preserves bio-molecular structures to near-atomic detail. While vitrification is a common process for structural investigations on isolated macromolecular complexes, it is still a rather tricky process to be applied to cellular specimens (e.g. see: 26, 40). Attempts to create frozen-hydrated cellular preparations for electron microscopy date back to pioneering work by Christensen, 1971 (41) and later McDowall et al. 1983 (42). However, cryo-EM as we know it today was not yet invented, or just about in its very early stages of development (29), and the real breakthrough for vitrified sections came much later with work from Hsieh et al. 2002 (30) and Al-Amoudi et al. 2004 (31).

To further strengthen the data that we have obtained from plastic sections, we also prepared vitrified sections from intact *spn*2Δ cells in exponential growth (Fig. 5A) and after seven days of glucose starvation (Fig. 5B & C). As explained above, the rational for using vitrified sectioning was to obtain sufficient resolution and unobstructed molecular detail that would allow us to directly distinguish F-actin bundles from filamentous spn3p-GFP assemblies by their individually different morphologies, without having to worry about chemical fixation and/or dehydration artifacts. Interestingly, we could not detect any structure convincingly showing F-actin bundles in any of the glucose-starved cells, although the strong fluorescence signal suggested the presence of 1-2 prominent F-actin cables that should be visible in any of the sections (Fig. 4). It is therefore possible that the architecture of this starvation-specific actin cables that we found in our preparations (Fig. 5C) differ considerably from that of F-actin stress fibers (Fig. 5D). To illustrate the different morphologies of F-actin bundles and filamentous spn3p-GFP assemblies we resorted to a picture of vitrified, cultured 3T3 fibroblast cells as shown in Fig. 5D (see also: 26), acting as a control for actin bundle dimensions and packing. This vitrified section reveals projections at various angles through actin stress fibers (blue arrows in Fig. 5D). These clearly show a very different morphology when compared to the filamentous spn3p-GFP assemblies we had identified. Similarly, in exponentially growing cells the much shorter, curvier, and less abundant spn3p-GFP structures showed a characteristic morphology that differed substantially from actin filament arrangements such as found in stress

fibers (Fig. 5D). The pattern of the filamentous spn3p-GFP assemblies (Fig. 5 red frame with a blow-up in the inset panel) often resembled a tightly pitched staggered assembly, which lack the long-pitched, helical pattern and stiffness of actin filaments (e.g. see: 43). All four panels of figure 5 are at the same magnification (see scale bars), and by comparing these images actin bundles appear significantly narrower and more tightly packed than filamentous spn3p-GFP assemblies. In addition, filamentous spn3p-GFP assemblies or clusters appear less ordered. Nevertheless, assuming that the overall structure of F-actin should still be the same despite some differences in arrangement, the bundles in figure 5C show a F-actin packing arrangement that is very different from what we find in filamentous spn3p-GFP assemblies or clusters (Fig. 5A & B). On the other hand, the pattern of the spn3p-GFP assemblies in our images match quite well the structure and dimensions of the EM 3-D reconstructions that have been presented by other groups (44).

Conclusions:

This work combines a technical component with a biological application. On the biology side, we investigated the behavior of septins in *S. pombe* upon extended glucose starvation. Thereby we made some unexpected observations, A: upon glucose depletion, septin-1 and -3 in *S. pombe* cells with a *spn2*Δ background aggregate into filamentous assemblies (Figs. 1-5). In all types of starved cells explored here, actin forms cables, which do not co-localize with the filamentous septin assemblies or other septin aggregates (Figs. 3-5). Regarding functional aspects of septins in *S. pombe*, we could demonstrate that *S. pombe* cells with a *spn2*Δ background still grow normally (based on observed growth rate and density the cultures reached after the exponential phase), despite aggregating the majority of GFP-labeled Septin-3 into small particles throughout the cytosol. Spn3p-GFP is clearly present in septa of wildtype cells (wildtype with respect to Spn2p deletion), and *spn*2Δ spn3p-GFP mutant cells. However, the septa of *spn*2Δ spn3p-GFP mutant cells do not seem to contain any traces of spn1p-RFP anymore. Hence, the overall structure of septa in *spn*2Δ spn3p-GFP cells seems to be insensitive to the absence of Septin-3 (see Fig. 1) and still function normally. Under wildtype conditions, Septin-1, -2, -3, and -4 are expressed in vegetatively growing cells and form hetero-octamer septin rod, which can further assemble into regular septin assemblies (14).

F-actin cables in starved *S-pombe* cells (Fig. 5C), mutants or wildtype, appear less densely packed than F-actin stress fibers such as in fibroblasts and other motile cells (Fig. 5D; 3T3 cells). There is no indication that any type of myosin motors co-localizes with the starvation-induced F-actin bundles. The bundles would be too tight to accommodate myosin motors and cargo within. However, any myosin mediated transport processes could take place on their outer surface.

On the technical side this work is a CLEM study (Figs. 2-4; 33, 34, 35), where we investigate the structure of a novel septin protein-assembly that we found in mutant, glucose starved *S. pombe* cells. Our work correlated light- (LM) and electron microscopy (EM) 3-D data of a complex protein structure within the cytosol of *S. pombe*. Due to the crowded density of a cytosol, electron microscopy alone often may not be sufficient to unambiguously identify such structures, unless they are of very obvious shape and size (e.g. microtubules, ribosomes). Clonable high-density labels for EM, somewhat analogous to GFP are available but difficult to handle and still part of an emerging technology (45, 46).

Here we could demonstrate the power of correlative light and electron microscopy for molecular studies in intact cells. By blanking out all unlabeled cellular structures, a fluorescence microscopy image is reduced to one or few fluorescently labeled target structures within a cellular context. This greatly enhances visibility and renders it a highly complementary tool for an unambiguous identification of the structures of interest within the complex density pattern of electron micrographs. We present results on spn3p-GFP in the presence or absence of septin-2 because this combination produced morphologically striking results that could be easily observed by both, light and electron microscopy. Wildtype or other mutants did not show such an obvious phenotype.

Our results that we have obtained with vitrified sectioning on frozen-hydrated cells, opened another perspective to septin assemblies and polymers. Omitting staining and/or any type of chemical fixation produces the true protein density of a macromolecular assembly. However, vitrified sectioning is still an emerging technology and will require further refinements, or other means of production. Producing vitrified sections of cellular specimens with a cryo-microtome is difficult and sometimes tedious (e.g. see: 26, 40), and correlative approaches are even more difficult because the handling of vitrified material requires uninterrupted cryo-conditions. This means keeping specimens at, or below -140C and access to specialized tools (34, 35). Also, despite using a newly developed cryo-light microscope in our lab (34, 35) we could not produce enough fluorescence for an unambiguous localization of spn3p-GFP polymers within vitrified sections. Unlike plastic sections of 200 – 300 nm thickness that we regularly use for tomographic data acquisition (see Fig. 2) our vitrified sections seem to be either too cold and/or too thin (~80 nm) and therefore do not contain enough active fluorochromes to produce sufficient signal at temperature below -140C^{o} (the vitrification boundary of water). Nevertheless, the accurate structural preservation of biological matter in vitrified sections sometimes allows for a direct *in situ* interpretation and comparison of large macromolecular densities such as the two types of filamentous structures found here. As demonstrated in figure 5, examining their morphology in frozen-hydrated preparations was sufficient to assign septin3 to the filamentous polymers that we find in *spn*2Δspn3p-GFP cells with a high probability.

Material & Methods

Cell culture and starvation

S. pombe cells were plated by autoclaved toothpicks from frozen glycerol stock for 48hrs at 32 °C on YE5S (general purpose rich media) plate made from YE5S powder (Sunrise Science Products). Colonies were picked up by autoclaved toothpicks and put in 10ml homemade EMM supplemented with the relevant extra amino acids in 200ml flask, shaking at 25°C, 220 rpm for 15~17 hours to 0.4~0.8 OD. The liquid culture was then diluted to OD 0.05 in fresh EMM and relevant extra amino acids, shaking at 25 °C for 13~15 hours to 0.4~0.8 OD. Subsequently, the culture was diluted to OD 0.05 in fresh EMM (regular (20 g/L glucose) or low glucose (5 g/L glucose) with the respective extra amino acids and left shaking at 25 °C, 220 rpm. All flasks were covered with stainless steel caps without any additional sealing. To analyze cells at an exponential growth phase, cells were harvested about 13~15 hours after the last dilution step. To obtain fully starved conditions, cells were harvested 7 days after the last dilution.

Homemade Edinburgh Minimal Media (EMM): This EMM was made by 3.0 g/L potassium hydrogen phthalate, 2.2 g/L Na2HPO4, 5.0 g/l NH4Cl, 20.0 g/L glucose, 20 ml/L 50x salts stock (52.5 g/L MaCl2 • 6H2O, 0.735 g/L CaCl2 • 2H2O, 50.0 g/L KCl and 2.0 g/L Na2SO4), 1 ml/L 1000x vitamins stock (1.0 g/L pantothenic acid, 10.0 g/L nicotinic acid, 10 g/L inositol and 10 mg/L biotin) and 0.1 ml/L 10,000x minerals stock (5.0 g/L boric acid, 4.0 g/L MnSO4, 4.0 g/L ZnSO4 • 7H2O, 2.0 g/L FeCl2 • 6H2O, 0.4 g/L molybdic acid, 1.0 g/L KI, 0.4 g/L CuSO4 • 5H2O and 10.0 g/L citric acid). All the solution stocks were filtered and the media solution was autoclaved at 108 °C for 12 min before use.

Light microscopy

Glass slides were discharged by Emitech K100X Glow Discharge (Emitech, Fall River, MA) then covered with 8 µl Lectin from *Bandeiraea Simplicifolia* solution (2 mg/mL) (Sigma, St. Louis, MO) and air-dried. A drop of yeast culture was placed on the slides and after 10min incubation was rinsed with culture supernatant. Observations were made at 25°C under Nikon Plan Fluor 100x oil lens (Nikon, Japan) by Nikon Eclipse 80i (Nikon, Japan) and Zeiss 510 Laser Scanning Confocal Microscope (Zeiss, Germany). Data was collected and processed by NIS-Elements AR 3.2 for Nikon Eclipse 80i and ZEN 2009 for Zeiss 510. Actin was

fluorescently stained with LifeAct®-MCherry (36) or with Rhodamine-Phalloidin (Molecular Probes / Thermo Fisher Scientific, Waltham, MA).

Electron Microscopy and Tomography

Schizosaccharomyces pombe cells were directly high pressure frozen as a solution, while the fibroblast cells of Fig. 5D were plated onto carbon-coated sapphire discs as previously described (reviewed in: 40). Both specimens were high pressure frozen using a Wohlwend Compact-2 high-pressure freezer (Martin Wohlwend AG, Sennwald Switzerland). *S. pombe* samples destined for plastic section microtomy were freeze-substituted in 0.1% glutaraldehyde and 1% uranyl acetate in acetone for 48hrs and warmed from -90°C to -50°C in 8hrs (5°C per hour). Cells were then washed by acetone for 3 times and infiltrated in HM20 solution (25%, 33%, 50%, 67%, 75%, 100% in acetone) (Lowicryl HM20 Embedding Kit, Electron Microscopy Science, Hatfield, PA) over 5 days using Leica EMAFS (Leica, Vienna, Austria). Samples were then polymerized to blocks under Leica EMAFS UV light unit for 72hrs.

Plastic blocks were cut into ribbons of 80 (for single projection images) – 250 nm thick plastic sections (for tomographic reconstructions), depending on the questions asked, by Leica Ultracut microtome (Leica Inc., Vienna, Austria) using Diatome Ultra 45° (Diatome AG, Biel, Switzerland). For electron tomography, (Figs. 2D, 4A, 5B & C) the thickness of section was around 250nm. For immuno-labeling, the thickness of a section was around 80nm (Fig. 3). Ribbons were collected on formvar-coated Cu-Rn grids (Electron Microscopy Science, Hatfield, PA) or Carbon Film Finder grids (Electron Microscopy Science, Hatfield, PA), immuno-labeled (optional), stained by uranyl acetate (2% uranyl acetate in 70% methanol) for ~4min and Reynold's lead citrate for ~2min (the staining time was adjusted based on the thickness of the sections).

The immuno-labeling process was done in a humid chamber to prevent evaporation of the solvents. Sample grids were blocked in 1% non-fat dry milk in PBST (Phosphate Buffered Saline, Tween-20) for 30min. Primary antibody (homemade poly-clonal Rabbit IgG anti GFP, a generous gift from Pearson Lab, University of Colorado at Denver) was diluted in blocking buffer as 1:100. Second antibody (EM Goat anti-Rabbit IgG 15nm Gold, Ted Pella, Redding, CA), was diluted 1:20 in blocking buffer. Grids were placed on the drop of primary antibody solution for 2 hours. Grids were rinsed 3 times with PBST and then placed on the drop of

secondary antibody solution for 1 hour. Grids were again rinsed with PBST for 3 times and then with distilled water for another 3 times. Grids were finally dried by air at room temperature.

Single pictures of immuno-labeled sections were acquired with a FEI Philips CM100 TEM and AMT 2Kx2K bottom-mount digital camera. Dual-axis serial section montaged tomograms were acquired with a Tecnai TF30 300 kV FEG (FEI-Company, Hillsboro, OR, and Eindhoven, The Netherlands) transmission electron microscope using SerialEM (47) from ± 60° with 1° increments, recorded with a 4K GATAN Ultrascan-895 CCD camera (GATAN Inc. Pleasanton, CA). R-weighted back projection tomograms were computed using IMOD (48).

2-D projections and tomograms of vitrified sections (Fig. 5) were obtained by a similar procedure as described above, but with some obvious adaptations to the nature of frozen-hydrated specimens, following modified protocols originally described in Al-Amoudi et al. 2004 (31; see also: 26). Essentially, the specimens were high-pressure frozen as described above, but then the freeze-substitution step was omitted and the frozen blocks were directly sectioned with a cryo-ultra microtome into ~80nm thick vitrified sections (about the maximum thickness achievable that still induces only minor artefacts). Grids with vitreous cytoskeletons were mounted on a GATAN-626 cryo-holder and imaged in a Tecnai TF30. Images were obtained through a Tridiem Gatan Imaging Filter operating with a slit width of 20 eV around the zero-loss range and recorded onto the Ultracam-868, a prototype 4K lens-coupled CCD camera (Gatan Inc., Pleasanton, CA). A typical tilt-series ranged from ± 60° tilt angles with 2° tilting increments and a pixel size of 0.776 nm2. The imaging defocus was either -6 µm or -4 µm to produce sufficient phase contrast. Tomograms were calculated with R-weighted back projection using IMOD, the contrast transfer function (CTF) was corrected (49) and the strong, spread-out signals of the gold fiducial markers were computationally erased.

Acknowledgments:

We would like to thank Cindi Schwartz (Univ. of Colorado at Boulder, now at the Rocky Mountain Laboratories NIAID, Hamilton, MT) and Dr. Cedric Bouchet-Marquis (Univ. of Colorado at Boulder, now at FEI-Company, Hillsboro, OR) for their micrographs used in figures 2C & D and 5D respectively.

This work was supported by the following grants: Human Frontier Science Programme RGP0007-2010 (to D.B. (PI), A.H. and E.F. (co-PIs), NIH-NCRR P41-RR000594, NIH-NIGMS P41-GM103431 and P41-GM103431-43S1 (to A.H.) and a NIH-NIGMS / University of Colorado Biophysics training grant (T32 GM-065103) to M.L. C.I. acknowledges support by the Schlumberger Foundation / Faculty for the Future Fellowship.

References:

1: An H, Morrell JL, Jennings JL, Link AJ, Gould KL. (2004) Requirements of fission yeast septins for complex formation, localization, and function. Mol. Biol. Cell. **15**:5551-64.

2: De Virgilio C. (2012) The essence of yeast quiescence. FEMS Microbiol. Rev. **36**:306-39.

3: Su, S. S., Tanaka, Y., Samejima, I., Tanaka, K. and Yanagida, M. (1996). A nitrogen starvation-induced dormant G0 state in fission yeast: the establishment from uncommitted G1 state and its delay for return to proliferation. J. Cell. Sci. **109**:1347-1357.

4: Rødkaer SV, Faergeman NJ. (2014) Glucose- and nitrogen sensing and regulatory mechanisms in Saccharomyces cerevisiae. FEMS Yeast Res. **14**:683-96.

5: Makushok T, Alves P, Huisman SM, Kijowski AR, Brunner D. (2016) Sterol-Rich Membrane Domains Define Fission Yeast Cell Polarity. Cell. **165**:1182-96.

6: Sajiki K, Hatanaka M, Nakamura T, Takeda K, Shimanuki M, Yoshida T, Hanyu Y, Hayashi T, Nakaseko Y, Yanagida M. (2009) Genetic control of cellular quiescence in S. pombe. J. Cell. Sci. **122**:1418-29.

7: Laporte D, Courtout F, Salin B, Ceschin J, Sagot I. (2013) An array of nuclear microtubules reorganizes the budding yeast nucleus during quiescence. J. Cell. Biol. **203**:585-94.

8: Laporte D, Courtout F, Pinson B, Dompierre J, Salin B, Brocard L, Sagot I. (2015) A stable microtubule array drives fission yeast polarity reestablishment upon quiescence exit. J. Cell. Biol. **210**:99-113.

9: Spiliotis, E.T., and Nelson, W.J. (2006). Here come the septins: novel polymers that coordinate intracellular functions and organization. J. Cell. Sci. **119**:4-10.

10: Hartwell, L.H. (1971). Genetic control of the cell division cycle in yeast. IV. Genes controlling bud emergence and cytokinesis. Exp. Cell. Res. **69**:265-276.

11: Byers, B., and Goetsch, L. (1976). A highly ordered ring of membrane-associated filaments in budding yeast. J. Cell. Biol. **69**:717-721.

12: Weirich, C.S., Erzberger, J.P., and Barral, Y. (2008). The septin family of GTPases: architecture and dynamics. Nature reviews Mol. Cell. Biol. **9**:478-489.

13: Fares, H., Peifer, M., and Pringle, J.R. (1995). Localization and possible functions of Drosophila septins. Mol. Biol. Cell. **6**:1843-1859.

14: Hall, P.A., Russell, H.S.E., and Pringle, J.R. (2009). The Septins (Chichester, UK: Wiley InterScience).

15: Mostowy, S., Bonazzi, M., Hamon, M.A., Tham, T.N., Mallet, A., Lelek, M., Gouin, E., Demangel, C., Brosch, R., Zimmer, C., et al. (2010). Entrapment of intracytosolic bacteria by septin cage-like structures. Cell host & microbe **8**:433-444.

16: Hall, P.A., and Russell, S.E. (2004). The pathobiology of the septin gene family. The Journal of pathology **204**:489-505.

17: Roeseler, S., Sandrock, K., Bartsch, I., and Zieger, B. (2009). Septins, a novel group of GTP-binding proteins: relevance in hemostasis, neuropathology and oncogenesis. Klinische Pediatrie **221**:150-155.

18: Versele M, Thorner J. (2005) Some assembly required: yeast septins provide the instruction manual. Trends Cell Biol. **15**:414-24.

19: Wu JQ, Ye Y, Wang N, Pollard TD, Pringle JR. (2010) Cooperation between the septins and the actomyosin ring and role of a cell-integrity pathway during cell division in fission yeast. Genetics. 2010 Nov;186(3):897-915.

20: Bähler J, Wu JQ, Longtine MS, Shah NG, McKenzie A 3rd, Steever AB, Wach A, Philippsen P, Pringle JR. (1998) Heterologous modules for efficient and versatile PCR-based gene targeting in Schizosaccharomyces pombe. Yeast **14**:943-51.

21: Onishi M1, Koga T, Hirata A, Nakamura T, Asakawa H, Shimoda C, Bähler J, Wu JQ, Takegawa K, Tachikawa H, Pringle JR, Fukui Y. (2010) Role of septins in the orientation of forespore membrane extension during sporulation in fission yeast. Mol. Cell. Biol. **30**:2057-74.

22: Bertin A, McMurray MA, Thai L, Garcia G, 3rd, Votin V, Grob P, Allyn T, Thorner J, Nogales E (2010) Phosphatidylinositol-4,5-bisphosphate promotes budding yeast septin filament assembly and organization. J. Mol. Biol. **404**:711-731.

23: Sirajuddin M, Farkasovsky M, Hauer F, Kuhlmann D, Macara IG, Weyand M, Stark H, Wittinghofer A. (2007) Structural insight into filament formation by mammalian septins. Nature **449**:311-315.

24: Petrovska I, Nüske E, Munder MC, Kulasegaran G, Malinovska L, Kroschwald S, Richter D, Fahmy K, Gibson K, Verbavatz JM, Alberti S. (2014) Filament formation by metabolic enzymes is a specific adaptation to an advanced state of cellular starvation. eLife. **3**:e02409.

25: Hoenger A, McIntosh JR. (2009) Probing the macromolecular organization of cells by electron tomography. Curr. Opin. Cell Biol. **21**:89-96.

26: Bouchet-Marquis C, Hoenger A. (2011) Cryo-electron tomography on vitrified sections: a critical analysis of benefits and limitations for structural cell biology. Micron **42**:152-62.

27: Liu Z, Lavis LD, Betzig E. (2015) Imaging Live-Cell Dynamics and Structure at the Single-Molecule Level. Mol. Cell. **58**:644-659.

28: Evans JE, Browning ND. (2013) Enabling direct nanoscale observations of biological reactions with dynamic TEM. Microscopy (Oxford). **62**:147-56.

29: Dubochet, J., Adrian, M., Chang, J.J., Homo, J.C., Lepault, J., McDowall, A.W., Schultz, P., (1988). Cryo-electron microscopy of vitrified specimens. Q. Rev. Biophys. **21**:129-228.

30: Hsieh, C.E., Marko, M., Frank, J., and Mannella, C.A. (2002) Electron tomographic analysis of frozen-hydrated tissue sections. J. Struct. Biol. **138**:63-73.

31: Al-Amoudi, A., Chang, J.J., Leforestier, A., McDowall, A., Salamin, L.M., Norlén, L.P.O., Richter, K., Sartori Blanc, N., Studer, D., and Dubochet, J. (2004) Cryo-electron microscopy of vitreous sections. EMBO J. **23**:3583-8.

32: Kolotuev I, Schwab Y, Labouesse M. (2009) A precise and rapid mapping protocol for correlative light and electron microscopy of small invertebrate organisms. Biol. Cell. **102**:121-32.

33: Kukulski W, Schorb M, Welsch S, Picco A, Kaksonen M, Briggs JA. (2011) Correlated fluorescence and 3D electron microscopy with high sensitivity and spatial precision. J. Cell. Biol. **192**:111-119.

34: Schwartz CL, Sarbash VI, Ataullakhanov FI, McIntosh JR, Nicastro D. (2007) Cryo-fluorescence microscopy facilitates correlations between light and cryo-electron microscopy and reduces the rate of photobleaching. J. Microsc. **227**:98-109.

35: Briegel A, Chen S, Koster AJ, Plitzko JM, Schwartz CL, Jensen GJ. (2010) Correlated light and electron cryo-microscopy. Methods Enzymol. **481**:317-41.

36: Riedl J, Crevenna AH, Kessenbrock K, Yu JH, Neukirchen D, Bista M, Bradke F, Jenne D, Holak TA, Werb Z, Sixt M, Wedlich-Soldner R. (2008) Lifeact: a versatile marker to visualize F-actin. Nat. Methods. **5**:605-7.

37: Griffiths G, Lucocq JM. (2014) Antibodies for immunolabeling by light and electron microscopy: not for the faint hearted. Histochem. Cell Biol. **142**:347-60.

38: Kellenberger, E. (1991). The potential of cryofixation and freeze substitution: observations and theoretical considerations. J. Microscopy **161**:183-203.

39: McDonald K, Schwarz H, Müller-Reichert T, Webb R, Buser C, Morphew M. (2010) "Tips and tricks" for high-pressure freezing of model systems. Methods Cell Biol. **96**:671-93.

40: Dubochet J, Zuber B, Eltsov M, Bouchet-Marquis C, Al-Amoudi A, Livolant F. (2007) How to "read" a vitreous section. Methods Cell Biol. **79**:385-406.

41: Christensen, AK. (1971) Frozen thin sections of fresh tissue for electron microscopy, with a description of pancreas and liver. J. Cell Biol. **51**:772-804.

42: McDowall AW, Chang JJ, Freeman R, Lepault J, Walter CA, Dubochet J. (1983) Electron microscopy of frozen hydrated sections of vitreous ice and vitrified biological samples. J. Microsc. **131**:1-9.

43: Bremer A, Millonig RC, Sütterlin R, Engel A, Pollard TD, Aebi U. (1991) The structural basis for the intrinsic disorder of the actin filament: the "lateral slipping" model. J. Cell Biol. **115**:689-703.

44: Lukoyanova N, Baldwin SA, Trinick J. (2008) 3D reconstruction of mammalian septin filaments. J Mol. Biol. **376**:1-7.

45: Bouchet-Marquis C, Pagratis M, Kirmse R, Hoenger A. (2012) Metallothionein as a clonable high-density marker for cryo-electron microscopy. J. Struct. Biol. **177**:119-27.

46: Morphew MK, O'Toole ET, Page CL, Pagratis M, Meehl J, Giddings T, Gardner JM, Ackerson C, Jaspersen SL, Winey M, Hoenger A, McIntosh JR. (2015) Metallothionein as a clonable tag for protein localization by electron microscopy of cells. J. Microsc. **260**:20–29.

47: Mastronarde DN. (2005) Automated electron microscope tomography using robust prediction of specimen movements. J. Struct. Biol. **152**:36-51.

48: Kremer, J.R., Mastronarde, D.N. & McIntosh, J.R. (1996) Computer visualization of three-dimensional image data using IMOD. J. Struct. Biol. **116**:71-76.

49: Xiong Q, Morphew MK, Schwartz CL, Hoenger A, Mastronarde DN. (2009) CTF determination and correction for low dose tomographic tilt series. J. Struct. Biol. **168**:378-87.

Figure Legends

Figure 1:

Spn1p-RFP and spn3p-GFP expression and localization patterns. (**A1-3**) Exponentially growing cells expressing spn3p-GFP (**A1**; green) spn1p-RFP (**A2** red), overlaid with a DIC image in **A3**. Both proteins can be found together, evenly distributed throughout the entire cytosol forming little clusters, and accumulated at the periphery of septa in dividing cells (arrows; see also Fig. 4B). However, spn1p-RFP appears to be less abundant. (**B1-3**) Exponentially growing *spn2*Δ cells expressing spn3p-GFP (**B1**) and spn1p-RFP (**B2**). The panels are merges of two different images indicated by the dotted line. Both proteins assemble into globular clusters (see also Fig. 5A) or short filamentous assemblies. Spn3p-GFP can be found on septa while spn1p-RFP seems absent, or only present at very low concentration (see also overlay (**B3**) and arrows). (**C1-3**) Starved cells expressing spn3p-GFP (**C1**) and spn1p-RFP (**C2**), after seven days of culturing in low glucose medium (LMM). Both proteins aggregate and merge together into one single clump per cell, except for minor traces of protein that remain distributed throughout the cytosol. Evident from the overlay panel, not all clusters contain both proteins (arrows). (**D1-3**) Starved *spn*Δ cells expressing spn3p-GFP (**D1**) and spn1p-RFP (**D2**) after seven days of culturing in low glucose medium. Both proteins form prominent elongated filamentous structures, typically only one per cell. The large elongated assemblies in each cell, all seem to contain spn1p-RFP or both, but interestingly, some cells lack the spn3p-GFP component (arrows; see overlay **D3**).

Figure 2:

Correlative light and electron microscopy performed on *spn2*Δ cells expressing spn3p-GFP. Arrows connect identical features that we can identify in the phase contrast image, fluorescence image and tomographic reconstruction of starved cells that have formed filamentous spn3p-GFP assemblies after seven days of culturing in low glucose medium. A 250-nm thick plastic section of high-pressure-frozen, lowicryl-K4M embedded, cells were mounted on an electron microscopy grid. An identical region on the grid was imaged on the grid by phase contrast (**A**: LM), by fluorescence light microscopy (**B**) and, after transfer to a 300kV Tecnai-F30, with low-magnification as micrograph (**C**: EM) and a thin (4.0 nm) computational section through an electron tomogram (**D**). Green arrows connect the sites of the spn3p-GFP assemblies. Blue arrows connect other easily recognizable common features of the

different panels such as high-density polymers, granules and entire cells. The red frame in (**A**) corresponds to the image area shown in (**B**). The red frame in (**C**) corresponds to the image area shown in (**D**).

Figure 3:

Immuno-gold-labeling on spn3p-GFP expressing *spn2*Δ (**A**) and wild type cells (**B**). Labeling was achieved with an anti-GFP primary antibody and a secondary antibody conjugated to 15nm gold particles (arrows). (**A**) Immunolabeling provides another mode of correlation between the fluorescence signals (inset panel) and EM density data and confirms the presence of spn3p-GFP in the filamentous structures observed in starved *spn2*Δ cells after seven days of culturing in low glucose medium (red arrows in both panels). The inset panels in **A** and **B** show Spn3GFP fluorescence images of the corresponding cells in green, and actin staining in red (upper panels: LifeAct®-mCherry, lower panels: Rhodamine-Phalloidin). The lower insets display actin staining with Rhodamine-Phalloidin, overlaid with a phase-contrast image, to test for potential differences with LifeAct®-mCherry (see also, Fig. 4). **B**: The anti-GFP primary antibody binds to spn3p-GFP at the outer ring formed by the septa and the old cell wall in dividing wild type cells during exponential growth (red arrow). The inset panels show dividing cells in a projection of a thin, confocal slice (lower insets), and of an entire confocal 3-D image stack that is slightly tilted to better visualize the ring shaped spn3p-GFP and inner actin distribution (upper inset). In septa, actin (red: Phalloidin, or LifeAct-mCherry labeled) is surrounded by spn3p-GFP (green), confirming that the latter mostly locates closer to the cell periphery, forming a ring like structure.

Figure 4:

Filamentous septin assemblies in plastic sections: Comparison of 80-nm plastic sections of high-pressure frozen, freeze-substituted and plastic-embedded starved, spn3p-GFP expressing *spn2*Δcells (**A**), and spn3p-GFP expressing cells (**B**). Both cells were starved for seven days in low glucose medium, as described. The upper inset panels show the corresponding spn3p-GFP fluorescence (green) as well as LifeAct®-mCherry, which marks F-actin (see also Fig. 3). In starvation F-actin forms long filamentous structures in both cell types. The lower inset panels show EM overviews of cells at corresponding conditions. (**A**) In *spn2*Δ spn3p-GFP cells, the F-actin bundles and filamentous spn3p-GFP assemblies do not overlap (upper inset panel). (**B**) None of the filamentous spn3p-GFP assemblies were present in starved wild type cells even though F-actin forms the same type of bundles as in *spn2*Δ cells (upper inset panel). Otherwise,

the cytosol of both cell types look very similar. Note the dense vacuoles, and the lighter stained, fragmented mitochondria, which are densely decorated with ribosomes.

Figure 5:

Septin and F-actin bundles observed in sections of unstained, frozen-hydrated specimens: We have taken advantage of the superb molecular structure preservation of vitrified sections to compare the morphology of F-actin bundles with that of spn3p-GFP aggregates in wildtype (**A**: exponentially growing; **C**: starved) and *spn2*Δ cells and after seven days of glucose starvation (**B**). Panel **C** shows a starved wildtype cell that shows F-actin bundles, but no septin assemblies (see also Fig. 4B). Panel **D** shows a vitrified section through the stressfibers of a 3T3 fibroblast, allowing for a direct comparison of shape and dimensions with the F-actin bundles in **C**. The excellent molecular preservation in frozen-hydrated specimens reveals distinct differences between septin (**A,** including insets; **B**) and actin bundles (**C**) or actin stressfibers (**D**). Both, F-actin bundles and stress fibers are morphologically quite different from spn3p-GFP assemblies, which form tighter curves and show a fine, but well visible, repetitive pattern of globular domains while appearing less ordered at the overall bundle level, especially in the clusters found in exponentially growing state (**A**). The lateral packing of F-actin bundles is much tighter than that of septin bundles (compare the width of 5 strands within actin bundles (visible in panels **C & D**) and septin bundles (panels **A & B**). Insets in **A**, **B** and **C** show corresponding cells with fluorescence labeling of septin-3 (spn3p-GFP) and actin (LifeAct®-mCherry).

Figure 6:

Western blot with anti-GFP antibodies marking septin-GFP constructs (spn1-GFP to spn7-GFP) and, as control, wildtype during exponential growing phase (EG) and after six days of starvation (SD6). Septins 5-7 are septins expressed mostly during meiosis, and therefore are relatively sparse, especially in non-dividing, starved cell cultures. Septins 1-4 are strongly expressed under both conditions, EG and SD6, but seem to fragment much more during starvation, most likely caused by a tuned-down expression of fresh protein. Tubulin and actin expressions are significantly reduced after six days of starvation.

Tables:

Table 1:

558	wildtype strain	h-	Fig. 1
2738	spn2Δ spn3p-GFP	h+ spn3p-GFP::KanR spn2::ura4 ade6-M210 ura4-D18 leu1-32	Figs. 1-5
2739	spn3p-GFP	h- spn3p-GFP::KanR ade6-M210 ura4-D18 leu1-32	Figs. 1, 3 & 4
2740	spn2p-GFP	h- spn2-GFP::KanR ade6-M210 ura4-D18 leu1-32	Fig. 1
4956	spn1p‐tagRFP spn3p‐GFP	h- spn1-TagRFP::kanR spn3-GFP::kanR	Fig. 1
5053	spn2Δ spn1p- tagRFP spn3-GFP	h- spn1-TagRFP::kanR spn2-Δ1::ura4+ spn3-GFP-kanR ura4-D18	Fig. 1
3476	spn2Δspn3p-GFP LifeAct®-mCherry	h- spn2-Δ1::ura4+ spn3p-GFP-kanR leu1-32::pAct1:LifeAct®-mCherry::leu1+ ura4-D18	Fig. 3
3480	spn3p-GFP LifeAct®-mCherry	h- spn3p-GFP-kanR leu1-32::pAct1:LifeAct®-mCherry::leu1+ ura4-D18	Fig. 3

Strain codes and genetic details (for strains 2738, 2739 and 2740 see (1))

Figure 1

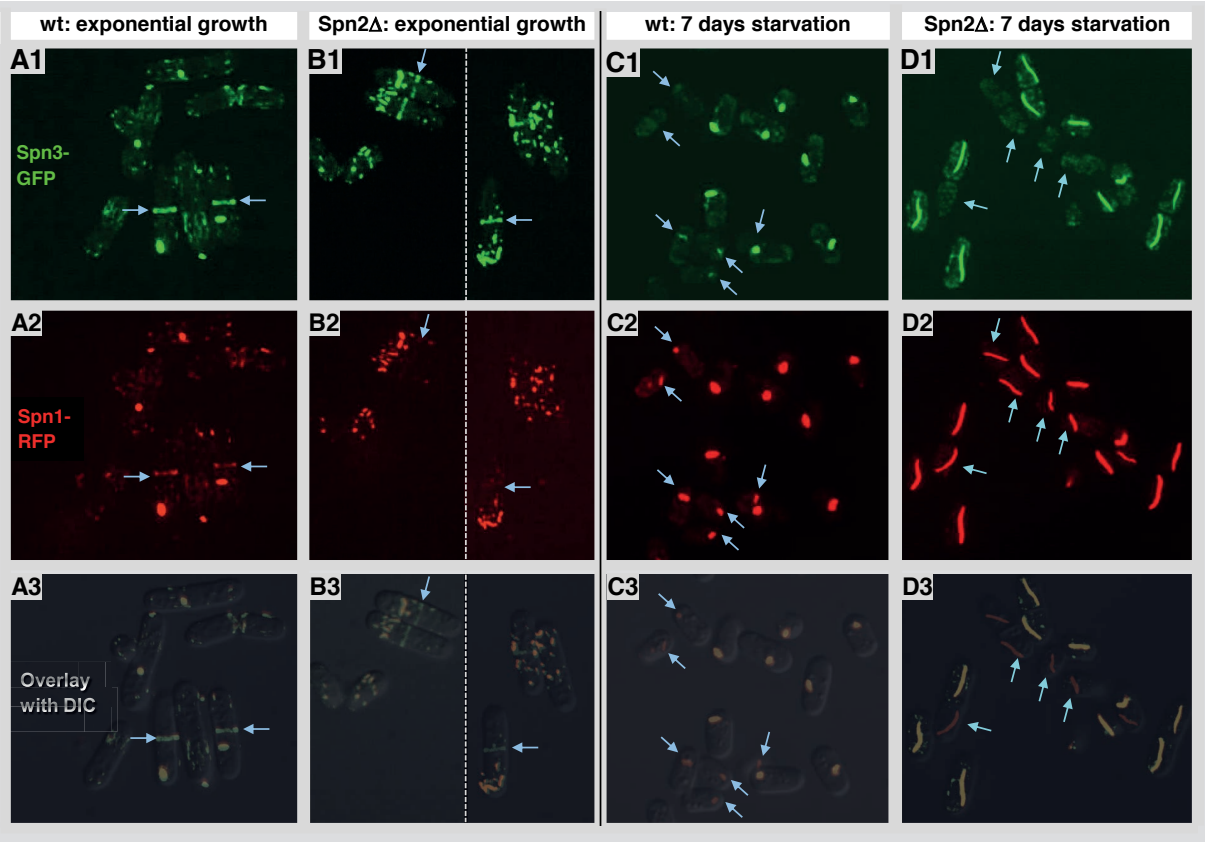

Figure 2

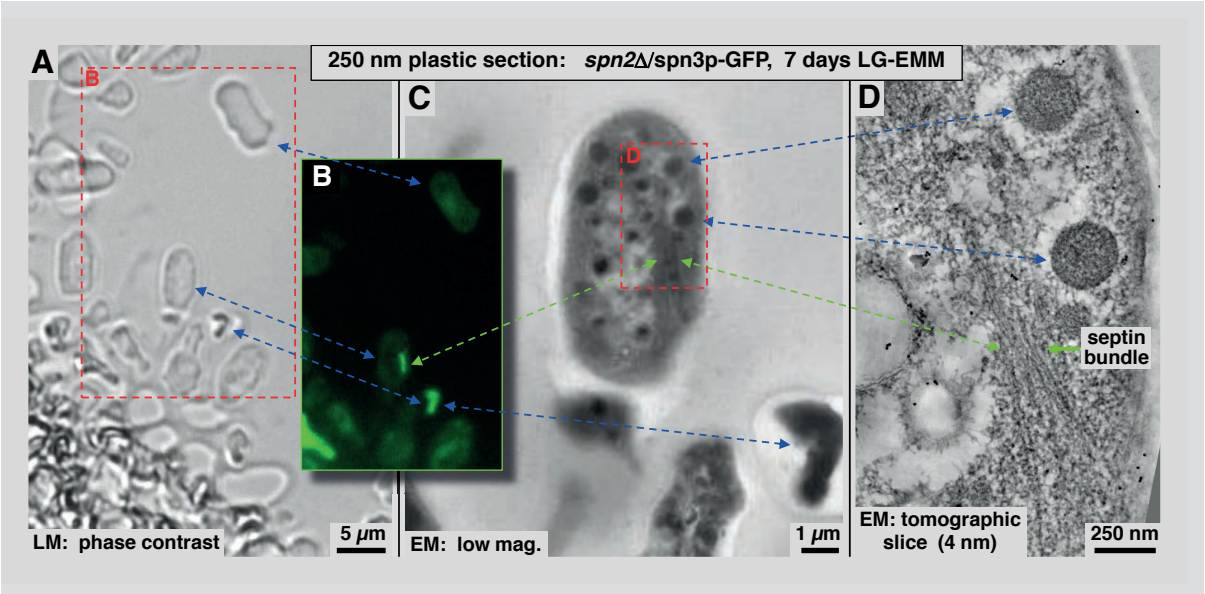

Figure 3

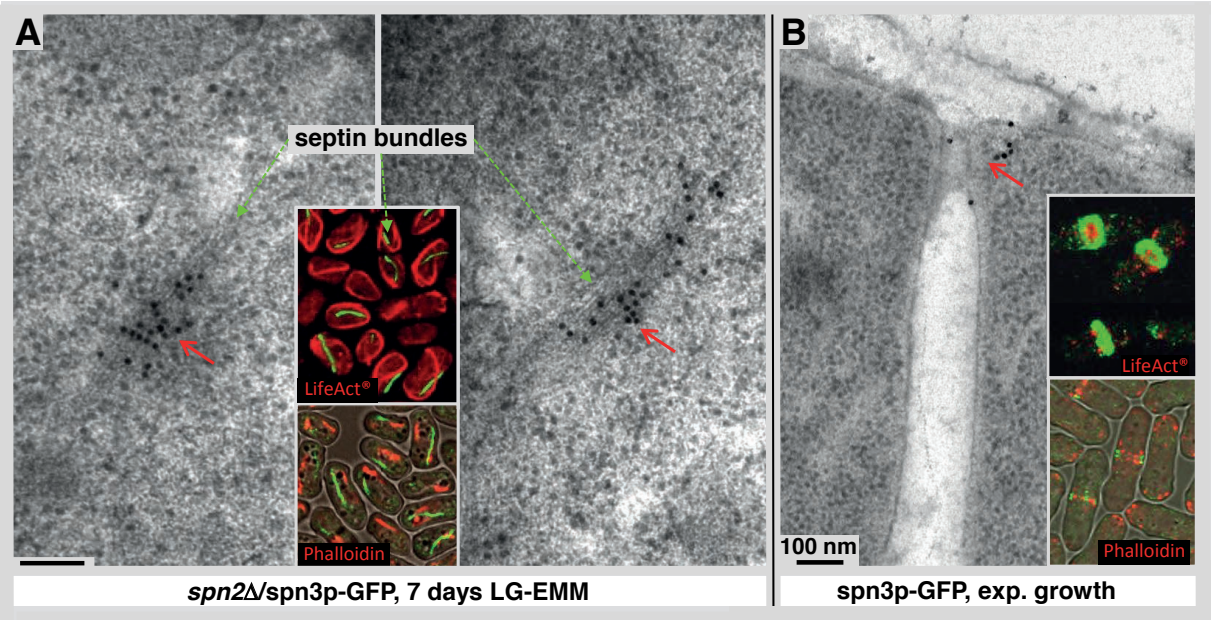

Figure 4

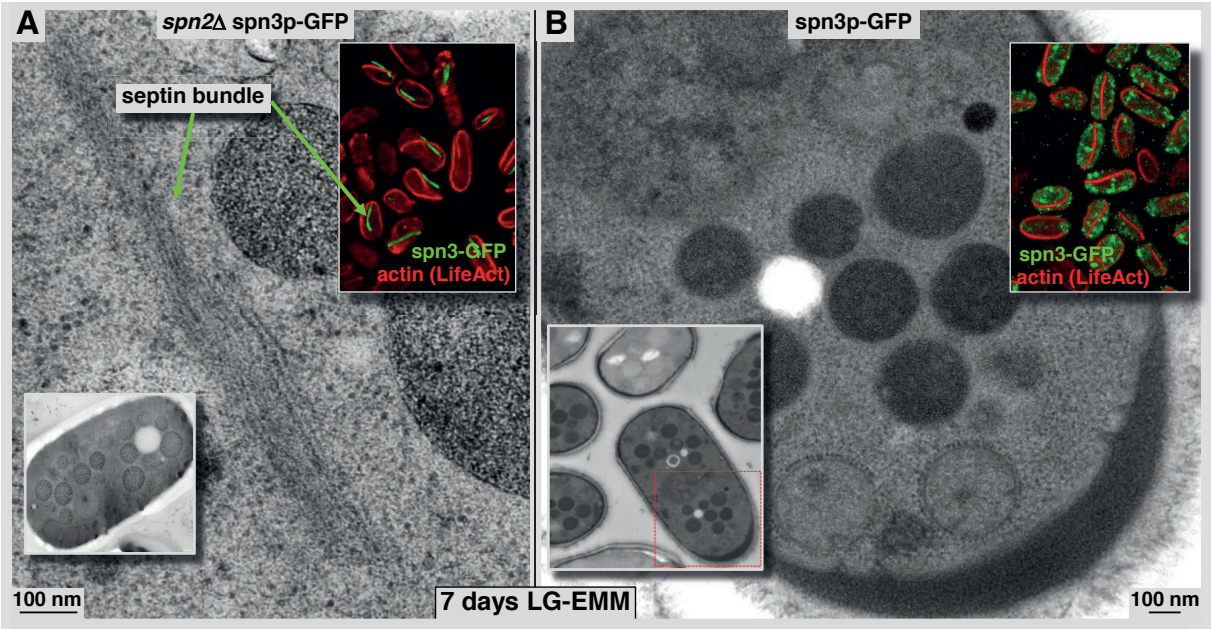

Figure 5

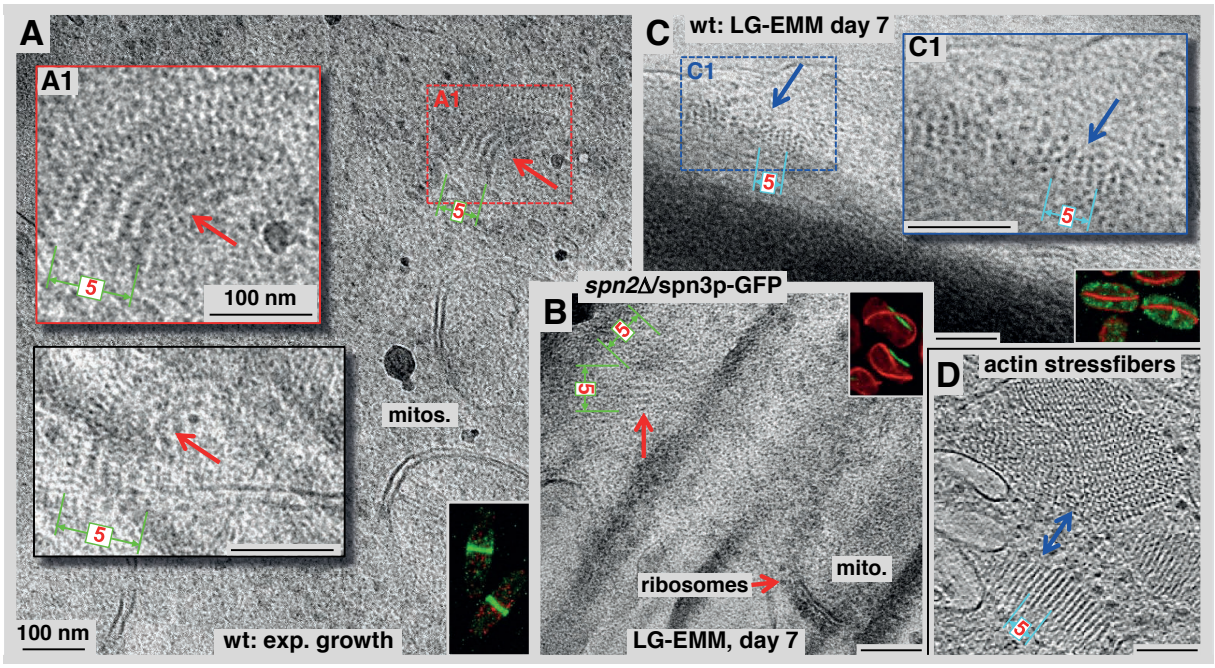

Figure 6

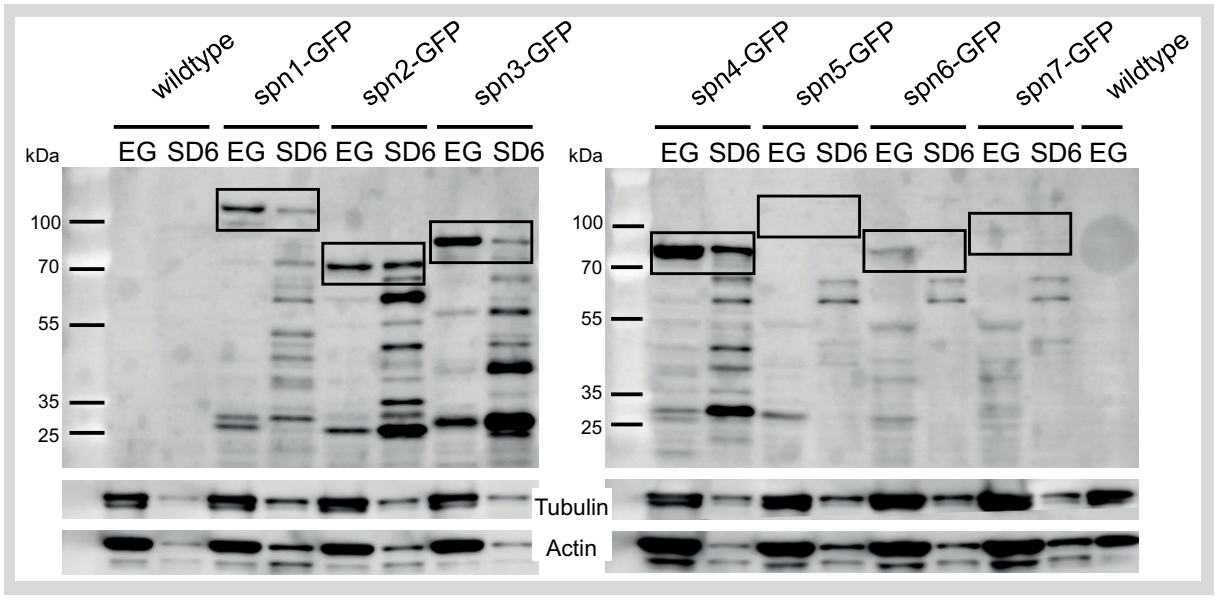

3 Results – Part 2: Unpublished Data

3.1 Experimental conditions influence the cytoplasmic state of cells

In order to describe and investigate the phenomenon of cytoplasmic freezing (CF), I first had to develop standardized assays to induce, capture and measure the cytoplasmic state. This was necessary, since the investigation of CF was mainly done in Prof. Ernst-Ludwig Florin's laboratory in Austin (Tx, USA) before I started my PhD. The challenge was, to obtain comparable results in both laboratories despite having very different infrastructure.

The first challenge was to measure the cytoplasmic state of cells. In the Florin lab they used optical tweezers and single particle tracking (SPT) of lipid droplets with an extremely high acquisition frame rate to precisely determine a measure for the viscosity of the cytoplasm, the alpha value (see section 0). We had neither an optical tweezer setup nor the possibility to image fast enough to apply their SPT analysis strategy. In addition, we needed fast and easy methods to check for CF in different conditions and in various mutant strains.
I developed several methods to evaluate the cytoplasmic state of cells: a qualitative, fast, non-invasive method to evaluate lipid droplet motion (qualitative readout), a quantitative description of lipid droplet dynamics by determining the co-localization of the lipophilic dye Bodipy over time using the Pearson correlation coefficient (Bodipy CC readout), and a quantitative description of mitochondria dynamics by SPT and subsequent mean squared displacement analysis (mitochondria MSD readout). All these methods are described in the manuscript in section 2.1.
The second challenge was to capture the cytoplasmic state of cells in the starvation culture by microscopy imaging. For this, the cells needed to be mounted for microscopy, meaning that a small aliquot of cells needed to be transferred from its culturing environment to a container where the cells could be imaged in. The cytoplasmic state of the imaged cells needed to reflect the state of cells in the starvation culture, not a cytoplasmic state that cells adopted acutely during the imaging or the prior preparation. If not stated otherwise, I used an imaging chamber similar to one developed by Chieze Ibeneche in the Florin lab. She built this small imaging chamber by gluing two coverslips together with parafilm, whereby the parafilm additionally acted as a spacer, protecting the cells from mechanical compression. Instead of two coverslips, I used an imaging dish we commonly use in the lab (see materials and methods) with a round

coverslip on top of its glass bottom (see Figure 5A). To immobilize the cells on the glass bottom, I used a coating of poly-L-lysine if not stated otherwise. Poly-L-lysine is a positively charged polymer that binds negatively charged cells by electrostatic interaction. In the next section, I will describe the factors that can acutely influence the cytoplasmic state.
Thirdly, the exact experimental conditions used for culturing the cells during the long starvation period needed to be standardized. In the following section, I will describe the culturing parameters that I found to influence the cytoplasmic state of cells in deep starvation.

Generally, in this chapter I will describe the cytoplasmic state of cells primarily by using a 2-D visualization of the qualitative readout. As we showed in detail in the manuscript in section section 2.1, this nicely revealed CF – the drastic immobilization that the cytoplasm undergoes upon entering deep starvation under standard conditions (see Figure 5B). For these experiments, we dilute exponentially growing cells with low glucose EMM medium (EMMLG: 0.5% glucose instead of 2% for EMM2). In this medium, the culture reaches stationary phase after 2 days and is continuously cultured for up to 8 days. We call this cell culture "starvation culture" and refer to the time the cells spend in this culture as starvation days (SD2-SD8). We divide the 8- starvation period into two phases with SD5, the day around which the cells usually induce CF. The first phase from SD2-4/5 is referred to as "early starvation" and the second phase from SD5/6-8 as "deep starvation".

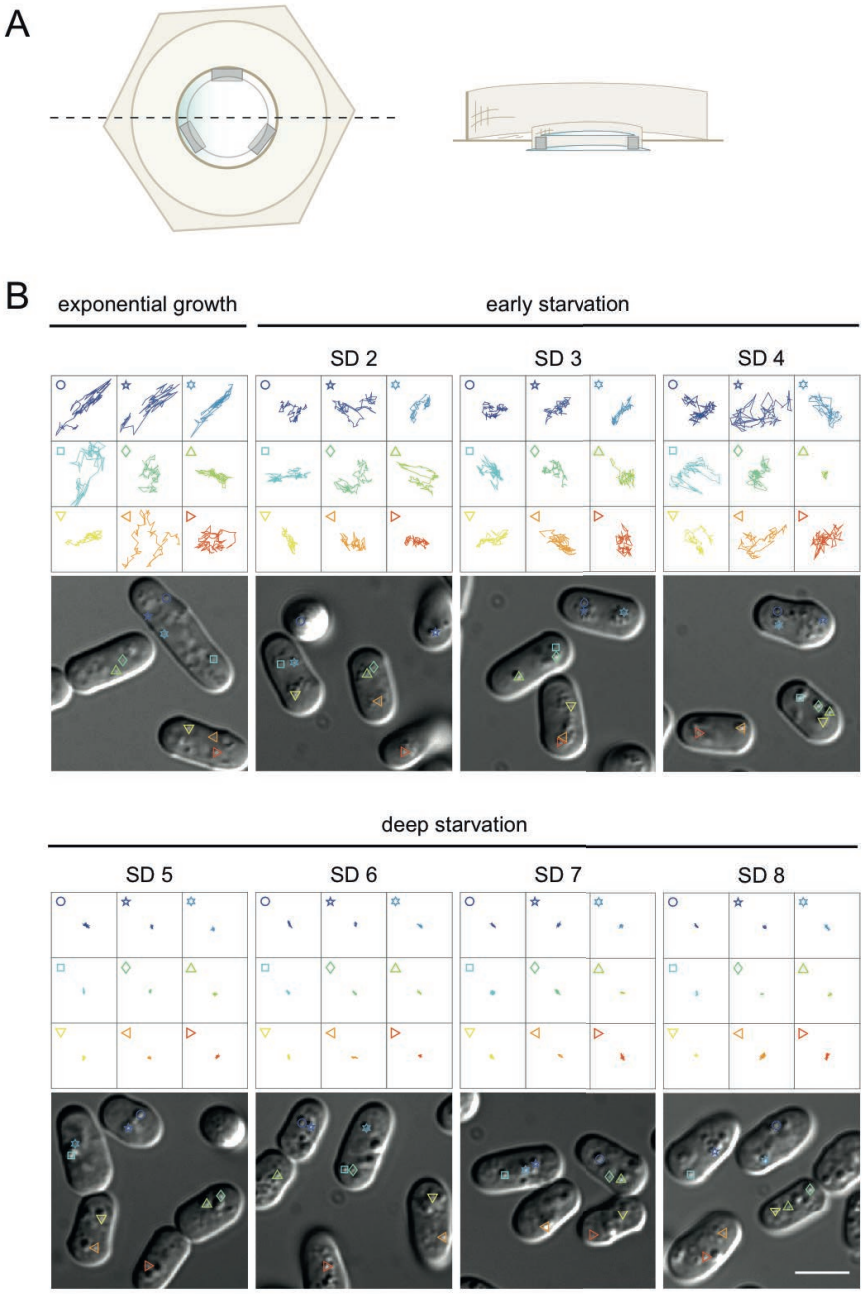

Figure 5. Qualitative evaluation of the cytoplasmic state of cells during starvation.

(**A**) Schematic drawing of the imaging chamber (top view and cross section). It consists of a live imaging dish with a coverslip on top of the glass bottom, with parafilm acting as a spacer in between. (**B**) Lipid droplet trajectories extracted from 25sec movies (4frames/sec, droplets depicted in lower DIC images) of cells in exponential growth (upper panel, left), cells in early starvation (SD 2-4; upper panel, right) and cells in deep starvation (SD 5-8; lower panel). Scale bar is 5µm in all panels.

3.1.1 Cell mounting conditions influence the cytoplasmic state of cells

3.1.1.1 Cell mounting conditions can fluidize the cytoplasm of CF cells

At the beginning of my PhD, I imaged cells by mounting them on a standard microscopy slide. I used cells from a starvation culture aliquot that I had left to sediment prior to imaging, which

increased the cell density. When observing lipid droplets from movies acquired under these conditions, I saw motion in every cell. The first, easy to resolve issue was the actual microscopy. In the lab, we had used bright field imaging mainly for finding cells. We had the optics necessary for differential interference contrast imaging (DIC), but it was not commonly applied. I acquired DIC images, but the movies I acquired were rather noisy. Flickering background noise interferes heavily with the perception of structural motion, making it hard to evaluate the degree of motion. I resolved this technical issue by improving the DIC imaging conditions, and was able to acquire movies with a good quality. However, we realized that the lipid droplets were still not as completely immobilized at SD6-8, as we would have expected for CF cells.

We started to suspect that the acquired movies did not reflect the actual cytoplasmic state of cells in culture, but rather that the mounting had acutely influenced the mechanical properties of the cytoplasm.

Thus, I tested the influence of the mounting method on the cytoplasmic state of cells in deep starvation by comparing different methods. As the default method, I used an imaging chamber as described above (see Figure 5A), equivalent to the mounting method that Chieze Ibeneche had been using for years to investigate CF cells. In order to evaluate the cytoplasmic state of cells, I used the motion of lipid droplets captured in DIC movies, as introduced above.

It is difficult not to become biased when staring at and evaluating many movies of barely moving lipid droplets. To minimize this bias, I anonymized the file names such that I did not know the mounting condition leading to the movie I analysed. I made the motion evaluation more quantitative by classifying the cells into 8 classes depending on the cell's lipid droplet motion. Cells where every single lipid droplet was clearly moving were classified into class 1 cells, and cells where no lipid droplet displayed any visible motion at all into class 8. The classes in between were defined rather cryptically by the kind of lipid droplet motion and distribution of cells. In the end, I used the amount of class 8 cells to define the cytoplasmic state of a cell population.

When imaging cells in deep starvation using the imaging chamber described above, an average of 60% of the cells showed no lipid droplet motion at all. With cells from the same starvation culture, I carried out the following tests.

The first condition I tested was the standard mounting method for live imaging of exponentially growing cells we used in the lab. Cells were transferred to a live imaging dish, where they were washed and covered with medium. Normally, standard EMM medium is used for the washing and incubation. However, we wanted to avoid a change of culturing medium for our CF cells,

since we were not sure if such a change had an influence on the cytoplasmic state. Therefore, I used original starvation culture medium that I had filtered to exclude the cells. Under these conditions the cells stayed in CF similar to the imaging chamber condition, with around 60% of cells displaying no motion at all (see also Figure 6B).

Next, I tested if I could concentrate the cells by letting them sediment in an Eppendorf tube prior to the mounting and imaging under the standard live imaging conditions. After 100 minutes of sedimentation, the number of cells showing no motion at all dropped to 30% (see also Figure 6C). This indicated that cell sedimentation indeed acutely influenced the cytoplasmic state to become slightly more fluid-like.

Lastly, I tested whether I could capture the cytoplasmic state using a conventional microscope slide with a coverslip on top of the cells. Instead of coating the slide with poly-L-lysine, I immobilized the cells mechanically. I used a minimal culture volume to prevent the coverslip from sliding on the medium film. Additionally, I gently pushed the coverslip to one side as far as possible, thereby gently compressing the cells and immobilizing on one side of the coverslip. This was the mounting method I had used initially and where I hardly observed cells with no lipid droplet motion. Indeed, this method also reduced the fraction of cells showing no lipid droplet motion to around 30% (see also Figure 6D).

In summary, I showed that sedimentation and mechanical compression have an influence on the cytoplasmic fluidity. Therefore, it was very likely that the residual lipid droplet motion I had observed was indeed based on an acute liquidation of the cytoplasm by my mounting method.

From then on, my mounting method of choice for a fast evaluation of the cytoplasmic state of a cell population was the imaging chamber. With this method, the time from taking out the cells from the starvation culture to the actual imaging was very short. The cells did not experience any manipulation and stayed in their culturing medium at the same cell concentration. Additionally, the DIC imaging I applied for capturing the lipid droplet motion gave the best results using this method, since the water phase that the polarized light passed was very small.

The second mounting method used later in my PhD, was the standard live imaging method. When establishing the experimental methods for screening the deletion library with the aim of identifying genes that were required for CF, I found that the cells stayed in CF even when I used standard EMM without glucose (EMM0) instead of the filtered original starvation medium (see section 3.4.1.1). I used this method, when I had to do prolonged imaging of up to 1h, or when I needed to incubate cells with a defined concentration of a drug or a fluorescent dye.

On a technical note: I realized while writing this thesis, that the effect of the mounting method on the cytoplasmic fluidity was actually very small. It was so small that it was hard to visualize with the 9 lipid droplet trajectories. I will discuss this in more depth in section 4.1.

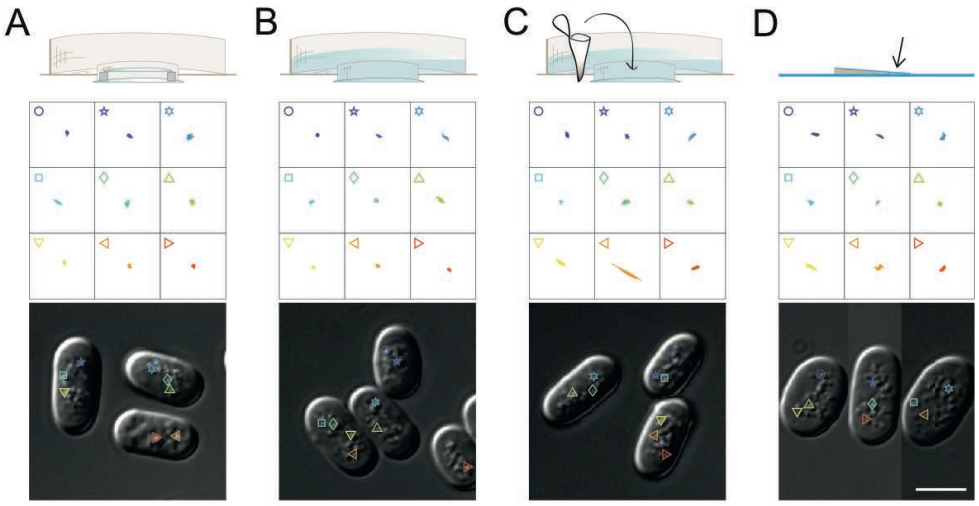

Figure 6. Different cell mounting conditions.

(**A**) Lipid droplet trajectories extracted from 25sec movies (4frames/sec, droplets depicted in lower DIC images) of cells imaged from the default imaging chamber (schematically drawn on top). The chamber consists of the glass bottom of a live imaging dish, and a coverslip that is glued onto and spaced from the bottom by parafilm. (**B**) Lipid droplet trajectories as in (A) but from cells mounted onto the live imaging dish that were covered with the filtered original starvation medium. (**C**) Lipid droplet trajectories as in (A) from cells mounted as in (B) but with 100min sedimentation prior to the mounting. (**D**) Lipid droplet trajectories as in (A) of cells mounted on a conventional microscope slide covered by a coverslip under minimal culture volume to add stability. Additionally, the coverslip was gently moved sideward as far as possible to mechanically immobilize the cells by gentle compression. The image is a combination of 3 cells from one movie that were initially further apart. Scale bar is 5µm.

3.1.1.2 Mounting conditions that immobilize the cytoplasm in non-CF cells

After having established the imaging chamber as the best method to capture CF cells, I used this method to describe the CF state in more detail. We were interested in the structure of the cytoskeleton in CF, and quickly realized that the microtubules disappeared and F-actin rearranged into prominent shoelace cables in CF (see manuscripts in section 2.1 and 2.2).

I imaged the fluorescent cytoskeletal marker strains in early starvation to see when and how the cytoskeleton changed its structure. I soon realized that the cytoskeletal phenotypes from cells in early starvation were very heterogeneous. After a while I started to suspect that this was due to the time the cells spent in the imaging chamber prior to the imaging.

To test this, I imaged SD2 cells expressing fluorescent markers for microtubules (GFP-atb2; (Pardo & Nurse, 2005)) and for F-actin (Lifeact-mCherry; (J. Huang et al., 2012; Riedl et al., 2008)) in 10 minute intervals. To exclude a phototoxic effect from the fluorescence imaging, I

prepared 3 parallel imaging chambers that I kept in the dark. Strikingly, the morphology and dynamics of the cytoskeletal elements were indeed quite different in cells that were in the imaging chamber for 24 min compared to cells that were in the chamber for only 3 min (see Figure 7A). The microtubules gradually disappeared, whereas the F-actin formed big assemblies and lost its dynamicity.

I repeated the same experiment with cells expressing the mitochondria marker cox4p (see section 3.3 and (Yaffe et al., 2003)). Mitochondria fragment during early starvation, and the fragmented mitochondria in CF cells in deep starvation are completely immobilized, similar to the lipid droplets (see manuscript in section 2.1, and section 3.3). I found that over time, the mitochondria increasingly fragmented and significantly reduced their mobility while in the imaging chamber (see Figure 7B).

I quantified this effect by single particle tracking and subsequent mean squared displacement (MSD) analysis of fragmented mitochondria (see Figure 7C and section section 2.1). The MSD of mitochondria in SD3 cells was highest immediately after the cell mounting and gradually decreased during time that the cells spent in the imaging chamber (see Figure 7D; left panel). With mitochondria from CF cells at SD6 no such effect was observed (see Figure 7D; right panel). The timing of the acute immobilization in this experiment seems accelerated compared to the qualitative experiments described above. This may be due to the fact that here the 3 movies came from cells in the same imaging chamber instead of different chambers, which seems to accelerate the immobilization of the mitochondria.

Taken together, early starvation cells showed a behaviour very reminiscent of CF after a short time in the imaging chamber. They rearranged their cytoskeleton, and fragmented and immobilized their mitochondria. I call this phenomenon “rapid freezing”, as the immobilization and intracellular rearrangement occurred within minutes in contrast to several days in the case of CF.

Interestingly, the induction of rapid freezing depended on the position of the cells in the imaging chamber. Cells in the centre of the chamber immobilized their cytoplasm whereas cells at the periphery stayed very dynamic (see Figure 7C). This remained the case when I sealed the chamber off using silicone or VALAP – both air permeable materials – to prevent the cells from drying out.

These results strongly suggested, that for cells to undergo rapid freezing, they required low oxygen conditions. Another observation supporting this hypothesis was that the GFP of the

mitochondria marker cox4-GFP became a red fluorescent protein under rapid freezing conditions. GFP was previously reported to be photoactivatable under near-anaerobic conditions (Elowitz, Surette, Wolf, Stock, & Leibler, 1997; Sawin & Nurse, 1997). I tried testing this dependency on oxygen levels by incubating cells under conditions where argon gas had replaced the air surrounding the cells, but I did not see a short-term effect. Experiments studying the long term effects of several hours incubation are not trivial to set up. Preliminary experiments failed since the control cells without argon had also changed their behaviour during the experiment.

To find out if the cells needed to be in early starvation to undergo rapid freezing when put into the imaging chamber, I followed the mitochondria in SD1 cells in the imaging chamber. SD1 cells are cells that have been growing in low glucose medium (EMMLG) for 1 day from a very diluted starting culture. They are basically in a late exponential growth phase, reaching stationary phase by SD2. The mitochondria of fresh SD1 cells looked similar to exponentially growing cells in standard EMM2 medium with 2% glucose (data not shown). I started to image the cells 20 min after having mounted them (see Figure 7E). At this time, the mitochondria have fragmented quite a bit, but after their first and only division (3h4min), the mitochondria reversed to their normal reticulated morphology. The cells did not grow substantially, but the mitochondria started to fragment at around 6h post mounting. The process of fragmentation was finished at around 15h post mounting. The dynamic behaviour of the mitochondria decreased drastically during this time (see Figure 7E).
From this, I concluded that the cells can undergo rapid freezing in the imaging dish independent of their growth phase while the time it takes for them to undergo rapid freezing was highly dependent on their growth phase. An open question is what induced rapid freezing. Do the cells only undergo rapid freezing in medium without glucose, or does the induction of rapid freezing depend on the cell concentration, maybe translating into how fast they metabolize oxygen, or on some compound the cells excrete to the medium after entering starvation?

We did not continue investigating the rapid freezing phenomenon for various reasons. The cell number per experiment was limited and could not be scaled up. The cells that had undergone rapid freezing could no longer be easily manipulated, since every manipulation would change the environment, foremost the oxygen conditions, surrounding the cells.
However, we learned from these experiments, that the imaging chamber mounting method only provided trustworthy results if the cells were imaged within the first minutes after mounting.

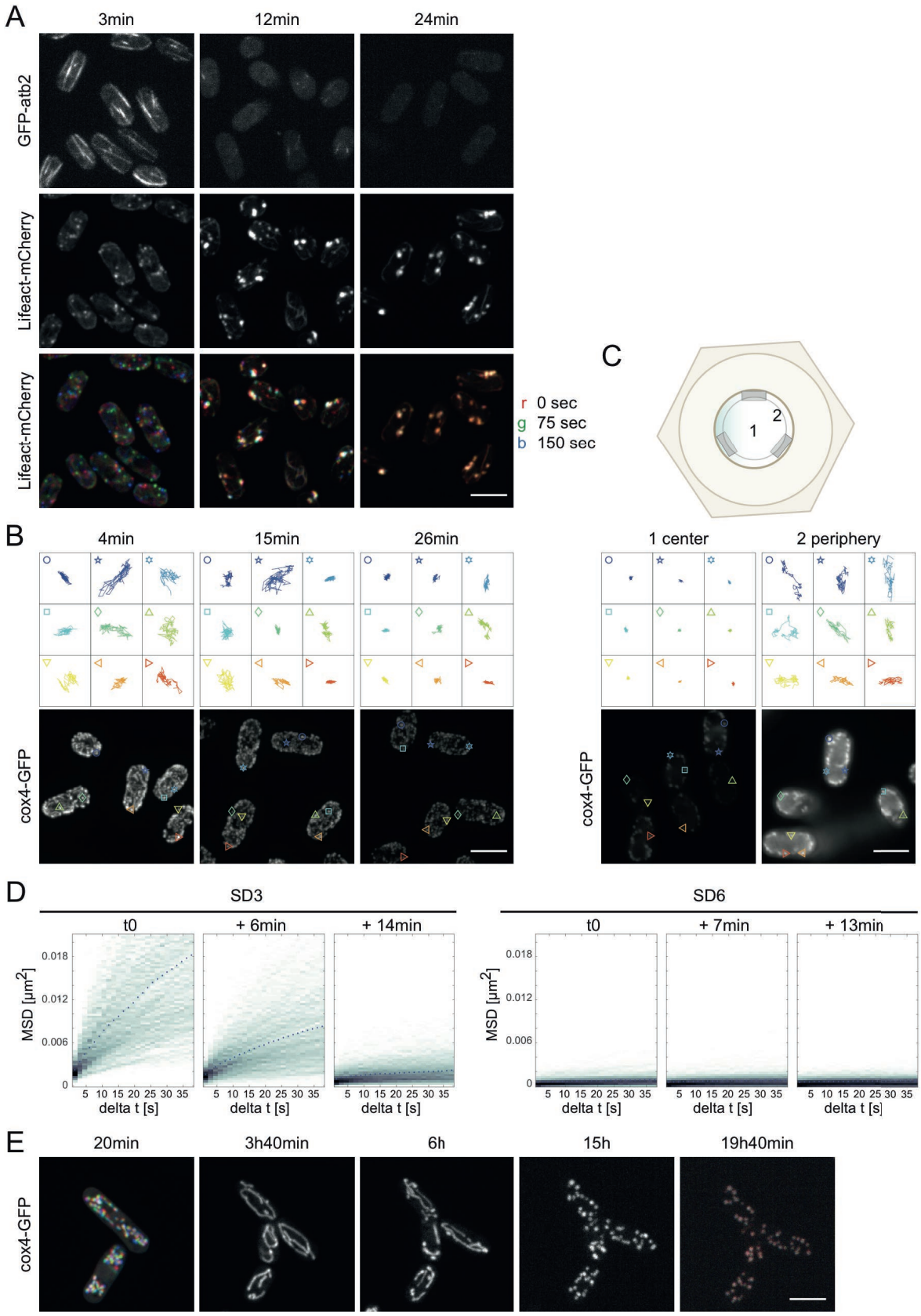

Figure 7. Rapid freezing – acute cytoplasmic immobilization in non-CF cells mounted under specific conditions.

(**A**) Images show microtubules (GFP-atb2; top) and F-actin (Lifeact-mCherry; middle) in SD2 cells immediately after mounting (3min, left), 12min and 24min after mounting (to the right). The 3 images come from 3 independent imaging chambers kept in the dark prior to imaging. The dynamics of F-actin can be

3.1.2 Culturing conditions influence the cytoplasmic state of cells in deep starvation

After having found mounting, imaging and evaluation conditions allowing precise conclusions about the cytoplasmic state of cells, I next wanted to investigate the experimental parameters during the starvation period that influenced the cytoplasmic state of cells in deep starvation. The main reason for this was that the starved cell populations did not consistently show CF in deep starvation even after the standardization of cell mounting, imaging and cytoplasmic state evaluation. We suspected that we were not aware of an important parameter influencing the cytoplasmic state, and which we therefore did not keep constant during the starvation. We hoped that by gaining knowledge about the influence of culturing parameters, we could identify and standardize all the parameters and get consistent CF.

First, I tested different culturing conditions. As a readout for the cytoplasmic state, I used the short 25sec DIC movies to qualitatively classify the lipid droplet motion in each cell without knowing the experimental background of a given population (see also section 3.1.1.1). I measured the portion of cells where no lipid droplet showed visible motion as a readout for the degree of CF in a given cell population.

The default method for liquid culturing we used in the lab was to culture cells in a 25°C incubator on a shaking platform in an Erlenmeyer flask sealed with aluminium foil, or sealed with a screw top for bigger flasks. We aimed at a culture volume of around 1/5-1/10 of the flask volume (eg. 5ml in 25ml flask). Under these conditions, 60-70% of cells showed no lipid droplet motion in a CF cell population (see also Figure 8A).

In contrast to this, culturing cells in a closed plastic screw cap tube of similar dimensions never led to CF (0% cells without lipid droplet motion; see also Figure 8B). The cell and lipid droplet

estimated from the colour spectrum revealed by a pseudo-colour image constructed from 3 time points merged to an RGB image (t1 in red, t2 = t1+75sec in green, t3=t1+150sec in blue). (**B**) Mitochondria (visualized by cox4-GFP) trajectories extracted from 99 frames from a 99s movie (tracked mitochondria fragments indicated in the lower fluorescence image) from SD2 cells immediately after mounting (4min; left) and 11 and 22min after mounting (to the right). All 3 movies were acquired from 3 separate imaging dishes. (**C**) Mitochondria trajectories extracted from 99 frames from a 25s movie (tracked mitochondria fragments indicated in the lower fluorescence image) from SD2 cells that were in the imaging chamber for 3h in the dark prior to the image acquisition. The imaging position is indicated in the schematic imaging chamber (top). (**D**) Mean squared displacement (MSD) of fragmented mitochondria particles at SD 3 (left panel) and SD6 (right panel). The trajectories were extracted from 300 frame movies, 1.5s time interval, of maximum intensity projections. The plot shows a color-coded histogram of each particle's time-averaged MSD; the black dashed line indicates the ensemble- and time-averaged MSD's. (**E**) Images show SD1 cells (late exponential growth phase in EMMLG) put into an imaging dish 20min prior to the first image of an almost 20h long movie. The first and last frame show a color-coded image, where 3 time points of a short, fast movie are merged to an RGB image (t1 in red, t2=t1+60sec in green, t3=t1+120sec in blue) to indicate the dynamics of the mitochondria. All images are maximum intensity projections, except for the images in (C) that are single planes. Scale bar is 5µm in all panels.

morphology was similar to cells from standard conditions with a few big lipid droplets (see Figure 8B). The lipid droplet motion in the closed tube condition was unlike the motion in early starvation, spatially very confined (see Figure 8B) and is therefore more obvious when playing the movie than in the 2-D representation. The absence of cells without visible lipid droplet motion strongly depended on the tight closure of this culture flask to the degree that there was a clear build up of pressure, audibly released with the first opening of the culture flask. When closing the flask loosely, approximately 35% of the cells displayed no lipid droplet motion.

By increasing the culture volume to culture flask ratio significantly (>½), cells did not undergo CF (0% cells without lipid droplet motion; see Figure 8C), independent of the culture flask or closure condition. The cells were a bit longer than those from standard conditions, with a few big lipid droplets and many small lipid droplets (see Figure 8C). Sometimes there were rather big vacuoles visible. The lipid droplet motion in those cells was spatially less confined and is thus more obvious in the 2-D visualization than in the closed tube case (compare Figure 8B and C).

When culturing cells anaerobically (Jara et al., 2007) in medium filling the whole Erlenmeyer flask, the cells never showed CF (0% cells without lipid droplet motion; see also Figure 8D). The lipid droplet motion was very obvious (see Figure 8D). In addition, the cells showed a distinct morphology, appearing blown up and round with a very smooth cytoplasmic background and some vacuoles (see Figure 8D). This phenotype was observed in Erlenmeyer flasks that were kept without shaking, but also in tightly closed screw cap tubes that were kept on the shaker. The density of such starvation cultures was significantly lower than standard starvation cultures, indicating that the glucose was mostly metabolized by less efficient fermentation rather than respiration.

When culturing cells under default conditions but without the constant shaking on the incubator, the cells in deep starvation showed a mixed lipid droplet motion phenotype. In around half the cells there was clear motion, whereas in the other half of the cells there were no visible lipid droplet dynamics. However, the motionless cells appeared rather rough and vacuolated, and could be categorized, from experience, as unhealthy. The same phenotype was observed for fully filled, tightly closed screw cap tubes cultured without shaking, probably due to the conic bottom facilitating sedimentation and pellet formation.

In summary, the occurrence of CF in deep starvation strongly depended on the culturing container. The cells required a large medium-to-air interphase, with good aeration of the medium to undergo CF. Anaerobic conditions prevented CF, but the limited aeration of cells in cultures with a high culture to flask volume ratio, or in a tightly closed culture container also,

prevented CF induction. This indicated that successful CF induction relies on a minimal rate of respiration instead of pure fermentation.

To test this, I tried inducing CF in cultures grown with glycerol as a non-fermentable carbon source (EMMLG+3% glycerol). Indeed, I already found cells with immobilized lipid droplets and mitochondria at SD3. However, the cell population was extremely heterogeneous, and at SD6 all cells looked virtually dead. One reason for this might be that the cells reached a very high density in stationary phase, about 3 times denser than a standard starvation culture.

Another possible parameter influencing the possible outcome of deep starvation, was the pH of the culturing medium. However, the pH for all the above discussed cultures was between 5.1 and 5.9, even though the cytoplasmic state in deep starvation differed quite dramatically. Therefore, we concluded that there was no straight forward link between CF and the extracellular pH.

The exact medium composition could be another factor potentially influencing the cytoplasmic state in deep starvation. Usually, the defined minimal medium EMM2 is used for culturing wildtype cells. However, many strains contain mutations in biosynthetic enzymes such as leu1 and ura4. Such strains (auxotrophes) grow only if supplemented with the appropriate amino acid or nucleobase (supplements). This enables the selection for plasmids, gene replacements or transgenes marked by a wildtype copy of such a gene by the strain's ability to grow in medium without the supplement. Even though these strains are widely used, it is known, that these auxotrophic alleles have an effect on the physiology of the cells (Ian M Hagan et al., 2016). Also, the addition of supplements to the medium of wildtype cells influences their physiology (Ian M Hagan et al., 2016).

I aimed to test if the addition of supplements to the starvation medium had an effect on CF induction. I found that the addition of these supplements to the starvation medium delayed the onset of CF by about 2 days to SD7 (see Figure 8F). Additionally, the CF cells from supplemented starvation medium (EMMLG + ALU) showed a different morphology. They were often highly vacuolated, with large grey value intensity fluctuations within the vacuoles. In conclusion, the use of supplements in CF experiments should be avoided if possible. Consequently, from this point onwards we crossed out all the auxotrophic alleles from strains that we wanted to use for detailed analysis. For preliminary experiments with auxotrophic strains, we tested for CF at SD7 or later.

The last parameter I briefly tested was the glucose concentration of the medium. For CF induction, cells were inoculated in EMMLG (0.5% glucose) from an exponential culture in EMM2 (2% glucose). The exact volume of exponential culture that needed to be transferred to

EMMLG varied slightly from experiment to experiment, depending on the exact cell density. Consequently, the exact glucose concentration in the starvation culture was not entirely constant.

Chieze Ibeneche from the Florin lab had already performed experiments with different glucose concentrations (see Figure 3C). She showed that CF was induced in cells grown with 0.1-0.5% glucose at SD5. From this, we knew that less glucose did not negatively influence CF induction. Only cells transferred to EMM0G (0% glucose), what we called shock starvation, did never induce CF.

However, cells that were grown to stationary phase and subsequently cultured for 7 days in standard EMM2, instead of EMMLG did not homogeneously undergo CF as under standard conditions. They showed a very heterogeneous phenotype, similar to cells grown under standard conditions without shaking. Many cells showed no lipid droplet motion, but had a very rough and uneven cytoplasmic background DIC signal (see Figure 8G). However, some cells looked rather smooth, with lipid droplets displaying some motion (see Figure 8G). Therefore, a glucose concentration in excess of 0.5% can influence the induction of CF. Instead of testing this further, I adjusted the protocol to minimize the glucose variation. Firstly, I centrifuged the necessary exponential culture aliquot, discarded the medium and transferred only the cells to the starvation culture. Secondly, I always measured the optical density of the starvation culture prior to data acquisition. Since the stationary cell culture density correlates with the initial glucose concentration, I could indirectly monitor the glucose concentration of the initial starvation culture.

In summary, the cytoplasmic state of cells in deep starvation is highly susceptible to changes in the exact experimental conditions. Therefore, I was especially careful in keeping the culturing conditions as constant as possible.

However, disappointingly, in a 6-month period only 60% (33/56) of wildtype starvation cultures showed CF, as defined by a majority of cells showing no lipid droplet motion at all. Strikingly, I observed that of two parallel starvation cultures originating from the same exponential culture, grown in the same flasks with the exact same medium, only one of the cultures showed CF. This indicated the possibility that there was an intrinsic variability in the cell's response to deep starvation, with a high, but not total penetrance of CF.

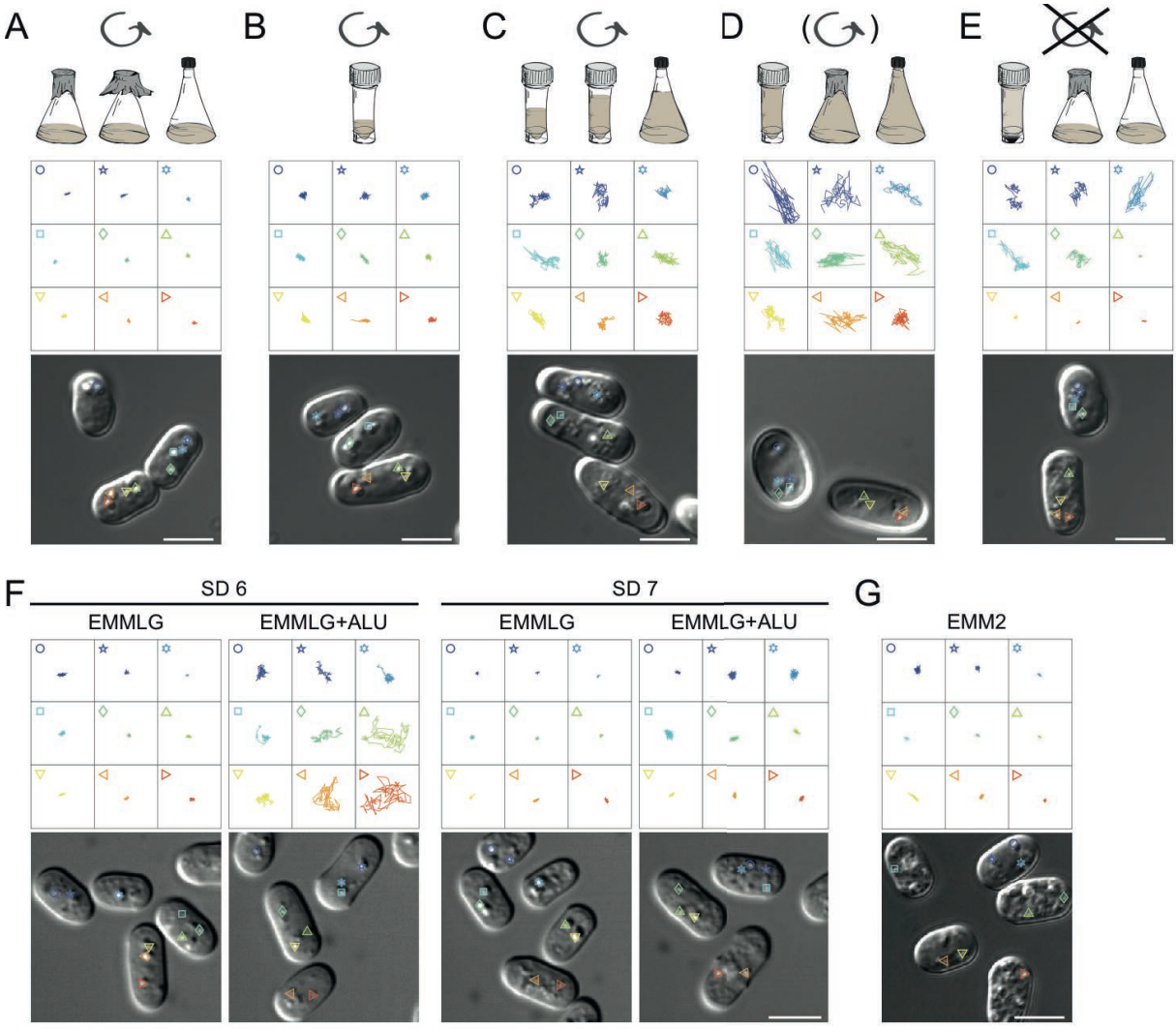

Figure 8. Culture conditions influence the cytoplasmic state of cells in deep starvation.

(**A**) Lipid droplet trajectories extracted from 25sec movies (4frames/sec, droplets depicted in lower DIC images) of SD7 cells cultured under default culturing conditions (in Erlenmeyer flask on shaking incubator, with a low volume to flask ratio, EMMLG starvation medium). (**B**) Lipid droplet trajectories as in (A) of SD7 cells cultured in tightly closed screw cap plastic tubes, otherwise standard conditions as in (A). (**C**) Lipid droplet trajectories as in (A) of SD7 cells cultured in various flasks all with a high culture to flask volume ratio. The example here is from a 100ml culture in a 125ml Erlenmeyer flask. (**D**) Lipid droplet trajectories as in (A) of SD7 cells cultured anaerobically in culture flasks filled to the top with medium. The example here is from a full 125ml Erlenmeyer that was kept without shaking. (**E**) Lipid droplet trajectories as in (A) of cells that were cultured under default conditions as in (A) but without shaking. (**F**) Lipid droplet trajectories as in (A) of SD6 and SD7 cells that were either cultured in standard EMMLG medium or in EMMLG supplemented with adenine, leucine and uracil (ALU). (**G**) Lipid droplet trajectories as in (A) of SD7 cells that were cultured in EMM2 (2% glucose) instead of EMMLG (0.5% glucose). Scale bar is 5µm in all panels.

3.2 Mechanical stability of protoplasts in the context of CF

As we presented in the manuscript in section 2.1, CF cells kept their cylindrical shape even in the absence of the rigid cell wall. This was in contrast to exponentially growing cells, where the protoplasts (cells without cell wall) adopt a spherical shape.
In this chapter I will describe the more detailed experiments I have performed to shed light on the protoplast shape and stability in the context of CF.

3.2.1 Cylindrical shape of protoplasts correlates with the onset of CF

After having found that CF protoplasts were still cylindrical, we wanted to know if only CF cells became cylindrical protoplasts or if this was a behaviour of starved cells in general. To that end I removed the cell wall of cells at each day of starvation up to SD8.
In most experiments, the protoplasts were round for cells in early starvation at SD2-SD5 showing no CF yet, but mostly cylindrical for CF cells in deep starvation (SD6-8; see Figure 9A). This indicated that indeed the cylindrical protoplasts were specific to CF cells and not to starved cells in general.
In order to ensure, that the cell wall was indeed removed, I stained the presumable protoplasts with rhodamine lectin. Lectins are glycoproteins that bind the carbohydrates of the cell wall with high affinity. Indeed, what we assumed to be protoplasts never showed rhodamine signal along their circumference (see Figure 9B). Cells where the cell wall was not removed in the given time were mostly distinguishable by a more specific signal along the outline (see white arrows in Figure 9B). However, this signal was not always as convincing, probably depending on the thickness of the cell wall remnants. With time and experience I started to recognize the intact cells in DIC images by the sharper contrast at the cell borders compared to protoplasts.
Next, I wanted to confirm the correlation of cylindrical protoplasts with CF more quantitatively. For this, I quantified the shape of the protoplasts by comparing manually measured protoplast length to width. The ratio of length to width was 1 for spherical protoplasts, and around 2 for the cylindrical protoplasts (see Figure 9C; lower panel), as for intact cells in starvation. The ratio confirmed a very sharp transition from round to mostly cylindrical protoplasts between SD5 and SD6. Additionally, I quantified the cytoplasmic state of the corresponding intact cells by measuring the correlation coefficient of Bodipy-stained lipid droplets over time (Bodipy CC readout; see sections 2.1 and 3.4.1). The correlation coefficient reached the plateau indicating CF at SD6 (see Figure 9C, upper panel). Together, the quantitative description of CF induction correlated perfectly with the occurrence of mainly cylindrical protoplasts from SD6 onwards, revealed by a length to width ratio of 2 (see Figure 9C).

However, the strongly immobilized cytoplasm characterizing CF cells was not the only potentially shape preserving feature of cells in deep starvation. The actin cytoskeleton was strongly remodelled in CF cells to form the characteristic shoelace bundles around the cell cortex (see section 2.1). Cortical actin is known to be key for cell shape control in eukaryotic cells without cell wall (Alberts, 2008). Moreover, the surface of the protoplasts was wrinkled and contained some strong indentations (see arrows in Figure 9D; left panel). These indentations were reminiscent of the shoelace structures that F-actin formed in deep starvation. We therefore investigated a potential shape preserving role of the shoelace actin bundles in CF protoplasts.

First, I wanted to see if indeed the protoplast indentations followed the shoelace actin bundle. In order to do this, I visualized the actin cables in protoplasts using Lifeact-GFP. I did not see a correlation between the indentations and the F-actin structures (see arrows in Figure 9D; left panel).

Furthermore, when I prevented the formation of the shoelace F-actin bundles by culturing the cells in the presence of latB from SD3 onwards (see Methods and section 2.1), the protoplasts still showed similar indentations (see arrows in Figure 9D; right panel).

Together, these results demonstrated that the shoelace actin bundles were not required for the cylindrical shape of CF protoplasts. The question remains, what underlying structure, if any, do those indentations follow in the CF protoplasts.

All together, these results strongly suggested, that the immobilized cytoplasm characterizing CF cells was indeed responsible for the preserved cylindrical shape in the absence of the cell wall.

When the cylindrical shape of CF protoplasts was due to their solid cytoplasm, the protoplasts would round up if they were recovering from starvation and thus exit the CF state. I tried to recover the cylindrical protoplasts by adding glucose to the protoplasts in their high sorbitol buffer. The cell wall digestion for the protoplast generation was performed in a hyperosmotic buffer containing high sorbitol (1.2M sorbitol), as was published previously (Kelly & Nurse, 2011). This was done to osmotically stabilize the protoplasts by preventing water influx and subsequent rupture following the removal of the cell wall. In this high sorbitol buffer, the protoplasts showed no sign of starvation exit upon glucose addition. However, when I exchanged the high sorbitol buffer with normal EMM2, the protoplasts rounded up prior to cell lysis (see Figure 9E).

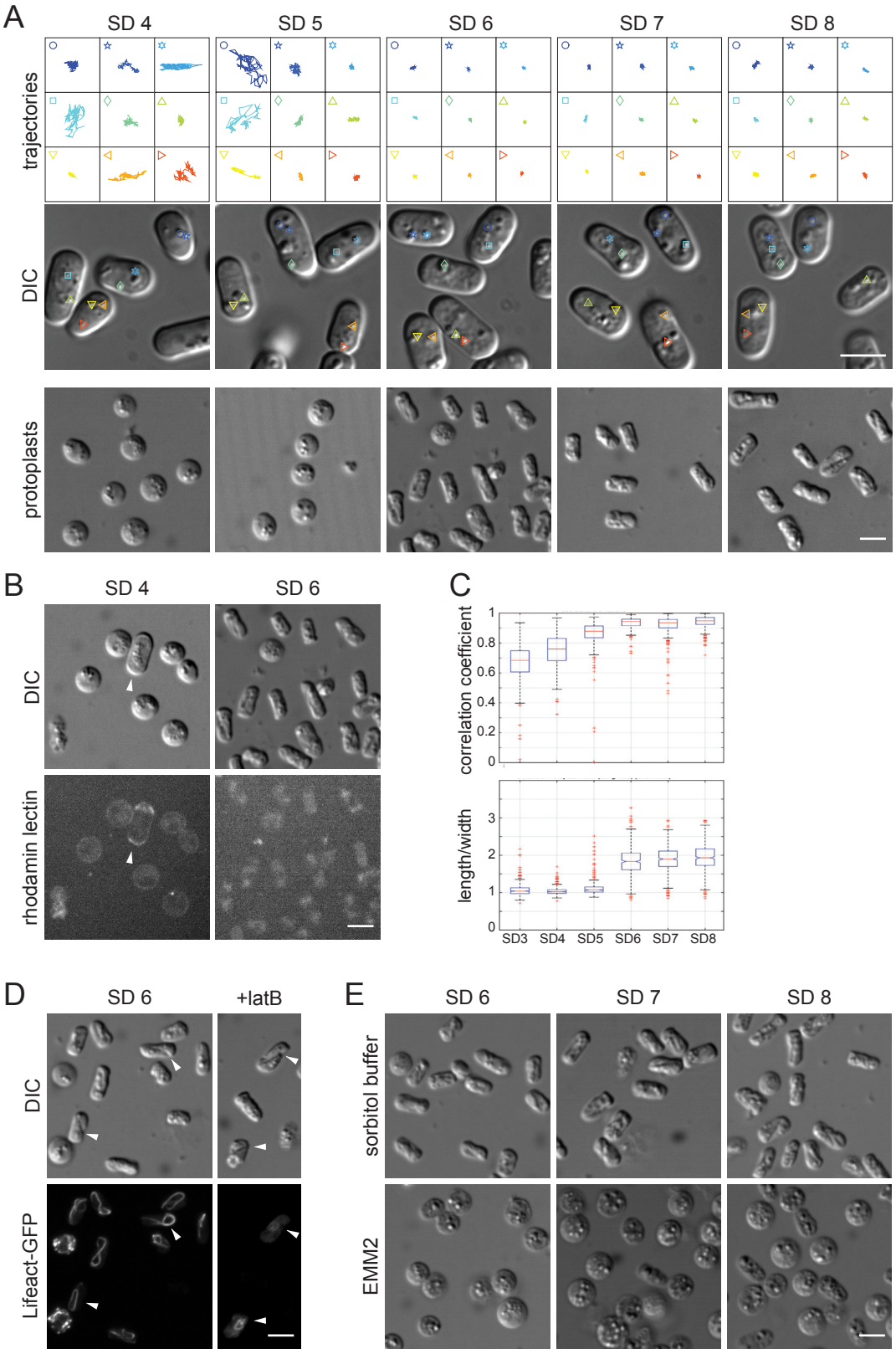

Figure 9. Protoplast shape in the context of CF.

(**A**) Lipid droplet trajectories extracted from 25sec movies (4frames/sec, droplets depicted in lower DIC images) of SD4-SD8 cells and the corresponding protoplasts from the same starvation cultures (lowest panel). (**B**) Images showing protoplasts of SD4 and SD6 cells (top panel) with the corresponding rhodamine lectin staining (bottom panel). Amongst the protoplasts of SD4 there is one cell with intact cell wall (white arrow). (**C**) Standard boxplot showing single cell correlation coefficients from Bodipy signal of two consecutive time points

This rounding up may be due to protoplasts recovering from starvation and thus exiting from CF by fluidizing the cytoplasm. Alternatively, the cylindrical protoplasts may require the osmotic pressure from the hyper-osmotic environment for their stability. Releasing the protoplasts from this pressure would thus induce their rounding up.

However, we have additional evidence supporting our hypothesis that the cylindrical shape is due to the solid cytoplasm of CF cells holding everything in place, independent of the hyper-osmolarity of the protoplast generation buffer. We address this issue in the manuscript in section 2.1 and further in this chapter in section 3.2.3.

3.2.2 Exceptions to the rule – challenging the interdependence of cylindrical protoplasts and CF

In the previous section I showed that only CF cells were able to keep their cylindrical shape as protoplasts. Here I will present two exceptions to this rule. As we showed in the manuscript in section 2.1, CF onset happened either between SD4-5 or SD5-6. From the 7 experiments, where I investigated the correlation of CF with the shape of protoplasts by examining the cells every day of starvation, 5 cultures showed CF from SD6 onwards. One culture was frozen at SD5 and one culture did not freeze during the 8-day experiment. The experiments where CF occurred from SD6 onwards all showed cylindrical protoplasts from SD6 on (see Figure 9A and C), indicating that the cylindrical shape preservation was due to the solid cytoplasm characterizing CF cells.

The culture already showing CF at SD5, only had cylindrical protoplasts from SD6 onwards (see Figure 10A and B). The cells at SD5 rounded up without cell wall, even though they had immobilized their lipid droplets already (see Figure 10A and B). This result showed that the immobilization of lipid droplets alone was not enough to predict the protoplast shape.

(45sec interval; upper panel) of SD3-8 cells from the same starvation culture as in (A). The shape of the corresponding protoplasts was quantified by the ratio of length and width summarized in a standard boxplot (lower panel). (**D**) SD6 protoplasts (DIC) with the corresponding Lifeact-GFP signal (maximum intensity projections) from a standard starvation culture (left) and from a starvation culture incubated with latB from SD3 (right). The arrows indicate the indentations visible in DIC. (**E**) DIC images showing standard SD6-8 protoplasts in high sorbitol buffer (upper panel) and SD6-8 protoplasts after 1 incubation in EMM2 without sorbitol. All protoplasts were generated in a buffer containing 1.2M sorbitol (Methods). Scale bar is 5µm for all panels.

SD5 cells are just at the transition to CF induction, since they do not always show CF. Therefore, CF cells from SD5 have most likely freshly transitioned from non-CF to CF. We hypothesize that the freshly frozen cytoplasm characterized by immobilized organelles undergoes a maturation process before becoming solid enough to prevent its components from rearranging. Translated to our hypothesized polymer network underlying the cytoplasmic immobilization in CF cells, this could mean that the crosslinks in freshly formed networks are not yet as stably established as in later phases of CF.

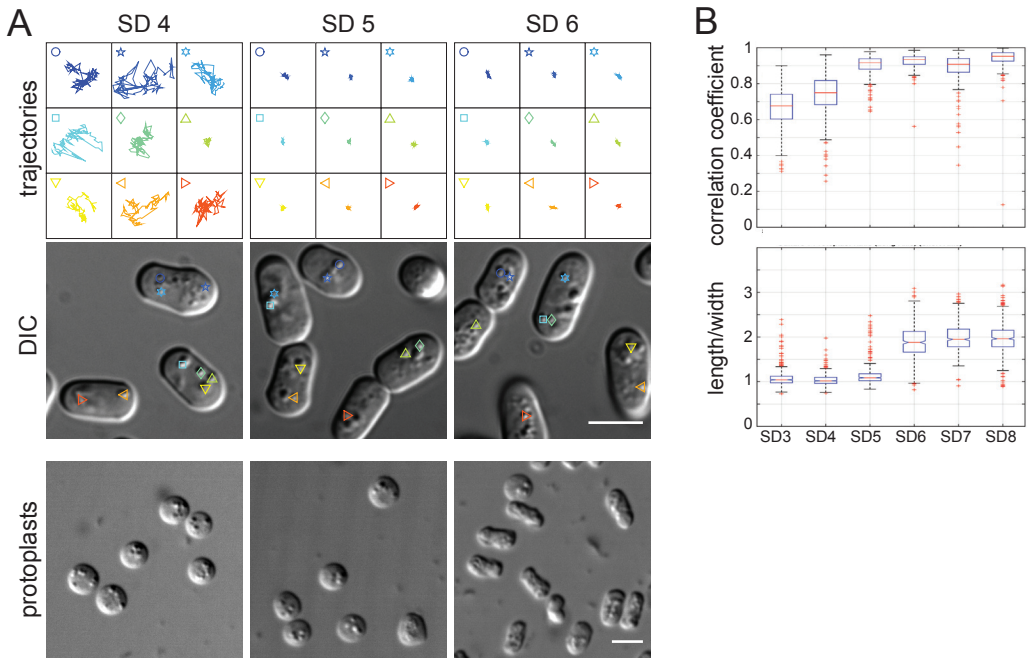

Figure 10. An example where CF preceded cylindrical protoplast shape.

(**A**) Lipid droplet trajectories extracted from 25sec movies (4frames/sec, droplets depicted in lower DIC images) of SD4-SD6 cells and the corresponding protoplasts from the same cell cultures (lowest panel). (**B**) Standard boxplot showing single cell correlation coefficients from Bodipy signal of two consecutive time points (45sec interval; upper panel) of SD3-8 cells from the same culture as in (A). The shape of the corresponding protoplasts was quantified by the ratio of length and width summarized in a standard boxplot (lower panel). All protoplasts were generated in a buffer containing 1.2M sorbitol (Methods). Scale bar is 5µm for all panels.

The most exceptional culture of the above described set of experiments was the one where I did not observe clear CF during any of the 8 starvation days. Even though I had already observed that CF did not always occur (see section 3.1.2), I had never followed such a starvation culture on a daily basis from early to deep starvation. When qualitatively evaluating the lipid droplets dynamics, they were clearly mobile throughout starvation – almost similar to the dynamics in cells in early starvation (see Figure 11A). The Bodipy correlation coefficients never reached high values clearly above 0.9 as for starvation cultures in CF (see Figure 11B). Interestingly however, the correlation coefficient still increased from SD3 onwards, reaching a plateau at SD6 (see Figure 11B and Discussion).

Regarding the protoplast shape of such a starvation culture: I strongly expected the protoplasts of such cells to be spherical, but to our great surprise, the protoplasts from those cells did not round up, but stayed elongated (see Figure 11A).

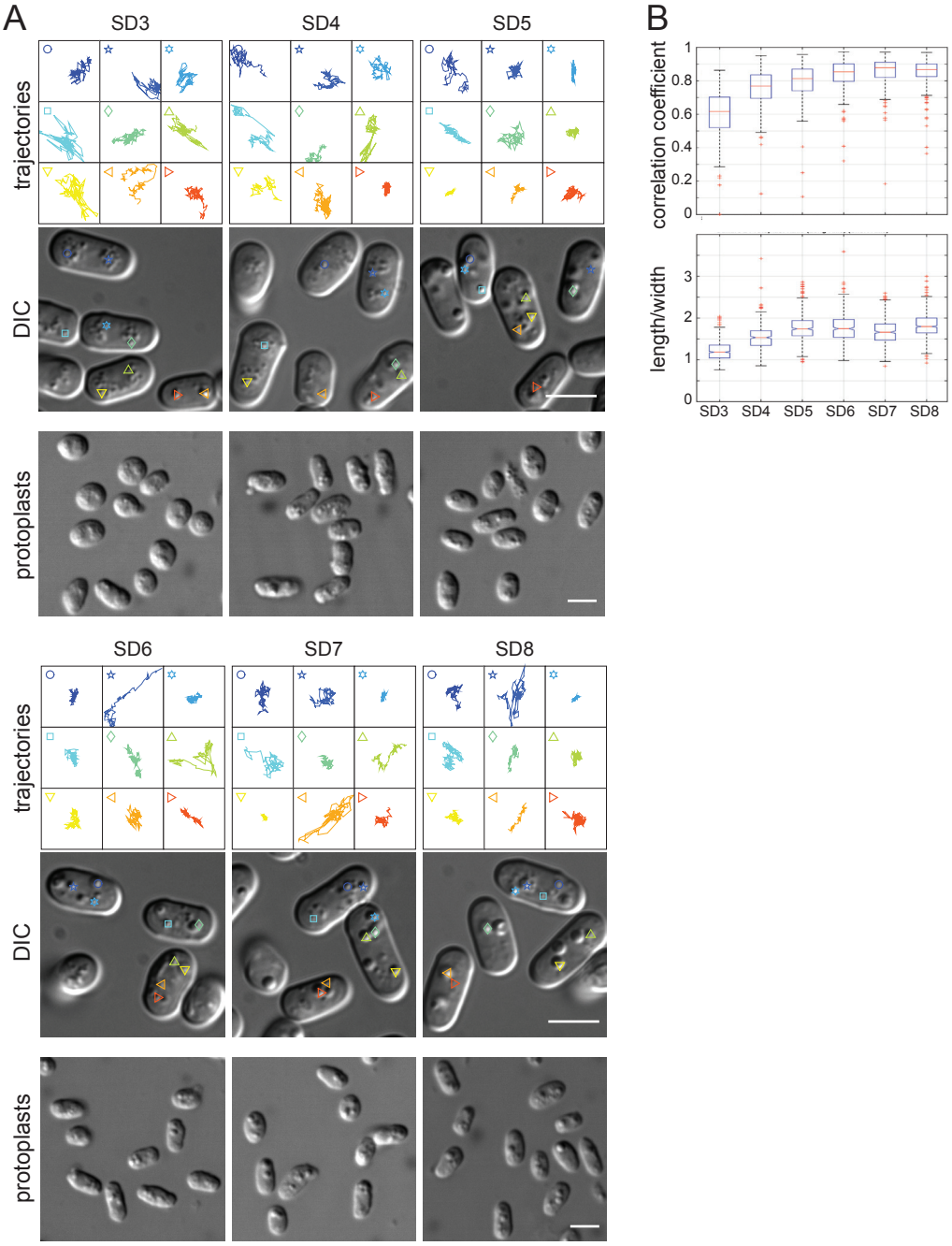

Figure 11. An example of elongated protoplasts in the absence of clear CF.

(**A**) Lipid droplet trajectories extracted from 25sec movies (4frames/sec, droplets depicted in lower DIC images) of SD3-SD8 cells and the corresponding protoplasts from the same cell cultures (lowest panel). (**B**) Standard boxplot showing single cell correlation coefficients from the Bodipy signal of two consecutive time points (45sec interval; upper panel) of SD3-8 cells from the same culture as in (A). The shape of the corresponding protoplasts was quantified by the ratio of length and width summarized in a standard boxplot (lower panel). All protoplasts were generated in a buffer containing 1.2M sorbitol (Methods). Scale bar is 5µm for all panels.

However, even though the protoplasts were clearly elongated, the shape was not as cylindrical as for CF protoplasts, but rather oval. Further, in starvation cultures that had undergone CF, the transition from round protoplasts to cylindrical protoplasts was always very sharp. In contrast to this, the protoplasts here became gradually more elongated (see Figure 11A). Already at SD3, most protoplasts were not perfectly spherical. At SD4, most of the protoplasts were clearly elongated, oval instead of round (see Figure 11A). As before I quantified the protoplast shape by the length to width ratio as a measure for roundness (see Figure 11B). This confirmed the qualitative impression that already at SD3, the roundness factor was distributed more broadly, with a median above 1. This ratio gradually increased until from SD5-8, the ratio was almost 2.
I speculate about the implications of this result on the molecular mechanism mediating CF in the Discussion.

The question arising was: How could these cells that were clearly not frozen, stabilize their shape to such a degree? Before this, we had simply thought that only a solid-like cytoplasm such as in CF cells could mediate shape preservation in the absence of cell wall. Reminiscent of this result, in the manuscript in section 2.1, we show that acutely starved cells according to (Joyner et al., 2016) and (Munder et al., 2016) showed cylindrical protoplasts, even though the cytoplasm in those cells was significantly less immobilized compared to CF cells. We hypothesized that the initial shape preservation was an acute result of the cell wall digestion protocol. Cell wall digestion is usually performed under hyperosmotic conditions. Aside from preventing the protoplast from cell lysis, this also leads to significant volume loss and hence increased macromolecular crowding. We hypothesized that only thereby the cytoplasm of acutely starved cells became sufficiently dense, such that the shape was preserved in the absence of cell wall. Supporting this hypothesis, we were able to show that the cylindrical protoplast shape for acutely starved cells was not nearly as stable as for CF protoplasts. Solids are characterized by a specific order of components whereas in liquids the components can rearrange (Alberti, 2017). The viscosity of complex liquids influences the timescale with which its components rearrange. Therefore, the rounding up of protoplasts from acutely starved cells indicated the cytoplasm to be liquid-like, albeit with a high viscosity. Additionally, we found that only CF cells but not acutely starved cells, could form stable cylindrical protoplasts under hypo-osmotic conditions where no additional macromolecular crowding was induced.

In line with these results, we hypothesized that volume loss upon transfer to hyperosmotic medium could be responsible for the initially cylindrical shape of protoplasts from the non-CF cells. Supporting this, the oval-cylindrical protoplasts of the non-CF cells were clearly less stable over time than CF protoplasts (see Figure 12). Whereas the CF protoplasts did not change their shape, the non-CF protoplasts were clearly rounder already 2 days after protoplast formation, and even more so after 11 days (see Figure 12). Additionally, when incubating the non-CF cells in high sorbitol buffer without enzymes, I found that lipid droplet motion significantly decreased. I acquired data to quantify the cytoplasmic state with the Bodipy CC readout (see sections 3.4.1 and 2.1), but unfortunately the quality of the data was not good enough. Nevertheless, this indicated that hyperosmotic pressure indeed solidified the cytoplasm but did not induce a phase transition to a solid. It rather led to a highly viscous fluid with solid-like properties on a short time scale.

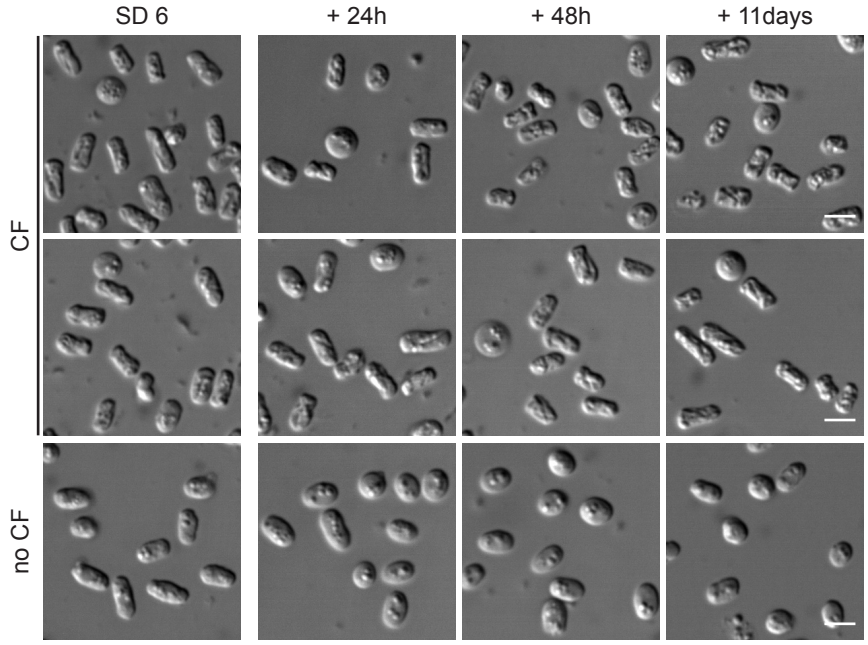

Figure 12. Protoplast shape stability over time.

Images show protoplasts of 3 starvation cultures at SD6, 2 of which showed CF (upper panels). The protoplasts were imaged again after 1,2 and 11 days. All protoplasts were generated in a buffer containing 1.2M sorbitol (Methods). Scale bar is 5µm.

According to this hypothesis, the spherical protoplasts of cells from early starvation would indicate that hyperosmotic pressure on these cells did not induce the same increase in macromolecular crowding and thus decrease in intracellular mobility. It would be interesting to test.

Furthermore, it would have been very interesting to see what shape the protoplasts of the non-CF culture had when generated under hypo-osmotic conditions. Unfortunately, I did not do

these experiments at the time. The idea to perform them basically arose from these results. Since we did not know why this exact starvation culture did not undergo CF at any time during the 8 days experiment, we could not easily generate such a starvation culture on demand.

3.2.3 Protoplast shape under hypo-osmotic conditions

In the previous section, I was able to show that established CF cells always formed cylindrical protoplasts, indicating that these cells were inherently stable. Challenging this idea were the oval-cylindrical protoplasts of the non-CF cells in deep starvation. We found evidence showing that these protoplasts were cylindrical due to acute cytoplasmic immobilization by hyper-osmotic pressure during the protoplast generation.
We could therefore not exclude that the same increased macromolecular crowding happened to the CF cells, and that this was responsible for their cylindrical shape. Supporting this, the CF protoplasts looked wrinkled and shrunk as one would expect after significant water loss. Moreover, the protoplasts were significantly smaller than cells with cell walls (see Figure 13B). In order to test this, we sought to generate protoplasts of CF cells in iso-osmotic or hypo-osmotic medium that would not induce cell shrinkage. If such protoplasts were cylindrical, this would strongly indicate that the shape preserving ability was inherent to CF cells and not due to acute cytoplasmic mobility reduction by water loss induced by the experimental procedure.
I tested cell wall digestion in 0.5M sorbitol buffer instead of 1.2M sorbitol. The key results for this are presented in the manuscript (see section 2.1). Here I will briefly summarize the results concerning CF cells and present supplemental details.

The low sorbitol buffer was indeed hypo-osmotic to fission yeast cells. Exponentially growing cells lysed within minutes after cell wall digesting enzyme addition (see Figure 13A; top panel). Interestingly, this was different for starved cells. Most of them did not lyse under low sorbitol conditions, but instead formed intact protoplasts. Under standard, high sorbitol conditions, the protoplasts of exponential cells squeeze out of the first weak spot in the cell wall. I could never convincingly follow the protoplast formation of CF cells under these conditions live, since there was no apparent cell wall evasion of the protoplast as for exponential cells. In contrast to this, the protoplast generation from starved cells under low sorbitol conditions was very easy to follow. These protoplasts flowed out from their cell walls as cylinders, often after the cell wall opened up on one of the poles – as if the pole were a door (see section 2.1). Only after this cylindrical protoplast release did the CF protoplasts showed a different behaviour than the protoplasts from cells in early starvation. Within an hour, most initially cylindrical SD2-5

protoplasts rounded up, whereas on average 60% of CF protoplasts remained cylindrical (see Figure 13A).

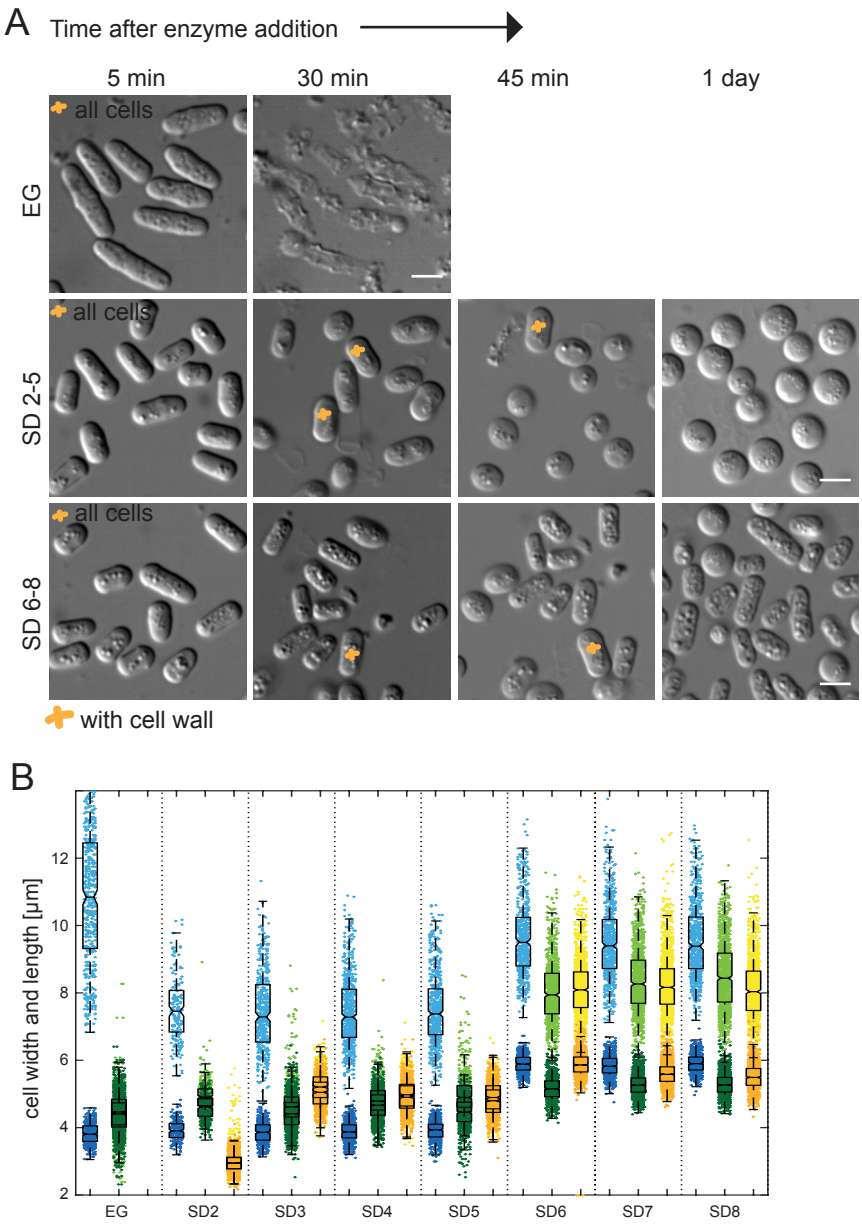

Figure 13. Cell wall digestion under low sorbitol conditions.

(**A**) DIC images showing protoplast generation (cells with cell wall are indicated by an orange cross) under low sorbitol conditions (0.5M sorbitol) for exponentially growing cells (EG), cells from early (SD2-5, example from SD3) and deep starvation (SD6-8, example from SD7). Scale bar is 5µm. (**B**) Dot plot with overlaid standard boxplot showing cell length and width (brighter and darker shade of colour) of exponentially growing and SD2-SD8 cells (blue), of protoplasts generated in 1.2M sorbitol containing buffer (green) and protoplasts generated in 0.5M sorbitol containing buffer (yellow).

As we had hoped for when designing these experiments, the cylindrical CF protoplasts generated under low sorbitol conditions looked very similar to intact cells, unlike the high sorbitol protoplasts. They had a smooth surface with no strong indentations. The width of low sorbitol protoplasts was significantly higher than that of high sorbitol protoplasts (see Figure

13B). For CF protoplasts from SD6 the width was even comparable to the width of intact cells (see Figure 13B). This indicated that the low sorbitol protoplasts had not experienced significant water loss during the protoplast generation experiment.

The macromolecular crowding in CF protoplasts from low sorbitol conditions was significantly less severe than for high sorbitol protoplasts. This strongly argues against a pure macromolecular crowding effect, if these cylinders were still stable over time. To tackle this, I measured the length and width of SD7 protoplasts from 4 experiments 1, 2 and 4 days after enzyme addition. As mentioned earlier, the proportion of round protoplasts in a population was significant, varying between 20-60%. However, the distribution of the 2 major shapes – the spheres and the cylinders – stayed constant for days (see Figure 14). Also, the cylinders did not show any evidence for slowly rounding up, as the length of them stayed constant (see Figure 14).

In summary, we could show that the shape preserving ability of CF protoplasts was not strictly dependent on an acute molecular crowding response induced by the experimental procedure of protoplast formation. There were stable cylindrical protoplasts from CF cells that did not experience apparent water loss. Therefore, we conclude that the cytoplasmic solidity can convey a strong inherent shape preservation ability to CF cells. This strongly argues against macromolecular crowding as a sole mechanism responsible for the solidity of the cytoplasm in CF cells.

However, only a subset of CF cells intrinsically possesses this strong solid-like state, as the number of cylinders is notably lower in protoplasts from low sorbitol conditions than from high sorbitol conditions. Thus, the macromolecular crowding induced by high sorbitol in the digestion buffer contributes to the stability of cell shape.

The proportion of cylindrical protoplasts from low sorbitol conditions varies between experiments between 40-80%. Interestingly, when I manually evaluated the lipid droplet dynamics of single cells, the proportion where no lipid droplet displayed any visible motion at all varied similarly (see section 3.1.2). This may indicate that only such cells possessed a cytoplasm solid enough to convey shape preservation in the absence of cell wall. Furthermore, this experimental procedure could be useful to quickly assess the strength of CF of a population, as the result is much clearer and faster than manually evaluating lipid droplet motion in single cells.

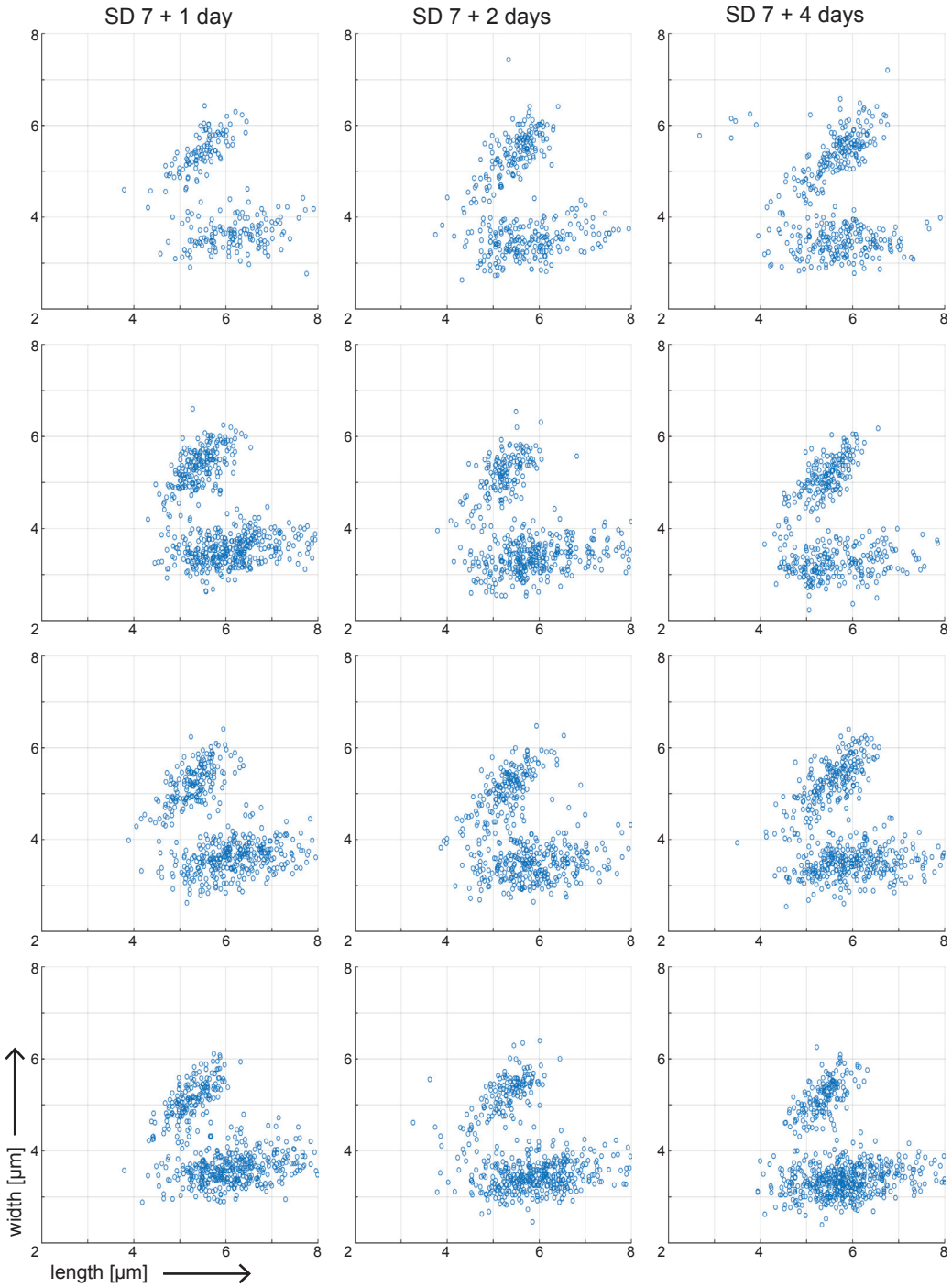

Figure 14. Stability of protoplasts in low sorbitol buffer.

Scatterplots showing cell length (horizontal) versus cell width (vertical) of CF protoplasts from SD7 generated in 0.5M sorbitol buffer 1, 2 and 4 days after enzyme addition.

3.3 Mitochondria during starvation

In order to better understand the phenomenon of cytoplasmic freezing in deep starvation of fission yeast cells, we wanted to know how the structure of intracellular entities evolves during the course of glucose starvation, and how it ends in deep starvation. To that end, I imaged fluorescent marker proteins for organelles like the mitochondria, the endoplasmic reticulum (ER) and Golgi apparatus, or followed the structures via DIC or a fluorescent dye for lipid droplets. The main results are presented in the manuscript in section 2.1. Here I will briefly summarize the behaviour of mitochondria during starvation and show supplemental results.

3.3.1 Mitochondria reversibly fragment during starvation and stop visible motion in deep starvation

Mitochondria in exponentially growing fission yeast cells form tubular bundles (see Figure 15A). They undergo fission and fusion and distribute through the cell in a microtubule-dependent manner (Yaffe et al., 2003). We wanted to investigate the effect of starvation on the mitochondria structure. We visualized mitochondria with cox4p, a widely used live marker for mitochondria (Yaffe et al., 2003). Cox4 encodes for the mitochondrial targeting signal domain of the *S. cerevisiae* cytochrome c oxidase subunit IV (Yaffe et al., 2003) that localizes to the mitochondria inner membrane (www.uniprot.org). As shown in the manuscript in section 2.1, we found that the total mitochondria network fragments during the course of glucose starvation (see Figure 15A). In early starvation at SD 2-4/5, the cells still contain some short tubular mitochondria, but also many globular mitochondria. In deep starvation after the cell has undergone CF between SD 5 and SD 6, all the mitochondria are fragmented, resulting in many globular mitochondria of similar size. These mitochondria are not distributed uniformly throughout the cell, but are located mostly at the cell cortex (see Figure 15A; right panel). In many cells, these cortical mitochondria additionally show a polarized distribution.

The complete fragmentation of the mitochondria occurs at the time when cells usually undergo CF characterized by lipid droplet immobilization. We wanted to know if the dynamics and the mobility of the mitochondria progress similarly to lipid droplets during starvation. For this we analysed time lapse movies of cox4-GFP during starvation. We found that the dynamic behaviour of mitochondria is the same as that of lipid droplets (see Figure 15B). Whereas in exponential growth and in early starvation the organelles are highly dynamic, the fragmented mitochondria in deep starvation display no visible motion at all – they appear frozen (see Figure 15B). We quantified the motion of the globular mitochondria by SPT and subsequent MSD

analysis and showed that the MSDs that are less than 10 times smaller in deep starvation as compared to early starvation (see section 2.1).
The correlation of lipid droplet and mitochondria dynamics was not only high on a population level, but also on a single cell level. In a population of CF cells there are often a few cells that still display observable motion of some lipid droplets (see section 3.1.2). In these cells, also the motion of globular mitochondria was discernibly higher than in the completely frozen cells of the population.
Thus, we learned that at least two abundant organelles – the lipid droplets and the mitochondria – get immobilized in deep starvation. While lipid droplets in deep starvation are located inside the cells, mitochondria are at the cell cortex. This strengthens our hypothesis that the entire cytoplasm becomes immobilized upon CF induction.

After having observed this complete mitochondrial fragmentation and immobilization in deep starvation, we wanted to know how the reversion back to a dynamic reticulated network occurs. We expected the fragmentation of the mitochondria to be reversible, since we knew that cells can revert from deep starvation to a proliferative state after glucose addition. We recovered cells from SD 6 in deep starvation by glucose addition and followed the mitochondria over time. Within 20 minutes after glucose addition, the first short tubular mitochondria appear (see Figure 15C). After 30-40 minutes, there are dynamic tubular bundles spanning the whole cell (see Figure 15C). Thus, the mitochondria can revert fast to a dynamic state, undergoing fusion, fission and translocation similar to mitochondria in exponentially growing cells. Cell growth is initiated at around 5h and the first cell division could be seen 8h post glucose addition (see Figure 15C).

It is interesting that the timeline of fragmentation correlates with the disappearance of microtubule bundles (see section 2.1). Fission yeast uses a microtubule-dependent but motor-independent mechanism for positioning the mitochondria (Yaffe et al., 2003). It has been shown before, that when microtubules are disturbed either by drugs or genetically, the mitochondria no longer form extended tubular structures but instead start to aggregate ending in two clumps located towards the cells ends (Chiron, Bobkova, Zhou, & Yaffe, 2008; Fu, Jain, Costa, Velve-Casquillas, & Tran, 2011). Why and how the aggregates are polarized towards the cells ends upon microtubule depolymerisation is still unclear, but the same mechanism could be responsible for the polarized localization of fragmented mitochondria in deep starvation.

The microtubule-dependent fragmentation was reported to be dependent on the dynamin related protein (DRP) dnm1 (Jourdain, Sontam, Johnson, Dillies, & Hyams, 2008; Röthlisberger, Jourdain, Johnson, Takegawa, & Hyams, 2009), a large GTPase mediating mitochondria fission. In order to test if the fragmentation we observed upon starvation is dmn1 dependent, we studied the mitochondria in dnm1-deleted cells during starvation. In early starvation at SD 2, the mitochondria were highly reticulated (see Figure 15D), similar to what was published previously for dnm1Δ cells in exponential growth (Jourdain et al., 2008). However, in deep starvation at SD 7 all the mitochondria were fragmented as in wildtype cells (see Figure 15D). Thus, the complete fragmentation of mitochondria upon cells entering deep starvation is independent of dnm1. This is interesting, since mitochondria fission mediated by the dynamin related protein DRP1 is the conserved mechanism causing most mitochondria fission events, such as general fission, fission upon stress like apoptosis or oxidative stress (Frank et al., 2001; Karbowski & Youle, 2003; S. Wu, Zhou, Zhang, & Xing, 2011; Youle & Karbowski, 2005). There is one study that reports a unique drp1-independent fragmentation of the mitochondrial network, induced by the foodborne bacterial pathogen Listeria monocytopgenes (Stavru, Palmer, Wang, Youle, & Cossart, 2013). They report an important role of the ER in the drp1-independent fragmentation for the mitochondria (Stavru et al., 2013). It would therefore be interesting to investigate the role of the ER in the fragmentation of the mitochondria network upon deep starvation.

Even though the complete fission of the mitochondria network occurs in dnm1Δ cells, the distribution of the globular mitochondria and the incomplete fragmentation in early starvation do not happen. This possibly indicates that the complete fission in deep starvation is a process independent of the shortening of the mitochondria tubules and their polarized positioning in early starvation. It is possible that the earlier processes are microtubule dependent, in contrast to the complete fragmentation upon deep starvation. To investigate this, the first step would be to follow the mitochondria in dnm1-del more closely over the starvation period to see whether there is indeed no step in between elongated and completely fragmented mitochondria.

In some cells, we observed some fragmented mitochondria to be localized like beads on an invisible string (see Figure 15H). The shape of the string was reminiscent of the characteristic actin shoelace bundles that appear in deep starvation (see section 2.1). We wanted to see whether the invisible string could actually be an actin bundle. To determine this, we did a co-localization analysis of cox4-GFP with Lifeact-mCherry and found that the mitochondria beads on a string run independent of the shoelace-like F-actin bundles (see Figure 15H). This is in

agreement with the fact that mitochondria localization runs independent of actin in fission yeast (T. Li, Zheng, Cheung, Wang, & Fu, 2015), and this does not seem to change in deep starvation. It remains to be seen if there is another structure underlying the shape of the mitochondria string.

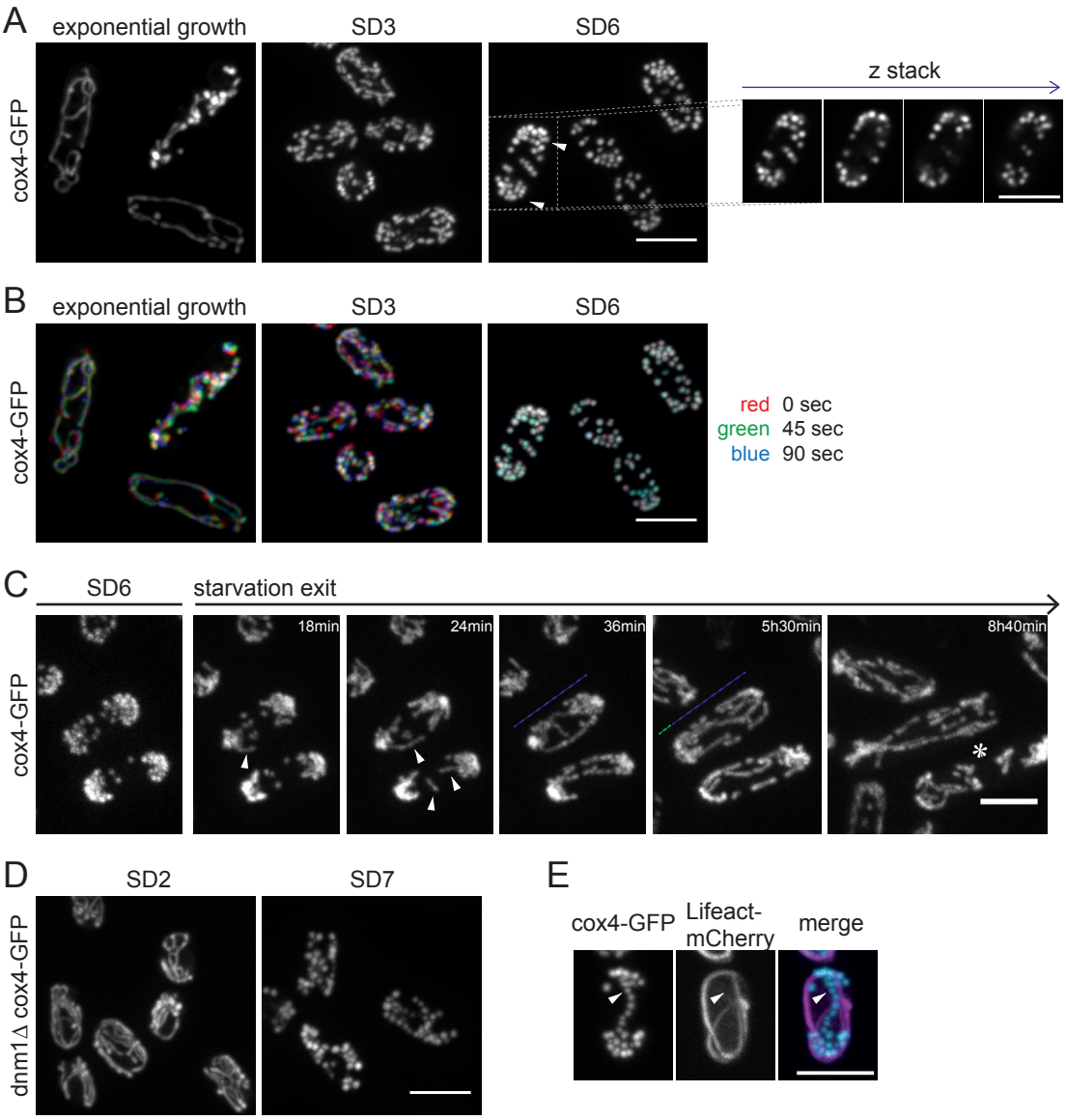

Figure 15. Mitochondria morphology and dynamics during starvation.

(**A**) Images showing mitochondria visualized by cox4-GFP during starvation. The fragmented mitochondria at SD6 are often polarized (white arrows) and mostly cortical, as seen in the single planes of a z stack (lower panel; cell marked by the dotted square in upper panel). (**B**) Mitochondria dynamics visualized by pseudo-colour images constructed from 3 time points of cox4-GFP images (t1 in red, t2 = t1+45sec in green, t3=t1+90sec in blue). The dynamics can be estimated from the colour spectrum. (**C**) Images showing cox4-GFP of SD6 cells and the same cells after addition of fresh EMM2 medium. Tubular mitochondria appear within minutes after starvation exit (white arrows), cells start to grow around 5h after starvation exit (dotted line) and the first cells divide around 8h after starvation exit (asterisk). (**D**) Images showing cox4-GFP in dnm1Δ cells at SD2 and SD7. (**E**) Images showing co-localisation of cox4-GFP with Lifeact-mCherry in SD6 cell. Sometimes fragmented mitochondria arrange like beads on a string, but the string is not mirrored by actin (white arrows). All images show maximum intensity projections. Scale bar is 5µm in all panels.

3.3.2 Autofluorescence from mitochondria increases during starvation

When illuminating wildtype cells not expressing any ectopic fluorescent protein in deep starvation with blue light, we found that these cells showed strong green autofluorescence (see Figure 16A, section 2.1). The nature of this signal was very much reminiscent of the structure of the fragmented mitochondria at this starvation stage. We tested if the strong autofluorescence indeed comes from the mitochondria by co-localization analysis of the mitochondria marker cox4-RFP with the green autofluorescence. We saw, that the signal overlaps perfectly (see Figure 16B, section 2.1).

This is not totally surprising, since mitochondria are visible by autofluorescence in exponentially growing cells. However, there the intensity of this signal is very low. When following the autofluorescence over starvation, we found a gradual increase in autofluorescence over the course of starvation until in the end the signal intensity was comparable to many GFP-labelled structures.

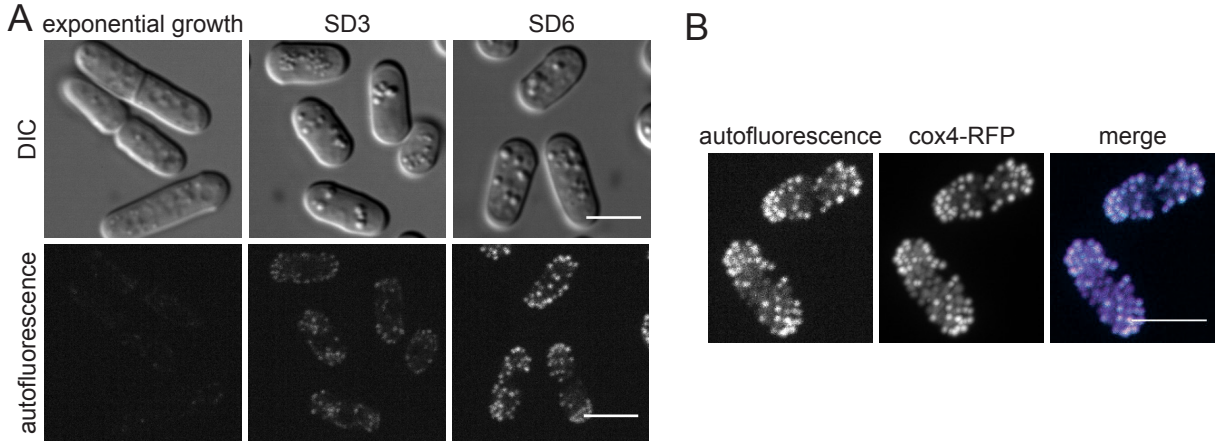

Figure 16. Mitochondria become increasingly autofluorescent during starvation.

(**A**) Maximum intensity projections of green autofluorescence in exponentially growing cells, at SD3 and SD6 (lower panel) and the corresponding cells in DIC images (upper panel). (**B**) Maximum intensity projections showing co-localization of the green autofluorescence and mitochondria visualised by cox4-RFP in SD6 cells. Scale bar is 5µm in all panels.

The metabolic coenzymes NAD(P)H and FAD are the compounds best known to show autofluorescence and are present in the mitochondria (Heikal, 2010). They are increasingly used as intrinsic biomarkers for cellular redox reactions, energy metabolism and mitochondrial anomalies under different pathophysiological conditions (Heikal, 2010). Only the fluorescent spectrum of FAD is in the range of GFP, with an excitation peak of 460nm and an emission peak of 540nm (Islam, Honma, Nakabayashi, Kinjo, & Ohta, 2013; R.-K. Zhao et al., 2011). I therefore hypothesize that it is an increase of flavoproteins that leads to the significant increase

in autofluorescence. It would be interesting to investigate what physiological change underlies this increased autofluorescence.

3.3.3 Fragmented mitochondria are coated by ribosomes

In order to ensure that what we see with the cox4p marker in deep starvation indeed reflects the structure of the mitochondria, our collaborators from the Hoenger lab in Boulder, Colorado investigated cells in deep starvation with electron microscopy. They solely found globular mitochondria in deep starvation. In addition, and to our great surprise these mitochondria were all totally covered with ribosomes. To our knowledge, this is the first description of mitochondria with ribosomes on their membrane, similar to the rough ER in normal cells.

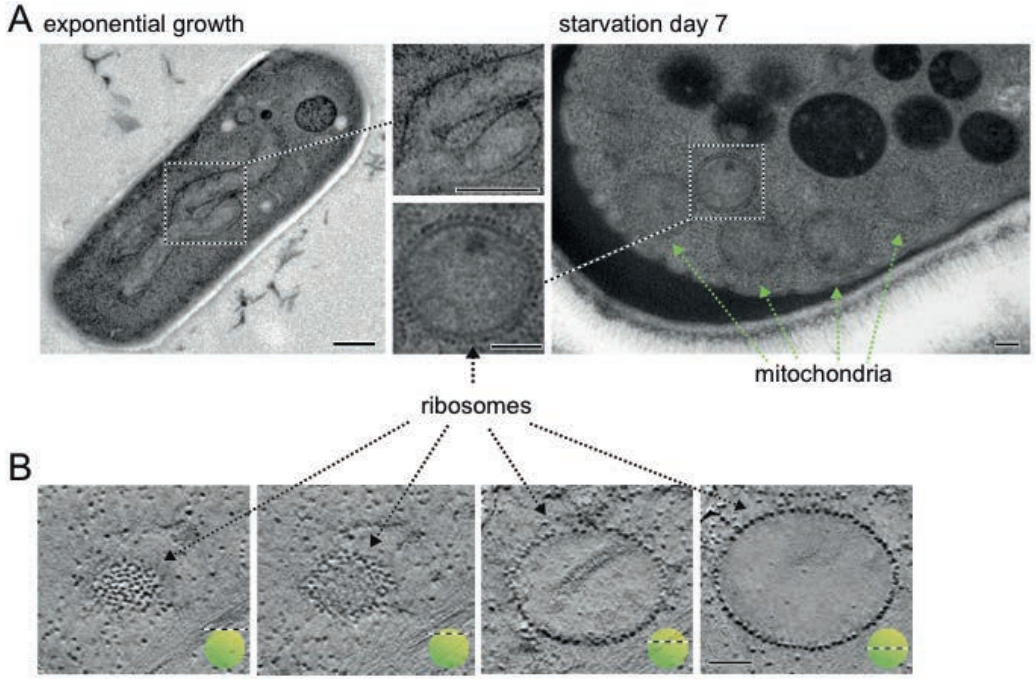

Figure 17. Fragmented mitochondria in deep starvation are coated with ribosomes.

(**A**) Electron micrographs of freeze-substituted, plastic-embedded and sectioned cells during exponential growth (left and upper centre inset) and after seven days of starvation (right, and lower centre inset). Starvation induces mitochondria fission that transforms them from long tubes to small spheres. In addition, while under exponential growth conditions the outer membranes of mitochondria are smooth, they become studded with ribosomes after starvation and fission (see marked area in the right panel, and its magnified view in the lower central panel. Several more studded mitochondria spheres are visible in the lower section of the starved cell (green arrows). (**B**) Tomographic slices (ca. 2.4 nm thick) through a ribosome-studded mitochondrion, starting at the top surface (left) followed by three gradually lower sections down the centre region of the mitochondrion, exposing the ribosomes from their side (see sketches at the lower right corner). Specimen preparation is equivalent to (A). Images courtesy of Prof. Andreas Hoenger.

3.4 Screen for the identification of candidate genes involved in cytoplasmic freezing

Thus far, none of the obvious candidate proteins or mechanisms looked at showed any functional correlation with CF (see section 2.1): Of the cytoskeleton, the microtubules disappeared in deep starvation, whereas the F-actin structures, though prominently rearranging, were not required for CF establishment. Importantly, the previously proposed requirement for septin1-septin3 could not be confirmed (discussed in section 4.2). Furthermore, we did not observe any fluid loss around the time of CF onset, as was proposed in (Joyner et al., 2016), nor could we detect any widespread macromolecular assemblies, as was proposed in (Munder et al., 2016).

In order to begin dissecting the molecular mechanism underlying CF, we performed a genome-wide high throughput screen of gene deletions. For this we used a gene deletion library, made of haploid fission yeast strains carrying deletions of all non-essential genes available (Bioneer, (Kim et al., 2010)). We purchased the latest version of this collection (version 5) and developed a screening strategy for identifying candidate genes that were required for CF.

Prior to establishing the actual screen, I had to device protocols to be able to handle of hundreds of strains in parallel. This involved purchasing appropriate material, like multi-channel pipettes and a replicator pin tool to replica plate 96 strains at a time or to inoculate them into liquid medium on 96-well plates. Protocols for general yeast handling had to be adapted for a high-throughput procedure, for example how to grow and freeze strains in 96-well plates, to allow generating library replicates and a working copy. Only after this, I could proceed to develop and perform the actual genome-wide screen.

In the following chapter I will describe the entire screening procedure, from the first steps to the actual results. First, I will describe the preparations that were necessary prior to the actual screen of the gene deletion library. These started with the establishment of the experimental conditions to induce CF under high-throughput conditions. This meant to scale up the number of strains to process in parallel to 96 strain units, and to scale down the culture volume and imaging to fit into 96-well plates. This was not trivial for two main reasons. On the one hand, the occurrence of CF was strongly dependent on the exact culturing conditions (see section 3.1.2). On the other hand, the capturing of the actual cytoplasmic state of a cell culture was a delicate matter (see section 3.1.1).

Following the detailed description of cell handling I will then go on to describe how I established an automated image analysis workflow, allowing me to obtain information about

the cytoplasmic state of all viable deletion strains in deep starvation. Next, I will report the results of the actual screen. Last, I will present the status of the evaluation of the identified candidate genes.

3.4.1 Establishment of the screen

3.4.1.1 Experimental Setup

In a first step, I had to establish cell mounting conditions for image acquisition on a 96-well plate, that would not acutely influence the cytoplasmic state of cells. This was not trivial, since I had observed before that the cytoplasmic mobility of cells could both increase and decrease within minutes of mounting the cells, depending on the mounting strategy (see section 3.1.1). For a successful identification of gene deletions that prevented CF, I needed to be able to capture CF cells. Therefore, I was mostly concerned about a scenario, where CF cells would acutely fluidize their cytoplasm upon cell mounting and thus appear as non-CF cells.

I designed a testing experiment where I varied the live imaging culture volume, the medium, and the cell concentration. I used CF cells from SD7 starved under standard conditions (see section 3), and evaluated their cytoplasmic state 1h after mounting, as this was the time frame I set for the data acquisition of one 96-well plate to take maximally. Unfortunately, I could not use the standard DIC imaging of lipid droplets for the evaluation of the cytoplasmic state, since DIC imaging of cells on 96-well imaging plates yielded movies of insufficient quality. Instead, I indirectly monitored the cytoplasmic state of cells by observing the cytoskeleton. In CF cells, microtubules mostly disappear or form one very short bundle, and F-actin forms the characteristic shoelace bundles (see section 2.1). When cells exit CF during starvation recovery, the first actin patches and exploring microtubule bundles reappear within minutes. Therefore, the monitoring of F-actin and microtubules immediately reveals a release from CF. The results for a strain expressing GFP-tagged alpha2-tubulin (GFP-atb2), that fluorescently labels the microtubules, and for another strain expressing Lifeact-GFP, that fluorescently labels F-actin, are shown in Figure 18.

First, I simply transferred 100µl from a starvation culture to a well on the 96-well imaging dish, thus incubating cells in their own starvation medium. When imaging such cells live, microtubules were absent and the shoelace actin bundles were present, as expected for CF cells (see Figure 18A; left panel). However, these cells were quite densely packed at the bottom of the well, as they were no longer mixed by the shaking incubator. Interestingly, when I added only about a third of the starvation culture volume (30µl), quite a few cells showed signs of release from CF, with longer microtubule bundles and F-actin patches (see Figure 18B; middle

panel). However, when I removed the supernatant of such a 30µl starvation culture aliquot by gentle centrifugation, and subsequently replenished the cells with 100µl of filtered starvation medium, the cytoskeleton did not show any sign of release from CF (see Figure 18A; right panel). A favourable side effect of this procedure was that the cells were nicely spread into a single layer of attached cells. This facilitated automated image analysis compared to a condition where on top of the attached cell layer additional cells were floating freely.

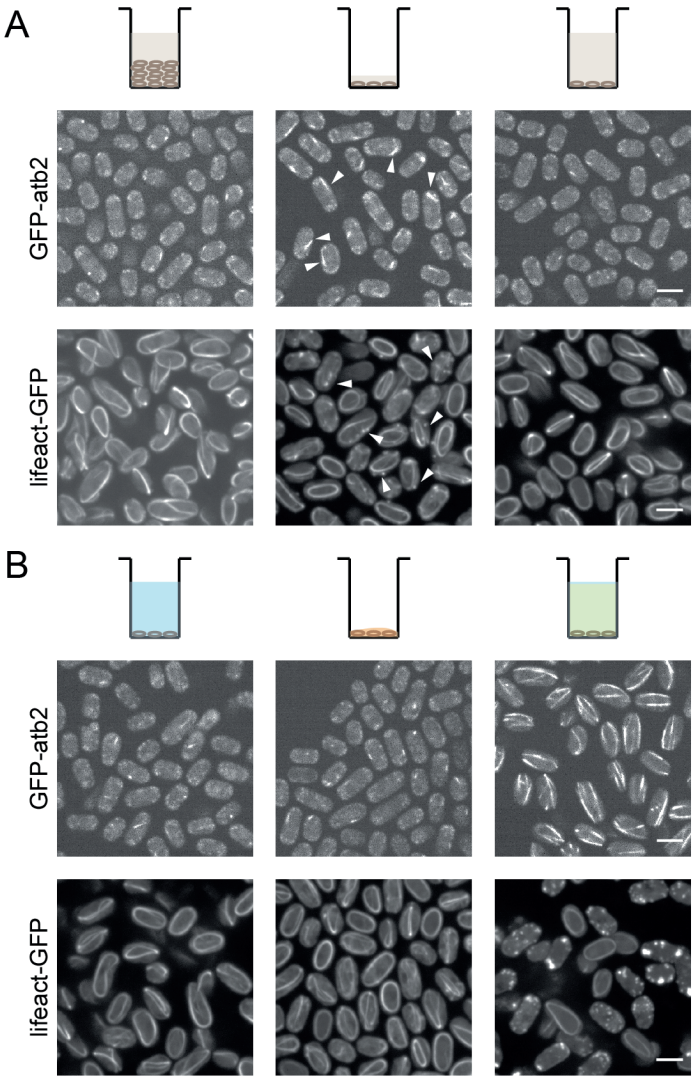

Figure 18. Mounting conditions to capture cytoplasmic freezing on 96-well imaging plates.

(**A**) SD 7 cells with fluorescently labelled microtubules (GFP-atb2, single planes, upper panel) and F-actin (Lifeact-GFP, maximum intensity projections, lower panel) were imaged from a 96-well imaging plate. Left panels: 100µl of starvation culture was transferred to the well. Middle panels: 30µl of starvation culture was transferred. White arrowsheads indicate cells showing signs of release from CF. Right panels: the medium of 30µl of transferred starvation culture was exchanged with 100µl of filtered starvation medium. (**B**) SD7 cells as in (A). Left panels: the medium of 30µl of transferred starvation culture was exchanged with 100µl EMM0 (standard EMM2 medium without glucose). Middle panels: the medium of 30µl of transferred starvation culture was removed and the cells were covered with Voltalef oil. Right panels: the medium of 30µl of transferred starvation culture was exchanged with fresh EMM2. Scale bar is 5µm in all panels.

Next, I tested if cells would stay in CF if instead of the filtered starvation medium, I added minimal EMM medium without glucose (EMM0). Indeed, the cells showed no sign of release from CF (see Figure 18B; left panel). The same was true for cells without any culture medium but protected from dying out by a layer of Voltalef oil (see Figure 18B; middle panel). As a control for recovery, I monitored a well where I added fresh EMM2 to the cells. In these controls, most cells showed long microtubule bundles and F-actin patches instead of the shoelace bundles (see Figure 18B; right panel).
Taken together, these results showed, that CF cells would stay in CF if kept with enough medium without glucose, for at least 1h I tested. For convenience, I decided to go for the EMM0 option from now on.

Knowing that I could keep CF cells in a stable sate for imaging in the 96-well format, I wanted to find conditions where cells cultured in 96-well plates would undergo CF. Already when working with few strains at a time in larger liquid cultures, I had found that CF induction depended on the exact culturing conditions (see section 3.1.2), mostly concerning the amount of aeration of the starvation cultures. Therefore, it was plausible that this would also be the case which the much smaller cultures in the 96-well plates. I started testing various parameters that could potentially have an influence and hoped that I would find conditions where CF was induced. The first parameters I tested were the shape of the wells on the 96-well plate, culturing under static versus shaking conditions, the culture volume, and the temperature. As a readout, I monitored the phenotype and dynamics of mitochondria, which are fragmented and immobile in CF cells (see section 2.1 and 3.3.1). As expected, CF occurred only under very specific conditions on 96-well plates similar to the induction of CF in large volume starvation cultures. No starvation culture incubated in 96-well plates with flat well bottoms (F plates) showed CF (see Figure 19A; right panels), independent of culture volume and shaking conditions. For cells cultured in 96-well plates with conic well bottoms (U plates) under static conditions I found heterogeneous populations with about 50% CF cells and 50% non-CF cells (see Figure 19A; middle panels) independent of the culture volume, similar to large volume starvation cultures in Erlenmeyer flasks under static conditions (see section 3.1.2). Fortunately, I found homogeneous CF cell populations, but only when culturing cells in a specific volume on U plates and in a shaking device (see Figure 19A; left panels). Furthermore, it was crucial that the culture volume and the shaking frequency were balanced such that both, cell sedimentation and medium overflow to neighbouring wells were minimized. All results were similar for a culturing temperature of 25°C and 30°C. I chose to continue with 25°C, since that's what I used

for large volume starvation cultures, and the cells could be imaged at room temperature without experiencing a temperature shock.

When culturing cells on 96-well plates on a shaker with a frequency just high enough to avoid cell sedimentation, culture medium would not overflow to the neighbouring wells, but still wet the gas permeable seal I used, sometimes forming droplets. This was not ideal. Therefore, I tested whether CF would occur if I sealed the wells with plastic foil instead. The result was very clear, showing homogeneous non-CF cell populations (see Figure 19B). This confirmed the need for air exchange as already revealed when culturing yeast cells in a tightly closed screw cap tube (see section 3.1.2).

In summary, I found many conditions where CF did not occur. Luckily, there was a combination of parameters, where cells showed CF: in U plates, closed with a gas permeable seal and a culture volume carefully adjusted to the frequency of the shaker.

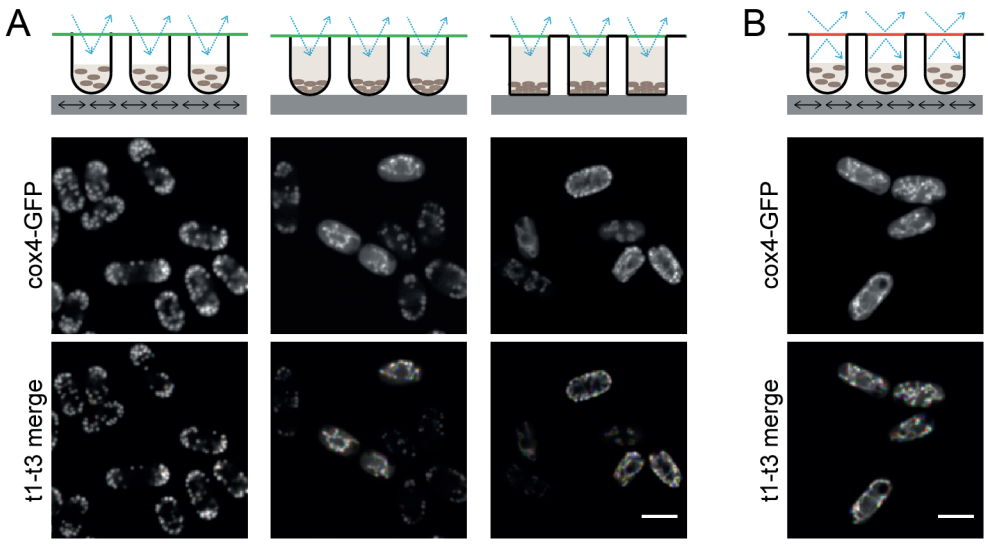

Figure 19. Testing various conditions to induce CF on a 96-well plate.

(**A**) The images show the phenotype (upper panel) and the dynamics (lower panel, 3 time points merged, t1 in red, t2 in green, t3 in blue, time interval 25s) of mitochondria in SD5 cells that were either kept on a shaker during the starvation period (left panels) or cultured under static conditions (middle and right panels). The plates either had flat bottomed wells (right panels) or U-shaped wells (left and middle panels). All culturing plates were incubated at 25°C and sealed with gas permeable seals. (**B**) Images as in (A) with SD6 cells cultured on a shaker in U shaped plates sealed with plastic foil. Scale bar is 5µm in all panels.

After having found conditions where CF was induced in cells cultured on 96-well plates, the next step was to determine a readout for the cytoplasmic state suitable for experimentally handling thousands of strains and subsequently analysing the acquired images using an automated image analysis workflow. So far, I had either used DIC movies to determine the dynamics of lipid droplets, or movies of cox4-GFP to visualize the dynamics of mitochondria.

On the automated screening microscope that I was going to use for data acquisition, DIC or other bright field imaging were not possible. I therefore needed to use fluorescence to determine the cytoplasmic state of the cells. Using the mitochondrial marker cox4-GFP was not an option, as this meant to bring the cox4-GFP into all 3500 deletion strains, either by crossing or by plasmid transformation. This would only be doable with the help of robots, which would have needed additional setting up, and therefore was not my first choice. Instead, I tested different fluorescent dyes labelling mitochondria or lipid droplets, which were the two organelles that we had already established as excellent CF markers.

First, I tested mitotracker red, a red fluorescent dye that is routinely used for imaging mitochondria (the aliquot used was a kind gift of Lucas Pelkmans). I saw fluorescent signal reminiscent of mitochondria as expected in SD7 cells that I incubated for 1h with mitotracker red in fresh EMM2, thus releasing them from CF and starvation (see Figure 20A; right panels). Unfortunately, SD7 cells incubated with mitotracker red in starvation medium did not show any fluorescent signal reminiscent of mitochondria in CF cells neither after a 1h-incubation (Figure 20A) nor after an incubation overnight (Figure 20B). There was strong intracellular fluorescence in some SD7 cells, that I assumed to be dead. Since the accumulation of the mitotracker dye was described to be dependent on the mitochondrial membrane potential, this suggests that the membrane potential in CF cells differs from that of interphase cells. Another explanation for the lack of signal in CF cells is that the dye could not enter CF cells.

In addition to the standard mitotracker I also tested a reduced form of the standard dye that only becomes fluorescent upon oxidation. Also with this dye I could not detect mitochondria in CF cells.

Next, I tested the lipophilic dyes Bodipy493/503, LD540 (the aliquot used was a kind gift of Robin Klemm) and NileRed (see Figure 20C). Bodipy stained the lipid droplets in CF cells quite homogeneously. A downside of this dye was the high rate of photo bleaching as evident when comparing signal intensities of the first and the last time point of a 1 minute movie (Figure 20C). LD540 stained the lipid droplets nicely and showed less photobleaching in the red fluorescent channel (see Figure 20C). Unfortunately, this dye in addition to its red fluorescence also emitted green fluorescence (see Figure 20C). This was problematic, as I was planning to do two colour imaging, whereby one colour would be used to detect the cell outlines. In addition, I saw some signs of recovery from CF in the cells stained with LD540.

Finally, I also tried the dye NileRed, which also is well established and in addition inexpensive. Unfortunately, also NileRed was not suitable for staining the lipid droplets in CF cells, as only

a subset of CF cells showed fluorescent signal (see Figure 20C). Taken together, these results suggested that Bodipy was the best option for lipid droplet imaging in CF.

Finally, I aimed to find a fluorescent dye that labelled the cell outlines to serve as a basis for single cell segmentation. This was important, as I wanted to monitor the cytoplasmic state in single cells. The dye needed to be red fluorescent, as the green channel was occupied by Bodipy-labelled lipid droplets. I knew of two dyes that could potentially work – rhodamine lectin and Phloxine B. Lectins are glycoproteins that bind the carbohydrates of the cell wall with high affinity, and together with rhodamine consistently labels cell outlines. Phloxine B is an established marker for identifying dead cells, as it is passively taken up by fission yeast cells but actively excreted only from metabolically active cells (Roux et al., 2006). I had used it before for this purpose, and observed that it nicely stains the cell outlines of metabolically active cells (see Figure 20D). Thus, Phloxine B staining simultaneously provided cell outlines and a method to discriminate dead cells. This was very fortunate, since the identification and exclusion of dead cells was of central importance for the analysis of the screen, as the cytoplasmic state of dead cells is naturally static. I had initially planned to exclude the dead cells based on their complete lipid droplet immobilisation, but had already anticipated problems in the clear distinction to CF cells. Additionally, the intracellular signal of Phloxine B in living cells was higher than in cells stained with rhodamine lectin. This facilitated the identification of single cells with our segmentation strategy. Therefore, I decided to use Phloxine B for cell segmentation and simultaneous identification of dead cells.

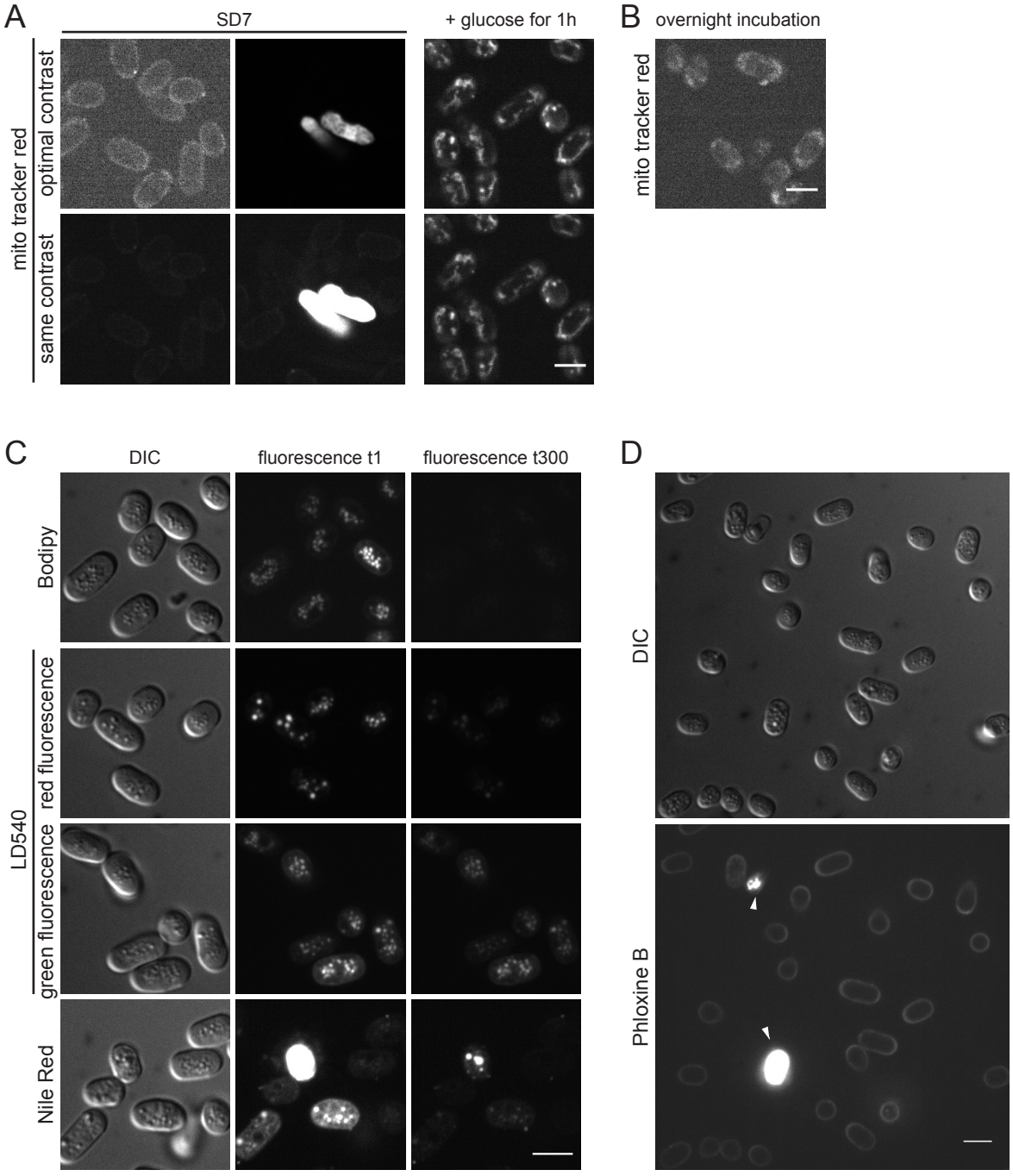

Figure 20. Testing dyes for visualizing mitochondria or lipid droplets, and cell outlines.

(**A**) Images show cells stained with mitotracker red after 1h of incubation in SD7 cells (upper left panel) or SD7 cells recovered from starvation by incubation in fresh EMM2 at the same time as incubating with mitotracker red (right panels). The visible fluorescence around the SD7 cells was very low compared to the specific mitochondria signal (lower panels shows images with same contrast settings for comparison of signal intensities). Only a few cells showed a very high intracellular signal, these were presumably the dead cells (middle panels). (**B**) Image shows mitotracker red in SD7 cells after overnight incubation. (**C**) Images show cells labelled with Bodipy (top), LD540 (middle) and NileRed (bottom) at SD8 (for cell location see DIC images, left panels). The photo bleaching can be estimated by comparing the first frame (middle) to the last frame (right) of a 1 minute movie of 300 frames. (**D**) Images show Phloxine B in SD8 cells (lower panel; for cell location see DIC image, upper panel), staining the cell outlines of metabolically active cells and the entire cell of dead cells (white arroweadss). Scale bar is 5µm in all panels.

3.4.1.2 Image analysis

After having found experimental conditions where CF occurred on 96-well plates and could be monitored in a way that was easily scalable to thousands of strains, the next step was to develop an analysis pipeline for the automated determination of the cytoplasmic state of single cells. First, I describe how I segmented the cells labelled with Phloxine B. After this, I report the CF index that I developed to describe the dynamics of lipid droplets from the Bodipy signal as a measure for the cytoplasmic state of cells.

3.4.1.2.1 From Phloxine B signal to segmented cells

I started the segmentation pipeline with preprocessing the raw Phloxine B images (see Figure 21A) in cellprofiler (Carpenter et al., 2006). I corrected for the camera noise and the uneven illumination of the camera chip by subtracting the dark frame and dividing the resulting image by a normalized image generated by the microscope for this purpose. As a result, the background pixels had near zero values and the signal intensities were even across the image (compare Figure 21A and Figure 21B; intensity profile 1).

The pixel classification software ilastik (Sommer, Straehle, Köthe, & Hamprecht, 2011) that I wanted to use next, could not handle the large 16-bit images acquired by the microscope. Therefore, I needed to convert the 16-bit images (65535 grey values) to 8-bit images (255 grey values) to reduce the file size. The main challenge for this were the dead cells that were present in some images but not in others. The fluorescent signal of these dead cells was about 20x higher than the cell outline signal. By simple linear down sampling of the covered intensity range in an image to 255 values, the actual cell outline intensities covered only around 10 grey values, while the dead cells occupied the rest (see Figure 21C; upper panel). Moreover, if there were no dead cells present in a particular image, the cell outlines had intensities that were 10x higher than the outlines in images containing dead cells (see Figure 21C; lower panel). This would complicate the actual cell segmentation. To circumvent these problems, I processed the images in Fiji (Rueden et al., 2017; Schindelin et al., 2012) prior to the 8-bit conversion. I applied a logarithmic transformation to boost the lower signals in respect to the higher signals. Subsequently I reduced the thereby increased background noise by applying a background subtraction filter. To avoid the problem of images without any dead cells having very different absolute values in cell outlines after the conversion, I reset the dynamic range to the global minimum and maximum of all images of a 96-well plate prior to the final 8-bit conversion. In this manner, I could reduce the relative intensity difference between living and dead cells, and the cell outlines covered a reasonable 100 grey values independent of the presence of dead cells in the image (see Figure 21D).

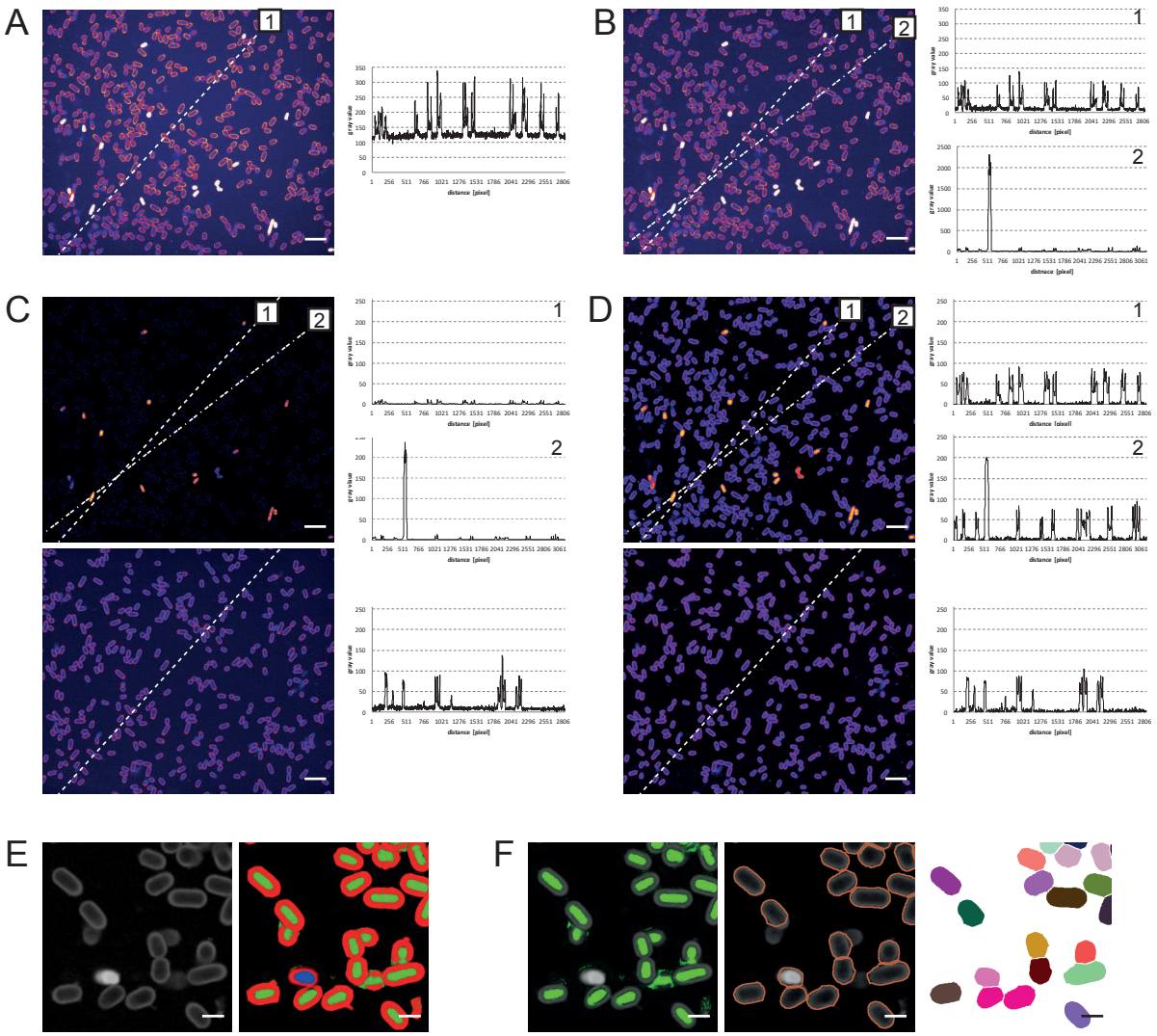

Figure 21. Establishment of a cell segmentation workflow.

(**A**) The raw Phloxine B image is shown colour-coded with a look-up-table from blue to yellow (low to high; left). The intensity profile (right) shows the grey values of the pixels indicated by the dashed line (1). (**B**) Shown is the image from (A) corrected for camera noise and uneven illumination. The intensity profile of the dashed line (1, top) covers alive cells only, while the profile of the dotted-dashed line (2, bottom) covers one dead cell. (**C**) Shown is the image as in (B) but reduced to 8-bit by linear downsampling from a 16-bit image rescaled to its minimum and maximum grey value (top), with intensity profile as in (B). Bottom panel: the same processing steps applied on an image without any dead cells. (**D**) The images, preprocessed as described in (B) are shown after applying a logarithmic transformation followed by a background subtraction. The 8-bit conversion was done after rescaling the grey values from a global minimum to maximum, thereby minimizing the dependence on the number of dead cells present. (**E**) The processed Phloxine B images (left) were classified pixel-wise (right) into 4 classes: "background" (black), "cell outline" (red), "cell inside" (green), "dead cell" (blue). (**F**) The "cell inside" class served as the input for cellprofiler to segment into seeds (left), from which the cell outlines were found based on the Phloxine B signal (middle: Phloxine B overlaid with red cell outlines; right: the segmented cells). Scale bar is 20µm in (A)-(D) and 5µm in (E)-(F).

In order to actually segment the cells from the Phloxine B images, I had to do a small detour. The idea for the strategy I followed in the end, came from Yauhen Yakimovich, a former member of the group of Prof. Lucas Pelkmans, during the preparation for a student course. The main challenge in image segmentation is to separate objects that touch each other. For

stereotypically shaped cells like fission yeast, people often use shape preconditions in order to segment the clumped cells, for example: tell a software to best fit cylinders or ellipses of a certain size range to a clump of signal. In my case this was not an option, since I wanted to perform a genome-wide screen of deletion mutants, many of which had shape defects like being round, bent, long or even T-shaped. Therefore, we went for a strategy that is often applied to mammalian cells. Here the nuclei are segmented first from a nuclear staining. This can be accomplished by simple thresholding, since nuclei do not touch each other but are separated by the surrounding cytoplasm. With the segmented nuclei, the software knows how many cells there are on an image, and where to look for them. The only thing left to do, is to find the cell outlines going out from these cell seeds.

In our lab, we did not have an established fluorescent dye for nuclei. Instead of finding a suitable dye and having to go for 3 colour imaging, we generated pseudo-nuclei by using pixel classification in ilastik on the processed Phloxine B images. I trained the software such that it classified the pixels into the classes “dead cell”, “cell outline”, “cell inside” and “background” (see Figure 21E). The “cell inside” class were my pseudo-nuclei. The aim of the cell outline class was simply to separate the cell insides of neighbouring cells, similar to the role of the cytoplasm in the mammalian cells. The dead cell class allowed me to exclude the dead cells from the later analysis. The output of this pixel classification were pseudo-images with intensity values indicating the probability to belong to a certain class.

I segmented the seeds from the pseudo-images showing the probability to belong to the class “cell inside” in cellprofiler. Going out from these seeds, cellprofiler found the outlines of the cells with the help of the processed Phloxine B image (see Figure 21F).

3.4.1.2.2 The CF index

After having developed a segmentation workflow, I aimed to determine the lipid droplet motion in cells as a readout for the cytoplasmic state. For the screen, I imaged the lipid droplet dynamics using Bodipy (see section 3.4.1.1). I did not want to manually evaluate the lipid droplet dynamics for each of the 3500 gene deletion strains. Instead, I aimed to generate a quantitative measure for the cytoplasmic state by automated image analysis. Previously, I had quantified the dynamics of fragmented mitochondria by single particle tracking and subsequent mean squared displacement analysis (see section 2.1), which is an established method to quantify motion. However, this was not the ideal method for this screen mainly due to the high photobleaching that the Bodipy signal was subject to. This made it impossible to follow the lipid droplets through enough time frames that would allow me to quantify a reasonable mean

squared displacement while limiting the acquisition time for one 96-well plate to 1h, the time I had established the experimental conditions for.

Taking a step back, we asked ourselves whether it was necessary to segment the lipid droplets in the first place. Could not just the change of their localization provide enough information to distinguish static from dynamic lipid droplet compositions? The change of their localization can be viewed as the degree of co-localization between two time points. A quantification that is often applied to estimate the degree of co-localization of two fluorescent markers is the Pearson Correlation Coefficient (CC). The CC is a measure for the linear correlation between two variables (Wikipedia). The CC ranges from -1 to 1 with 1 being perfect correlation, 0 no linear correlation and -1 perfect anti-correlation (see Figure 23A). In my case the variables were the grey values of all the pixels of two time points. In order to see if the CC could be used to describe the lipid droplet dynamics, I compared the CC with the qualitative impression of the dynamics of lipid droplets of reference cell populations. I found a good correlation, but only after a multi-step processing of the Bodipy images prior to computing the CC.

First, I applied the same preprocessing steps as for the Phloxine B signal to correct for camera noise and for uneven illumination (see Figure 22A). To correct for the xy-drift within the focal plane I applied the Fiji/ImageJ plugin *StackReg*. I had no means to correct for z-drift of the focal plane, since I only acquired a single plane to minimize the photo bleaching. This was no problem if I acquired just one 42sec movie of 6 frames, since the focal plane stayed very constant during that time. However, it made the acquisition of more data per one strain/well impossible. The 42 seconds was the maximum time to spend per well, if I wanted to limit the acquisition time for one plate to about 1 hour. Therefore, the only option to increase the amount of data per well was the acquisition of multiple movies in parallel (eg. first frame for 3 positions, then second frame for the 3 positions etc.). In theory, this would have been no problem, the microscope could change positions very fast, but unfortunately the auto focus was not accurate enough to repeatedly find the exact same plane. Therefore, such movies acquired in parallel were very unstable could thus not be used to determine lipid droplet dynamics. Luckily the screening microscope I used was equipped with a large camera chip, allowing the acquisition of around 300 cells at once. 300 cells we thought were enough to reasonably estimate the cytoplasmic state of a cell population allowing me to make only a single movie per strain. Next, I corrected for the acquisition photobleaching with the Fiji function *Bleach Correction* (compare Figure 22A with Figure 22B).

The main challenge of the Bodipy staining was, similar to the Phloxine B signal, the uneven intensity among cells of the same population. In some populations, some cells had very intense

lipid droplets compared to the rest of the cells (orange arrows in Figure 22B). Therefore, the lipid droplet intensity in the last time frame was hardly distinguishable from the background noise in some cells. Applying the same image processing steps in Fiji as I did for Phloxine B (logarithmic transformation, background subtraction, see section 3.4.1.2.1) improved the images (orange arrows in Figure 22C). However, the correlation coefficient from these corrected images still did not correlate strongly with the qualitative evaluation of lipid droplet motion.

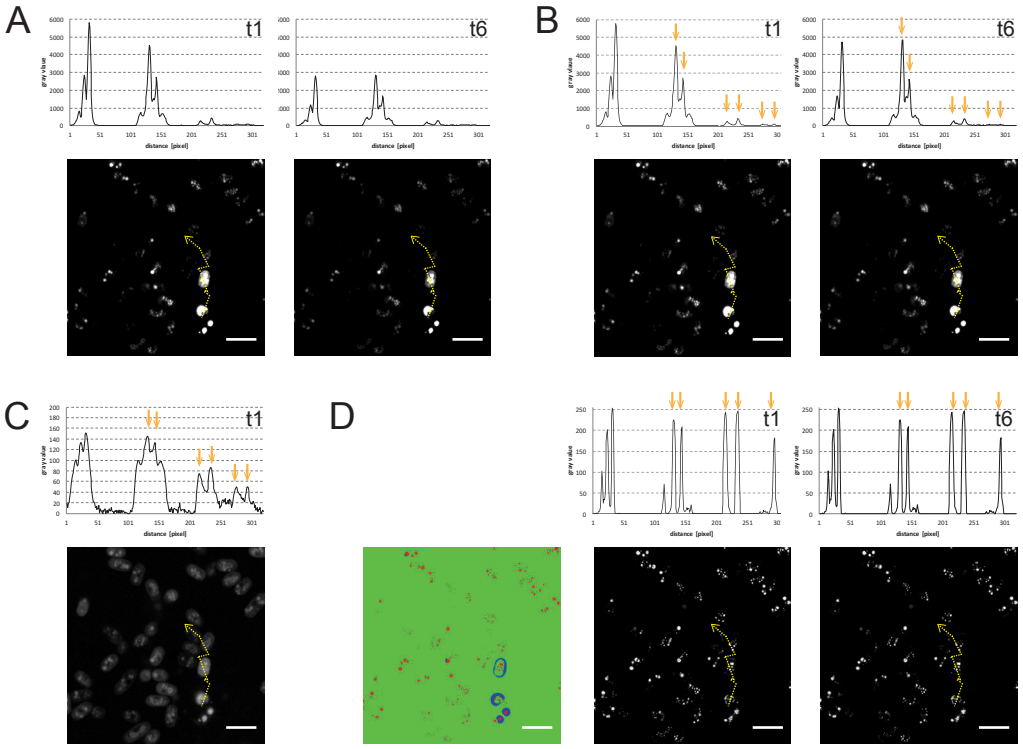

Figure 22. Processing the Bodipy signal of lipid droplets.

(**A**) The images show the first (t1; left) and last (t6; right) frame from a 42s movie of Bodipy-labelled lipid droplets. The images were corrected for camera noise, uneven illumination and xy-drift in the focal plane. The intensity profiles displayed above the images represent the grey values of the pixels indicated by the dashed yellow line. (**B**) Shown are the images and profiles as in (A) after correction for acquisition photobleaching. The Bodipy signal intensities varied greatly between different cells (orange arrows). (**C**) The first movie frame as in (B) after a logarithmic transformation followed by a background subtraction. (**D**) The processed Bodipy images were pixel-wise classified in ilastik into 3 classes (left): "background" (green), "lipid droplets" (red) and "intense cytoplasm" (blue). Shown are the first and last frame of the "lipid droplet" class ilastik output (middle and right), where the orange arrows indicate the lipid droplets in the intensity profiles. Scale bars is 5µm in all panels.

Whereas before I hypothesized that the presence of the high intensity lipid droplets influenced the correlation coefficient very strongly, the problem with the processed images was likely the increased cytoplasmic noise. To decrease this noise and thereby increase the signal to noise ratio of lipid droplets to cytoplasm I used again the pixel classification software ilastik. I trained ilastik to classify the pixels into the 3 classes "lipid droplets", "background", and a "helper

class" for high cytoplasmic signal. The output of this step were pseudo-images, showing the probability for each pixel to belong to the 3 classes, colour coded as an RGB image (see Figure 22D). The "lipid droplet" class image showed lipid droplets that were now very clearly distinguishable from the cytoplasm and the background. When evaluating the CC computed from these pseudo-images there was a clear correlation with the qualitative evaluation of example populations.

After processing the Bodipiy signal of lipid droplets as described above, I had an improved input to compute CCs. I had acquired 6 time points every 7s for each position. I could compute the CC from each time point versus the first time point for each single cell. With this I could be was confident to discriminate frozen from non-frozen cell populations, as I had assayed on example cell populations.

Therefore, I performed the actual genome-wide screen of the gene deletion library with 38 96-well plates in 2 independent repeats (screen 1 and screen 2).

After the data acquisition and data processing as described above, I computed the CCs for each single cell for the time points 2-6 versus the first time point (example plate shown in Figure 23B; the corners of the plates could not be imaged for technical reasons). To facilitate the identification of interesting candidate genes, I wanted to describe the cytoplasmic state by a single number instead of having CCs for each cell for 5 time intervals. I hoped, that the median of CCs might serve as such a number. To test this, I manually classified 3 plates with 91 deletion mutants plus 1 wildtype control per plate into three classes: "clearly non-CF", "possibly CF" and "CF". I then compared the medians of CCs from the manually classified as frozen and the totally non-frozen cell populations from t2-t6 versus t1 (see Figure 23C). The CC medians from frozen and non-frozen populations were clearly different for all the 5 time intervals, with the highest difference in CC medians from the last to the first time point (t6 vs t1 in Figure 23C).

Therefore, I defined the CF index as the median of Pearson correlation coefficients from all cells in a population. The values well above 0.9 indicated clear CF, whereas lower values in the 0.8 range indicated clear non-CF cell populations. The absolute values for the CF index were dependent on the ilastik training I applied on the Bodipy images prior to computing the CCs. Therefore, to be comparable, I applied the same training on all the plates of both screens and all the wildtype control plates. I found, that indeed the CF index nicely separated the manually classified frozen vs non-frozen populations for both screens (see Figure 23D).

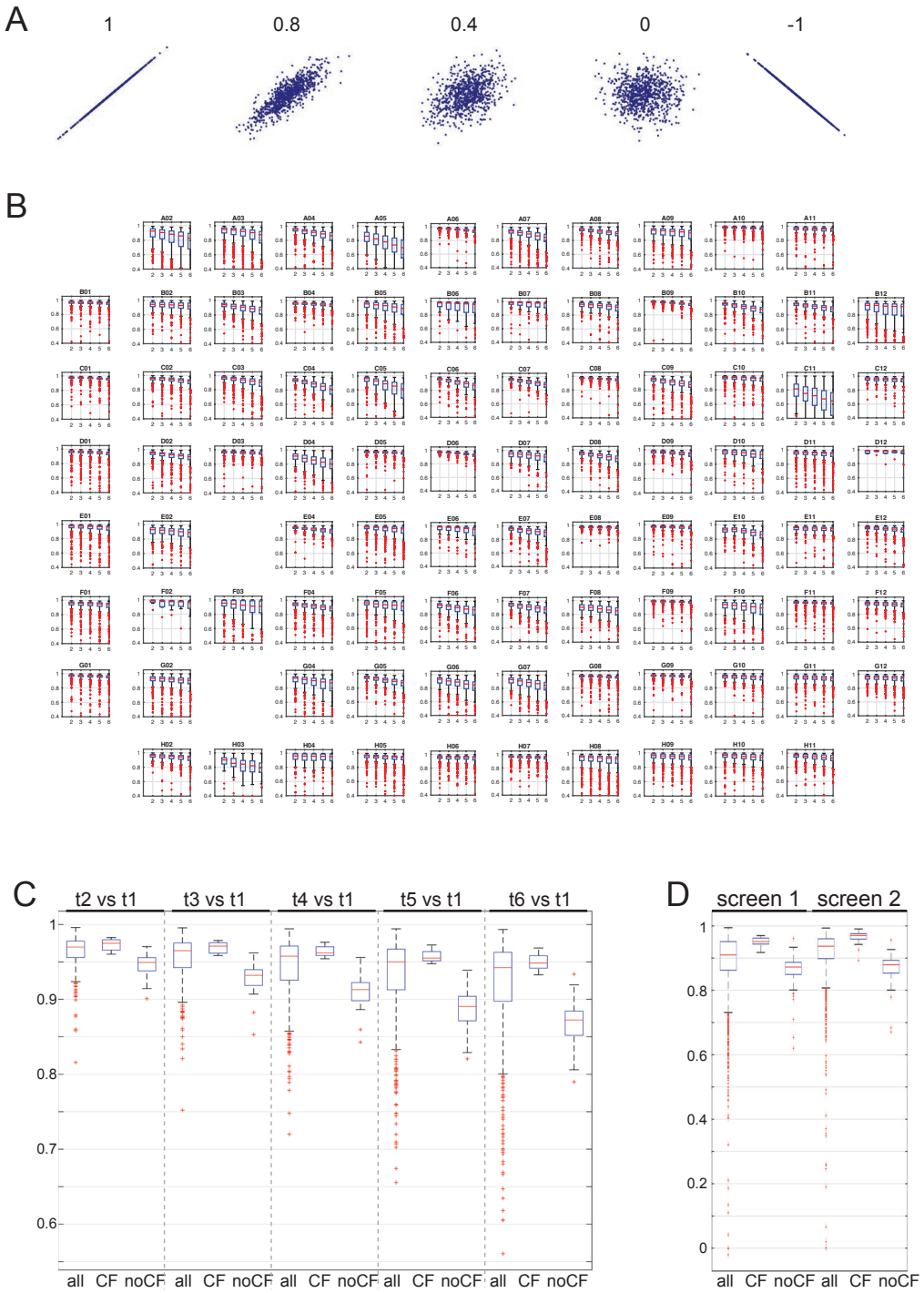

Figure 23. The cytoplasmic freezing index.

(**A**) Examples of the Pearson correlation coefficient (CC). (**B**) The boxplots show correlation coefficients of single cells from t2 vs t1 to t6 vs t1 for all the wells on a 96-well plate. The corner wells are empty because they could not be imaged on the microscope. In the other two empty wells, no cells were detected. (**C**) The boxplots show medians of single cell CCs from all the screen 1 deletion mutants, and the subsets of manually classified as frozen and non-frozen populations for time points t2-t6 vs t1. (**D**) The boxplots show the CF index for all deletions and the manually classified frozen and non-frozen subsets for the two independent genome-wide deletion mutant screens. The CF index was defined as the population median of single cell CCs from t6 vs t1 (time interval 42s).

3.4.2 Results of screen 1 and screen 2

3.4.2.1 General overview

In the last chapter I described, how I established the experimental conditions to induce CF in a large number of samples. I also described how I developed an analysis workflow that ended in the CF index, one number that characterized the cytoplasmic state of a population of cells with values close to 1 for CF cell populations.

In the following section I will describe the results of the actual screens (1 and 2), where I subjected all 3500 strains from the gene deletion library to a starvation protocol that induces CF in wildtype cells, and subsequently evaluated the cytoplasmic state of all cell populations using the data acquisition strategy and analysis workflow introduced above. The resulting CF indices (the median of the cell-based Pearson correlation coefficients of the processed Bodipy labelled lipid droplets of a cell population) are summarized in Figure 24. A histogram of the CF indices of the deletion strains from screen 1 (see Figure 24A; left) revealed a clear bimodal structure, with the two peaks correlating with the peaks of the subset of strains manually classified as non-frozen and frozen. Interestingly, the bimodality of the CF indices for screen 2 was less unambiguous (see Figure 24A; right). While the distribution could be bimodal with the two maxima closer together than for screen 1, or with significantly more populations in the CF mode, it could also be a skewed unimodal distribution. However, since we had the results from screen 1, and the two subsets of manually classified strains, I did not test this further but assumed the first, i.e. that it was a bimodal distribution. If the two maxima were closer together, this would indicate a higher CF index for non-CF populations, whereas the same distance between the maxima of the two modes but a larger number of strains in the CF mode, would indicate more strains entering into CF. Qualitatively, the latter seems more likely, especially since the subpopulations that I classified manually to be CF or non-CF have CF indices comparable to screen 1.

Next, I was interested in the CF indices of the wildtype control populations. On each of the 38 96-well plates I screened, there was one wildtype control well. Additionally, the first and the last plate I imaged each day during the screen data acquisition were control plates filled with wildtype starvation cultures. For screen 1 this resulted in 6 full control plates, and for screen 2 in 8 full control plates. The CF indices for the screen 1 and the screen 2 control populations were, as expected, mostly in the very high CF index range (see Figure 24B), with the distribution maxima at CF index values comparable to the higher maxima of the bimodal

distribution of all populations. This indicated that most wildtype control populations were able to induce CF under the experimental conditions applied.

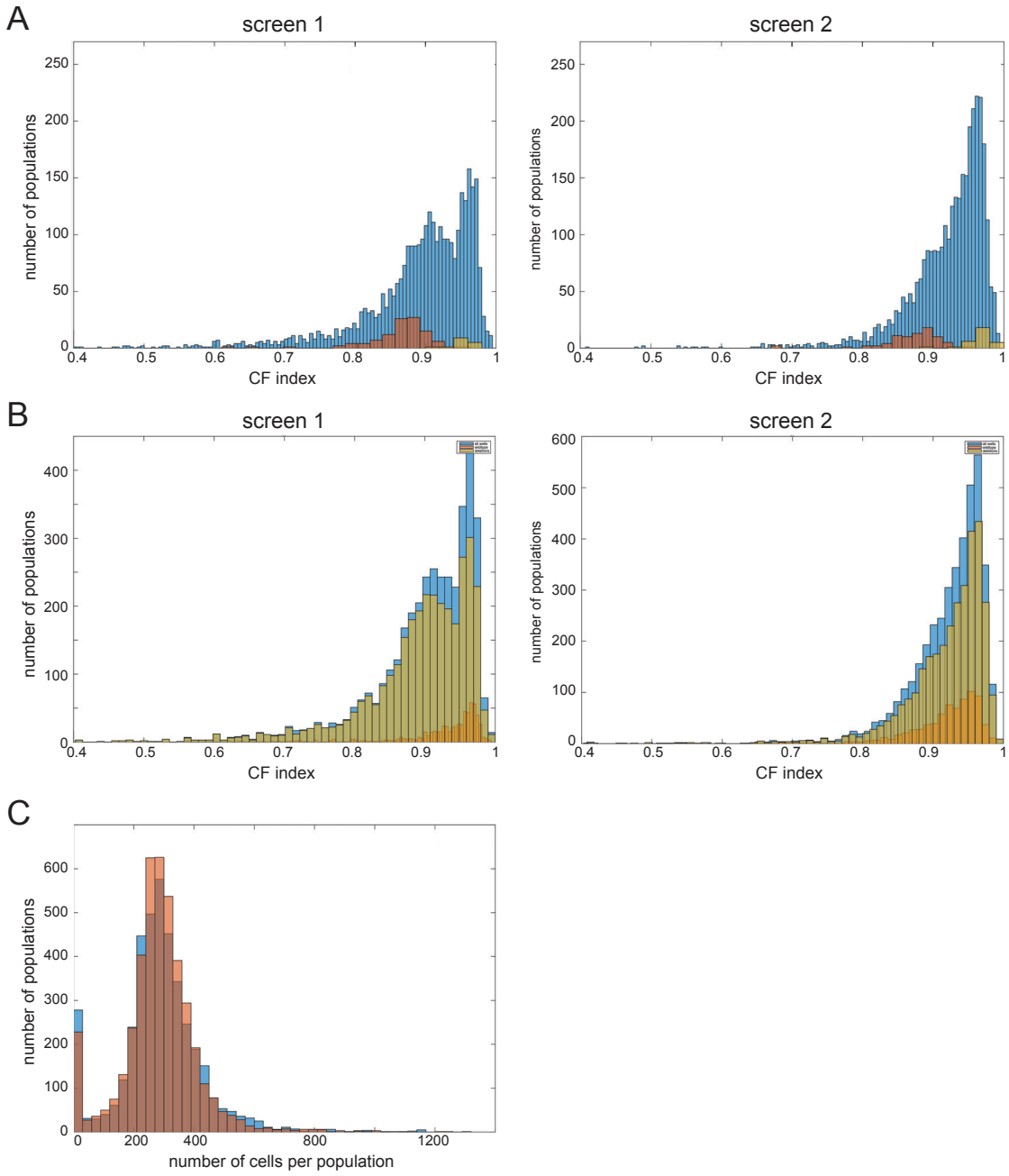

Figure 24. Overview of screen results.

(**A**) The histograms show the distribution of the CF index of all deletion mutants (blue), only the subset I manually classified as non-CF (red), and the subset manually classified as CF cell populations (yellow) for screen 1 (left) and screen 2 (right). (**B**) The histograms show the CF index distribution for all the populations including the wildtype controls (blue; left panel screen 1, right panel screen 2). Overlaid are the cytoplasmic freezing indices of only the deletion mutants (yellow) and only the wildtype control populations (orange). (**C**) The histogram shows the distribution of cell numbers per population for screen 1 (blue) and screen 2 (red).

Aside from the pure CF index, I also looked at the number of cells behind the CF index. For both screens the cell number distribution was very similar, with a maximum around 300 cells

(see Figure 24C). Some deletion strains did not grow up, explaining the many populations without any cells.

Taken together, the results looked promising, with the deletions spanning the whole range of CF index values and the wildtype controls being clearly shifted towards the high CF index values.

3.4.2.2 Identification of candidate genes that are potentially required for CF

After this general evaluation of the screen results, I wanted to identify interesting candidate genes that were potentially required for CF. These were the genes where the corresponding deletion strains were not frozen in neither of the 2 screen repeats (see Figure 25A for comparison of CF indices from screen 1 and screen 2).

To separate CF from non-CF populations we decided to follow a straight-forward strategy and define a CF index threshold, below which I would consider populations as non-CF. I chose a CF index threshold of 0.9, which nicely separated the manually classified frozen and non-frozen subsets (see Figure 25B). As an entry point to the molecular mechanism of CF we wanted to go for the clear candidates, with the possibility to go back to the strains with indices close to the threshold in a second step.

In total, I prepared 3420 deletion strains for deep starvation. In screen 1, 3254 strains grew up while in screen 2, 3304 strains grew up, such that I could segment cells and compute a CF index. In screen 1, 1452 strains had an index of below 0.9 whereas only 894 strains of screen 2 had an index under 0.9. There were 550 strains with a CF index below 0.9 in both screens (see Figure 25C). These were the candidate genes I wanted to further evaluate. This also meant that by repeating the screen, I could reduce the number of possible candidates by 38%.

As I described previously, wildtype cell population did not always undergo CF (see section 3.1.2). However, in screen 2 there was a significant number of wildtype populations with a very low CF index (see Figure 25D. I excluded those as artefacts, as they all originated from one half of a control plate, where cells apparently had not been immobilised properly. After this, the number of wildtype populations classified as non-CF (index < 0.9) added up to 103/624 (16%) in screen 1 and 193/766 (25%) in screen 2. When combining the two screens, only 60 wells were left that did not show freezing at least once. Like this, I could estimate a false positive rate of candidate genes of 10% (see Figure 25D). In other words, at least 10% of my candidate genes were not actually required for CF, but had a potential similar to wildtype cells to undergo CF. Therefore these 550 candidate genes needed to be carefully evaluated and rescreened.

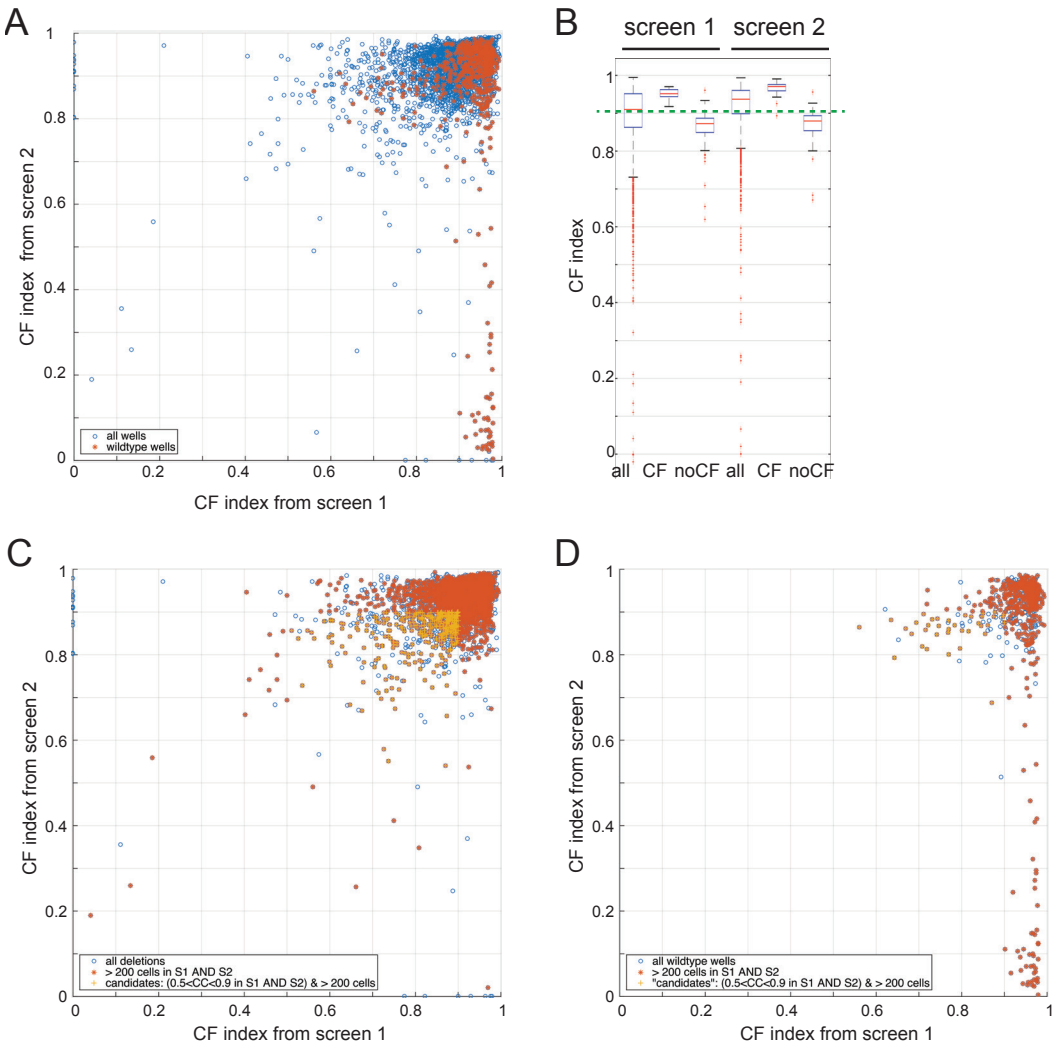

Figure 25. Finding candidate genes that were potentially required for cytoplasmic freezing.

(**A**) Scatter plot comparing the CF index of all deletions (blue) and wildtype control populations (red) from screen 1 and screen 2. (**B**) Boxplot visualizing the CF index of all deletions and of the manually classified subsets from both screens. The green dashed line indicates the threshold I defined for the selection of candidate genes. (**C**) Scatter plot as in (A) but with the identified candidate genes indicated in yellow. (**D**) Scatter plot as in (A) showing all the wildtype populations (red), and the wildtype populations that would classify as candidate populations (yellow), indicating the scale of false positives among the candidate genes.

Before the validation of the identified candidate genes, I wanted to investigate the influence of the position on the 96-well plate on the CF index. During the data acquisition I had already seen, that not all the wells contained the same culture volume. Some wells mainly from the circumference of the plate were even dried out. To prevent a well bias coming from the incubation position, I positioned the plates the opposite way in the incubator during the starvation period for screen 1 and screen 2. The imaging however, was always done from well A2-H11. To visualize a potential well bias, I plotted the median of all CF indices from wildtype control populations grown in a given well as a color-coded square on a schematic 96-well plate (see Figure 26).

Interestingly, there was a clear well bias, with lower CF indices in the upper central wells for both screen repeats (see Figure 26A). The reason for this could not be the orientation of the plates in the incubator during the starvation period, as the plates were purposely placed the opposite way for screen 1 and screen 2.
Another possible reason for an uneven distribution of CF indices over control plates, was that I used two control strains that differed in their ade6 mutation – one had ade6-M210 and the other ade6-M216. These were the two parental strains used for constructing the library from diploid cells, so some of the deletion strains contained one mutation and some the other (see Appendix). However, for each day of screen data acquisition, I imaged 2 wildtype plates, one with ade6-M210 filling the wells A1-D12 and ade6-M216 filling the lower wells E1-H12 and vice versa. Therefore, the observed well bias could not originate from a potential effect of the ade6-mutation on the CF index, since its effect would be erased by averaging over all the plates. So there seemed to be an intrinsic well bias for no obvious reason. From personal communication, I heard that this is not uncommon for such screens. The question was, how much did it influence the selection of candidate genes. To find out, I plotted the medians of all candidate genes of a given well onto a representative 96-well plate (see Figure 26B). There were candidate genes from most wells of the plate. Hence, the candidate genes were not purely defined by their well position, but by their cytoplasmic state. However, the absolute CF index clearly depended on the well position, as it was significantly lower for the deletion strains that had grown up in the upper central wells.

In summary, I applied a rather raw but fast strategy for the selection of candidate genes from the CF indices. Behind this was the notion, that our immediate aim was not the identification of all genes that are required for CF in a lengthy analysis, but to identify a small set of genes that was required for CF without spending too much time on the actual identification process. This would provide us with an entry point to elucidate the molecular mechanism causing CF in a more directed approach.

Assuming I had more time, I would attempt to develop a more sophisticated candidate gene selection approach than a simple threshold of the CF index. I would try to take into account the well bias that I observed, for example by weighing the CF index of a deletion population in a given well with the CF index of wildtype control populations grown in the same well. Moreover, I would try to test statistically if the CF index distributions were indeed bimodal and try to describe the two underlying distributions for both screens. This would allow the

determination of a probability for each deletion population for each screen to belong to the non-CF class. From these probabilities, I would define a threshold with which I would likely identify a more complete list of candidate genes.

Assuming I had even more time, I would attempt to select candidate genes not only based on the CF index – the median of the cell-based Pearson correlation coefficients of the processed Bodipy labelled lipid droplets of a cell population, but also the distribution of correlation coefficients. This would provide information about the heterogeneity of cell populations, and potentially allow the exclusion of candidate genes that showed heterogeneous cell populations where a subpopulation of cells still managed to induce CF.

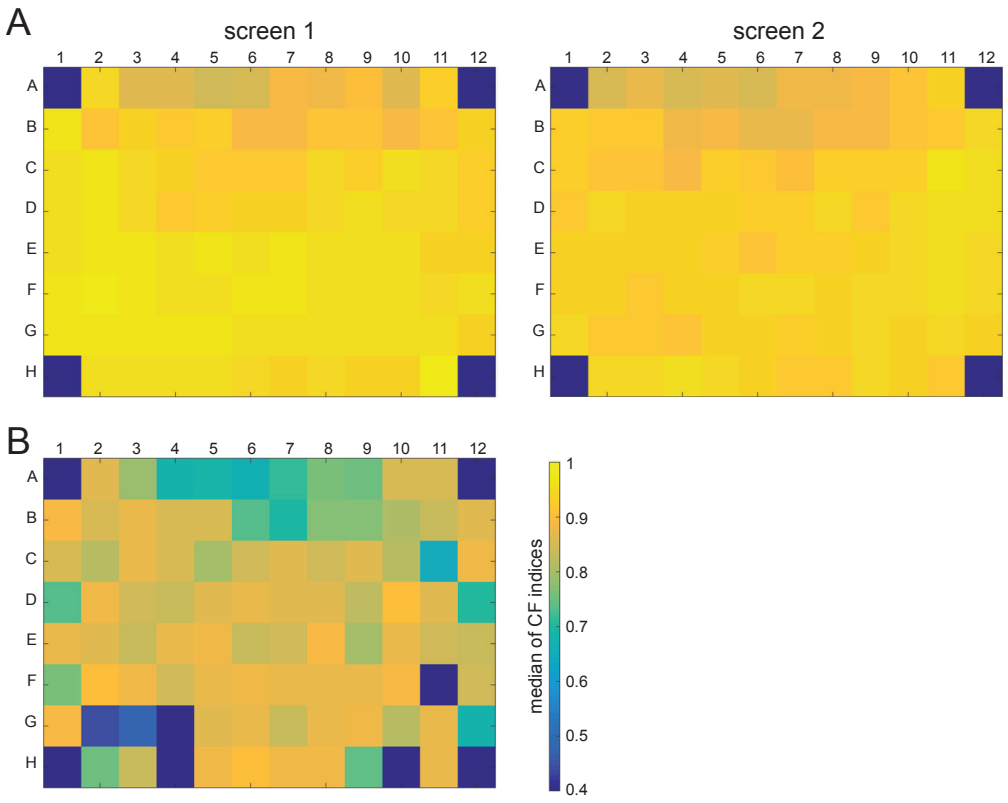

Figure 26. Influence of a strain's position on 96-well plate on CF index.

(**A**) The images represent 96-well plates showing the color-coded median of all 6-9 cytoplasmic indices from the wildtype control populations for screen 1 (left) and screen 2 (right). (**B**) The image represents a 96-well plate as in (A) with the median of cytoplasmic indices from the candidate gene deletions. The colour code is the same for all panels.

Next, I subjected my candidate list to a gene ontology (GO) term enrichment analysis (http://go.princeton.edu/cgi-bin/LAGO; (Boyle et al., 2004)) to see, whether a special group of genes was overrepresented among the candidates in comparison to the whole genome. There was no molecular function term significantly overrepresented, but in both the GO terms describing cellular components and the biological processes, autophagy-related terms were

significantly overrepresented (see Figure 27A). Indeed, when I summarized the CF indices of all known autophagy genes in fission yeast, more than half of them did not undergo CF in both screens (see Figure 27B, modified from (Mukaiyama, Nakase, Nakamura, Kakinuma, & Takegawa, 2010)).

This was very interesting, as autophagy is an evolutionarily conserved mechanism used by cells to remove damaged organelles and to recycle cellular components (Yang & Klionsky, 2010). Notably, this might be the first indication that autophagy is induced under specific glucose starvation conditions in fission yeast, as autophagy was thus far reported to be induced only by nitrogen starvation but not carbon starvation in fission yeast (Kohda et al., 2007), (Nakashima et al., 2006). Could this process be required for CF to recycle the proper building blocks, or provide energy necessary for the rebuilding? We followed this hypothesis up by selectively evaluating two major factors required for autophagy, atg1 and atg8 (Kohda et al., 2007). As described in the manuscript (see section 2.1), we found that these genes were not required for cytoplasmic freezing. However, the onset of CF was delayed by about 2 days in strains deleted for atg1 and atg8.

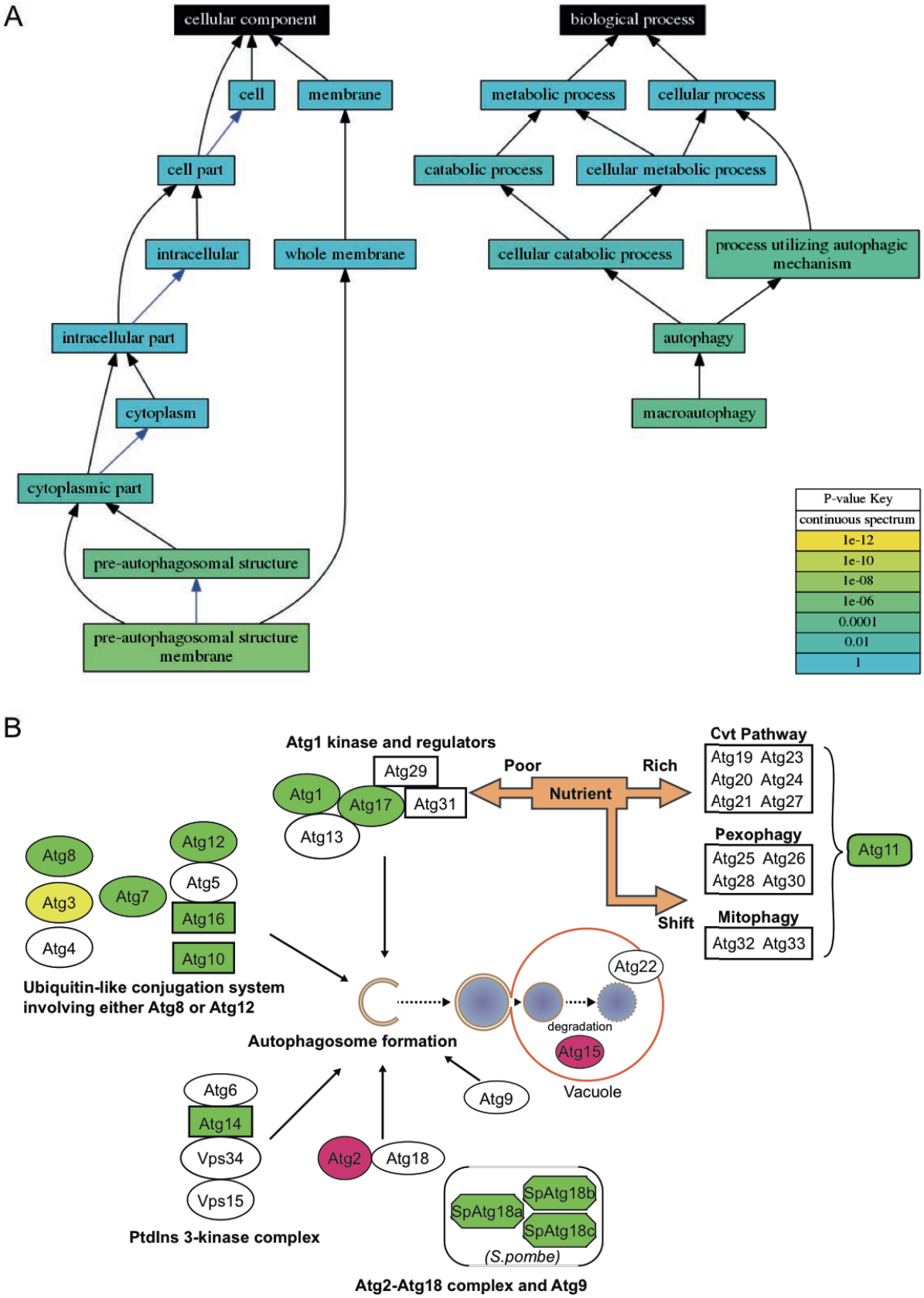

Figure 27. GO term enrichment and overview of autophagy candidate genes.

(**A**) GO terms enrichment analysis showing colour coded significance of term enrichment. (**B**) Overview of autophagy in fission yeast modified from (Mukaiyama et al., 2010). Many genes were not frozen in both screens (green), not frozen in 1 screen but did not grow up in the other (yellow), or clearly non-frozen in one screen but with a CF index value close to the threshold in the other screen (pink).

3.4.3 Validating the candidate genes

After having identified 550 candidate genes, of which the deletion strains clearly did not undergo CF in two experiments, I wanted to evaluate these candidate genes further. This was of vital importance, since I expected to have a rate of false positive candidates of 10%, similar to the non-frozen wildtype culture wells. Another class of deletions might have the potential to undergo CF but do so with less penetrance than wildtype. Summarizing, I expected to have many false positive candidates in my list. I wanted to exclude as many of those as possible, before starting to thoroughly speculate about possible molecular mechanisms and performing follow up experiments.

In order to validate the candidate genes, I had to reposition the candidate deletion strains onto new 96-well plates. In addition to the 550 candidate gene deletions, I took along the strains, that only grew up once but showed a CF phenotype. This resulted in a total of 600 strains to validate. Since I observed a well bias in the first two screens, and the end volume was always lowest in the outermost row of a 96-well plate, I only used the 60 centre wells of the plates (B2-G11). This yielded a total of 10 plates to rescreen.

I planned to apply the exact same experimental setup for the rescreen as I developed and used for the two primary screens (see 3.4.1). Prior to the actual experiment, I performed imaging tests, to see if the dyes were still working well with the same imaging settings, and everything was as it used to be. Only when I started the experiment, I realized to my great surprise, that another research group had changed parameters on the shared incubator I had used previously. The diameter of the shaking was changed from 25mm to 50mm. Now the shaking speed that I had carefully and extensively established was no longer suitable for the experiment. As I reported in section 3.4.1.1, the shaking frequency for a certain culture volume needed to be carefully balanced between cell sedimentation and liquid overflowing from one well to the other for successful CF induction. I continued with the experiment and troubleshooted on the go. While the plates with the starvation cultures were already incubating, I had to adjust the shaking speed several times before I had found a speed where there was no major cell sedimentation but no major culture volume changes either.

With the help of another PhD student, Mirjam Bächler, I rescreened the candidate genes twice. However, when I analysed the data, I found that the results were not convincing at all. Many wildtype control wells I imaged did not seem to show CF. In fact, they showed a CF index distribution very similar to the CF distribution of all the deletion strains (see Figure 28). I strongly suspect that the above described problems during the starvation period of the strains were the reason for the poor CF induction rate. We concluded, that it was not worth analysing

the dataset any further. Instead one would need to establish new culturing conditions suitable for inducing CF with the current hardware, before repeating the validation screen. Unfortunately, this goes beyond the scope of this thesis.

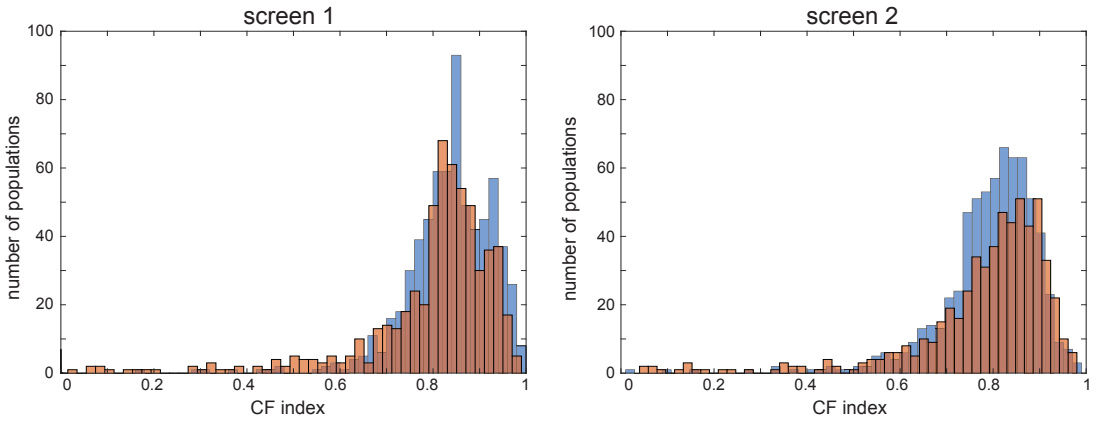

Figure 28. Overview of validation screen results.

The histograms show the CF index distribution for all the candidate gene deletion mutants (blue; left panel: validation screen 1, right panel: validation screen 2). Overlaid are the cytoplasmic freezing indices of only the wildtype control populations (red).

4 Discussion

4.1 Reproducibility of CF – a question of terminology

4.1.1 Definition of CF

An important parameter to know about a novel phenomenon such as CF is its reproducibility. In theory, this appears trivial to determine. However, in reality the situation was not so clear. In the early years of my PhD when I investigated how the experimental conditions influenced the occurrence of CF, I found that even under standardized conditions, CF occurred in around 60% of experiments only (see section 3.1.2). Conversely, CF seemed to occur much more consistently in the recent years, with an outlier experiment showing no CF occurring only approximately every 10 to 20 times. This was confusing to me and brought about that I was rather hesitant to make a clear statement about the reproducibility of CF.

While writing this thesis, I realised that the question of CF reproducibility is actually a question of how one defines CF. What made me hesitant to a clear statement, was that the CF definition rather than the actual experimental outcome evolved during my PhD time. Whereas in the early years of my PhD I considered cells to be CF cells only if absolutely no lipid droplet motion was visible, I later considered cells as CF cells also, if some lipid droplets showed residual motion, as long as the residual motion was clearly restricted compared to lipid droplet motion of cells in early starvation. Thus, I evolved to view CF as the striking cytoplasmic solidification happening upon deep starvation instead of a complete immobilisation of all lipid droplets. This overall phase transition from a fluid-like to a solid-like cytoplasm happens very consistently, while the efficiency of cytoplasmic solidification in single cells varies between populations (see section 3.1.2).

In the next sections I will discuss the reasons behind this evolution of CF definition.

4.1.2 Reasons for evolution of CF definition during my PhD

When I started my PhD, CF was defined as a solid cytoplasmic state where endogenous lipid droplets could not be moved by optical tweezers. This state was induced in cells in deep glucose starvation. This was a purely qualitative description that was very clear for single lipid droplets but did not specify the population behaviour.

Alternatively, the lipid droplet motion was quantified by the determination of the alpha value, a measure for the anomalous subdiffusion. If alpha was below a certain threshold, these cells were thought to be in CF. Whereas this description of the dynamic behaviour of single lipid droplets was highly quantitative, its value for estimating the behaviour of cells or populations

was limited. First, the high acquisition frame rate required for the estimation of the alpha value limited the number of cells that could be imaged at once to a few cells. Next, only a subset of lipid droplets was actually eligible for the single particle tracking (SPT). The reason for this was that segmenting objects from DIC images is by no means trivial. The main challenge is the lack of an absolute intensity difference between the object and its surrounding. To circumvent this issue, Chieze Ibeneche, a former PhD student in the Florin laboratory, had to manually crop suitable lipid droplets from the movies, such that in the cropped movie, the only contrast came from one lipid droplet. Therefore, lipid droplets in the vicinity of other lipid droplets, or close to the cell border could not be analysed. Consequently, the alpha value accurately described the behaviour of selected single lipid droplets but not of all lipid droplets of individual cells or across cell populations.

This lack of a description of the cytoplasmic state on a population level has not been a problem thus far, since the difference between early and late starvation was very clear. It was clear from the alpha values, but even from observing lipid droplet motion by eye from DIC movies. This made us confident that we could investigate CF in Zürich without an optical tweezer setup or the high time resolution and stability necessary to reasonably determine alpha values.

Indeed, after improvements of DIC imaging and mounting of cells, I saw cells in deep starvation having totally immobilized lipid droplets. We were quite confident that this was CF. However, I saw the same in septin deletion mutants, where there was no CF according to previous results on alpha value quantification done by Chieze Ibeneche from the Florin lab.

In hindsight, this controversy was the turning point, from when I started to judge the cytoplasmic state of cells much more strictly. Even though I saw cells without lipid droplet motion in deep starvation, I found that the portion of such cells varied between experiments. This was not described before. Now it was not clear whether this indicated that I induced CF poorly in wildtype or mutant cells, or whether this was a general feature of CF that just got unnoticed since the bigger picture was very clear.

I developed a semi-quantitative readout for the cytoplasmic state, where I strictly scored every cell according to the motion of its lipid droplets in a completely unbiased manner. This allowed to estimate the cytoplasmic state of a cell population without the need to exclude certain droplets or cells from the analysis based on their specific morphology. I anonymized the identity of the movies to be blind for the experimental/genetic background in order to reduce personal bias. With this, I explored all the experimental parameters we could think of (see section **3.1**). Thereby I gained a lot of experience and confidence in judging the cytoplasmic state of cell populations. Indeed, I found culturing conditions that would never lead to a complete lipid

droplet immobilization. But I repetitively found many cells without any lipid droplet motion in deep starvation cultured under standard conditions. This was exactly how CF was described before. Therefore, we concluded that we could indeed detect CF with our methods and by our qualitative or semi-quantitative readout. What implications this had on the septin story, I discuss in detail in section 4.2.

These experiments confirmed that the actual efficiency of CF varied quite significantly between experiments even under the same conditions. What varied, was the portion of cells with totally immobilized cytoplasm judged by no visible motion of any of its lipid droplets (10-80%). At this time, we interpreted these results as revealing poor reproducibility of CF. This could either be an intrinsic feature of CF, or there could be an experimental parameter that was important but we were still not aware of and therefore did not keep constant.

Instead of continuing the search for such a parameter, we decided to prioritize finding an entry point into the molecular mechanism behind CF, especially since the evidence for septins to form a network in CF cells has become weak. We wanted to first identify genes that were strictly required. Only in a later step would we be interested in the factors modulating the efficiency of CF. Consequently, I reduced my focus on the penetrance of CF. I still judged the cytoplasmic state of cells by the qualitative lipid droplet readout, albeit without classifying the motion in each cell.

4.1.3 Implications of the changing definition of CF on the perception of reproducibility

Interestingly, the CF reproducibility issue became less pronounced after I had changed my focus to finding an entry point into the molecular mechanism behind CF. Only occasionally I encountered starvation cultures that had not undergone CF as expected. This appeared to be in controversy with my previous results that indicated CF reproducibility to be low. In retrospect, I consider most likely that the actual results were the same as before, but my perception of a cell population in CF changed. I did not judge a cell population with only 30% of totally immobilized cells as non-CF. I acknowledged that all the cells induced a drastic cytoplasmic immobilisation compared to cells in early starvation, albeit with less efficiency than other times, leading to totally frozen and moderately frozen cells.

The fact that I can only hypothesize about this change of perception, reveals a limitation of the qualitative lipid droplet readout for the cytoplasmic state. The qualitative estimation of motion is no absolute measure. I cannot be sure to judge a lipid droplet to be wiggling a tiny little bit or be immobile the same at any time. Additionally, it does not provide information about the amount of motion. I suspect that I judged a particle's motion very strictly, when all I was

looking at for days were almost to totally immobilized lipid droplets. Conversely, I might subconsciously judge more casually, when mostly comparing lipid droplet motion of cells in early and late starvation.

Supporting this, I consider the recently developed visualization of 9 lipid droplet trajectories to accurately describe the immobilization characterizing CF, as it clearly and consistently showed a strong lipid droplet motion reduction between SD4/5 or SD5/6. However, preparing this thesis made me realize that it did not reveal the variation in efficiency of CF to the extent I had perceived it. Even the inability of cells to induce CF when grown under conditions of reduced aeration (see section 3.1.2) was not obvious from the 9 trajectories. In my memory, these lipid droplets were totally dynamic, but their trajectories revealed that they are actually quite restricted in their dynamics.

In this context, it would be very valuable to know how the Bodipy CC readout performs to distinguish this different efficiency of cytoplasmic immobilisation. The absolute value of the median of correlation coefficients varies between experiments. I always generously attributed this to technical issues like variations in signal intensities, or to slightly different lipid droplet morphology influencing the size of the lipid droplets and thereby the correlation coefficients. Also, the initial purpose of the Bodipy CC readout was to identify candidate genes that were clearly not able to induce CF, therefore I did never associate this readout with being very accurate in describing the exact details of the cytoplasmic state of cells. Maybe I was wrong to do so, and the Bodipy CC readout accurately describes the efficiency of CF by its absolute values. However, the application of the Bodipy CC readout for general CF description indeed came along with some problems that I will discuss in the following section.

4.1.4 How to quantitatively describe the cytoplasmic state of cells during starvation

When we aimed to quantitatively describe the cytoplasmic state of cells from exponential growth to deep starvation, we had the choice between two quantitative readouts I had developed previously. On the one hand the mitochondria MSD readout, where I computed the MSD of single particle trajectories from mitochondria (see section 2.1). On the other hand, the Bodipy CC (correlation coefficient) readout that I had used as a fast readout for the screen (see section 3.4).

I had used the mitochondria MSD readout to investigate the role of septins in CF. It is a highly accurate measure of the cytoplasmic state, but it requires fragmented mitochondria to track over time as it is not possible to deduce a simple trajectory from a dynamic tubular structure. Sadly, the mitochondria only fragment during starvation. Therefore, we could not use this method to

consistently describe the cytoplasmic state of cells from exponential growth to early and deep starvation.

Consequently, we chose to use the Bodipy CC readout, which convincingly worked to discriminate CF from non-CF starvation cultures. Additionally, we knew that lipid droplets were present in cells from exponential growth to deep starvation, and had extensively used their dynamics to qualitatively describe the cytoplasmic state.

For the screen data acquisition where I identified candidate genes required for CF using the Bodipy CCs, I was kindly allowed to use the high throughput screening microscope from the group of Prof. Lucas Pelkmans (see Methods). For the quantitative cytoplasmic state description over time, I acquired the necessary data using our laboratory spinning disc microscope (see Methods). I found that the resulting Bodipy CC values reflected our qualitative impression of high mobility in exponentially growing cells, intermediate mobility in early starvation and very restricted mobility in CF cells in deep starvation.

However, an observation from these data left me with a slightly uneasy feeling. I found when establishing the conditions for the deletion library screening experiment that the Bodipy fluorescence was subject to notable acquisition photobleaching. To keep it minimal I applied mild imaging conditions. However, when acquiring data on our laboratory microscope, I found the opposite result: often the Bodipy fluorescence of cells increased over time rather than decreased. This was most pronounced for cells in early starvation, where the initial signal was very weak, but became significantly stronger over the next acquisition time points (see Methods). Again, I was very conservative in imaging frequency, only acquiring 3 single planes every 45 seconds. This indicates that the cells suffer from notable phototoxicity, as I found that when imaging exponentially growing cells more frequently, the Bodipy fluorescence starts to increase dramatically at some point, and minutes later the cells are dead, indicated by cytoplasmic Phloxine B signal. I did not encounter a similar phototoxic effect when imaging strains that expressed an ectopic fluorescent marker, like Lifeact-GFP. I could acquire data much more intensely, acquiring z stacks every 10 seconds without any hint for phototoxicity. Therefore, I suspected that one of the dyes I used was responsible for the increased phototoxicity.

Initially, I suspected Bodipy rather than Phloxine B, as I had to apply quite intense imaging conditions like a high laser power for a decent Bodipy signal when applying the Bodipy CC readout to cells in general compared to only cells in deep starvation. I identified several possible reasons for this. First of all, Bodipy-stained lipid droplets in cells in early starvation fluoresced very weakly compared to lipid droplets of cells in deep starvation or exponential growth.

Moreover, the light-sensitivity of the system that I used on our laboratory microscope was weaker than of the screening microscope. Furthermore, it is possible that the Bodipy dye had a weaker fluorescent signal than when I used it for the screen. We used frozen liquid aliquots prepared for the screen for up to two years later, and Bodipy can oxidize over time in solution which impairs its fluorescence. Together, I suspected that the image acquisition settings for Bodipy on our microscope were much harsher than what I used for the screen. This could be responsible for the observed phototoxicity. However, preparation of new Bodipy aliquots did not improve the situation.

I initially considered Phloxine B as unlikely to be harmful to the cells, as it is widely used as a food colourant or in cosmetics. Also, it seemed to be an established marker for cell death, where no negative effects were mentioned (Roux et al., 2006). After the new Bodipy did not improve the situation, I checked again for reports on harmful effects of Phloxine B. Indeed, I found several reports stating that Phloxine B damages cellular membranes in combination with exposure to sunlight. Therefore, it is used as a photo-activated pesticide, most probably by stimulating the production of ROS under light illumination (Goyal et al., 2016; Inbaraj, Kukielczak, & Chignell, 2005; Liquido, McQuate, & Cunningham, 1995). I even found a report from *S. pombe* where it was shown to have pro-oxidant action under illumination with light (Mutoh, Kawabata, Nakagawa, & Kitajima, 2005). This strongly suggests that Phloxine B induced the observed phototoxicity when I was acquiring data for the Bodipy CC, and the above discussed reasons for using more intense imaging conditions might have notably increased its phototoxic effect. Therefore, the choice for using Phloxine B to segment cells and identify metabolically inactive cells might need to be reconsidered for the future. An alternative for cell segmentation could be fluorescently labelled lectin.

4.2 The role of septins in CF

4.2.1 Controversial results

Septins are highly conserved among eukaryotes and came into the focus of CF research due to their filament forming abilities. Already before I started my PhD, the CF researchers had hypothesized that a filamentous network spanning the intracellular space was responsible for the cytoplasmic immobilization in CF. The protein x forming such a network would have to be strongly expressed in the cytoplasm of CF cells. Furthermore, the absence of the protein x would prevent cells from undergoing CF.

As I presented in the introduction (see section 1.4), Chieze Ibeneche, a former PhD student in the Florin lab in Austin, Texas, had obtained strong evidence indicating that septins could be the filament formers for the hypothesized network. She found that septin 1-3 showed strong, homogeneous cytoplasmic localization in deep starvation. With fluorescence recovery after photobleaching (FRAP) experiments she found a significant immobile fraction of septins in cells in deep starvation, indicating that at least a part of the septins were stably integrated into some structure. Moreover, she found that deletion mutants of septin 1-3 did not show CF in deep starvation. Together, the septins 1-3 behaved exactly as one would expect for the protein x.

However, as we presented in the manuscript in section 2.1, I could not reproduce any of these results. In my hands, the GFP-tagged septins did not show homogenous cytoplasmic signal in CF cells. On the contrary, I found that they formed a few very bright structures, sometimes with interesting spring-like shapes for septin1. Otherwise, the signal that dominated in these cells was dot-like and rather polarized instead of homogeneously cytoplasmic. I found that this dot-like signal was autofluorescence that appeared in wildtype cells that did not express any ectopic fluorescent marker protein. By co-localization analysis I showed that this autofluorescence emanated from mitochondria.

We were puzzled by this discrepancy. Even though the previous localization data showing the homogeneous cytoplasmic signal was done with the exact same strains with GFP as a fluorescent marker, we thought that the mitochondria autofluorescence might mask a cytoplasmic septin signal. Since this mitochondria autofluorescence was not visible in the red fluorescence range, I tagged the septins 1-4 with the red fluorescent tagRFP and mCherry. These red fluorescent septins showed similar bright structures in CF cells, but still no homogeneous cytoplasmic signal. I also tried to perform FRAP on spn2-tagRFP, but with very noisy, inconclusive results, since the cytoplasmic signal was basically at background level.

We could think of two possible reasons for these different results. On the one hand a technical reason, where the resolution of the microscope that Chieze Ibeneche used could have been too low to resolve the dot-like pattern of mitochondria autofluorescence. Instead these dots would appear as homogeneous signal. On the other hand, it could be that the cells where Chieze looked at the septin localization, were actually not in CF. This could be, since at those early days of CF research, a systematic control for the cytoplasmic state was not established as it is now for any CF experiments. Nobody was aware of the fact that CF happened only under certain conditions and even then, not in 100% of experiments. Moreover, the GFP-tagged strains that Chieze used, contained auxotrophic markers and needed to be grown in EMMLG with

supplements. As I found later, these supplements delayed CF by at least 2 days (see section 3.1.2). Also, I had the feeling that CF was induced with less efficiency for many strains that contained transgenes. It could correlate with the marker used for transgene selection, but I did not investigate this systematically.

Even though I could not confirm the homogeneous cytoplasmic localization for septins in CF, we still had the septin deletion mutants that did not show CF. Unfortunately, I could not confirm these results either. I found that deletions in septin 1-4 did not interfere with the induction of CF (see section 2.1). I showed this qualitatively from the motion of lipid droplets from DIC movies and quantitatively, with the determination of Bodipy-labelled lipid droplet dynamics by the Pearson correlation coefficient and with the MSD from SPT of fragmented mitochondria.

Again, I can only speculate about the cause for the inconsistent results. For me, the most likely reason for the absence of CF in Chieze's hands is similar to the septin-GFP situation – nobody was aware that one needed to carefully control CF experiments. Again, the septin deletion strains that Chieze looked at contained auxotrophic marker alleles, and therefore would have shown CF earliest at SD7 without any mutant-specific reason. Additionally, the spn1Δ cells for which Chieze observed the strongest suppression of cytoplasmic immobilization, show a strong septation defect in starvation. Cells often comprise 4 or more cells, and are very long and sticky. These cells clump, such that it is difficult to find cells to image. It is possible that the data acquisition took longer for those cells. This might have influenced the results, since I found that the time in the imaging chamber can influence the cytoplasmic state of cells (see section 3.1.1.2).

Taken together, the evidence for CF weighs stronger than the absence of CF. Therefore, we concluded that neither of the septins 1-3 alone was crucial for CF.

We cannot unambiguously exclude a role for septins in CF, since septins are known for their mutual redundancy. We tried to address this issue by investigating a septin 1-4 quadruple mutant (kindly provided by Kathy Gould). In preliminary experiments, this mutant showed CF. However, we could only confirm the presence of the spn2 and spn4 deletions by colony PCR. From crossing this strain against a wildtype strain, we know that there must be at least one additional mutation/transgene marked by geneticin resistance in this strain. Therefore, this strain needs careful evaluation before we can draw a final conclusion.

4.2.2 Concluding remarks

All together, these controversial results had a positive influence on both CF research and my personal development. On the research side, we would probably not have investigated the conditions that influenced the cytoplasmic state. In the beginning, we indeed had problems to

capture and measure the cytoplasmic state of cells in Zürich. It was therefore very important to realize the challenges concerning CF induction, and to establish systematic control experiments to always monitor the cytoplasmic state. If we had not done it early on, we would probably have run into similar reproducibility issues later on. Moreover, the different readouts for the cytoplasmic state I developed were really pushed by the need to convincingly show my points. Lastly, I really enjoyed the development and realization of the experiment, where I screened the deletion library for the identification of candidate genes involved in CF. I would not have done this, had the septins proven to be responsible for CF. On the personal side, I learned to very critically evaluate my experimental approaches and results, and then trust them. Additionally, I had the possibility for a short research stay in Austin, Texas, that I greatly enjoyed, which would not have been necessary had we always obtained comparable results.

4.3 Ideas about the molecular mechanism underlying CF

By screening the deletion library for mutants that were unable to undergo CF, I identified 500 candidate genes that are potentially required for CF. Among them, autophagy-related genes were overrepresented, presenting a possible entry point to the molecular mechanism. However, we found that autophagy is not strictly required for CF but influences the timing of CF induction. The validation of the remaining candidate genes is still ongoing, but we expect the candidate list to shorten significantly (see section 3.4.3). Therefore, it is too early to speculate on a possible molecular mechanism from those candidate genes.

Nevertheless, I have collected many bits and pieces of information about cells under glucose starvation and in CF. Some of these results invite to speculate about the nature of the molecular mechanism underlying CF.

In general, we see two mechanisms for cytoplasmic solidification. On the one hand, diffusive motion could be impaired by increased macromolecular crowding, leading to a glass-like cytoplasmic state (crowding hypothesis). Such a mechanism has previously been proposed for cytoplasmic solidifications in spores (Sun & Leopold, 1997), bacteria (Parry et al., 2014) and *S. cerevisiae* (Joyner et al., 2016). This could either be mediated by a severe loss of water leading to a concentration of intracellular structures, or involve the production of a compound like trehalose or another stress protectant that accumulates in excess (see section 1.1). Both scenarios would lead to a steady increase in macromolecular crowding, eventually leading to a glassy cytoplasmic state.

On the other hand, cytoplasmic solidification could be achieved by globally crosslinking cellular structures or by embedding them in a stable matrix-like gel or network (network

hypothesis). A mechanism in this direction has been proposed for *S. cerevisiae*, where widespread macromolecular assemblies as a collective are proposed to impair cytoplasmic mobility (Munder et al., 2016).

As discussed in the manuscript in section 2.1, we have evidence that the molecular mechanism underlying CF differs from other solid-like cytoplasmic states. We do not measure any cell volume loss upon CF induction as was proposed to be the cause for the mobility reduction under acute glucose depletion (AGD; (Joyner et al., 2016)). Likewise, we do not find evidence for widespread macromolecular assemblies as are forming under drug-induced energy depletion (DED), causing the observed intracellular immobilization (Munder et al., 2016). Moreover, while we still observe clear particle motion in cells acutely depleted of energy, we do not in CF cells, thus the restriction of particle motion in CF cells is considerably more complete. Reflecting this, CF cells can keep their cylindrical shape in the absence of a cell wall for multiple days, while cells acutely depleted of energy adopt a spherical shape on a remarkably shorter time scale. Together, these results indicate that CF represents a yet unreached solidification of the cytoplasm caused by a so far unknown mechanism.

4.3.1 Macromolecular crowding unlikely to cause the cytoplasmic solidification in CF cells

In general, we doubt that pure macromolecular crowding could mediate a cytoplasmic solidification as strong as seen in CF cells. A highly crowded cytoplasm can still be viewed as a complex fluid with very high viscosity. Its components should be able to rearrange, albeit on a long timescale. A glass-like cytoplasm that was solid enough to preserve its shape for several days without the shape-determining cell wall as we see it for CF cells, would most likely require a very high molecular crowding. However, even cylindrical CF protoplasts generated and kept under normally hypotonic conditions thus lacking the stabilization by hyperosmotic pressure, do not show any signs of rounding up for multiple days. We know from budding yeast that severe osmotic pressure significantly impairs the mobility of smaller cytoplasmic components like proteins via increased macromolecular crowding (Miermont et al., 2013). Therefore, we expect that a macromolecular crowding, which is strong enough to mediate CF, would inhibit the diffusive motion of smaller components like single proteins. Indeed, preliminary experiments on performing FRAP on exponentially growing cells under hyper-osmotic pressure in 1.2M sorbitol buffer already revealed a slower diffusional mobility. These cells do not possess any shape-preserving ability as their protoplasts are perfectly spherical. However, we found that the diffusive motion of Lifeact-GFP, a small protein, is not impaired in CF cells compared to exponentially growing cells. Additionally, an external force like the optical

tweezers would be expected to be able to still move a component of a highly crowded system, even if slower and to a lesser extent, but in CF cells the lipid droplets cannot be moved at all.
If the crowding hypothesis were true, one would expect a gradual increase in cytoplasmic viscosity already before CF induction, culminating in the observed immobilisation of organelles upon CF induction. Conversely, a network could be formed reasonably fast, given that the building blocks are present.
Therefore, one major question we asked was, if the induction of CF was sudden or gradual. We found that entry into stationary phase was accompanied by a first reduction of the space that lipid droplets explored. They did not notably translocate anymore, but rather wiggled around the same spot. As discussed in the manuscript, this difference is hard to visualize by lipid droplet trajectories since the lipid droplets that move notably are hard to follow. But the Bodipy CC readout indicated this initial reduction of motion. This could of course be due to increased macromolecular crowding upon entry into quiescence by some unknown mechanism. An alternative scenario of the highly speculative sort, is that the constriction of lipid droplet dynamics during early starvation is caused by a reticulation of endomembrane structures like the ER. ER structure in starvation is hard to investigate by light microscopy, as we show in the manuscript in section 2.1. One problem is the strong autofluorescence of mitochondria in the green fluorescent range. But even more puzzling is the behaviour of ER marker proteins labelled with red fluorescent proteins, be it TagRFP or mCherry. The signal accumulates strongly in vacuolar structures, which is often neglected as an artefact of the fluorescent protein, but could also indicate active autophagy (D. Zhao et al., 2016), (Hamasaki, Noda, Baba, & Ohsumi, 2005). This strong vacuolar signal is very dominant, making it hard to identify intracellular ER structures. But when looking at it extensively, it appeared to me that there were highly reticulated membranous structures throughout all the cytoplasm. If indeed the ER was highly reticulated in starved cells, this would possibly impair the diffusive motion of large organelles and could thus explain the moderately restricted mobility of lipid droplets already in early starvation. From the electron microscopy data that we have, it is hard to draw conclusions about endomembranes, as the staining used is not optimal for visualisation of membrane structures (personal communication with Prof. Andreas Hoenger). It would thus be interesting to reconstruct ER membranes from electron microscopy data specifically stained for visualising membranes.
After this initial reduction of cytoplasmic motion at SD2, the lipid droplets displayed similar dynamics at SD3. However, from SD3 to CF induction we had controversial results whether there was a gradual solidification or a sudden CF induction. Depending on the readout for the

cytoplasmic state, the results were different. Quantitative descriptions of the cytoplasmic state like the alpha value and the Bodipy CC readout displayed a gradual increase in cytoplasmic viscosity before reaching the CF state. Conversely, qualitative readouts like the evaluation of lipid droplet motion by eye, the optical tweezer experiments or the cell wall digestion experiments clearly supported a switch-like induction of CF.

A prime example for this discrepancy was a recent experiment. I aimed to answer exactly the question, how long it takes for cells to induce CF. I acquired data suitable for the qualitative readout as well as the Bodipy CC readout. Since the time of CF induction varies around SD5, I set up 3 starvation cultures with 3h starting time difference between them. I evaluated their lipid droplet motion when the oldest culture was incubating for exactly 5 days. I saw clear lipid droplet motion only in the youngest of the three starvation cultures, incubated for 5 days minus 6h. This was promising, as it suggested that within 3-6h this starvation culture would induce CF as well. I imaged aliquots of said starvation culture and a negative control starvation culture from SD4 every 30min. There were several reasons why this experiment proved not to be conclusive. One of them was that the Bodipy CC distribution did not gradually increase over all time points but showed random drop outs. But important for this discussion is that the actual difference in Bodipy CC between the 3 parallel starvation cultures around SD5 (medians at 0.75, 0.6, 0.45) was marginal compared to the difference to the starvation culture from SD4 (median at 0.76). These values suggested that a significant transition happened between SD4 and SD5, not within hours before SD5. This result alone does not exclude that the major increase in viscosity happens fast at some period between SD4 and SD5. However, the Bodipy CC consistently showed intermediate values one day prior to CF induction determined by the qualitative readout or by Bodipy CC reaching its high plateau, whereas from the qualitative evaluation no such intermediate state was evident.

Therefore, the unbiased, quantitative cytoplasmic state readouts (alpha value and Bodipy CC) suggest that indeed there is a gradual increase in cytoplasmic viscosity prior to CF. Additionally, this shows that the qualitative readout is inherently non-linear. Our brain seems to scale up small differences around the threshold of visible motion, but is rather poor in ranking clear motion.

Now the question is, whether the non-linearity of our brain's motion detection presents us with the false impression of a switch-like CF induction, or whether it reveals a biologically meaningful transition that is small in terms of its effect on particle dynamics. Here the cell wall digestion experiments give a clear answer. From a gradual increase in cytoplasmic viscosity that was capable of solidifying the cytoplasm enough to preserve the cylindrical shape in cells

without cell wall (protoplasts), one would expect an intermediate protoplast shape at least one day prior to CF induction. However, the shape-preserving capability of protoplasts does not increase gradually over time of starvation, but appears suddenly from one day to the next at or at most one day after CF induction. While the protoplasts from cells in early starvation are all perfectly spherical, protoplasts from cells in deep starvation with CF induction are predominantly cylindrical but not oval. This demonstrates that the cells either possess the shape-preserving ability or not, and clearly supports a switch-like induction of CF.

What we interpreted for long as conflicting results, can be alternatively interpreted to demonstrate that CF establishment involves a gradual increase in cytoplasmic viscosity as well as a sudden finish that most likely involves crosslinking of some sort.

Whether these two processes are coupled, or the increase in cytoplasmic viscosity is independent of CF induction is totally open. It is plausible that the increased viscosity is caused by macromolecular crowding, be it from excess production of network components or by an unrelated crowding agent.

4.3.2 Preparation phase prior to CF induction suggests de novo production of components required for CF

As I discussed, simple macromolecular crowding cannot convincingly explain the cytoplasmic solidity of CF cells. In order to crosslink components to form a network that immobilises the cytoplasmic content there are two possible scenarios: either already existing cellular components are crosslinked or the components for crosslinking need to be generated specifically for this purpose.

An example for filament formation of existing components is the acute energy depletion response reported in budding yeast (Munder et al., 2016). The authors report a widespread formation of protein assemblies or filaments upon intracellular acidification caused by energy depletion. However, we do not find evidence for such a mechanism in CF cells, plus such a mechanism is unlikely to be strong enough for causing a solidity as profound as observed in CF cells.

A protective state mediated by the excess production of specific components was reported for tardigrades (water bears). These microscopic animals are well known for their ability to survive a vast array of environmental extremes, including essentially complete desiccation for up to a decade (Goldstein & Blaxter, 2002). It was long known that tardigrades die if dried too quickly, suggesting that they need time to produce protectants (J. C. Wright, 1989). Indeed it was recently shown that de novo transcription and translation are required for the robust survival of a tardigrade species (Kondo, Kubo, & Kunieda, 2015). Moreover, the proposed protectants

were identified as intrinsically disordered proteins (IDPs) that are thought to mediate protection by vitrification (Boothby et al., 2017).

The tardigrade's desiccation tolerance differs from CF in fission yeast, as tardigrades enter an anhydrobiosis state where they have essentially lost all their intracellular water (Boothby et al., 2017) while CF cells clearly are not desiccated. However, we have evidence for a preparation phase prior to CF induction, suggesting that the cells need time and energy to produce components necessary for CF similar to the tardigrades.

Evidence that important processes for CF happen days prior to CF induction comes from a result I described earlier, where one starvation culture happened to induce CF extremely poorly, whereas two parallel cultures induced CF normally around SD5. I could see clear lipid droplet motion throughout the starvation period, and the Bodipy CC, even though increasing until SD6, never reached a level usual for decent CF. It is interesting to note that the difference between the two starvation cultures that induced CF well and the extremely poor CF culture was evident already at SD3. There, the protoplasts from the poor CF culture were not perfectly spherical in contrast to the two more conventional cultures. This result shows that crucial processes regarding CF are happening in cells 2-3 days prior to the actual phase transition to CF.

Interestingly, we also observed a cytoplasmic immobilization that was very reminiscent of CF but occurred within minutes instead of days (see section 3.1.1.2). I observed rearrangement of F-actin, microtubules and mitochondria together with cytoplasmic immobilization all reminiscent of CF within minutes after transferring early starvation cells to an imaging chamber – a phenomenon we call rapid freezing. However, for this to happen within minutes, the cells needed to be in stationary phase. I showed that when mounting exponentially growing cells, the rapid freezing was induced only after a day in the chamber. Additionally, we do not know, if the extent of cytoplasmic solidification after rapid freezing is comparable to CF, or if its incomplete. Together, these results indicate that establishment of CF might require preparation time in the range of days.

Moreover, we have demonstrated that autophagy, a cytoplasmic recycling process, is involved in the timing of CF induction. Inhibition of autophagy delays CF onset by at least two days. Additionally, it appears as if the absence of autophagy also increases the variation in induction time, as cells deleted for atg8 show CF anywhere between SD8-10. These results indicate that either a crucial component or an energy source for producing a crucial component for CF is preferably provided by autophagy recycling. We know that in nitrogen starved fission yeast cells, autophagy is mainly required for recycling nitrogen, more specifically amino acids that

are then used for de novo protein synthesis to allow for sporulation or for adaptation to a quiescence state in the absence of mating partners (Kohda et al., 2007; Mukaiyama et al., 2009). In this situation, prototrophy or auxotrophy with excess supplementation of the amino acids for which cells are auxotroph, partially suppressed sporulation defects of autophagy mutants. In the absence of mating partners, preventing autophagy in nitrogen starved cells partially reduced the viability of quiescent cells (Kohda et al., 2007). However, viability was extremely reduced in leu1-32 cells that are unable to produce leucine (Kohda et al., 2007). In our case where cells are starving of glucose, nitrogen recycling by autophagy is unlikely, as there is no shortage of nitrogen. In addition, excess supplementation of amino acids like leucine also delayed CF induction in wildtype cells by two days and is thus unlikely to rescue the CF induction delay of autophagy mutants similar to its rescuing effect in nitrogen starved cells.

Together, this suggests that cells in glucose starvation-induced quiescence rely on autophagy to provide energy, which is necessary for an adaptation process prior to CF induction. If autophagy is inhibited, cells likely use alternative energy-recycling mechanisms that might be less efficient, and therefore providing the required energy for finishing the preparation for CF takes longer. Additionally, this suggests a mechanism explaining the CF induction delay observed in the excess of amino acid supplements. Amino acids like leucine are known to activate TORC1, the negative regulator of autophagy (Avruch et al., 2009; Binda et al., 2009). Therefore, an excess amount of leucine might lead to a CF induction delay by keeping TORC1 activated, thus delaying autophagy induction and the energy necessary for CF.

In summary, it is unlikely that CF is caused by crosslinking existing structures or molecules, as cells apparently cannot spontaneously enter CF. It rather seems as if the cells need to specifically prepare themselves before being able to induce CF. This preparation probably relies on energy recycling that could be required to generate specific components necessary for the formation of a crosslinked network.

4.3.3 Specific quiescence state as a likely prerequisite for successful CF induction

So far, we hypothesize that the early starvation period might be required to produce components that crosslink to mediate CF in deep starvation. The first global transition that marks the beginning of early starvation happens when cells run out of glucose and enter a quiescent state. Such cellular quiescence is characterized by growth arrest, long viability and increased resistance to stress (Wei et al., 1993). However, quiescence is not a very specific term. Even narrowed down more specifically to quiescence induced by carbon exhaustion by reaching stationary phase describes cellular states with quite variable features. For example, it was reported previously that the chronological lifespan of fission yeast cells in stationary phase

depends on the initial glucose concentration of the medium (B.-R. Chen & Runge, 2009; Roux et al., 2009; Zuin et al., 2010).

We have evidence that also the comprehensive induction of CF depends on an initially low glucose concentration in the medium, as cells cultured with 2% glucose instead of 0.5% induce CF inhomogeneously in a subset of cells only within a population. Furthermore, we know from results obtained by Chieze Ibeneche that cells induced CF around the same time for glucose concentrations between 0.5%-0.1%, but cells acutely depleted for glucose could not induce CF at all. When I repeated these glucose depletion experiments, I observed two different phenotypes of such cells in deep starvation. Either there was no apparent drop of cytoplasmic mobility for up to 8 days as Chieze reported, or cells appeared to have a solid cytoplasm but at the same time displayed large vacuoles. I tried to recover such cells from starvation but without success. In line with this, it was previously reported that acute glucose depletion leads to a rapid loss of viability. Also, these cells did not show increased stress resistance, which is a characteristic feature of successful quiescence (Pluskal et al., 2011). Although I did not follow up on this systematically, it invites to speculate that cells require a minimal amount of glucose to be able to prepare for the establishment of CF. Also, the preparation time preceding CF induction cannot be sped up simply by lowering the glucose concentration. Therefore, we conclude that simple glucose exhaustion is not directly causing CF induction. Rather, it seems likely that low glucose concentration and exhaustion regulates CF induction indirectly, by inducing an adaptation program for successful quiescence. This program seems to be a prerequisite for CF induction in deep starvation.

The mechanism through which calorie restriction induces lifespan extension was proposed to be dependent on activation of the stress-dependent Sty1 MAP kinase via high respiratory rates which stimulate the production of ROS (Zuin et al., 2010). We have evidence that for successful CF induction also the metabolic state of cells entering quiescence is important. Under limited glucose concentrations, oxygen is the key determinant of the cellular metabolism, low oxygen condition favours fermentation while high oxygen levels stimulate respiration (van Dijken et al., 1993). I could show that reduced aeration or even near-anaerobic conditions during the entire starvation period prevented CF induction. This suggests that successful CF induction relies on a certain level of respiration when cells enter quiescence. Yet, the rapid cytoplasmic immobilisation (rapid freezing) that cells can undergo when transferred to near-anaerobic conditions in early starvation, provides evidence that near-anaerobic conditions may not generally prevent CF induction assuming that both conditions induce the same mechanism of cytoplasmic immobilization.

Together, these results suggest that successful CF induction might rely on the same mechanism of sty1 activation upon entry into quiescence as the lifespan extension by calorie restriction. To test this, I performed starvation experiments with a strain harbouring a sty1-deletion. Unfortunately, the results were not conclusive. First, the lipid droplet distribution was extremely inhomogeneous, with parts of the long cells full of lipid droplets and other parts totally lacking any lipid droplets. This made the evaluation of cytoplasmic mobility from lipid droplet dynamics impossible. Furthermore, the mitochondria that I usually used as an alternative way to judge cytoplasmic mobility, could not be used as they were not fragmented in the mutant. Third, overall the cells were very inhomogeneous, some clearly dead, some looking quite unhealthy but with immobilized organelles, and some rather healthy and dynamic. At that time, I did not systematically test metabolic activity with Phloxine B, therefore it was very hard for me to determine if there were CF cells or not.

Nevertheless, all together these results strongly indicate that successful CF induction relies on a very specific entry into quiescence, whether depending on sty1 or not. This implies several consequences. Firstly, it shows that a cell needs to be in a certain state for CF induction and cannot just induce CF from any point. This supports our hypothesis that CF induction requires a preparation phase for the production of components rather than just using and crosslinking whatever is present in the cells. This compound production might well be regulated by the quiescence adaptation program. Secondly, it implies a connection between CF induction and longevity.

So far, we did not find any experimental evidence for an effect of CF on longevity. In contrary, cells that were cultured under near-anaerobic conditions seemed to exit starvation faster than CF cells and more consistently, giving them a growth advantage. Also, there was no clear viability difference between cells cultured in 0.5% glucose versus 2% glucose. Nevertheless, it is possible that we used the wrong controls. Maybe CF is beneficial for cells grown under aerobic conditions, and this effect is only obvious when compared to conditions where glucose can infer its pro-aging effect. So far it was shown that the pro-aging effect of glucose was only notable in cells cultured in rich medium or minimal medium other than EMM2 (B.-R. Chen & Runge, 2009; Roux et al., 2009). This seems consistent with the reported finding that the respiration rate, as revealed by oxygen consumption, is generally higher in cells grown in minimal medium than in cells grown in rich medium (Zuin et al., 2008). Consequently, sty1 is activated in EMM2 with 2% glucose similar to rich medium with 1% glucose but not in rich medium with 3% glucose (Zuin et al., 2010). However, this sty1 activation was deduced from bulk cell populations. Indeed, there is a subset of CF cells in starvation cultures from EMM2.

It is possible that these had activated sty1 only. Therefore, it would be interesting to investigate if CF is induced under conditions where Sty1 is inactive and the lifespan of quiescent cells is short.

The inhomogeneous phenotype of cytoplasmic states found when cells are cultured in EMM2 is interesting from another aspect. It was reported that *S. cerevisiae* populations can undergo differentiation that results in the formation of specialized cell types (Palková, Wilkinson, & Váchová, 2014). This typically occurs during chronological aging as a result of environmental changes like starvation (Palková et al., 2014). Such a specialization can occur in colonies developing on solid media, but also during liquid cultivation (Palková et al., 2014). It is intriguing to speculate that CF is a specialized cell type of *S. pombe*. The conditions that the cells experience when entering quiescence in a shaking culture under low glucose conditions might mimic conditions that a subset of cells experience depending on their position within a colony. Supporting this, I found cells to show inhomogeneous cytoplasmic states, some immobilised and some still very dynamic in cell populations that were not cultured on a shaker and where cells thus had a more defined environment. Also, I found that sedimentation of cells in early starvation influenced the cytoplasmic state of cells, and even induced CF occasionally. Investigating this further might eventually lead to more insight about a biological function of CF.

4.3.4 Indications for a second global transition after entry into quiescence that might regulate CF induction

An important question is, what triggers CF induction around SD5. It is interesting to note that CF induction happens with remarkable synchrony across a cell population. This could best be achieved by a global transition similar to the metabolic change that induces quiescence when cells run out of glucose. Besides CF induction, I encountered several other structural changes in cells at around SD5, which suggest a global transition occurring in cells: First, the dynamic microtubule bundles disappear almost completely. Second, filamentous actin undergoes a striking rearrangement resulting in the presence of long, prominent, shoelace-like actin bundles at the cell periphery and the total absence of actin patches. Third, the mitochondria undergo global fragmentation during early starvation, and end up fully fragmented at around SD5. Fourth, the lipid droplets changed their morphology from mostly grape-like aggregations of multiple lipid droplets in early starvation to a few, larger lipid droplets rather dispersed through the cell after SD5. Additionally, many times we had the feeling that fluorescent markers seemed to lose their signal around SD5, as for example sec24 – a copII cargo receptor (data not shown).

We always evaluated these changes based on their likelihood to be functionally relevant to CF but we could not find any evidence. All together, these changes strongly support the occurrence of a major transition in global sub-cellular organization at around SD5.

Even though the specific rearrangements of cellular content may not be involved in the induction of CF, the nature of the rearrangements can easily be conceived as supporting the crosslinking of components to a dense network. For example, the presence of dynamic F-actin and microtubules might very well disturb the proper formation of a network by pure mechanical interference. Supporting this I have never seen fully dynamic cytoskeleton in CF cells. Even when preventing the formation of the shoelace actin cables by latB, the occurring structures were hardly dynamic. Conversely, in the case of no or extremely poor CF induction under reduced aeration conditions, the F-actin and the mitochondria were still very dynamic.

Of course, it is well possible that the cytoplasmic solidification upon induction of CF causes these changes for example by sterically hindering cytoskeletal dynamics. However, even though I do not have systematic evidence, I often found these transitions to rather precede fully formed CF than lagging behind.

4.3.5 Conclusion

All the results that we have collected over the years and that I have discussed above, have led me to think about CF in the following highly speculative way.

Organisms live in highly unpredictable environments. Therefore, survival strategies in times of scarceness are crucial for a successful persistence of organisms. Strategies for saving energy involve slowing down the metabolism. But the anisotropic organization of intracellular structures needs to somehow be maintained, since equilibration of the latter means cell death. Solidification of the cytoplasm provides preservation of the intracellular organization at low cost. Fission yeast has developed CF, a strategy of complete cytoplasmic immobilization that cells preferably undergo when there is sufficient adaptation time and energy. This CF adaptation process is triggered by cells running slowly out of glucose, as it might happen naturally for example in a yeast colony. Entry into quiescence might thus induce the excess generation of components that have the potential to form a network, a stable matrix, where cytoplasmic components would be trapped and thus hindered from deleterious equilibration or aggregation. Such a cytoplasmic solidification might potentially be harmful for cells in times when they need to highly perform, grow and metabolize in a dynamic environment. Therefore, the specific production of such components only in scarce conditions as confirmed by entry into quiescence, will protect cells from aberrant cytoplasmic solidification. Also, the benefits of a complete cytoplasmic solidification might outweigh the resulting serious impairment of

intracellular processes only at times of prolonged starvation. Therefore, CF is only induced when the cells experience prolonged starvation. The way that cells are informed about their prolonged starvation state might involve the observed global transition that the cells experience rather stereotypically after around 3 days of quiescence at SD5. When nutrients are provided again by a changed environment, the network disassembles within minutes, possibly by a global metabolic transition that inverses the inductive transition.

Such a network might arise through polymerization of filamentous structure and subsequent crosslinking, or by liquid phase transition and subsequent maturation of the liquid compartments into solid-like entities (Alberti & Hyman, 2016). Such a solidification has been suggested to be an intrinsic property of membraneless compartments (Alberti & Hyman, 2016). Moreover, it was shown that quiescent oocytes of Xenopus use such a mechanism to form the Balbiani body, a membraneless storage organelle (Boke et al., 2016).

The simple conclusion from all these speculations clearly is that it is of central importance to now identify factors that are required for CF. Only then can we advance from speculations about the molecular mechanism underlying CF to clear evidence. After their careful evaluation and validation, the candidate genes that I identified by screening the deletion library, will thus provide an invaluable entry point for elucidating the molecular mechanism mediating CF.

5 Materials and Methods

5.1 Yeast handling

5.1.1 Standard yeast handling and starvation exit

Cells were grown at 25°C in EMM2 with supplements as required, as described in (Moreno, Klar, & Nurse, 1991). All strains used are listed in Table 1. Gene tagging was done as published previously (Bähler et al., 1998) using the primers listed in Table 2.
For starvation exit experiments used for CF quantification by Bodipy staining, 4 volumes fresh EMM2 was added to the starvation cultures and incubated in Erlenmeyer flasks on the shaker at 25°C.

5.1.2 Standard protocol for CF induction

For CF analysis, cells were cultured in Erlenmeyer flasks on a shaker (New Brunswick scientific innova 4230; 220rpm) for up to 8 days. To set up a standard starvation culture for CF induction, first, 5ml of EMM2 were inoculated with a fresh patch of a strain that had not been stored in the cold, and incubated on the shaker for at least half a day but maximally until early stationary phase. This preculture was used to inoculate a 5ml EMM2 culture in a 25ml Erlenmeyer flask. This culture was incubated on the shaker, typically overnight, until it reached mid exponential growth (OD_{595} of 0.1-0.4, where OD_{595} of 0.1 is equivalent to $3x10^6$ wildtype cells/ml measured with the spectrophotometer Genesys 10S Vis, Thermo Fisher Scientific, Waltham, Massachusetts). This exponential culture was then used to start the starvation culture. For this, usually 10ml of EMMLG (EMM with 0.5% glucose instead of 2% glucose) in a 100ml Erlenmeyer flask was inoculated with the exponential culture to a concentration of $6x10^5$ cells/ml (equivalent to OD_{595} of 0.02), whereby only the cell pellet was used for inoculation without the medium from the exponential culture, to avoid changing the initial glucose concentration in the starvation culture. Typically, this Erlenmeyer flask had a screw top cap, which was almost closed for the incubation period, with half a turn left to complete closure. The starvation culture was incubated on the shaker for up to 8 days. It is possible to set up starvation cultures for CF analysis with different culture volumes, but the culture volume should not exceed 1/10 of the total volume of the flask to ensure sufficient aeration. Furthermore, the culture flask should not be closed airtight for successful CF induction.

For the variations of the standard protocol applied in section 3.1.2 everything else than the indicated differences was done as described above.

5.1.3 Protocols for acute energy depletion

AGD for fission yeast was done as described in (Joyner et al., 2016). DED was done as described in (Munder et al., 2016); Antimycin A from Streptomyces sp., Merck, Darmstadt, Germany, A8674; 2-Deoxy-D-glucose, Merck, D8375). Incubation time for DED was 30 min (personal communication) unless stated otherwise.

5.1.4 LatB treatment

LatB (Latrunculin B, Latrunculia magnifica, Merck; 428020) was added from a stock solution of 10mM in DMSO to a final concentration of 100µM (1% DMSO). Control cultures were treated with 1% DMSO. For the short-term effect of this latB concentration, the stock solution was diluted in EMM2 for exponentially growing cells, and EMM0G for SD3 and SD6 cells. For 3-day latB incubations, starved cultures were split in half at SD3. One half was supplemented with latB, the other with DMSO to serve as a control. Both cultures were incubated at 25°C on the shaker for another 3 days.

5.2 Microscopy

5.2.1 Standard microscopy

Live imaging was performed at room temperature on a spinning disc microscope (Zeiss Axio Observer Z1, Yokogawa CSU-X) using 63x and 100x NA 1.4 oil plan apo objectives, Andor iQ2.9 software and Andor Neo sCMOS and iXon3 EMMCCD cameras (Andor Technology, Belfast, UK) using 488nm and 561nm laser excitation and 525/50 BP and 568 LP emission filter sets. If not stated otherwise, z stacks with 0.5µm step size were acquired. Live cell imaging of starved cells was performed on lectin coated (griffonia (bandeiraea) simplicifolia lectin 1; Vector laboratories, Burlingame, California; L-1100; diluted in water to 1mg/ml or 2mg/ml) live imaging dishes where cells were incubated with EMM0 (EMM without glucose) unless stated otherwise. For coating single live imaging dishes (Bioswisstec, Schaffhausen, Switzerland; 5160) with lectin, 1.5 µl of 2mg/ml lectin was spread on the glass bottom and set aside to dry. For coating multi-well imaging slides (8 well: ibidi, Martinsried, Germany; 80827;

10 well: Greiner Bio-One, Kremsmünster, Austria; 543079), 1mg/ml lectin was distributed to the wells to cover the glass bottoms, left for ~5min, pipetted off (reused) and set aside to dry.
DIC imaging for cytoplasmic state evaluation using the qualitative DIC readout
DIC imaging of starved cells for the qualitative evaluation of the cytoplasmic state was done on poly-L-lysine (2mg/ml, Merck, P1399) coated glass bottom dishes (Bioswisstec, Schaffhausen, Switzerland; 5160). The reason for poly-L-lysine instead of the default lectin coating was that undiluted starvation culture cells were not immobilized on lectin coated glass slides. A chamber was constructed (see Figure 5A) by adding a cover slip on top of parafilm spacers that simultaneously acted as glue when shortly heated on a prewarmed heating plate (approx. 100°C, heat until parafilm turns transparent, gently push down the coverslip). This chamber was filled with cell culture (~30µl). The cells were centrifuged at low speed (100 rpm with Multifuge 1S-R centrifuge from Thermo Fisher Scientific) and imaged immediately (5-15 min after mounting) as prolonged residence in the chamber could cause artefacts, especially on cells from early starvation. 100 frames at 4fps using a 100x objective were acquired.

5.2.2 Fluorescence imaging for quantification of the cytoplasmic state using Bodipy and Phloxine B staining

Live cell imaging for quantifying the cytoplasmic state using the Bodipy CC readout was done on lectin coated glass bottom 8 well slides (ibidi) or 10 well slides (Greiner Bio-One). Bodipy (BODIPY 493/503, Thermo Fisher Scientific; D3922) was dissolved in DMSO (1mg/ml) and used at a final concentration of 4µg/ml in EMM0G (EMM without glucose). Phloxine B (Merck, P4030) was dissolved in water to 5mg/ml (long term storage at 4°C), diluted again to 100µg/ml in water (shorter term storage at 4°C), and used at a final concentration of 10µg/ml. When imaging, we first acquired one red fluorescent Phloxine B single focal plane image followed by 3 green fluorescent Bodipy single focal plane images with a time interval of 45s. Imaging was done on the spinning disc microscope (Zeiss Axio Observer Z1, Yokogawa CSU-X) using the 63x NA 1.4 oil plan apo objective, the Andor Neo sCMOS camera (Andor Technology), with the acquisition settings for 488nm: 200ms acquisition time, 14% laser power, and for 561nm: 150ms acquisition time, 12% laser power.

5.2.3 Directly monitoring cells during starvation exit

For directly monitoring cells during starvation exit, cells were mounted on a lectin (Vector laboratories) coated imaging dish. The first time point before glucose addition was acquired

with EMM0G, then 2% glucose was added and the cells were imaged at the indicated time points.

5.2.4 Cell staining

- **Phloxine B** (Merck, P4030) was dissolved in water to 5mg/ml, diluted to 100µg/ml in water, and used at a final concentration of 10µg/ml in EMM medium.
- **Bodipy** (BODIPY 493/503, Thermo Fisher Scientific; D3922) was dissolved in DMSO (1mg/ml) and used at a final concentration of 4µg/ml in EMM medium.
- **Mitotracker red** (MitoTracker Red CMXRos or CM-H_2Xros, Thermo Fisher Scientific, M7512 or M7513, the used aliquot was a kind gift from Lucas Pelkmans) was dissolved in DMSO to a 1mM stock solution that was stored at -20°C. From this, a 100µM working stock solution was generated in DMSO. Mito tracker red was used at a final concentration of 100nM in EMM medium.
- **NileRed** (Sigma, N-3013) was dissolved in acetone to a 1mg/ml stock solution and used at a final concentration of 1µg/ml in EMM medium.

5.3 Cell wall digestion

5.3.1 1.2M Sorbitol buffer

For protoplast generation, approx. 0.3 OD ($1x10^6$ cell) units of cells were transferred to a 2ml Eppendorf tube for a final cell wall digestion volume of 500µl. Cells were washed twice in E buffer + sorbitol (E buffer: 50 mM sodium citrate, 100 mM sodium phosphate buffer pH 5.6; +1.2 M Sorbitol; (Kelly & Nurse, 2011)). Then, cells were resuspended in prewarmed enzyme digestion buffer consisting of E buffer + sorbitol plus cell wall digesting enzymes from Trichoderma (lysing enzymes from Trichoderma Harzianum, Merck; L1412) and zymolyase (MP Biomedicals, Santa Ana, California; 320921) at a final concentration of 5mg/ml. The enzyme stock solutions (25mg/ml enzymes in E buffer + sorbitol) were stored at 4°C for the duration of an experiment. The cells in the digestion buffer were then incubated for 1h on a rotor at 25°C unless stated otherwise. The protoplasts were washed once with E buffer + sorbitol, with centrifugation at minimum speed for 5min (no visible protoplast pellet). If necessary, the protoplasts were incubated for 15min on the rotor at 25°C in the presence of 8µg/ml rhodamine lectin (stock solution 2mg/ml in water; Rhodamine labelled griffonia (bandeiraea) simplicifolia lectin 1; Vector laboratories; RL-1102) in the dark. For observation,

protoplasts were transferred to a lectin coated imaging chamber and sealed with VALAP (Vaseline, Lanoline, Parafilm; 1:1:1) to prevent dehydration. For the protoplast shape stability experiments in the unpublished results of this thesis, the protoplasts were kept in the imaging chamber for as long as indicated.
For DED {Munder et al 2016.}, protoplasts were generated in the continued presence of 20 mM 2-deoxyglucose and 10 mM antimycin A in E buffer + sorbitol.

5.3.2 0.5M Sorbitol buffer

Approx. 0.2 OD units of cells were washed with 500µl 0.5M sorbitol solution (2:3 E buffer + 1.2M sorbitol to EMM0G). The pellet was resuspended in 30µl EMM0G, 10µl of each enzyme stock solution (Zymolyase 20-T (MP Biomedicals, 320921) and lysing enzymes from Trichoderma Harzianum (sigma-aldrich, L1412); stock concentration 25mg/ml in E buffer +1.2MSorbitol) and immediately put into an imaging chamber, sealed off with VALAP and imaged.

5.4 FLIP acquisition and analysis

Fluorescence loss in photobleaching (FLIP) experiments were performed at room temperature on cells mounted to an imaging chamber as described above that was sealed with VALAP (Vaseline, Lanoline, Parafilm; 1:1:1) to prevent dehydration. A spinning disc microscope (Nikon Eclipse Ti, VisiScope system, Yokogawa W1) with a 60x water objective, VisiView software and an Andor EMCCD camera was used. A z stack of 3 planes at a 1µm step size was acquired every second for 100 seconds, and a small region near one cell pole was bleached every 5 seconds. The mean fluorescence intensity loss of a region at the opposite pole (reference region) was then measured using Fiji. The analysis was done using Matlab, as described in (Bancaud, Huet, Rabut, & Ellenberg, 2010). For background subtraction, the mean signal of a background region close to the bleached cell was selected. The acquisition photobleaching was estimated by fitting an exponential function to the signal of a neighbouring cell, and dividing the background subtracted signal of the reference region by the exponential function. The signal was normalized to the last pre-bleach time point.

5.5 Electron microscopy

Cells were directly high pressure frozen as a solution (reviewed in (McDonald et al., 2010)). Both specimens were high pressure frozen using a Wohlwend Compact-2 high-pressure freezer

(Martin Wohlwend AG, Sennwald Switzerland). *S. pombe* samples destined for plastic section microtomy were freeze-substituted in 0.1% glutaraldehyde and 1% uranyl acetate in acetone for 48hrs and warmed from -90°C to -50°C in 8hrs (5°C per hour). Cells were then washed by acetone for 3 times and infiltrated in HM20 solution (25%, 33%, 50%, 67%, 75%, 100% in acetone) (Lowicryl HM20 Embedding Kit, Electron Microscopy Science, Hatfield, PA) over 5 days using Leica EMAFS (Leica, Vienna, Austria). Samples were then polymerized to blocks under Leica EMAFS UV light unit for 72hrs.

Plastic blocks were cut into ribbons of 80 (for single projection images) – 250 nm thick plastic sections (for tomographic reconstructions), by a Leica Ultracut microtome (Leica Inc., Vienna, Austria) using Diatome Ultra 45° (Diatome AG, Biel, Switzerland). Ribbons were collected on formvar-coated Cu-Rn grids (Electron Microscopy Science, Hatfield, PA) or Carbon Film Finder grids (Electron Microscopy Science, Hatfield, PA), immuno-labeled (optional), stained by uranyl acetate (2% uranyl acetate in 70% methanol) for ~4min and Reynold's lead citrate for ~2min (the staining time was adjusted based on the thickness of the sections).

Individual pictures of plastic sections, mostly used as a control, were acquired with a FEI Philips CM100 TEM and AMT 2Kx2K bottom-mount digital camera.

5.6 Image analysis

Routine image processing was done using Fiji/ImageJ (Rueden et al., 2017; Schindelin et al., 2012). Deconvolution was done using Huygens software (Scientific Volume Imaging) on image stacks acquired using Nyquist criteria. Plots were made using Matlab (MathWorks).

5.6.1 Single particle tracking of lipid droplets from DIC movies for qualitative DIC readout

The DIC movies (100frames, 4fps) were stack registered (Fiji plugin *StackReg*, (Thévenaz, Ruttimann, & Unser, 1998)). Lipid droplets were tracked with the Fiji plugin *Manual Tracking with TrackMate* (Tinevez et al., 2017), settings for semi-automated tracking: Quality threshold: 0.2, Distance tolerance: 0.1, Max nFrames: 0). The lipid droplets were manually seeded in the first time-frame, and the trajectory was considered if the particle could be tracked for more than ~95/100 frames. The manually seeded first trajectory point was excluded from the final trajectory, such that all LD positions were automatically detected.

5.6.2 Mean squared displacement (MSD) of mitochondria

Cox4-GFP labelled mitochondria were tracked using the *Mosaic particle tracking* plugin in Fiji (Mosaic Toolsuite, (Sbalzarini & Koumoutsakos, 2005); Settings: radius: 4, cutoff: 0, per/abs: 2, link: 3, displacement: 2). The subsequent analysis was done in Matlab (Mathworks). In section 2.1, only trajectories longer than 160 frames were considered, and the MSD up to a time lag of 40 frames was computed. For Figure 7 in the unpublished results, the trajectory length threshold was 100 frames, and the maximum time lag was 25 frames. The time-averaged MSD for each particle is plotted as a colour-coded histogram, and additionally the ensemble-averaged mean is shown.

5.6.3 Determination of the Bodipy correlation coefficient for quantification of lipid droplet motion (Bodipy CC readout)

For cell segmentation, first the signal from the image with the Phloxine B stain was log transformed and background subtracted (Mosaic ToolSuite, (Sbalzarini & Koumoutsakos, 2005)) in Fiji. Using pixel classification in ilastik (Sommer et al., 2011) the cell's inside was separated from the outline and the background. At the same time, the dead cells revealed by being filled with Phloxine B signal, were marked as a separate class and were excluded from the subsequent analysis. The cell insides were segmented in cellprofiler (Module: identify primary objects. Settings: Typical diameter of objects: 25-100 px; Threshold strategy: Manual, 0.85) after a smoothing step (Median Filter, typical artefact diameter: 2px). Next, the segmented cell insides were filtered (Module: filter objects. Settings: measurements to filter by: Solidity, 0.8-1) and used as seeds for segmentation (Module: identify secondary objects, applied twice in a row. Settings for first time: Method to identify the secondary object: Distance – N; expand primary objects by 6 px. Settings used second time: Distance – B; Threshold strategy: automatic; expand primary objects by 6px.) of all the alive cells (see section 2.1, Figure 1 – figure supplement 2 A).

Subsequently, the 3 Bodipy images, taken at a time interval of 45s (t1-t3), were stack registered using the *StackReg* plugin in Fiji. Since the signal intensity of Bodipy varied significantly within a population of cells in deep starvation (SD6, SD7, SD8; see section 2.1, Figure 1 – figure supplement 2B, white arrows) as well as throughout starvation, with particularly low signal at SD2 and SD3 (see section 2.1, Figure 1 – figure supplement 2 B), we included additional procedures. In addition, the Bodipy signal increased over the 3 time points, with the major increase between t1 and t2 (see section 2.1, Figure 1 – figure supplement 2 C). During SD2 and SD3 more LDs were detectable at t2 and t3 than at t1, which is why we decided to use

only t2 and t3. Because signal intensities do not matter when extracting LD dynamics, we equalized them by performing a log transform and background subtraction (Moasaic ToolSuite) on the fluorescent images. The signals were further equalised by pixel classification using ilastik. This procedure resulted in pseudoimages with pixel values representing the probability to belong to a lipid droplet instead of the actual fluorescence intensities (see section 2.1, Figure 1 – figure supplement 2 D). From the pseudoimages we computed the Pearson's correlation coefficient (CC) between t2 and t3 for the pixels of individual cells in cellprofiler. In the absence of LD motion during the 45s separating t2 and t3, the co-localization was very high leading to a CC close to 1. For cells with high LD motion, the co-localization was low, leading to a lower CC accordingly. A CC close to 0, or even below was rarely obtained, showing that a situation where all LDs of a cell completely changed their localization within the 45s time interval was unusual.

In section 3, I present the Bodipy CC values as standard boxplots. In the manuscript in section 2.1, I present CC values as dot plots showing individual CC values using the function plotSpread from the MathWorks File Exchange (Jonas Dorn, https://ch.mathworks.com/matlabcentral/fileexchange/37105-plot-spread-points--beeswarm-plot-). I overlay a boxplot indicating the median and the 25th to 75th percentile of the values. Where several experiments were pooled, the mean of the medians of the single experiments was plotted in blue. As a measure for the variance between individual experiments, blue error bars indicate the 95% confidence interval (95% CI) of the medians. This variance does not describe the variance of the individual medians, and might thus underestimate the true variance of the median.

5.6.4 Cell size measurements

For comparison of cell size in standard and high sorbitol medium (see section 2.1, Figure 2 E, Figure 2 – figure supplement 1 C), cell length and width were measured manually from DIC images using Fiji. Subsequently, the means of the mean cell length, measured independently in 3 experiments each for cells grown in standard and high sorbitol medium, were extracted. We then divided the mean of EMM cells by the mean of high Sorbitol cells (EMMLength1 + EMMLength2 + EMMLength3) / (SorbLength1 + SorbLength2 + SorbLength3) to define the amount of shrinkage upon transfer to 1.2M sorbitol. To estimate the variance of this ratio, bootstrapping was performed (999x resampling of each individual experiment) in Matlab, leading to 999 fractions from bootstrapped samples. The mean and 95% CI of these normally distributed fractions are shown in section 2.1, Figure 2E.

Measurements of protoplast length and width were done manually from DIC images using Fiji. Measurements of cell length and width throughout starvation were done in an automated fashion using Phloxine B signal, as described above.

5.7 Yeast handling of gene deletion library in 96-well format

5.7.1 Transfer 96 strains using the replicator pin tool or multi-channel pipettes

We have two methods, how to handle 96 strains: either by pipetting with multi-channel pipettes (Eppendorf Xplorer plus) where 12 strains can be handled at once, or by using the replicator pin tool (Multi-Blot Floating E-Clip Style Replicator, 96 FP13 pins, 3.18mm pin diameter, single robotic float plate plus BGPK-E manual use kit, delivers µ3µl hanging drop; V&P Scientific, San Diego, CA) where 96 strains can be transferred at once. The replicator pin tool method is fast and inexpensive, but I found that there is a notable risk of cross contamination of neighbouring wells during the transfer of the 96 hanging drops, especially when transferring from agar plates to liquid cultures. The pipetting method is a lot slower and more expensive, but also safer in respect of cross contamination.

For replicating strains using the replicator pin tool, a *library copier* was placed onto the plates containing the strains, where two long guide pins on the replicator pin tool fitted nicely into alignment holes, such that the pins could be aligned to the wells. For replica plating from or to liquid cultures, the replicator pin tool was carefully pushed up and down three times through the meniscus.

During the use of the replicator pin tool, a strict washing routine of the pins was maintained, according to the manufacturers recommendation. After each replication step, the replicator pin tool was washed with 10% bleach (Javelwasser 13-14% Aktivchlor; Thommen-Furler AG; 649-VS36TE/1; dilute this to 10% in water) and subsequently twice with water in 2 separate containers. For each step, the replicator pin tool was dipped 3 times into a container filled with the washing solution, and subsequently blotted onto lint-free blotting paper. After the second water step, the pins were dipped into isopropanol and briefly flamed. The pin tool was cooled prior to the next strain transfer. Before and after each experiment, the washing routine was performed using a mild detergent (Extran; Merck; 1.07553.2500, use at 2.5%) instead of the bleach solution. When after extensive use, the pins were not floating neatly anymore, the pin tool was disassembled very carefully, and the single pins were gently washed using the mild detergent and a gentle brush.

5.7.2 Generation of working replicas from the original gene deletion library

The pipetting method was used for re-isolation of the original gene deletion library (M-4030H-U5; *S. pombe* Haploid Deletion Mutant Set; Bioneer Coorporation, Republic of Korea) to generate two library replicates that were used for experiments, to leave the original plates as untouched as possible. For this, the frozen 96-well plates were processed in batches of 6 plates. The plates were taken out of the freezer and the aluminium seals were removed immediately while the strains were still frozen to reduce the contamination risk during this step. Then, the plates were let to thaw completely. After thawing, the now liquid cell cultures were carefully mixed with the multi-channel pipette (5-100µl), then 5µl were transferred to U-bottomed 96-well plates (Tissue culture test plate, 96 wells, U-bottom, TPP AG, Trasadingen, Switzerland; 92697) prepared with 120µl YE5S + G419 (100µg/ml, Geneticin G418; Bioconcept; 4-15P01-GA) + amp (100µg/ml; ampicillin. Na-salt; Serva, 13399) (fill the medium to the plates the day before, then you see if a well was contaminated). These plates were sealed with breathe-easier seals (Diversified Biotech, Dedham, Massachusetts; BERM-2000) and incubated at 30°C for 4 days. The plate numbers are encoded by an empty well at the well number that equals the plate number. Luckily, these wells were still empty after the 4-day incubation, indicating no contamination.

Next, the plates were prepared for long term storage by generating 25% glycerol stocks. For this, 75µl of 2/3 x 100% glycerol in YE5s + G418 (100µg/ml) + amp (100µg/ml) were added to the wells and thoroughly (!) mixed. From this, 5µl was transferred to 96-well plates filled with 120µl YE5S +G419 (100µg/ml) + amp (100µg/ml) for the generation of replica 2. The replica 1 plates were sealed with aluminium foil (AlumaSeal CS Films for cold storage, Merck, Z722642) and immediately frozen at -80°C. The plates for replica 2 were processed as replica 1.

5.7.3 Generation of glycerol stocks for long term storage on 96-well plates

Strains were grown in U-bottomed 96-well plates (TPP AG) prepared with 120µl YE5S + amp (100µg/ml ampicillin) plus G418 if required (fill the medium to the plates the day before, then you see if a well was contaminated). The plates were sealed with breathe-easier seals (Diversified Biotech; BERM-2000) and incubated at 30°C for 2-4 days. Next, the plates were prepared for long term storage by generating 25% glycerol stocks. For this, 75µl of 2/3 x 100% glycerol in YE5s + amp (100µg/ml) plus G418 if necessary, were added to the wells and thoroughly (!) mixed. The plates were sealed with aluminium foil (AlumaSeal CS Films for cold storage, Merck, Z722642) and immediately frozen at -80°C.

5.7.4 Re-isolation of frozen (-80°C) cultures in 96-well plates

5.7.4.1 Re-isolation of entire 96-well plate

The plate was taken out from -80°C incubator and the aluminium seal was removed immediately while the strains were still frozen to reduce the contamination risk during this step. Then, the plates were let to thaw completely. After thawing, the now liquid cell cultures were mixed and transferred carefully with the replicator pin tool to an agar plate (OmniTray; Therm Fisher Scientific; 242811, ~35ml YE5s + amp (100µg/ml), + G418 if necessary, per plate). The strains were incubated at 25°C or 30°C until colonies have formed.

5.7.4.2 Re-isolation of single strains

The re-isolation of single strains from glycerol stocks on 96-well plates was first tried according to re-isolation of strains from single tubes, by scraping cells off the glycerol stock from the top of the frozen stock and streaking onto an agar plate. Only in a second step, if no colonies formed with the default method, the plates were let to thaw, the liquid culture was mixed and 10µl transferred to an agar plate.

5.8 Screening the gene deletion library for the identification of strains required for CF

5.8.1 Starvation protocol for CF induction on 96-well plates

The strains were inoculated from agar plates to U-bottom 96-well plates (Tissue culture test plate, 96 wells, U-bottom, TPP AG, Trasadingen, Switzerland; 92697) filled with 200µl EMM2+ (EMM2 supplemented with 2.5mg/ml ALU: adenine (Merck, A9126), leucine (Merck, L8000) and uracil (Merck; U0750)) per well using the replicator pin tool. The plates were incubated overnight at 25°C without shaking (due to space limitations on the shaking incubator). The next morning before 10am, the strains were diluted to 150µl EMMLG+ (EMM with 0.5% glucose supplemented with ALU) using the replicator pin tool, which delivers ~3µl hanging drops per well (approx. 1: 50 dilution). The plates were sealed with breathe-easier seals (Diversified Biotech; BERM-2000) and incubated at 25°C in a shaking incubator (kühner shaker ISF-1-W; Adolf Kühner AG, Birsfelden, Switzerland; 25mm shaking diameter and 350rpm shaking speed for genome-wide screens; 50mm shaking diameter and (in the end) 270rpm shaking speed for evaluation screen) for 8 days.

5.8.2 Microscopy of cells on 96-well plates

Imaging plates (glass bottom 96-well plates from Zellkontakt (Bioswisstec); 5241; glass thickness 145µm, distance plate bottom to image focus plane 400µm) were coated up to a day prior to the data acquisition with poly-L-lysine (1mg/ml, Merck, P1399) by distributing 50µl poly-L-lysine to each well, letting it incubate for 5 minutes, removing the poly-L-lysine and letting the wells dry fully (takes a while). The residual poly-L-lysine was reused.

Cells were stained with Bodipy at a final concentration of 1µg/ml (BODIPY 493/503, Thermo Fisher Scientific; D3922) and Phloxine B (Merck, P4030) at a final concentration of 10-20µg/ml (screen 1 and screen 2, respectively). The staining mix for each 96-well plate was prepared freshly (11.4ml EMM0G, 12µl Bodipy stock solution 1mg/ml in DMSO, 24/48µl Phloxine B stock solution 5mg/ml) and protected from light. The staining mix was distributed to the imaging plate to a volume of 95µl per well. Then, 5µl of starvation culture was added to the wells using a 12-channel multi-pipette (Eppendorf Xplorer plus, 5-100µl) and mixed thoroughly but carefully with the staining mix (Pipet/Mix program: 5µl/60µl, 5x, speed up/down 5). Next, the imaging plates were sealed with aluminium seals (AlumaSeal CS Films for cold storage, Merck, Z722642) and centrifuged for 1 minute at 1000rpm (Multifuge 1S-R centrifuge, Thermo Fisher Scientific). After this, the plate was imaged immediately and up to maximally 1h after cell mounting.

Live imaging was performed at room temperature on a high throughput screening spinning disc microscope (Yokogawa CV7000, CSU-W1 Nipkow disc, Group of Prof. Lucas Pelkmans) using a 60x 1.2NA water objective and an Andor sCMOS camera (2560×2160 pixels, 14×16.6mm wide-view area; Andor Technology). First a single focal plane of Phloxine B (561 laser, 40%laser power, 200ms exposure time) and subsequently a Bodipy timelapse of single focal planes (6x every 7s, 488 laser, 40% laser power, 100ms exposure time) was acquired in the centre of each well.

For testing whether cells were able to recover the 8 days starvation period, an aliquot of each starvation culture was replica-plated onto an agar plate (YE5S + amp (100µg/ml)) using the replicator pin tool, and incubated at 25°C for several days until colonies were visible.

5.8.3 Data analysis

5.8.3.1 Cell segmentation

The raw Phloxine B images were preprocessed in cellprofiler (Carpenter et al., 2006) by correcting for the camera noise and the uneven illumination of the camera chip by subtracting

the dark frame and dividing the resulting image by a normalized image generated by the microscope for this purpose.

The preprocessed images were processed further using Fiji (Rueden et al., 2017; Schindelin et al., 2012). On the preprocessed images, a logarithmic transformation followed by background subtraction (Mosaic distribution, (Sbalzarini & Koumoutsakos, 2005)) was applied. Subsequently, the intensity values were set to the global minimum and maximum of all images from one 96-well plate, and converted to 8-bit.

Next, the processed images were subjected to pixel classification using ilastik (Sommer et al., 2011). The software was trained to classify the pixels into the classes *dead cell*, *cell outline*, *cell inside* and *background*. This training was applied on all processed Phloxine B images. The output was saved as pseudo-images (.png) with intensity values indicating the probability to belong to a certain class.

Last, seeds (inside of cells, equivalent to nuclei in mammalian cells) segmented in cellprofiler from the pseudo-images showing the probability to belong to the class *cell inside* (Module: identify primary objects. Settings: Typical diameter of objects: 6-100 px; Threshold strategy: Manual, 0.5) after a smoothing step (Median Filter, typical artefact diameter: 10px). Going out from these seeds, the cells were segmented in cellprofiler with the help of the processed Phloxine B images (Module: identify secondary objects. Settings: Method to identify secondary objects: Distance – B, Threshold strategy: Automatic, Number of pixels by which to expand primary objects: 20).

5.8.3.2 Determination of CF index

The raw Bodipy images were preprocessed in cellprofiler (Carpenter et al., 2006) by correcting for the camera noise and the uneven illumination of the camera chip by subtracting the dark frame and dividing the resulting image by a normalized image generated by the microscope for this purpose.

The preprocessed images were processed further using Fiji (Rueden et al., 2017; Schindelin et al., 2012). The movies were stack registred using the imageJ plugin *StackReg* (Thévenaz et al., 1998). Next, the acquisition photobleaching was corrected with the Fiji function *Bleach Correction*. Subsequently, a logarithmic transformation followed by background subtraction (Mosaic distribution, (Sbalzarini & Koumoutsakos, 2005)) was applied. Finally, the intensity values were set to the global minimum and maximum of all images from one 96-well plate, and converted to 8-bit.

Next, the processed images were subjected to pixel classification using ilastik (Sommer et al., 2011). The software was trained to classify the pixels into the 3 classes *lipid droplets*,

background, and a *helper class* for high cytoplasmic signal. This training was applied on all processed Bodipy images. The output was saved as pseudo-images (.png) with intensity values indicating the probability to belong to a certain class.

Last, cellprofiler was used to compute the Pearson correlation coefficient for each cell from the from the pseudo-images showing the probability to belong to the class *lipid droplet*. The CF index was the median of all single cell correlation coefficients of a given strain/cell population.

5.8.3.3 Selection of candidate genes

The criteria for selecting the candidate genes that were subjected to further validation were a CF index<0.9 in both screen repeats, or a CF index<1 in one screen repeat and no CF index (no cells) in the other repeat.

6 List of Figures

7 List of Tables

8 References

Abada, A., & Elazar, Z. (2014). Getting ready for building: signaling and autophagosome biogenesis. *EMBO Reports*, *15*(8), 839–852. http://doi.org/10.15252/embr.201439076

Abe, H., & Shimoda, C. (2000). Autoregulated expression of Schizosaccharomyces pombe meiosis-specific transcription factor Mei4 and a genome-wide search for its target genes. *Genetics*, *154*(4), 1497–1508.

Aiba, H., Yamada, H., Ohmiya, R., & Mizuno, T. (1995). The osmo-inducible gpd1+ gene is a target of the signaling pathway involving Wis1 MAP-kinase kinase in fission yeast. *FEBS Letters*, *376*(3), 199–201.

Alberti, S. (2017). The wisdom of crowds: regulating cell function through condensed states of living matter. *Journal of Cell Science*, *130*(17), 2789–2796. http://doi.org/10.1242/jcs.200295

Alberti, S., & Hyman, A. A. (2016). Are aberrant phase transitions a driver of cellular aging? *BioEssays : News and Reviews in Molecular, Cellular and Developmental Biology*, *38*(10), 959–968. http://doi.org/10.1002/bies.201600042

Alberts, B. (2008). Molecular Biology of the Cell. Garland Science.

Alvarez-Tabarés, I., Grallert, A., Ortiz, J.-M., & Hagan, I. M. (2007). Schizosaccharomyces pombe protein phosphatase 1 in mitosis, endocytosis and a partnership with Wsh3/Tea4 to control polarised growth. *Journal of Cell Science*, *120*(Pt 20), 3589–3601. http://doi.org/10.1242/jcs.007567

An, H., Morrell, J. L., Jennings, J. L., Link, A. J., & Gould, K. L. (2004). Requirements of fission yeast septins for complex formation, localization, and function. *Molecular Biology of the Cell*, *15*(12), 5551–5564. http://doi.org/10.1091/mbc.E04-07-0640

Atilgan, E., Magidson, V., Khodjakov, A., & Chang, F. (2015). Morphogenesis of the Fission Yeast Cell through Cell Wall Expansion. *Current Biology : CB*, *25*(16), 2150–2157. http://doi.org/10.1016/j.cub.2015.06.059

Avruch, J., Long, X., Ortiz-Vega, S., Rapley, J., Papageorgiou, A., & Dai, N. (2009). Amino acid regulation of TOR complex 1. *American Journal of Physiology. Endocrinology and Metabolism*, *296*(4), E592–602. http://doi.org/10.1152/ajpendo.90645.2008

Banani, S. F., Lee, H. O., Hyman, A. A., & Rosen, M. K. (2017). Biomolecular condensates: organizers of cellular biochemistry. *Nature Reviews. Molecular Cell Biology*, *18*(5), 285–298. http://doi.org/10.1038/nrm.2017.7

Bancaud, A., Huet, S., Rabut, G., & Ellenberg, J. (2010). Fluorescence perturbation techniques to study mobility and molecular dynamics of proteins in live cells: FRAP, photoactivation, photoconversion, and FLIP. *Cold Spring Harbor Protocols*, *2010*(12), pdb.top90–pdb.top90. http://doi.org/10.1101/pdb.top90

Barros, M. H., Bandy, B., Tahara, E. B., & Kowaltowski, A. J. (2004). Higher respiratory activity decreases mitochondrial reactive oxygen release and increases life span in Saccharomyces cerevisiae. *The Journal of Biological Chemistry*, *279*(48), 49883–49888. http://doi.org/10.1074/jbc.M408918200

Bähler, J., Wu, J. Q., Longtine, M. S., Shah, N. G., McKenzie, A., Steever, A. B., et al. (1998). Heterologous modules for efficient and versatile PCR-based gene targeting in Schizosaccharomyces pombe. *Yeast (Chichester, England)*, *14*(10), 943–951. http://doi.org/10.1002/(SICI)1097-0061(199807)14:10<943::AID-YEA292>3.0.CO;2-Y

Berlin, A., Paoletti, A., & Chang, F. (2003). Mid2p stabilizes septin rings during cytokinesis in fission yeast. *The Journal of Cell Biology*, *160*(7), 1083–1092. http://doi.org/10.1083/jcb.200212016

Binda, M., Péli-Gulli, M.-P., Bonfils, G., Panchaud, N., Urban, J., Sturgill, T. W., et al. (2009). The Vam6 GEF controls TORC1 by activating the EGO complex. *Molecular Cell*, *35*(5), 563–573. http://doi.org/10.1016/j.molcel.2009.06.033

Binns, D., Januszewski, T., Chen, Y., Hill, J., Markin, V. S., Zhao, Y., et al. (2006). An intimate collaboration between peroxisomes and lipid bodies. *The Journal of Cell Biology*, *173*(5), 719–731. http://doi.org/10.1083/jcb.200511125

Boisvert, F.-M., van Koningsbruggen, S., Navascués, J., & Lamond, A. I. (2007). The multifunctional nucleolus. *Nature Reviews. Molecular Cell Biology*, *8*(7), 574–585. http://doi.org/10.1038/nrm2184

Boke, E., Ruer, M., Wühr, M., Coughlin, M., Lemaitre, R., Gygi, S. P., et al. (2016). Amyloid-like Self-Assembly of a Cellular Compartment. *Cell*, *166*(3), 637–650. http://doi.org/10.1016/j.cell.2016.06.051

Boldogh, I. R., & Pon, L. A. (2006). Interactions of mitochondria with the actin cytoskeleton. *Biochimica Et Biophysica Acta*, *1763*(5-6), 450–462. http://doi.org/10.1016/j.bbamcr.2006.02.014

Bonawitz, N. D., Chatenay-Lapointe, M., Pan, Y., & Shadel, G. S. (2007). Reduced TOR signaling extends chronological life span via increased respiration and upregulation of mitochondrial gene expression. *Cell Metabolism*, *5*(4), 265–277. http://doi.org/10.1016/j.cmet.2007.02.009

Boothby, T. C., Tapia, H., Brozena, A. H., Piszkiewicz, S., Smith, A. E., Giovannini, I., et al. (2017). Tardigrades Use Intrinsically Disordered Proteins to Survive Desiccation. *Molecular Cell*, *65*(6), 975–984.e5. http://doi.org/10.1016/j.molcel.2017.02.018

Boyle, E. I., Weng, S., Gollub, J., Jin, H., Botstein, D., Cherry, J. M., & Sherlock, G. (2004). GO::TermFinder--open source software for accessing Gene Ontology information and finding significantly enriched Gene Ontology terms associated with a list of genes. *Bioinformatics (Oxford, England)*, *20*(18), 3710–3715. http://doi.org/10.1093/bioinformatics/bth456

Brangwynne, C. P., Eckmann, C. R., Courson, D. S., Rybarska, A., Hoege, C., Gharakhani, J., et al. (2009). Germline P granules are liquid droplets that localize by controlled dissolution/condensation. *Science (New York, N.Y.)*, *324*(5935), 1729–1732. http://doi.org/10.1126/science.1172046

Brunner, D., & Nurse, P. (2000). CLIP170-like tip1p spatially organizes microtubular dynamics in fission yeast. *Cell*, *102*(5), 695–704.

Buchan, J. R., & Parker, R. (2009). Eukaryotic stress granules: the ins and outs of translation. *Molecular Cell*, *36*(6), 932–941. http://doi.org/10.1016/j.molcel.2009.11.020

Cano, R. J., & Borucki, M. K. (1995). Revival and identification of bacterial spores in 25- to 40-million-year-old Dominican amber. *Science (New York, N.Y.)*, *268*(5213), 1060–1064.

Carpenter, A. E., Jones, T. R., Lamprecht, M. R., Clarke, C., Kang, I. H., Friman, O., et al. (2006). CellProfiler: image analysis software for identifying and quantifying cell phenotypes. *Genome Biology*, *7*(10), R100. http://doi.org/10.1186/gb-2006-7-10-r100

Chang, F. (2017). Forces that shape fission yeast cells. *Molecular Biology of the Cell*, *28*(14), 1819–1824. http://doi.org/10.1091/mbc.E16-09-0671

Chen, B.-R., & Runge, K. W. (2009). A new Schizosaccharomyces pombe chronological lifespan assay reveals that caloric restriction promotes efficient cell cycle exit and extends longevity. *Experimental Gerontology*, *44*(8), 493–502. http://doi.org/10.1016/j.exger.2009.04.004

Chen, H., & Chan, D. C. (2005). Emerging functions of mammalian mitochondrial fusion and fission. *Human Molecular Genetics*, *14 Spec No. 2*(suppl_2), R283–9. http://doi.org/10.1093/hmg/ddi270

Chiron, S., Bobkova, A., Zhou, H., & Yaffe, M. P. (2008). CLASP regulates mitochondrial distribution in Schizosaccharomyces pombe. *The Journal of Cell Biology*, *182*(1), 41–49. http://doi.org/10.1083/jcb.200712147

Choudhary, V., Ojha, N., Golden, A., & Prinz, W. A. (2015). A conserved family of proteins facilitates nascent lipid droplet budding from the ER. *The Journal of Cell Biology*, *211*(2), 261–271. http://doi.org/10.1083/jcb.201505067

Coelho, M., Dereli, A., Haese, A., Kühn, S., Malinovska, L., DeSantis, M. E., et al. (2013). Fission yeast does not age under favorable conditions, but does so after stress. *Current Biology : CB*, *23*(19), 1844–1852. http://doi.org/10.1016/j.cub.2013.07.084

Coelho, M., Lade, S. J., Alberti, S., Gross, T., & Tolić, I. M. (2014). Fusion of protein aggregates facilitates asymmetric damage segregation. *PLoS Biology*, *12*(6), e1001886. http://doi.org/10.1371/journal.pbio.1001886

Coller, H. A., Sang, L., & Roberts, J. M. (2006). A new description of cellular quiescence. *PLoS Biology*, *4*(3), e83. http://doi.org/10.1371/journal.pbio.0040083

Costello, G., Rodgers, L., & Beach, D. (1986). Fission yeast enters the stationary phase G0 state from either mitotic G1 or G2. *Current Genetics*, 1–7.

Cowan, A. E., Koppel, D. E., Setlow, B., & Setlow, P. (2003). A soluble protein is immobile in dormant spores of Bacillus subtilis but is mobile in germinated spores: implications for spore dormancy. *Proceedings of the National Academy of Sciences of the United States of America*, *100*(7), 4209–4214. http://doi.org/10.1073/pnas.0636762100

De Deken, R. H. (1966). The Crabtree effect: a regulatory system in yeast. *Journal of General Microbiology*, *44*(2), 149–156. http://doi.org/10.1099/00221287-44-2-149

Decker, C. J., & Parker, R. (2012). P-bodies and stress granules: possible roles in the control of translation and mRNA degradation. *Cold Spring Harbor Perspectives in Biology*, *4*(9), a012286–a012286. http://doi.org/10.1101/cshperspect.a012286

Dijksterhuis, J., Nijsse, J., Hoekstra, F. A., & Golovina, E. A. (2007). High viscosity and anisotropy characterize the cytoplasm of fungal dormant stress-resistant spores. *Eukaryotic Cell*, *6*(2), 157–170. http://doi.org/10.1128/EC.00247-06

Dilova, I., Easlon, E., & Lin, S.-J. (2007). Calorie restriction and the nutrient sensing signaling pathways. *Cellular and Molecular Life Sciences : CMLS*, *64*(6), 752–767. http://doi.org/10.1007/s00018-007-6381-y

Elbein, A. D., Pan, Y. T., Pastuszak, I., & Carroll, D. (2003). New insights on trehalose: a multifunctional molecule. *Glycobiology*, *13*(4), 17R–27R. http://doi.org/10.1093/glycob/cwg047

Elowitz, M. B., Surette, M. G., Wolf, P. E., Stock, J., & Leibler, S. (1997). Photoactivation turns green fluorescent protein red. *Current Biology : CB*, *7*(10), 809–812.

Fels, J., Orlov, S. N., & Grygorczyk, R. (2009). The hydrogel nature of mammalian cytoplasm contributes to osmosensing and extracellular pH sensing. *Biophysical Journal*, *96*(10), 4276–4285. http://doi.org/10.1016/j.bpj.2009.02.038

Feng, Y., Yao, Z., & Klionsky, D. J. (2015). How to control self-digestion: transcriptional, post-transcriptional, and post-translational regulation of autophagy. *Trends in Cell Biology*, *25*(6), 354–363. http://doi.org/10.1016/j.tcb.2015.02.002

Flores, C. L., Rodríguez, C., Petit, T., & Gancedo, C. (2000). Carbohydrate and energy-yielding metabolism in non-conventional yeasts. *FEMS Microbiology Reviews*, *24*(4), 507–529.

Frank, S., Gaume, B., Bergmann-Leitner, E. S., Leitner, W. W., Robert, E. G., Catez, F., et al. (2001). The role of dynamin-related protein 1, a mediator of mitochondrial fission, in apoptosis. *Developmental Cell*, *1*(4), 515–525.

Fu, C., Jain, D., Costa, J., Velve-Casquillas, G., & Tran, P. T. (2011). mmb1p binds mitochondria to dynamic microtubules. *Current Biology : CB*, *21*(17), 1431–1439. http://doi.org/10.1016/j.cub.2011.07.013

Goldstein, B., & Blaxter, M. (2002). Tardigrades. *Current Biology : CB*, *12*(14), R475.

Goyal, S., Amar, S. K., Srivastav, A. K., Chopra, D., Pal, M. K., Arjaria, N., & Ray, R. S. (2016). ROS mediated crosstalk between endoplasmic reticulum and mitochondria by Phloxine B under environmental UV irradiation. *Journal of Photochemistry and Photobiology. B, Biology*, *161*, 284–294. http://doi.org/10.1016/j.jphotobiol.2016.05.031

Grygorczyk, R., Boudreault, F., Platonova, A., & Orlov, S. N. (2015). Salt and osmosensing: role of cytoplasmic hydrogel. *Pflugers Archiv : European Journal of Physiology*, *467*(3), 475–487. http://doi.org/10.1007/s00424-014-1680-2

Hagan, I M. (1998). The fission yeast microtubule cytoskeleton. *Journal of Cell Science*, *111 (Pt 12)*, 1603–1612.

Hagan, Ian M, Carr, A. M., Grallert, A., & Nurse, P. (Eds.). (2016). Fission Yeast. John Inglis.

Hamasaki, M., Noda, T., Baba, M., & Ohsumi, Y. (2005). Starvation triggers the delivery of the endoplasmic reticulum to the vacuole via autophagy in yeast. *Traffic (Copenhagen, Denmark)*, *6*(1), 56–65. http://doi.org/10.1111/j.1600-0854.2004.00245.x

Han, T. W., Kato, M., Xie, S., Wu, L. C., Mirzaei, H., Pei, J., et al. (2012). Cell-free formation of RNA granules: bound RNAs identify features and components of cellular assemblies. *Cell*, *149*(4), 768–779. http://doi.org/10.1016/j.cell.2012.04.016

Hayles, J., & Nurse, P. (2001). A journey into space. *Nature Reviews. Molecular Cell Biology*, *2*(9), 647–656. http://doi.org/10.1038/35089520

Heikal, A. A. (2010). Intracellular coenzymes as natural biomarkers for metabolic activities and mitochondrial anomalies. *Biomarkers in Medicine*, *4*(2), 241–263. http://doi.org/10.2217/bmm.10.1

Herman, P. K. (2002). Stationary phase in yeast. *Current Opinion in Microbiology*, *5*(6), 602–607.

Heslot, H., Goffeau, A., & Louis, C. (1970). Respiratory metabolism of a “petite negative”yeast Schizosaccharomyces pombe 972h-. *Journal of Bacteriology*, *104*(1), 473–481.

Hollenbeck, P. J., & Saxton, W. M. (2005). The axonal transport of mitochondria. *Journal of Cell Science*, *118*(Pt 23), 5411–5419. http://doi.org/10.1242/jcs.02745

Höög, J. L., Schwartz, C., Noon, A. T., O'Toole, E. T., Mastronarde, D. N., McIntosh, J. R., & Antony, C. (2007). Organization of interphase microtubules in fission yeast analyzed by electron tomography. *Developmental Cell*, *12*(3), 349–361. http://doi.org/10.1016/j.devcel.2007.01.020

Huang, J., Huang, Y., Yu, H., Subramanian, D., Padmanabhan, A., Thadani, R., et al. (2012). Nonmedially assembled F-actin cables incorporate into the actomyosin ring in fission yeast. *The Journal of Cell Biology*, *199*(5), 831–847. http://doi.org/10.1083/jcb.201209044

Huisman, S. M., & Brunner, D. (2011). Cell polarity in fission yeast: a matter of confining, positioning, and switching growth zones. *Seminars in Cell & Developmental Biology*, *22*(8), 799–805. http://doi.org/10.1016/j.semcdb.2011.07.013

Hyman, A. A., Weber, C. A., & Jülicher, F. (2014). Liquid-liquid phase separation in biology. *Annual Review of Cell and Developmental Biology*, *30*(1), 39–58. http://doi.org/10.1146/annurev-cellbio-100913-013325

Ibeneche, C. C. (2011, December 8). *Cell Freezing in Response to Advanced Glucose Starvation: A Novel Cytoplasmic State in Fission Yeast*.

Inbaraj, J. J., Kukielczak, B. M., & Chignell, C. F. (2005). Phloxine B phototoxicity: a mechanistic study using HaCaT keratinocytes. *Photochemistry and Photobiology*, *81*(1), 81–88. http://doi.org/10.1562/2003-11-04-RA-002

Islam, M. S., Honma, M., Nakabayashi, T., Kinjo, M., & Ohta, N. (2013). pH dependence of the fluorescence lifetime of FAD in solution and in cells. *International Journal of Molecular Sciences*, *14*(1), 1952–1963. http://doi.org/10.3390/ijms14011952

Jacquier, N., Choudhary, V., Mari, M., Toulmay, A., Reggiori, F., & Schneiter, R. (2011). Lipid droplets are functionally connected to the endoplasmic reticulum in Saccharomyces cerevisiae. *Journal of Cell Science*, *124*(Pt 14), 2424–2437. http://doi.org/10.1242/jcs.076836

Jara, M., Vivancos, A. P., Calvo, I. A., Moldón, A., Sansó, M., & Hidalgo, E. (2007). The peroxiredoxin Tpx1 is essential as a H2O2 scavenger during aerobic growth in fission yeast. *Molecular Biology of the Cell*, *18*(6), 2288–2295. http://doi.org/10.1091/mbc.E06-11-1039

Jourdain, I., Sontam, D., Johnson, C., Dillies, C., & Hyams, J. S. (2008). Dynamin-dependent biogenesis, cell cycle regulation and mitochondrial association of peroxisomes in fission yeast. *Traffic (Copenhagen, Denmark)*, *9*(3), 353–365. http://doi.org/10.1111/j.1600-0854.2007.00685.x

Joyner, R. P., Tang, J. H., Helenius, J., Dultz, E., Brune, C., Holt, L. J., et al. (2016). A glucose-starvation response regulates the diffusion of macromolecules. *eLife*, *5*, 833. http://doi.org/10.7554/eLife.09376

Karbowski, M., & Youle, R. J. (2003). Dynamics of mitochondrial morphology in healthy cells and during apoptosis. *Cell Death and Differentiation*, *10*(8), 870–880. http://doi.org/10.1038/sj.cdd.4401260

Kassi, E., & Papavassiliou, A. G. (2008). Could glucose be a proaging factor? *Journal of Cellular and Molecular Medicine*, *12*(4), 1194–1198. http://doi.org/10.1111/j.1582-4934.2008.00329.x

Kato, M., Han, T. W., Xie, S., Shi, K., Du, X., Wu, L. C., et al. (2012). Cell-free formation of RNA granules: low complexity sequence domains form dynamic fibers within hydrogels. *Cell*, *149*(4), 753–767. http://doi.org/10.1016/j.cell.2012.04.017

Kelly, F. D., & Nurse, P. (2011). De novo growth zone formation from fission yeast spheroplasts. *PloS One*, *6*(12), e27977. http://doi.org/10.1371/journal.pone.0027977

Kim, D. U., Hayles, J., Kim, D., Wood, V., Park, H.-O., Won, M., et al. (2010). Analysis of a genome-wide set of gene deletions in the fission yeast Schizosaccharomyces pombe. *Nature Biotechnology*, *28*(6), 617–623. http://doi.org/10.1038/nbt.1628

Kobori, H., Yamada, N., Taki, A., & Osumi, M. (1989). Actin is associated with the formation of the cell wall in reverting protoplasts of the fission yeast Schizosaccharomyces pombe. *Journal of Cell Science*, *94 (Pt 4)*, 635–646.

Kohda, T. A., Tanaka, K., Konomi, M., Sato, M., Osumi, M., & Yamamoto, M. (2007). Fission yeast autophagy induced by nitrogen starvation generates a nitrogen source that drives adaptation processes. *Genes to Cells : Devoted to Molecular & Cellular Mechanisms*, *12*(2), 155–170. http://doi.org/10.1111/j.1365-2443.2007.01041.x

Kondo, K., Kubo, T., & Kunieda, T. (2015). Suggested Involvement of PP1/PP2A Activity and De Novo Gene Expression in Anhydrobiotic Survival in a Tardigrade, Hypsibius dujardini, by Chemical Genetic Approach. *PloS One*, *10*(12), e0144803. http://doi.org/10.1371/journal.pone.0144803

Kopecká, M., Fleet, G. H., & Phaff, H. J. (1995). Ultrastructure of the cell wall of Schizosaccharomyces pombe following treatment with various glucanases. *Journal of Structural Biology*, *114*(2), 140–152. http://doi.org/10.1006/jsbi.1995.1013

Kovar, D. R., Sirotkin, V., & Lord, M. (2011). Three's company: the fission yeast actin cytoskeleton. *Trends in Cell Biology*, *21*(3), 177–187. http://doi.org/10.1016/j.tcb.2010.11.001

Laplante, M., & Sabatini, D. M. (2012). mTOR signaling in growth control and disease. *Cell*, *149*(2), 274–293. http://doi.org/10.1016/j.cell.2012.03.017

Laporte, D., Courtout, F., Pinson, B., Dompierre, J., Salin, B., Brocard, L., & Sagot, I. (2015). A stable microtubule array drives fission yeast polarity reestablishment upon quiescence exit. *The Journal of Cell Biology*, *210*(1), 99–113. http://doi.org/10.1083/jcb.201502025

Laporte, D., Salin, B., Daignan-Fornier, B., & Sagot, I. (2008). Reversible cytoplasmic localization of the proteasome in quiescent yeast cells. *The Journal of Cell Biology*, *181*(5), 737–745. http://doi.org/10.1083/jcb.200711154

Lennon, J. T., & Jones, S. E. (2011). Microbial seed banks: the ecological and evolutionary implications of dormancy. *Nature Reviews. Microbiology*, *9*(2), 119–130. http://doi.org/10.1038/nrmicro2504

Li, P., Banjade, S., Cheng, H.-C., Kim, S., Chen, B., Guo, L., et al. (2012). Phase transitions in the assembly of multivalent signalling proteins. *Nature*, *483*(7389), 336–340. http://doi.org/10.1038/nature10879

Li, T., Zheng, F., Cheung, M., Wang, F., & Fu, C. (2015). Fission yeast mitochondria are distributed by dynamic microtubules in a motor-independent manner. *Scientific Reports*, *5*, 11023. http://doi.org/10.1038/srep11023

Lin, S.-J., Kaeberlein, M., Andalis, A. A., Sturtz, L. A., Defossez, P.-A., Culotta, V. C., et al. (2002). Calorie restriction extends Saccharomyces cerevisiae lifespan by increasing respiration. *Nature*, *418*(6895), 344–348. http://doi.org/10.1038/nature00829

Liquido, N. J., McQuate, G. T., & Cunningham, R. T. (1995). Light- activated toxicity of phloxine B and uranine to Mediterranean fruit fly, Ceratitis capitata (Wiedemann) (Diptera: Tephritidae), adults. In *Light-Activated Pest Control*.

Long, A. P., Manneschmidt, A. K., VerBrugge, B., Dortch, M. R., Minkin, S. C., Prater, K. E., et al. (2012). Lipid droplet de novo formation and fission are linked to the cell cycle in fission yeast. *Traffic (Copenhagen, Denmark)*, *13*(5), 705–714. http://doi.org/10.1111/j.1600-0854.2012.01339.x

Longtine, M. S., DeMarini, D. J., Valencik, M. L., Al-Awar, O. S., Fares, H., De Virgilio, C., & Pringle, J. R. (1996). The septins: roles in cytokinesis and other processes. *Current Opinion in Cell Biology*, *8*(1), 106–119.

Luby-Phelps, K., Taylor, D. L., & Lanni, F. (1986). Probing the structure of cytoplasm. *The Journal of Cell Biology*, *102*(6), 2015–2022.

Mahen, R., & Venkitaraman, A. R. (2012). Pattern formation in centrosome assembly. *Current Opinion in Cell Biology*, *24*(1), 14–23. http://doi.org/10.1016/j.ceb.2011.12.012

Makushok, T., Alves, P., Huisman, S. M., Kijowski, A. R., & Brunner, D. (2016). Sterol-Rich Membrane Domains Define Fission Yeast Cell Polarity. *Cell*, *165*(5), 1182–1196. http://doi.org/10.1016/j.cell.2016.04.037

Manners, D. J., & Meyer, M. T. (1977). The molecular structures of some glucans from the cell walls of Schizosaccharomyces pombe. *Carbohydrate Research*.

Martin, S., & Parton, R. G. (2006). Lipid droplets: a unified view of a dynamic organelle. *Nature Reviews. Molecular Cell Biology*, *7*(5), 373–378. http://doi.org/10.1038/nrm1912

Mata, J., & Nurse, P. (1997). tea1 and the microtubular cytoskeleton are important for generating global spatial order within the fission yeast cell. *Cell*, *89*(6), 939–949.

Mata, J., Lyne, R., Burns, G., & Bähler, J. (2002). The transcriptional program of meiosis and sporulation in fission yeast. *Nature Genetics*, *32*(1), 143–147. http://doi.org/10.1038/ng951

Matsuzawa, T., Ohashi, T., Hosomi, A., Tanaka, N., Tohda, H., & Takegawa, K. (2010). The gld1+ gene encoding glycerol dehydrogenase is required for glycerol metabolism in Schizosaccharomyces pombe. *Applied Microbiology and Biotechnology*, *87*(2), 715–727. http://doi.org/10.1007/s00253-010-2586-3

McDonald, K., Schwarz, H., Müller-Reichert, T., Webb, R., Buser, C., & Morphew, M. (2010). "Tips and tricks" for high-pressure freezing of model systems. *Methods in Cell Biology*, *96*, 671–693. http://doi.org/10.1016/S0091-679X(10)96028-7

Miermont, A., Waharte, F., Hu, S., McClean, M. N., Bottani, S., Léon, S., & Hersen, P. (2013). Severe osmotic compression triggers a slowdown of intracellular signaling, which can be explained by molecular crowding. *Proceedings of the National Academy of Sciences of the United States of America*, *110*(14), 5725–5730. http://doi.org/10.1073/pnas.1215367110

Minc, N., Boudaoud, A., & Chang, F. (2009). Mechanical forces of fission yeast growth. *Current Biology : CB*, *19*(13), 1096–1101. http://doi.org/10.1016/j.cub.2009.05.031

Mitchison, T. J., Charras, G. T., & Mahadevan, L. (2008). Implications of a poroelastic cytoplasm for the dynamics of animal cell shape. *Seminars in Cell & Developmental Biology*, *19*(3), 215–223. http://doi.org/10.1016/j.semcdb.2008.01.008

Mitchison, T., & Kirschner, M. (1984). Dynamic instability of microtubule growth. *Nature*, *312*(5991), 237–242.

Moeendarbary, E., Valon, L., Fritzsche, M., Harris, A. R., Moulding, D. A., Thrasher, A. J., et al. (2013). The cytoplasm of living cells behaves as a poroelastic material. *Nature Materials*, *12*(3), 253–261. http://doi.org/10.1038/nmat3517

Molliex, A., Temirov, J., Lee, J., Coughlin, M., Kanagaraj, A. P., Kim, H. J., et al. (2015). Phase separation by low complexity domains promotes stress granule assembly and drives pathological fibrillization. *Cell*, *163*(1), 123–133. http://doi.org/10.1016/j.cell.2015.09.015

Moreno, S., Klar, A., & Nurse, P. (1991). Molecular genetic analysis of fission yeast Schizosaccharomyces pombe. *Methods in Enzymology*, *194*, 795–823.

Mostowy, S., & Cossart, P. (2012). Septins: the fourth component of the cytoskeleton. *Nature Reviews. Molecular Cell Biology*, *13*(3), 183–194. http://doi.org/10.1038/nrm3284

Mukaiyama, H., Kajiwara, S., Hosomi, A., Giga-Hama, Y., Tanaka, N., Nakamura, T., & Takegawa, K. (2009). Autophagy-deficient Schizosaccharomyces pombe mutants undergo partial sporulation during nitrogen starvation. *Microbiology (Reading, England)*, *155*(Pt 12), 3816–3826. http://doi.org/10.1099/mic.0.034389-0

Mukaiyama, H., Nakase, M., Nakamura, T., Kakinuma, Y., & Takegawa, K. (2010). Autophagy in the fission yeast Schizosaccharomyces pombe. *FEBS Letters*, *584*(7), 1327–1334. http://doi.org/10.1016/j.febslet.2009.12.037

Munder, M. C., Midtvedt, D., Franzmann, T., Nüske, E., Otto, O., Herbig, M., et al. (2016). A pH-driven transition of the cytoplasm from a fluid- to a solid-like state promotes entry into dormancy. *eLife*, *5*, 59. http://doi.org/10.7554/eLife.09347

Murakami, T., Qamar, S., Lin, J. Q., Schierle, G. S. K., Rees, E., Miyashita, A., et al. (2015). ALS/FTD Mutation-Induced Phase Transition of FUS Liquid Droplets and Reversible Hydrogels into Irreversible Hydrogels Impairs RNP Granule Function. *Neuron*, *88*(4), 678–690. http://doi.org/10.1016/j.neuron.2015.10.030

Mutoh, N., Kawabata, M., Nakagawa, C. W., & Kitajima, S. (2005). Pro-oxidant action of phloxine B on fission yeast Schizosaccharomyces pombe. *Yeast (Chichester, England)*, *22*(2), 91–97. http://doi.org/10.1002/yea.1196

Nakashima, A., Hasegawa, T., Mori, S., Ueno, M., Tanaka, S., Ushimaru, T., et al. (2006). A starvation-specific serine protease gene, isp6+, is involved in both autophagy and sexual development in Schizosaccharomyces pombe. *Current Genetics*, *49*(6), 403–413. http://doi.org/10.1007/s00294-006-0067-0

Narayanaswamy, R., Levy, M., Tsechansky, M., Stovall, G. M., O'Connell, J. D., Mirrielees, J., et al. (2009). Widespread reorganization of metabolic enzymes into reversible assemblies upon nutrient starvation. *Proceedings of the National Academy of Sciences of the United States of America*, *106*(25), 10147–10152. http://doi.org/10.1073/pnas.0812771106

Neuman, K. C., & Block, S. M. (2004). Optical trapping. *The Review of Scientific Instruments*, *75*(9), 2787–2809. http://doi.org/10.1063/1.1785844

Noree, C., Sato, B. K., Broyer, R. M., & Wilhelm, J. E. (2010). Identification of novel filament-forming proteins in Saccharomyces cerevisiae and Drosophila melanogaster. *The Journal of Cell Biology*, *190*(4), 541–551. http://doi.org/10.1083/jcb.201003001

Nott, T. J., Petsalaki, E., Farber, P., Jervis, D., Fussner, E., Plochowietz, A., et al. (2015). Phase transition of a disordered nuage protein generates environmentally responsive membraneless organelles. *Molecular Cell*, *57*(5), 936–947. http://doi.org/10.1016/j.molcel.2015.01.013

Nunnari, J., & Suomalainen, A. (2012). Mitochondria: in sickness and in health. *Cell*, *148*(6), 1145–1159. http://doi.org/10.1016/j.cell.2012.02.035

O'Connell, J. D., Zhao, A., Ellington, A. D., & Marcotte, E. M. (2012). Dynamic reorganization of metabolic enzymes into intracellular bodies. *Annual Review of Cell and Developmental Biology*, *28*(1), 89–111. http://doi.org/10.1146/annurev-cellbio-101011-155841

Onishi, M., Koga, T., Hirata, A., Nakamura, T., Asakawa, H., Shimoda, C., et al. (2010). Role of septins in the orientation of forespore membrane extension during sporulation in fission yeast. *Molecular and Cellular Biology*, *30*(8), 2057–2074. http://doi.org/10.1128/MCB.01529-09

Otsubo, Y., Nakashima, A., Yamamoto, M., & Yamashita, A. (2017). TORC1-Dependent Phosphorylation Targets in Fission Yeast. *Biomolecules*, *7*(3), 50. http://doi.org/10.3390/biom7030050

Otsuga, D., Keegan, B. R., Brisch, E., Thatcher, J. W., Hermann, G. J., Bleazard, W., & Shaw, J. M. (1998). The dynamin-related GTPase, Dnm1p, controls mitochondrial morphology in yeast. *The Journal of Cell Biology*, *143*(2), 333–349.

Palková, Z., Wilkinson, D., & Váchová, L. (2014). Aging and differentiation in yeast populations: elders with different properties and functions. *FEMS Yeast Research*, *14*(1), 96–108. http://doi.org/10.1111/1567-1364.12103

Pan, F., Malmberg, R. L., & Momany, M. (2007). Analysis of septins across kingdoms reveals orthology and new motifs. *BMC Evolutionary Biology*, *7*(1), 103. http://doi.org/10.1186/1471-2148-7-103

Pardo, M., & Nurse, P. (2005). The nuclear rim protein Amo1 is required for proper microtubule cytoskeleton organisation in fission yeast. *Journal of Cell Science*, *118*(Pt 8), 1705–1714. http://doi.org/10.1242/jcs.02305

Parry, B. R., Surovtsev, I. V., Cabeen, M. T., O'Hern, C. S., Dufresne, E. R., & Jacobs-Wagner, C. (2014). The Bacterial Cytoplasm Has Glass-like Properties and Is Fluidized by Metabolic Activity. *Cell*, *156*(1-2), 183–194. http://doi.org/10.1016/j.cell.2013.11.028

Patel, A., Lee, H. O., Jawerth, L., Maharana, S., Jahnel, M., Hein, M. Y., et al. (2015). A Liquid-to-Solid Phase Transition of the ALS Protein FUS Accelerated by Disease Mutation. *Cell*, *162*(5), 1066–1077. http://doi.org/10.1016/j.cell.2015.07.047

Petrovska, I., Nüske, E., Munder, M. C., Kulasegaran, G., Malinovska, L., Kroschwald, S., et al. (2014). Filament formation by metabolic enzymes is a specific adaptation to an advanced state of cellular starvation. *eLife*, *3*, 6063. http://doi.org/10.7554/eLife.02409

Piper, P. W., Harris, N. L., & MacLean, M. (2006). Preadaptation to efficient respiratory maintenance is essential both for maximal longevity and the retention of replicative potential in chronologically ageing yeast. *Mechanisms of Ageing and Development*, *127*(9), 733–740. http://doi.org/10.1016/j.mad.2006.05.004

Pluskal, T., Hayashi, T., Saitoh, S., Fujisawa, A., & Yanagida, M. (2011). Specific biomarkers for stochastic division patterns and starvation-induced quiescence under limited glucose levels in fission yeast. *The FEBS Journal*, *278*(8), 1299–1315. http://doi.org/10.1111/j.1742-4658.2011.08050.x

Riedl, J., Crevenna, A. H., Kessenbrock, K., Yu, J. H., Neukirchen, D., Bista, M., et al. (2008). Lifeact: a versatile marker to visualize F-actin. *Nature Methods*, *5*(7), 605–607. http://doi.org/10.1038/nmeth.1220

Rojas, E. R., & Huang, K. C. (2017). Regulation of microbial growth by turgor pressure. *Current Opinion in Microbiology*, *42*, 62–70. http://doi.org/10.1016/j.mib.2017.10.015

Roux, A. E., Leroux, A., Alaamery, M. A., Hoffman, C. S., Chartrand, P., Ferbeyre, G., & Rokeach, L. A. (2009). Pro-aging effects of glucose signaling through a G protein-coupled glucose receptor in fission yeast. *PLoS Genetics*, *5*(3), e1000408. http://doi.org/10.1371/journal.pgen.1000408

Roux, A. E., Quissac, A., Chartrand, P., Ferbeyre, G., & Rokeach, L. A. (2006). Regulation of chronological aging in Schizosaccharomyces pombe by the protein kinases Pka1 and Sck2. *Aging Cell*, *5*(4), 345–357. http://doi.org/10.1111/j.1474-9726.2006.00225.x

Röthlisberger, S., Jourdain, I., Johnson, C., Takegawa, K., & Hyams, J. S. (2009). The dynamin-related protein Vps1 regulates vacuole fission, fusion and tubulation in the fission yeast, Schizosaccharomyces pombe. *Fungal Genetics and Biology : FG & B*, *46*(12), 927–935. http://doi.org/10.1016/j.fgb.2009.07.008

Rueden, C. T., Schindelin, J., Hiner, M. C., DeZonia, B. E., Walter, A. E., Arena, E. T., & Eliceiri, K. W. (2017). ImageJ2: ImageJ for the next generation of scientific image data. *BMC Bioinformatics*, *18*(1), 529. http://doi.org/10.1186/s12859-017-1934-z

Russo, G. J., Louie, K., Wellington, A., Macleod, G. T., Hu, F., Panchumarthi, S., & Zinsmaier, K. E. (2009). Drosophila Miro is required for both anterograde and retrograde axonal mitochondrial transport. *The Journal of Neuroscience : the Official Journal of the Society for Neuroscience*, *29*(17), 5443–5455. http://doi.org/10.1523/JNEUROSCI.5417-08.2009

Saarikangas, J., & Barral, Y. (2011). The emerging functions of septins in metazoans. *EMBO Reports*, *12*(11), 1118–1126. http://doi.org/10.1038/embor.2011.193

Sagot, I., Pinson, B., Salin, B., & Daignan-Fornier, B. (2006). Actin bodies in yeast quiescent cells: an immediately available actin reserve? *Molecular Biology of the Cell*, *17*(11), 4645–4655. http://doi.org/10.1091/mbc.E06-04-0282

Sawin, K. E., & Nurse, P. (1997). Photoactivation of green fluorescent protein. *Current Biology : CB*, *7*(10), R606–7.

Saxton, M. J., & Jacobson, K. (1997). Single-particle tracking: applications to membrane dynamics. *Annual Review of Biophysics and Biomolecular Structure*, *26*(1), 373–399. http://doi.org/10.1146/annurev.biophys.26.1.373

Sbalzarini, I. F., & Koumoutsakos, P. (2005). Feature point tracking and trajectory analysis for video imaging in cell biology. *Journal of Structural Biology*, *151*(2), 182–195. http://doi.org/10.1016/j.jsb.2005.06.002

Schindelin, J., Arganda-Carreras, I., Frise, E., Kaynig, V., Longair, M., Pietzsch, T., et al. (2012). Fiji: an open-source platform for biological-image analysis. *Nature Methods*, *9*(7), 676–682. http://doi.org/10.1038/nmeth.2019

Schuldiner, M., & Bohnert, M. (2017). A different kind of love - lipid droplet contact sites. *Biochimica Et Biophysica Acta*, *1862*(10 Pt B), 1188–1196. http://doi.org/10.1016/j.bbalip.2017.06.005

Sigova, A., Rhind, N., & Zamore, P. D. (2004). A single Argonaute protein mediates both transcriptional and posttranscriptional silencing in Schizosaccharomyces pombe. *Genes & Development*, *18*(19), 2359–2367. http://doi.org/10.1101/gad.1218004

Smirnova, E., Griparic, L., Shurland, D. L., & van der Bliek, A. M. (2001). Dynamin-related protein Drp1 is required for mitochondrial division in mammalian cells. *Molecular Biology of the Cell*, *12*(8), 2245–2256.

Sommer, C., Straehle, C., Köthe, U., & Hamprecht, F. A. (2011). **Ilastik: Interactive learning and segmentation toolkit**. Presented at the Biomedical Imaging.

Soto, T., Fernandez, J., Vicente-Soler, J., Cansado, J., & Gacto, M. (1999). Accumulation of trehalose by overexpression of tps1, coding for trehalose-6-phosphate synthase, causes increased resistance to multiple stresses in the fission yeast schizosaccharomyces pombe. *Applied and Environmental Microbiology*, *65*(5), 2020–2024.

Spector, I., Shochet, N. R., Kashman, Y., & Groweiss, A. (1983). Latrunculins: novel marine toxins that disrupt microfilament organization in cultured cells. *Science (New York, N.Y.)*, *219*(4584), 493–495.

Stavru, F., Palmer, A. E., Wang, C., Youle, R. J., & Cossart, P. (2013). Atypical mitochondrial fission upon bacterial infection. *Proceedings of the National Academy of Sciences of the United States of America*, *110*(40), 16003–16008. http://doi.org/10.1073/pnas.1315784110

Su, S. S., Tanaka, Y., Samejima, I., Tanaka, K., & Yanagida, M. (1996). A nitrogen starvation-induced dormant G0 state in fission yeast: the establishment from uncommitted G1 state and its delay for return to proliferation. *Journal of Cell Science*, *109 (Pt 6)*, 1347–1357.

Sun, W. Q., & Leopold, A. C. (1997). Cytoplasmic Vitrification and Survival of Anhydrobiotic Organisms. *Comparative Biochemistry and Physiology Part a Physiology*, *117*(3), 327–333. http://doi.org/https://doi.org/10.1016/S0300-9629(96)00271-X

Takeshige, K., Baba, M., Tsuboi, S., Noda, T., & Ohsumi, Y. (1992). Autophagy in yeast demonstrated with proteinase-deficient mutants and conditions for its induction. *The Journal of Cell Biology*, *119*(2), 301–311.

Tasto, J. J., Morrell, J. L., & Gould, K. L. (2003). An anillin homologue, Mid2p, acts during fission yeast cytokinesis to organize the septin ring and promote cell separation. *The Journal of Cell Biology*, *160*(7), 1093–1103. http://doi.org/10.1083/jcb.200211126

Thazar-Poulot, N., Miquel, M., Fobis-Loisy, I., & Gaude, T. (2015). Peroxisome extensions deliver the Arabidopsis SDP1 lipase to oil bodies. *Proceedings of the National Academy of Sciences of the United States of America*, *112*(13), 4158–4163. http://doi.org/10.1073/pnas.1403322112

Thévenaz, P., Ruttimann, U. E., & Unser, M. (1998). A pyramid approach to subpixel registration based on intensity. *IEEE Transactions on Image Processing : a Publication of the IEEE Signal Processing Society*, *7*(1), 27–41. http://doi.org/10.1109/83.650848

Tinevez, J.-Y., Perry, N., Schindelin, J., Hoopes, G. M., Reynolds, G. D., Laplantine, E., et al. (2017). TrackMate: An open and extensible platform for single-particle tracking. *Methods (San Diego, Calif.)*, *115*, 80–90. http://doi.org/10.1016/j.ymeth.2016.09.016

Tolić-Nørrelykke, I. M., Munteanu, E. L., Thon, G., Oddershede, L., & Berg-Sørensen, K. (2004). Anomalous diffusion in living yeast cells. *Physical Review Letters*, *93*(7), 078102. http://doi.org/10.1103/PhysRevLett.93.078102

Toretsky, J. A., & Wright, P. E. (2014). Assemblages: functional units formed by cellular phase separation. *The Journal of Cell Biology*, *206*(5), 579–588. http://doi.org/10.1083/jcb.201404124

Tran, P. T., Marsh, L., Doye, V., Inoué, S., & Chang, F. (2001). A mechanism for nuclear positioning in fission yeast based on microtubule pushing. *The Journal of Cell Biology*, *153*(2), 397–411.

van Dijken, J. P., Weusthuis, R. A., & Pronk, J. T. (1993). Kinetics of growth and sugar consumption in yeasts. *Antonie Van Leeuwenhoek*, *63*(3-4), 343–352.

Vasicova, P., Lejskova, R., Malcova, I., & Hasek, J. (2015). The stationary phase cells of S. cerevisiae display dynamic actin filaments required for processes extending chronological life span. *Molecular and Cellular Biology*, *35*(22), MCB.00811–15–3908. http://doi.org/10.1128/MCB.00811-15

Vejrup-Hansen, R., Fleck, O., Landvad, K., Fahnøe, U., Broendum, S. S., Schreurs, A.-S., et al. (2014). Spd2 assists Spd1 in the modulation of ribonucleotide reductase architecture but does not regulate deoxynucleotide pools. *Journal of Cell Science*, *127*(Pt 11), 2460–2470. http://doi.org/10.1242/jcs.139816

Visser, W., Scheffers, W. A., Batenburg-van der Vegte, W. H., & van Dijken, J. P. (1990). Oxygen requirements of yeasts. *Applied and Environmental Microbiology*, *56*(12), 3785–3792.

Vjestica, A., Tang, X.-Z., & Oliferenko, S. (2008). The actomyosin ring recruits early secretory compartments to the division site in fission yeast. *Molecular Biology of the Cell*, *19*(3), 1125–1138. http://doi.org/10.1091/mbc.E07-07-0663

Vreeland, R. H., Rosenzweig, W. D., & Powers, D. W. (2000). Isolation of a 250 million-year-old halotolerant bacterium from a primary salt crystal. *Nature*, *407*(6806), 897–900. http://doi.org/10.1038/35038060

Walther, T. C., & Farese, R. V. (2012). Lipid droplets and cellular lipid metabolism. *Annual Review of Biochemistry*, *81*(1), 687–714. http://doi.org/10.1146/annurev-biochem-061009-102430

Wang, H., Tang, X., Liu, J., Trautmann, S., Balasundaram, D., McCollum, D., & Balasubramanian, M. K. (2002). The multiprotein exocyst complex is essential for cell separation in Schizosaccharomyces pombe. *Molecular Biology of the Cell*, *13*(2), 515–529. http://doi.org/10.1091/mbc.01-11-0542

Watanabe, T., Miyashita, K., Saito, T. T., Yoneki, T., Kakihara, Y., Nabeshima, K., et al. (2001). Comprehensive isolation of meiosis-specific genes identifies novel proteins and unusual non-coding transcripts in Schizosaccharomyces pombe. *Nucleic Acids Research*, *29*(11), 2327–2337.

Weber, S. C., & Brangwynne, C. P. (2015). Inverse size scaling of the nucleolus by a concentration-dependent phase transition. *Current Biology : CB*, *25*(5), 641–646. http://doi.org/10.1016/j.cub.2015.01.012

Wei, W., Nurse, P., & Broek, D. (1993). Yeast cells can enter a quiescent state through G1, S, G2, or M phase of the cell cycle. *Cancer Research*, *53*(8), 1867–1870.

Weisman, R., Roitburg, I., Schonbrun, M., Harari, R., & Kupiec, M. (2007). Opposite effects of tor1 and tor2 on nitrogen starvation responses in fission yeast. *Genetics*, *175*(3), 1153–1162. http://doi.org/10.1534/genetics.106.064170

Weiss, M., Elsner, M., Kartberg, F., & Nilsson, T. (2004). Anomalous subdiffusion is a measure for cytoplasmic crowding in living cells. *Biophysical Journal*, *87*(5), 3518–3524. http://doi.org/10.1529/biophysj.104.044263

Welte, M. A. (2015). Expanding roles for lipid droplets. *Current Biology : CB*, *25*(11), R470–81. http://doi.org/10.1016/j.cub.2015.04.004

Wen, X., & Klionsky, D. J. (2016). An overview of macroautophagy in yeast. *Journal of Molecular Biology*, *428*(9), 1681–1699. http://doi.org/10.1016/j.jmb.2016.02.021

Wilfling, F., Thiam, A. R., Olarte, M.-J., Wang, J., Beck, R., Gould, T. J., et al. (2014). Arf1/COPI machinery acts directly on lipid droplets and enables their connection to the ER for protein targeting. *eLife*, *3*, e01607. http://doi.org/10.7554/eLife.01607

Wirawan, E., Vanden Berghe, T., Lippens, S., Agostinis, P., & Vandenabeele, P. (2012). Autophagy: for better or for worse. *Cell Research*, *22*(1), 43–61. http://doi.org/10.1038/cr.2011.152

Wirtz, D. (2009). Particle-tracking microrheology of living cells: principles and applications. *Annual Review of Biophysics*, *38*(1), 301–326. http://doi.org/10.1146/annurev.biophys.050708.133724

Wood, V., Gwilliam, R., Rajandream, M.-A., Lyne, M., Lyne, R., Stewart, A., et al. (2002). The genome sequence of Schizosaccharomyces pombe. *Nature*, *415*(6874), 871–880. http://doi.org/10.1038/nature724

Wright, J. C. (1989). Desiccation tolerance and water-retentive mechanisms in tardigrades. *Journal of Experimental Biology*.

Wu, J.-Q., Ye, Y., Wang, N., Pollard, T. D., & Pringle, J. R. (2010). Cooperation between the septins and the actomyosin ring and role of a cell-integrity pathway during cell division in fission yeast. *Genetics*, *186*(3), 897–915. http://doi.org/10.1534/genetics.110.119842

Wu, S., Zhou, F., Zhang, Z., & Xing, D. (2011). Mitochondrial oxidative stress causes mitochondrial fragmentation via differential modulation of mitochondrial fission-fusion proteins. *The FEBS Journal*, *278*(6), 941–954. http://doi.org/10.1111/j.1742-4658.2011.08010.x

Yaffe, M. P., Harata, D., Verde, F., Eddison, M., Toda, T., & Nurse, P. (1996). Microtubules mediate mitochondrial distribution in fission yeast. *Proceedings of the National Academy of Sciences of the United States of America*, *93*(21), 11664–11668.

Yaffe, M. P., Stuurman, N., & Vale, R. D. (2003). Mitochondrial positioning in fission yeast is driven by association with dynamic microtubules and mitotic spindle poles. *Proceedings of the National Academy of Sciences of the United States of America*, *100*(20), 11424–11428. http://doi.org/10.1073/pnas.1534703100

Yanagida, M. (2009). Cellular quiescence: are controlling genes conserved? *Trends in Cell Biology*, *19*(12), 705–715. http://doi.org/10.1016/j.tcb.2009.09.006

Yang, Z., & Klionsky, D. J. (2010). Eaten alive: a history of macroautophagy. *Nature Cell Biology*, *12*(9), 814–822. http://doi.org/10.1038/ncb0910-814

Youle, R. J., & Karbowski, M. (2005). Mitochondrial fission in apoptosis. *Nature Reviews. Molecular Cell Biology*, *6*(8), 657–663. http://doi.org/10.1038/nrm1697

Zhang, D., Vjestica, A., & Oliferenko, S. (2010). The cortical ER network limits the permissive zone for actomyosin ring assembly. *Current Biology : CB*, *20*(11), 1029–1034. http://doi.org/10.1016/j.cub.2010.04.017

Zhang, D., Vjestica, A., & Oliferenko, S. (2012). Plasma membrane tethering of the cortical ER necessitates its finely reticulated architecture. *Current Biology : CB*, *22*(21), 2048–2052. http://doi.org/10.1016/j.cub.2012.08.047

Zhao, D., Liu, X.-M., Yu, Z.-Q., Sun, L.-L., Xiong, X., Dong, M.-Q., & Du, L.-L. (2016). Atg20- and Atg24-family proteins promote organelle autophagy in fission yeast. *Journal of Cell Science*, *129*(22), 4289–4304. http://doi.org/10.1242/jcs.194373

Zhao, R.-K., Lukacs, A., Haigney, A., Brust, R., Greetham, G. M., Towrie, M., et al. (2011). Ultrafast transient mid IR to visible spectroscopy of fully reduced flavins. *Physical Chemistry Chemical Physics : PCCP*, *13*(39), 17642–17648. http://doi.org/10.1039/c1cp22097g

Zuin, A., Carmona, M., Morales-Ivorra, I., Gabrielli, N., Vivancos, A. P., Ayté, J., & Hidalgo, E. (2010). Lifespan extension by calorie restriction relies on the Sty1 MAP kinase stress pathway. *The EMBO Journal*, *29*(5), 981–991. http://doi.org/10.1038/emboj.2009.407

Zuin, A., Gabrielli, N., Calvo, I. A., García-Santamarina, S., Hoe, K.-L., Kim, D. U., et al. (2008). Mitochondrial dysfunction increases oxidative stress and decreases chronological life span in fission yeast. *PloS One*, *3*(7), e2842. http://doi.org/10.1371/journal.pone.0002842

9 Appendix

9.1 Strains used in this thesis

Table 1. List of *S. pombe* strains used in this thesis

Strains	Genotype	Source
DB404	h- Sec63-GFP::KanMX6 ura4-D18, leu-32	(Vjestica, Tang, & Oliferenko, 2008)
DB558	h- wild-type	Laboratory collection
DB933	h- nup85-GFP::kanMX6 ade6-M216, leu1	This study
DB2003	h+ cnx1-linkerGFP::kanMX6 ura4-D18 leu1-32 ade6-M216	This study
DB2057	h- SV40p-GFP-atb2::LEU2 leu1-32	(Pardo & Nurse, 2005)
DB2400	h+ anp1-GFP::ura4+ ade6-216 ura4-D18 leu1-32	(Vjestica et al., 2008)
DB2401	h+ sec72-GFP::ura4+ ade6-216 ura4-D18 leu1-32	(Vjestica et al., 2008)
DB2402	h+ anp1- mCherry::ura4+ ade6-216 leu1-32 ura4-D18	(Vjestica et al., 2008)
DB2403	h+ uch2-mCherry::ura4+ ade6-216 leu1-32 ura4-D18	(Vjestica et al., 2008)
DB2404	h- ost1::GFP-ura4+ ura4-D18 leu1-32	(Vjestica et al., 2008)
DB2405	h+ ost1-mCherry::ura4+ ade6-210 leu1-32 ura4-D18	(Vjestica et al., 2008)
DB3287	h- spn1Δ::kanMX6	(J.-Q. Wu, Ye, Wang, Pollard, & Pringle, 2010)
DB3293	h- spn2Δ::ura4+ ura4D18	(An et al., 2004)
DB3297	h+ spn2-GFP::kanMX6 *	(An et al., 2004)
DB3310	h+ spn3-GFP::kanMX6 *	(An et al., 2004)
DB3324	h- spn4-Δ1::kanMX6 *	(J.-Q. Wu et al., 2010)
DB3326	h+ spn5-GFP::kanMX6	This study
DB3340	h+ spn6-GFP::kanMX6	This study
DB3410	h- leu1-32::pAct1-Lifeact-GFP::leu1+ *	(J. Huang et al., 2012)
DB3422	h- spn1-GFP::kanMX6 *	(J.-Q. Wu et al., 2010)
DB3426	h+ spn3-Δ::ura4+ ura4-D18	(An et al., 2004)
DB3455	h+ spn7-GFP::kanMX6 *	(Onishi et al., 2010)
DB3587	h- spn4-tagRFP::kanMX6	This study
DB3623	h- Pbip1-GFP-AHDL::leu1+ ura4-D18 leu1-32 ade6	(D. Zhang, Vjestica, & Oliferenko, 2010)
DB3624	h- Pbip1-mCherry-AHDL::leu1+	(D. Zhang et al., 2010)
DB3726	h- cox4-GFP::LEU2 leu1-32 *	(Fu et al., 2011)
DB3856	h- hsp104-mCherry::kanMX	(Coelho et al., 2013)
DB4192	h- GMA12-GFP::ura4+ ura4-D18 *	(H. Wang et al., 2002)
DB4672	h+ Pnmt1-Tts-2TM(1-83aa)-linker-mCherry::leu+	(D. Zhang, Vjestica, & Oliferenko, 2012)
DB5013	h- atg8Δ::kanMX *	Bioneer M-4030H-U5, (Kim et al., 2010)
DB5018	h- atg1Δ::kanMX *	Bioneer M-4030H-U5, (Kim et al., 2010)
DB5160	h- cts1-GFP::kanMX	This study

DB5162	h- pre6-mGFP::kanMX6	This study
DB5209	h+ suc22-GFP	(Vejrup-Hansen et al., 2014)
DB5310	h- gln1-mCherry::natR	(Coelho, Lade, Alberti, Gross, & Tolić, 2014)
DB5315	h+ dis2-NEGFP::ura4 ura4-D18*	(Alvarez-Tabarés, Grallert, Ortiz, & Hagan, 2007)
DB5320	h+ adh1-GFP::kanMX*	(Sigova, Rhind, & Zamore, 2004)
DB5380	h+ cts1-mCherry::kanMX*	(Coelho et al., 2014)
DB5381	h- hsp104-GFP::kanMX*	(Coelho et al., 2013)
DB5470	h- tif221-GFP::kanMX	This study
DB5730	h? nmt1:GFP-spac11D3.06::kanMX gln1-mCherry::natR	This study
	* the auxotrophic alleles were crossed out from the original strain	

9.2 Primers used in this thesis

Table 2. List of primers used in this thesis

DB3340	DPE872	CTGAATATCACGAAAGGATCCGTGCTTTGGAGACCCAAATTGAAAGTT TGAAAAGTTACAAGGGCCGCGGTCATAAAAAAATCCTTGGAGCTCCTT CAGGA
	DPE873	AATTGCAAATTTAGTAAGAAAAAGCCATCAGATGAGCAAATAAAAGG AGATGGAAAAGTTAAAAGTTTGACTTGAGACTT GAATTCGAGCTCGTTTAAAC
DB933	DPE 275	GTCAACTGTAAAGGACCAGCAGCTTTTACTATCCATTCATGAGCGTCT TTCTTCTGCGATATCATGGTATTTTCTTCACTTAAAAAAAATCCTTGGA GCTCCTTCAGGA
	DPE 274	GTATCTTAATAAAAACATGTATGAAGCTTCTATGTTACAGAAAGATTA AAATGTCAAGTAACAGAAATAGCCTAATTTAAATCCCgaattcgagctcgtttaa ac
DB2003	DPE739	TAAGCAAGAGACTGAGACTGAGAAGATAGACGTTTCTTACGCTCCCG AAACTGAATCACCAACTGCGAAGAATGAAGACATCCTTGGAGCTCCTT CAGGA
	DPE740	GATAGTACTACCCACGATTTATAAATTCATAGTCTATTTATTGATATTA CTCATAATAAGAACTAGAGAAAACAGAATTCGAGCTCGTTTAAAC
DB5160	DPE1495	ATTTTAACGCTGAATCTGCCTTAGCTGACATGAATGACTCTGTTGAAG TTACTGAAGAAGCCACTGTCGTCACCATCAGT ATCCTTGGAGCTCCTTCAGG
	DPE1496	CACCCCAGAACCCAATTTTTCCTATAGATAAAGAAAAACACACCAAC AAACACACATTATTTCCTAATTCCCGGAATCCC GAATTCGAGCTCGTTTAAAC
DB5162	DPE1450	AAGATGAGAAAGAAGCTGAAGCTGCTCGTAAAAAGAGTGGCCGTTCT GCCCCTGGAGTCTCTACAACTTCTACGATTCAA ATCCTTGGAGCTCCTTCAGG
	DPE1451	CAAAAGGGAAAAGACATATGAACCTTATAAACAAGAAATTCTTAAGT CGGTTTGCATGTAATGAAATAAAAGAGGTATCA GAATTCGAGCTCGTTTAAAC
DB5470	DPE1535	TTGTCTCAGGTCTCATTACCGATTTAGGGATCATTGATTCGAAGAGTG GGGTAAGCGAAGAGCTAATTAAATTGTATCTT ATCCTTGGAGCTCCTTCAGG
	DPE1536	AAGACTTATGAGAAATTTAAGTCAACTCAAAGTACAATCTATTCATAT TTTATTTTTAAGATCAGGAGAATCTGATTG GAATTCGAGCTCGTTTAAACTG
DB5730	DPE1473	GGTTCCATCCGTTCAATCAATATGATAAAAGCTTAGTAAACTTTTATT AAAGGAAAATTTGAACCTTCGGTGAACAGACAgaattcgagctcgtttaaac
	DPE1474	GAGTTTTGCAAGGCATATCCAAGGATTACCGGAGCTGAATTTATCAAA AGGTATTTCACCTCTGTAAGTGGTCTACCCATaattaaccccgcaggtccac

9.3 Results from genome-wide screen for the identification of genes required for CF

9.3.1 CF index and cell numbers of all deletion strains from the two experimental repeats

Table 3. CF index and cell numbers of all deletion strains used in screen for the identification of genes required for CF

Systematic ID	Gene name	Gene description	CF index screen 1	Cell number	CF index screen 2	Cell number
SPAC27D7.14c	tpr1	RNA polymerase II associated Paf1 complex subunit Tpr1	NaN	0	0.000	1
SPAC2E1P3.05c		fungal cellulose binding domain protein	NaN	0	0.000	22
SPAC3F10.04	gsa1	glutathione synthetase large subunit Gsa1	0.000	3	NaN	0
SPBC21C3.13	rps1901	40S ribosomal protein S19	NaN	0	0.000	3
SPCC338.05c	mms2	ubiquitin conjugating enzyme Mms2	0.000	1	NaN	0
SPAC22F8.04		triose phosphate transporter	0.041	253	0.190	344
SPBC1921.06c	pvg3	beta-1,3-galactosyltransferase	0.135	312	0.260	330
SPAC17A5.04c	mde10	spore wall assembly peptidase Mde10	0.110	303	0.356	175
SPAC22F8.02c	pvg5	PvGal biosynthesis protein Pvg5	-0.002	268	0.480	332
SPAC7D4.04	taf1	Taz1 interacting factor 1	0.567	175	0.066	319
SPBC36.04	cys11	cysteine synthase	0.321	1	NaN	0
SPBP8B7.28c		sequence orphan	0.186	299	0.559	353
SPCC285.09c	cgs2	cAMP-specific phosphodiesterase Cgs2	0.774	1	0.001	106
SPAC29A4.18	prw1	Clr6 histone deacetylase complex subunit Prw1	0.000	3	0.803	7
SPAC144.02		transcription factor	0.000	3	0.804	292
SPCC1739.12	ppe1	serine/threonine protein phosphatase Ppe1	0.823	338	0.000	1
SPAC1093.01		PPR repeat protein	0.000	7	0.869	1
SPBC216.03		conserved fungal protein	0.000	1	0.877	374
SPAC13G6.10c		O-glucosyl hydrolase	0.900	267	0.000	1
SPAC6B12.08	mug185	DNAJ domain protein Jjj family	0.000	2	0.910	3
SPBCPT2R1.08c	tlh2	RecQ type DNA helicase Tlh1	0.000	7	0.911	296
SPAC12B10.06c		DUF339 family protein	0.000	1	0.911	12
SPAPB1E7.02c	mcl1	DNA polymerase alpha accessory factor Mcl1	0.000	12	0.912	168
SPAC22F8.11	plc1	phosphoinositide phospholipase C Plc1	0.662	325	0.256	400
SPCC23B6.04c		sec14 cytosolic factor family	0.000	1	0.928	204
SPCC16C4.17	mug123	meiotically upregulated gene Mug123	0.929	3	0.000	11
SPBC1604.20c	tea2	kinesin-like protein Tea2	0.000	12	0.936	450
SPBC839.17c	fkh1	FKBP-type peptidyl-prolyl cis-trans isomerase Fkh1	0.000	6	0.938	350
SPBC27B12.09c		FAD transporter	0.000	1	0.948	9
SPBC4C3.12	sep01	fork head transcription factor Sep1	0.964	21	0.000	36
SPBC1105.02c	lys4	homocitrate synthase	-0.020	11	0.988	2
SPAP8A3.14c		mitochondrial inner membrane protein	0.975	2	0.000	3
SPAC343.15	tit1	tRNA isopentenyltransferase	0.976	2	0.000	14
SPAC1805.05	cki3	serine/threonine protein kinase Cki3	0.000	7	0.979	339
SPBC428.02c	eca39	branched chain amino acid aminotransferase Eca49	0.980	1	0.000	1
SPBC215.01		GTPase activating protein	0.970	232	0.020	205
SPAC3A11.04		siepin homolog	0.561	240	0.491	269
SPBC543.07	pek1	MAP kinase kinase Pek1	0.403	218	0.660	333
SPAC2F7.17		peptide chain release factor	0.888	175	0.247	103
SPAC13G6.15c		calcipressin	0.575	103	0.566	176
SPBC3B9.06c	apg3	autophagy associated protein Apg3	NaN	0	0.575	296
SPBC21C3.03		ABC1 kinase family protein	0.412	290	0.741	260
SPAC23H4.12	alp13	Clr6 histone deacetylase complex subunit Alp13	0.473	2	0.683	198
SPAC25H1.03	mug66	meiotically upregulated gene Mug66	0.809	236	0.348	223
SPAC824.03c		conserved fungal protein	0.749	225	0.412	274
SPCC1682.11c		DUF580 family protein	0.458	222	0.717	214
SPCC895.06		RNA polymerase II elongator complex subunit Elp2	0.211	5	0.971	379
SPBC6B1.05c		ubiquitin-like conjugating enzyme	0.500	221	0.693	286
SPAC4F10.13c	mpd2	GYF domain	NaN	0	0.597	194
SPAC3G9.08	png1	ING family homolog Png1	0.439	212	0.765	289
SPBC18H10.19		human UVRAG (UV radiation resistance) homolog	0.477	338	0.741	227

Systematic ID	Gene name	Gene description	CF index screen 1	Cell number	CF index screen 2	Cell number
SPBC3B9.11c	ctf1	mRNA cleavage and polyadenylation specificity factor complex subunit Ctf1	0.535	392	0.728	295
SPBC56F2.05c		transcription factor	0.477	218	0.799	233
SPCC63.08c	ppk36	serine/threonine protein kinase Ppk36	0.737	232	0.551	290
SPBC21D10.09c		ubiquitin-protein ligase E3	0.921	274	0.370	127
SPBC1711.13	his2	histidinol dehydrogenase His2	NaN	0	0.648	43
SPAC25B8.06c		serine-tRNA ligase	0.806	183	0.491	218
SPAC13D6.02c	byr3	zinc finger protein Byr3	0.727	226	0.579	325
SPAC8F11.10c	pvg1	pyruvyltransferase	0.460	330	0.848	298
SPAC24B11.06c	sty1	MAP kinase Sty1	0.661	247	NaN	0
SPCC736.08	cbf11	transcription factor	0.641	285	0.681	152
SPCC162.05	coq3	hexaprenyldihydroxybenzoate methyltransferase	0.661	231	NaN	0
SPAC25A8.02		sequence orphan	0.647	317	0.684	242
SPAC630.13c	tsc2	tuberin	NaN	0	0.667	312
SPBC405.05		sequence orphan	0.667	195	0.671	343
SPAC458.06		phosphoinositide binding protein	0.675	238	0.670	287
SPAC1A6.10		Moeb/ThiF domain	0.491	337	0.855	308
SPAC22H12.05c		fasciclin domain protein	0.406	357	0.946	402
SPCC1919.04		sequence orphan	0.527	308	0.838	425
SPAC11G7.02	pub1	ubiquitin-protein ligase E3	0.472	84	0.893	185
SPCC320.12		mitochondrial inner membrane peptidase Atp23	0.512	352	0.857	530
SPAC227.04		autophagy C terminal domain family protein	0.602	301	0.775	365
SPBC18H10.14	rps1601	40S ribosomal protein S16	0.529	271	0.854	192
SPAC1A6.06c	meu31	sequence orphan	0.600	416	0.784	399
SPAC4F10.14c	btf3	nascent polypeptide-associated complex subunit	0.563	397	0.838	368
SPBC83.18c		C2 domain protein	0.548	231	0.857	217
SPCC191.01		sequence orphan	NaN	0	0.705	4
SPBP4H10.04	ppb1	calcineurin catalytic subunit Ppb1	0.558	285	0.852	388
SPAC1952.05	gcn5	histone acetyltransferase Gcn5	0.871	281	0.540	286
SPBC839.05c	rps1701	40S ribosomal protein S17	0.521	175	0.891	208
SPBC31E1.01c	atg2	autophagy associated protein Mug36	0.679	291	0.736	251
SPCC1259.07		transcriptional regulatory protein Rxt3	0.534	3	0.883	205
SPAC23G3.02c	sib1	ferrichrome synthetase Sib1	0.720	256	0.697	312
SPAC1F5.10		ATP-dependent RNA helicase, eIF4A related	0.618	212	0.803	188
SPBC365.10		actin-like protein Arp5	NaN	0	0.711	34
SPBC1718.01	pop1	F-box/WD repeat protein Pop1	0.714	213	0.710	217
SPAC4F10.15c	wsp1	WASp homolog	0.710	291	0.715	197
SPCC16C4.10		6-phosphogluconolactonase	0.753	227	0.673	239
SPCC790.03		protease	0.484	32	0.947	44
SPAC19E9.01c	nup40	nucleoporin Nup40	0.605	376	0.828	370
SPAC13G7.09c		sequence orphan	0.499	279	0.939	264
SPAC1687.10	mcp1	sequence orphan	0.598	379	0.841	371
SPAC1834.07	klp3	kinesin-like protein Klp3	0.637	353	0.804	331
SPBC1105.14	rsv2	transcription factor Rsv2	0.747	434	0.695	268
SPAC57A7.08	pzh1	serine/threonine protein phosphatase Pzh1	0.675	180	0.770	175
SPCC794.12c	mae2	malic enzyme	0.567	168	0.882	219
SPCC13B11.04c		glutathione-dependent formaldehyde dehydrogenase	0.629	309	0.820	328
SPBC30D10.09c		HVA22/TB2/DP1 family protein	0.733	237	0.716	258
SPBC1539.08	arf6	ADP-ribosylation factor, Arf family	0.603	112	0.848	288
SPAC1952.11c	ure2	urease	0.605	353	0.846	265
SPBC25B2.04c		mitochondrial ribosome assembly protein	0.668	42	0.790	207
SPAC19B12.08		peptidase family C54	0.924	363	0.537	344
SPACUNK4.09		conserved protein	0.681	276	0.783	242
SPAC56F8.06c	alg10	dolichyl-phosphate-glucose-glycolipid alpha-glucosyltransferase Alg10	0.714	202	0.751	179
SPBP8B7.24c	atg8	autophagy associated protein Atg8	0.587	410	0.878	475
SPAC27F1.03c	uch1	ubiquitin C-terminal hydrolase Uch1	0.745	263	0.721	287
SPAC1783.06c	atg12	autophagy associated protein Atg12	0.823	208	0.643	166
SPAC31A2.12		arrestin/PY protein 1	0.590	22	0.878	197
SPBC577.15c	sim3	NASP family histone binding protein	0.735	273	NaN	0
SPAC4F10.04		protein phosphatase type 2A, intrinsic regulator	0.813	58	0.659	130
SPAC2C4.15c	ubx2	UBX domain protein Ubx2	0.731	323	0.741	222
SPCC417.09c		transcription factor	0.704	264	0.771	355
SPBC2F12.03c		EST1 family protein	0.699	238	0.778	184
SPAC12G12.15	sif3	Sad1 interacting factor 3	0.761	301	0.719	247
SPAC30D11.14c		RNA-binding protein	0.579	335	0.901	252

Systematic ID	Gene name	Gene description	CF index screen 1	Cell number	CF index screen 2	Cell number
SPBC1778.04	spo6	Spo4-Spo6 kinase complex regulatory subunit Spo6	0.603	483	0.880	308
SPAPB17E12.02	yip12	SMN family protein Yip12	0.603	229	0.881	374
SPBP35G2.14		RNA-binding protein	0.607	256	0.880	225
SPAC513.04		sequence orphan	NaN	0	0.744	4
SPAC1D4.03c	aut12	autophagy associated protein Aut12	0.706	160	0.781	182
SPBC28E12.04		sequence orphan	0.740	200	0.749	152
SPAC23H4.09	cdb4	curved DNA-binding protein Cdb4	0.647	362	0.842	247
SPAC4D7.03	pop2	F-box/WD repeat protein Pop2	0.628	244	0.862	264
SPAC29B12.03	spd1	ribonucleotide reductase (RNR) inhibitor	0.745	298	0.746	305
SPAC4F8.11		WD repeat protein, human WDR24 family	0.707	319	0.787	302
SPAC17A5.14	exo2	exonuclease II Exo2	0.748	294	NaN	0
SPBC3E7.11c		DNAJ protein Caj1/Djp1-type	0.680	242	0.816	211
SPBC3B8.02	php5	CCAAT-binding factor complex subunit Php5	0.600	112	0.897	83
SPBC1604.12		sequence orphan	0.729	291	0.770	294
SPBP4H10.07		ubiquitin-protein ligase E3	0.627	274	0.873	394
SPAC3F10.09		1-(5-phosphoribosyl)-5-[(5-phosphoribosylamino) methylideneamino]imidazole-4-carboxamide isomerase	0.727	217	0.773	217
SPAC4C5.01		haloacid dehalogenase-like hydrolase	0.599	260	0.902	222
SPBC29A10.02	spo5	meiotic RNA-binding protein 1	0.757	299	0.746	475
SPAC869.11	cat1	amino acid permease, unknown 6	0.632	458	0.871	390
SPBP8B7.08c		leucine carboxyl methyltransferase	0.714	252	0.791	249
SPAC3A11.08	pcu4	cullin 4	0.770	82	0.739	127
SPAC56F8.12		conserved fungal protein	0.772	244	0.738	276
SPBC1861.05		carbohydrate kinase	0.600	275	0.915	216
SPBP26C9.03c	fet4	iron ion transporter	0.614	227	0.905	315
SPAC14C4.08	mug5	meiotically upregulated gene Mug5	0.649	217	0.870	195
SPAC1D4.01		sequence orphan	0.666	366	0.857	226
SPAPB2B4.06		conserved fungal protein	0.663	317	0.863	366
SPAC23H4.10c	thi4	thiamine-phosphate dipyrophosphorylase/hydroxyethylthiazole kinase	0.629	181	0.899	58
SPBC26H8.01	thi2	thiazole biosynthetic enzyme	0.655	87	0.873	368
SPBC16H5.12c		conserved fungal protein	0.620	163	0.910	330
SPBC6B1.03c		Pal1 family protein	0.559	192	0.971	209
SPBC1703.11		optic atrophy 3 family protein	0.873	229	0.657	217
SPAC56F8.04c	coq2	para-hydroxybenzoate--polyprenyltransferase Coq2	NaN	0	0.765	174
SPAC6G9.01c		conserved protein	0.716	194	0.817	218
SPAC4G8.05	ppk14	serine/threonine protein kinase Ppk14	0.711	277	0.822	262
SPBC83.03c	tas3	RITS complex subunit 3	0.595	334	0.940	297
SPAC4F8.08	mug114	sequence orphan	0.643	565	0.894	266
SPAC5D6.13		Golgi phosphoprotein 3 family	0.664	408	0.874	307
SPBC725.15	ura5	orotate phosphoribosyltransferase Ura5	0.572	236	0.967	233
SPAC31A2.13c	sft1	SNARE Sft1	0.697	176	0.843	203
SPBC16E9.19		sequence orphan	0.686	355	0.857	398
SPAC31G5.17c	rps1001	40S ribosomal protein S10	0.722	296	0.821	358
SPBP16F5.07	apm1	AP-1 adaptor complex subunit Apm1	0.635	2	0.910	296
SPAC16E8.12c		sequence orphan	0.724	338	0.822	305
SPBC26H8.05c		serine/threonine protein phosphatase	0.746	216	0.799	192
SPBC23E6.03c	nta1	protein N-terminal amidase Nta1	0.575	260	0.972	281
SPAC56E4.06c	ggt2	gamma-glutamyltranspeptidase Ggt2	0.764	190	0.782	160
SPBC17G9.10	rpl1102	60S ribosomal protein L11	0.708	391	0.839	325
SPAPB8E5.08		sequence orphan	0.578	286	0.973	278
SPBC23E6.01c		RNA-binding protein	0.701	233	0.851	259
SPAC23A1.19c		RecQ type DNA helicase Hrq1	0.675	239	0.878	140
SPAC10F6.13c		aspartate aminotransferase	0.667	52	0.885	162
SPAC1F7.12	yak3	aldose reductase YakC	0.688	383	0.870	259
SPCC576.01c		sulfonate dioxygenase	0.674	227	0.884	291
SPBC19G7.16	iws1	transcription elongation factor complex subunit Iws1	NaN	0	0.779	257
SPAC10F6.11c		kinase activator	0.776	260	0.782	266
SPBC557.02c		sequence orphan	NaN	0	0.780	2
SPBC1711.11		autophagy associated protein	0.636	325	0.925	247
SPAC167.06c	mug143	sequence orphan	0.839	258	0.723	299
SPAC1805.11c	rps2602	40S ribosomal protein S26	0.786	248	0.777	236
SPCC663.06c		short chain dehydrogenase	0.669	270	0.894	238
SPAC4A8.14	prs1	ribose-phosphate pyrophosphokinase Prs1	0.823	221	0.741	244
SPAC4H3.01		DNAJ domain protein Caj1/Djp1 type	0.747	323	0.817	271
SPAPB1E7.06c	eme1	Holliday junction resolvase subunit Eme1	0.911	274	0.653	175

Systematic ID	Gene name	Gene description	CF index screen 1	Cell number	CF index screen 2	Cell number
SPBC20F10.03		conserved eukaryotic protein	0.601	240	0.964	238
SPAC23H3.09c	gly1	threonine aldolase	0.704	224	0.861	2
SPAC27D7.08c		DUF890 family protein	0.711	306	0.854	171
SPAC3F10.16c		GTP binding protein, HSR1-related	0.699	5	0.867	128
SPAC12B10.03		WD repeat protein, human WDR20 family	0.614	211	0.952	220
SPAPB2B4.04c		P-type ATPase, calcium transporting Pmc1	0.721	196	0.850	226
SPAC1F8.05	isp3	sequence orphan	0.650	304	0.921	262
SPBC16A3.08c		nuclear telomere cap complex subunit	0.706	338	0.865	191
SPAC8C9.05		D-Tyr-tRNA deacylase	0.649	216	0.923	193
SPAC15A10.11	ubr11	N-end-recognizing protein	0.767	239	0.805	289
SPBC56F2.10c	alg5	dolichyl-phosphate beta-glucosyltransferase Alg5	0.730	229	0.843	220
SPAP7G5.03		conjugation protein	0.654	7	0.919	400
SPBC16H5.02	pfk1	6-phosphofructokinase	0.670	283	0.904	359
SPCP1E11.05c		sterol O-acyltransferase	0.750	406	0.825	378
SPBC19F8.03c		clathrin binding protein	0.692	185	0.883	276
SPBC17G9.07	rps2402	40S ribosomal protein S24	0.690	186	0.887	235
SPBC4B4.12c		sequence orphan	0.641	223	0.937	330
SPAP8A3.04c	hsp9	heat shock protein Hsp9	0.748	286	0.830	245
SPAC589.07c		WD repeat protein Atg18	0.784	312	0.795	319
SPBC106.07c		N alpha-acetyltransferase Nat2	0.737	207	0.842	269
SPAC15A10.16	bud6	actin interacting protein 3 homolog Bud6	0.812	263	0.767	334
SPAC664.04c	rps1602	40S ribosomal protein S16	0.777	230	0.803	225
SPBP8B7.09c		karyopherin	0.757	239	0.823	253
SPAC15A10.08	ain1	alpha-actinin	0.742	327	0.839	282
SPAC6G10.06		amino acid oxidase	0.750	339	0.831	232
SPAC4G8.04		GTPase activating protein	0.800	312	0.782	273
SPCC18.06c	caf1	CCR4-Not complex subunit Caf1	0.791	184	NaN	0
SPAPB1A10.14		F-box protein, unnamed	0.663	305	0.920	362
SPBC36.11		sequence orphan	0.784	385	0.801	226
SPBC2A9.05c		DUF846 family protein	0.757	327	0.829	248
SPBC11C11.02	imp2	contractile ring protein Imp2	0.636	166	0.951	143
SPAC144.11	rps1102	40S ribosomal protein S11	0.709	270	0.878	278
SPAC1565.03		sequence orphan	0.684	252	0.904	210
SPBC646.06c	agn2	glucan endo-1,3-alpha-glucosidase Agn2	0.621	239	0.968	215
SPBC56F2.11	met6	homoserine O-acetyltransferase	0.930	1	0.660	3
SPBC215.10		haloacid dehalogenase-like hydrolase	0.715	287	0.875	264
SPBC19G7.10c		topoisomerase associated protein	0.695	134	0.897	165
SPAC17G8.08c		human TMEM165 homolog	0.818	176	0.774	280
SPBC25H2.15		programmed cell death protein homolog	0.703	1	0.890	2
SPAC5D6.10c	mug116	sequence orphan	0.737	368	0.857	269
SPBC651.11c	apm3	AP-3 adaptor complex subunit Apm3	0.778	142	0.816	164
SPBC776.09	ste13	ATP-dependent RNA helicase Ste13	0.797	315	NaN	0
SPAC4H3.07c		protein phosphatase Fmp31	0.705	270	0.889	238
SPAC186.01		DIPSY family	0.710	439	0.886	264
SPAC1A6.09c	lag1	sphingosine N-acyltransferase Lag1	0.700	242	0.895	118
SPAC227.17c		conserved protein (fungal and plant)	NaN	0	0.798	174
SPBC3H7.11		actin binding methyltransferase	0.794	260	0.803	260
SPBC2G2.02	syj1	inositol polyphosphate phosphatase	0.740	267	0.857	235
SPBC685.03		sequence orphan	0.810	238	0.787	257
SPCC550.03c		RNA helicase involved in mRNA catabolism	0.638	193	0.960	186
SPCC1322.12c	bub1	serine/threonine protein kinase Bub1	0.815	265	0.784	234
SPAC17A5.10		conserved fungal protein	0.640	100	0.960	294
SPAC25B8.19c		transcription factor	0.719	192	0.880	13
SPCC550.01c		CHCH domain protein	0.726	393	0.874	316
SPAPJ698.02c	rps002	40S ribosomal protein S0B	0.800	218	NaN	0
SPAC3H5.09c		conserved fungal protein	0.873	222	0.728	272
SPAC16A10.05c	dad1	DASH complex subunit Dad1	0.782	176	0.819	329
SPBC2D10.11c		nucleosome assembly protein Nap2	0.666	530	0.936	343
SPCC1753.03c	rec7	meiotic recombination protein Rec7	0.843	236	0.760	207
SPBC1D7.04	mlo3	RNA annealing factor Mlo3	0.709	45	0.893	1
SPAC6F6.03c		ribosome export GTPase	0.894	222	0.709	291
SPAC56E4.03		aromatic aminotransferase	0.778	171	0.824	169
SPAC2G11.03c	vps45	vacuolar sorting protein Vps 45	0.855	5	0.750	203
SPAC6B12.15	cpc2	RACK1 homologue Cpc2	0.789	194	0.817	210
SPBC25B2.10		Usp (universal stress protein) family protein	0.628	283	0.979	248
SPAC17H9.08		mitochondrial coenzyme A transporter	NaN	0	0.804	178
SPBC1773.09c	mug184	meiotically upregulated gene Mug184	0.671	423	0.937	309

Systematic ID	Gene name	Gene description	CF index screen 1	Cell number	CF index screen 2	Cell number
SPAC13G6.09		zf-MYND type	0.823	174	0.784	254
SPAC2H10.02c		26S proteasome regulator	0.724	516	0.884	340
SPAC31G5.03	rps1101	40S ribosomal protein S11	0.738	225	0.871	181
SPAC9.02c		N-acetyltransferase	0.691	253	0.919	303
SPBC13G1.10c	mug81	ATP-dependent RNA helicase Slh1	0.722	145	0.889	480
SPAC22F3.06c	lon1	Lon protease homolog Lon1	0.740	229	0.871	210
SPAC18B11.04	ncs1	related to neuronal calcium sensor Ncs1	0.678	275	0.933	227
SPAC22F3.11c	snu23	U4/U6 x U5 tri-snRNP complex subunit Snu23	0.828	186	0.784	269
SPBP16F5.04	ubc7	ubiquitin conjugating enzyme Ubc3	0.732	300	0.881	265
SPAC323.05c		S-adenosylmethionine-dependent methyltransferase	0.808	218	0.805	2
SPCC1393.03	rps1501	40S ribosomal protein S15	0.807	262	NaN	0
SPBC12D12.07c	trx2	mitochondrial thioredoxin Trx2	0.911	343	0.704	2
SPBPB7E8.02		conserved protein (fungal bacterial protazoan)	0.814	301	0.802	279
SPCC553.08c		GTPase Ria1	0.808	292	NaN	0
SPCC18B5.05c		phosphomethylpyrimidine kinase	0.697	317	0.920	243
SPCC14G10.03c	ump1	proteasome maturation factor Ump1	0.793	235	0.825	277
SPAC22F3.10c	gcs1	glutamate-cysteine ligase Gcs1	0.832	277	0.786	2
SPBP4H10.14c		sequence orphan	0.707	316	0.913	212
SPAC1486.10	thi1	transcription factor Thi1	0.781	11	0.838	21
SPCC645.08c	snd1	RNA-binding protein Snd1	0.736	357	0.884	263
SPAC1296.06		NADPH cytochrome reductase	NaN	0	0.811	222
SPCC417.02	dad5	DASH complex subunit Dad5	0.688	379	0.935	227
SPAC977.10	sod2	CPA1 sodium ion/proton antiporter	0.868	258	0.755	225
SPAC31A2.06		conserved fungal protein	0.812	5	NaN	0
SPBC26H8.12		cytochrome c heme lyase	0.640	56	0.985	1
SPCC548.05c		ubiquitin-protein ligase E3	0.850	346	0.775	279
SPCC1739.13	ssa2	heat shock protein Ssa2	0.813	3	NaN	0
SPBC2G2.01c	liz1	pantothenate transporter	0.727	228	0.899	237
SPBC365.16		sequence orphan	0.813	255	NaN	0
SPBC1289.11	spf38	splicing factor Spf38	0.756	395	0.871	276
SPAC9E9.09c		aldehyde dehydrogenase	0.676	91	0.951	99
SPCC1739.06c		uroporphyrin methyltransferase	0.814	4	NaN	0
SPBC428.06c		histone deacetylase complex subunit, RXT2 family	0.763	96	0.865	137
SPBC1539.04		conserved eukaryotic protein	0.687	183	0.943	245
SPBC1861.09	ppk22	serine/threonine protein kinase Ppk22	0.775	283	0.855	252
SPAC29A4.05	cam2	myosin I light chain Cam2	0.714	290	0.916	251
SPBC2A9.07c		zf-PARP-type zinc finger protein	0.770	229	0.862	262
SPAC25H1.04	mug105	DUF1671 family protein	0.733	327	0.899	225
SPCC794.08		HEAT repeat protein, unknown biological role	0.703	91	0.930	29
SPCC1183.06	ung1	uracil DNA N-glycosylase Ung1	0.766	230	0.867	261
SPBC1683.02		adenine deaminase	0.686	287	0.947	201
SPAC22F3.03c	rdh54	ATP-dependent DNA helicase Rdh54	0.769	303	0.864	290
SPAC22E12.05c	rer1	Rer1 family protein	0.797	119	0.837	199
SPAC2F7.07c	cph2	histone deacetylase complex subunit Rco1	0.773	35	0.861	7
SPBC651.09c		RNA polymerase II associated Paf1 complex	0.682	194	0.953	285
SPAPJ760.02c	app1	App1 protein	0.808	176	0.828	185
SPAP8A3.03		ZIP zinc transporter 1	0.878	198	0.759	223
SPCC1672.04c		mitochondrial copper ion transport protein	0.818	113	NaN	0
SPAC589.08c	dam1	DASH complex subunit Dam1	0.838	263	0.800	238
SPBC1652.01		conserved fungal protein	0.862	271	0.777	234
SPAC11D3.04c		SnoaL	0.867	254	0.772	149
SPBC16G5.17		transcription factor	0.736	332	0.903	305
SPAC9.11		sequence orphan	0.868	201	0.772	199
SPBC530.15c		spermidine family transporter	0.722	310	0.919	194
SPBC776.17		rRNA processing protein Rrp7	0.808	264	0.833	114
SPCC126.02c	pku70	Ku domain protein Pku70	0.754	184	0.888	239
SPBC19C7.09c	uve1	endonuclease Uve1	0.711	219	0.932	244
SPCC1682.07	ssl1	transcription factor TFIIH complex subunit Ssl1	0.871	187	0.773	168
SPAC25B8.01	dap1	cytochrome P450 regulator Dap1	0.725	292	0.919	329
SPCC5E4.05c		serine hydrolase	0.811	179	0.834	174
SPBC83.02c	rpl4302	60S ribosomal protein L37a	0.971	458	0.675	191
SPAC17G8.14c	pck1	protein kinase C (PKC)-like Pck1	0.763	208	0.884	179
SPAC2F3.05c		xylose and arabinose reductase	0.766	360	0.881	225
SPBC16G5.15c	fkh2	fork head transcription factor Fkh2	0.791	234	0.857	296
SPBP4H10.19c		calreticulin/calnexin homolog	0.673	218	0.975	253
SPAPYUG7.03c	mid2	anillin homologue Mid2	0.785	93	0.864	99

Systematic ID	Gene name	Gene description	CF index screen 1	Cell number	CF index screen 2	Cell number
SPBC336.01	fbh1	DNA helicase I	0.711	234	0.939	225
SPCC970.06		cargo receptor for soluble proteins	0.871	329	0.779	6
SPAC4F10.07c	atg13	autophagy associated protein Atg13	0.977	386	0.673	237
SPBC19C7.04c		conserved fungal protein	0.722	333	0.929	288
SPAC19D5.11c	ctf8	DNA replication factor C complex subunit Ctf8	0.772	266	0.879	274
SPCC126.10	iah1	isoamyl acetate hydrolytic enzyme Iah1	0.703	290	0.950	347
SPAC1F8.06	fta5	Sim4 and Mal2 associated (4 and 2 associated) protein 5	0.755	249	0.898	250
SPBC21B10.12	rec6	meiotic recombination protein Rec6	0.760	523	0.893	315
SPBC15D4.02		transcription factor	0.827	3	NaN	0
SPAC1142.03c	swi2	Swi5 complex subunit Swi2	0.751	358	0.903	302
SPAC14C4.10c		Nudix family hydrolase	0.824	236	0.830	214
SPAC630.06c		conserved fungal protein	0.750	253	0.905	198
SPBC2G2.17c		beta-glucosidase Psu2	0.827	283	NaN	0
SPCC285.17	spp27	RNA polymerase I upstream activation factor complex subunit Spp27	0.773	182	0.882	278
SPAC1F7.06		ThiJ domain protein	0.770	389	0.886	309
SPCC4G3.11	mug154	conserved fungal protein	0.863	414	0.793	305
SPAC20H4.03c	tfs1	transcription elongation factor TFIIS	0.747	25	0.909	315
SPAC24H6.13		DUF221 family protein	0.789	270	0.867	289
SPBC1734.07c		TRAPP complex subunit Trs85	0.963	218	0.694	109
SPCC162.04c	wtf13	wtf element Wtf13	0.771	179	0.886	223
SPBC27B12.03c		lathosterol oxidase	0.700	149	0.957	262
SPBC577.06c		phosphatidylinositol kinase	0.706	364	0.952	308
SPAC2E1P3.02c	amt3	ammonium transporter Amt3	0.859	277	0.799	256
SPBC15C4.01c	oca3	TPR repeat protein Oca3	0.871	271	0.788	251
SPCPJ732.02c		xylulose kinase	0.750	229	0.909	208
SPBC19G7.18c		sequence orphan	0.810	311	0.848	275
SPCC4B3.02c		Golgi transport protein Got1	0.842	350	0.817	245
SPAC8C9.06c		mitochondrial translation regulator	NaN	0	0.830	255
SPAC56F8.16	esc1	transcription factor Esc1	0.817	296	0.842	254
SPBC16D10.05	mok13	alpha-1,3-glucan synthase Mok13	0.763	283	0.897	179
SPBC3H7.15	hhp1	serine/threonine protein kinase Hhp1	0.831	201	0.829	218
SPAC806.04c		DUF89 family protein	0.787	288	0.875	280
SPAP8A3.07c		phospho-2-dehydro-3-deoxyheptonate aldolase	0.831	260	NaN	0
SPAC12B10.01c		ubiquitin-protein ligase E3	0.696	376	0.965	353
SPBC1734.05c	spf31	DNAJ protein Spf31	0.847	397	0.816	152
SPBC12C2.03c		FAD binding protein	0.814	260	0.850	220
SPCC132.04c		NAD-dependent glutamate dehydrogenase	0.818	505	0.846	528
SPBC887.18c		transcription adaptor protein	0.832	237	NaN	0
SPCC1672.06c	asp1	inositol hexakisphosphate kinase	0.940	280	0.725	33
SPBC29B5.02c	isp4	OPT oligopeptide transporter family	0.752	266	0.914	268
SPAC10F6.12c	mam4	protein-S isoprenylcysteine O-methyltransferase Mam4	0.803	293	0.862	219
SPAC821.11	pro1	gamma-glutamyl phosphate reductase Pro1	NaN	0	0.833	317
SPAC23G3.03	sib2	ornithine N5 monooxygenase	0.817	327	0.849	367
SPAPB17E12.04c	csn2	COP9/signalosome complex subunit Csn2	0.779	209	0.887	362
SPCC1235.06	sif1	Sad1 interacting factor 1	0.805	182	0.861	268
SPCC364.03	rpl1702	60S ribosomal protein L17	0.800	362	0.867	334
SPBC543.03c	pku80	Ku domain protein Pku80	0.812	226	0.855	323
SPAC1296.02	cox4	cytochrome c oxidase subunit IV	0.802	91	0.865	161
SPAPB24D3.03		agmatinase	0.823	305	0.845	240
SPAC57A7.12		heat shock protein Pdr13	0.819	199	0.849	202
SPAC6G10.11c	ubi3	ribosomal ubiquitin fusion protein Ubi3	0.704	166	0.965	190
SPBC3B9.04		mitochondrial methyltransferase	0.825	283	0.844	245
SPBC16A3.02c		mitochondrial peptidase	0.740	265	0.929	196
SPCC285.15c	rps2802	40S ribosomal protein S28	0.849	247	0.821	306
SPCC24B10.04		sequence orphan	NaN	0	0.835	263
SPCC1322.15	rpl3402	60S ribosomal protein L34	0.795	225	0.875	321
SPBC428.14		1-acylglycerol-3-phosphate acyltransferase	0.787	185	0.885	190
SPBC8E4.05c		fumarate lyase superfamily	0.803	254	0.869	266
SPAC3C7.07c		arginine-tRNA protein transferase	0.838	195	0.834	206
SPBC106.03		DUF1776 family protein	0.735	359	0.938	213
SPAC328.10c	rps502	40S ribosomal protein S5	0.827	249	0.847	306
SPAC26A3.16	dph1	UBA domain protein Dph1	0.951	208	0.725	156
SPAC1002.20		sequence orphan	0.915	311	0.761	378
SPAPYUK71.03c		C2 domain protein	0.752	246	0.925	289

Systematic ID	Gene name	Gene description	CF index screen 1	Cell number	CF index screen 2	Cell number
SPAC1782.02c		conserved fungal protein	0.788	361	0.889	278
SPAC26H5.04		vacuolar import and degradation protein Vid28	0.820	323	0.856	329
SPBC1A4.09		pseudouridine synthase	NaN	0	0.838	3
SPAC1142.02c		TPR repeat protein	0.794	294	0.883	337
SPAC18G6.13		sequence orphan	0.744	229	0.933	131
SPBC577.11		sequence orphan	0.893	208	0.784	152
SPAC2C4.10c		sequence orphan	0.725	169	0.952	272
SPAP14E8.05c		UPF0136 family protein	0.880	264	0.798	239
SPAC1D4.11c	lkh1	dual specificity protein kinase Lkh1	0.849	115	0.828	154
SPBC800.11		inosine-uridine preferring nucleoside hydrolase	0.822	226	0.856	234
SPBC15D4.09c		cystathionine gamma-synthase	0.819	59	0.859	28
SPAC1B2.04	cox6	cytochrome c oxidase subunit VI	0.839	10	NaN	0
SPAC2G11.15c	tgs1	RNA methyltransferase Tgs1	0.746	220	0.933	234
SPAC2E12.03c		G-protein coupled receptor	0.781	423	0.898	263
SPAC1610.01		conserved fungal protein	0.773	70	0.906	132
SPBC19C2.14	smd3	Sm snRNP core protein Smd3	0.812	100	0.867	76
SPAC20H4.02		conserved fungal protein	0.865	395	0.814	515
SPAC6C3.03c		sequence orphan	0.837	269	0.843	296
SPAC869.09		conserved fungal protein	0.739	271	0.942	285
SPAC694.06c	mrc1	mediator of replication checkpoint 1	0.722	199	0.958	218
SPAC2F7.04	pmc2	RNA polymerase II holoenzyme mediator complex subunit	0.768	319	0.913	263
SPAC57A10.03	cyp1	cyclophilin family peptidyl-prolyl cis-trans isomerase Cyp1	0.875	153	0.806	328
SPAC22A12.06c		serine hydrolase	0.815	244	0.867	212
SPAC23H3.15c		sequence orphan	0.838	135	0.845	261
SPCC584.15c		arrestin/PY protein 2	0.785	180	0.898	238
SPAC23C11.08	php3	CCAAT-binding factor complex subunit Php3	0.830	84	0.853	272
SPAC227.07c	pab1	protein phosphatase regulatory subunit Pab1	0.773	164	0.911	47
SPAC821.05		translation initiation factor eIF3h	0.761	113	0.922	125
SPCC14G10.04		sequence orphan	0.787	247	0.898	261
SPBC27B12.10c	tom7	mitochondrial TOM complex subunit Tom7	0.862	319	0.823	198
SPAC6G10.10c		human hmmtag2 homolog	0.837	337	0.847	217
SPCC18.13		tRNA (guanine-N7-)-methyltransferase subunit Trm82	0.796	315	0.888	285
SPBC8E4.02c		sequence orphan	0.861	246	0.824	293
SPCC11E10.05c	ynd1	nucleoside diphosphatase	0.833	209	0.852	220
SPBC354.03	swd3	WD repeat protein Swd3	0.772	192	0.913	245
SPCC126.15c	sec65	signal recognition particle subunit Sec65	0.739	392	0.946	291
SPAC2G11.07c	ptc3	protein phosphatase 2C Ptc3	0.795	316	0.891	157
SPAC823.12		zinc finger protein Pep5/Vps11	0.787	1	0.898	78
SPAC750.05c		S. pombe specific 5Tm protein family	0.850	392	0.836	358
SPAC22F8.12c	shf1	sequence orphan	0.842	112	0.844	357
SPAC683.03		sequence orphan	0.878	310	0.809	278
SPAC3H5.10	rpl3202	60S ribosomal protein L32	0.843	217	NaN	0
SPAC17C9.07	alg8	glucosyltransferase Alg8	0.850	280	0.838	235
SPBC16C6.06	pep1	sorting receptor for CPY	0.752	253	0.935	279
SPCC16C4.09	sts5	RNB-like protein	0.868	193	0.819	250
SPBC1921.07c		SAGA complex subunit Sgf29	0.859	191	0.828	270
SPAC18G6.12c		hypothetical protein	0.755	214	0.933	211
SPBC20F10.10		cyclin pho85 family	0.857	216	0.832	231
SPAC9G1.06c	cyk3	cytokinesis protein Cyk3	0.850	289	0.838	291
SPAC8C9.19		conserved fungal protein	0.833	330	0.856	337
SPBC336.13c		mitochondrial inner membrane peptidase complex catalytic subunit 2	0.840	225	0.850	148
SPCC1259.12c		Ran GTPase binding protein	0.808	199	0.881	263
SPCC1020.09		WD repeat protein, human WDR79 family	0.765	319	0.925	269
SPAC15E1.03	rpl42	60S ribosomal protein L36/L42	0.810	50	0.880	273
SPCC613.08		CDK regulator	0.821	249	0.870	215
SPBC29A3.09c		AAA family ATPase Gcn20	0.814	169	0.877	312
SPAC2G11.04		RNA-binding protein	0.798	208	0.893	224
SPBC1709.10c		metallochaperone	0.739	278	0.952	356
SPAC13D6.01	pof14	F-box protein Pof14	0.785	302	0.907	401
SPAC1F8.01	ght3	hexose transporter Ght3	0.789	231	0.902	350
SPAC20G4.05c		UPF0061 family protein	0.952	396	0.741	317
SPBC530.06c		translation initiation factor eIF3 alpha subunit	0.846	2	NaN	0
SPAC24C9.15c	spn5	septin Spn5	NaN	0	0.847	91

Systematic ID	Gene name	Gene description	CF index screen 1	Cell number	CF index screen 2	Cell number
SPBC1734.04		alpha-1,6-mannosyltransferase	0.847	6	NaN	0
SPBC1861.07		elongin C	0.763	359	0.930	245
SPCC1020.10	oca2	serine/threonine protein kinase Oca2	0.877	196	0.817	193
SPAPB18E9.01	trm5	tRNA (guanine) methyltransferase Trm5	0.847	397	NaN	0
SPAC3C7.06c	pit1	serine/threonine protein kinase Pit1	0.728	462	0.966	460
SPCC576.17c		membrane transporter	0.882	261	0.812	250
SPAC30C2.08		conserved fungal protein	0.808	285	0.886	356
SPBC27B12.08		AP-1 accessory protein	0.720	188	0.975	197
SPCC306.05c	ins1	INSIG domain protein	0.813	204	0.882	226
SPAC1071.11		NADH-dependent flavin oxidoreductase	0.810	127	0.885	58
SPCC1620.07c		lunapark homolog	0.840	237	0.855	193
SPAC22E12.06c	gmh3	alpha-1,2-galactosyltransferase Gmh3	0.780	358	0.915	297
SPAC1F5.09c	shk2	PAK-related kinase Shk2	0.745	384	0.951	251
SPCC24B10.19c		sequence orphan	0.884	285	0.813	254
SPAC750.06c		S. pombe specific DUF999 protein family 4	0.803	224	0.894	227
SPBC16E9.16c	lsd90	sequence orphan	0.822	239	0.876	371
SPAC25B8.17		peptidase family A22	0.802	170	0.896	52
SPAC6F12.09	rdp1	RNA-directed RNA polymerase Rdp1	0.771	177	0.927	230
SPAC11E3.03	pcs1	chromosome segregation protein Pcs1	0.801	222	0.896	227
SPAC29B12.06c	rcd1	RNA-binding protein Rcd1	0.820	224	0.878	247
SPBC2A9.04c		Sir Antagonist ortholog	0.837	308	0.861	439
SPCC4G3.17		HD domain	0.796	358	0.902	257
SPAC3H5.05c	rps1401	40S ribosomal protein S14	0.861	215	0.837	218
SPBC21C3.06		sequence orphan	0.881	208	0.817	176
SPBC3E7.09		Sad1-UNC-like C-terminal	0.815	196	0.884	187
SPAC13G6.14	aps1	diadenosine 5,5-p1,p6-hexaphosphate hydrolase Aps1	0.875	147	0.824	175
SPBC1709.16c		conserved protein (fungal bacterial plant)	0.803	324	0.896	171
SPAC23A1.14c		cystathionine gamma-synthase	0.836	181	0.863	196
SPCC1450.02		bromodomain protein	0.862	217	0.837	196
SPAC56E4.07		N-acetyltransferase	0.821	278	0.878	264
SPAC26F1.07		2-methylbutyraldehyde reductase	0.772	196	0.927	265
SPAC1687.15	gsk3	serine/threonine protein kinase Gsk3	0.911	332	0.789	349
SPAC343.20		sequence orphan	0.804	262	0.896	294
SPCP1E11.06	apl4	AP-1 adaptor complex gamma subunit Apl4	0.816	315	0.884	320
SPAC13G7.12c		choline kinase	0.852	175	0.849	175
SPAC3A12.17c	cys12	cysteine synthase Cys12	0.755	231	0.945	290
SPAC977.17		MIP water channel	NaN	0	0.851	693
SPAPJ695.01c		S. pombe specific UPF0321 family protein 3	0.832	238	0.869	242
SPBC106.04	ada1	adenosine deaminase Ada1	0.907	94	0.795	39
SPBC32F12.03c	gpx1	glutathione peroxidase Gpx1	0.868	312	0.834	308
SPBC32H8.03	bem46	esterase/lipase	0.762	259	0.940	211
SPCC1235.12c	mug146	meiotically upregulated gene Mug46	0.863	236	0.839	250
SPAC3G9.11c		pyruvate decarboxylase	0.775	218	0.928	215
SPBC29A3.05		chromatin remodeling complex subunit	0.813	165	0.890	262
SPAC1639.02c	trk2	potassium ion transporter Trk2	0.746	219	0.957	191
SPCC1906.04	wtf20	wtf element Wtf20	0.845	160	0.858	210
SPBP4H10.17c		carboxyl methyl esterase	0.815	271	0.888	318
SPAC637.06		alpha-1,2-galactosyltransferase	0.832	157	0.872	194
SPCC1682.08c		RNA-binding protein Mcp2	0.815	4	0.888	216
SPBC25H2.14	mug16	UNC-50 family protein	0.787	284	0.917	295
SPAC1952.06c		DUF1716 family protein	0.856	259	0.848	211
SPBC24C6.09c		phosphoketolase	0.798	305	0.907	198
SPAC30D11.06c		DUF300 family protein	0.840	295	0.865	321
SPCC970.02		mannan endo-1,6-alpha-mannosidase	0.819	248	0.886	246
SPAC13C5.02	dre4	DNA replication protein Dre4	0.860	231	0.845	237
SPBC405.04c	ypt7	GTPase Ypt7	0.720	144	0.986	84
SPAC6F12.12	par2	protein phosphatase regulatory subunit Par2	0.876	165	0.829	178
SPCC1020.08		wybutosine biosynthesis protein Tyw1	0.889	214	0.818	197
SPCC613.11c	meu23	DUF1773 family protein 2	0.758	423	0.948	276
SPBC16C6.04		sequence orphan	0.919	191	0.788	202
SPAC4G9.02		ribonuclease H2 complex subunit	0.835	342	0.872	300
SPBC26H8.08c	grn1	GTPase Grn1	NaN	0	0.854	300
SPBC1306.02		WD repeat protein, human WDR6 family	0.808	245	0.899	326
SPAC14C4.09	agn1	glucan endo-1,3-alpha-glucosidase Agn1	0.811	121	0.897	109
SPAC4G9.19		DNAJ domain protein DNAJB family	0.747	244	0.961	210
SPBC409.07c	wis1	MAP kinase kinase Wis1	0.873	156	0.836	155

Systematic ID	Gene name	Gene description	CF index screen 1	Cell number	CF index screen 2	Cell number
SPBCPT2R1.03		hypothetical protein	0.865	341	0.844	325
SPAC688.10	rev3	DNA polymerase zeta catalytic subunit Rev3	0.888	364	0.822	316
SPAC18B11.03c		N-acetyltransferase	0.812	209	0.898	205
SPBC2D10.06	rep1	MBF transcription factor complex subunit Rep1	0.749	213	0.962	223
SPCC1235.09		histone deacetylase complex subunit	0.808	266	0.903	415
SPBC1718.07c	zfs1	transcription factor Zfs1	NaN	0	0.856	332
SPAC24H6.10c		phospho-2-dehydro-3-deoxyheptonate aldolase	0.775	289	0.937	276
SPAC13F5.05		thioredoxin family protein	0.735	161	0.977	291
SPBC3H7.07c		phosphoserine phosphatase	NaN	0	0.856	374
SPCC1739.05	set5	histone lysine methyltransferase Set5	0.757	242	0.955	321
SPAC644.15	rpp101	60S acidic ribosomal protein Rpp1-1	0.749	262	0.964	247
SPBC29A10.11c	vps902	guanyl-nucleotide exchange factor Vps902	0.821	225	0.892	263
SPAC664.03		RNA polymerase II associated Paf1 complex	0.785	147	0.928	299
SPBC3B8.10c		NLI interacting factor family	NaN	0	0.857	256
SPBPB2B2.07c		S. pombe specific DUF999 protein family 7	0.872	224	0.841	238
SPAC4C5.04	rad31	SUMO E1-like activator enzyme Rad31	0.854	184	0.859	166
SPCC794.02	wtf5	wtf element Wtf5	0.842	179	0.872	207
SPCC1739.03	hrr1	Helicase Required for RNAi-mediated heterochromatin assembly Hrr1	0.923	378	0.791	63
SPAC8F11.02c		diphthamide biosynthesis protein Dph3	0.888	385	0.826	268
SPBC1773.15		membrane transporter	0.924	295	0.790	308
SPBC1604.19c		TRAPP complex subunit Trs85	0.865	226	0.850	304
SPCC1393.07c	mug4	sequence orphan	0.796	241	0.919	243
SPAC1851.03	ckb1	CK2 family regulatory subunit	0.866	119	0.849	104
SPBC215.04	git11	heterotrimeric G protein gamma subunit Git11	0.816	241	0.899	207
SPCC965.05c	thp1	uracil DNA N-glycosylase Thp1	0.793	332	0.922	227
SPBC16E9.11c	pub3	ubiquitin-protein ligase E3	0.885	265	0.831	223
SPBPB10D8.04c		membrane transporter	0.795	264	0.920	288
SPBC2A9.06c		di-trans,poly-cis-decaprenylcistransferase	0.866	271	0.850	288
SPAC3F10.12c		transcription factor	0.778	288	0.938	217
SPCC285.14		TRAPP complex subunit Trs130	NaN	0	0.858	2
SPACUNK4.10		hydroxyacid dehydrogenase	0.850	384	0.866	275
SPCC1795.01c	mad3	mitotic spindle checkpoint protein Mad3	0.864	322	0.852	200
SPAC12B10.07	acp1	F-actin capping protein alpha subunit	0.893	315	0.823	401
SPBC23E6.09	ssn6	transcriptional corepressor Ssn6	0.858	4	NaN	0
SPAC16E8.17c		succinate-CoA ligase	0.762	265	0.955	205
SPAC1486.01		manganese superoxide dismutase (AF069292)	0.736	42	0.981	222
SPBC725.10		tspO homolog	0.775	219	0.943	265
SPAC29A4.20		RNA polymerase II elongator complex, histone acetyltransferase subunit	0.845	300	0.872	231
SPAC56F8.09	rrp8	rRNA methyltransferase Rrp8	0.845	182	0.873	167
SPAC29E6.01	pof11	F-box protein Pof11	0.887	200	0.830	242
SPAC17A2.01	bsu1	high-affinity import carrier for pyridoxine, pyridoxal, and pyridoxamine Bsu1	0.849	304	0.868	281
SPCC24B10.11c		THO complex subunit 7	0.837	208	0.881	166
SPBC24C6.06	gpa1	G-protein alpha subunit	0.813	279	0.905	170
SPAC23G3.04		DUF1711 family protein	0.840	204	0.878	290
SPBC1685.14c		Vid27 family protein	0.874	303	0.844	165
SPAC27E2.11c		sequence orphan	0.918	40	0.801	276
SPAC57A7.05		conserved protein (fungal and plant)	0.889	185	0.829	215
SPCC757.09c	rnc1	RNA-binding protein that suppresses calcineurin deletion Rnc1	0.869	229	0.850	251
SPAC767.01c	vps1	dynamin family protein Vps1	0.830	243	0.889	258
SPAC24B11.07c		ketopantoate reductase	0.821	234	0.898	199
SPCC962.05		sequence orphan	0.835	248	0.884	381
SPAC4F8.03		SBDS family protein	0.895	3	0.824	264
SPAC19G12.11	coq9	ubiquinone biosynthesis protein Coq9	0.820	289	0.900	196
SPBC21D10.11c	nfs1	iron-sulfur cluster assembly protein Nfs1	0.810	220	0.910	277
SPAC15A10.09c		conserved fungal protein	0.859	293	0.861	237
SPBC31F10.05	mug37	sequence orphan	0.854	195	0.866	232
SPAC14C4.14	atp1	F1-ATPase alpha subunit	0.874	315	0.847	321
SPAC2G11.06	vps4	AAA family ATPase Vps4	0.829	318	0.892	293
SPAC9G1.12	cpd1	tRNA (m1A) methyltransferase complex subunit Cpd1	0.792	308	0.929	182
SPAC24B11.10c	chr3	chitin synthase regulatory factor Chr3	0.838	124	0.883	173
SPAC4A8.04	isp6	vacuolar serine protease Isp6	0.800	154	0.921	210
SPBC1709.06	dus2	tRNA dihydrouridine synthase Dus2	NaN	0	0.861	265

Systematic ID	Gene name	Gene description	CF index screen 1	Cell number	CF index screen 2	Cell number
SPBC1815.01	eno101	enolase	0.831	294	0.891	211
SPBC405.02c		sequence orphan	0.853	169	0.869	196
SPBP8B7.27	mug30	ubiquitin-protein ligase E3	0.856	346	0.866	289
SPBC21H7.06c		inositol metabolism protein Opi10	0.869	293	0.853	266
SPBC16G5.02c		ribokinase	0.796	260	0.926	218
SPCC1494.03	arz1	sequence orphan	0.774	551	0.949	316
SPAC869.08	pcm2	protein-L-isoaspartate O-methyltransferase	0.763	212	0.960	330
SPAC27E2.01		alpha-amylase homolog	0.782	1	0.942	2
SPCC1672.03c		guanine deaminase	0.783	404	0.940	269
SPAC343.10	met11	methylenetetrahydrofolate reductase Met11	0.795	38	0.929	252
SPBC409.16c		sequence orphan	0.751	239	0.973	233
SPAC11D3.18c		nicotinic acid plasma membrane transporter	0.896	335	0.828	422
SPBC2F12.11c	rep2	transcriptional activator Rep2	0.797	196	0.927	282
SPAC17G8.07		YEATS family protein	0.911	236	0.813	312
SPBC20F10.05		DuF1740 family protein	0.846	194	0.878	341
SPBP4H10.20	nhm1	m7G(5)pppN diphosphatase	0.821	281	0.904	386
SPCC1223.11	ptc2	protein phosphatase 2C Ptc2	0.810	230	0.915	149
SPAP11E10.01		ornithine cyclodeaminase family	0.883	369	0.842	358
SPBC649.04	uvi15	UV-induced protein Uvi15	0.905	37	0.820	109
SPAC11D3.17		zinc finger protein	0.903	367	0.822	304
SPAC25H1.09	mde5	alpha-amylase homolog Mde5	0.886	233	0.840	277
SPBC16E9.03c		DUF1783 family protein	0.850	185	0.875	223
SPCC1259.01c	rps1802	40S ribosomal protein S18	0.834	273	0.892	302
SPAC343.06c		scramblase	0.837	365	0.888	264
SPBC17G9.09	tif213	translation initiation factor eIF2 gamma subunit	0.896	256	0.830	294
SPAC824.05	vps16	HOPS complex subunit Vps16	0.851	153	0.875	170
SPBC1604.02c		PPR repeat protein	0.845	237	0.882	228
SPCC1494.01		iron/ascorbate oxidoreductase family	0.798	217	0.929	234
SPBC19C2.06c	mug124	sequence orphan	0.786	224	0.940	335
SPBC543.09		mitochondrial m-AAA protease	0.852	281	0.874	56
SPBP4H10.16c		phosphatase activator	0.790	222	0.937	377
SPAC17A2.10c		sequence orphan	0.841	245	0.885	402
SPAC6F6.12		autophagy associated protein Atg24	0.813	130	0.914	118
SPAC1A6.01c		human thyroid receptor interacting protein homolog	0.824	271	0.904	332
SPAC26A3.14c		DUF1748 family protein	0.798	312	0.929	320
SPCC550.09		peroxin Pex32	0.848	181	0.880	357
SPBC23G7.12c	rpt6	19S proteasome regulatory subunit Rpt6	0.771	234	0.956	305
SPCC24B10.08c		histone acetyltransferase complex subunit Ada2	0.866	274	0.862	315
SPAC16C9.04c		CCR4-Not complex subunit Mot2	0.839	213	0.890	245
SPCC1020.07		haloacid dehalogenase-like hydrolase	0.826	280	0.903	326
SPAC20G4.07c	sts1	C-24(28) sterol reductase Sts1	0.888	395	0.841	4
SPAC186.05c		human TMEM165 homolog	0.873	298	0.856	234
SPBPB2B2.01		amino acid permease, unknown 12	0.754	172	0.976	237
SPBC12C2.08	dnm1	dynamin Dnm1	0.875	256	0.855	347
SPAC24C9.02c		cytochrome c1 heme lyase	0.850	281	0.880	309
SPAC23D3.09	arp42	SWI/SNF and RSC complex subunit Arp42	0.827	318	0.903	295
SPBC27.06c	mgr2	mitochondrial membrane protein Mgr1	0.817	246	0.913	261
SPAC23D3.01		PWWP domain protein	0.854	295	0.877	301
SPCC777.07		alpha-1,2-mannosyltransferase	0.877	310	0.854	311
SPCPB16A4.05c		urease accessory protein UREG	0.871	220	0.860	250
SPAC1610.03c	crp79	poly(A) binding protein Crp79	0.824	262	0.907	282
SPCC553.07c	mug40	DinB translesion DNA repair polymerase	0.886	304	0.845	300
SPBC20F10.02c		DUF1741 family protein	0.792	183	0.939	328
SPCC1442.01	ste6	guanyl-nucleotide exchange factor Ste6	0.842	200	0.890	237
SPCC1494.08c		conserved fungal protein	0.899	232	0.833	216
SPBC365.07c		TATA element modulatory factor homolog	0.810	235	0.922	200
SPCC794.07		dihydrolipoamide S-acetyltransferase E2	0.901	337	0.831	2
SPBPB2B2.08		conserved fungal protein	0.783	218	0.949	202
SPBC29A3.08	pof4	elongin-A, F-box protein Pof4	0.911	284	0.821	275
SPAC4G8.08		iron ion transporter	0.873	296	0.859	199
SPCC24B10.09	rps1702	40S ribosomal protein S17	0.823	272	0.909	330
SPAC30D11.07	nth1	DNA endonuclease III	0.858	341	0.874	390
SPCC1223.10c	eaf1	RNA polymerase II transcription elongation factor SpEAF	0.796	226	0.937	239
SPBC106.20	exo70	exocyst complex subunit Exo70	0.827	399	0.905	441
SPCC16C4.01	sif2	Sad1 interacting factor 2	0.810	298	0.922	337
SPBC1347.02	fkbp39	FKBP-type peptidyl-prolyl cis-trans isomerase	0.777	635	0.956	312

Systematic ID	Gene name	Gene description	CF index screen 1	Cell number	CF index screen 2	Cell number
SPAC17D4.03c	cis4	membrane transporter	0.882	240	0.850	305
SPCC13B11.02c		sequence orphan	0.902	270	0.831	251
SPBC1539.03c		argininosuccinate lyase	0.912	241	0.820	286
SPBC336.03	efc25	exchange factor Cdc25p-like	0.931	74	0.802	131
SPBC21D10.07		UPF0287 family protein	0.865	224	0.868	261
SPCC830.04c	mug128	sequence orphan	0.883	220	0.850	251
SPBC36B7.02		Svf1 family protein Svf2	NaN	0	0.866	309
SPBC3E7.12c	chr1	chitin synthase regulatory factor Chr1	0.866	272	0.867	170
SPCC1223.02	nmt1	no message in thiamine Nmt1	0.821	332	0.912	26
SPBC557.05		arrestin	0.793	384	0.941	324
SPBC1347.08c		ribonuclease H2 complex subunit	0.870	290	0.863	240
SPAC9.05	mfh1	ATP-dependent DNA helicase Mfh1	0.817	296	0.917	291
SPAC4F10.06		BUD22 family protein	0.894	307	0.839	318
SPAC10F6.08c		HMG box protein	0.796	224	0.938	224
SPAC15E1.04		thymidylate synthase	0.839	10	0.896	22
SPAC17H9.19c	cdt2	WD repeat protein Cdt2	0.858	243	0.877	188
SPAC630.10		conserved fungal protein	0.837	310	0.898	287
SPBC651.06	mug166	sequence orphan	0.801	247	0.934	321
SPBC359.04c		DIPSY family	0.876	274	0.859	272
SPCC553.04	cyp9	cyclophilin family peptidyl-prolyl cis-trans isomerase Cyp9	0.881	2	0.855	235
SPAC19B12.12c	yip11	SMN family protein Yip11	0.804	307	0.932	291
SPBC2D10.13	est1	telomerase regulator Est1	0.793	173	0.943	168
SPBC25B2.11	pof2	F-box protein Pof2	0.881	277	0.855	314
SPAC4D7.11		conserved fungal protein	0.756	182	0.981	143
SPAC8E11.04c		phospholipase	0.872	354	0.864	371
SPAPYUG7.02c	sin1	stress activated MAP kinase interacting protein Sin1	0.853	226	0.884	211
SPBP8B7.04	mug45	sequence orphan	0.872	229	0.865	302
SPBC354.05c	sre2	membrane-tethered transcription factor	0.816	18	0.921	28
SPAC1834.04	hht1	histone H3 h3.1	0.923	297	0.814	255
SPAC607.07c		sequence orphan	0.803	231	0.934	242
SPAC17G6.15c		MTC tricarboxylate transporter	0.869	188	0.869	245
SPBC36B7.04		tRNA dihydrouridine synthase Dus1	0.899	338	0.839	290
SPAC23C4.17		tRNA (cytosine-5-)-methyltransferase	0.854	290	0.884	326
SPAC694.03		conserved fungal protein	0.865	259	0.873	281
SPBC216.01c		DNA damage response protein	0.901	223	0.837	232
SPAC22G7.05		krr family protein	0.863	232	0.875	144
SPBC1271.03c		phosphoprotein phosphatase	0.861	286	0.878	272
SPCC188.12	spn6	septin Spn6	0.837	188	0.902	324
SPAC25H1.02	jmj1	Jmj1 protein	0.893	309	0.846	265
SPBC29A10.01	ccr1	NADPH-cytochrome p450 reductase	0.812	164	0.927	221
SPCC74.06	mak3	histidine kinase Mak3	0.780	208	0.959	364
SPAC26A3.17c		N-methyltransferase	0.947	280	0.793	282
SPAC1F3.09	mug161	CwfJ family protein	0.818	106	0.922	70
SPBC12D12.04c	pck2	protein kinase C (PKC)-like Pck2	0.816	415	0.924	180
SPAC664.15		CCR4-Not complex subunit Caf4/Mdv1	0.852	286	0.888	280
SPCC1840.07c		phosphoprotein phosphatase	0.902	315	0.839	252
SPBC216.06c	swi1	replication fork protection complex subunit Swi1	0.892	269	0.849	242
SPAC6F6.09		NuA4 histone acetyltransferase complex subunit	0.884	471	0.857	367
SPBC32F12.05c	cwf12	complexed with Cdc5 protein Cwf12	0.859	133	0.882	36
SPBC3D6.10	apn2	AP-endonuclease Apn2	0.783	192	0.959	155
SPBC3E7.16c	leu3	2-isopropylmalate synthase	0.816	214	0.926	215
SPAC25B8.13c	isp7	2-OG-Fe(II) oxygenase superfamily protein	0.907	256	0.835	280
SPAP27G11.12		human down-regulated in multiple cancers-1 homolog 1	0.855	242	0.887	262
SPCC126.01c		conserved fungal protein	0.828	204	0.914	274
SPCC4B3.08		C-terminal domain kinase I (CTDK-I) gamma subunit	0.931	296	0.811	327
SPCC126.11c		RNA-binding protein	0.843	188	0.900	207
SPAC26F1.04c	etr1	enoyl-[acyl-carrier protein] reductase	0.879	733	0.864	276
SPBC2F12.12c		conserved eukaryotic protein	0.833	7	0.910	7
SPBC30B4.08	eri1	double-strand siRNA ribonuclease	0.809	261	0.934	413
SPBC336.05c		S-adenosylmethionine-dependent methyltransferase	0.889	283	0.854	216
SPBC13E7.03c		RNA hairpin binding protein	0.865	302	0.878	161
SPAC3A11.11c		pyridoxal reductase	0.840	204	0.903	204
SPAC977.16c	dak2	dihydroxyacetone kinase Dak2	0.857	531	0.886	373

Systematic ID	Gene name	Gene description	CF index screen 1	Cell number	CF index screen 2	Cell number
SPBC1711.01c	matmi_1	mating-type m-specific polypeptide mi	0.788	266	0.956	319
SPAC688.06c	slx4	structure-specific endonuclease subunit	0.829	331	0.914	196
SPBC11B10.10c	pht1	histone H2A variant	0.831	144	0.913	144
SPAC4C5.03		CTNS domain protein	0.796	361	0.948	291
SPBC1271.06c	mug96	sequence orphan	0.789	314	0.955	195
SPAC11E3.09	pyp3	protein-tyrosine phosphatase Pyp3	0.856	292	0.888	357
SPBC16G5.13		sequence orphan	0.854	294	0.890	330
SPCC23B6.01c		oxysterol binding protein	NaN	0	0.872	326
SPBC21B10.03c		ataxin-2 homolog	0.935	180	0.809	126
SPAC821.04c	cid13	poly(A) polymerase Cid13	0.816	175	0.928	105
SPBC11C11.06c		sequence orphan	0.872	286	0.872	320
SPAC6G9.05	pcd1	peroxisomal coenzyme A diphosphatase	0.828	178	0.916	226
SPAC22G7.06c	ura1	carbamoyl-phosphate synthase (glutamine hydrolyzing), aspartate carbamoyltransferase Ura1	0.798	302	0.946	427
SPAC25G10.06	rps2801	40S ribosomal protein S28	0.859	248	0.886	324
SPCC4B3.07		nuclear pore associated protein	0.805	170	0.940	280
SPAC32A11.03c	phx1	homeobox transcription factor Phx1	0.882	324	0.863	430
SPBC713.02c	ubp21	ubiquitin C-terminal hydrolase Ubp21	0.893	329	0.852	334
SPBC1289.10c		transcription factor	NaN	0	0.873	246
SPAC11G7.03	idh1	isocitrate dehydrogenase (NAD+) subunit 1 Idh1	0.868	162	0.878	91
SPBC409.17c		DUF1769 family protein	0.897	267	0.849	264
SPAC22F8.05		alpha,alpha-trehalose-phosphate synthase	0.914	315	0.832	160
SPAC9E9.05		sequence orphan	0.873	250	0.873	252
SPAC1565.07c		TATA binding protein interacting protein	0.942	262	0.804	300
SPCC11E10.09c		alpha-amylase homolog	0.872	237	0.875	235
SPBC651.04		sequence orphan	0.811	199	0.936	273
SPBC28F2.10c	kap1	chromatin remodeling complex subunit Ngg1	0.874	224	0.873	201
SPCC1450.12		conserved fungal protein	0.862	325	0.885	156
SPBC36B7.03	sec63	ER protein translocation subcomplex subunit Sec63	0.813	221	0.935	305
SPAC11H11.02c	mug162	sequence orphan	0.894	282	0.854	308
SPAC343.09	ubx3	UBX domain protein Ubx3	0.860	174	0.888	224
SPBC13G1.14c		RNA-binding protein	0.887	446	0.861	217
SPAC25B8.10		trans-aconitate 3-methyltransferase	0.855	328	0.893	377
SPCC74.04		amino acid permease, unknown 15	0.874	319	0.875	261
SPCC736.11	ago1	argonaute	0.906	538	0.843	274
SPAC22F3.02	atf31	transcription factor Atf31	0.857	308	0.892	272
SPBC359.01		amino acid permease, unknown 7	0.835	248	0.914	293
SPBC21B10.10	rps402	40S ribosomal protein S4	0.857	385	0.892	209
SPAC13G7.03		up-frameshift suppressor3 family	0.849	315	0.900	315
SPCC16C4.11	pef1	Pho85/PhoA-like cyclin-dependent kinase Pef1	0.798	249	0.951	276
SPBP8B7.22	erd2	HDEL receptor	0.872	296	0.877	238
SPCC24B10.12		CGI121 family protein	0.781	186	0.968	226
SPAC4D7.06c		siroheme synthase	0.801	252	0.948	4
SPCC1620.12c		GTPase activating protein	0.889	218	0.860	309
SPBC3B9.05		helper of TIM (Predicted)	0.901	186	0.849	288
SPAC1F8.08		sequence orphan	0.902	236	0.848	278
SPBC317.01	mbx2	MADS-box transcription factor Pvg4	0.801	319	0.949	419
SPCC1322.09		conserved fungal protein	0.847	322	0.903	293
SPBC32H8.06	mug93	TPR repeat protein, meiotically spliced	0.784	169	0.966	347
SPCC830.10		nucleoside triphosphatase	0.816	261	0.935	349
SPAC11H11.01	sst6	ESCRT I complex subunit Vps23	0.879	166	0.872	228
SPBC21C3.16c	spt4	transcription elongation factor complex subunit Spt4	0.852	234	0.899	265
SPAC167.04	pam17	presequence translocase-associated motor subunit Pam17	0.875	222	NaN	0
SPBC29A10.05	exo1	exonuclease I Exo1	0.810	215	0.941	242
SPAC29A4.17c		FUN14 family protein	0.804	215	0.947	290
SPBC16G5.03		ubiquitin-protein ligase E3	0.934	303	0.817	262
SPCC1183.11		MS ion channel protein 1	0.847	341	0.904	229
SPAC10F6.17c		pyruvate dehydrogenase (lipoamide) phosphatase	0.886	348	0.865	313
SPBC24C6.05	sec28	coatomer epsilon subunit	0.884	274	0.867	247
SPCPB16A4.06c		sequence orphan	0.892	340	0.860	315
SPBC8D2.04	hht2	histone H3 h3.2	0.826	245	0.925	222
SPCC4B3.12	set9	histone lysine methyltransferase Set9	0.817	235	0.935	280
SPBPB2B2.13		galactokinase Gal1	0.844	345	0.907	459
SPBC83.01	ucp8	UBA/EH/EF hand domain protein Ucp8	0.826	233	0.926	285

Systematic ID	Gene name	Gene description	CF index screen 1	Cell number	CF index screen 2	Cell number
SPBC713.05		WD repeat protein, human MAPK organizer 1 (MORG1) family	0.854	249	0.899	220
SPCC126.07c		ubiquitin-protein ligase E3	0.839	215	0.914	252
SPBC15D4.05		conserved protein	0.885	343	0.867	260
SPAC23G3.05c		regulator of G-protein signaling (RGS) domain	0.895	357	0.857	240
SPBP35G2.04c		sequence orphan	0.868	198	0.885	192
SPAC1782.04	cox24	mitochondrial mRNA processing protein Cox24	0.903	300	0.850	273
SPBC1685.08		histone deacetylase complex subunit Cti6	0.847	201	0.906	201
SPAC5D6.02c	mug165	sequence orphan	0.859	294	0.895	246
SPAC1782.01		proteasome component	0.790	201	0.964	278
SPBC19F8.02		nuclear distribution protein NUDC	0.809	335	0.944	365
SPBC354.08c		DUF221 family protein	0.885	305	0.869	364
SPAPB1E7.05	gde1	glycerophosphoryl diester phosphodiesterase	0.876	315	0.878	263
SPAC15F9.01c		sequence orphan	0.864	217	0.889	250
SPAC19A8.05c	sst4	sorting receptor for ubiquitinated membrane proteins	0.852	231	0.901	244
SPCC1620.02	wtf23	wtf element Wtf23	NaN	0	0.877	276
SPCP31B10.02		conserved eukaryotic protein	0.870	210	0.884	191
SPBC3B9.08c		Mago-nashi homolog	0.891	262	0.864	221
SPBC651.03c	gyp10	GTPase activating protein Gyp10	0.826	224	0.928	305
SPAPB1E7.08c		membrane transporter	0.864	239	0.890	256
SPAC8C9.14	prr1	transcription factor Prr1	0.876	319	0.878	326
SPAC869.02c		nitric oxide dioxygenase	0.782	241	0.973	255
SPBC31F10.17c		sequence orphan	0.863	289	0.892	282
SPBC4F6.16c	ero11	ER oxidoreductin Ero1a	0.857	300	0.897	255
SPAC1687.12c	coq4	ubiquinone biosynthesis protein Coq4	0.879	234	0.876	207
SPCC1672.09		triglyceride lipase-cholesterol esterase	0.893	241	0.862	268
SPBC16A3.06		tRNA specific adenosine deaminase	0.833	307	0.922	226
SPAC18G6.01c		conserved fungal protein	0.854	192	0.901	238
SPBC19C7.01		Mago binding protein homolog	0.797	266	0.958	261
SPAC20G4.01		CCR4-Not complex subunit Caf16	0.879	232	0.876	194
SPBC32F12.09	rum1	CDK inhibitor Rum1	0.874	269	0.881	248
SPAC1D4.09c		DUF602 family protein	0.850	214	0.905	216
SPAC15E1.05c		ethanolamine-phosphate cytidylyltransferase	0.900	400	0.856	337
SPAC19A8.14		aminoacyl-tRNA hydrolase	0.814	353	0.942	342
SPAC19E9.02	fin1	serine/threonine protein kinase Fin1	0.915	298	0.841	259
SPCC1393.08		transcription factor	0.820	171	0.936	157
SPBC409.20c	psh3	ER chaperone SHR3 homologue Psh3	0.878	258	NaN	0
SPCC1183.02		glutathione S-transferase	0.823	227	0.934	262
SPAC6B12.06c		conserved fungal protein	0.879	344	0.877	314
SPAC1556.08c	cbs2	protein kinase activator Snf4	0.912	103	0.844	258
SPCC1827.03c		acetyl-CoA ligase	NaN	0	0.878	287
SPBC18H10.15	ppk23	serine/threonine protein kinase Ppk23	0.811	252	0.946	317
SPAC1F7.08	fio1	iron transport multicopper oxidase Fio1	0.879	5	NaN	0
SPCC18.17c		sequence orphan	0.941	317	0.816	211
SPAC30D11.10	rad22	DNA repair protein Rad22	0.806	308	0.951	252
SPAC227.06		Rab GTPase binding	0.867	299	0.891	290
SPBC32F12.07c		ubiquitin-protein ligase E3	0.803	185	0.955	211
SPBC29A3.07c		U2 snRNP-associated protein Sf3b14 homolog	0.807	222	0.951	279
SPAC343.19		phosphatidylinositol 4-kinase Lsb6	0.826	248	0.932	224
SPCC1393.12		sequence orphan	0.822	234	0.935	231
SPBC28E12.03	rga4	GTPase activating protein Rga4	0.816	211	0.942	280
SPBC13A2.04c		PTR family peptide transporter	0.860	339	0.898	324
SPBC3H7.14	mug176	BRCT domain protein	0.875	253	0.884	242
SPAC664.02c		actin-like protein Arp8	0.883	155	0.876	188
SPAC637.09		ribonuclease H70	0.845	2	0.914	224
SPBC1734.06	rhp18	Rad18 homolog Rhp18	0.855	78	0.904	208
SPAC6B12.16	meu26	conserved fungal protein	0.908	229	0.851	280
SPBC19C2.10		BAR adaptor protein	0.809	224	0.951	280
SPAC14C4.13	rad17	RFC related checkpoint protein Rad17	0.831	296	0.928	287
SPAPB2C8.01		glycoprotein	0.876	243	0.883	253
SPBC16E9.14c	zrg17	membrane transporter	0.925	331	0.835	460
SPCC1442.05c		conserved fungal protein	0.895	278	0.865	239
SPBC428.04		sequence orphan	0.921	130	0.839	160
SPAC1D4.05c		Erd1 homolog	0.863	251	0.897	241
SPBC106.16		20S proteasome component alpha 4	0.868	153	0.892	196
SPBC27.02c	ask1	DASH complex subunit Ask1	0.860	219	0.900	194

Systematic ID	Gene name	Gene description	CF index screen 1	Cell number	CF index screen 2	Cell number
SPAC16C9.06c	upf1	ATP-dependent RNA helicase Upf1	0.905	203	0.856	240
SPCC1223.04c	set11	lysine methyltransferase	0.861	227	0.899	254
SPCC1884.02	nic1	NiCoT heavy metal ion transporter Nic1	0.824	427	0.936	480
SPBC11G11.03		60S acidic ribosomal protein	0.791	306	0.970	535
SPBC3H7.12		sequence orphan	0.901	255	0.860	289
SPAP27G11.07c		serine/threonine protein kinase	0.880	289	0.881	351
SPCC1919.07		sequence orphan	0.912	373	0.849	390
SPCC1322.02		sequence orphan	0.936	316	0.824	190
SPBC56F2.14	mrpl44	mitochondrial ribosomal protein subunit l44	0.890	277	0.871	259
SPBC1734.11		DNAJ domain protein Mas5	0.790	46	0.971	341
SPCC622.01c		sequence orphan	0.808	417	0.953	284
SPAC664.10	klp2	kinesin-like protein Klp2	0.872	281	0.889	269
SPCC188.13c	dcr1	dicer	0.837	580	0.924	375
SPAC1805.04	nup132	nucleoporin Nup132	0.880	234	0.881	292
SPCC550.15c		ribosome biogenesis protein	0.795	218	0.967	209
SPCC622.15c		double-strand break repair protein	0.853	228	0.909	221
SPBC713.06	adl1	DNA ligase	0.827	1	0.935	368
SPAC2F3.02		ER protein translocation subcomplex subunit	0.870	281	0.892	321
SPAC1002.07c	ats1	N-acetyltransferase Ats1	0.893	272	0.869	243
SPBC23E6.10c		methylthioribose-1-phosphate isomerase	0.819	236	0.943	288
SPCC338.11c	rrg1	methyltransferase	0.879	342	0.883	326
SPAC19A8.01c	sec73	guanyl-nucleotide exchange factor Sec73	0.907	215	0.855	262
SPAC6G9.04	mug79	meiotically upregulated gene Mug79	0.901	215	0.861	235
SPBC215.02	bob1	prefoldin subunit 5	0.856	374	0.907	341
SPCC777.12c		sequence orphan	0.894	224	0.869	261
SPAC13F5.01c	msh1	MutS protein homolog 1	0.876	221	0.887	183
SPCC1393.09c		RWD domain	0.945	478	0.818	409
SPBC25H2.11c		bromodomain protein	0.954	1	0.809	298
SPCC584.11c		Svf1 family protein Svf1	0.818	189	0.946	246
SPCC2H8.05c		sequence orphan	0.896	249	0.867	265
SPAC8C9.04		sequence orphan	0.811	228	0.953	248
SPAC1002.06c	bqt2	bouquet formation protein Bqt2	0.907	266	0.856	308
SPBC83.10		conserved eukaryotic protein	0.867	271	0.897	247
SPAC1071.02		TFIIH regulator	0.801	299	0.963	13
SPAC30C2.02	mmd1	deoxyhypusine hydroxylase	0.849	359	0.915	174
SPBC1604.04		thiamine pyrophosphate transporter	0.878	265	0.887	311
SPAC3G6.02	dss1	mRNA export protein Dss1	0.833	37	0.932	89
SPBC4B4.10c	mug77	autophagy associated protein Atg5	0.836	211	0.929	336
SPAC17G6.08	pep7	prevacuole/endosomal FYVE tethering component Pep7	NaN	0	0.883	242
SPAC23C11.15	pst2	Clr6 histone deacetylase complex subunit Pst2	0.853	253	0.912	505
SPAC23C4.05c		LEA domain protein	0.873	257	0.893	239
SPAC13G6.13		sequence orphan	0.899	296	0.866	371
SPAC13D6.04c	btb3	BTB/POZ domain protein Btb3	0.876	200	0.889	269
SPCC24B10.16c		sequence orphan	0.904	323	0.861	301
SPBC4C3.06		actin cytoskeletal protein Syp1	0.824	265	0.941	217
SPBC1683.06c		uridine ribohydrolase	0.897	403	0.869	578
SPAC323.01c		mitochondrial NADH kinase	0.890	20	0.876	85
SPCC965.09		nitrilase	0.876	216	0.890	277
SPAC10F6.07c	mug94	sequence orphan	0.886	269	0.879	326
SPBC14F5.12c	cbh2	centromere binding protein Cbh2	NaN	0	0.883	325
SPBC3B9.13c	rpp102	60S acidic ribosomal protein Rpp1-2	0.827	327	0.939	377
SPBC1711.09c		SNARE associated Golgi protein	0.901	270	0.865	263
SPAC2F3.01		mannosyltransferase complex subunit	0.891	353	0.875	211
SPAC1952.15c	rec24	meiotic recombination protein Rec24	0.897	262	0.869	252
SPAC8E11.05c		conserved fungal protein	0.836	389	0.931	195
SPCC1259.14c	meu27	S. pombe specific UPF0300 family protein 5	0.878	295	0.889	277
SPAC14C4.04	B22918-2	hypothetical protein	0.815	250	0.952	372
SPBPB10D8.02c		arylsulfatase	0.882	210	0.885	260
SPAP32A8.02		xylose and arabinose reductase	0.950	375	0.817	392
SPBC902.05c	idh2	isocitrate dehydrogenase (NAD+) subunit 2	0.875	194	0.892	246
SPAC1399.02		membrane transporter	0.878	298	0.889	245
SPAC6B12.09	trm10	tRNA m(1)G methyltransferase Trm10	0.839	277	0.928	381
SPAC25A8.01c		fun thirty related protein Fft3	0.818	135	0.949	130
SPBC29B5.04c		conserved fungal protein	0.907	270	0.860	268
SPAC688.13	scn1	TatD DNase family Scn1	0.967	245	0.800	262

Systematic ID	Gene name	Gene description	CF index screen 1	Cell number	CF index screen 2	Cell number
SPBP4H10.12		conserved protein (fungal and bacterial)	0.904	264	0.864	254
SPAC513.03	mfm2	M-factor precursor Mfm2	0.895	294	0.872	376
SPBC31F10.08	mde2	Mde2 protein	0.861	278	0.906	276
SPAC11D3.07c		transcription factor	0.938	450	0.830	406
SPAC926.09c	fas1	fatty acid synthase beta subunit Fas1	0.870	337	0.898	217
SPBP35G2.02		DUF1000 family protein	0.880	194	0.888	265
SPAC57A10.10c	sla1	La protein homolog	0.831	390	0.937	259
SPBC21B10.08c		sequence orphan	0.851	220	0.916	309
SPAC26A3.11		amidohydrolase	0.855	344	0.913	340
SPBC19C7.11		ClC chloride channel	0.928	240	0.840	322
SPBC1709.13c		lysine methyltransferase	0.839	262	0.929	301
SPAC15A10.10	mde6	Muskelin homolog	0.909	260	0.859	329
SPCC1919.13c		conserved eukaryotic protein	0.796	284	0.972	216
SPCC61.05		S. pombe specific multicopy membrane protein family 1	0.860	321	0.909	498
SPAC19B12.09	srp14	signal recognition particle subunit Srp14	0.888	284	0.881	258
SPCC576.13	swc5	chromatin remodeling complex subunit Swc5	0.885	163	0.884	190
SPAC23A1.16c		DUF408 family protein	0.867	194	0.902	1
SPAC12B10.10		sequence orphan	0.907	287	0.862	252
SPBC36.06c	spo9	farnesyl pyrophosphate synthetase	0.900	317	0.869	283
SPBC28F2.02	mep33	mRNA export protein Mep33	0.916	237	0.853	281
SPAC12B10.14c	ppk2	serine/threonine protein kinase Ppk2	0.811	276	0.959	285
SPBC3D6.06c		ribose-phosphate pyrophosphokinase	0.840	256	0.930	261
SPBC17D11.02c		synoviolin homolog	0.843	277	0.927	307
SPAC17H9.13c		glutamate 5-kinase	0.855	206	0.915	3
SPAC3G6.06c	rad2	FEN-1 endonuclease	0.825	270	0.946	199
SPBC1709.19c		NifU-like protein	0.907	292	0.864	339
SPAC823.15	ppa1	minor serine/threonine protein phosphatase Ppa1	0.837	192	0.933	287
SPBC13G1.08c	ash2	Ash2-trithorax family protein	0.847	223	0.924	248
SPAC1782.06c		prohibitin Phb1	0.915	210	0.855	277
SPAC27D7.04	omt2	4-alpha-hydroxytetrahydrobiopterin dehydratase	0.880	315	0.891	320
SPBC3H7.05c		sequence orphan	0.823	214	0.948	188
SPCC126.04c		SAGA complex subunit Sgf73	0.923	247	0.848	207
SPAC4D7.01c	sec71	Sec7 domain	0.877	234	0.894	300
SPAC1B3.07c	vps28	ESCRT I complex subunit Vps28	0.877	261	0.894	240
SPBC16A3.03c	lyn1	sequence orphan	NaN	0	0.885	258
SPCC1902.02	mug72	ketopantoate reductase	0.931	18	0.840	237
SPAC1006.01	psp3	serine protease Psp3	0.920	295	0.852	326
SPBC776.15c		dihydrolipoamide S-succinyltransferase, e2 component of oxoglutarate dehydrogenase complex	0.918	261	0.853	234
SPAC23G3.10c	ssr3	SWI/SNF and RSC complex subunit Ssr3	0.878	246	0.894	369
SPBC16H5.06	rip1	ubiquinol-cytochrome-c reductase complex subunit 5	0.829	336	0.942	385
SPBC2G2.06c	apl1	AP-2 adaptor complex subunit Apl1	0.848	271	0.923	227
SPAC139.02c	oac1	anion transporter	0.892	255	0.879	210
SPCP1E11.03	mug170	arrestin	0.949	187	0.823	303
SPBC8D2.11		sequence orphan	0.803	311	0.969	255
SPBC19G7.17		translocon subunit Sec61 homolog	0.903	264	0.869	238
SPBCPT2R1.02		sequence orphan	0.892	328	0.881	247
SPBC337.07c		carboxypeptidase	0.877	222	0.896	277
SPBC36B7.06c	mug20	sequence orphan	0.955	251	0.818	417
SPAC1782.09c	clp1	Cdc14-related protein phosphatase Clp1/Flp1	0.812	166	0.961	195
SPCC297.05		diacylglycerol binding protein	0.807	212	0.966	220
SPAC16E8.18		sequence orphan	0.895	290	0.878	273
SPAC9.13c	cwf16	splicing factor	0.819	300	0.954	267
SPCC24B10.20		short chain dehydrogenase	0.822	372	0.951	299
SPBP22H7.08	rps1002	40S ribosomal protein S10	0.845	218	0.928	233
SPBC409.03	swi5	Swi5 protein	0.852	257	0.921	256
SPBC16G5.06		sequence orphan	0.875	310	0.899	340
SPCC338.14		adenosine kinase	0.925	314	0.848	148
SPAC23E2.01	fep1	iron-sensing transcription factor Fep1	NaN	0	0.887	51
SPBC365.12c	ish1	LEA domain protein	0.863	140	0.911	407
SPCC1259.09c		pyruvate dehydrogenase protein x component	0.887	294	0.887	700
SPBC14F5.09c	ade8	adenylosuccinate lyase Ade8	0.920	211	0.854	154
SPBC713.03		D-lactate dehydrogenase (cytochrome)	0.922	295	0.852	194
SPAC11D3.09		agmatinase	0.830	332	0.945	410
SPCC1919.11	mug137	BAR adaptor protein	0.856	348	0.919	276

Systematic ID	Gene name	Gene description	CF index screen 1	Cell number	CF index screen 2	Cell number
SPBP4H10.08	qcr10	ubiquinol-cytochrome-c reductase complex subunit Qcr10	0.876	269	0.899	282
SPAC27F1.10		sequence orphan	0.886	349	0.889	439
SPAC22H10.11c		sequence orphan	0.820	399	0.955	255
SPCC1450.16c		triacylglycerol lipase	0.857	273	0.918	367
SPAC823.16c	mug179	WD repeat protein Mug179	0.898	26	0.878	182
SPAC806.08c	mod21	gamma tubulin complex subunit Mod21	0.873	247	0.902	252
SPCC1235.11		conserved eukaryotic protein	0.921	217	0.854	130
SPBC16C6.10	chp2	chromodomain protein 2	0.879	278	0.897	396
SPCC162.06c		vacuolar sorting protein Vps60	0.834	259	0.942	278
SPAC1687.21		phosphoglycerate mutase family	0.873	245	0.903	295
SPAC16.04	dus3	tRNA dihydrouridine synthase Dus3	0.835	435	0.941	317
SPCC4G3.03		WD repeat protein	0.924	317	0.853	323
SPAC823.10c		mitochondrial carrier with solute carrier repeats	0.845	228	0.931	294
SPBC11C11.07	rpl1801	60S ribosomal protein L18	0.935	363	0.842	330
SPBC2G2.14		sequence orphan	0.870	312	0.907	205
SPCC1620.03	mug163	sequence orphan	0.896	274	0.880	290
SPBC2D10.14c	myo51	myosin type V	0.871	284	0.906	227
SPCC330.11	btb1	BTB/POZ domain protein Btb1	0.842	237	0.935	247
SPBC25B2.08		sequence orphan	0.890	285	0.887	445
SPBC1348.02		S. pombe specific 5Tm protein family	0.847	309	0.931	304
SPBC776.06c		spindle pole body interacting protein	0.855	219	0.923	396
SPAC1296.05c		cyclin L family cyclin	0.911	396	0.868	161
SPBC28E12.06c	lvs1	beige protein homolog	0.931	179	0.848	246
SPBP35G2.08c	air1	TRAMP complex subunit	0.858	291	0.920	207
SPCC417.03		sequence orphan	0.873	236	0.905	286
SPBC3B8.08		Sjogrens syndrome/scleroderma autoantigen 1 family	0.864	301	0.914	301
SPCC1020.01c	pma2	P-type proton ATPase Pma2	0.813	279	0.966	165
SPBC21B10.02		sequence orphan	NaN	0	0.889	382
SPBC1105.01	rrp12	rRNA processing protein Rrp12	0.824	576	0.955	309
SPAC139.03		transcription factor	0.825	279	0.954	297
SPBC2F12.15c		palmitoyltransferase	0.971	46	0.807	91
SPCC18B5.07c	nup61	nucleoporin Nup61	0.861	319	0.917	374
SPAC17A2.07c		sequence orphan	0.823	246	0.956	205
SPBC428.10		sequence orphan	0.893	279	0.886	165
SPAC1002.05c	jmj2	histone demethylase Jmj2	0.880	292	0.899	277
SPBC18H10.18c		sequence orphan	0.875	290	0.904	265
SPAC732.02c		6-phosphofructo-2-kinase	0.874	215	0.905	311
SPBC17D11.08		WD repeat protein, human WDR68 family	0.887	297	0.892	419
SPCC794.01c		glucose-6-phosphate 1-dehydrogenase	0.862	321	0.917	205
SPAC14C4.16	dad3	DASH complex subunit Dad3	0.900	355	0.880	477
SPBC713.08	tom13	mitochondrial TOM complex subunit Tom13	0.838	89	0.941	328
SPAC1952.02		ribosome biogenesis protein	0.825	293	0.954	239
SPBP4H10.10		protease	0.893	325	0.887	439
SPCC1450.08c	wtf16	wtf element Wtf16	0.896	446	0.884	342
SPAC23H3.06	apl6	AP-3 adaptor complex subunit Apl6	0.891	89	0.889	95
SPCC191.09c	gst1	glutathione S-transferase Gst1	0.854	255	0.926	266
SPAC637.07	moe1	translation initiation factor eIF3d Moe1	NaN	0	0.890	51
SPCC1223.15c	spc19	DASH complex subunit Spc19	0.848	308	0.932	362
SPAC23H3.14		LAlv9 family protein	0.907	292	0.873	204
SPCC1235.02	bio2	biotin synthase	0.917	242	0.863	282
SPAC1952.08c		pyridoxamine 5-phosphate oxidase	0.887	228	0.893	183
SPAC3A11.14c	pkl1	kinesin-like protein Pkl1	0.906	307	0.874	285
SPAC31A2.14		WD repeat protein, human WRDR48 family	0.861	261	0.919	300
SPAC1786.02		phospholipase	0.893	346	0.888	258
SPBC32C12.03c	ppk25	serine/threonine protein kinase Ppk25	0.844	189	0.937	306
SPAC4F8.10c	stg1	SM22/transgelin-like actin modulating protein Stg1	0.842	327	0.939	297
SPCC23B6.03c	tel1	ATM checkpoint kinase	0.825	284	0.956	230
SPAC1006.04c	mcp3	sequence orphan	0.874	274	0.907	299
SPAC22H12.02	tfg3	transcription factor TFIIF complex subunit Tfg3	NaN	0	0.891	226
SPBC36B7.05c		phosphatidylinositol(3)-phosphate binding protein	0.862	236	0.919	208
SPAC1420.01c		DUF1752 family protein	0.880	272	0.901	300
SPAC1786.01c		triacylglycerol lipase	0.869	314	0.913	247
SPAC977.14c		aldo/keto reductase, unknown biological role	0.882	249	0.900	263
SPCC1322.01		3-5 exonuclease for RNA 3 ss-tail	0.843	10	0.938	4
SPAC3A12.08		conserved fungal protein	0.888	308	0.894	292

Systematic ID	Gene name	Gene description	CF index screen 1	Cell number	CF index screen 2	Cell number
SPAC8E11.07c	alp31	tubulin specific chaperone cofactor A	0.865	198	0.917	55
SPAC13G6.03	gpi7	GPI anchor biosynthesis protein Gpi7	0.809	254	0.973	270
SPCC1259.04		sequence orphan	0.861	9	0.921	388
SPAC3C7.02c		protein kinase inhibitor	0.828	217	0.954	262
SPCC569.02c		S. pombe specific UPF0321 family protein 2	0.922	320	0.860	263
SPBP4H10.03	oxa102	mitochondrial inner membrane translocase Oxa102	0.889	95	0.893	132
SPAC4G8.13c	prz1	transcription factor Prz1	0.891	265	0.892	217
SPAC688.04c	gst3	glutathione S-transferase	0.841	275	0.941	307
SPBC725.05c		nucleotide pyrophosphatase	0.846	266	0.937	191
SPCC16C4.13c	rpl1201	60S ribosomal protein L12.1/L12A	0.893	448	0.890	520
SPAC1527.02	sft2	Golgi transport protein Sft2	0.924	264	0.860	359
SPAC1687.08		sequence orphan	0.840	243	0.943	258
SPAC26H5.03		WD repeat protein Cac2	0.884	325	0.899	266
SPAC607.02c		conserved fungal protein	0.972	296	0.812	291
SPBC18H10.13	rps1402	40S ribosomal protein S14	0.849	253	0.935	274
SPBC1861.02	abp2	ARS binding protein Abp2	0.845	268	0.939	357
SPCC594.06c		SNARE Vam7	0.833	133	0.951	168
SPCC825.05c		splicing coactivator SRRM1	0.840	262	0.944	278
SPAC1002.03c	gls2	glucosidase II Gls2	0.872	248	0.912	275
SPAPB1A10.07c		sphingolipid biosynthesis protein	0.817	118	0.967	179
SPBC31F10.07		cortical component Lsb5	0.864	208	0.921	341
SPAC23G3.07c	snf30	SWI/SNF complex subunit Snf30	0.875	238	0.910	243
SPCC417.06c	ppk35	serine/threonine protein kinase Ppk35	0.891	303	0.894	378
SPAC3C7.05c	mug191	alpha-1,6-mannanase	0.818	305	0.967	291
SPAC8C9.07		rRNA processing protein Fyv7	0.885	336	0.899	259
SPCC1442.03		ATP-Mg/Pi carrier homolog	0.954	481	0.831	484
SPAC26F1.05	mug106	sequence orphan	0.869	310	0.916	264
SPAC6F6.11c		pyridoxal kinase	0.832	394	0.953	270
SPCC663.03	pmd1	leptomycin efflux transporter Pmd1	0.867	202	0.918	170
SPBC14F5.10c		ubiquitin-protein ligase E3	0.823	287	0.963	351
SPAC1851.02		1-acylglycerol-3-phosphate O-acyltransferase	0.917	320	0.869	253
SPAC23C4.16c	atg15	triacylglycerol lipase Atg15	0.876	243	0.910	333
SPAC57A10.08c		esterase/lipase	0.839	248	0.947	282
SPAC5D6.01	rps2202	40S ribosomal protein S15a	0.901	286	0.885	283
SPBC947.01		AAA family ATPase Sur2	0.900	244	0.886	188
SPAC869.05c		sulfate transporter	0.860	228	0.926	225
SPCC4G3.15c		CCR4-Not complex subunit Not2	0.879	304	0.907	247
SPBPB21E7.05		sequence orphan	0.836	238	0.950	292
SPBC26H8.11c		conserved fungal protein	0.896	213	0.891	271
SPAC23C11.14	zhf1	zinc ion transporter Zhf1	0.839	178	0.948	366
SPAPB1A11.01		membrane transporter	0.954	248	0.833	302
SPAC31G5.04		homoisocitrate dehydrogenase	0.895	289	0.892	215
SPCC24B10.07	gad8	serine/threonine protein kinase Gad8	0.827	155	0.960	272
SPAC1F5.07c	hem14	protoporphyrinogen oxidase	0.912	209	0.875	279
SPAC1486.04c	alm1	medial ring protein Alm1	0.942	374	0.845	337
SPAC959.07	rps403	40S ribosomal protein S4	0.840	230	0.947	232
SPBC2D10.07c		mitochondrial inner membrane peptidase complex catalytic subunit	0.919	337	0.868	4
SPAC5H10.07		sequence orphan	0.835	274	0.953	351
SPAC521.04c		calcium permease	0.881	208	0.907	218
SPAC926.05c		diphthamide biosynthesis protein Dph4	0.838	357	0.950	256
SPAC31G5.12c	maf1	repressor of RNA polymerase III Maf1	NaN	0	0.894	382
SPCC736.07c		cell polarity protein	0.872	201	0.917	239
SPBC947.11c	elg1	DNA replication factor C complex subunit Elg1	0.844	297	0.944	290
SPCC24B10.02c		NAD/NADH kinase	0.887	194	0.901	267
SPAC3G6.13c	rpl4101	60S ribosomal protein L41	0.885	293	0.904	259
SPAC6G9.10c	sen1	splicing endonuclease Sen1	0.858	428	0.930	328
SPAC23C11.02c	rps23	40S ribosomal protein S23	0.855	400	0.933	413
SPAC1805.03c	trm13	tRNA 2-O-methyltransferase Trm13	0.820	237	0.969	227
SPAC20G8.07c	erg2	C-8 sterol isomerase Erg2	0.860	304	0.929	332
SPCC5E4.10c		sequence orphan	0.821	240	0.968	281
SPBC1773.06c		alcohol dehydrogenase	0.883	314	0.906	293
SPBC1604.16c		RNA-binding protein	0.921	450	0.868	406
SPCC1795.10c		Sed5 Vesicle Protein Svp26	0.910	590	0.879	356
SPAC22A12.07c	ogm1	protein O-mannosyltransferase Ogm1	0.876	152	0.913	162
SPAC23H3.08c	bub3	mitotic spindle checkpoint protein Bub3	0.842	321	0.948	350
SPAC9E9.14	vps24	vacuolar sorting protein Vps24	0.852	359	0.938	402

Systematic ID	Gene name	Gene description	CF index screen 1	Cell number	CF index screen 2	Cell number
SPBC887.06c	snx3	sorting nexin Snx3	0.905	298	0.885	210
SPAC13A11.04c	ubp8	ubiquitin C-terminal hydrolase Ubp8	0.848	459	0.942	406
SPAC21E11.04	ppr1	L-azetidine-2-carboxylic acid acetyltransferase	0.868	284	0.922	311
SPBC887.17		uracil permease	0.872	245	0.918	204
SPBC16H5.14c		short chain dehydrogenase DHRS family	0.849	211	0.941	256
SPAC1F5.03c		FAD-dependent oxidoreductase	0.898	229	0.893	317
SPAC31A2.02	trm112	tRNA (guanine-N2-)-methyltransferase regulatory subunit Trm112	0.915	264	0.875	263
SPCC4B3.15	mid1	medial ring protein Mid1	0.879	130	0.911	224
SPAC20H4.08		phosphatase activator	0.834	231	0.956	265
SPAC9G1.04	oxa101	mitochondrial inner membrane translocase Oxa101	0.899	240	0.891	246
SPBC2D10.20	ubc1	ubiquitin conjugating enzyme Ubc1	0.911	142	0.880	263
SPCC4G3.09c	gyp3	GTPase activating protein Gyp3	0.962	546	0.829	298
SPAC12B10.13		CTLH domain	0.898	228	0.893	201
SPAPB17E12.08		N-glycosylation protein	0.930	201	0.861	291
SPBC530.08		transcription factor	0.870	221	0.921	247
SPAC10F6.05c	ubc6	ubiquitin conjugating enzyme Ubc6	0.850	291	0.941	184
SPCC16A11.04	snx12	sorting nexin Snx12	0.913	195	0.879	243
SPAC3A12.12	atp11	F1-ATPase chaperone Atp11	0.905	243	0.886	292
SPAC19B12.10	sst2	human amsh protein homolog	0.912	235	0.880	206
SPBC28F2.11		INO80 complex subunit	0.928	434	0.863	335
SPCC4G3.19	alp16	gamma tubulin complex ubunit Alp16	0.845	208	0.947	167
SPAC3C7.01c		inositol polyphosphate phosphatase	0.877	307	0.915	349
SPCC663.10		methyltransferase, DUF1613 family	0.864	278	0.927	213
SPBC725.12	mug118	sequence orphan	0.833	271	0.959	228
SPAC1527.01	mok11	alpha-1,3-glucan synthase Mok11	0.910	199	0.882	265
SPAP27G11.08c	meu32	sequence orphan	0.880	294	0.912	258
SPAC3C7.10	pex13	peroxin-13	0.868	188	0.924	168
SPAC6F12.03c	fsv1	SNARE Fsv1	0.848	312	0.945	327
SPCC1020.05		phosphoprotein phosphatase	0.824	244	0.969	297
SPCC790.02	pep3	ubiquitin-protein ligase E3	NaN	0	0.896	2
SPBC530.13		cyclin Ctk2	0.824	249	0.969	293
SPBC16C6.03c		sequence orphan	0.878	287	0.915	335
SPBC776.16		sequence orphan	0.861	200	0.931	201
SPCC1223.03c	gut2	glycerol-3-phosphate dehydrogenase Gut2	0.879	322	0.914	368
SPBC530.01	gyp1	GTPase activating protein Gyp1	0.917	302	0.875	306
SPAC19G12.05		mitochondrial citrate transporter	0.981	223	0.812	316
SPBC31F10.15c	atp15	F0-ATPase epsilon subunit	0.844	267	0.949	414
SPAC17G8.10c	dma1	mitotic spindle checkpoint protein Dma1	0.915	337	0.878	375
SPBC2A9.13		sequence orphan	0.875	254	0.919	362
SPBC1778.01c	zuo1	zuotin	0.892	115	0.901	12
SPBC2G2.13c		deoxycytidylate deaminase	0.845	199	0.948	244
SPAC5D6.12		sequence orphan	0.973	1	0.821	220
SPBC3D6.13c		protein disulfide isomerase	0.849	294	0.944	167
SPAC20G4.08		sequence orphan	0.897	243	0.898	233
SPAPB1A11.02		esterase/lipase	0.909	293	0.885	387
SPAC1834.10c		sequence orphan	0.849	262	0.945	283
SPAC4H3.04c		UPF0103 family	0.880	283	0.914	237
SPBC14F5.07		ER-localized ubiquitin ligase	0.844	197	0.950	350
SPAC29B12.10c		OPT oligopeptide transporter family	0.902	333	0.893	324
SPAC22G7.07c		mRNA (N6-adenosine)-methyltransferase	0.840	278	0.955	363
SPAC18G6.09c		sequence orphan	0.859	233	0.936	218
SPAC3G6.03c		Maf-like protein	0.850	297	0.945	289
SPBP8B7.13		conserved fungal protein	0.921	188	0.874	227
SPBC2D10.15c		peptidyl-tRNA hydrolase Pth1	0.867	243	0.929	417
SPBC23G7.08c	rga7	GTPase activating protein Rga7	0.848	206	0.948	277
SPBC2G2.09c	crs1	meiosis specific cyclin Crs1	0.884	245	0.912	327
SPBC4C3.09		acetylglucosaminyltransferase	0.906	295	0.890	215
SPBC56F2.01	pof12	F-box protein Pof12	0.921	1	0.875	3
SPBC13G1.02		mannose-1-phosphate guanyltransferase	0.872	89	0.924	333
SPCC18.01c	adg3	beta-glucosidase Adg3 (predicted)	0.896	227	0.900	252
SPAC6B12.03c		HbrB family protein	0.834	256	0.962	294
SPAC630.15	mug177	sequence orphan	0.833	218	0.963	294
SPAC22H10.09		sequence orphan	NaN	0	0.898	14
SPBP4H10.18c		sequence orphan	0.837	245	0.959	313
SPAC24H6.08		sequence orphan	0.857	251	0.940	336
SPBC21.03c		DUF55 family protein	0.941	270	0.855	313

Systematic ID	Gene name	Gene description	CF index screen 1	Cell number	CF index screen 2	Cell number
SPAC521.05	rps802	40S ribosomal protein S8	0.908	381	0.888	281
SPCC830.06		calcineurin regulatory subunit	0.883	124	0.913	166
SPAC27D7.02c		conserved eukaryotic protein	0.898	203	0.899	312
SPBC1685.07c		amino acid transporter	0.860	219	0.938	261
SPBC16E9.08	mcp4	sequence orphan	0.898	317	0.899	243
SPBC15D4.13c		sequence orphan	0.881	203	0.916	191
SPAC869.06c		cation binding protein	0.876	354	0.922	422
SPBC1198.11c	reb1	RNA polymerase I transcription termination factor Reb1	0.899	130	0.899	225
SPAC25H1.06		histone acetyltransferase complex subunit	0.858	291	0.940	350
SPCC31H12.05c	sds21	serine/threonine protein phosphatase Sds21	0.884	363	0.914	249
SPAC3F10.18c	rpl4102	60S ribosomal protein L41	0.908	382	0.890	337
SPAPB18E9.04c		sequence orphan	0.896	271	0.901	351
SPBC15C4.04c		amino acid permease, unknown 10	0.844	315	0.953	380
SPAC2F3.18c		sequence orphan	0.835	258	0.963	246
SPAC20G4.03c	hri1	eIF2 alpha kinase Hri1	0.876	264	0.922	238
SPBC27.03	meu25	sequence orphan	0.909	313	0.889	322
SPAC926.06c		leucine-rich repeat protein, unknown	0.889	227	0.909	420
SPBC685.02		conserved eukaryotic protein	0.896	285	0.902	299
SPAC13C5.05c		N-acetylglucosamine-phosphate mutase	0.915	213	0.883	260
SPAC16E8.05c	mde1	sequence orphan	0.832	99	0.967	77
SPCC550.10	meu8	betaine aldehyde dehydrogenase	0.913	309	0.885	335
SPBC1703.12	ubp9	ubiquitin C-terminal hydrolase Ubp9	0.891	291	0.907	391
SPBC887.15c		sphingosine hydroxylase	0.860	121	0.939	260
SPAC57A10.02	cdr2	GIN4 family protein kinase Cdr2	0.892	180	0.907	182
SPCC965.14c		cytosine deaminase	0.890	245	0.909	259
SPCC1223.05c	rpl3702	60S ribosomal protein L37	0.876	434	0.923	363
SPAC869.04		formamidase-like protein	0.867	272	0.932	264
SPAC1039.08		serine acetyltransferase	0.836	311	0.964	245
SPAC607.09c	btn1	battenin CLN3 family protein	0.900	211	0.900	358
SPAC11D3.15		oxoprolinase	0.904	316	0.896	285
SPAC29E6.07		sequence orphan	0.912	336	0.887	262
SPBC1271.15c		translation initiation factor IF-2Mt	0.934	192	0.865	22
SPBC13E7.07		sequence orphan	0.886	226	0.913	231
SPBC1709.01	chs2	chitin synthase homolog Chs2	0.862	305	0.938	390
SPAC589.05c		conserved eukaryotic protein	0.906	298	0.894	251
SPCC1183.04c	pet127	mitochondrial membrane protein Pet127	0.850	237	0.950	350
SPAC3A11.03		methyltransferase	0.851	254	0.949	254
SPCC16A11.01		conserved fungal protein	0.847	352	0.953	242
SPAC664.07c	rad9	checkpoint clamp complex protein Rad9	NaN	0	0.900	286
SPAC19G12.09		NADH/NADPH dependent indole-3-acetaldehyde reductase AKR3C2	0.863	329	0.937	296
SPBC2G2.05	rpl1603	60S ribosomal protein L13/L16	0.908	293	0.892	239
SPBC17A3.03c		phosphoprotein phosphatase	0.914	354	0.886	173
SPAC17C9.05c	pmc3	mediator complex subunit Pmc3	0.869	227	0.931	267
SPAC26F1.02		pinin homologue	0.926	277	0.874	296
SPCC663.04	rpl39	60S ribosomal protein L39	0.908	400	0.892	384
SPBC23G7.10c		NADH-dependent flavin oxidoreductase	0.872	276	0.929	302
SPBC11G11.05	rpa34	DNA-directed RNA polymerase I complex subunit Rpa34	0.872	220	0.928	432
SPBC36.10		mitochondrial intermembrane space protein sorting protein	0.876	198	0.925	174
SPAC1486.02c	ucp14	UBA domain protein Ucp14	0.884	407	0.917	165
SPCC1259.05c	cox9	cytochrome c oxidase subunit VIIa	0.966	432	0.835	431
SPCC24B10.10c		mitochondrial outer membrane ATPase Msp1	0.899	225	0.902	302
SPCC1442.07c		ubiquitin/metalloprotease fusion protein	0.890	219	0.911	269
SPBC27B12.14		mitochondrial membrane protein complex assembly protein	0.849	239	0.953	191
SPAC25G10.03	zip1	transcription factor Zip1	0.990	4	0.811	2
SPAC4H3.03c		glucan 1,4-alpha-glucosidase	0.828	326	0.973	314
SPBC1271.08c		sequence orphan	0.839	282	0.962	278
SPCC297.04c	set7	histone lysine methyltransferase Set7	0.836	223	0.965	368
SPAP27G11.05c	vps41	vacuolar protein sorting-associated protein Vps41	0.927	213	0.875	206
SPAC1F12.10c		NADPH-hemoprotein reductase	0.947	482	0.855	293
SPAC607.10	spo3	sporulation protein Spo3	0.881	259	0.921	237
SPBC31A8.01c	cwl1	reticulon-like protein	0.877	254	0.924	265
SPBC685.07c	rpl2701	60S ribosomal protein L27	0.916	340	0.886	371

Systematic ID	Gene name	Gene description	CF index screen 1	Cell number	CF index screen 2	Cell number
SPAC17G6.06	rps2401	40S ribosomal protein S24	0.926	724	0.876	357
SPCC1020.03		mitochondrial iron ion transporter	0.967	330	0.835	312
SPAC12B10.05		metallopeptidase	0.894	211	0.908	223
SPCC1739.04c		sequence orphan	0.885	319	0.917	334
SPAC19G12.04		ureidoglycolate hydrolase	0.886	220	0.916	245
SPAC16E8.08		sequence orphan	0.851	295	0.952	241
SPBC1105.04c	cbp1	CENP-B homolog	0.898	252	0.905	150
SPBC1683.10c	pcl1	ferrous iron transporter Pcl1	0.889	315	0.914	297
SPBC691.05c		membrane transporter	0.873	329	0.929	224
SPAC14C4.11		polyphosphate synthetase	0.828	139	0.975	292
SPAC4G9.05	mpf1	meiotic PUF family protein 1	0.851	324	0.952	227
SPBC21C3.18	spo4	serine/threonine protein kinase Spo4	0.882	202	0.921	278
SPAP7G5.05	rpl1002	60S ribosomal protein L10	0.908	276	0.895	442
SPAC9E9.12c	ybt1	ABC transporter Ybt1	0.910	385	0.893	292
SPCC970.01	rad16	DNA repair endonuclease XPF	0.905	276	0.898	260
SPAC5D6.05	39702.000	mediator complex subunit Pmc6	0.952	365	0.851	257
SPAC1610.04	mug99	meiotically upregulated gene Mug99	0.884	461	0.919	429
SPAPB1A10.13		sequence orphan	0.917	337	0.886	243
SPBC1271.12	kes1	oxysterol binding protein	0.920	272	0.883	315
SPAC1093.03		polyphosphoinositide phosphatase	0.868	771	0.936	478
SPCC550.14	vgl1	vigilin	0.862	291	0.942	452
SPAC1093.06c	dhc1	dynein heavy chain	0.876	415	0.927	706
SPAC12G12.13c	cid14	poly(A) polymerase Cid14	0.898	219	0.906	359
SPBC428.11		homocysteine synthase	0.896	224	0.908	295
SPBC32F12.01c		inositol phosphosphingolipid phospholipase C	0.941	205	0.863	281
SPAC683.02c		zf-CCHC type zinc finger protein	0.903	331	0.902	304
SPAP27G11.15	slx1	structure-specific endonuclease catalytic subunit	0.905	299	0.899	306
SPAC3F10.17		ribosome biogenesis protein Ltv1	NaN	0	0.902	365
SPBC1D7.03	mug80	cyclin Clg1	0.882	204	0.923	244
SPBC8D2.12c		mitochondrial DNA binding protein	0.881	228	0.924	205
SPBC32H8.05		conserved fungal protein	0.904	342	0.901	221
SPCC338.02	mug112	sequence orphan	0.916	297	0.889	304
SPAC4H3.13		transcription factor Pcc1	NaN	0	0.902	1
SPAC19A8.03		phosphatidylinositol-3-phosphatase	0.910	394	0.895	322
SPAC6C3.04	cit1	citrate synthase	0.913	278	0.892	300
SPBC16D10.11c	rps1801	40S ribosomal protein S18	0.926	450	0.879	271
SPBP23A10.14c	ell1	RNA polymerase II transcription elongation factor SpELL	0.858	211	0.947	254
SPBC30D10.14		dienelactone hydrolase family	0.836	215	0.969	191
SPAC959.08	rpl2102	60S ribosomal protein L21	0.880	38	0.925	126
SPCC1393.05		sequence orphan	0.883	471	0.922	464
SPBC4B4.02c	nca2	mitochondrial protein Nca2	0.903	304	0.903	274
SPAC26A3.07c	rpl1101	60S ribosomal protein L11	0.921	292	0.885	277
SPAC25A8.03c		conserved protein (broad species distribution)	0.894	286	0.911	258
SPAC20G8.02		phospholipase	0.891	280	0.915	222
SPAC1327.01c		transcription factor	0.863	139	0.942	93
SPBC23E6.02		ATP-dependent DNA helicase	0.886	228	0.919	256
SPAC1805.01c	ppk6	serine/threonine protein kinase Ppk6	0.884	262	0.922	304
SPAC1071.09c		DNAJ domain protein, DNAJC9 family	0.879	217	0.927	260
SPBC32F12.02	rec14	recombination protein Rec14	0.895	130	0.911	326
SPAC589.12		cell wall organization membrane protein	0.915	240	0.891	284
SPCC757.11c		membrane transporter	0.900	303	0.906	287
SPBC2G5.04c		COPII-coated vesicle component Erv41/46	0.891	417	0.915	299
SPAC12G12.09		sequence orphan	0.966	380	0.840	356
SPBC1A4.04		sequence orphan	0.871	166	0.935	123
SPCC1281.08	wtf11	wtf element Wtf11	0.909	299	0.898	278
SPBC577.12	mug71	endoribonuclease	0.902	276	0.905	320
SPAC1635.01		voltage-dependent anion-selective channel	0.899	179	0.907	307
SPAC13G6.02c	rps101	40S ribosomal protein S3a	0.885	330	0.922	302
SPAC140.02	gar2	GAR family	0.922	296	0.885	343
SPBC2G5.06c	hmt2	sulfide-quinone oxidoreductase	NaN	0	0.903	299
SPCC1795.03	gms1	UDP-galactose transporter Gms1	0.933	237	0.874	278
SPBC902.06	mto2	MT organizer Mto2	0.908	357	0.899	210
SPBC2A9.03		conserved protein (fungal and plant)	0.904	277	0.903	463
SPBC106.08c	mug2	DUF1773 family protein 1	0.876	305	0.931	269

Systematic ID	Gene name	Gene description	CF index screen 1	Cell number	CF index screen 2	Cell number
SPBC25H2.03		vacuolar protein involved in phosphoinositide metabolism	0.881	365	0.926	470
SPBC3D6.02	but2	neddylation pathway protein But2	0.893	227	0.914	205
SPCC338.12		protease inhibitor	0.904	5	NaN	0
SPAP8A3.02c		2 OG-Fe(II) oxygenase superfamily	0.855	273	0.952	259
SPCC24B10.22		mitochondrial DNA polymerase gamma catalytic subunit	0.961	424	0.846	304
SPAC3H1.08c		DUF1640 family protein	0.920	299	0.887	258
SPBC8E4.04		aldo/keto reductase involved in pentose catabolism	0.882	260	0.925	357
SPBC1198.08		dipeptidase Dug1	0.844	333	0.964	276
SPAC10F6.06	vip1	RNA-binding protein Vip1	0.904	436	0.903	498
SPAC1F5.05c		sequence orphan	0.897	207	0.910	219
SPAC977.11		conserved fungal protein	0.907	264	0.900	283
SPAC1002.17c	urg2	uracil phosphoribosyltransferase	0.954	330	0.853	214
SPAC637.10c	rpn10	19S proteasome regulatory subunit Rpn10	0.931	247	0.877	206
SPBC26H8.03	cho2	phosphatidylethanolamine N-methyltransferase Cho2	0.847	141	0.961	4
SPAC30C2.06c	dml1	mitochondrial genome maintenance protein	0.903	301	0.905	174
SPBC725.07	pex5	peroxisomal targeting signal receptor	0.887	243	0.921	219
SPBC16A3.13	meu7	alpha-amylase homolog Aah4	0.847	295	0.961	331
SPAC23C4.03		haspin related kinase	0.909	252	0.899	282
SPBC16A3.16		mitochondrial inner membrane protein involved in cytochrome c oxidase assembly Pet191	0.846	84	0.963	226
SPCC364.07		D-3 phosphoglycerate dehydrogenase	0.899	213	0.909	195
SPAC15E1.02c		DUF1761 family protein	0.838	249	0.970	296
SPBC3D6.04c	mad1	mitotic spindle checkpoint protein Mad1	0.856	219	0.952	263
SPAC694.02		DEAD/DEAH box helicase	0.924	227	0.885	230
SPAC7D4.06c	alg3	dolichol-P-Man dependent alpha(1-3) mannosyltransferase Alg3	0.852	230	0.956	205
SPBC1271.01c	pof13	F-box protein Pof13	0.895	356	0.914	273
SPAC16C9.02c		S-methyl-5-thioadenosine phosphorylase	0.910	588	0.899	397
SPAC23D3.03c		GTPase activating protein	0.927	261	0.882	243
SPAC12B10.09		S-adenosylmethionine transporter	0.877	210	0.932	524
SPBC56F2.08c		RNA-binding protein	0.855	281	0.954	276
SPAC1687.23c		sequence orphan	0.884	307	0.925	238
SPAC890.07c	rmt1	type I ribosomal protein arginine N-methyltransferase Rmt1	0.849	274	0.960	307
SPACUNK4.07c	cta4	P-type ATPase, calcium transporting Cta4	0.841	263	0.968	303
SPBC1539.07c		glutathione-dependent formaldehyde dehydrogenase	0.915	240	0.894	325
SPAC19A8.08	upf2	nonsense-mediated decay protein Upf2	0.849	266	0.961	998
SPBC1685.11	rlp1	RecA family ATPase Rlp1	0.882	295	0.927	246
SPAC13G7.05		acyl-coA-sterol acyltransferase	0.852	254	0.957	265
SPBC15D4.06		NatC N-acetyltransferase complex catalytic subunit	0.909	192	0.900	136
SPBC1271.10c		membrane transporter	0.926	619	0.884	285
SPAC13C5.07	rad32	Rad32 nuclease	0.934	243	0.876	258
SPAC652.01		conserved eukaryotic protein	0.898	72	0.912	306
SPBC1773.13		aromatic aminotransferase	0.873	305	0.937	273
SPBC577.05c	rec27	meiotic recombination protein Rec27	0.862	412	0.948	317
SPBC839.04	rpl803	60S ribosomal protein L8	0.878	339	0.932	320
SPAC3C7.04		transcription factor	0.920	342	0.890	272
SPAC27E2.09	mak2	histidine kinase Mak2	0.851	164	0.959	221
SPAC11D3.13		ThiJ domain protein	0.848	242	0.963	319
SPBPB21E7.04c		S-adenosylmethionine-dependent methyltransferase	0.865	342	0.945	268
SPCC1620.13		phosphoglycerate mutase family	0.905	318	0.906	462
SPBC11B10.05c	rsp1	random septum position protein Rsp1	0.851	386	0.960	266
SPAC9E9.08	rad26	ATRIP	0.914	571	0.897	560
SPAC6G9.16c		sequence orphan	0.910	286	0.901	286
SPBC691.01		palmitoyltransferase	0.882	176	0.929	191
SPBC18H10.11c		conserved fungal protein	0.881	211	0.930	222
SPCC1322.06	kap113	karyopherin Kap113	0.895	259	0.916	269
SPAC13G7.07	arb2	argonaute binding protein 2	0.919	406	0.893	344
SPAC17G6.05c		Rhophilin-2 homolog	0.901	193	0.910	217
SPAC4G9.16c	rpl901	60S ribosomal protein L9	0.864	262	0.948	305
SPCC330.19c		sequence orphan	0.919	307	0.892	270
SPBC947.09		ThiJ domain protein	0.901	275	0.910	260

Systematic ID	Gene name	Gene description	CF index screen 1	Cell number	CF index screen 2	Cell number
SPBC23G7.13c		urea transporter	0.895	317	0.916	179
SPBC3D6.05	ptp4	phosphatidate cytidylyltransferase Ptp4	0.864	212	0.948	256
SPAC1420.03	rpn501	19S proteasome regulatory subunit Rpn501	0.918	495	0.893	418
SPAC19A8.02		transcriptional coactivator	0.894	248	0.918	264
SPCC24B10.03		sequence orphan	0.873	346	0.938	231
SPBP8B7.31		acid phosphatase	0.840	321	0.972	286
SPCC24B10.17	emp24	COPII-coated vesicle component Emp24	0.908	441	0.904	388
SPCC1442.15c	cox18	mitochondrial inner membrane protein Cox18	0.927	315	0.885	261
SPBC1198.09	ubc16	ubiquitin conjugating enzyme Ubc16	0.874	235	0.938	246
SPBC725.09c	hob3	BAR adaptor protein Hob3	NaN	0	0.906	55
SPAC11E3.10		VanZ-like family protein	0.939	434	0.873	400
SPCC553.03	pex1	AAA family ATPase Pex1	0.887	287	0.926	298
SPAC6G9.12	cfr1	Chs five related protein Cfr1	0.881	213	0.931	333
SPCC1020.11c		DUF786 family protein	0.892	383	0.921	346
SPBC19C2.04c	ubp11	ubiquitin C-terminal hydrolase Ubp11	0.882	247	0.931	324
SPAC4G9.09c	arg11	N-acetyl-gamma-glutamyl-phosphate reductase/acetylglutamate kinase	NaN	0	0.906	3
SPAC23C11.07		sequence orphan	0.911	329	0.901	328
SPAC1002.01		conserved fungal protein	0.882	258	0.930	264
SPBC30B4.04c	sol1	SWI/SNF complex subunit Sol1	0.862	282	0.951	313
SPCC895.07	alp14	Mad2-dependent spindle checkpoint component	0.845	172	0.968	210
SPAC22H12.01c	mug35	sequence orphan	0.889	413	0.924	263
SPAC823.09c		L-asparaginase	0.885	205	0.928	235
SPAC11E3.06	map1	MADS-box transcription factor Map1	0.941	361	0.872	313
SPAC1B3.15c		membrane transporter	0.898	273	0.915	306
SPBC15C4.05		ATP-dependent RNA/DNA helicase	0.886	181	0.927	240
SPAC688.14		lysine methyltransferase	0.915	224	0.898	274
SPAC3F10.05c	mug113	DUF1766 family protein	0.851	411	0.963	243
SPCC1906.02c		CUE domain protein Cue3	0.878	47	0.936	227
SPBC651.10	nse5	Smc5-6 complex non-SMC subunit Nse5	0.940	402	0.874	421
SPAC4A8.02c		conserved protein (broad species distribution)	0.858	332	0.955	380
SPAC1952.10c		conserved fungal protein	0.861	287	0.953	320
SPAC644.13c		Rab GTPase binding	0.858	257	0.956	291
SPCC1393.13		DUF89 family protein	0.880	372	0.934	282
SPAPB1A10.09	ase1	microtubule-associated protein Ase1	0.858	246	0.957	299
SPCP20C8.01c		B13958 domain	NaN	0	0.907	4
SPBC215.03c	csn1	COP9/signalosome complex subunit Csn1	0.907	175	0.907	130
SPAC20G8.08c	fft1	fun thirty related protein Fft1	0.914	399	0.900	456
SPAC22F3.08c	rok1	ATP-dependent RNA helicase Rok1	0.922	376	0.892	415
SPAC19D5.02c		peroxisomal membrane protein Pex22	0.890	295	0.924	277
SPAC144.05		ATP-dependent DNA helicase	0.900	300	0.915	289
SPBC115.03		gfo/idh/mocA family oxidoreductase	0.892	240	0.922	235
SPCC1840.02c	bgs4	1,3-beta-glucan synthase subunit Bgs4	0.923	355	0.892	216
SPAP8A3.13c		conserved protein family	0.914	303	0.901	255
SPBC2D10.16		sequence orphan	0.865	233	0.950	234
SPAPB1E7.12	rps602	40S ribosomal protein S6	0.896	313	0.919	290
SPCC1827.08c	pof7	F-box protein Pof7	0.855	286	0.960	225
SPCC736.06		aspartate-tRNA ligase	0.839	243	0.977	111
SPAC22E12.04	ccs1	metallochaperone Ccs1	0.880	452	0.935	329
SPAC4G9.20c		mitochondrial carrier with solute carrier repeats	0.904	229	0.911	233
SPBC1778.05c		sequence orphan	0.906	396	0.910	377
SPBC354.12	gpd3	glyceraldehyde 3-phosphate dehydrogenase Gpd3	0.915	236	0.900	352
SPBC1105.08		EMP70 family	0.962	443	0.853	634
SPBC15C4.06c		ubiquitin-protein ligase E3	0.915	177	0.900	226
SPBC8D2.10c	rmt3	type I ribosomal protein arginine N-methytransferase Rmt3	0.855	318	0.960	228
SPAC824.07		hydroxyacylglutathione hydrolase	0.857	203	0.958	336
SPCC1919.05		TPR repeat protein Ski3	0.908	261	0.908	307
SPAC1B3.10c		SEL1 repeat protein, unknown biological role	0.927	301	0.889	275
SPAC22F3.12c	rgs1	regulator of G-protein signaling Rgs1	0.908	212	0.908	359
SPCC1682.13		SWIRM domain protein	0.893	196	0.923	281
SPBC3E7.02c	hsp16	heat shock protein Hsp16	0.902	356	0.914	254
SPAC4A8.07c		sphingoid long chain base (LCB) kinase	0.867	247	0.949	241
SPBC14C8.11c		sequence orphan	0.872	371	0.944	293
SPAC23C11.06c		hydrolase	0.877	345	0.940	310
SPBC530.04	mod5	Tea1 anchoring protein Mod5	0.866	338	0.950	301
SPAPB21F2.02		Dopey family protein	0.889	162	0.928	246

Systematic ID	Gene name	Gene description	CF index screen 1	Cell number	CF index screen 2	Cell number
SPCC70.06		nuclear export factor	0.898	281	0.918	264
SPBC31F10.12		RNA-binding protein Tma20	0.955	191	0.861	443
SPAC17H9.03c	rdl1	RAD51D-like protein 1	0.916	331	0.900	396
SPAC9.08c		steroid reductase	0.913	468	0.904	244
SPAC3C7.14c	obr1	ubiquitinated histone-like protein Uhp1	0.865	130	0.952	226
SPBC16E9.02c		CUE domain protein Cue5	0.893	403	0.924	400
SPBC14C8.16c	bot1	mitochondrial ribosomal protein subunit S35	0.876	195	0.941	162
SPAC2C4.06c		rRNA methyltransferase	0.870	510	0.947	315
SPAC22F8.03c		sequence orphan	0.901	261	0.916	313
SPCC126.08c		lectin	0.894	268	0.924	312
SPAC3H1.05		CAAX prenyl protease	0.949	373	0.869	533
SPCC1739.07		substrate-specific nuclear cofactor for exosome activity	0.906	209	0.912	294
SPBC365.03c	rpl2101	60S ribosomal protein L21	0.899	544	0.919	427
SPCC550.08		N-acetyltransferase	0.929	240	0.888	223
SPBC1778.07		methyltransferase N2227 family	0.919	261	0.898	250
SPAC15E1.09	grx2	glutaredoxin Grx2	0.921	277	0.896	246
SPAC12B10.15c		ribonuclease H2 complex subunit	0.865	272	0.952	168
SPAC167.07c		ubiquitin-protein ligase E3	0.885	288	0.933	312
SPAC17A5.02c	dbr1	RNA lariat debranching enzyme Dbr1	0.909	143	NaN	0
SPAC17G6.02c	tco1	RTA1-like protein	0.871	250	0.947	317
SPAC13G6.08		Cdc20/Fizzy family WD repeat protein	0.864	318	0.954	368
SPBP4H10.09	rsv1	transcription factor Rsv1	0.934	223	0.885	226
SPAC4H3.02c		sequence orphan	0.919	221	0.899	202
SPBC32F12.11	tdh1	glyceraldehyde-3-phosphate dehydrogenase Tdh1	0.938	362	0.881	379
SPBC19C2.02	pmt1	DNA methyltransferase homolog	0.901	233	0.917	221
SPAC19G12.13c		sequence orphan	0.897	163	0.922	276
SPAC4G8.06c	trm12	tRNA methyltransferase Trm12	0.874	432	0.944	400
SPBC2G5.02c		CK2 family regulatory subunit	0.898	218	0.920	319
SPAC1952.12c	csn71	COP9/signalosome complex subunit 7a	0.881	300	0.938	218
SPBC29A3.12	rps902	40S ribosomal protein S9	0.914	292	0.904	347
SPAC6F6.01		VIC sodium channel	0.954	356	0.864	254
SPBC685.04c	aps2	AP-2 adaptor complex subunit Aps2	0.900	286	0.918	260
SPBC1773.02c		thioredoxin peroxidase	0.890	288	0.929	296
SPBCPT2R1.01c		S. pombe specific DUF999 protein family 9	0.871	365	0.948	345
SPAC9E9.13	wos2	p23 homolog	0.934	256	0.885	274
SPBC29A3.02c	his7	phosphoribosyl-AMP cyclohydrolase/phosphoribosyl-ATP pyrophosphohydrolase His7	0.901	270	0.919	366
SPAC5D6.08c	mes1	meiosis II protein Mes1	0.871	313	0.949	267
SPAC3H1.04c	mdm31	mitochondrial inner membrane protein Mdm31	0.899	285	0.920	277
SPBC4B4.03	rsc1	RSC complex subunit Rsc1	0.893	255	0.926	312
SPBC21C3.11	ubx4	UBX domain protein Ubx4	0.885	150	0.935	73
SPBC1198.12	mfr1	fizzy-related protein Mfr1	0.884	381	0.935	331
SPAC1142.07c	vps32	vacuolar sorting protein Vps32	0.859	183	0.961	262
SPBPJ4664.02		glycoprotein	0.902	252	0.918	388
SPBC2F12.09c	atf21	transcription factor Atf21	0.859	299	0.960	261
SPBC8D2.17		alpha-1,2-galactosyltransferase	0.892	205	0.928	260
SPCC757.03c		ThiJ domain protein	0.896	391	0.924	289
SPAC26A3.10		Arf GAP protein	0.961	321	0.858	361
SPCC338.06c		heat shock protein Hsp20 family	0.907	181	0.913	258
SPBC17G9.08c	csx2	Arf GAP protein	0.887	114	0.933	237
SPAC869.10c		proline specific permease	0.856	264	0.964	276
SPAC23H3.12c		conserved protein (fungal and plant)	0.896	295	0.924	280
SPBC947.15c		NADH dehydrogenase	0.862	243	0.958	256
SPBC25B2.07c	mug164	microtubule-associated protein	0.871	228	0.949	289
SPAC9.07c		GTPase Rbg1	0.933	490	0.887	257
SPBC17D1.07c		GTPase regulator	0.855	226	0.966	226
SPBC16C6.08c	qcr6	ubiquinol-cytochrome-c reductase complex subunit 8	0.858	221	0.962	186
SPAC144.13c	srw1	CDK inhibitor Srw1	0.903	253	0.917	254
SPAC4A8.09c	cwf21	complexed with Cdc5 protein Cwf21	0.949	401	0.872	433
SPCC1919.15	brl1	zinc finger protein	0.858	224	0.963	162
SPAPB1A11.03		FMN dependent dehydrogenase	0.890	298	0.931	273
SPAC11E3.08c	nse6	Smc5-6 complex non-SMC subunit Nse6	0.889	319	0.932	329
SPAC6F6.02c	pof5	F-box protein Pof5	0.935	635	0.886	505
SPBC18H10.05		WD repeat protein	0.960	235	0.861	134
SPBC6B1.06c	ubp14	ubiquitin C-terminal hydrolase Ubp14	0.888	339	0.933	539

Systematic ID	Gene name	Gene description	CF index screen 1	Cell number	CF index screen 2	Cell number
SPAC4F10.20	grx1	glutaredoxin Grx1	0.863	184	0.958	255
SPAC6F6.04c		membrane transporter	0.895	234	0.926	240
SPBC1778.03c		NADH pyrophosphatase	0.920	306	0.902	4
SPAC328.06	ubp2	ubiquitin C-terminal hydrolase Ubp2	0.912	296	0.910	303
SPAC11H11.04	mam2	pheromone p-factor receptor	0.890	315	0.932	365
SPAC5D6.09c	mug86	acetate transporter	0.911	353	0.911	450
SPCC1393.02c		non-specific DNA binding protein Spt2	0.886	259	0.936	270
SPCC757.02c		epimarase	0.930	367	0.892	391
SPAC2F7.08c	snf5	chromatin remodeling complex subunit Snf5	0.918	272	0.904	366
SPBC1539.06		acyl-coenzyme A binding protein	0.928	202	0.894	200
SPBC1685.05		serine protease	0.889	255	0.933	212
SPCC364.02c	bis1	stress response protein Bis1	0.860	105	0.962	281
SPAC22F3.09c	res2	MBF transcription factor complex subunit Res2	0.889	344	0.934	407
SPAC1039.01		amino acid permease, unknown 5	0.867	257	0.956	204
SPAC23H3.13c	gpa2	heterotrimeric G protein alpha-2 subunit Gpa2	0.960	338	0.863	244
SPCC1235.03		SMR and CUE domain protein	0.914	445	0.908	604
SPBC800.05c	tub1	tubulin alpha 2	0.882	82	0.940	108
SPAC27F1.06c		FKBP-type peptidyl-prolyl cis-trans isomerase	0.943	318	0.879	318
SPAC4G9.14		Mvp17/PMP22 family	0.919	343	0.904	237
SPAC144.08		DNAJ domain protein Jac1	0.848	169	0.975	95
SPAC13G6.12c	chs1	chitin synthase I	0.908	310	0.915	223
SPBP4G3.03		PI31 proteasome regulator related	0.868	342	0.954	301
SPAC1B1.02c		NAD/NADH kinase	0.895	222	0.928	231
SPAC3G9.03	rpl2301	60S ribosomal protein L23	0.873	347	0.950	316
SPAC19D5.01	pyp2	tyrosine phosphatase Pyp2	0.901	264	0.922	367
SPAC186.08c		L-lactate dehydrogenase	0.872	279	0.951	307
SPAC3H8.04		chromosome segregation protein	0.925	239	0.898	267
SPAC26F1.12c		conserved eukaryotic protein	0.889	255	0.934	330
SPAC186.06		human MAWBP homolog	0.872	236	0.951	264
SPAC323.04		mitochondrial ATPase	0.936	207	0.888	224
SPAC13G7.06	met16	phosphoadenosine phosphosulfate reductase	0.912	5	NaN	0
SPBPB21E7.09		L-asparaginase	0.914	327	0.909	343
SPAC3G6.01	hrp3	ATP-dependent DNA helicase Hrp3	0.882	342	0.942	351
SPAC13D6.03c		tRNA (uridine) methyltransferase Trm9	0.900	320	0.924	315
SPAC23C4.06c		methyltransferase	0.914	71	0.910	257
SPAC2F3.08	sut1	alpha-glucoside transporter	0.870	295	0.954	399
SPCC777.02		transcription factor	0.918	361	0.906	454
SPAC24H6.07	rps901	40S ribosomal protein S9	0.903	238	0.921	309
SPBC14F5.11c	mug186	sorting nexin Snx41	0.928	300	0.897	251
SPAC458.02c		mRNP complex	0.879	283	0.946	269
SPAC926.07c	dlc2	dynein light chain Dlc2	0.881	310	0.944	287
SPCC576.02		hydantoin racemase family	0.898	255	0.927	197
SPAC890.02c	alp7	TACC homolog	0.850	367	0.975	240
SPBC21B10.09		acetyl-CoA transporter	0.898	321	0.927	275
SPAC13C5.03	tht1	nuclear membrane protein involved in karyogamy	0.901	276	0.924	340
SPCC757.07c	ctt1	catalase	0.886	284	0.939	194
SPBC1778.10c	ppk21	serine/threonine protein kinase Ppk21	0.881	313	0.945	352
SPAC2C4.05		cornichon family protein	0.879	264	0.946	249
SPBC32H8.01c		conserved fungal protein	0.911	295	0.915	288
SPBC1773.16c		transcription factor	0.970	276	0.856	279
SPAC2G11.09		DUF221 family protein	0.873	214	0.953	227
SPBC776.14	plh1	phospholipid-diacylglycerol acyltransferase Plh1	0.865	351	0.961	360
SPCC1442.11c		sequence orphan	0.872	232	0.954	251
SPBC18H10.10c	cwc16	complexed with Cdc5 protein Cwf16	0.932	263	0.895	249
SPAC23H4.16c		sequence orphan	0.897	248	0.929	261
SPCC2H8.02		inorganic phosphate transporter	0.914	259	0.912	256
SPAC186.09		pyruvate decarboxylase	0.898	306	0.928	269
SPAC8E11.06		sequence orphan	0.902	372	0.925	409
SPAC11D3.03c		meiotic chromosome segregation protein	0.929	314	0.897	248
SPCC553.12c		conserved fungal protein	0.937	388	0.890	326
SPAC2C4.16c	rps801	40S ribosomal protein S8	0.915	603	0.912	282
SPAC20G8.09c		N-acetyltransferase Nat10	0.891	141	0.936	268
SPAC17A2.05	osm1	fumerate reductase	0.888	282	0.939	305
SPCC4G3.05c	mus81	Holliday junction resolvase subunit Mus81	0.961	639	0.866	355
SPCC1682.14	rpl1902	60S ribosomal protein L19B	0.895	324	0.932	342
SPAC22G7.11c		conserved fungal protein	0.883	255	0.944	316
SPBC15D4.01c		kinesin-like protein	0.920	189	0.907	208

Systematic ID	Gene name	Gene description	CF index screen 1	Cell number	CF index screen 2	Cell number
SPBC25H2.05	egd2	nascent polypeptide-associated complex alpha subunit Egd1	0.852	401	0.976	376
SPAC328.07c		heavy metal ion homeostasis protein	0.927	212	0.900	317
SPAC16A10.04	rho4	Rho family GTPase Rho4	0.896	219	0.932	204
SPAC521.03		short chain dehydrogenase	0.861	249	0.967	242
SPBP8B7.26		sequence orphan	0.895	271	0.932	281
SPCC777.13	vps35	retromer complex subunit Vps35	0.933	238	0.894	283
SPAC513.07		flavonol reductase/cinnamoyl-CoA reductase family	0.905	354	0.922	388
SPBC1604.09c		exoribonuclease Rex4	0.928	248	0.899	183
SPAC630.14c	tup12	transcriptional corepressor Tup12	0.914	19	NaN	0
SPCC4G3.08	psk1	serine/threonine protein kinase Psk1	0.872	411	0.955	315
SPAC5H10.04		NADPH dehydrogenase	0.905	186	0.923	202
SPBC2D10.09		3-hydroxyisobutyryl-CoA hydrolase	0.955	275	0.872	327
SPAC824.08	gda1	guanosine-diphosphatase Gda1	0.911	287	0.916	190
SPBC17A3.09c		lipoate-protein ligase A	0.890	267	0.938	247
SPCC338.18		sequence orphan	0.900	301	0.928	180
SPAC140.03	arb1	argonaute binding protein 1	0.864	321	0.964	353
SPBC354.04		sequence orphan	0.871	277	0.957	257
SPAC227.01c		Erd1 homolog	0.883	178	0.946	120
SPBC19F8.04c		nuclease	0.852	280	0.977	261
SPAC8C9.09c	mug129	sequence orphan	0.906	170	0.923	229
SPBC1289.09	tim21	mitochondrial inner membrane presequence translocase complex subunit Tim21	0.879	248	0.950	226
SPCC584.03c		RanGTP-binding protein	0.877	385	0.952	278
SPAC22G7.02	kap111	karyopherin Kap111	0.861	289	0.967	390
SPBC25B2.06c	btb2	BTB/POZ domain protein Btb2	0.880	203	0.949	284
SPBC713.07c		vacuolar polyphosphatase	0.904	181	0.925	242
SPAC13A11.03	mcp7	meiosis specific coiled-coil protein Mcp7	0.922	375	0.907	326
SPBC32H8.08c		mannosyltransferase complex subunit	0.842	194	0.987	292
SPCPB16A4.03c	ade10	IMP cyclohydrolase	0.990	1	0.839	5
SPCC569.01c		DUF1773 family protein 5	0.906	329	0.923	338
SPBC28E12.02		RNA-binding protein	0.924	178	0.905	197
SPCC4G3.02	aph1	bis(5-nucleosidyl)-tetraphosphatase	0.865	244	0.965	277
SPAC1783.08c	rpl1502	60S ribosomal protein L15b	0.905	312	0.925	268
SPCC1494.09c		sequence orphan	0.912	324	0.918	306
SPCC4E9.01c	rec11	meiotic cohesin complex subunit Rec11	0.915	314	0.915	242
SPBC8D2.02c		vacuolar sorting protein Vps68	NaN	0	0.915	282
SPCC645.11c	mug117	meiotically upregulated gene Mug117	0.917	193	0.912	230
SPAC27D7.11c		S. pombe specific But2 family protein	0.946	452	0.884	385
SPBC4B4.06	vps25	ESCRT II complex subunit Vps25	0.874	191	0.956	177
SPAPB24D3.02c		amino acid permease, unknown 3	0.947	290	0.883	338
SPAC1A6.07		sequence orphan	0.875	511	0.955	287
SPAC3C7.12	tip1	CLIP170 family protein Tip1	0.904	266	0.926	239
SPCC320.14		threo-3-hydroxyaspartate ammonia-lyase	0.895	384	0.936	318
SPAC806.03c	rps2601	40S ribosomal protein S26	0.911	497	0.919	360
SPBC1709.09		mitochondrial translation termination factor	0.867	47	0.963	76
SPBC83.19c		sequence orphan	0.912	348	0.918	239
SPCC61.03		conserved protein (broad species distribution)	0.902	345	0.928	254
SPAC1F7.13c	rpl801	60S ribosomal protein L8	0.912	347	0.918	549
SPAC637.11	suv3	ATP-dependent RNA helicase Suv3	0.963	223	0.868	376
SPBC839.03c		neddylation protein Dcn1	0.869	307	0.962	358
SPAC17A5.07c	ulp2	SUMO deconjugating peptidase Ulp2	0.894	273	0.937	308
SPBC29A10.08		1,3-beta-glucanosyltransferase	0.913	293	0.917	360
SPBC409.08		spermine family transporter	0.887	373	0.943	413
SPCC663.08c		short chain dehydrogenase	0.908	269	0.922	210
SPBC4F6.12	pxl1	LIM domain	0.911	88	0.919	300
SPBC1604.01	mug158	sulfatase modifying factor 1 related	0.889	259	0.941	227
SPAC1B3.03c	wis2	cyclophilin family peptidyl-prolyl cis-trans isomerase Wis2	0.876	467	0.955	300
SPBC1734.08	hse1	STAM like protein	0.934	197	0.897	268
SPAC1565.04c	ste4	adaptor protein Ste4	0.864	281	0.967	316
SPBC1861.06c	mug131	S. pombe specific UPF0300 family protein 4	0.887	379	0.944	355
SPAC1687.16c	erg3	C-5 sterol desaturase Erg3	0.869	270	0.961	299
SPAC1039.10	mmf2	homologous Pmf1p factor 1	0.890	214	0.941	321
SPBC25D12.05	trm1	N2,N2-dimethylguanosine tRNA methyltransferase	0.897	255	0.934	153
SPCC74.09	mug24	RNA-binding protein	0.978	603	0.853	242
SPBC24C6.04		delta-1-pyrroline-5-carboxylate dehydrogenase	0.931	278	0.900	258

Systematic ID	Gene name	Gene description	CF index screen 1	Cell number	CF index screen 2	Cell number
SPAC4F10.17		conserved fungal protein	0.893	301	0.938	318
SPBC1652.02	aap1	APC amino acid transporter	0.924	279	0.907	293
SPBC947.06c		spermidine family transporter	0.873	242	0.958	236
SPBC16A3.01	spn3	septin Spn3	0.876	348	0.955	319
SPAC8C9.16c	mug63	TLDc domain protein 1	0.863	274	0.968	200
SPBC800.07c	tsf1	mitochondrial translation elongation factor EF-Ts Tsf1	0.848	75	0.984	82
SPAC15E1.06	vps29	retromer complex subunit Vps29	0.929	284	0.902	321
SPAC16C9.07	ppk5	serine/threonine protein kinase Ppk5	0.928	216	0.903	194
SPAC9E9.03	leu2	3-isopropylmalate dehydratase Leu2	0.901	316	0.930	292
SPAC4H3.06		sequence orphan	0.891	193	0.941	228
SPAC18B11.08c		conserved fungal protein	0.868	280	0.964	299
SPBC1683.11c		isocitrate lyase	0.875	280	0.957	291
SPAPB21F2.03		conserved fungal protein	0.905	495	0.927	656
SPBP23A10.05	ssr4	SWI/SNF and RSC complex subunit Ssr4	0.927	226	0.905	27
SPBC16A3.10		membrane bound O-acyltransferase, MBOAT	0.960	292	0.872	234
SPBC3B8.07c	dsd1	dihydroceramide delta-4 desaturase	0.864	250	0.968	299
SPAC1851.04c		guanyl-nucleotide exchange factor	0.877	210	0.955	154
SPAC6F6.06c	rax2	cell polarity factor Rax2	0.864	290	0.968	216
SPAC22A12.11	dak1	dihydroxyacetone kinase Dak1	0.889	406	0.943	397
SPCC1322.14c	vtc4	vacuolar transporter chaperone (VTC) complex subunit	0.872	182	0.960	180
SPBC582.06c	mcp6	meiosis specific coiled-coil protein Mcp6	0.913	302	0.919	241
SPAC8F11.09c	nnt1	nicotinamide N-methyltransferase Nnt1	0.872	512	0.960	439
SPAC11D3.02c		ELLA family acetyltransferase	0.895	269	0.937	348
SPBC16E9.15		heat shock factor binding protein	0.861	192	0.971	204
SPAC637.13c		cytoskeletal signaling protein	0.864	340	0.969	296
SPBC29A3.14c	trt1	telomerase reverse transcriptase 1 protein Trt1	0.900	253	0.933	255
SPBC947.14c		sequence orphan	0.847	1	0.986	149
SPAP8A3.12c		tripeptidylpeptidase	0.936	305	0.897	322
SPAC4G8.03c		RNA-binding protein	0.910	318	0.923	248
SPAC16C9.01c		carbohydrate kinase	0.869	301	0.964	303
SPAC2G11.13	atg22	autophagy associated protein Atg22	0.899	434	0.934	322
SPAC22F8.07c	rtf1	replication termination factor Rtf1	0.909	258	0.924	282
SPBC32H8.11	mei4	meiotic forkhead transcription factor Mei4	0.852	209	0.981	241
SPAC1399.01c		purine permease	0.874	241	0.960	241
SPAC7D4.12c		DUF1212 family protein	0.949	225	0.885	216
SPAC8E11.03c	dmc1	RecA family ATPase Dmc1	0.883	294	0.951	329
SPAC6B12.12	tom70	mitochondrial TOM complex subunit Tom70	0.915	423	0.919	291
SPBC14C8.05c	meu17	glucan-alpha-1,4-glucosidase	0.873	393	0.961	241
SPAC31A2.16	gef2	RhoGEF Gef2	0.943	299	0.892	287
SPAC869.07c	mel1	alpha-galactosidase	0.863	289	0.972	250
SPAC3A12.10	rpl2001	60S ribosomal protein L20a	0.880	439	0.955	309
SPAC3F10.06c		initiator methionine tRNA 2-O-ribosyl phosphate transferase	0.920	323	0.914	336
SPBP23A10.10	ppk32	serine/threonine protein kinase Ppk32	0.901	275	0.933	262
SPBC3E7.06c		membrane transporter	0.901	365	0.934	436
SPAC1705.02		human 4F5S homolog	0.873	271	0.962	272
SPAC14C4.12c		SWIRM domain protein	0.976	326	0.858	141
SPAC27D7.12c	but1	neddylation pathway protein But1	0.863	334	0.972	395
SPCC24B10.15		PINc domain	0.909	246	0.925	195
SPBC3B8.04c		membrane transporter	0.900	262	0.935	400
SPBC428.15		GTP binding protein	0.852	201	0.983	276
SPBC19C7.10		transcription factor	0.885	201	0.950	236
SPCC338.16	pof3	F-box protein Pof3	0.896	243	0.939	267
SPAC14C4.07		membrane transporter	0.900	279	0.935	121
SPCC320.03		transcription factor	0.900	362	0.935	310
SPAC30.03c	tsn1	translin	0.934	316	0.901	455
SPCC1919.12c		aminopeptidase	0.905	263	0.930	240
SPBC11C11.10		tRNA pseudouridine synthase	0.920	165	0.915	268
SPCC576.11	rpl15	60S ribosomal protein L15	0.893	247	0.942	256
SPCC364.01		sequence orphan	0.878	284	0.957	315
SPBC19G7.01c	msh2	MutS protein homolog 2	0.915	235	0.921	278
SPAC186.07c		hydroxyacid dehydrogenase	0.865	309	0.970	389
SPAC3G9.07c	hos2	histone deacetylase (class I) Hos2	0.883	290	0.952	282
SPCC306.02c		Rab GTPase binding	0.864	211	0.971	267
SPAC19G12.15c	tpp1	trehalose-6-phosphate phosphatase Tpp1	0.892	368	0.944	260

Systematic ID	Gene name	Gene description	CF index screen 1	Cell number	CF index screen 2	Cell number
SPBC582.04c		sequence orphan	0.921	340	0.915	316
SPAC1805.09c	fmt1	methionyl-tRNA formyltransferase Fmt1	0.940	378	0.896	380
SPBC839.13c	rpl1601	60S ribosomal protein L13/L16	0.897	220	0.939	335
SPAC823.02		sequence orphan	0.877	384	0.959	333
SPBC725.06c	ppk31	serine/threonine protein kinase Ppk31	0.893	301	0.943	339
SPAC3H1.11	hsr1	transcription factor Hsr1	0.912	244	0.924	184
SPAC4G9.13c	vps26	retromer complex subunit Vps26	NaN	0	0.918	410
SPCC1322.08	srk1	MAPK-activated protein kinase Srk1	0.914	432	0.922	337
SPBC18H10.16		amino acid permease, unknown 9	0.937	282	0.900	287
SPBC19F8.08	rps401	40S ribosomal protein S4	0.869	341	0.968	316
SPAPB1E7.04c		chitinase	0.869	208	0.967	238
SPBC13G1.12	did2	vacuolar sorting protein Did2	0.936	201	0.901	219
SPCC364.04c		CASP family protein	0.931	254	0.906	344
SPBC8E4.03		agmatinase 2	0.904	213	0.933	252
SPAC5D6.06c		UDP-GlcNAc transferase associated protein Alg14	0.955	217	0.882	161
SPBC1773.14	arg7	argininosuccinate lyase	0.911	234	0.926	311
SPAP7G5.04c	lys1	aminoadipate-semialdehyde dehydrogenase	0.978	2	0.858	250
SPCC31H12.03c		transcriptional regulator	NaN	0	0.918	452
SPAC212.08c		S. pombe specific GPI anchored protein family 1	0.875	265	0.962	206
SPBC15D4.15	pho2	4-nitrophenylphosphatase	0.933	272	0.904	263
SPBC725.14	arg6	acetylglutamate synthase Arg6	0.919	259	NaN	0
SPBC16C6.01c		lysine methyltransferase	0.900	231	0.937	266
SPBC405.06		DNAJ protein Xdj1	0.866	199	0.972	187
SPAC31A2.15c	dcc1	DNA replication factor C complex subunit Dcc1	0.907	172	0.930	280
SPBC12D12.06	srb11	cyclin Srb11	0.904	187	0.933	21
SPCC417.12		carboxylesterase-lipase family	0.910	206	0.927	250
SPBC23G7.14		sequence orphan	0.877	237	0.960	266
SPBC28F2.03	ppi1	cyclophilin family peptidyl-prolyl cis-trans isomerase Cyp2	0.896	328	0.941	346
SPAC328.04		AAA family ATPase, unknown biological role	0.908	334	0.930	261
SPBC106.17c	cys2	homoserine O-acetyltransferase	0.981	1	0.857	280
SPAC1296.01c		phosphoacetylglucosamine mutase	0.865	319	0.973	294
SPAC32A11.01	mug8	conserved fungal protein	0.931	282	0.907	315
SPAC15A10.07		sequence orphan	0.907	280	0.931	283
SPBP35G2.12		nucleoside diphosphate-sugar hydrolase	0.896	296	0.942	305
SPAC29B12.08		sequence orphan	0.919	247	0.919	221
SPAC1142.06	get3	GET complex ATPase subunit	0.883	252	0.955	315
SPCC550.11		karyopherin	0.919	270	0.919	266
SPCC16A11.08	atg20	sorting nexin Atg20	0.886	296	0.952	264
SPAC1805.14		sequence orphan	0.870	250	0.969	238
SPBC12C2.09c		Haemolysin-III family protein	0.862	155	0.976	147
SPCC4B3.03c		DUF21 domain protein	0.922	218	0.916	244
SPAC4G8.07c		tRNA (m5U54) methyltransferase Trm2	0.899	261	0.940	344
SPBC660.07	ntp1	alpha,alpha-trehalase Ntp1	0.890	347	0.948	377
SPBC1709.14		peptide N-glycanase	0.880	229	0.959	286
SPCC1742.01		sequence orphan	0.845	247	0.993	845
SPBC947.05c		ferric-chelate reductase	0.888	208	0.951	321
SPCC1259.13	chk1	chk1 protein kinase	0.963	299	0.875	294
SPAC4A8.10		lipase	0.887	295	0.951	279
SPAC1834.08	mak1	histidine kinase Mak1	0.928	312	0.911	277
SPAC17H9.10c	ddb1	damaged DNA binding protein Ddb1	0.921	248	0.917	198
SPBC8D2.03c	hhf2	histone H4 h4.2	0.913	491	0.926	368
SPCC622.14		GTPase activating protein	0.886	302	0.953	411
SPAC1071.12c	stp1	low molecular weight phosphotyrosine protein phosphatase	0.904	264	0.935	244
SPAC1B3.08		COP9 signalosome complex subunit 12	0.915	208	0.924	199
SPBC119.04	mei3	meiosis inducing protein Mei3	0.928	564	0.912	282
SPAC12G12.16c		nuclease, XP-G family	0.945	465	0.895	333
SPCC285.16c	msh6	MutS protein homolog	0.889	206	0.951	302
SPCC4B3.06c		NADPH-dependent FMN reductase	0.972	552	0.868	445
SPAC1556.04c	cdd1	cytidine deaminase Pcd1	0.872	311	0.968	333
SPCC188.07	ccq1	telomere maintenence protein	0.941	220	0.899	303
SPCC306.07c		U3 snoRNP-associated protein Cic1/Utp30 family	0.890	235	0.950	269
SPBC31F10.16		ChAPs family protein	0.863	234	0.977	175
SPCC70.09c	mug9	conserved fungal protein	0.871	218	0.969	278
SPAC56F8.05c	mug64	conserved fungal protein	0.873	355	0.967	259
SPCC1450.07c		D-amino acid oxidase	0.886	179	0.954	178

Systematic ID	Gene name	Gene description	CF index screen 1	Cell number	CF index screen 2	Cell number
SPAC824.04		WD repeat protein	0.888	236	0.952	269
SPCC1259.08		conserved fungal protein	0.877	265	0.963	309
SPAC1B3.06c		UbiE family methyltransferase	0.866	333	0.974	252
SPCC191.05c		nucleoside 2-deoxyribosyltransferase	0.860	190	0.980	190
SPBC6B1.09c	nbs1	Mre11 complex subunit Nbs1	0.954	672	0.886	429
SPBC582.05c	brc1	BRCT domain protein Brc1	0.954	141	0.886	275
SPBC21C3.19		DUF1960 family protein	0.871	297	0.970	366
SPBC23G7.04c	nif1	SEL1 repear protein Nif1	0.898	302	0.943	280
SPCC1223.12c	meu10	conserved fungal family	0.939	218	0.901	228
SPAC11H11.03c		SMR and DUF1771 domain protein	0.877	321	0.964	374
SPAC17A5.18c	rec25	meiotic recombination protein Rec25	0.903	250	0.937	272
SPAC27D7.03c	mei2	RNA-binding protein involved in meiosis Mei2	0.913	291	0.928	328
SPAC22A12.03c	csn4	COP9/signalosome complex subunit Csn4	0.969	231	0.871	256
SPAC5H10.13c	gmh2	alpha-1,2-galactosyltransferase Gmh2	0.872	290	0.969	371
SPBC1289.16c		copper amine oxidase	0.872	284	0.969	287
SPAC11E3.01c	swr1	SNF2 family helicase Swr1	0.954	246	0.887	254
SPBC887.05c	cwf29	RNA-binding protein Cwf29	0.925	430	0.916	280
SPBC660.10		translation elongation factor G	0.946	206	0.895	199
SPAC23H4.17c	srb10	cyclin-dependent protein kinase Srb10	0.946	398	0.895	11
SPCC1183.10	wtf10	wtf element Wtf10	0.883	374	0.958	422
SPAC24B11.13	hem3	hydroxymethylbilane synthase	0.882	305	0.960	281
SPCPJ732.01	vps5	retromer complex subunit Vps5	0.924	464	0.918	340
SPBC8D2.16c		DUF171 family protein	0.870	278	0.972	298
SPAC2F7.06c	pol4	DNA polymerase X family	0.914	271	0.928	310
SPBC1685.04		sequence orphan	0.960	597	0.882	423
SPBC17D1.02		diphthamide biosynthesis protein	0.894	348	0.948	303
SPCC162.03		short chain dehydrogenase	0.885	328	0.958	360
SPCC965.04c		mitochondrial inner membrane i-AAA protease complex subunit Yme1	0.937	410	0.906	540
SPAC23C11.10		conserved eukaryotic protein	0.916	231	0.927	318
SPCC4B3.01		thiosulfate sulfurtransferase	0.919	269	0.924	176
SPBPB8B6.05c		L-asparaginase	0.886	265	0.956	399
SPBC2G2.03c	sbh1	translocon beta subunit Sbh1	0.917	332	0.926	384
SPAC1B3.16c	vht1	vitamin H transporter Vth1	0.925	42	0.918	5
SPBC2F12.05c		sterol binding ankyrin repeat protein	0.982	67	0.861	652
SPCC16A11.15c		sequence orphan	0.928	319	0.915	392
SPBC29A3.13		PWWP domain protein	0.932	335	0.911	606
SPBC1271.14		glutamate N-acetyltransferase	0.903	386	0.941	331
SPAC1805.08	dlc1	dynein light chain Dlc1	0.891	222	0.953	265
SPCC737.07c		DNA polymerase alpha-associated DNA helicase A	0.939	269	0.905	199
SPCC4B3.10c	ipk1	inositol 1,3,4,5,6-pentakisphosphate (IP5) kinase	0.922	453	NaN	0
SPCC285.13c		nucleoporin Nup60	0.934	63	0.910	55
SPCC1259.03	rpa12	DNA-directed RNA polymerase complex I subunit Rpa12	0.947	467	0.897	365
SPBC26H8.09c	snf59	SWI/SNF complex subunit Snf59	0.889	287	0.955	377
SPBC30D10.10c	tor1	phosphatidylinositol kinase Tor1	0.946	279	0.897	135
SPCC417.11c		glutamate-1-semialdehyde 2,1-aminomutaseaminotransferase	0.944	159	0.900	266
SPAC9G1.07		sequence orphan	0.888	346	0.956	223
SPBPJ4664.06	gpt1	UDP-glucose-glycoprotein glucosyltransferase Gpt1	0.873	218	0.971	251
SPAC19D5.06c	din1	Dhp1p-interacting protein Din1	0.907	355	0.937	217
SPAC2C4.08		conserved fungal protein	0.869	259	0.975	273
SPAC6F6.13c		DUF726 family protein	0.956	377	0.888	365
SPBC776.03		homoserine dehydrogenase	0.909	408	0.935	263
SPAC3G6.11		ATP dependent DNA helicase Chl1	0.946	641	0.898	341
SPBC21C3.09c		fumarylacetoacetate (FAA) hydrolase	0.892	324	0.952	229
SPBC1289.08		UDP-N-acetylglucosamine diphosphorylase	0.908	249	0.937	326
SPAC24C9.05c	mug70	conserved protein (fungal and plant)	0.926	331	0.919	335
SPBPJ4664.05		conserved fungal protein	0.875	336	0.970	343
SPBC31F10.10c		zf-MYND type zinc finger protein	0.922	46	NaN	0
SPAPJ691.02		yippee-like protein	0.889	315	0.956	243
SPAC6B12.05c		chromatin remodeling complex subunit	0.888	109	0.957	142
SPBC15D4.10c	amo1	nuclear rim protein Amo1	0.946	306	0.899	395
SPAC4D7.10c		SAGA complex subunit Spt20	0.869	117	0.976	104
SPCC757.12		alpha-amylase homolog	0.873	277	0.972	280
SPCC63.06		human WDR89 family WD repeat protein	0.882	556	0.963	325
SPAC11D3.01c		conserved fungal protein	0.967	418	0.878	364

Systematic ID	Gene name	Gene description	CF index screen 1	Cell number	CF index screen 2	Cell number
SPAC10F6.14c		ABC1 kinase family protein	0.922	311	0.923	302
SPAPB2B4.07		ubiquitin family protein, human UBTD1 homolog	0.891	414	0.954	345
SPAC13C5.06c	mug121	sequence orphan	0.879	310	0.966	312
SPAC4G9.10	arg3	ornithine carbamoyltransferase Arg3	0.886	264	0.960	254
SPAC823.05c	tlg2	SNARE Tlg2	NaN	0	0.923	4
SPBC29A3.03c		ubiquitin-protein ligase E3	0.885	397	0.960	555
SPAC57A7.07c		homocysteine methyltransferase	0.937	332	0.908	292
SPAC12B10.12c	rhp41	DNA repair protein Rhp41	0.889	527	0.956	347
SPAC2G11.12	rqh1	RecQ type DNA helicase Rqh1	0.965	308	0.881	328
SPAC1039.06		alanine racemase	0.911	363	0.934	405
SPCC191.06		sequence orphan	0.880	285	0.965	276
SPBC106.05c	tim11	F0-ATPase subunit E	0.946	286	0.900	249
SPBC3B9.09	vps36	RBZ zinc finger protein Vps36	0.961	222	0.885	283
SPAC17H9.12c		NADH-cytochrome reductase	0.899	164	0.947	209
SPAC21E11.05c	cyp8	cyclophilin family peptidyl-prolyl cis-trans isomerase Cyp8	0.903	392	0.943	305
SPCC1827.04		ankyrin repeat protein, unknown biological role	0.939	239	0.907	331
SPBC1734.12c	alg12	dolichyl pyrophosphate Man7GlcNAc2 alpha-1,3-glucosyltransferase Alg12	0.907	284	0.939	315
SPAC57A7.04c	pabp	mRNA export shuttling protein	0.953	225	0.893	214
SPAC20G4.04c	hus1	checkpoint clamp complex protein Hus1	0.884	282	0.962	262
SPAC17H9.01	cid16	poly(A) polymerase Cid16	0.886	326	0.961	294
SPCC737.03c		conserved eukaryotic protein	0.890	565	0.956	411
SPCC4B3.11c		conserved eukaryotic protein	0.970	553	0.877	422
SPAC23C4.02	crn1	actin binding protein, coronin Crn1	0.875	304	0.971	286
SPAC2E1P3.04		copper amine oxidase	0.918	194	0.928	278
SPAC18B11.09c		N-acetyltransferase	0.905	199	0.941	268
SPAC18G6.04c	shm2	serine hydroxymethyltransferase Shm2	0.901	281	0.946	302
SPAC16.05c	sfp1	transcription factor Sfp1	0.889	251	0.958	253
SPCC63.14		conserved fungal protein	0.923	214	0.924	254
SPBC13E7.06	msd1	spindle pole body protein Msd1	0.875	357	0.972	290
SPAC9.12c	atp12	F1-ATPase chaperone Atp12	0.917	222	0.930	269
SPBC365.11		GRIP domain protein	0.885	391	0.962	394
SPBC1289.15		glycoprotein	0.924	270	0.923	313
SPAC1F3.10c	39722.000	mitochondrial intermediate peptidase Oct1	0.958	236	0.889	143
SPAPB8E5.03	mae1	malic acid transport protein Mae1	0.912	266	0.936	229
SPAC3H1.12c	snt2	Lid2 complex subunit Snt2	0.891	362	0.956	275
SPAC222.05c	mss1	COX RNA-associated protein	0.906	334	0.941	46
SPCC569.04		sequence orphan	0.884	368	0.963	409
SPAC3H1.07		arginase	0.890	379	0.957	224
SPBC17A3.02		conserved fungal protein	0.888	293	0.959	280
SPAC4F10.19c		zf-HIT protein Hit1	0.887	467	0.961	332
SPAPB24D3.07c		sequence orphan	0.886	429	0.962	250
SPAP27G11.14c		sequence orphan	0.907	234	0.940	158
SPAP11E10.02c	mam3	cell agglutination protein Mam3	0.902	367	0.946	230
SPBC21D10.08c		sequence orphan	0.875	290	0.972	247
SPAC13F5.04c		endosomal sorting protein	0.982	433	0.866	221
SPBC21C3.12c		DUF953 family protein	0.884	225	0.964	370
SPAC23D3.04c	gpd2	glycerol-3-phosphate dehydrogenase Gpd2	0.891	40	0.957	59
SPAC31G5.14	gcv1	glycine decarboxylase T subunit	0.904	359	0.944	346
SPBC20F10.06	mad2	spindle checkpoint protein Mad2	0.899	211	0.949	277
SPBC947.03c		sequence orphan	0.924	250	0.924	294
SPAC1834.09	mug51	conserved fungal protein	0.892	330	0.956	266
SPCC320.05		sulphate transporter	0.919	260	0.929	251
SPCC645.12c		sequence orphan	0.883	231	0.965	313
SPAC823.14		phosphoric monoester hydrolase	0.951	183	0.897	224
SPCP31B10.03c	med31	mediator complex subunit Med31	0.908	70	0.940	314
SPAC9G1.05		actin cortical patch component Aip1	0.932	558	0.916	422
SPAC630.09c	mug58	glycerate kinase	0.927	138	0.921	272
SPAC2E1P5.01c	mns1	mannosyl-oligosaccharide 1,2-alpha-mannosidase	0.880	215	0.969	231
SPBC25H2.10c		tRNA acetyltransferase	0.954	218	0.894	244
SPBPB10D8.05c		membrane transporter	0.883	286	0.966	249
SPAC2H10.01		transcription factor	0.930	379	0.918	352
SPCC338.08	ctp1	sequence orphan	0.918	206	0.931	220
SPCC663.14c		membrane transporter	0.916	339	0.933	316
SPAC12B10.02c		sequence orphan	0.931	316	0.918	335

Systematic ID	Gene name	Gene description	CF index screen 1	Cell number	CF index screen 2	Cell number
SPBC1347.09		hexaprenyldihydroxybenzoate methyltransferase	0.887	474	0.962	212
SPCC1840.08c		protein disulfide isomerase	0.882	201	0.967	486
SPBC1604.08c	imp1	importin alpha	0.941	205	0.908	246
SPBC342.06c	rtt109	RTT109 family histone lysine acetyltransferase Rtt109	0.880	211	0.969	345
SPCC63.03		DNAJ domain protein, DNAJC11 family	0.930	288	0.920	297
SPBC27.08c	sua1	sulfate adenylyltransferase (ATP)	NaN	0	0.925	207
SPAC4F8.01	did4	vacuolar sorting protein Did4	0.938	173	0.912	243
SPCC320.07c	mde7	RNA-binding protein Mde7	0.949	276	0.900	278
SPCC777.17c		mitochondrial ribosomal protein subunit L9	0.881	253	0.969	218
SPBC1347.01c	rev1	deoxycytidyl transferase Rev1	0.918	314	0.931	279
SPAC23D3.13c		guanyl-nucleotide exchange factor	0.896	243	0.954	259
SPCC4B3.05c	hem12	uroporphyrinogen decarboxylase	0.974	616	0.876	549
SPAC1399.04c		uracil phosphoribosyltransferase	0.881	312	0.969	264
SPCC970.10c	brl2	ubiquitin-protein ligase E3	0.929	184	0.921	169
SPBC14C8.09c		conserved fungal protein	0.923	237	0.927	283
SPAC1F7.07c	fip1	iron permease Fip1	NaN	0	0.925	226
SPAC15A10.03c	rhp54	Rad54 homolog Rhp54	NaN	0	0.925	244
SPCC13B11.03c		hydroxyacylglutathione hydrolase	0.900	376	0.951	304
SPBC3H7.10		elongator homolog	0.900	265	0.950	314
SPAC23H3.05c	swd1	COMPASS complex subunit Swd1	0.893	212	0.957	194
SPBC354.09c		Tre1 family protein	0.899	369	0.951	221
SPAC22A12.04c	rps2201	40S ribosomal protein S15a	0.959	559	0.892	243
SPBC6B1.04	mde4	monopolin-like complex subunit Mde4	0.921	215	0.930	141
SPAP32A8.03c		ubiquitin-protein ligase E3	0.959	308	0.891	346
SPAC23D3.10c	eng2	endo-1,3-beta-glucanase Eng2	0.884	305	0.966	239
SPBC25H2.16c		adaptin	0.944	238	0.907	240
SPAC30D11.05	aps3	AP-3 adaptor complex subunit Aps3	0.973	87	0.878	117
SPAC227.15		protein phosphatase regulatory subunit Reg1	0.939	280	0.913	355
SPAC1071.08	rpp203	60S acidic ribosomal protein P2C subunit	0.900	361	0.952	493
SPAC17A5.08		COPII-coated vesicle component Erp2/3/4	0.892	171	0.959	209
SPAPB1A11.04c		transcription factor	0.905	411	0.947	480
SPAC17G6.13		sequence orphan	0.890	316	0.962	241
SPAC23C4.12	hhp2	serine/threonine protein kinase Hhp2	0.921	416	0.930	445
SPAC57A10.14	sgf11	SAGA complex subunit Sgf11	0.914	280	0.937	401
SPAC821.09	eng1	endo-1,3-beta-glucanase Eng1	0.942	368	0.910	297
SPCC757.04		transcription factor	0.900	281	0.952	254
SPAC6C3.08		gankyrin	0.880	337	0.971	233
SPBC17G9.02c		RNA polymerase II accessory factor, Cdc73 family	0.926	242	0.926	344
SPAC29A4.13		urease accessory protein UreF	0.964	301	0.888	315
SPBC354.07c		oxysterol binding protein	0.939	291	0.913	313
SPBC1711.06	rpl401	60S ribosomal protein L2	0.878	259	0.974	267
SPAPJ691.03		DUF543 family protein	0.951	261	0.901	331
SPBC19F8.06c	meu22	amino acid permease, unknown 11	0.880	299	0.972	310
SPCC663.15c		conserved fungal protein	0.887	427	0.966	307
SPBC1773.04		flavonol reductase/cinnamoyl-CoA reductase family	0.914	429	0.939	410
SPCP1E11.09c	rpp103	60S acidic ribosomal protein Rpp1-3	0.903	347	0.949	304
SPBC32H8.07	git5	heterotrimeric G protein beta subunit Git5	0.925	345	0.927	451
SPBC543.08		phosphoinositide biosynthesis protein	0.911	427	0.941	491
SPBC19G7.02		4-amino-4-deoxychorismate lyase	0.883	5	0.969	479
SPBC12C2.12c	glo1	glyoxalase I	0.892	216	0.960	279
SPAC24C9.08		vacuolar carboxypeptidase	0.965	214	0.887	283
SPCC364.06	nap1	nucleosome assembly protein Nap1	0.914	235	0.939	180
SPAC6G10.12c	ace2	transcription factor Ace2	0.883	195	0.969	211
SPAC18B11.02c		pseudouridylate synthase	0.902	299	0.951	284
SPBC18H10.08c	ubp4	ubiquitin C-terminal hydrolase Ubp4	0.981	1029	0.872	507
SPCC1682.12c	ubp16	ubiquitin C-terminal hydrolase Ubp16	0.955	469	0.898	270
SPACUNK4.14	mdb1	BRCT domain protein	0.891	241	0.962	284
SPAC607.08c		DUF726 family protein	0.919	328	0.934	240
SPBC12D12.05c		mitochondrial carrier, calcium binding subfamily	0.929	1110	0.924	420
SPAC1142.08	fhl1	fork head transcription factor Fhl1	0.871	379	0.982	590
SPAPB1A10.03	nxt1	mRNA export receptor Nxt1	0.916	313	0.938	365
SPBC428.07	meu6	meiotic chromosome segregation protein Meu6	0.898	283	0.955	317
SPBC3B8.03		saccharopine dehydrogenase	0.944	260	0.910	226
SPAC5H10.08c	pan6	pantoate-beta-alanine ligase	0.910	283	0.943	347
SPAC2C4.07c		ribonuclease II (RNB) family	0.908	372	0.945	643
SPAC9.06c		adducin	0.951	298	0.902	284

Systematic ID	Gene name	Gene description	CF index screen 1	Cell number	CF index screen 2	Cell number
SPAC1F12.04c		conserved fungal protein	0.911	272	0.942	391
SPAC26A3.06		methyltransferase	0.926	272	0.927	262
SPCC4G3.13c		CUE domain protein Cue1/4 family	0.976	581	0.878	382
SPACUNK4.12c	mug138	metallopeptidase	0.925	452	0.929	406
SPBC30B4.01c	wsc1	transmembrane receptor Wsc1	0.895	370	0.959	457
SPCC320.06		sequence orphan	0.893	247	0.961	257
SPAC644.08		haloacid dehalogenase-like hydrolase	0.972	337	0.882	280
SPAC56F8.02		AMP binding enzyme	0.946	336	0.908	231
SPAC5H10.01		DUF1445 family protein	0.939	441	0.915	284
SPCC16C4.03	pin1	peptidyl-prolyl cis-trans isomerase Pin1	0.901	227	0.954	251
SPBC3E7.07c		DUF757 family protein	0.883	319	0.972	263
SPBC4F6.11c		asparagine synthase	0.908	362	0.946	421
SPBC1778.02	rap1	telomere binding protein Rap1	0.896	394	0.958	299
SPBC2D10.04		arrestin Aly1 related	NaN	0	0.927	256
SPBC337.04	ppk27	serine/threonine protein kinase Ppk27	0.955	249	0.899	417
SPAC631.01c	acp2	F-actin capping protein beta subunit	0.936	223	0.919	290
SPAC343.11c	msc1	multi-copy suppressor of Chk1	0.953	535	0.902	277
SPAC20G8.04c		electron transfer flavoprotein-ubiquinone oxidoreductase	0.887	305	0.968	191
SPBC14C8.03	fma2	methionine aminopeptidase Fma2	0.895	401	0.960	206
SPAC922.03		1-aminocyclopropane-1-carboxylate deaminase	0.949	286	0.906	219
SPAC30C2.05	erv14	cornichon family protein Erv14	0.928	371	0.927	324
SPCC1259.02c		aminopeptidase	0.944	337	0.911	230
SPAC1556.05c		CGR1 family	0.890	362	0.965	213
SPAC3H8.10	spo20	sec14 cytosolic factor family Sec14	NaN	0	0.928	252
SPCC550.12	arp6	actin-like protein Arp6	0.875	151	0.980	209
SPBC13E7.08c		RNA polymerase II associated Paf1 complex	0.924	416	0.931	408
SPBC2D10.12	rhp23	Rad23 homolog Rhp23	0.924	413	0.931	392
SPBC28F2.05c		xylose and arabinose reductase	0.910	216	0.946	356
SPBC336.10c	tif512	translation initiation factor	0.911	296	0.945	395
SPAC16A10.03c		zinc finger protein Pep5/Vps11	0.964	187	0.892	156
SPBC16A3.12c		triglyceride lipase-cholesterol esterase	0.908	349	0.947	344
SPCC1223.01		ubiquitin-protein ligase E3	0.917	309	0.938	446
SPCC965.12		dipeptidyl aminopeptidase	0.914	290	0.942	826
SPAC3A11.02	cps3	zinc finger protein Cps3	0.942	373	0.914	226
SPCC162.11c		uridine kinase	0.931	379	0.925	288
SPBC16A3.07c	nrm1	negative regulator of MBF	0.916	210	0.940	182
SPAC17H9.11		cofilin/tropomyosin family protein	0.887	329	0.969	289
SPAC631.02		bromodomain protein	0.964	278	0.892	138
SPAC1039.03		esterase/lipase	0.898	677	0.958	416
SPAC105.01c		potassium ion/proton antiporter	0.911	273	0.945	162
SPAC328.05		RNA-binding protein involved in export of mRNAs	0.930	279	0.926	737
SPBC1604.11	atp17	F-0 ATPase subunit F	0.928	160	NaN	0
SPAC6B12.02c	mus7	DNA repair protein Mus7	0.960	199	0.897	337
SPCC18.03		shuttle craft like transcriptional regulator	0.894	289	0.962	431
SPAC1A6.08c	mug125	sequence orphan	0.893	342	0.963	298
SPCPB1C11.01	amt1	ammonium transporter Amt1	0.941	432	0.915	976
SPBC776.11	rpl2801	60S ribosomal protein Ll28B 27a	0.898	269	0.959	367
SPBC1347.11	sro1	sequence orphan	0.883	355	0.974	408
SPAC22H10.04		protein phosphatase type 2A	0.905	317	0.951	333
SPAC139.04c	fap2	L-saccharopine oxidase	0.929	321	0.928	315
SPCC1902.01	gaf1	transcription factor Gaf1	0.885	231	0.972	171
SPAPB24D3.01		transcription factor	0.958	350	0.898	570
SPBC19G7.08c		arrestin	0.930	202	0.927	162
SPBP8B7.05c		carbonic anhydrase	0.916	220	0.941	170
SPAP14E8.04	oma1	metallopeptidase Oma1	0.942	357	0.916	281
SPAC57A10.04	mug10	sequence orphan	0.899	359	0.958	278
SPBC1773.05c	tms1	hexitol dehydrogenase	0.893	143	0.964	208
SPAC23G3.12c		serine protease	0.916	296	0.941	246
SPBC660.14	mik1	mitotic inhibitor kinase Mik1	0.887	338	0.970	287
SPCC569.07		aromatic aminotransferase	0.889	313	0.968	431
SPBP4G3.02	pho1	acid phosphatase Pho1	0.966	320	0.892	275
SPAC18G6.02c	chp1	chromodomain protein Chp1	0.896	369	0.962	342
SPAC926.02		conserved fungal protein	0.890	282	0.968	321
SPBC1289.14		adducin	0.899	272	0.959	77
SPBC18E5.08		N-acetyltransferase	0.907	189	0.951	345
SPACUNK4.19	mug153	sequence orphan	0.886	385	0.972	385

Systematic ID	Gene name	Gene description	CF index screen 1	Cell number	CF index screen 2	Cell number
SPAC11E3.14		conserved protein	0.882	301	0.977	277
SPAC11E3.12		conserved eukaryotic protein	0.924	429	0.934	361
SPBC405.03c		membrane transporter	0.906	299	0.952	333
SPAC5D6.04		auxin family	0.920	432	0.938	446
SPAC144.01		sequence orphan	0.906	385	0.953	350
SPAC11D3.14c		oxoprolinase	0.887	431	0.971	197
SPAC31G5.09c	spk1	MAP kinase Spk1	0.888	268	0.970	241
SPCC23B6.02c		sequence orphan	0.911	502	0.948	471
SPCC18B5.09c		sequence orphan	0.908	274	0.951	314
SPCC1620.04c	mug55	Cdc20/Fizzy family WD repeat protein	0.898	221	0.961	318
SPBC17D11.03c		conserved fungal protein	0.896	253	0.963	181
SPBC30D10.13c	pdb1	pyruvate dehydrogenase e1 component beta subunit Pdb1	0.929	110	NaN	0
SPAC11E3.11c		guanyl-nucleotide exchange factor	0.951	298	0.908	410
SPCC1322.16	phb2	prohibitin Phb2	0.879	680	0.980	488
SPBC1347.03	meu14	sporulation protein Meu14	0.902	339	0.957	345
SPBC646.08c		oxysterol binding protein	0.936	251	0.923	224
SPCC63.13		DNAJ domain protein	0.910	261	0.949	300
SPAC7D4.02c		src (SH3) homology domain protein, unknown family	0.924	251	0.935	210
SPCC895.05	for3	formin For3	0.894	215	0.965	204
SPAC12G12.07c		conserved fungal protein	0.934	262	0.925	329
SPAC343.12	rds1	conserved fungal protein	0.913	389	0.947	289
SPAC139.01c		nuclease, XP-G family	0.942	258	0.917	109
SPBC27B12.05		WD repeat protein	0.885	339	0.974	308
SPBC146.06c		human MTMR15 homolog	0.959	318	0.900	216
SPCC24B10.18		human Leydig cell tumor 10 kDa protein homolog	0.900	379	0.960	437
SPBC1703.07		ATP citrate synthase subunit 1	0.956	324	0.903	217
SPAC6C3.02c		CHCH domain protein	0.893	216	0.967	279
SPAC688.12c		sequence orphan	0.897	314	0.963	382
SPCC825.01		ribosome biogenesis ATPase, Arb family	0.917	407	0.943	326
SPBC25H2.09		DUF1690 family protein	0.910	426	0.950	259
SPBC1706.03	fzo1	mitochondrial fusion GTPase protein	0.924	355	0.936	382
SPCC794.11c		ENTH domain protein Ent3	NaN	0	0.930	257
SPBC839.06	cta3	P-type ATPase, calcium transporting Cta3	0.901	298	0.959	282
SPBP8B7.02		sequence orphan	0.897	268	0.963	326
SPBC1604.03c		sequence orphan	0.891	291	0.969	258
SPCC16C4.04		sequence orphan	0.894	304	0.966	437
SPAC222.13c		6-phosphofructo-2-kinase	0.906	263	0.954	253
SPBC56F2.09c	arg5	arginine specific carbamoyl-phosphate synthase Arg5	NaN	0	0.930	7
SPAC1F5.08c	yam8	calcium transport protein	0.916	344	0.944	162
SPAC3H1.14		cytoplasmic vesicle protein, Vid24 family	0.888	278	0.973	354
SPAC23H4.01c		sterol binding ankyrin repeat protein	0.956	280	0.905	265
SPBC25B2.02c	mam1	M-factor transporter Mam1	0.904	336	0.956	337
SPBPB8B6.04c	grt1	transcription factor Grt1	0.909	275	0.952	468
SPBC530.10c	anc1	adenine nucleotide carrier Anc1	0.874	157	0.986	125
SPCC1259.11c	gyp2	GTPase activating protein Gyp2	0.914	298	0.946	219
SPBC577.13	syj2	inositol polyphosphate phosphatase	0.882	213	0.978	353
SPBC354.14c	vac8	vacuolar protein Vac8	0.935	341	0.925	370
SPAC22E12.14c	sck2	serine/threonine protein kinase Sck2	0.967	460	0.894	562
SPBC30B4.02c		R3H and G-patch domain, unknown biological role	0.883	257	0.978	377
SPACUNK4.17		NAD binding dehydrogenase family protein	0.887	315	0.973	320
SPAC15E1.07c	moa1	meiotic cohesin complex associated protein Moa1	0.909	337	0.952	271
SPAC23D3.11	ayr1	1-acyldihydroxyacetone phosphate reductase	0.897	324	0.964	257
SPCC330.12c	sdh3	succinate dehydrogenase (ubiquinone)	0.873	85	0.988	123
SPAC16C9.05	cph1	PHD finger containing protein	0.951	288	0.910	263
SPCC18.09c		conserved eukaryotic protein	0.899	259	0.962	293
SPBC21C3.07c		actin binding methyltransferase	0.947	458	0.914	225
SPAC1F12.05		conserved fungal protein	0.894	223	0.967	204
SPCC364.05	vps3	GTPase regulator Vps3	0.961	361	0.900	319
SPCC613.06	rpl902	60S ribosomal protein L9	0.917	411	0.944	308
SPAC458.04c		sequence orphan	0.903	376	0.959	314
SPAC1D4.06c	csk1	cyclin-dependent kinase activating kinase Csk1	0.921	169	0.940	299
SPCC1827.02c		cholinephosphate cytidylyltransferase	0.970	389	0.891	208
SPAC29E6.05c		peptide methionine sulfoxide reductase	0.927	414	0.935	328
SPAC17H9.06c		conserved fungal protein	0.887	311	0.974	299
SPCC777.04		amino acid transporter	0.971	612	0.891	318
SPCC569.03		DUF1773 family protein 4	0.935	232	0.927	235

Systematic ID	Gene name	Gene description	CF index screen 1	Cell number	CF index screen 2	Cell number
SPAPB1A10.15		Arv1-like family protein	0.910	481	0.952	329
SPAC22G7.04	ubp13	poly(A)-specific ribonuclease complex subunit Pan2	0.969	329	0.892	275
SPBC23G7.06c		conserved eukaryotic protein	0.931	616	NaN	0
SPCC613.02		membrane transporter	0.891	276	0.971	425
SPCC1753.02c	git3	G-protein coupled receptor Git3	0.903	313	0.959	248
SPAC57A10.06	mug15	sequence orphan	0.893	274	0.969	275
SPAC1B1.04c		poly(A)-specific ribonuclease complex subunit Pan3	0.902	283	0.960	275
SPAC8F11.03	msh3	MutS protein homolog 3	0.907	296	0.955	243
SPAC6C3.06c		P-type ATPase, calcium transporting	0.944	474	0.918	532
SPBC32H8.13c	mok12	alpha-1,3-glucan synthase Mok12	0.878	233	0.984	358
SPCC1450.11c	cek1	serine/threonine protein kinase Cek1	0.972	315	0.891	251
SPBC725.11c	php2	CCAAT-binding factor complex subunit Php2	0.937	270	0.926	260
SPCC825.02		glucosidase II Gtb1	0.898	294	0.964	222
SPBC2F12.04	rpl1701	60S ribosomal protein L17	0.905	413	0.958	361
SPAC9E9.11	plr1	pyridoxal reductase	0.926	268	0.937	306
SPAC1002.12c		succinate-semialdehyde dehydrogenase	0.964	325	0.898	309
SPAC1071.06	arp9	SWI/SNF and RSC complex subunit Arp9	0.974	454	0.889	225
SPAC5H10.10		NADPH dehydrogenase	0.970	330	0.893	241
SPCC1682.15	mug122	PX/PXA domain protein	0.899	355	0.964	341
SPBC2D10.17	clr1	cryptic loci regulator Clr1	0.922	97	0.941	114
SPBC4B4.11		conserved fungal protein	NaN	0	0.932	277
SPAC22H10.08		conserved protein	0.928	578	0.935	383
SPAC17G8.05	med20	TATA-box related factor (TRF)	0.905	188	0.959	346
SPBC106.12c		THO complex subunit	0.954	416	0.909	507
SPAC222.12c	atp2	F1-ATPase beta subunit	0.911	2	0.953	383
SPAC144.03	ade2	adenylosuccinate synthetase Ade2	0.923	259	0.940	390
SPBC609.04	caf5	spermine family transporter	0.927	218	0.937	306
SPBC577.04		human THOC5 homolog	0.898	159	0.965	229
SPAC22F3.13	tsc1	hamartin	0.965	2	0.899	290
SPAC25B8.08		conserved fungal family	0.963	256	0.901	231
SPAC664.12c		LYR family protein	0.931	433	0.933	270
SPBC887.01		acireductone dioxygenase family	0.894	104	0.970	299
SPAC1783.02c	vps66	acyltransferase	0.955	411	0.909	465
SPAC4F10.11	spn1	septin Spn1	0.970	56	0.894	116
SPBC56F2.06	mug147	sequence orphan	0.961	383	0.903	402
SPBC211.06	gfh1	gamma tubulin complex subunit Gfh1	0.908	299	0.956	222
SPAC6C3.07	mug68	sequence orphan	0.958	214	0.906	387
SPCC777.10c	ubc12	ubiquitin conjugating enzyme Ubc12	0.966	699	0.899	312
SPAC4F10.02		aspartyl aminopeptidase	0.928	388	0.936	248
SPAC12B10.16c	mug157	conserved protein (fungal and bacterial)	0.888	336	0.977	292
SPAC1F7.01c	spt6	transcription elongation factor Spt6	0.914	143	0.950	183
SPAC694.04c		conserved eukaryotic protein	0.947	234	0.918	461
SPAC1002.18	urg3	DUF1688 family protein	0.967	323	0.898	305
SPBC1718.03	ker1	RNA polymerase I transcription factor subunit Ker1	0.947	290	0.918	322
SPAC13C5.04		glutamine amidotransferase	0.887	327	0.978	268
SPBC713.09		sequence orphan	0.906	256	0.959	291
SPAC4G8.10	gos1	SNARE Gos1	0.910	427	0.955	293
SPBC29A3.01		heavy metal ATPase	0.959	311	0.906	245
SPAC1006.03c		human CCDC131 homolog	0.905	314	0.961	295
SPBC21B10.05c	pop3	WD repeat protein Pop3	0.933	1	NaN	0
SPAC8E11.10		short chain dehydrogenase	0.905	206	0.960	231
SPBC405.07	rpl3602	60S ribosomal protein L36	0.914	518	0.951	327
SPBC19F5.01c	puc1	cyclin Puc1	0.902	443	0.963	385
SPAC23H4.08		RNA polymerase II associated protein	0.910	430	0.956	239
SPBC651.12c		sequence orphan	0.920	250	0.945	304
SPBC1105.18c		peptide release factor	0.929	294	0.937	281
SPAC1039.09	isp5	amino acid permease Isp5	0.896	483	0.970	411
SPAC13G6.01c	rad8	ubiquitin-protein ligase E3	0.896	395	0.970	335
SPAC2E1P5.02c	mug109	sequence orphan	NaN	0	0.933	268
SPBC336.06c	rnh1	ribonuclease H Rnh1	0.928	395	0.938	400
SPAC11G7.04	ubi1	ribosomal-ubiquitin fusion protein Ubi1	0.927	356	0.939	286
SPBC1604.18c		vacuolar sorting protein	0.900	325	0.966	228
SPBC725.01		aspartate aminotransferase	0.885	235	0.981	321
SPAC1071.04c		signal peptidase subunit	0.922	405	0.944	582
SPCC576.14		diphthine synthase	0.973	376	0.893	437
SPBC4.02c		conserved fungal protein	0.947	715	0.919	414
SPAC24H6.09	gef1	RhoGEF Gef1	0.963	428	0.904	412

Systematic ID	Gene name	Gene description	CF index screen 1	Cell number	CF index screen 2	Cell number
SPAC25B8.05		pseudouridylate synthase	0.906	343	0.961	106
SPAC20H4.11c	rho5	Rho family GTPase Rho5	0.942	345	0.924	277
SPAC13F5.07c		sequence orphan	0.948	582	0.918	346
SPBC18H10.04c	sce3	translation initiation factor eIF4B	0.942	239	0.924	263
SPCC162.10	ppk33	serine/threonine protein kinase Ppk33	0.905	392	0.962	282
SPBC36.07	iki3	RNA polymerase II elongator subunit Iki3	0.960	215	0.907	548
SPAPJ696.01c	vps17	retromer complex subunit Vps17	0.934	276	0.932	336
SPAC9G1.08c		phospholipase	0.906	378	0.961	264
SPBC16G5.09		serine carboxypeptidase	0.898	289	0.969	370
SPBC1773.17c		hydroxyacid dehydrogenase	0.950	378	0.917	367
SPAC1805.02c		electron transfer flavoprotein beta subunit	0.917	324	0.951	353
SPAC959.04c		mannosyltransferase complex subunit	0.911	269	0.956	235
SPAC19B12.04	rps3001	40S ribosomal protein S30	0.957	380	0.910	415
SPCC16A11.03c		conserved protein (fungal and protazoan)	0.954	302	0.914	244
SPCC1281.07c		glutathione S-transferase Gst3	0.910	317	0.957	404
SPCC5E4.07	rpl2802	60S ribosomal protein L27a.2/L28A	0.931	699	0.937	537
SPBC1718.02	hop1	linear element associated protein Hop1	0.904	228	0.964	280
SPBC1773.12		transcription factor	0.913	378	0.954	274
SPBC1734.13	atp3	F1-ATPase gamma subunit	0.929	221	0.938	297
SPAC959.05c		protein disulfide isomerase	0.921	783	0.946	350
SPBC119.03		S-adenosylmethionine-dependent methyltransferase	0.935	620	0.932	412
SPAC25G10.09c		actin cortical patch component, with EF hand and WH2 motif	0.894	159	0.974	258
SPBC11C11.08	srp1	SR family protein Srp1	0.930	191	0.938	227
SPBC2A9.02		NAD dependent epimerase/dehydratase family protein	0.942	263	0.926	276
SPAPB24D3.08c		NADP-dependent oxidoreductase	0.956	338	0.912	362
SPAC30.02c		RNA polymerase II elongator complex subunit	0.921	345	0.947	294
SPBPB2B2.14c		S. pombe specific DUF999 protein family 8	0.935	368	0.933	301
SPBC4.05	mlo2	zinc finger protein Mlo2	0.928	199	0.941	321
SPBC21H7.04		ATP-dependent RNA helicase Dbp7	0.892	356	0.977	357
SPAC22G7.08	ppk8	serine/threonine protein kinase Ppk8	0.900	292	0.969	447
SPAPB17E12.03		ubiquitin-protein ligase E3	0.925	320	0.944	467
SPBC106.19		sequence orphan	0.887	359	0.982	3
SPAC27E2.03c		GTP binding protein	0.953	326	0.915	289
SPAC4D7.02c		glycerophosphoryl diester phosphodiesterase	0.915	488	0.954	318
SPAC5H10.06c	adh4	alcohol dehydrogenase Adh4	0.935	454	0.934	345
SPBC21C3.15c		aldehyde dehydrogenase	0.904	333	0.965	328
SPAC29B12.04	snz1	pyridoxine biosynthesis protein	0.935	4	NaN	0
SPCC74.05	rpl2702	60S ribosomal protein L27	0.960	493	0.909	832
SPAC1002.19	urg1	GTP cyclohydrolase	0.978	423	0.891	519
SPAC869.01		amidase	0.935	284	0.934	499
SPCC191.10		sequence orphan	0.952	372	0.917	241
SPAC1039.05c	klf1	conserved fungal protein	0.904	395	0.965	591
SPCC31H12.02c	mug73	membrane transporter	0.902	283	0.967	291
SPBC359.03c		amino acid permease, unknown 8	0.906	274	0.964	266
SPAC6F12.06		Rho GDP dissociation inhibitor Rdi1	0.907	281	0.962	406
SPCC1672.12c		DUF410 family protein	0.931	375	0.938	317
SPAC323.07c		MatE family transporter	0.918	374	0.952	324
SPAC13A11.06		pyruvate decarboxylase	0.899	410	0.971	334
SPAC2F3.15	lsk1	latrunculin sensitive kinase Lsk1	0.935	273	0.935	306
SPAC343.07	mug28	RNA-binding protein Mug28	0.965	391	0.905	378
SPBC83.13		mitochondrial tricarboxylic acid transporter	0.939	582	0.931	405
SPAC6G10.02c	tea3	cell end marker Tea3	0.968	313	0.902	308
SPAC6G9.09c	rpl24	60S ribosomal protein L24	0.949	307	0.921	376
SPAC1805.07c	dad2	DASH complex subunit Dad2	0.934	272	0.936	370
SPAC17D4.01	pex7	peroxin-7	0.963	230	0.907	257
SPAC343.16	lys2	homoaconitate hydratase Lys2	0.900	245	0.970	4
SPBPB10D8.06c		membrane transporter	0.911	442	0.960	364
SPAC1556.01c	rad50	DNA repair protein Rad50	0.946	214	0.924	216
SPCC330.14c	rpl2402	60S ribosomal protein L24	0.902	328	0.968	304
SPAC17C9.11c		zinc finger protein	0.910	364	0.960	370
SPAC29B12.05c		S-adenosylmethionine-dependent methyltransferase	NaN	0	0.935	22
SPBC646.09c	int6	translation initiation factor eIF3e	0.950	379	0.921	256
SPCC1020.06c	tal1	transaldolase	0.926	284	0.945	240

Systematic ID	Gene name	Gene description	CF index screen 1	Cell number	CF index screen 2	Cell number
SPAC3G6.05		Mvp17/PMP22 family	0.946	248	0.925	274
SPBC337.10c		anamorsin family protein	0.974	266	0.897	329
SPBC342.03		1,3-beta-glucanosyltransferase	0.943	258	0.928	293
SPCC1223.09		uricase	NaN	0	0.936	410
SPCC74.02c		mRNA cleavage and polyadenylation specificity factor complex associated protein	0.950	288	0.921	246
SPAC26H5.07c		seven transmembrane receptor-like protein	0.921	443	0.950	287
SPBC30D10.04	swi3	replication fork protection complex subunit Swi3	0.905	244	0.967	292
SPBC1105.05	exg1	glucan 1,3-beta-glucosidase I/II precursor	0.970	199	0.901	141
SPBC19C7.05		cell wall organization protein	0.899	267	0.973	400
SPBC16G5.05c		MSP domain	0.922	230	0.950	339
SPAC24H6.11c		sulfate transporter	0.912	288	0.959	322
SPAC57A10.09c		High-mobility group non-histone chromatin protein	0.904	211	0.967	246
SPAC1565.02c		GTPase activating protein	0.912	389	0.959	384
SPAC22A12.14c		BSD domain protein, unknown biological role	0.959	448	0.912	412
SPAC17G6.03		phosphoprotein phosphatase	0.910	330	0.962	291
SPAC1250.05	rpl3002	60S ribosomal protein L30	0.942	323	0.929	436
SPAC2G11.10c		URM1 activating enzyme	0.909	324	0.962	217
SPBC887.04c	lub1	WD repeat protein Lub1	0.902	334	0.970	226
SPBC21C3.17c		conserved fungal protein	0.899	514	0.972	373
SPBC15D4.03	slm9	hira protein Slm9	0.932	262	0.940	258
SPAC29B12.11c		human WW domain binding protein-2 ortholog	0.914	398	0.958	596
SPBC4F6.10	vps901	guanyl-nucleotide exchange factor Vps901	0.964	133	0.908	258
SPBC1105.10	rav1	RAVE complex subunit Rav1	0.938	351	0.934	687
SPCC126.03	pus1	tRNA pseudouridylate synthase Lsp1	0.959	248	0.913	378
SPAC630.07c		sequence orphan	0.932	353	0.940	414
SPCC970.07c	raf2	Rik1-associated factor Raf2	0.903	258	0.969	212
SPAC23H3.03c		nitrogen permease regulator family	0.963	2	0.909	397
SPBC3B8.05		diphthamide biosynthesis protein	0.910	392	0.962	394
SPAC10F6.15		S. pombe specific UPF0300 family protein 1	0.913	403	0.959	221
SPAC1071.03c		sequence orphan	0.903	605	0.969	400
SPAC922.06		short chain dehydrogenase	0.916	325	0.956	375
SPAC1F7.11c		transcription factor	0.967	353	0.905	548
SPBC11G11.01	fis1	mitochondrial fission protein Fis1	0.930	308	0.943	316
SPAC3H8.09c	nab3	poly(A) binding protein Nab3	0.935	187	0.938	174
SPBC1215.01	shy1	SURF-family protein Shy1	0.959	593	0.913	40
SPAC1782.08c	rex3	exonuclease Rex3	0.962	228	0.910	242
SPBC660.09	mug168	sequence orphan	0.900	345	0.973	283
SPAC26H5.05		IPT/TIG ankyrin repeat protein	0.944	388	0.929	260
SPAC110.02	pds5	cohesin-associated protein Pds5	0.941	219	0.932	266
SPCC1753.05	rsm1	RNA export factor Rsm1	0.902	458	0.971	396
SPBC27B12.11c		transcription factor	0.923	304	0.950	342
SPBC1711.04		methylenetetrahydrofolate reductase	0.942	200	0.932	261
SPCC645.14c	sti1	chaperone activator Sti1	0.924	172	0.949	263
SPBC1683.13c		transcription factor	0.948	278	0.926	272
SPCP1E11.07c	cwf18	complexed with Cdc5 protein Cwf18	0.903	263	0.970	240
SPCC569.05c		spermidine family transporter	0.915	335	0.959	412
SPAC2E1P5.03		DNAJ domain protein Erj5	0.934	631	0.940	398
SPCC622.18	rpl6	60S ribosomal protein L6	0.962	357	0.912	331
SPBC3B8.06		conserved fungal protein	0.931	232	0.943	211
SPBP26C9.02c	car1	arginase Car1	0.951	537	0.923	436
SPBC16C6.02c	vps1302	chorein homolog	0.903	315	0.972	253
SPBC530.14c	dsk1	SR protein-specific kinase Dsk1	0.950	347	0.925	478
SPAC824.02		GPI inositol deacylase	0.947	69	0.928	195
SPCC63.04	mok14	alpha-1,3-glucan synthase Mok14	0.905	302	0.969	361
SPAC7D4.08		sequence orphan	0.956	233	0.919	301
SPBC36.03c		spermidine family transporter	0.930	233	0.945	345
SPAC22G7.03		sequence orphan	0.910	522	0.964	260
SPAC3H1.03	mug151	transcriptional regulator, HCNGP-like	0.930	106	0.945	295
SPAC2G11.05c		BRO1 domain protein	0.930	282	0.945	377
SPBC29A10.03c	rlf2	chromatin remodeling complex subunit Rlf2	0.959	243	0.916	245
SPAC19G12.03	cda1	chitin deacetylase Cda1	0.910	406	0.964	343
SPAC343.04c	gnr1	heterotrimeric G protein beta subunit Gnr1	0.926	338	0.949	371
SPAC27D7.06		electron transfer flavoprotein alpha subunit	0.908	275	0.967	539
SPAC22G7.01c		aminopeptidase	0.948	209	0.927	220
SPCC18.10		pyridoxine-pyridoxal-pyridoxamine kinase	0.967	318	0.908	505
SPAC24C9.16c	cox8	cytochrome c oxidase subunit VIII	0.913	527	0.962	325

Systematic ID	Gene name	Gene description	CF index screen 1	Cell number	CF index screen 2	Cell number
SPBC1683.03c		membrane transporter	0.908	440	0.967	291
SPAC8C9.10c		ribosome biogenesis protein Rrp14-N	0.938	150	0.938	373
SPBC3E7.01	fab1	1-phosphatidylinositol-3-phosphate 5-kinase Fab1	0.945	175	0.930	216
SPAC22A12.10		diacylglycerol cholinephosphotranferase/ diacylglycerol ethanolaminesphotranferase	0.934	275	0.941	296
SPAC13C5.01c		20S proteasome component alpha 3	0.956	420	0.920	279
SPBC56F2.02	rpl1901	60S ribosomal protein L19	0.952	312	0.924	484
SPCC320.04c		GTPase Gem1	0.905	287	0.971	375
SPBP35G2.03c	sgo1	shugoshin Sgo1	0.919	258	0.957	328
SPAC3G9.01		sequence orphan	0.908	295	0.968	373
SPBC1105.11c	hht3	histone H3 h3.3	0.970	469	0.906	788
SPCC16A11.10c	oca8	cytochrome b5	0.957	463	0.919	759
SPCC965.11c		amino acid transporter	0.903	288	0.974	326
SPAC22A12.17c		short chain dehydrogenase	0.909	302	0.967	359
SPBC800.02	whi5	cell cycle transcriptional repressor Whi5	0.921	314	0.955	460
SPAC637.03		conserved fungal protein	0.912	181	0.964	319
SPBC215.07c		PWWP domain protein	0.899	250	0.977	268
SPAC3F10.02c	trk1	potassium ion transporter Trk1	0.940	391	0.936	358
SPAC22F3.07c	atp20	F0-ATPase subunit G	0.922	353	0.954	363
SPBC14F5.13c		alkaline phosphatase	0.934	226	0.943	263
SPBC342.05	crb2	DNA repair protein RAD9 homolog, Rhp9	0.919	260	0.957	292
SPAC17G6.17	pof8	F-box protein Pof8	0.943	303	0.934	315
SPAC977.15		dienelactone hydrolase family	0.975	343	0.901	309
SPAC17G8.09	shg1	Csp15 family protein	0.921	306	0.955	318
SPAC1952.03		cysteine protease	0.929	270	0.948	351
SPAC31G5.15		phosphatidylserine decarboxylase	0.938	979	NaN	0
SPAC17D4.04		tRNA (cytosine-5-)-methyltransferase	0.911	392	0.966	355
SPAC688.03c		human AMMECR1 homolog	0.935	317	0.941	333
SPCC306.11		sequence orphan	0.968	216	0.909	191
SPAC5H10.02c		ThiJ domain protein	0.908	222	0.969	178
SPAC27D7.05c	apc14	anaphase-promoting complex subunit Apc14	0.926	368	0.950	430
SPBC2G2.08	ade9	C-1-tetrahydrofolatesynthase/methylenetetrahydrofolatedehydrogenase/methylenetetrahydrofolatecyclohydrolase/formyltetrahydrofolate synthetase	0.945	223	0.932	302
SPAC977.06		S. pombe specific DUF999 family protein 3	0.912	349	0.966	373
SPCC622.19	jmj4	Jmj4 protein	0.912	290	0.965	313
SPBC1348.07		S. pombe specific DUF999 protein family 6	NaN	0	0.939	363
SPAC25B8.18		mitochondrial electron carrier	0.919	446	0.958	303
SPCC70.08c		methyltransferase	0.921	482	0.957	273
SPAC750.08c		NAD-dependent malic enzyme	0.942	324	0.936	329
SPAC24H6.03	cul3	cullin 3	0.905	337	0.973	291
SPAC31G5.18c		ubiquitin family, human C1ORF55 related	0.927	277	0.951	293
SPBC1683.09c	frp1	ferric-chelate reductase Frp1	0.964	222	0.914	302
SPCC188.02	par1	protein phosphatase regulatory subunit Par1	0.908	212	0.969	222
SPAC4D7.07c		sequence orphan	0.904	253	0.974	270
SPCC16A11.07	coq10	ubiquinone binding protein Coq10	0.960	21	0.917	186
SPAC23A1.09		RNA-binding protein	0.946	232	0.932	246
SPBC32F12.12c		conserved fungal protein	0.912	341	0.966	364
SPAC17A5.09c		protein phosphatase regulatory subunit Glc9	0.938	157	0.940	286
SPBC15D4.07c	atg9	autophagy associated protein Atg9	0.923	453	0.955	183
SPBP8B7.21	ubp3	ubiquitin C-terminal hydrolase Ubp3	0.918	319	0.960	319
SPAC212.01c		S. pombe specific DUF999 family protein 2	0.908	429	0.970	263
SPAC1093.02		pyridoxamine 5-phosphate oxidase	0.908	420	0.970	355
SPCC31H12.06	mug111	sequence orphan	0.936	268	0.942	227
SPCC11E10.07c		translation initiation factor eIF2B alpha subunit	0.924	382	0.954	308
SPAC18B11.11		GTPase activating protein	0.904	27	0.974	20
SPBC337.13c	gtr1	Gtr1/RagA G protein Gtr1	NaN	0	0.939	298
SPBC23G7.15c	rpp202	60S acidic ribosomal protein P2B subunit	0.903	239	0.975	292
SPAC167.01	ppk4	serine/threonine protein kinase Ppk4	0.969	163	0.910	161
SPAC11E3.04c	ubc13	ubiquitin conjugating enzyme Ubc13	0.962	228	0.916	270
SPBC337.03		conserved eukaryotic protein	0.960	331	0.919	501
SPAC29B12.14c		purine transporter	0.919	476	0.959	310
SPAC11D3.05		membrane transporter	0.926	379	0.952	230
SPCC794.15		sequence orphan	0.966	377	0.912	624
SPCC1442.02		DUF1760 family protein	NaN	0	0.939	274
SPCC622.08c	hta1	histone H2A alpha	0.918	524	0.960	321
SPAC17A2.13c	rad25	14-3-3 protein Rad25	0.939	8	0.939	514

Systematic ID	Gene name	Gene description	CF index screen 1	Cell number	CF index screen 2	Cell number
SPBPB10D8.01		cysteine transporter	0.916	347	0.962	312
SPBC646.12c	gap1	GTPase activating protein Gap1	NaN	0	0.939	1
SPCC569.08c	ade5	glycinamide ribonucleotide transformylase	0.974	570	0.905	361
SPBC4F6.15c	swi10	DNA repair endonuclease	0.945	302	0.934	212
SPCC18.15		WD repeat protein, human WRDR85 family	0.914	360	0.965	339
SPBC3D6.09	dpb4	DNA polymerase epsilon subunit Dpb4	0.906	251	0.973	237
SPCC306.04c	set1	histone lysine methyltransferase Set1	0.922	240	0.957	260
SPAC12G12.01c		ubiquitin-protein ligase E3	0.957	245	0.922	415
SPAC1071.07c	rps1502	40S ribosomal protein S15	0.923	341	0.956	292
SPAC29A4.19c		P-type ATPase	0.905	281	0.974	372
SPCC1795.06	map2	P-factor	0.914	359	0.966	395
SPAPB8E5.02c	rpn502	19S proteasome regulatory subunit Rpn502	0.969	335	0.910	346
SPCC1235.13	ght6	hexose transporter Ght6	0.911	353	0.968	338
SPBC25H2.08c	mrs2	magnesium ion transporter Mrs2	0.924	211	0.956	332
SPCP25A2.02c	rhp26	SNF2 family helicase Rhp26	0.947	375	0.933	360
SPAC29E6.10c		kinetochore protein	0.934	320	0.945	494
SPAC6F6.17	rif1	telomere length regulator protein Rif1	0.920	631	0.959	325
SPBC12D12.09	rev7	DNA polymerase zeta Rev7 (predicted)	0.923	189	0.957	206
SPAC6B12.14c		conserved fungal protein	0.962	235	0.918	381
SPBC31F10.13c	hip1	hira protein Hip1	0.951	288	0.929	298
SPBC32F12.08c	duo1	DASH complex subunit Duo1	0.903	157	0.977	247
SPAC1A6.05c		triacylglycerol lipase	0.928	303	0.952	320
SPBC216.05	rad3	ATR checkpoint kinase	0.934	343	0.946	456
SPBC337.11		mitochondrial peptidase	0.939	254	0.941	188
SPCC1529.01		membrane transporter	0.936	276	0.944	252
SPBC12C2.05c		diacylglycerol binding protein Bzz1	0.930	344	0.951	484
SPBC215.05	gpd1	glycerol-3-phosphate dehydrogenase Gpd1	0.914	291	0.967	334
SPAC694.05c	rps2502	40S ribosomal protein S25	0.910	300	0.971	432
SPAC30.04c	abc4	glutathione S-conjugate-exporting ATPase Abc4	0.975	343	0.906	385
SPAC15A10.15	sgo2	shugoshin Sgo2	0.932	377	0.949	362
SPAC27E2.02		IMPACT homolog	0.902	299	0.979	999
SPAC22E12.11c	set3	histone lysine methyltransferase Set3	0.964	543	0.917	385
SPBC16C6.11	rpl3201	60S ribosomal protein L32	0.913	41	0.967	67
SPBC365.20c		nicotinamidase	0.905	269	0.976	207
SPAC1006.06	rgf2	RhoGEF Rgf2	0.947	554	0.934	605
SPAC1039.04		nicotinic acid plasma membrane transporter	0.913	449	0.968	388
SPBC428.17c	wpl1	conserved fungal protein	0.953	444	0.928	386
SPAC17A2.09c	csx1	RNA-binding protein Csx1	0.921	327	0.960	212
SPAC7D4.14c		sequence orphan	0.919	376	0.962	438
SPAC17A5.16		human down-regulated in multiple cancers-1 homolog 3	0.923	394	0.959	402
SPCC622.12c		NADP-specific glutamate dehydrogenase	0.976	346	0.905	320
SPAC13A11.05		peptidase family M17	0.909	270	0.973	335
SPAC589.03c		sequence orphan	0.922	348	0.960	121
SPAC9G1.11c	spn4	septin Spn4	0.921	147	0.961	174
SPAC9.10	thi9	amino acid permease, unknown 2	0.948	297	0.934	243
SPBP23A10.12		FRG1 family protein	0.975	385	0.907	304
SPAC26A3.04	rpl2002	60S ribosomal protein L20	0.927	491	0.955	370
SPBC337.16	cho1	phosphatidyl-N-methylethanolamine N-methyltransferase	NaN	0	0.941	4
SPAC630.05	gyp7	GTPase activating protein Gyp7	0.936	281	0.946	320
SPBC530.09c		cation dependent mannose-6-phosphate cargo receptor	0.937	341	0.945	395
SPAC25B8.11		transcription factor	0.959	259	0.923	259
SPAC22E12.03c		THIJ/PFPI family peptidase	0.928	464	0.955	461
SPBC36B7.08c		nucleosome assembly protein	0.906	215	0.976	297
SPCC594.04c		steroid oxidoreductase superfamily protein	0.964	227	0.919	195
SPAC4H3.14c		sequence orphan	0.959	338	0.924	411
SPBC16E9.07	mug100	sequence orphan	0.945	406	0.938	398
SPAC14C4.06c		poly(A) binding protein Nab2	0.909	339	0.974	294
SPAC869.03c		urea transporter	0.973	572	0.910	528
SPAC3C7.13c		glucose-6-phosphate 1-dehydrogenase	0.944	417	0.938	464
SPAC821.06	spn2	septin Spn2	0.949	292	0.934	278
SPAC18B11.07c	rhp6	Rad6 homolog Rhp6	0.954	286	0.929	296
SPAC10F6.04		RCC domain protein Ats1	0.911	509	0.972	550
SPCC663.09c		short chain dehydrogenase	0.969	359	0.914	401
SPAC513.01c	eft201	translation elongation factor 2	0.962	326	0.921	328

Systematic ID	Gene name	Gene description	CF index screen 1	Cell number	CF index screen 2	Cell number
SPAC1399.03	fur4	uracil permease	0.987	60	0.896	88
SPAC29A4.09		rRNA processing protein Rrp17	0.942	415	0.941	498
SPAC22A12.01c	pso2	DNA 5 exonuclease	0.949	498	0.934	346
SPAC1782.05		phosphotyrosyl phosphatase activator homolog	0.954	188	0.930	228
SPBC2G2.07c	mug178	mitochondrial ribosomal protein subunit L51-b	NaN	0	0.942	280
SPCC132.01c		DUF814 family protein	0.920	319	0.964	228
SPAC9G1.10c		inositol polyphosphate phosphatase	0.956	366	0.927	285
SPCC613.03		conserved fungal protein	0.923	223	0.961	334
SPAC1687.17c		Der1-like (degradation in the ER) family	0.906	246	0.977	302
SPBC21B10.07		glycosyl hydrolase family 16	0.929	218	0.954	295
SPAC607.06c		metallopeptidase	0.966	497	0.918	536
SPAC323.03c		sequence orphan	0.949	318	0.934	239
SPBC4C3.04c		guanyl-nucleotide exchange factor	0.914	185	0.970	366
SPAC977.05c		conserved fungal protein	0.952	333	0.932	354
SPAC13F5.03c		glycerol dehydrogenase (Phlippen, Stevens, Wolf, Zimmermann manuscript in preparation)	0.954	344	0.930	233
SPBC83.17		transcriptional coactivator, multiprotein bridging factor Mbf1	0.918	274	0.966	248
SPAPB24D3.09c	pdr1	ABC transporter Pdr1	0.927	217	0.957	363
SPBC25B2.01		elongation factor 1 alpha related protein	0.959	224	0.925	200
SPAC13A11.01c	rga8	GTPase activating protein Rga8	0.912	297	0.972	287
SPBP22H7.06		nicotinamide riboside kinase	0.946	392	0.939	318
SPBC365.01		sec14 cytosolic factor family	0.906	162	0.979	295
SPCC1235.05c	fft2	fun thirty related protein Fft2	0.975	372	0.909	357
SPAC20G4.02c	fus1	formin Fus1	0.918	487	0.966	385
SPAPB2B4.03	cig2	cyclin Cig2	0.910	344	0.975	294
SPBC11C11.01		RNA-binding protein	0.918	227	0.966	228
SPAC20G8.10c		beclin family protein	0.922	320	0.963	312
SPAC19G12.16c	adg2	conserved fungal protein	0.911	315	0.974	375
SPAC19B12.07c		human ZNF277P homolog	0.944	325	0.941	318
SPBC30D10.03c		IMP 5-nucleotidase	0.934	334	0.951	383
SPBC19C2.09	sre1	sterol regulatory element binding protein Sre1	0.970	255	0.915	193
SPBP35G2.05c	cki2	serine/threonine protein kinase Cki2	0.951	406	0.934	331
SPACUNK4.13c		GTPase Ylf2	0.967	311	0.918	312
SPBC1703.03c		armadillo repeat protein, unknown biological role	0.955	430	0.930	430
SPAC890.03	ppk16	serine/threonine protein kinase Ppk16	0.950	216	0.935	278
SPCC965.13		membrane transporter	0.919	207	0.966	266
SPBC354.13	rga6	GTPase activating protein Rga6	0.920	175	0.965	749
SPAC105.03c		transcription factor	0.921	318	0.965	380
SPAC23A1.03	apt1	adenine phosphoribosyltransferase (APRT)	0.954	352	0.931	383
SPBC1734.15	rsc4	RSC complex subunit Rsc4	0.928	394	0.958	325
SPAC23H3.11c		glucosidase	0.936	367	0.950	341
SPBC530.07c		TENA/THI domain	0.954	320	0.931	254
SPCC1442.04c		conserved fungal protein	0.929	587	0.957	395
SPBC29A10.07		nucleoporin Pom152	0.909	319	0.976	277
SPBC2D10.19c		sequence orphan	0.965	405	0.921	475
SPAC212.04c		S. pombe specific DUF999 family protein 1	0.925	793	0.961	352
SPBC30D10.05c		sepiapterin reductase	0.917	851	0.969	406
SPBC1D7.01		prefoldin subunit 1	0.911	277	0.974	324
SPCC965.10		transcription factor	0.920	397	0.966	335
SPAC13G6.04	tim8	TIM22 inner membrane protein import complex subunit Tim8	0.904	265	0.982	255
SPAC1687.14c		EF hand family protein, unknown role	0.918	298	0.968	325
SPAC23C4.07	tht2	meiotically upregulated gene Mug22	0.925	342	0.961	265
SPAC30D11.01c		alpha-glucosidase	0.928	375	0.959	310
SPBC21C3.02c		Sds3-like family	0.937	307	0.949	337
SPAC25B8.15c		wybutosine biosynthesis protein Tyw3	0.953	374	0.934	342
SPAPJ760.03c	adg1	sequence orphan	0.976	293	0.911	263
SPAC9G1.03c	rpl3001	60S ribosomal protein L30	0.931	436	0.956	781
SPBC1A4.02c	leu1	3-isopropylmalate dehydrogenase Leu1	0.960	946	0.927	266
SPCC4F11.04c		mannosyltransferase complex subunit	0.946	297	0.940	289
SPBC19C2.13c	ctu2	conserved eukaryotic protein	0.933	327	0.954	270
SPBC31F10.14c	hip3	HIRA interacting protein Hip3	0.935	407	0.952	310
SPAC26F1.10c	pyp1	tyrosine phosphatase Pyp1	0.941	236	0.946	247
SPAC6C3.05		sequence orphan	0.943	290	0.944	324
SPBC1D7.05	byr2	MAP kinase kinase kinase Byr2	0.931	384	0.957	475
SPAC513.02		phosphoglycerate mutase family	0.937	312	0.951	282

Systematic ID	Gene name	Gene description	CF index screen 1	Cell number	CF index screen 2	Cell number
SPCC285.05		purine nucleoside transporter	0.957	281	0.930	245
SPAC343.18	rfp2	ubiquitin-protein ligase E3	0.953	628	0.935	363
SPBC651.05c	dot2	EAP30 family protein Dot2	NaN	0	0.944	301
SPBC1347.07	rex2	RNA exonuclease	0.917	335	0.971	440
SPBC1105.12	hhf3	histone H4 h4.3	0.921	369	0.967	324
SPAPYUG7.06	mug67	PPPDE peptidase family	0.936	248	0.952	336
SPBC29A3.11c		mitochondrial carboxylic acid transporter	0.953	311	0.934	316
SPBC2F12.13	klp5	kinesin-like protein Klp5	0.967	255	0.921	272
SPCC663.13c		N-acetyltransferase	0.908	279	0.980	207
SPBC725.03		conserved fungal protein	0.972	381	0.916	541
SPCP1E11.11		Puf family RNA-binding protein	0.913	287	0.975	383
SPCC613.10	qcr2	ubiquinol-cytochrome-c reductase complex core protein Qcr2	0.961	1	0.927	13
SPBC947.10		ubiquitin-protein ligase E3	0.942	256	0.946	74
SPAC25H1.05	meu29	sequence orphan	0.932	136	0.956	269
SPAC30D11.13	hus5	SUMO conjugating enzyme	0.954	311	0.934	351
SPBC30D10.16	pha2	phrenate dehydratase	0.955	2	0.933	177
SPAC1039.07c		2,2-dialkylglycine decarboxylase	0.971	467	0.917	323
SPAC1687.09		conserved fungal protein	0.947	323	0.941	395
SPBC16A3.19		histone acetyltransferase complex subunit Eaf7	0.933	433	0.955	338
SPCC569.06		S. pombe specific multicopy membrane protein family 1	0.921	254	0.967	208
SPBC1683.07	mal1	alpha-glucosidase Mal1	0.957	290	0.931	313
SPAC17C9.16c		spermine family transporter	0.918	296	0.970	467
SPBC17G9.12c		conserved fungal protein	0.948	223	0.941	279
SPAC23C11.13c	hpt1	xanthine phosphoribosyltransferase	0.930	543	0.959	459
SPBC16H5.13		WD repeat protein (possible)	0.930	196	0.958	293
SPAC23C11.04c	pnk1	DNA kinase/phosphatase Pnk1	0.921	623	0.968	256
SPAC22H10.07	scd2	scaffold protein Scd2	0.927	121	0.961	241
SPAC1002.02	mug31	nucleoporin Pom34	0.947	332	0.942	323
SPAC26F1.01	sec74	guanyl-nucleotide exchange factor Sec74	0.956	323	0.933	379
SPBC418.02		NatA N-acetyltransferase complex subunit	0.921	231	0.968	236
SPBC11G11.02c	end3	actin cortical patch component End3	0.959	285	0.929	337
SPBC365.06	pmt3	SUMO	0.952	336	0.937	358
SPAC1399.05c		transcription factor	0.924	287	0.965	310
SPBC409.10	ade7	phosphoribosylamidoimidazolesuccinocarboxamide synthase Ade7	0.926	385	0.963	184
SPBC1271.11		tricarboxylate transporter	0.948	298	0.941	338
SPAPB8E5.06c	rpl302	60S ribosomal protein L3	0.943	440	0.946	434
SPBC557.04	ppk29	Ark1/Prk1 family protein kinase Ppk29	0.912	271	0.977	477
SPAC7D4.05		hydrolase	0.937	260	0.952	269
SPCC622.16c	epe1	transcription factor Epe1	0.926	342	0.963	269
SPBC29A10.10c		tRNA-splicing endonuclease positive effector	0.925	280	0.964	364
SPAC5H10.05c		NADHdh_2 domain protein	0.964	422	0.926	452
SPAC8E11.02c	rad24	14-3-3 protein Rad24	0.950	104	0.940	179
SPBC16E9.06c	uvi31	BolA domain UV inducedv protein Uvi31	0.970	199	0.920	252
SPAC1039.02		phosphoprotein phosphatase	0.939	283	0.951	259
SPCC584.16c		sequence orphan	0.926	300	0.964	236
SPCC1840.03	sal3	karyopherin Sal3	0.919	388	0.970	194
SPAC26A3.01	sxa1	aspartic protease Sxa1	0.910	215	0.979	306
SPAC890.05		ribosome biogenesis protein	0.933	404	0.957	365
SPCC1494.07		conserved eukaryotic protein	0.961	359	0.928	296
SPCC338.04	cid2	caffeine induced death protein Cid2	0.965	278	0.925	320
SPCPB1C11.03		cysteine transporter	0.928	551	0.962	411
SPAC22H10.13	zym1	metallothionein	0.963	370	0.927	249
SPBC1271.07c		N-acetyltransferase	0.938	284	0.952	381
SPBC800.03	clr3	histone deacetylase (class II) Clr3	0.934	74	0.956	67
SPBC31F10.03		ChaC-like protein	0.946	271	0.945	390
SPAC4G9.11c	cmb1	cytosine-mismatch binding protein 1	0.949	374	0.941	324
SPCP31B10.07	eft202	translation elongation factor 2	0.921	427	0.969	443
SPAC2F7.03c	pom1	DYRK family protein kinase Pom1	0.953	260	0.938	412
SPCC188.08c	ubp22	ubiquitin C-terminal hydrolase Ubp22	0.923	358	0.968	301
SPAC11G7.06c	mug132	S. pombe specific UPF0300 family protein 3	0.963	260	0.928	258
SPBC1861.03	mak10	NatC N-acetyltransferase complex subunit Mak10	0.924	246	0.966	267
SPBP8B7.07c	set6	histone lysine methyltransferase Set6	0.920	401	0.970	338
SPBC16D10.02	trm11	tRNA (guanosine) methyltransferase Trm11	0.922	353	0.969	323
SPBC16A3.18	cip1	RNA-binding protein Cip1	0.931	419	0.959	436

Systematic ID	Gene name	Gene description	CF index screen 1	Cell number	CF index screen 2	Cell number
SPBC1198.06c		mannan endo-1,6-alpha-mannosidase	0.973	296	0.917	149
SPBC3E7.05c		conserved eukaryotic protein	0.914	242	0.977	71
SPAC22H10.02		conserved fungal protein	0.961	333	0.930	351
SPAC1805.06c	hem2	porphobilinogen synthase Hem2	0.967	380	0.924	400
SPAC1B3.02c		transcription elongation factor, Elf1 family	0.917	253	0.974	272
SPAC644.06c	cdr1	GIN4 family protein kinase Cdr1	0.930	332	0.961	260
SPBC146.10	mug57	meiotically upregulated gene Mug57	0.948	483	0.944	390
SPBC3H7.09	mug142	palmitoyltransferase	0.919	220	0.972	314
SPAC630.11	vps55	vacuolar sorting protein Vps55	0.941	299	0.950	285
SPBC56F2.03		actin-like protein Arp10	0.912	242	0.979	242
SPAC25G10.05c	his1	ATP phosphoribosyltransferase	NaN	0	0.946	169
SPAC1B3.05		CCR4-Not complex subunit Not3/5	0.932	259	0.959	341
SPBP16F5.08c		flavin dependent monooxygenase	0.915	292	0.976	221
SPBC9B6.11c		cr4p-like	0.970	419	0.921	454
SPAC22E12.01		triose phosphate transporter	0.953	408	0.939	245
SPAC140.01	sdh2	succinate dehydrogenase (ubiquinone) iron-sulfur protein subunit	0.913	203	0.979	213
SPAC16.03c	ura2	dihydroorotase Ura2	0.922	247	0.970	266
SPBC31F10.02		thioesterase superfamily protein	0.934	439	0.958	358
SPBC12D12.02c	cdm1	DNA polymerase delta subunit Cdm1	0.927	415	0.965	413
SPAC521.02		WLM domain protein	0.946	235	0.946	213
SPCC1223.06	tea1	cell end marker Tea1	0.971	300	0.922	296
SPAC821.07c	moc3	transcription factor Moc3	0.959	274	0.933	279
SPAC1B3.04c		mitochondrial GTPase Guf1	0.947	276	0.945	280
SPAC12B10.11	exg2	glucan 1,3-beta-glucosidase Exg2	0.932	488	0.960	380
SPBC83.09c		GYF domain	0.986	23	0.907	491
SPAC13G7.04c	mac1	membrane anchored protein Mac1	0.941	558	0.951	338
SPBC713.11c	pmp3	plasma membrane proteolipid Pmp3	0.917	360	0.975	270
SPBC12C2.04		NAD binding dehydrogenase family protein	0.939	310	0.954	289
SPAC2C4.17c		MS ion channel protein 2	0.929	299	0.964	325
SPCC18.02		membrane transporter	0.943	294	0.950	240
SPAC1783.01		FAD binding protein	0.911	262	0.982	122
SPCC16A11.16c		ARM1 family	0.934	474	0.959	287
SPBC1198.01		glutathione-dependent formaldehyde dehydrogenase	0.961	354	0.932	379
SPAC1002.14	itt1	ubiquitin-protein ligase E3	0.922	290	0.971	323
SPAC5H10.12c		acetylglucosaminyltransferase	0.934	397	0.959	296
SPAC1F7.10		hydantoin racemase family	NaN	0	0.947	521
SPAC644.14c	rhp51	recombinase Rhp51	0.955	106	0.939	194
SPBC11C11.09c	rpl502	60S ribosomal protein L5	0.928	386	0.966	368
SPAC30D11.12	rpl3802	60S ribosomal protein L38	0.963	340	0.931	345
SPCC548.07c	ght1	hexose transporter Ght1	0.969	354	0.925	608
SPAC3A11.05c	kms1	meiotic spindle pole body protein Kms1	NaN	0	0.947	235
SPBC83.04	apc15	anaphase-promoting complex subunit Apc15	0.918	228	0.976	299
SPAC1952.07	rad1	checkpoint clamp complex protein Rad1	0.941	389	0.953	344
SPAC16E8.06c	nop12	RNA-binding protein Nop12	0.948	405	0.946	274
SPCC31H12.04c	rpl1202	60S ribosomal protein L12.1/L12A	0.952	307	0.942	219
SPAC12G12.12		NST UDP-galactose transporter	0.967	183	0.928	291
SPCC1235.01		sequence orphan	0.950	261	0.944	235
SPAC3H8.03		mitochondrial ribosomal protein subunit Img2	0.950	513	0.945	363
SPBC1A4.03c	top2	DNA topoisomerase II	0.963	280	0.932	443
SPAC1751.04		sequence orphan	0.952	263	0.942	284
SPBC4C3.08	mug136	acetylglucosaminyltransferase	0.968	276	0.926	292
SPBC354.10		RNAPII degradation factor	0.978	392	0.917	259
SPAC23A1.04c	mnl1	alpha mannosidase-like protein	0.945	337	0.950	429
SPAC31G5.19		ATPase with bromodomain protein	0.936	284	0.959	210
SPBC800.12c		ubiquitin family protein, unknown	0.956	289	0.939	286
SPCC553.01c		meiotic chromosome segregation protein	0.954	246	0.941	204
SPCC1739.08c		short chain dehydrogenase	0.949	597	0.946	256
SPAC513.05	ams1	alpha-mannosidase	0.936	321	0.959	386
SPBC428.08c	clr4	histone H3 methyltransferase Clr4	0.937	241	0.958	272
SPBC13A2.02		nucleoporin Nup82	0.954	414	0.941	429
SPCC1840.04		caspase	0.921	341	0.974	296
SPBC1711.12		serine peptidase	0.930	145	0.965	308
SPBC3B9.15c	scp1	sterol regulatory element binding protein Scp1	0.938	230	0.957	332
SPAC2F3.07c		sequence orphan	0.937	352	0.958	308
SPAC186.03		L-asparaginase	0.949	311	0.947	389

Systematic ID	Gene name	Gene description	CF index screen 1	Cell number	CF index screen 2	Cell number
SPCC1795.09	yps1	aspartic protease Yps1	0.932	304	0.963	247
SPBC365.14c		UDP-glucose 4-epimerase	0.944	137	0.951	129
SPAC3C7.08c	elf1	AAA family ATPase ELf1	0.952	498	0.943	499
SPBC646.13	sds23	inducer of sexual development Sds23/Moc1	0.912	286	0.984	227
SPBC17G9.05	rct1	cyclophilin family peptidyl-prolyl cis-trans isomerase Cyp6	0.971	271	0.924	476
SPAC222.07c	hri2	eIF2 alpha kinase Hri2	0.922	302	0.973	279
SPCC1739.10	mug33	conserved fungal protein	0.962	222	0.934	271
SPAC1250.03	ubc14	ubiquitin conjugating enzyme Ubc14	0.949	424	0.947	286
SPAC56F8.14c	mug115	sequence orphan	0.938	264	0.958	320
SPCC548.06c	ght8	hexose transporter Ght8	0.922	254	0.974	1
SPAC17C9.15c		sequence orphan	0.928	269	0.968	237
SPAC14C4.15c		dipeptidyl aminopeptidase	0.962	418	0.935	344
SPBC609.05	pob3	FACT complex component Pob3	0.925	474	0.972	523
SPCC297.06c		mitochondrial ribosomal protein subunit 8	0.964	549	0.933	395
SPBC1683.08	ght4	hexose transporter Ght4	0.936	536	0.961	374
SPBC16H5.11c	skb1	arginine N-methyltransferase Skb1	0.962	165	0.934	183
SPCC16C4.20c		sequence orphan	0.943	322	0.954	291
SPBC16G5.16		transcription factor	0.944	191	0.952	245
SPAC1783.04c	hst4	Sir2 family histone deacetylase Hst4	0.921	258	0.976	244
SPAC29E6.09		sequence orphan	0.952	395	0.945	186
SPCC1322.07c	mug150	sequence orphan	0.921	408	0.976	331
SPAC22F3.04	mug62	AMP binding enzyme	0.924	535	0.973	490
SPBPB7E8.01		sequence orphan	0.958	235	0.939	189
SPAPB24D3.04c	mag1	DNA-3-methyladenine glycosylase Mag1	0.927	524	0.970	505
SPAC3H5.07	rpl702	60S ribosomal protein L7	0.957	430	0.940	504
SPCC126.12		NGG1p interacting factor 3 family	0.954	551	0.943	434
SPAC1F8.02c		sequence orphan	0.934	405	0.963	361
SPBC16H5.03c	fub2	SUMO E1-like activator enzyme Fub2	0.967	256	0.930	258
SPBC887.02		ClC chloride channel	NaN	0	0.949	397
SPBC577.02	rpl3801	60S ribosomal protein L38	0.925	315	0.973	292
SPAC1805.16c		purine nucleoside phosphorylase	0.950	267	0.947	261
SPAC11E3.13c		1,3-beta-glucanosyltransferase	0.953	376	0.945	340
SPAC20H4.06c		RNA-binding protein	0.949	488	0.948	342
SPCC23B6.05c	ssb3	DNA replication factor A subunit Ssb3	0.947	3	0.951	312
SPBP22H7.04		sequence orphan	0.968	395	0.930	488
SPAC17A2.11		sequence orphan	0.955	346	0.944	350
SPBC17A3.06		phosphoprotein phosphatase	0.928	368	0.971	351
SPCC1223.13	cbf12	transcription factor	0.974	349	0.924	320
SPAC20H4.07	rhp57	RecA family ATPase Rhp57	0.957	260	0.942	205
SPAC1783.07c	pap1	transcription factor Caf3	0.949	281	0.949	186
SPAC589.11	mug82	translation release factor	0.956	228	0.943	302
SPCC1322.03		membrane transporter	0.944	223	0.955	215
SPCC330.03c		NADPH-hemoprotein reductase	0.963	258	0.936	302
SPBC1105.09	ubc15	ubiquitin conjugating enzyme Ubc15	0.965	299	0.933	277
SPAC3C7.03c	rhp55	RecA family ATPase Rhp55	0.951	229	0.948	227
SPAC222.08c		imidazoleglycerol-phosphate synthase	0.931	138	0.968	69
SPCC777.08c	bit61	HbrB family protein	0.955	253	0.944	265
SPBC342.01c	alg6	glucosyltransferase Alg6	0.944	211	0.955	288
SPBC119.16c		conserved fungal protein	0.973	411	0.927	264
SPAC140.04		conserved fungal protein	0.933	165	0.967	205
SPBC1539.10		ribosome biogenesis protein Nop16	0.951	304	0.948	257
SPAC1F3.03		Lgl family protein	0.952	311	0.948	439
SPCC962.01		C2 domain protein	0.942	284	0.958	306
SPAC2F3.12c		conserved eukaryotic protein	0.930	229	0.969	273
SPCC31H12.08c	ccr4	CCR4-Not complex subunit Ccr4	NaN	0	0.950	201
SPBC4.06		acid phosphatase	0.953	294	0.947	284
SPAC664.13		sequence orphan	0.972	436	0.928	363
SPAC25G10.01		RNA-binding protein	0.949	146	0.951	180
SPAC15A10.06		CPA1 sodium ion/proton antiporter	0.973	279	0.927	409
SPAC23D3.12		inorganic phosphate transporter	0.946	389	0.954	286
SPBC16H5.05c	cyp7	cyclophilin family peptidyl-prolyl cis-trans isomerase Cyp7	0.969	236	0.931	219
SPAC12G12.03	cip2	RNA-binding protein Cip2	0.925	411	0.975	451
SPAC18G6.05c		translation elongation regulator Gcn1	0.944	346	0.956	283
SPAC31A2.09c	apm4	AP-2 adaptor complex subunit Apm4	0.932	406	0.969	269
SPBC19C7.12c		alpha-1,2-mannosyltransferase	0.934	447	0.967	315

Systematic ID	Gene name	Gene description	CF index screen 1	Cell number	CF index screen 2	Cell number
SPAC6G9.03c	mug183	histone chaperone Rtt106-like	0.936	278	0.964	359
SPAC11G7.01		sequence orphan	0.950	288	0.951	306
SPAC6G9.15c		sequence orphan	0.944	176	0.957	140
SPCC736.09c		TRAX	0.952	366	0.948	395
SPBPB21E7.01c	eno102	enolase	0.923	243	0.978	375
SPAC922.07c		aldehyde dehydrogenase	0.962	443	0.939	438
SPBC1709.12	rid1	GTPase binding protein Rid1	0.971	347	0.930	335
SPAC664.01c	swi6	chromodomain protein Swi6	0.972	143	0.929	164
SPAC328.01c		karyopherin	0.942	287	0.959	271
SPBC1347.13c		ribose methyltransferase	0.941	227	0.960	295
SPBC11B10.08		conserved fungal protein	0.946	312	0.955	317
SPAC22H10.03c	kap114	karyopherin Kap14	0.954	345	0.947	358
SPBC902.04		RNA-binding protein	0.936	624	0.965	376
SPBC16H5.07c	ppa2	serine/threonine protein phosphatase Ppa2	0.961	276	0.940	337
SPAC3H1.06c		membrane transporter	0.960	390	0.941	457
SPBC21H7.07c	his5	imidazoleglycerol phosphate dehydratase	0.975	29	0.926	513
SPBC800.08	gcd10	translation initiation factor eIF-3 gamma subunit Gcd10	0.956	342	0.945	466
SPAC13G7.13c	msa1	RNA-binding protein Msa1	0.962	514	0.939	379
SPBC25D12.02c	dnt1	sequence orphan	0.934	449	0.967	544
SPAC30.01c	sec72	Sec7 domain	0.953	318	0.948	525
SPACUNK4.16c		alpha,alpha-trehalose-phosphate synthase	0.957	309	0.944	325
SPBC11B10.02c	his3	histidinol-phosphate aminotransferase imidazole acetol phosphate transaminase His3	0.951	4	NaN	0
SPBC409.19c		metaxin	0.944	199	0.958	258
SPAC1805.15c	pub2	ubiquitin-protein ligase Pub2	0.943	291	0.959	216
SPBC6B1.02	ppk30	Ark1/Prk1 family protein kinase Ppk30	0.928	154	0.973	294
SPCC162.12	tco89	sequence orphan	0.970	383	0.931	405
SPCC1450.06c	grx3	monothiol glutaredoxin Grx3	NaN	0	0.951	328
SPBC16D10.01c		TPR repeat protein Tci1	0.936	440	0.966	307
SPAC2F7.02c		phosphoprotein phosphatase	0.954	302	0.948	281
SPBC776.02c	dis2	serine/threonine protein phosphatase PP1	0.946	269	0.956	345
SPAC7D4.13c		sequence orphan	0.951	220	0.951	245
SPCC70.10		sequence orphan	0.952	320	0.950	310
SPAC1952.17c		GTPase activating protein	0.948	990	0.954	365
SPBC19G7.04		HMG box protein	0.918	128	0.984	364
SPAC8C9.17c	spc34	DASH complex subunit Spc34	0.955	233	0.947	208
SPAC2F7.09c		sequence orphan	0.936	265	0.966	273
SPAC26A3.09c	rga2	GTPase activating protein Rga2	0.922	255	0.981	285
SPCPB16A4.04c	trm8	tRNA (guanine-N7-)-methyltransferase catalytic subunit Trm8	0.972	328	0.930	731
SPBC215.11c		aldo/keto reductase, unknown biological role	0.963	247	0.940	351
SPAC8E11.01c		beta-fructofuranosidase	0.947	216	0.955	247
SPCC736.02		sequence orphan	0.927	147	0.975	71
SPCC965.07c	gst2	glutathione S-transferase Gst2	0.925	454	0.978	346
SPAC23G3.08c	ubp7	ubiquitin C-terminal hydrolase Ubp7	0.954	230	0.949	324
SPBC3F6.05	rga1	GTPase activating protein Rga1	NaN	0	0.951	267
SPCC63.02c	aah3	alpha-amylase homolog Aah3	0.944	413	0.959	166
SPAC8C9.11		conserved protein (broad species distribution)	0.956	312	0.947	312
SPAC6G9.14		RNA-binding protein	0.954	313	0.949	354
SPAC589.10c		ribomal-ubiquitin fusion protein Ubi5	0.942	357	0.961	242
SPBC651.02		nitrilase	0.929	239	0.974	335
SPAC458.05	pik3	phosphatidylinositol 3-kinase Pik3	0.947	186	0.956	268
SPCC126.09		vacuolar membrane zinc transporter	0.951	264	0.952	272
SPBC1711.05		nucleocytoplasmic transport chaperone Srp40	0.936	471	0.967	634
SPBC14C8.15		triglyceride lipase-cholesterol esterase	NaN	0	0.952	227
SPBC21.05c	ral2	Ras guanyl-nucleotide exchange factor Ral2	0.940	279	0.964	351
SPCC1919.10c	myo52	myosin type V	0.917	261	0.986	82
SPBC1271.05c		zinc finger protein zf-AN1 type	0.960	388	0.943	547
SPAC3H8.02		sec14 cytosolic factor family	0.948	412	0.956	264
SPAC644.07		Rieske ISP assembly protein	0.978	21	0.925	6
SPBC1773.08c		mannosyltransferase complex subunit	0.971	559	0.932	481
SPBC839.02		arrestin Aly1 related	0.953	397	0.950	304
SPAC1F8.03c	str3	siderophore-iron transporter Str3	0.950	453	0.954	240
SPCC70.03c		proline dehydrogenase	0.926	268	0.977	272
SPBC887.08		sequence orphan	0.946	330	0.958	282
SPAC26H5.10c	tif51	translation initiation factor eIF5A	0.966	325	0.938	329

Systematic ID	Gene name	Gene description	CF index screen 1	Cell number	CF index screen 2	Cell number
SPCC757.05c		acetylornithine deacetylase	0.955	519	0.949	461
SPAC22E12.19		histone deacetylase complex subunit	0.945	293	0.959	279
SPAC16.01	rho2	Rho family GTPase Rho2	0.953	279	0.951	308
SPAC513.06c		dihydrodiol dehydrogenase	0.930	256	0.974	240
SPCC70.02c		mitochondrial ATPase inhibitor	0.942	320	0.961	272
SPAC4G9.12		gluconokinase	0.949	1142	0.955	327
SPAC1B3.01c		uracil phosphoribosyltransferase	0.971	5	0.933	3
SPCC757.13		membrane transporter	0.964	324	0.941	363
SPAC8C9.03	cgs1	cAMP-dependent protein kinase regulatory subunit Cgs1	NaN	0	0.952	35
SPBC146.12	coq6	monooxygenase Coq6	0.952	251	NaN	0
SPBC660.06		conserved fungal protein	0.963	271	0.941	174
SPBC29A10.06c		conserved fungal protein	0.973	271	0.932	332
SPCC285.04		transthyretin	0.932	558	0.972	200
SPBC660.17c		sequence orphan	0.966	249	0.938	246
SPBC577.08c	txl1	thioredoxin-like I protein Txl1	0.976	292	0.929	329
SPAPB8E5.10		sequence orphan	0.956	216	0.949	251
SPAC23A1.06c	cmk2	MAPK-activated protein kinase Cmk2	0.938	326	0.967	348
SPCC191.11	inv1	beta-fructofuranosidase	0.940	330	0.964	312
SPCC613.12c	raf1	Rik1-associated factor Raf1	0.924	155	0.981	248
SPCC1442.13c		RNA-binding protein	0.936	393	0.968	389
SPBC4F6.09	str1	siderophore-iron transporter Str1	0.943	336	0.961	285
SPBC530.02		membrane transporter	0.954	363	0.951	376
SPBC725.04		oxalyl-CoA decarboxylase	0.937	315	0.968	304
SPAC14C4.03	mek1	Cds1/Rad53/Chk2 family protein kinase Mek1	0.971	405	0.933	364
SPCC11E10.06c		RNA polymerase II elongator complex subunit Elp4	0.933	309	0.972	314
SPCC417.05c	chr2	chitin synthase regulatory factor Chr2	0.951	438	0.955	306
SPAC823.13c		mitochondrial inner membrane protein	0.968	216	0.937	265
SPCC285.11	ucp10	UBA/UAS domain protein Ucp10	0.965	282	0.940	295
SPAC3F10.11c	abc2	glutathione S-conjugate-exporting ATPase Abc2	0.938	307	0.967	109
SPCC1840.09		NAD dependent epimerase/dehydratase family protein	0.967	119	0.938	242
SPAC17A5.01	pex6	peroxin-6	0.962	301	0.943	334
SPAC17C9.10	stm1	G-protein coupled receptor Stm1	0.953	382	0.952	386
SPCC285.10c		SPRY domain protein	0.969	389	0.936	387
SPAC17C9.09c	tim13	TIM22 inner membrane protein import complex subunit Tim13	0.961	280	0.945	263
SPAC17H9.14c		protein disulfide isomerase	0.953	327	0.952	287
SPAC3F10.15c	spo12	Spo12 family protein	0.935	240	0.970	323
SPBC18A7.02c		seven transmembrane receptor-like protein	0.941	425	0.964	494
SPCC1322.05c		leukotriene A-4 hydrolase	0.966	464	0.940	328
SPCC4G3.12c		ubiquitin-protein ligase E3	0.963	279	0.942	318
SPAC12G12.10		WD repeat protein, human WDR21 family	0.946	559	0.959	321
SPBC16H5.04		pho88 family protein	0.956	190	0.949	274
SPAC1805.12c	uep1	ribosomal-ubiquitin fusion protein Ubi2	0.961	336	0.945	301
SPAC3A11.07		NADH dehydrogenase	0.931	183	0.974	268
SPBC354.15	fap1	L-pipecolate oxidase	0.951	300	0.954	362
SPCP31B10.04		conserved fungal protein	0.966	273	0.940	335
SPBC30D10.18c	rpl102	60S ribosomal protein L10a	0.956	404	0.950	456
SPBP4H10.05c	spe2	S-adenosylmethionine decarboxylase proenzyme Spe2	0.933	443	0.973	98
SPCP31B10.06	mug190	C2 domain protein Tcb3	0.941	428	0.965	299
SPBC83.11		triose phosphate transporter	0.952	441	0.954	380
SPBC530.05		transcription factor	0.953	332	NaN	0
SPBC1709.04c	cyp3	cyclophilin family peptidyl-prolyl cis-trans isomerase Cyp3	0.967	235	0.940	431
SPAC3A12.06c		sodium/calcium exchanger	0.955	332	0.952	378
SPAC926.03	rlc1	myosin II regulatory light chain	0.941	102	0.966	123
SPBC1709.11c	png2	ING family homolog Png2	0.964	373	0.943	314
SPAC26H5.02c		DNA replication ATPase	0.965	326	0.942	414
SPBC56F2.04	utp20	U3 snoRNP protein Utp20	0.957	281	0.950	255
SPAPYUG7.04c	rpb9	DNA-directed RNA polymerase II complex subunit Rpb9	0.945	401	0.962	394
SPBC16A3.14		mitochondrial ribosomal protein subunit S26	0.973	474	0.934	409
SPCC794.10		UTP-glucose-1-phosphate uridylyltransferase	0.944	179	0.963	141
SPBC4B4.04		translation initiation factor eIF2A	0.924	164	0.983	285
SPBC29A3.17	gef3	RhoGEF Gef3	0.953	214	0.954	281

Systematic ID	Gene name	Gene description	CF index screen 1	Cell number	CF index screen 2	Cell number
SPAC30D11.09	cwf19	complexed with Cdc5 protein Cwf19	0.953	445	0.954	278
SPCC306.08c		malate dehydrogenase	0.921	348	0.986	266
SPCC417.07c	mto1	MT organizer Mto1	0.974	147	0.934	275
SPAC29A4.14c		peroxin-3	0.935	466	0.973	482
SPAC139.05		succinate-semialdehyde dehydrogenase	0.941	383	0.966	327
SPAC23A1.11	rpl1602	60S ribosomal protein L13/L16	0.933	281	0.975	304
SPBC1711.08		chaperone activator Aha1	0.957	374	0.950	299
SPAPB1A10.10c	ypt71	GTPase Ypt71	0.936	180	0.971	190
SPBC649.03	rhp14	XP-A family homolog Rhp14	0.957	353	0.950	415
SPCC737.09c	hmt1	ATP-binding cassette-type vacuolar membrane transporter Hmt1	0.932	53	0.976	104
SPBC106.10	pka1	cAMP-dependent protein kinase catalytic subunit Pka1	0.966	478	0.941	523
SPAC25G10.02	cce1	mitochondrial cruciform cutting endonuclease Cce1	0.957	402	0.950	348
SPBC16E9.18		phosphatidylserine decarboxylase	0.949	239	0.958	217
SPCC777.06c		hydrolase	0.973	219	0.934	302
SPAC24C9.12c		glycine hydroxymethyltransferase	0.950	339	0.958	184
SPCC188.09c		glycoprotein	0.949	610	0.959	386
SPCC1620.08		succinate-CoA ligase	0.968	340	0.940	336
SPAP14E8.02		transcription factor	0.954	297	0.953	335
SPAC3H5.12c	rpl501	60S ribosomal protein L5	0.979	976	0.929	465
SPACUNK4.08		dipeptidyl aminopeptidase	0.925	197	0.983	300
SPCC965.08c	alr1	alanine racemase Alr1	0.954	253	0.954	375
SPAC57A7.13		RNA-binding protein	0.954	324	0.954	333
SPAP27G11.02		TPR repeat protein, unknown biological role	0.977	406	0.931	538
SPAC26F1.09	gyp51	GTPase activating protein Gyp51	0.960	373	0.949	299
SPBC359.06	mug14	adducin	0.932	156	0.977	308
SPAC14C4.01c		DUF1770 family protein	0.959	289	0.950	302
SPBC18E5.11c	edc3	enhancer of mRNA decapping Edc3	0.955	386	0.953	430
SPAC13G7.02c	ssa1	heat shock protein Ssa1	0.950	366	0.958	504
SPAC31G5.11	pac2	cAMP-independent regulatory protein Pac2	0.964	334	0.944	298
SPCC645.07	rgf1	RhoGEF for Rho1, Rgf1	0.932	172	0.976	476
SPAC24H6.02c		TIM23 translocase complex subunit Tim15	0.952	265	0.956	251
SPAC3A11.13		prefoldin subunit 6	0.941	239	0.968	272
SPCC24B10.13	skb5	Shk1 kinase binding protein 5	0.979	322	0.930	287
SPBC16G5.11c	bag101	BAG family molecular chaperone regulator	0.937	421	0.972	369
SPAC23H4.14	vam6	guanyl-nucleotide exchange factor Vma6	NaN	0	0.955	233
SPBC1706.01	tea4	tip elongation aberrant protein Tea4	0.937	318	0.972	214
SPBC2A9.11c		nuclear export factor	0.963	240	0.946	259
SPCC1739.09c	cox13	cytochrome c oxidase subunit VIa	0.967	199	0.943	206
SPCC18B5.03	wee1	dual specificity protein kinase Wee1	0.960	137	0.950	215
SPCC830.07c	psi1	DNAJ domain protein Psi1	0.959	359	0.950	243
SPCC1442.14c		adenosine 5-monophosphoramidase	0.974	228	0.936	265
SPBP8B7.10c		U3 snoRNP-associated protein Utp16	0.964	257	0.946	244
SPAC1786.04		sequence orphan	0.943	574	0.967	394
SPBC18E5.07		sequence orphan	0.942	258	0.967	256
SPAC11D3.10		nifs homolog	0.943	436	0.967	294
SPAC6G9.08	ubp6	ubiquitin C-terminal hydrolase Ubp6	0.961	488	0.949	550
SPAC4F8.15	itr1	myo-inositol transporter Itr1	0.962	397	0.948	390
SPAC922.04		sequence orphan	0.967	357	0.943	815
SPBC1709.05	sks2	heat shock protein Sks2	0.947	207	0.962	233
SPBC2G2.10c	mug110	sequence orphan	0.954	349	0.956	302
SPBC1685.15c	klp6	kinesin-like protein Klp6	0.945	420	0.965	317
SPBC20F10.07		GRAM domain protein	0.942	708	0.968	400
SPBC1347.06c	cki1	serine/threonine protein kinase Cki1	0.955	739	0.955	383
SPAC3G9.05		GTPase activating protein	0.934	227	0.977	159
SPBC18H10.20c		conserved fungal protein	0.959	498	0.951	460
SPBPB2B2.02	mug180	esterase/lipase	0.953	355	0.958	304
SPBC1347.12		actin-like protein Arp1	0.958	230	0.953	295
SPBC354.01	gtp1	GTP binding protein Gtp1	0.954	371	0.956	436
SPBC2G5.01		DUF1682 family protein	0.969	375	0.941	242
SPAC57A7.09		human RNF family homolog	0.942	786	0.968	494
SPCC13B11.01	adh1	alcohol dehydrogenase Adh1	0.958	267	0.952	301
SPBC947.04		DIPSY family	0.960	236	0.951	278
SPBC19C7.08c		leucine carboxyl methyltransferase	0.950	417	0.961	453
SPAC3H1.10		phytochelatin synthetase	0.951	301	0.960	432
SPBC17F3.01c	rga5	GTPase activating protein Rga5	0.981	287	0.930	398

Systematic ID	Gene name	Gene description	CF index screen 1	Cell number	CF index screen 2	Cell number
SPCC895.08c		conserved fungal protein	0.959	311	0.952	262
SPCC126.06	twf1	twinfilin	0.974	389	0.938	294
SPCC663.12	cid12	poly(A) polymerase Cid12	0.939	282	0.972	308
SPBC146.11c	mug97	meiotically upregulated gene Mug97	0.949	358	0.962	423
SPAC821.03c		sequence orphan	0.954	459	0.958	377
SPAC1296.03c	sxa2	serine carboxypeptidase Sxa2	0.971	338	0.940	249
SPAC20H4.05c		adducin	0.960	434	0.951	404
SPBC83.12		sequence orphan	0.946	157	0.966	268
SPCC737.04		S. pombe specific UPF0300 family protein 6	0.951	295	0.960	276
SPBC21C3.20c	git1	C2 domain protein Git1	0.959	297	0.952	321
SPBC31E1.02c	pmr1	P-type ATPase, calcium transporting Pmr1	0.951	193	0.961	78
SPAC24H6.04	hxk1	hexokinase 1	0.958	357	0.954	292
SPAC24B11.12c		P-type ATPase	0.947	329	0.964	234
SPBC21D10.10		bromodomain protein	0.956	300	0.956	228
SPAC3A12.03c	mug145	ubiquitin-protein ligase E3	0.960	347	0.952	328
SPBPB10D8.07c		membrane transporter	0.931	432	0.981	564
SPCC550.07		acetamidase	0.970	83	0.942	330
SPAC3F10.13	ucp6	UBA domain protein Ucp6	0.937	290	0.975	380
SPCC1795.02c		CaCA proton/calcium exchanger	0.980	223	0.932	298
SPBC2D10.03c		DUF866 domain protein	0.942	362	0.970	396
SPAC1A6.03c		phospholipase	0.944	281	0.968	365
SPBC776.04	sec2302	GTPase activating protein Sec23b	0.977	786	0.935	337
SPBC1921.01c	rpl3701	60S ribosomal protein L37	0.946	295	0.967	263
SPBC3H7.13		FHA domain protein Far10	0.952	283	0.960	277
SPBC1289.06c		sequence orphan	0.938	202	0.975	17
SPCC594.05c		COMPASS complex subunit	0.949	259	0.964	243
SPBC18H10.09		zinc finger protein	0.972	491	0.941	374
SPBC902.03		Spo7 homolog	0.932	313	0.981	273
SPAPJ696.02		actin cortical patch component Lsb4	0.956	456	0.957	337
SPBC18E5.01		cycloisomerase 2 family	0.934	518	0.979	335
SPAC23A1.07		ubiquitin-protein ligase E3	0.937	226	0.976	388
SPAC3C7.09	set8	lysine methyltransferase Set8	0.967	331	0.946	227
SPBC14C8.17c		SAGA complex subunit Spt8	0.971	99	0.942	74
SPBC16H5.08c		ribosome biogenesis ATPase, Arb family	0.970	201	0.943	240
SPAC3F10.10c	map3	pheromone M-factor receptor	0.954	221	0.959	267
SPAC57A10.12c	ura3	dihydroorotate dehydrogenase Ura3	0.951	59	0.962	64
SPAC22A12.16		ATP-citrate synthase subunit 2	0.950	307	0.963	329
SPAC17G8.06c		dihydroxy-acid dehydratase	NaN	0	0.957	15
SPCC4B3.13		MatE family transporter	0.968	288	0.945	282
SPBC32H8.02c	nep2	nedd8 protease Nep2	0.958	407	0.956	267
SPBC530.03c	bag102	BAG family molecular chaperone regulator	0.970	289	0.944	271
SPCC777.09c	arg1	acetylornithine aminotransferase	NaN	0	0.957	5
SPAC19B12.11c		zinc finger protein	0.968	342	0.946	346
SPCC663.11		ww domain binding protein 11 (wbp11) ortholog	0.939	219	0.975	194
SPBC776.05		membrane transporter	0.941	358	0.973	416
SPBC17D11.04c		histone acetyltransferase complex subunit Nto1	0.957	262	0.957	313
SPAC8C9.12c		iron ion transporter	0.962	425	0.952	432
SPAC14C4.05c	mug61	Sad1 interacting factor	0.968	362	0.946	386
SPBP8B7.30c	thi5	transcription factor Thi5	0.929	383	0.985	521
SPAC22E12.18		conserved fungal protein	0.957	289	NaN	0
SPAPB24D3.10c	agl1	alpha-glucosidase Agl1	0.954	324	0.960	302
SPAC212.02		sequence orphan	0.949	440	0.965	512
SPAC8F11.05c	mug130	sequence orphan	0.950	271	0.964	360
SPBPB2B2.09c		2-dehydropantoate 2-reductase	0.943	372	0.971	291
SPBC19G7.07c		conserved fungal protein	0.959	329	0.955	398
SPBC1703.14c	top1	DNA topoisomerase I	0.955	342	0.960	397
SPAC6F12.02	rst2	transcription factor Rst2	0.957	364	0.957	313
SPAC26F1.14c	aif1	apoptosis-inducing factor homolog Aif1	0.966	515	0.949	276
SPBC16E9.17c	rem1	meiosis-specific cyclin Rem1	0.952	453	0.963	344
SPBC2D10.18	abc1	ABC1 kinase family protein	0.985	1	0.929	195
SPCC1442.16c	zta1	quinone oxidoreductase	0.960	393	0.954	337
SPAC26H5.09c		GFO/IDH/MocA family oxidoreductase	0.968	308	0.947	276
SPAC31G5.10	eta2	Myb family transcriptional regulator Eta2	0.933	324	0.982	325
SPBC2G2.15c		rRNA methyltransferase Mrm2	0.964	334	0.951	320
SPBC3H7.03c		2-oxoglutarate dehydrogenase (lipoamide) (e1 component of oxoglutarate dehydrogenase complex)	0.932	5	0.983	144
SPAC1687.13c	csn5	COP9/signalosome complex subunit Csn5	0.967	387	0.948	362

Systematic ID	Gene name	Gene description	CF index screen 1	Cell number	CF index screen 2	Cell number
SPBC1734.09		NST UDP-N-acetylglucosamine transporter	0.947	239	0.968	209
SPBC106.02c	srx1	sulphiredoxin	0.976	292	0.939	463
SPBC1539.02		sequence orphan	0.957	301	0.959	259
SPCC1450.09c		phospholipase	0.975	368	0.940	334
SPCC576.04		bax inhibitor-like protein	0.971	627	0.944	381
SPBC17A3.10	pas4	ubiquitin-protein ligase E3	0.948	283	0.967	320
SPBC29A3.18	cyt1	cytochrome c1	0.975	155	0.940	390
SPAC1556.02c	sdh1	succinate dehydrogenase Sdh1	0.930	225	0.986	161
SPBC9B6.07		nucleolar protein Nop52 family	0.929	330	0.987	351
SPCC613.01		membrane transporter	0.972	251	0.944	242
SPBC29A10.12		HMG-box variant	NaN	0	0.958	284
SPCC70.04c		sequence orphan	0.969	246	0.946	230
SPAC16E8.01		cytoskeletal protein binding protein Sla1 family	0.958	206	NaN	0
SPBC4F6.08c	mrpl39	mitochondrial ribosomal protein subunit L39	0.965	177	0.950	242
SPBC27B12.07		conserved fungal protein	0.977	408	0.939	378
SPAC1142.01		DUF654 family protein	0.963	438	0.952	399
SPAC19A8.10	rfp1	ubiquitin-protein ligase E3	0.975	406	0.941	398
SPBC36.01c		spermidine family transporter	0.954	281	0.961	318
SPAC6G10.03c		abhydrolase family protein, unknown biological role	0.950	376	0.966	243
SPAPB1A10.12c	alo1	D-arabinono-1,4-lactone oxidase	0.946	437	0.969	352
SPBC1348.01		S. pombe specific DUF999 protein family 5	0.960	258	0.956	251
SPBC776.01	rpl29	60S ribosomal protein L29	0.930	212	0.986	287
SPCC1281.04		pyridoxal reductase	0.940	196	0.976	206
SPAC890.06		nucleoporin Nup157/170	0.969	373	0.947	428
SPAC2C4.14c	ppk11	PAK-related kinase Ppk11	0.948	310	0.968	133
SPAC15A10.05c	mug182	YjeF family protein	0.967	324	0.949	201
SPBC17A3.05c		DNAJ/DUF1977 DNAJB12 homolog	0.953	128	0.963	178
SPAC19D5.07	uga1	4-aminobutyrate aminotransferase (GABA transaminase)	0.957	326	0.959	285
SPAC1751.01c	gti1	gluconate transporter inducer Gti1	0.956	303	0.960	290
SPBC16G5.07c		prohibitin	0.945	438	0.971	458
SPAC19D5.03	cid1	poly(A) polymerase Cid1	0.959	302	0.957	423
SPAC23A1.02c		phosphoprotein phosphatase	0.969	434	0.947	362
SPBC839.11c	hut1	uridine diphosphate-N-acetylglucosamine transporter Hut1	0.954	867	0.962	413
SPCC1259.10	pgp1	metallopeptidase Pgp1	0.977	871	0.939	366
SPCPB1C11.02		amino acid permease, unknown 16	0.965	314	0.952	307
SPBC1683.04		glycosyl hydrolase family 3	0.962	337	0.955	257
SPAC24C9.14	otu1	ubiquitin-specific protease	0.955	233	0.962	264
SPAC22A12.02c	mug103	sequence orphan	0.974	588	0.943	399
SPAC222.14c		GTP binding protein Sey1	0.967	497	0.950	419
SPCP20C8.02c		S. pombe specific UPF0321 family protein 1	0.964	394	0.953	477
SPBC691.03c	apl3	AP-2 adaptor complex subunit Alp3	0.960	381	0.957	272
SPAC3H8.07c		prefoldin subunit 3	0.955	833	0.962	610
SPAC11H11.05c	fta6	Sim4 and Mal2 associated (4 and 2 associated) protein 6	0.966	651	0.951	344
SPBP35G2.11c		transcription related zf-ZZ type zinc finger protein	0.967	482	0.950	442
SPBC947.08c		histone promoter control protein Hpc2	0.965	418	0.952	450
SPAC4A8.05c	myp2	myosin II heavy chain	0.976	653	0.941	302
SPCC4F11.03c		sequence orphan	0.958	141	0.960	247
SPBC119.08	pmk1	MAP kinase Pmk1	0.963	240	0.955	283
SPAC7D4.03c		conserved fungal family	0.942	421	0.975	333
SPBC1773.01		striatin homolog	0.954	232	0.964	294
SPAC3G6.04	rnp24	RNA-binding protein Rnp24	0.956	388	0.962	346
SPCC576.12c		conserved eukaryotic protein	0.975	314	0.943	339
SPBC947.02	apl2	AP-1 adaptor complex subunit Apl2	0.989	1	0.929	366
SPBC1685.01	pmp1	dual-specificity MAP kinase phosphatase Pmp1	0.958	149	0.960	293
SPAC13G7.11		mitochondrial inner membrane protein	0.973	103	0.945	189
SPAC9E9.10c	cbh1	centromere binding protein (k-type repeat)	0.957	323	0.961	212
SPBC83.05		RNA-binding protein	0.978	237	0.940	210
SPCC330.07c		membrane transporter	0.967	456	0.951	335
SPAC1250.02	mug95	sequence orphan	0.947	246	0.971	346
SPCC736.13		short chain dehydrogenase	0.957	411	0.961	323
SPAC20H4.10	ufd2	ubiquitin-protein ligase E4	0.954	270	0.964	298
SPAC30C2.07		sequence orphan	0.962	281	0.956	325
SPAC26H5.08c	bgl2	glucan 1,3-beta-glucosidase Bgl2	0.959	616	0.959	258
SPBC839.14c		methyltransferase	0.950	292	0.969	278

Systematic ID	Gene name	Gene description	CF index screen 1	Cell number	CF index screen 2	Cell number
SPBC1289.01c	chr4	chitin synthase regulatory factor Chr4	0.958	229	0.961	241
SPAC5D6.07c	pxa1	PXA domain protein	0.970	433	0.949	451
SPBC13G1.03c	pex14	peroxisomal membrane anchor protein	0.966	428	0.953	250
SPBC1921.03c	mex67	mRNA export receptor Mex67	0.958	390	0.961	439
SPAC25B8.07c		hypoxia induced family protein	0.967	335	0.952	387
SPAC644.09		alanine racemase	0.957	268	0.962	285
SPCC594.07c		sequence orphan	0.972	341	0.947	362
SPBC8D2.01	gsk31	serine/threonine protein kinase Gsk31	0.933	265	0.986	337
SPBC418.01c	his4	imidazoleglycerol-phosphate synthase	0.967	375	0.952	356
SPBC21C3.08c		ornithine aminotransferase	0.958	123	0.962	28
SPBC2D10.05	exg3	glucan 1,3-beta-glucosidase Exg3	0.957	341	0.962	260
SPBC660.11	tcg1	single-stranded telomeric binding protein Tgc1	0.972	523	0.948	641
SPAC16E8.13		ubiquitin-protein ligase E3	0.972	324	0.948	449
SPBC3E7.08c	rad13	DNA repair nuclease Rad13	0.957	319	0.963	361
SPBPB2B2.11		nucleotide-sugar 4,6-dehydratase	0.950	443	0.970	351
SPBC3F6.01c		serine/threonine protein phosphatase	0.937	356	0.983	653
SPAC6G9.13c	bqt1	bouquet formation protein Bqt1	0.962	368	0.958	329
SPCPB16A4.02c		conserved fungal protein	0.953	333	0.967	291
SPCC825.04c		N-acetyltransferase	0.945	413	0.975	448
SPCC737.05		peroxin Pex28/29	0.964	357	0.956	358
SPBC19F8.01c	spn7	septin Spn7	0.959	302	0.962	285
SPAC21E11.03c	pcr1	transcription factor Pcr1	0.971	389	0.949	294
SPAC17A2.02c		DUF887 family protein	0.960	291	0.960	363
SPAC23H3.04		conserved fungal protein	0.963	417	0.957	382
SPBC13E7.11		mitochondrial rhomboid protease	0.946	330	0.974	361
SPBC1683.01		inorganic phosphate transporter	0.955	612	0.966	349
SPBC119.14	rti1	Rad22 homolog Rti1	0.960	297	0.961	379
SPBC21B10.13c		transcription factor	0.965	283	0.956	221
SPAC222.15	meu13	Tat binding protein 1(TBP-1)-interacting protein (TBPIP) homolog	0.964	493	0.957	375
SPBC18H10.02	lcf1	long-chain-fatty-acid-CoA ligase Lcf1	0.946	148	0.975	133
SPAC821.10c	sod1	superoxide dismutase Sod1	NaN	0	0.960	341
SPAC3H8.08c		transcription factor	0.971	344	0.950	791
SPAC1F7.09c		allantoicase	0.948	375	0.974	264
SPAC30D11.02c		sequence orphan	0.949	483	0.973	1060
SPAPB1A10.08		sequence orphan	0.976	582	0.946	518
SPCC11E10.03	mug1	dynactin complex subunit	0.960	407	0.962	372
SPBC4F6.05c		lectin	0.974	428	0.947	384
SPAC29A4.02c		translation elongation factor EF-1 gamma subunit	0.955	307	0.967	328
SPCC1494.10		transcription factor	0.955	292	0.967	230
SPAC2E1P3.01		zinc binding dehydrogenase	0.965	308	0.956	325
SPAC212.03		hypothetical protein	NaN	0	0.961	289
SPAC18G6.10		chromosome segregation protein	0.973	310	0.949	331
SPBC582.10c		ATP-dependent DNA helicase Rhp16b	0.976	286	0.945	259
SPAPB17E12.14c		6-phosphofructo-2-kinase	0.954	401	0.968	340
SPBC11C11.11c		ATP-dependent DNA helicase Irc3	0.944	514	0.978	434
SPBC21C3.14c		sequence orphan	0.946	427	0.976	293
SPBC359.05	abc3	ABC transporter Abc3	0.967	516	0.955	269
SPBC6B1.10	prp17	splicing factor Prp17	0.955	296	0.967	340
SPAC227.03c		mitochondrial NAD+ transporter	0.968	449	0.954	462
SPBC16E9.09c		COPII vesicle coat component Erp5/Erp6	0.968	201	0.954	227
SPAC17A5.05c		conserved fungal protein	0.960	355	0.962	297
SPBC8D2.18c		adenosylhomocysteinase	0.961	457	0.962	429
SPBC725.02	mpr1	response regulator phosphotransferase	0.961	324	NaN	0
SPBC18H10.07		WW domain-binding protein 4	0.957	176	0.966	366
SPAC3H1.09c		amino acid transporter	0.960	215	0.962	245
SPBC16D10.08c		heat shock protein Hsp104	0.961	257	0.962	255
SPAC12G12.11c		DUF544 family protein	0.970	422	0.953	326
SPAC24B11.08c		COPII-coated vesicle component Erv41/46	0.961	344	0.963	371
SPBC24C6.08c		vesicle coat protein	0.975	347	0.948	434
SPBC23E6.05	arx1	ribosomal export complex Arx1	0.953	255	0.970	268
SPBC1711.03		conserved eukaryotic protein	0.950	402	0.973	264
SPAC1527.03		RNA-binding protein	0.964	293	0.959	392
SPBC1198.03c		sequence orphan	0.958	445	0.965	498
SPAC806.07	ndk1	nucleoside diphosphate kinase	0.988	539	0.935	491
SPAC1556.03	azr1	serine/threonine protein phosphatase Azr1	0.981	270	0.942	369
SPAC29A4.11	rga3	GTPase activating protein Rga3	0.939	302	0.985	586

Systematic ID	Gene name	Gene description	CF index screen 1	Cell number	CF index screen 2	Cell number
SPCC970.05	rpl3601	60S ribosomal protein L36	0.966	293	0.958	445
SPBP8B7.11	nxt3	ubiquitin protease cofactor	0.956	502	0.968	397
SPAC1834.05	alg9	mannosyltransferase complex subunit Alg9	0.964	231	0.960	274
SPAC227.18	lys3	saccharopine dehydrogenase [NAD+, L-lysine forming]	0.972	507	0.952	320
SPBC29A3.21		sequence orphan	0.952	169	0.972	241
SPAPB17E12.05	rpl3703	60S ribosomal protein L37	0.952	403	0.972	489
SPAC4F10.18		WD repeat protein, human NUP37 family	NaN	0	0.962	123
SPBC1685.02c	rps1202	40S ribosomal protein S12	0.965	587	0.959	358
SPBC4F6.06	kin1	microtubule affinity-regulating kinase Kin1	NaN	0	0.962	27
SPBC11B10.06	sws1	SWIM domain containing-Srs2 interacting protein 1	0.973	473	0.951	360
SPBC1773.03c		aminotransferase class-III	0.965	295	0.960	293
SPAC3A12.13c		translation initiation factor eIF3 complex subunit	0.951	259	0.973	239
SPCC1739.01		zf-CCCH type zinc finger protein	0.963	801	0.961	430
SPBP18G5.03	toc1	sequence orphan	0.966	559	0.959	400
SPCC584.13		amino acid permease, unknown 14	0.968	283	0.956	273
SPBC1A4.05		sequence orphan	0.961	247	0.963	264
SPBC1685.13		non classical export pathway protein	0.975	138	0.949	137
SPAC3A12.09c		urease accessory protein UreD	0.957	229	0.967	295
SPAC2F7.10		palmitoyltransferase	0.951	291	0.974	350
SPCP31B10.05		tyrosyl-DNA phosphodiesterase	0.968	273	0.956	259
SPBC17D1.05		sequence orphan	0.959	351	0.966	212
SPAC144.14	klp8	kinesin-like protein Klp8	0.966	269	0.959	340
SPAP27G11.16		sequence orphan	0.954	494	0.971	506
SPBC660.05		conserved fungal protein	0.955	302	0.970	276
SPAC1D4.02c		human GRASP protein homolog	0.971	359	0.954	330
SPBC2G5.03	ctu1	ATP binding protein	0.963	330	0.962	337
SPBC1921.04c		sequence orphan	0.960	330	0.965	312
SPAC2F7.11	nrd1	RNA-binding protein Nrd1	0.959	237	0.966	301
SPBC21B10.06c		sequence orphan	0.964	308	0.961	393
SPAC17A2.06c	vps8	WD repeat protein Vps8	0.975	139	0.951	148
SPAC3G9.04	ssu72	phosphoric ester hydrolase	0.981	851	0.945	595
SPAC5H10.09c		3-methyl-2-oxobutanoate hydroxymethyltransferase	0.976	308	0.950	375
SPACUNK12.02c	cmk1	calcium/calmodulin-dependent protein kinase Cmk1	0.973	335	0.953	293
SPAC328.09		2-oxoadipate and 2-oxoglutarate transporter	0.955	460	0.971	283
SPBC23G7.07c		replication regulator	0.958	239	0.968	338
SPAC589.02c	med13	mediator complex subunit Srb9	0.941	132	0.985	662
SPAC17H9.09c	ras1	GTPase Ras1	NaN	0	0.963	225
SPBC3H7.06c	pof9	F-box protein Paf9	0.959	257	0.968	314
SPCC737.06c		glutamate-cysteine ligase regulatory subunit	0.969	314	0.958	337
SPBC21.07c	ppk24	serine/threonine protein kinase Ppk24	0.975	606	0.952	443
SPBC887.11	pus2	tRNA pseudouridylate synthase Pus2	0.962	594	0.965	386
SPBC29A10.16c		cytochrome b5	0.954	183	0.973	319
SPCC1450.05c	rox3	RNA polymerase II holoenzyme mediator complex subunit Med19	0.973	331	0.954	301
SPAC17H9.04c		RNA-binding protein	0.967	256	0.961	331
SPAC3A11.06	mvp1	sorting nexin Mvp1	0.964	429	0.963	456
SPAC16E8.14c		methyltransferase	0.962	373	0.966	311
SPCC4B3.14	cwf20	complexed with Cdc5 protein Cwf20	0.969	251	0.958	232
SPBPB2B2.12c		UDP-glucose 4-epimerase	0.943	433	0.985	390
SPAC1687.06c	rpl44	60S ribosomal protein L28/L44	0.963	344	0.965	383
SPBC29B5.03c	rpl26	60S ribosomal protein L26	0.964	293	0.964	248
SPAC17A2.14		CorA family magnesium ion transporter	0.974	411	0.954	308
SPAC1805.10		sequence orphan	0.951	275	0.977	306
SPBC3E7.15c	mug83	sphingosine N-acyltransferase Lac1	0.954	300	0.974	191
SPAC823.03	ppk15	serine/threonine protein kinase Ppk15	0.957	194	0.971	302
SPCC162.02c		AMP-binding dehydrogenase	0.957	393	0.971	313
SPCC4E9.02	cig1	cyclin Cig1	0.975	324	0.953	472
SPBC146.02		sequence orphan	0.961	271	0.967	278
SPBC582.08		alanine aminotransferase	0.951	324	0.977	320
SPAC1D4.13	byr1	MAP kinase kinase Byr1	0.970	345	0.958	330
SPBC1711.15c		sequence orphan	0.963	207	0.966	408
SPAC2C4.09		DUF1640 family protein	0.964	299	0.965	249
SPBC25B2.03		zf-C3HC4 type zinc finger	0.949	414	0.980	387
SPBC1683.12		nicotinic acid plasma membrane transporter	0.961	363	0.968	266
SPBC365.13c	hba1	Ran GTPase binding protein Hba1	0.968	297	0.961	314
SPBC12C2.01c		sequence orphan	0.983	1143	0.947	346

Systematic ID	Gene name	Gene description	CF index screen 1	Cell number	CF index screen 2	Cell number
SPAC4A8.06c		esterase/lipase	0.977	440	0.952	648
SPBC1289.13c		alpha-1,2-galactosyltransferase	0.979	618	0.950	316
SPAC27F1.05c		4-aminobutyrate transaminase	0.961	227	0.968	301
SPAC11D3.06		MatE family transporter	0.969	253	0.960	333
SPBC800.04c	rpl4301	60S ribosomal protein L37a	0.951	250	0.978	295
SPCC1919.03c		AMP-activated protein kinase beta subunit	0.990	231	0.939	276
SPAC1F12.06c		endonuclease	0.967	292	0.962	356
SPAC17C9.14		Pex19 protein family	0.950	286	0.979	290
SPAC16A10.02		transcription coactivator Sub1	0.973	310	0.957	292
SPBC24C6.10c		conserved eukaryotic protein	0.974	164	0.955	239
SPBC1709.18	tif452	translation initiation factor eIF4E 4F complex subunit	0.954	313	0.976	270
SPAC3H1.13	ppk13	serine/threonine protein kinase Ppk13	0.968	205	0.962	436
SPAC1565.01		conserved fungal protein	0.978	188	0.952	71
SPAC1B9.02c	sck1	serine/threonine protein kinase Sck1	0.971	156	0.959	65
SPBC16C6.05		translation initiation factor	0.966	320	0.964	236
SPBC12C2.07c		spermidine synthase	0.972	141	0.959	76
SPAC644.11c		pyruvate dehydrogenase (lipoamide) kinase	0.962	271	0.968	417
SPBC18E5.14c		sequence orphan	0.968	176	0.962	336
SPAPB8E5.05	mfm1	M-factor precursor Mfm1	0.950	510	0.981	953
SPAC20H4.09		ATP-dependent RNA helicase, spliceosomal	0.964	322	0.966	427
SPAPB1E7.07	glt1	glutamate synthase	0.965	442	NaN	0
SPAC1F3.06c	spo15	sporulation protein Spo15	0.974	312	0.957	440
SPBC27.04		sequence orphan	0.973	259	0.958	249
SPBC6B1.08c	ofd1	2-oxoglutarate and Fe(II) dioxygenase domain containing protein 1	0.960	628	0.971	354
SPAC6G10.08	idp1	isocitrate dehydrogenase Idp1	0.966	425	0.964	351
SPBC15D4.12c	mug98	sequence orphan	0.982	894	0.948	419
SPBC16E9.12c	pab2	poly(A) binding protein Pab2	0.966	313	0.965	314
SPAC12B10.04		tubulin-tyrosine ligase	0.973	304	0.958	384
SPAC1687.05	pli1	SUMO E3 ligase Pli1	0.963	364	0.968	377
SPAC19B12.06c		protease	0.962	398	0.969	305
SPAC1F3.05		adaptin	0.973	396	0.958	321
SPAC30D11.11		Haemolysin-III family protein	0.964	351	0.968	322
SPAC23E2.03c	ste7	meiotic suppressor protein Ste7	0.953	335	0.978	248
SPAC25H1.07		DUF1620 family protein	0.952	190	0.979	236
SPAC1B3.17	clr2	chromatin silencing protein Clr2	0.958	82	0.974	101
SPCC18B5.11c	cds1	replication checkpoint kinase Cds1	0.971	283	0.960	293
SPBC24C6.11	cwf14	G10 protein	NaN	0	0.966	3
SPAC3A11.10c		dipeptidyl aminopeptidase	0.971	437	0.961	406
SPCC18B5.06	erf1	translation release factor eRF1	0.977	366	0.954	411
SPBC1271.09		glycerophosphodiester transporter	0.960	549	0.972	449
SPAC4F10.16c		P-type ATPase	0.961	327	0.971	334
SPCP1E11.10		ankyrin repeat protein, unknown biological role	0.964	347	0.968	326
SPCC1840.05c		phosphomannomutase	0.958	411	0.974	331
SPAC1687.19c		queuine tRNA-ribosyltransferase	0.971	716	0.961	397
SPAC20H4.04	mfh2	ATP-dependent 3 to 5 DNA helicase	0.960	384	0.972	304
SPAC30C2.04		cofactor for methionyl-and glutamyl-tRNA synthetases	0.959	402	0.973	402
SPAC227.11c		sensor for misfolded ER glycoproteins Yos9	0.970	293	0.962	323
SPCC1450.03		ribonucleoprotein (RNP) complex	0.967	285	0.965	355
SPAC6B12.07c		ubiquitin-protein ligase E3	0.952	214	0.981	212
SPBC428.03c	pho4	thiamine-repressible acid phosphatase Pho4	0.968	200	0.965	107
SPAC664.14	amt2	ammonium transporter Amt2	0.962	490	0.971	662
SPBC30B4.03c		conserved protein (fungal and plant)	0.947	68	0.986	351
SPAC1687.07		conserved fungal protein	0.965	486	0.968	505
SPAC17C9.08	pnu1	endodeoxyribonuclease Pnu1	0.967	261	0.966	254
SPAC186.02c		hydroxyacid dehydrogenase	0.974	448	0.959	285
SPACUNK4.11c		sequence orphan	0.983	146	0.950	243
SPAC227.05		prefoldin subunit 4	0.969	548	0.963	417
SPBC4B4.07c	usp102	U1 snRNP-associated protein Usp102	0.949	7	0.984	334
SPCC11E10.08	rik1	silencing protein Rik1	0.967	1	NaN	0
SPAC3H5.04	aar2	U5 snRNP-associated protein Aar2	0.949	387	0.984	277
SPCC1739.14	npp106	nucleoporin Npp106	0.964	381	0.969	269
SPAC26A3.02	myh1	adenine DNA glycosylase	0.975	397	0.958	347
SPCC777.03c		nifs homolog	0.963	206	0.970	245
SPCC622.11		LMBR1-like membrane protein	0.969	429	0.964	342
SPAC19G12.12	dlp1	decaprenyl diphosphate synthase subunit 2 Dlp1	0.985	2	0.949	287

Systematic ID	Gene name	Gene description	CF index screen 1	Cell number	CF index screen 2	Cell number
SPCC548.04		ubiquitin family protein Urm1	0.959	76	0.974	88
SPAC57A10.07		conserved protein (fungal and protazoan)	0.973	369	0.960	277
SPAC10F6.16	mug134	endosulphine family protein	0.969	404	0.965	539
SPBC902.02c	ctf18	DNA replication factor C complex subunit Ctf18	0.971	413	0.963	422
SPAC1952.16	rga9	RhoGAp, GTPase activator towards Rho/Rac/Cdc42-like small GTPases	0.969	289	0.965	308
SPAPB1A10.05		sequence orphan	0.972	335	0.962	316
SPAC4H3.05	srs2	ATP-dependent DNA helicase, UvrD subfamily	0.962	866	0.972	357
SPAC922.05c		membrane transporter	0.963	125	0.971	107
SPBP35G2.13c	swc2	chromatin remodeling complex subunit Swc2	0.966	459	0.968	283
SPAC1296.04	mug65	spore wall assembly protein	0.984	342	0.950	422
SPAPB17E12.12c		mitochondrial transporter	0.963	293	0.971	400
SPAC1A6.04c	plb1	phospholipase B homolog Plb1	0.965	377	0.969	365
SPAC29B12.02c	set2	histone lysine methyltransferase Set2	0.973	267	0.961	327
SPAC1783.05	hrp1	ATP-dependent DNA helicase Hrp1	0.964	357	0.971	232
SPBC13E7.04	atp16	F1-ATPase delta subunit	0.989	4	0.945	215
SPAC1834.03c	hhf1	histone H4 h4.1	0.968	269	0.966	305
SPAC26F1.03	pda1	pyruvate dehydrogenase e1 component alpha subunit Pda1	NaN	0	0.967	307
SPBC1861.01c	cnp3	CENP-C	0.961	304	0.974	247
SPCC16C4.06c		tRNA pseudouridylate synthase (predicted)	0.975	320	0.960	266
SPBP22H7.05c		ATPase with bromodomain protein	0.966	335	0.969	293
SPBC1685.06	cid11	poly(A) polymerase Cid11	0.967	254	0.968	323
SPCC16C4.12		NatB N-acetyltransferase complex catalytic subunit Nat3	0.976	355	0.959	262
SPAC1071.05		S-adenosylmethionine-dependent methyltransferase	0.974	296	0.961	373
SPBC13E7.09	vrp1	verprolin	0.972	309	0.963	510
SPAC3G6.09c	tps2	trehalose-phosphate synthase Tps2	NaN	0	0.968	481
SPBC21D10.12	hob1	BAR adaptor protein Hob1	0.967	239	0.968	378
SPBC13G1.04c		alkB homolog	0.973	304	0.962	239
SPAC5H10.11	gmh1	alpha-1,2-galactosyltransferase Gmh1	0.968	271	0.967	337
SPAC17G8.11c		mannosyltransferase complex subunit	0.950	361	0.985	346
SPAC589.09		sec14 cytosolic factor family	0.971	263	0.965	271
SPAC144.04c	spe1	ornithine decarboxylase Spe1	0.967	163	0.968	169
SPAC17G6.04c	cpp1	protein farnesyltransferase beta subunit Cpp1	0.958	292	0.977	321
SPCC965.06		potassium channel subunit	0.962	291	0.973	299
SPBC19G7.03c	rps3002	40S ribosomal protein S30	0.964	432	0.972	450
SPAC27F1.08	pdt1	Nramp family manganese ion transporter	0.974	366	0.962	397
SPCC777.15		tRNA dihydrouridine synthase Dus4	0.971	294	0.965	260
SPAC18G6.15	mal3	EB1 family Mal3	0.968	266	0.968	263
SPBC649.02	rps1902	40S ribosomal protein S19	0.970	469	0.966	314
SPCC736.04c	gma12	alpha-1,2-galactosyltransferase Gma12	0.974	270	0.962	186
SPBC1198.07c		mannan endo-1,6-alpha-mannosidase	0.953	428	0.983	5
SPBC11B10.07c		CDC50 domain protein	0.961	399	0.976	338
SPBC1703.13c		inorganic phosphate transporter	0.946	3	0.991	1
SPBC17D11.01	nep1	nedd8 protease Nep1	0.967	397	0.970	503
SPAC4G9.06c		sequence orphan	0.961	400	0.976	360
SPAC11D3.16c		sequence orphan	0.965	262	0.972	298
SPBC409.11	meu18	sequence orphan	0.977	271	0.960	290
SPAC9E9.15		CIA30 family protein	0.974	249	0.963	311
SPBC31F10.09c	nut2	mediator complex subunit Med10	0.962	157	0.975	405
SPBC543.02c		DNAJ/TPR domain protein DNAJC7 family	0.950	231	0.987	454
SPCC1827.07c		SPX/EXS domain protein	0.960	348	0.977	280
SPBC32F12.06	pch1	cyclin Pch1	NaN	0	0.969	368
SPBC146.04		sulfhydryl oxidase	0.954	456	0.984	405
SPCC645.13		transcription elongation regulator	NaN	0	0.969	440
SPAC23C11.01		ER membrane protein, ICE2 family	0.971	556	0.967	351
SPAC27D7.13c	ssm4	p150-Glued	0.966	301	0.972	316
SPBC1703.08c		5-formyltetrahydrofolate cyclo-ligase	0.970	227	0.967	181
SPAC19G12.02c	pms1	MutL family mismatch-repair protein Pms1	0.971	273	0.967	291
SPBC18A7.01		X-Pro dipeptidase	0.971	408	0.967	341
SPAC4F10.08	mug126	sequence orphan	0.967	362	0.971	387
SPAC29B12.13		carbon-sulfur lyase	0.967	724	0.972	444
SPCP1E11.02	ppk38	Ark1/Prk1 family protein kinase Ppk38	0.971	326	0.967	412
SPBC16A3.17c		membrane transporter	0.958	411	0.980	381
SPCC1235.15	dga1	diacylglycerol O-acyltransferase	0.967	190	0.972	225

Systematic ID	Gene name	Gene description	CF index screen 1	Cell number	CF index screen 2	Cell number
SPBC21C3.01c	vps13a	chorein homolog	0.974	238	0.964	212
SPBC1348.14c	ght7	hexose transporter Ght7	0.969	268	0.970	290
SPCC132.02	hst2	Sir2 family histone deacetylase Hst2	0.974	420	0.964	431
SPBC609.02	ptn1	phosphatidylinositol-3,4,5-trisphosphate 3-phosphatase	0.984	111	0.955	357
SPBC14C8.04		acetolactate synthase regulatory unit	0.970	245	0.969	208
SPBC146.09c	lsd1	histone demethylase SWIRM1	NaN	0	0.970	329
SPBPB2B2.05		GMP synthase [glutamine-hydrolyzing]	0.953	393	0.986	367
SPCC794.03		amino acid permease, unknown 13	0.968	338	0.971	249
SPAC15F9.02	seh1	nucleoporin Seh1	0.966	524	0.973	382
SPAC23C4.08	rho3	Rho family GTPase Rho3	0.974	585	0.965	383
SPAC31A2.11c	cuf1	Cu metalloregulatory transcription factor Cuf1	0.970	232	NaN	0
SPBP16F5.03c	tra1	phosphatidylinositol kinase	0.970	204	0.970	265
SPAC4G8.11c	atp10	F1-F0 ATPase assembly protein	0.979	4	0.961	8
SPAC29B12.12		helper of TIM (Predicted)	0.994	1160	0.946	521
SPBC115.02c		AFG1 family mitochondrial ATPase	0.962	338	0.978	334
SPCC1020.13c		phospholipase	0.966	699	0.975	369
SPBPJ4664.03	mfm3	M-factor precursor Mfm3	0.951	484	0.989	391
SPAC227.14		nicotinamide riboside kinase	NaN	0	0.970	287
SPAC23C4.09c		DNA-binding TFAR19-related protein	0.981	583	0.959	332
SPBC30B4.06c		tRNA uridine 5-carboxymethylaminomethyl modification enzyme	0.956	273	0.984	54
SPBC8D2.19	mde3	serine/threonine protein kinase Mde3	0.952	403	0.988	393
SPCC830.08c		Golgi membrane protein	0.966	275	0.975	397
SPBC106.11c	plg7	phospholipase A2	0.969	338	0.972	310
SPBC106.01	mph1	dual specificity protein kinase Mph1	0.973	372	0.968	364
SPBC23E6.08	sat1	Golgi membrane exchange factor subunit Sat1	NaN	0	0.970	249
SPBC14F5.03c	kap123	karyopherin Kap123	NaN	0	0.970	96
SPAP27G11.10c	nup184	nucleoporin Nup184	0.972	296	0.968	334
SPCC1442.17c		DUF292 family protein	0.978	258	0.963	277
SPCC4G3.10c	rhp42	DNA repair protein Rhp42	0.982	162	0.959	252
SPBC21H7.03c		acid phosphatase	0.968	322	0.973	378
SPBP8B7.18c		phosphomethylpyrimidine kinase	0.970	236	0.971	272
SPCC794.09c	ef1a-a	translation elongation factor EF-1 alpha Ef1a-a	0.971	342	0.970	337
SPAC23H4.02	ppk9	serine/threonine protein kinase Ppk9	0.978	308	0.964	414
SPBC1778.09		GTPase activating protein	0.963	360	0.978	321
SPCC1183.09c	pmp31	plasma membrane proteolipid Pmp31	0.974	200	0.968	91
SPAC24C9.07c	bgs2	1,3-beta-glucan synthase subunit Bgs2	0.977	357	0.965	255
SPBC215.13		sequence orphan	0.967	367	0.975	266
SPAC144.17c		6-phosphofructo-2-kinase	0.956	366	0.986	409
SPBC16D10.07c	sir2	Sir2 family histone deacetylase Sir2	0.981	346	0.961	133
SPBC1921.05	ape2	aminopeptidase Ape1	0.963	285	0.979	198
SPBC1778.06c	fim1	fimbrin	0.956	56	0.986	90
SPBC530.11c		transcription factor	0.967	284	0.975	220
SPAC2F3.16		ubiquitin-protein ligase E3	0.964	264	0.978	271
SPBC28F2.08c		HRD ubiquitin ligase complex subunit	0.976	332	0.966	356
SPBC17A3.08		TatD	0.968	420	0.974	894
SPBC646.02	cwf11	complexed with Cdc5 protein Cwf11	0.970	235	0.973	157
SPBC18E5.10		iron sulfur cluster assembly protein	0.992	939	0.950	375
SPAC8F11.08c		esterase/lipase	0.960	9	0.983	17
SPAC25B8.09		trans-aconitate 3-methyltransferase	0.971	254	0.972	281
SPAC4C5.02c	ryh1	GTPase Ryh1	0.975	333	0.968	258
SPBP16F5.05c		ribosome biogenesis protein Nop8	0.963	218	0.980	412
SPAC630.04c		sequence orphan	0.969	219	0.975	93
SPAC32A11.02c		conserved fungal protein	0.970	375	0.974	541
SPAC823.11		sphingosine-1-phosphate phosphatase	0.965	284	0.979	277
SPBC1E8.02		ubiquitin family protein, unknown	0.971	224	0.972	265
SPBC146.13c	myo1	myosin type I	NaN	0	0.972	95
SPBC428.12c		RNA-binding protein	0.992	1293	0.951	446
SPCC1235.08c	pdh1	DUF1751 family protein	0.975	58	0.968	64
SPBC9B6.03		zinc finger protein	0.960	417	0.984	367
SPAC9G1.02	wis4	MAP kinase kinase kinase Wis4	0.981	168	0.963	233
SPAC6B12.04c		aminotransferase class I and II	0.958	342	0.986	300
SPBC17D1.06	dbp3	ATP-dependent RNA helicase Dbp3	0.969	310	0.975	443
SPBC23G7.16	ctr6	copper transporter Ctr6	0.977	240	0.967	276
SPBC16E9.13	ksp1	serine/threonine protein kinase Ksp1	0.975	810	0.970	385
SPAC26F1.08c		conserved protein	0.972	330	0.973	326

Systematic ID	Gene name	Gene description	CF index screen 1	Cell number	CF index screen 2	Cell number
SPBC119.12		Golgi matrix protein	0.958	353	0.987	1011
SPCC1840.06	atp5	F0-ATPase delta subunit	0.972	1	NaN	0
SPBC582.09	pex11	peroxisomal biogenesis factor 11	0.969	180	0.976	278
SPBC1703.06	pof10	F-box protein Pof10	0.966	278	0.979	303
SPAC824.09c		GTPase activating protein	0.971	243	0.974	254
SPCC594.02c		conserved fungal protein	0.990	250	0.955	255
SPBPB2B2.10c		galactose-1-phosphate uridylyltransferase	0.959	429	0.987	313
SPAPB8E5.04c		phosphatidylglycerol/phosphatidylinositol transfer protein	0.972	336	0.974	252
SPBC1711.14	rec15	meiotic recombination protein Rec15	0.972	345	0.974	270
SPBC19C7.02	ubr1	N-end-recognizing protein Ubr1	0.979	35	0.968	33
SPBC18E5.04	rpl1001	60S ribosomal protein L10	NaN	0	0.974	358
SPAC17A5.11	rec12	endonuclease Rec12	0.971	249	0.977	270
SPBC83.16c		conserved fungal protein	0.969	257	0.979	343
SPCC126.13c		histone deacetylase complex subunit, SAP128 family	0.979	233	0.969	319
SPBC609.03		WD repeat protein, human IQWD1 family	0.975	253	0.973	337
SPAC227.10		prefoldin subunit 2	0.976	585	0.972	523
SPBC543.05c		inorganic anion exchanger	0.961	194	0.987	297
SPCC1020.12c		xap-5-like protein	0.962	301	0.987	366
SPBC21B10.04c	nrf1	GTPase regulator Nrf1	NaN	0	0.975	264
SPBC29A10.09c		CAF1 family ribonuclease	0.971	343	0.979	343
SPCC74.03c	ssp2	serine/threonine protein kinase Ssp2	0.974	245	0.976	256
SPCC330.02	rhp7	Rad7 homolog Rhp7	0.972	350	0.978	331
SPBC1198.14c	fbp1	fructose-1,6-bisphosphatase Fbp1	0.976	347	0.975	359
SPBC839.07	ibp1	itty bitty phosphatase Ibp1	0.977	286	0.973	354
SPAC17A2.12		ATP-dependent DNA helicase	0.971	351	0.979	278
SPAC19A8.04	erg5	C-22 sterol desaturase Erg5	0.973	320	0.978	361
SPBC543.10		GET complex subunit	0.966	355	0.986	338
SPACUNK4.15		2,3-cyclic-nucleotide 3-phosphodiesterase	0.979	382	0.973	370
SPBP8B7.23		ubiquitin-protein ligase E3	0.961	429	0.991	523
SPCC1682.01	qcr9	ubiquinol-cytochrome-c reductase complex subunit 10	0.976	188	0.976	198
SPAPB2B4.02	grx5	monothiol glutaredoxin Grx5	NaN	0	0.976	139
SPCC1739.15	wtf21	wtf element Wtf21	0.978	374	0.974	804
SPAC105.02c		ankyrin repeat protein, unknown biological role	0.970	194	0.982	222
SPBP8B7.25	cyp4	cyclophilin family peptidyl-prolyl cis-trans isomerase Cyp4	0.966	290	0.986	317
SPBC1703.04	mlh1	MutL family protein Mlh1	0.983	278	0.970	345
SPBC428.05c	arg12	argininosuccinate synthase	NaN	0	0.976	7
SPBPJ4664.01	dps1	decaprenyl diphosphate synthase subunit Dps1	0.976	2	NaN	0
SPBC577.03c		GCN5-related N-acetyltransferase	0.971	274	0.982	259
SPBC336.14c	ppk26	serine/threonine protein kinase Ppk26	0.968	285	0.986	369
SPBC215.06c		human LYHRT homolog	0.973	268	0.981	305
SPBP19A11.02c		sequence orphan	0.970	267	0.984	394
SPAC11E3.05		ubiquitin-protein ligase E3	0.974	231	0.980	202
SPAC22F8.09	rrp16	rRNA processing protein Rrp16	0.981	424	0.973	382
SPBC29A10.14	rec8	meiotic cohesin complex subunit Rec8	0.970	369	0.985	409
SPBC216.04c		methionine sulfoxide	0.973	423	0.982	330
SPBC18E5.05c		RNA polymerase II elongator complex subunit	0.985	369	0.970	397
SPBP4H10.13	rps2302	40S ribosomal protein S23	0.967	407	0.988	453
SPAC1782.07	qcr8	ubiquinol-cytochrome-c reductase complex subunit 7	0.978	3	NaN	0
SPBP8B7.06	rpp201	60S acidic ribosomal protein P2A subunit	0.971	392	0.985	450
SPCC962.04	rps1201	40S ribosomal protein S12	0.990	72	0.966	383
SPBP35G2.10	mit1	SHREC complex subunit Mit1	0.971	296	0.986	410
SPBP35G2.06c	nup131	nucleoporin Nup131	0.972	344	0.985	441
SPAC17G8.13c	mst2	histone acetyltransferase Mst2	0.980	732	0.978	304
SPCC338.10c	cox5	cytochrome c oxidase subunit V	NaN	0	0.979	116
SPAC1610.02c		mitochondrial ribosomal protein subunit L1	0.967	45	0.990	94
SPBC685.06	rps001	40S ribosomal protein S0A (p40)	0.970	395	0.988	355
SPAC3H5.08c		WD repeat protein Wdr44 family	0.979	639	0.980	447
SPBC660.12c		peptide epimerase	0.975	299	0.985	466
SPBC26H8.14c	cox17	metallochaperone Cox17	NaN	0	0.980	4
SPAC1006.09	win1	MAP kinase kinase kinase Win1	0.983	308	0.977	350
SPAC19G12.08		fatty acid hydroxylase	0.970	187	0.989	119
SPBC25D12.06		RNA helicase	0.977	9	0.983	703
SPAC19E9.03	pas1	cyclin Pas1	NaN	0	0.980	562
SPBC23G7.11		DNA-3-methyladenine glycosidase Mag2	0.975	282	0.986	341

Systematic ID	Gene name	Gene description	CF index screen 1	Cell number	CF index screen 2	Cell number
SPBC18H10.06c	swd2	COMPASS complex subunit Swd2	0.981	261	0.979	92
SPAC144.06	apl5	AP-3 adaptor complex subunit Apl5	0.985	117	0.975	219
SPCC895.09c	ucp12	ATP-dependent RNA helicase Ucp1	0.979	331	0.982	254
SPBC9B6.09c	mdl1	mitochondrial peptide-transporting ATPase	0.972	245	0.989	235
SPCC306.09c	cap1	adenylyl cyclase-associated protein Cap1	0.981	4	NaN	0
SPCC4F11.02	ptc1	protein phosphatase 2C Ptc1	0.983	197	0.979	249
SPBC216.02	mcp5	cortical anchoring factor for dynein Mcp5/Num1	0.974	343	0.989	300
SPCC191.07	cyc1	cytochrome c	NaN	0	0.982	5
SPBC1604.07	atp4	F0-ATPase subunit	0.984	4	NaN	0
SPAC3H8.05c		conserved fungal protein	0.983	103	0.985	56
SPAC4A8.03c	ptc4	protein phosphatase 2C Ptc4	0.978	6	0.990	91
SPBC887.10	mcs4	two-component response regulator	0.981	269	0.988	142
SPAC222.04c	ies6	chromatin remodeling complex subunit Ies6	0.985	303	NaN	0
SPCC18B5.01c	bfr1	brefeldin A efflux transporter Bfr1	0.986	278	0.984	335
SPCC4B3.17	cbp3	ubiquinol cytochrome-c reductase assembly protein Cbp3	0.985	5	NaN	0
SPBC215.14c	vps20	vacuolar sorting protein Vps20	0.985	81	0.986	199
SPAC29A4.16	hal4	halotolerence protein 4	NaN	0	0.986	3
SPCC297.03	ssp1	serine/threonine protein kinase Ssp1	NaN	0	0.987	223
SPBP23A10.16	sdh4	TIM22 inner membrane protein import complex anchor subunit Tim18	0.988	152	NaN	0
SPAC1952.09c		acetyl-CoA hydrolase	0.987	209	0.992	253
SPAC1486.08		mitochondrial inner membrane protein involved in cytochrome c oxidase assembly Cox16	NaN	0	0.990	1
SPBC691.04		mitochondrial ATP-dependent RNA helicase Mss116	0.993	147	0.992	228
SPAC328.03	tps1	alpha,alpha-trehalose-phosphate synthase [UDP-forming]	0.993	400	0.993	180
SPBC119.06	sco1	copper chaperone Sco1	0.993	3	0.993	777
SPBC29A10.13	atp7	F0-ATPase subunit D	0.993	1	NaN	0
SPAC1006.05c	och1	alpha-1,6-mannosyltransferase Och1	NaN	0	NaN	0
SPAC1142.05	ctr5	copper transporter complex subunit Ctr5	NaN	0	NaN	0
SPAC167.05		Usp (universal stress protein) family protein, implicated in meiotic chromosome segregation	NaN	0	NaN	0
SPAC1782.11	met14	adenylyl-sulfate kinase	NaN	0	NaN	0
SPAC19A8.11c		recombination protein Irc6	NaN	0	NaN	0
SPAC1F3.07c	rsc58	RSC complex subunit Rsc58	NaN	0	NaN	0
SPAC1F8.04c		hydrolase	NaN	0	NaN	0
SPAC227.13c	isu1	iron-sulfur cluster assembly scaffold protein Isu1	NaN	0	NaN	0
SPAC23C4.11	atp18	F-0 ATPase subunit J	NaN	0	NaN	0
SPAC27E2.07	pvg2	galactose residue biosynthesis protein Pvg2	NaN	0	NaN	0
SPAC31F12.01	zds1	zds family protein Zds1	NaN	0	NaN	0
SPAC31G5.07		conserved fungal protein	NaN	0	NaN	0
SPAC31G5.21		human family 32A homolog	NaN	0	NaN	0
SPAC328.02		Ariadne homolog	NaN	0	NaN	0
SPAC3A11.09	sod22	plasma membrane alkali metal cation/H+ antiporter Sod22	NaN	0	NaN	0
SPAC4F10.05c		lipoate-protein ligase	NaN	0	NaN	0
SPAC688.11	end4	Huntingtin-interacting protein homolog	NaN	0	NaN	0
SPAC6F12.04		COPI-coated vesicle associated protein	NaN	0	NaN	0
SPAP27G11.06c		AP-1 adaptor complex subunit	NaN	0	NaN	0
SPAP8A3.05		ski complex subunit Ski7	NaN	0	NaN	0
SPAPB1E7.11c		sequence orphan	NaN	0	NaN	0
SPBC12C2.02c	ste20	sterility protein Ste20	NaN	0	NaN	0
SPBC16C6.09	ogm4	protein O-mannosyltransferase Ogm4	NaN	0	NaN	0
SPBC19G7.06	mbx1	MADS-box transcription factor Mbx1	NaN	0	NaN	0
SPBC215.08c	arg4	carbamoyl-phosphate synthase Arg4	NaN	0	NaN	0
SPBC29A3.10c	atp14	F1-ATPase subunit H	NaN	0	NaN	0
SPBC29B5.01	atf1	transcription factor Atf1	NaN	0	NaN	0
SPBC337.08c	ubi4	ubiquitin	NaN	0	NaN	0
SPBC337.09	erg28	Erg28 protein	NaN	0	NaN	0
SPBC337.15c	coq7	ubiquinone biosynthesis protein Coq7	NaN	0	NaN	0
SPBC365.08c		Der1-like (degradation in the ER) family	NaN	0	NaN	0
SPBC3D6.08c		mRNA decapping complex subunit	NaN	0	NaN	0
SPBC3E7.10	fma1	methionine aminopeptidase Fma1	NaN	0	NaN	0
SPBC409.06	uch2	ubiquitin C-terminal hydrolase Uch2	NaN	0	NaN	0
SPBC56F2.12	ilv5	acetohydroxyacid reductoisomerase	NaN	0	NaN	0
SPBC577.14c	spa1	ornithine decarboxylase antizyme Spa1	NaN	0	NaN	0

Systematic ID	Gene name	Gene description	CF index screen 1	Cell number	CF index screen 2	Cell number
SPBC839.15c	ef1a-c	translation elongation factor EF-1 alpha Ef1a-c	NaN	0	NaN	0
SPBC8E4.01c		inorganic phosphate transporter	NaN	0	NaN	0
SPBP35G2.07	ilv1	acetolactate synthase catalytic subunit	NaN	0	NaN	0
SPBP4H10.11c	lcf2	long-chain-fatty-acid-CoA ligase	NaN	0	NaN	0
SPBPB2B2.19c		S. pombe specific 5Tm protein family	NaN	0	NaN	0
SPCC11E10.04		ATPase expression protein homolog	NaN	0	NaN	0
SPCC1322.10		conserved fungal protein	NaN	0	NaN	0
SPCC1393.10	ctr4	copper transporter complex subunit Ctr4	NaN	0	NaN	0
SPCC1840.10	lsm8	U6 snRNP-associated protein Lsm8	NaN	0	NaN	0
SPCC1840.12		OPT oligopeptide transporter family	NaN	0	NaN	0
SPCC18B5.10c		TREX complex subunit Tex1	NaN	0	NaN	0
SPCC191.03c		sequence orphan	NaN	0	NaN	0
SPCC1919.01	ppk34	serine/threonine protein kinase Ppk34	NaN	0	NaN	0
SPCC4G3.04c	coq5	C-methytransferase	NaN	0	NaN	0
SPCC584.01c		sulfite reductase NADPH flavoprotein subunit	NaN	0	NaN	0
SPCC594.01		DUF1769 family protein	NaN	0	NaN	0
SPCC663.01c	ekc1	protein phosphatase regulatory subunit Ekc1	NaN	0	NaN	0
SPCC794.06		TDT malic acid transporter	NaN	0	NaN	0
SPCP1E11.04c	pal1	membrane associated protein Pal1	NaN	0	NaN	0

9.3.2 Identified candidate genes

Table 4. Candidate genes identified by genome-wide screen for genes required for CF, and the position of the corresponding deletion strains on the plates generated for the validation screens.

Rescreen Position	Bioneer Position	Systematic ID	CF index screen 1	Cell number	CF index screen 2	Cell number
RS-P01-14	P01-13	SPAC14C4.16	0.900	355	0.880	477
RS-P01-15	P01-18	SPAC16A10.05c	0.782	176	0.819	329
RS-P01-16	P01-20	SPAC16E8.18	0.895	290	0.878	273
RS-P01-17	P01-30	SPAC19A8.11c	NaN	0	NaN	0
RS-P01-18	P01-31	SPAC19D5.11c	0.772	266	0.879	274
RS-P01-19	P01-32	SPAC1D4.11c	0.849	115	0.828	154
RS-P01-20	P01-40	SPAC23C11.08	0.830	84	0.853	272
RS-P01-21	P01-43	SPAC23C4.17	0.854	290	0.884	326
RS-P01-22	P01-44	SPAC25B8.10	0.855	328	0.893	377
RS-P01-23	P01-45	SPAC25G10.06	0.859	248	0.886	324
RS-P01-26	P01-47	SPAC27F1.10	0.886	349	0.889	439
RS-P01-27	P01-55	SPAC343.20	0.804	262	0.896	294
RS-P01-28	P01-56	SPAC3A12.08	0.888	308	0.894	292
RS-P01-29	P01-67	SPAC664.10	0.872	281	0.889	269
RS-P01-30	P01-68	SPAC683.03	0.878	310	0.809	278
RS-P01-31	P01-69	SPAC694.03	0.865	259	0.873	281
RS-P01-32	P01-70	SPAC6B12.06c	0.879	344	0.877	314
RS-P01-33	P01-71	SPAC6B12.15	0.789	194	0.817	210
RS-P01-34	P01-72	SPAC6F6.09	0.884	471	0.857	367
RS-P01-35	P01-78	SPAC8C9.14	0.876	319	0.878	326
RS-P01-38	P01-79	SPAC8C9.19	0.833	330	0.856	337
RS-P01-39	P01-80	SPAC8E11.04c	0.872	354	0.864	371
RS-P01-40	P01-83	SPAP11E10.01	0.883	369	0.842	358
RS-P01-41	P01-85	SPAPB17E12.02	0.603	229	0.881	374
RS-P01-42	P01-87	SPAPB17E12.04c	0.779	209	0.887	362
RS-P01-43	P01-92	SPAPB18E9.01	0.847	397	NaN	0
RS-P01-44	P02-01	SPAPB2B4.06	0.663	317	0.863	366
RS-P01-45	P02-12	SPBC1539.08	0.603	112	0.848	288
RS-P01-46	P02-22	SPBC1703.11	0.873	229	0.657	217
RS-P01-47	P02-29	SPBC215.04	0.816	241	0.899	207
RS-P01-50	P02-36	SPBC24C6.05	0.884	274	0.867	247
RS-P01-51	P02-43	SPBC30D10.09c	0.733	237	0.716	258
RS-P01-52	P02-44	SPBC31F10.05	0.854	195	0.866	232
RS-P01-53	P02-54	SPBC56F2.14	0.890	277	0.871	259
RS-P01-54	P02-63	SPBCPT2R1.02	0.892	328	0.881	247
RS-P01-55	P02-66	SPBP4H10.08	0.876	269	0.899	282
RS-P01-56	P02-68	SPBP8B7.22	0.872	296	0.877	238
RS-P01-57	P02-72	SPBPB7E8.02	0.814	301	0.802	279
RS-P01-58	P02-85	SPCC576.01c	0.674	227	0.884	291
RS-P01-59	P03-05	SPAC11D3.18c	0.896	335	0.828	422
RS-P01-62	P03-07	SPAC11E3.09	0.856	292	0.888	357
RS-P01-63	P03-08	SPAC11G7.02	0.472	84	0.893	185
RS-P01-64	P03-11	SPAC12B10.07	0.893	315	0.823	401
RS-P01-65	P03-20	SPAC13G6.09	0.823	174	0.784	254
RS-P01-66	P03-21	SPAC144.02	0.000	3	0.804	292
RS-P01-67	P03-29	SPAC15A10.11	0.767	239	0.805	289
RS-P01-68	P03-30	SPAC15A10.16	0.812	263	0.767	334
RS-P01-69	P03-52	SPAC17D4.03c	0.882	240	0.850	305
RS-P01-70	P03-57	SPAC17H9.08	NaN	0	0.804	178

Rescreen Position	Bioneer Position	Systematic ID	CF index screen 1	Cell number	CF index screen 2	Cell number
RS-P01-71	P03-65	SPAC1851.03	0.866	119	0.849	104
RS-P01-74	P03-78	SPAC1B2.04	0.839	10	NaN	0
RS-P01-75	P03-87	SPAC20H4.02	0.865	395	0.814	515
RS-P01-76	P03-96	SPAC22F3.03c	0.769	303	0.864	290
RS-P01-77	P04-01	SPAC22F3.06c	0.740	229	0.871	210
RS-P01-78	P04-05	SPAC22F8.04	0.041	253	0.190	344
RS-P01-79	P04-06	SPAC22F8.11	0.662	325	0.256	400
RS-P01-80	P04-12	SPAC22H10.09	NaN	0	0.898	14
RS-P01-81	P04-17	SPAC23D3.01	0.854	295	0.877	301
RS-P01-82	P04-20	SPAC23E2.01	NaN	0	0.887	51
RS-P01-83	P04-21	SPAC23G3.02c	0.720	256	0.697	312
RS-P02-14	P04-22	SPAC23G3.05c	0.895	357	0.857	240
RS-P02-15	P04-31	SPAC25H1.02	0.893	309	0.846	265
RS-P02-16	P04-38	SPAC27D7.02c	0.898	203	0.899	312
RS-P02-17	P04-40	SPAC27D7.14c	NaN	0	0.000	1
RS-P02-18	P04-48	SPAC2F3.02	0.870	281	0.892	321
RS-P02-19	P04-68	SPAC328.10c	0.827	249	0.847	306
RS-P02-20	P04-82	SPAC3F10.16c	0.699	5	0.867	128
RS-P02-21	P04-85	SPAC3G9.08	0.439	212	0.765	289
RS-P02-22	P05-01	SPAC4D7.03	0.628	244	0.862	264
RS-P02-23	P05-04	SPAC4F8.11	0.707	319	0.787	302
RS-P02-26	P05-06	SPAC4G8.04	0.800	312	0.782	273
RS-P02-27	P05-07	SPAC4G8.05	0.711	277	0.822	262
RS-P02-28	P05-08	SPAC4G8.08	0.873	296	0.859	199
RS-P02-29	P05-09	SPAC4G9.02	0.835	342	0.872	300
RS-P02-30	P05-12	SPAC4H3.07c	0.705	270	0.889	238
RS-P02-31	P05-16	SPAC56E4.03	0.778	171	0.824	169
RS-P02-32	P05-17	SPAC56E4.06c	0.764	190	0.782	160
RS-P02-33	P05-19	SPAC56F8.06c	0.714	202	0.751	179
RS-P02-34	P05-20	SPAC56F8.09	0.845	182	0.873	167
RS-P02-35	P05-21	SPAC57A10.03	0.875	153	0.806	328
RS-P02-38	P05-22	SPAC57A7.05	0.889	185	0.829	215
RS-P02-39	P05-23	SPAC57A7.12	0.819	199	0.849	202
RS-P02-40	P05-28	SPAC637.06	0.832	157	0.872	194
RS-P02-41	P05-29	SPAC637.07	NaN	0	0.890	51
RS-P02-42	P05-32	SPAC664.02c	0.883	155	0.876	188
RS-P02-43	P05-41	SPAC6F12.12	0.876	165	0.829	178
RS-P02-44	P05-69	SPAC926.09c	0.870	337	0.898	217
RS-P02-45	P06-12	SPBC13G1.10c	0.722	145	0.889	480
RS-P02-46	P06-65	SPBC19G7.10c	0.695	134	0.897	165
RS-P02-47	P06-77	SPBC21C3.03	0.412	290	0.741	260
RS-P02-50	P06-85	SPBC25B2.04c	0.668	42	0.790	207
RS-P02-51	P06-96	SPBC29A3.05	0.813	165	0.890	262
RS-P02-52	P07-01	SPBC29A3.09c	0.814	169	0.877	312
RS-P02-53	P07-05	SPBC2A9.04c	0.837	308	0.861	439
RS-P02-54	P07-33	SPBC365.10	NaN	0	0.711	34
RS-P02-55	P08-12	SPCC132.04c	0.818	505	0.846	528
RS-P02-56	P08-17	SPCC1682.08c	0.815	4	0.888	216
RS-P02-57	P08-18	SPCC1795.01c	0.864	322	0.852	200
RS-P02-58	P08-27	SPCC338.11c	0.879	342	0.883	326
RS-P02-59	P08-28	SPCC417.06c	0.891	303	0.894	378
RS-P02-62	P08-29	SPCC417.09c	0.704	264	0.771	355
RS-P02-63	P08-31	SPCC553.08c	0.808	292	NaN	0
RS-P02-64	P08-40	SPCC736.08	0.641	285	0.681	152

Rescreen Position	Bioneer Position	Systematic ID	CF index screen 1	Cell number	CF index screen 2	Cell number
RS-P02-65	P08-41	SPCC74.04	0.874	319	0.875	261
RS-P02-66	P08-52	SPAC1002.05c	0.880	292	0.899	277
RS-P02-67	P08-54	SPAC10F6.11c	0.776	260	0.782	266
RS-P02-68	P08-68	SPAC1786.02	0.893	346	0.888	258
RS-P02-69	P08-91	SPAC32A11.03c	0.882	324	0.863	430
RS-P02-70	P09-05	SPAC688.10	0.888	364	0.822	316
RS-P02-71	P09-13	SPAC977.17	NaN	0	0.851	693
RS-P02-74	P09-14	SPAC9G1.06c	0.850	289	0.838	291
RS-P02-75	P09-15	SPAPB1E7.05	0.876	315	0.878	263
RS-P02-76	P09-17	SPAPB1E7.08c	0.864	239	0.890	256
RS-P02-77	P09-18	SPAPYUG7.03c	0.785	93	0.864	99
RS-P02-78	P09-28	SPBC1685.14c	0.874	303	0.844	165
RS-P02-79	P09-30	SPBC16E9.11c	0.885	265	0.831	223
RS-P02-80	P09-34	SPBC215.08c	NaN	0	NaN	0
RS-P02-81	P09-45	SPBC31E1.01c	0.679	291	0.736	251
RS-P02-82	P09-50	SPBC3E7.12c	0.866	272	0.867	170
RS-P02-83	P09-52	SPBC428.10	0.893	279	0.886	165
RS-P03-14	P09-54	SPBC530.06c	0.846	2	NaN	0
RS-P03-15	P09-64	SPCC11E10.04	NaN	0	NaN	0
RS-P03-16	P09-85	SPCC970.02	0.819	248	0.886	246
RS-P03-17	P09-86	SPCP1E11.05c	0.750	406	0.825	378
RS-P03-18	P09-96	SPAC10F6.13c	0.667	52	0.885	162
RS-P03-19	P10-01	SPAC1142.02c	0.794	294	0.883	337
RS-P03-20	P10-28	SPAC22A12.06c	0.815	244	0.867	212
RS-P03-21	P10-30	SPAC23C4.05c	0.873	257	0.893	239
RS-P03-22	P10-35	SPAC25A8.02	0.647	317	0.684	242
RS-P03-23	P10-50	SPAC4G8.13c	0.891	265	0.892	217
RS-P03-26	P10-67	SPAPB2C8.01	0.876	243	0.883	253
RS-P03-27	P10-68	SPAPYUG7.02c	0.853	226	0.884	211
RS-P03-28	P10-75	SPBC1289.10c	NaN	0	0.873	246
RS-P03-29	P10-77	SPBC12C2.08	0.875	256	0.855	347
RS-P03-30	P10-79	SPBC1604.02c	0.845	237	0.882	228
RS-P03-31	P11-06	SPBC2F12.03c	0.699	238	0.778	184
RS-P03-32	P11-07	SPBC2G2.01c	0.727	228	0.899	237
RS-P03-33	P11-08	SPBC2G2.02	0.740	267	0.857	235
RS-P03-34	P11-18	SPBC3E7.09	0.815	196	0.884	187
RS-P03-35	P11-19	SPBC3E7.11c	0.680	242	0.816	211
RS-P03-38	P11-21	SPBC428.14	0.787	185	0.885	190
RS-P03-39	P11-30	SPBC800.11	0.822	226	0.856	234
RS-P03-40	P11-32	SPBC839.15c	NaN	0	NaN	0
RS-P03-41	P11-39	SPCC1020.10	0.877	196	0.817	193
RS-P03-42	P11-40	SPCC11E10.05c	0.833	209	0.852	220
RS-P03-43	P11-41	SPCC11E10.09c	0.872	237	0.875	235
RS-P03-44	P11-43	SPCC1235.12c	0.863	236	0.839	250
RS-P03-45	P11-50	SPCC1450.02	0.862	217	0.837	196
RS-P03-46	P11-51	SPCC1620.07c	0.840	237	0.855	193
RS-P03-47	P11-68	SPCC584.01c	NaN	0	NaN	0
RS-P03-50	P11-90	SPAC15E1.05c	0.900	400	0.856	337
RS-P03-51	P11-96	SPAC17A5.04c	0.110	303	0.356	175
RS-P03-52	P12-02	SPAC17H9.19c	0.858	243	0.877	188
RS-P03-53	P12-03	SPAC186.01	0.710	439	0.886	264
RS-P03-54	P12-04	SPAC1952.11c	0.605	353	0.846	265
RS-P03-55	P12-05	SPAC19E9.01c	0.605	376	0.828	370
RS-P03-56	P12-06	SPAC1A6.09c	0.700	242	0.895	118

Rescreen Position	Bioneer Position	Systematic ID	CF index screen 1	Cell number	CF index screen 2	Cell number
RS-P03-57	P12-07	SPAC1D4.01	0.666	366	0.857	226
RS-P03-58	P12-08	SPAC1F5.10	0.618	212	0.803	188
RS-P03-59	P12-16	SPAC25B8.17	0.802	170	0.896	52
RS-P03-62	P12-17	SPAC25H1.04	0.733	327	0.899	225
RS-P03-63	P12-18	SPAC29A4.20	0.845	300	0.872	231
RS-P03-64	P12-19	SPAC2C4.15c	0.731	323	0.741	222
RS-P03-65	P12-20	SPAC2E12.03c	0.781	423	0.898	263
RS-P03-66	P12-21	SPAC2F3.05c	0.766	360	0.881	225
RS-P03-67	P12-22	SPAC2G11.07c	0.795	316	0.891	157
RS-P03-68	P12-25	SPAC31G5.12c	NaN	0	0.894	382
RS-P03-69	P12-26	SPAC323.05c	0.808	218	0.805	2
RS-P03-70	P12-38	SPAC57A7.08	0.675	180	0.770	175
RS-P03-71	P12-39	SPAC664.07c	NaN	0	0.900	286
RS-P03-74	P12-43	SPAC750.06c	0.803	224	0.894	227
RS-P03-75	P12-47	SPAC9E9.05	0.873	250	0.873	252
RS-P03-76	P12-50	SPAPB1E7.11c	NaN	0	NaN	0
RS-P03-77	P12-60	SPBC16A3.03c	NaN	0	0.885	258
RS-P03-78	P12-67	SPBC28F2.10c	0.874	224	0.873	201
RS-P03-79	P12-71	SPBC32F12.05c	0.859	133	0.882	36
RS-P03-80	P12-85	SPBC543.03c	0.812	226	0.855	323
RS-P03-81	P12-96	SPCC1223.04c	0.861	227	0.899	254
RS-P03-82	P13-21	SPAC1071.11	0.810	127	0.885	58
RS-P03-83	P13-28	SPAC15A10.09c	0.859	293	0.861	237
RS-P04-14	P13-29	SPAC167.04	0.875	222	NaN	0
RS-P04-15	P13-30	SPAC1687.12c	0.879	234	0.876	207
RS-P04-16	P13-31	SPAC186.05c	0.873	298	0.856	234
RS-P04-17	P13-33	SPAC1952.06c	0.856	259	0.848	211
RS-P04-18	P13-38	SPAC1D4.03c	0.706	160	0.781	182
RS-P04-19	P13-44	SPAC227.06	0.867	299	0.891	290
RS-P04-20	P13-60	SPAC589.07c	0.784	312	0.795	319
RS-P04-21	P13-82	SPBC15D4.09c	0.819	59	0.859	28
RS-P04-22	P14-21	SPBC947.01	0.900	244	0.886	188
RS-P04-23	P14-27	SPCC1020.08	0.889	214	0.818	197
RS-P04-26	P14-29	SPCC1442.01	0.842	200	0.890	237
RS-P04-27	P14-30	SPCC1753.03c	0.843	236	0.760	207
RS-P04-28	P14-31	SPCC24B10.11c	0.837	208	0.881	166
RS-P04-29	P14-33	SPCC306.05c	0.813	204	0.882	226
RS-P04-30	P14-38	SPCC548.05c	0.850	346	0.775	279
RS-P04-31	P14-39	SPCC553.04	0.881	2	0.855	235
RS-P04-32	P14-40	SPCC576.13	0.885	163	0.884	190
RS-P04-33	P14-44	SPCC663.06c	0.669	270	0.894	238
RS-P04-34	P14-49	SPCC757.09c	0.869	229	0.850	251
RS-P04-35	P14-51	SPCC777.12c	0.894	224	0.869	261
RS-P04-38	P14-52	SPCC794.12c	0.567	168	0.882	219
RS-P04-39	P14-53	SPCP1E11.04c	NaN	0	NaN	0
RS-P04-40	P14-55	SPAC1002.07c	0.893	272	0.869	243
RS-P04-41	P14-74	SPAC22F8.02c	-0.002	268	0.480	332
RS-P04-42	P14-87	SPAC4F10.06	0.894	307	0.839	318
RS-P04-43	P15-09	SPBC16C6.09	NaN	0	NaN	0
RS-P04-44	P15-16	SPBC20F10.10	0.857	216	0.832	231
RS-P04-45	P15-26	SPBC365.16	0.813	255	NaN	0
RS-P04-46	P15-42	SPCC1259.14c	0.878	295	0.889	277
RS-P04-47	P15-46	SPCC1494.08c	0.899	232	0.833	216
RS-P04-50	P15-58	SPCC576.17c	0.882	261	0.812	250

Rescreen Position	Bioneer Position	Systematic ID	CF index screen 1	Cell number	CF index screen 2	Cell number
RS-P04-51	P15-81	SPAC227.04	0.602	301	0.775	365
RS-P04-52	P15-85	SPAC23G3.10c	0.878	246	0.894	369
RS-P04-53	P15-91	SPAC323.01c	0.890	20	0.876	85
RS-P04-54	P15-96	SPAC5D6.02c	0.859	294	0.895	246
RS-P04-55	P16-03	SPAC806.04c	0.787	288	0.875	280
RS-P04-56	P16-04	SPAC8F11.10c	0.460	330	0.848	298
RS-P04-57	P16-06	SPACUNK4.09	0.681	276	0.783	242
RS-P04-58	P16-11	SPBC16G5.13	0.854	294	0.890	330
RS-P04-59	P16-17	SPBC215.10	0.715	287	0.875	264
RS-P04-62	P16-18	SPBC23E6.01c	0.701	233	0.851	259
RS-P04-63	P16-21	SPBC29A10.11c	0.821	225	0.892	263
RS-P04-64	P16-22	SPBC2A9.07c	0.770	229	0.862	262
RS-P04-65	P16-24	SPBC32F12.03c	0.868	312	0.834	308
RS-P04-66	P16-27	SPBC359.04c	0.876	274	0.859	272
RS-P04-67	P16-28	SPBC3B9.04	0.825	283	0.844	245
RS-P04-68	P16-29	SPBC3H7.11	0.794	260	0.803	260
RS-P04-69	P16-30	SPBC685.03	0.810	238	0.787	257
RS-P04-70	P16-31	SPBC8E4.02c	0.861	246	0.824	293
RS-P04-71	P16-32	SPBC8E4.05c	0.803	254	0.869	266
RS-P04-74	P16-33	SPBPB10D8.02c	0.882	210	0.885	260
RS-P04-75	P16-41	SPCC1739.06c	0.814	4	NaN	0
RS-P04-76	P16-43	SPCC2H8.05c	0.896	249	0.867	265
RS-P04-77	P16-65	SPAC1952.05	0.871	281	0.540	286
RS-P04-78	P16-76	SPAC4F8.03	0.895	3	0.824	264
RS-P04-79	P17-03	SPBC1709.16c	0.803	324	0.896	171
RS-P04-80	P17-09	SPBC29A3.10c	NaN	0	NaN	0
RS-P04-81	P17-10	SPBC2A9.05c	0.757	327	0.829	248
RS-P04-82	P17-12	SPBC337.15c	NaN	0	NaN	0
RS-P04-83	P17-20	SPBC83.18c	0.548	231	0.857	217
RS-P05-14	P17-21	SPBC839.05c	0.521	175	0.891	208
RS-P05-15	P17-28	SPCC162.04c	0.771	179	0.886	223
RS-P05-16	P17-29	SPCC162.05	0.661	231	NaN	0
RS-P05-17	P17-30	SPCC1682.11c	0.458	222	0.717	214
RS-P05-18	P17-40	SPAC14C4.08	0.649	217	0.870	195
RS-P05-19	P17-41	SPAC14C4.09	0.811	121	0.897	109
RS-P05-20	P17-45	SPAC17G8.14c	0.763	208	0.884	179
RS-P05-21	P17-48	SPAC23H4.10c	0.629	181	0.899	58
RS-P05-22	P17-51	SPAC29B12.06c	0.820	224	0.878	247
RS-P05-23	P17-52	SPAC2G11.04	0.798	208	0.893	224
RS-P05-26	P17-53	SPAC3A11.04	0.561	240	0.491	269
RS-P05-27	P17-64	SPAPB24D3.03	0.823	305	0.845	240
RS-P05-28	P17-66	SPBC1271.03c	0.861	286	0.878	272
RS-P05-29	P17-75	SPBC1921.06c	0.135	312	0.260	330
RS-P05-30	P18-02	SPAC13D6.02c	0.727	226	0.579	325
RS-P05-31	P18-03	SPAC14C4.10c	0.824	236	0.830	214
RS-P05-32	P18-04	SPAC167.06c	0.839	258	0.723	299
RS-P05-33	P18-05	SPAC1783.06c	0.823	208	0.643	166
RS-P05-34	P18-06	SPAC17G8.08c	0.818	176	0.774	280
RS-P05-35	P18-07	SPAC18B11.03c	0.812	209	0.898	205
RS-P05-38	P18-14	SPAC22E12.05c	0.797	119	0.837	199
RS-P05-39	P18-15	SPAC23A1.14c	0.836	181	0.863	196
RS-P05-40	P18-17	SPAC31A2.12	0.590	22	0.878	197
RS-P05-41	P18-19	SPAC31A2.13c	0.697	176	0.843	203
RS-P05-42	P18-38	SPBC902.05c	0.875	194	0.892	246

Rescreen Position	Bioneer Position	Systematic ID	CF index screen 1	Cell number	CF index screen 2	Cell number
RS-P05-43	P18-39	SPBP35G2.02	0.880	194	0.888	265
RS-P05-44	P18-40	SPBP35G2.04c	0.868	198	0.885	192
RS-P05-45	P18-50	SPAC13D6.04c	0.876	200	0.889	269
RS-P05-46	P18-52	SPAC13G7.12c	0.852	175	0.849	175
RS-P05-47	P18-93	SPBC1683.06c	0.897	403	0.869	578
RS-P05-50	P19-03	SPBC409.17c	0.897	267	0.849	264
RS-P05-51	P19-04	SPBP4H10.17c	0.815	271	0.888	318
RS-P05-52	P19-05	SPBP8B7.28c	0.186	299	0.559	353
RS-P05-53	P19-20	SPAC6G9.01c	0.716	194	0.817	218
RS-P05-54	P19-28	SPBC21C3.06	0.881	208	0.817	176
RS-P05-55	P19-30	SPBC3B8.10c	NaN	0	0.857	256
RS-P05-56	P19-38	SPCC965.09	0.876	216	0.890	277
RS-P05-57	P19-42	SPAC22F3.02	0.857	308	0.892	272
RS-P05-58	P19-44	SPAC31G5.03	0.738	225	0.871	181
RS-P05-59	P19-45	SPAC3H5.10	0.843	217	NaN	0
RS-P05-62	P19-51	SPAPJ698.02c	0.800	218	NaN	0
RS-P05-63	P19-53	SPBC15D4.05	0.885	343	0.867	260
RS-P05-64	P19-87	SPAC22F3.10c	0.832	277	0.786	2
RS-P05-65	P20-01	SPBC20F10.05	0.846	194	0.878	341
RS-P05-66	P20-06	SPBC405.05	0.667	195	0.671	343
RS-P05-67	P20-17	SPAC823.16c	0.898	26	0.878	182
RS-P05-68	P20-18	SPBC106.07c	0.737	207	0.842	269
RS-P05-69	P20-21	SPBC19G7.16	NaN	0	0.779	257
RS-P05-70	P20-22	SPBC1D7.04	0.709	45	0.893	1
RS-P05-71	P20-30	SPCP31B10.02	0.870	210	0.884	191
RS-P05-74	P20-31	SPAC10F6.07c	0.886	269	0.879	326
RS-P05-75	P20-32	SPAC139.02c	0.892	255	0.879	210
RS-P05-76	P20-33	SPCC830.04c	0.883	220	0.850	251
RS-P05-77	P20-34	SPAP27G11.12	0.855	242	0.887	262
RS-P05-78	P20-41	SPBPB2B2.07c	0.872	224	0.841	238
RS-P05-79	P20-44	SPAC1952.08c	0.887	228	0.893	183
RS-P05-80	P20-45	SPAC23G3.04	0.840	204	0.878	290
RS-P05-81	P20-52	SPCC1672.04c	0.818	113	NaN	0
RS-P05-82	P20-55	SPAC11G7.03	0.868	162	0.878	91
RS-P05-83	P20-57	SPAC22F8.12c	0.842	112	0.844	357
RS-P06-14	P20-64	SPBP8B7.04	0.872	229	0.865	302
RS-P06-15	P20-65	SPCC285.15c	0.849	247	0.821	306
RS-P06-16	P20-66	SPAC11H11.02c	0.894	282	0.854	308
RS-P06-17	P20-67	SPAC15F9.01c	0.864	217	0.889	250
RS-P06-18	P20-68	SPAC23H3.06	0.891	89	0.889	95
RS-P06-19	P20-69	SPAC25H1.09	0.886	233	0.840	277
RS-P06-20	P20-70	SPAC26H5.04	0.820	323	0.856	329
RS-P06-21	P20-80	SPCPB16A4.06c	0.892	340	0.860	315
RS-P06-22	P20-81	SPAC10F6.17c	0.886	348	0.865	313
RS-P06-23	P20-87	SPBC336.13c	0.840	225	0.850	148
RS-P06-26	P21-03	SPAC15A10.08	0.742	327	0.839	282
RS-P06-27	P21-04	SPAC1687.10	0.598	379	0.841	371
RS-P06-28	P21-05	SPAC1834.07	0.637	353	0.804	331
RS-P06-29	P21-06	SPAC1A6.06c	0.600	416	0.784	399
RS-P06-30	P21-08	SPAC1F7.06	0.770	389	0.886	309
RS-P06-31	P21-09	SPAC2H10.02c	0.724	516	0.884	340
RS-P06-32	P21-18	SPBC428.06c	0.763	96	0.865	137
RS-P06-33	P21-19	SPCC13B11.04c	0.629	309	0.820	328
RS-P06-34	P21-20	SPCC14G10.04	0.787	247	0.898	261

Rescreen Position	Bioneer Position	Systematic ID	CF index screen 1	Cell number	CF index screen 2	Cell number
RS-P06-35	P21-22	SPCC550.01c	0.726	393	0.874	316
RS-P06-38	P21-27	SPBC16G5.06	0.875	310	0.899	340
RS-P06-39	P21-29	SPAC31G5.17c	0.722	296	0.821	358
RS-P06-40	P21-30	SPAP8A3.04c	0.748	286	0.830	245
RS-P06-41	P21-31	SPAPJ695.01c	0.832	238	0.869	242
RS-P06-42	P21-40	SPAC17A2.10c	0.841	245	0.885	402
RS-P06-43	P21-42	SPBC25B2.08	0.890	285	0.887	445
RS-P06-44	P21-43	SPCC962.05	0.835	248	0.884	381
RS-P06-45	P21-45	SPAC30C2.08	0.808	285	0.886	356
RS-P06-46	P21-50	SPAC11D3.04c	0.867	254	0.772	149
RS-P06-47	P21-63	SPAC30D11.06c	0.840	295	0.865	321
RS-P06-50	P21-64	SPAC6C3.03c	0.837	269	0.843	296
RS-P06-51	P22-03	SPAC13C5.02	0.860	231	0.845	237
RS-P06-52	P22-04	SPAC458.06	0.675	238	0.670	287
RS-P06-53	P22-05	SPAC4H3.01	0.747	323	0.817	271
RS-P06-54	P22-06	SPAC5D6.10c	0.737	368	0.857	269
RS-P06-55	P22-07	SPBC17G9.10	0.708	391	0.839	325
RS-P06-56	P22-08	SPAC6G10.06	0.750	339	0.831	232
RS-P06-57	P22-09	SPBC1289.11	0.756	395	0.871	276
RS-P06-58	P22-11	SPBC36.04	0.321	1	NaN	0
RS-P06-59	P22-16	SPCC1906.04	0.845	160	0.858	210
RS-P06-62	P22-17	SPCC794.02	0.842	179	0.872	207
RS-P06-63	P22-18	SPAC3F10.09	0.727	217	0.773	217
RS-P06-64	P22-19	SPBC56F2.10c	0.730	229	0.843	220
RS-P06-65	P22-20	SPCC1183.06	0.766	230	0.867	261
RS-P06-66	P22-21	SPCC285.17	0.773	182	0.882	278
RS-P06-67	P22-23	SPAC17A2.01	0.849	304	0.868	281
RS-P06-68	P22-26	SPCC1259.07	0.534	3	0.883	205
RS-P06-69	P22-29	SPAC4F10.04	0.813	58	0.659	130
RS-P06-70	P22-30	SPAC9.11	0.868	201	0.772	199
RS-P06-71	P22-31	SPBC577.11	0.893	208	0.784	152
RS-P06-74	P22-32	SPBC713.05	0.854	249	0.899	220
RS-P06-75	P22-42	SPAC3H5.05c	0.861	215	0.837	218
RS-P06-76	P22-43	SPBC405.02c	0.853	169	0.869	196
RS-P06-77	P22-45	SPCC16C4.10	0.753	227	0.673	239
RS-P06-78	P22-51	SPAC12B10.13	0.898	228	0.893	201
RS-P06-79	P22-52	SPAC20G4.01	0.879	232	0.876	194
RS-P06-80	P22-62	SPAC15E1.03	0.810	50	0.880	273
RS-P06-81	P22-63	SPAC19B12.09	0.888	284	0.881	258
RS-P06-82	P22-77	SPCC24B10.08c	0.866	274	0.862	315
RS-P06-83	P23-01	SPBC1861.09	0.775	283	0.855	252
RS-P07-14	P23-03	SPBC776.17	0.808	264	0.833	114
RS-P07-15	P23-04	SPAC3C7.07c	0.838	195	0.834	206
RS-P07-16	P23-05	SPAC17G6.15c	0.869	188	0.869	245
RS-P07-17	P23-06	SPAC343.09	0.860	174	0.888	224
RS-P07-18	P23-09	SPAC1805.04	0.880	234	0.881	292
RS-P07-19	P23-16	SPBC14F5.12c	NaN	0	0.883	325
RS-P07-20	P23-18	SPAC24B11.10c	0.838	124	0.883	173
RS-P07-21	P23-22	SPAC17C9.07	0.850	280	0.838	235
RS-P07-22	P23-29	SPAC13G6.15c	0.575	103	0.566	176
RS-P07-23	P23-42	SPAPJ760.02c	0.808	176	0.828	185
RS-P07-26	P23-43	SPAC13F5.01c	0.876	221	0.887	183
RS-P07-27	P23-45	SPBC1711.13	NaN	0	0.648	43
RS-P07-28	P23-65	SPAC20G4.08	0.897	243	0.898	233

Rescreen Position	Bioneer Position	Systematic ID	CF index screen 1	Cell number	CF index screen 2	Cell number
RS-P07-29	P23-68	SPAC1952.15c	0.897	262	0.869	252
RS-P07-30	P23-85	SPAC1F8.06	0.755	249	0.898	250
RS-P07-31	P23-96	SPAC1A6.10	0.491	337	0.855	308
RS-P07-32	P24-01	SPAC23H4.12	0.473	2	0.683	198
RS-P07-33	P24-03	SPCC645.08c	0.736	357	0.884	263
RS-P07-34	P24-04	SPAC23H4.09	0.647	362	0.842	247
RS-P07-35	P24-05	SPAC1F7.12	0.688	383	0.870	259
RS-P07-38	P24-06	SPAC5D6.13	0.664	408	0.874	307
RS-P07-39	P24-07	SPBC18H10.19	0.477	338	0.741	227
RS-P07-40	P24-15	SPBC577.15c	0.735	273	NaN	0
RS-P07-41	P24-19	SPAC23A1.19c	0.675	239	0.878	140
RS-P07-42	P24-20	SPAC144.11	0.709	270	0.878	278
RS-P07-43	P24-23	SPAC343.06c	0.837	365	0.888	264
RS-P07-44	P24-26	SPBC3D6.08c	NaN	0	NaN	0
RS-P07-45	P24-27	SPAC56F8.16	0.817	296	0.842	254
RS-P07-46	P24-30	SPBC13E7.03c	0.865	302	0.878	161
RS-P07-47	P24-31	SPBC1734.05c	0.847	397	0.816	152
RS-P07-50	P24-32	SPAC6G10.10c	0.837	337	0.847	217
RS-P07-51	P24-33	SPAC10F6.12c	0.803	293	0.862	219
RS-P07-52	P24-40	SPBC83.10	0.867	271	0.897	247
RS-P07-53	P24-41	SPBP35G2.07	NaN	0	NaN	0
RS-P07-54	P24-50	SPAC3F10.04	0.000	3	NaN	0
RS-P07-55	P24-78	SPAC1B3.07c	0.877	261	0.894	240
RS-P07-56	P24-85	SPAC6F12.04	NaN	0	NaN	0
RS-P07-57	P25-04	SPAC869.11	0.632	458	0.871	390
RS-P07-58	P25-07	SPAC22F3.11c	0.828	186	0.784	269
RS-P07-59	P25-12	SPCC4G3.04c	NaN	0	NaN	0
RS-P07-62	P25-16	SPBC3B8.02	0.600	112	0.897	83
RS-P07-63	P25-27	SPAC767.01c	0.830	243	0.889	258
RS-P07-64	P25-28	SPAC11E3.03	0.801	222	0.896	227
RS-P07-65	P25-29	SPAC1296.02	0.802	91	0.865	161
RS-P07-66	P25-48	SPAC8C9.07	0.885	336	0.899	259
RS-P07-67	P25-52	SPBC1306.02	0.808	245	0.899	326
RS-P07-68	P25-59	SPBC17G9.07	0.690	186	0.887	235
RS-P07-69	P25-73	SPBP4H10.10	0.893	325	0.887	439
RS-P07-70	P25-75	SPCC1259.01c	0.834	273	0.892	302
RS-P07-71	P25-77	SPCC16C4.13c	0.893	448	0.890	520
RS-P07-74	P25-78	SPCC1739.12	0.823	338	0.000	1
RS-P07-75	P25-79	SPCC1919.04	0.527	308	0.838	425
RS-P07-76	P25-80	SPCC320.12	0.512	352	0.857	530
RS-P07-77	P25-88	SPBC776.09	0.797	315	NaN	0
RS-P07-78	P25-89	SPCC1259.09c	0.887	294	0.887	700
RS-P07-79	P25-96	SPAC750.05c	0.850	392	0.836	358
RS-P07-80	P26-05	SPBC18H10.14	0.529	271	0.854	192
RS-P07-81	P26-12	SPAC27D7.08c	0.711	306	0.854	171
RS-P07-82	P26-51	SPAC167.05	NaN	0	NaN	0
RS-P07-83	P26-82	SPAC23G3.03	0.817	327	0.849	367
RS-P08-14	P26-85	SPAC24H6.13	0.789	270	0.867	289
RS-P08-15	P26-96	SPAPB2B4.04c	0.721	196	0.850	226
RS-P08-16	P27-01	SPBC1105.14	0.747	434	0.695	268
RS-P08-17	P27-04	SPBC16A3.08c	0.706	338	0.865	191
RS-P08-18	P27-05	SPBC16D10.05	0.763	283	0.897	179
RS-P08-19	P27-06	SPBC1778.04	0.603	483	0.880	308
RS-P08-20	P27-10	SPBC21B10.10	0.857	385	0.892	209

Rescreen Position	Bioneer Position	Systematic ID	CF index screen 1	Cell number	CF index screen 2	Cell number
RS-P08-21	P27-11	SPBC26H8.05c	0.746	216	0.799	192
RS-P08-22	P27-23	SPBC543.07	0.403	218	0.660	333
RS-P08-23	P27-29	SPBP4H10.03	0.889	95	0.893	132
RS-P08-26	P27-33	SPCC126.11c	0.843	188	0.900	207
RS-P08-27	P27-85	SPAC25B8.19c	0.719	192	0.880	13
RS-P08-28	P27-96	SPAC977.16c	0.857	531	0.886	373
RS-P08-29	P28-01	SPACUNK4.10	0.850	384	0.866	275
RS-P08-30	P28-08	SPBP8B7.09c	0.757	239	0.823	253
RS-P08-31	P28-12	SPCC285.09c	0.774	1	0.001	106
RS-P08-32	P28-18	SPCC550.09	0.848	181	0.880	357
RS-P08-33	P28-19	SPCC5E4.05c	0.811	179	0.834	174
RS-P08-34	P28-22	SPAC24B11.07c	0.821	234	0.898	199
RS-P08-35	P28-26	SPBC12C2.03c	0.814	260	0.850	220
RS-P08-38	P28-29	SPBC1815.01	0.831	294	0.891	211
RS-P08-39	P28-33	SPBC337.07c	0.877	222	0.896	277
RS-P08-40	P28-40	SPCC584.15c	0.785	180	0.898	238
RS-P08-41	P28-41	SPCPB16A4.05c	0.871	220	0.860	250
RS-P08-42	P28-42	SPAC1399.02	0.878	298	0.889	245
RS-P08-43	P28-43	SPAC1D4.05c	0.863	251	0.897	241
RS-P08-44	P28-48	SPBC3B9.11c	0.535	392	0.728	295
RS-P08-45	P28-51	SPBC6B1.05c	0.500	221	0.693	286
RS-P08-46	P28-68	SPBC1604.12	0.729	291	0.770	294
RS-P08-47	P28-70	SPCC1450.08c	0.896	446	0.884	342
RS-P08-50	P28-81	SPAC31G5.04	0.895	289	0.892	215
RS-P08-51	P28-84	SPBC56F2.05c	0.477	218	0.799	233
RS-P08-52	P28-94	SPAC2F7.07c	0.773	35	0.861	7
RS-P08-53	P28-96	SPBC36.11	0.784	385	0.801	226
RS-P08-54	P29-01	SPBC651.11c	0.778	142	0.816	164
RS-P08-55	P29-02	SPCC4G3.11	0.863	414	0.793	305
RS-P08-56	P29-03	SPAC16E8.12c	0.724	338	0.822	305
RS-P08-57	P29-05	SPAC4F10.14c	0.563	397	0.838	368
RS-P08-58	P29-06	SPAC4F8.08	0.643	565	0.894	266
RS-P08-59	P29-08	SPBC21B10.12	0.760	523	0.893	315
RS-P08-62	P29-12	SPAC664.04c	0.777	230	0.803	225
RS-P08-63	P29-14	SPBC31F10.17c	0.863	289	0.892	282
RS-P08-64	P29-16	SPBC3H7.14	0.875	253	0.884	242
RS-P08-65	P29-22	SPAC1782.02c	0.788	361	0.889	278
RS-P08-66	P29-23	SPAC17A5.14	0.748	294	NaN	0
RS-P08-67	P29-26	SPBC336.05c	0.889	283	0.854	216
RS-P08-68	P29-27	SPAC12G12.15	0.761	301	0.719	247
RS-P08-69	P29-32	SPAC56E4.07	0.821	278	0.878	264
RS-P08-70	P29-42	SPCC364.03	0.800	362	0.867	334
RS-P08-71	P29-43	SPAC27D7.04	0.880	315	0.891	320
RS-P08-74	P29-47	SPCC1450.12	0.862	325	0.885	156
RS-P08-75	P29-52	SPBC21H7.06c	0.869	293	0.853	266
RS-P08-76	P29-62	SPAC13G6.13	0.899	296	0.866	371
RS-P08-77	P29-73	SPAC513.03	0.895	294	0.872	376
RS-P08-78	P29-79	SPAC2G11.06	0.829	318	0.892	293
RS-P08-79	P29-85	SPCC18.13	0.796	315	0.888	285
RS-P08-80	P29-96	SPBC19G7.18c	0.810	311	0.848	275
RS-P08-81	P30-01	SPCC613.08	0.821	249	0.870	215
RS-P08-82	P30-12	SPAC25H1.03	0.809	236	0.348	223
RS-P08-83	P30-19	SPBC19C2.14	0.812	100	0.867	76
RS-P09-14	P30-33	SPAC4D7.01c	0.877	234	0.894	300

Rescreen Position	Bioneer Position	Systematic ID	CF index screen 1	Cell number	CF index screen 2	Cell number
RS-P09-15	P30-34	SPCC1322.12c	0.815	265	0.784	234
RS-P09-16	P30-41	SPBC4F6.16c	0.857	300	0.897	255
RS-P09-17	P30-45	SPAC20G4.07c	0.888	395	0.841	4
RS-P09-18	P30-62	SPAC1F5.03c	0.898	229	0.893	317
RS-P09-19	P30-70	SPBC36B7.04	0.899	338	0.839	290
RS-P09-20	P30-74	SPAC26H5.03	0.884	325	0.899	266
RS-P09-21	P30-75	SPAC2F7.17	0.888	175	0.247	103
RS-P09-22	P30-83	SPAC22G7.05	0.863	232	0.875	144
RS-P09-23	P30-84	SPAC26F1.04c	0.879	733	0.864	276
RS-P09-26	P30-93	SPBP8B7.24c	0.587	410	0.878	475
RS-P09-27	P31-01	SPCC63.08c	0.737	232	0.551	290
RS-P09-28	P31-04	SPBC409.07c	0.873	156	0.836	155
RS-P09-29	P31-15	SPAC31A2.06	0.812	5	NaN	0
RS-P09-30	P31-18	SPAC227.17c	NaN	0	0.798	174
RS-P09-31	P31-24	SPBC13G1.14c	0.887	446	0.861	217
RS-P09-32	P31-30	SPAC29E6.01	0.887	200	0.830	242
RS-P09-33	P31-42	SPBC3B9.08c	0.891	262	0.864	221
RS-P09-34	P31-43	SPBC543.09	0.852	281	0.874	56
RS-P09-35	P31-51	SPBC1604.19c	0.865	226	0.850	304
RS-P09-38	P31-53	SPBC23E6.09	0.858	4	NaN	0
RS-P09-39	P31-84	SPBC216.03	0.000	1	0.877	374
RS-P09-40	P31-91	SPBC21B10.02	NaN	0	0.889	382
RS-P09-41	P32-05	SPAC630.10	0.837	310	0.898	287
RS-P09-42	P32-08	SPBC16E9.08	0.898	317	0.899	243
RS-P09-43	P32-09	SPCC1442.05c	0.895	278	0.865	239
RS-P09-44	P32-10	SPAC8F11.02c	0.888	385	0.826	268
RS-P09-45	P32-12	SPBC1347.08c	0.870	290	0.863	240
RS-P09-46	P32-17	SPBC26H8.11c	0.896	213	0.891	271
RS-P09-47	P32-20	SPAC11H11.01	0.879	166	0.872	228
RS-P09-50	P32-27	SPAC9G1.04	0.899	240	0.891	246
RS-P09-51	P32-34	SPBC106.16	0.868	153	0.892	196
RS-P09-52	P32-54	SPAC13G6.14	0.875	147	0.824	175
RS-P09-53	P32-59	SPAC1486.10	0.781	11	0.838	21
RS-P09-54	P32-62	SPAC15E1.04	0.839	10	0.896	22
RS-P09-55	P32-67	SPAC16C9.04c	0.839	213	0.890	245
RS-P09-56	P32-71	SPAC17G6.08	NaN	0	0.883	242
RS-P09-57	P32-85	SPAC1F7.08	0.879	5	NaN	0
RS-P09-58	P33-01	SPAC24C9.02c	0.850	281	0.880	309
RS-P09-59	P33-04	SPAC24C9.15c	NaN	0	0.847	91
RS-P09-62	P33-30	SPAC4C5.04	0.854	184	0.859	166
RS-P09-63	P33-38	SPAC607.09c	0.900	211	0.900	358
RS-P09-64	P33-41	SPAC664.15	0.852	286	0.888	280
RS-P09-65	P33-50	SPAC821.11	NaN	0	0.833	317
RS-P09-66	P33-52	SPAC824.05	0.851	153	0.875	170
RS-P09-67	P33-65	SPAP27G11.07c	0.880	289	0.881	351
RS-P09-68	P33-80	SPBC11C11.06c	0.872	286	0.872	320
RS-P09-69	P33-92	SPBC1604.04	0.878	265	0.887	311
RS-P09-70	P34-01	SPBC16C6.10	0.879	278	0.897	396
RS-P09-71	P34-03	SPBC16E9.16c	0.822	239	0.876	371
RS-P09-74	P34-04	SPBC16E9.19	0.686	355	0.857	398
RS-P09-75	P34-06	SPBC1709.06	NaN	0	0.861	265
RS-P09-76	P34-09	SPBC1718.01	0.714	213	0.710	217
RS-P09-77	P34-22	SPBC19F8.03c	0.692	185	0.883	276
RS-P09-78	P34-32	SPBC21D10.07	0.865	224	0.868	261

Rescreen Position	Bioneer Position	Systematic ID	CF index screen 1	Cell number	CF index screen 2	Cell number
RS-P09-79	P34-39	SPBC25B2.11	0.881	277	0.855	314
RS-P09-80	P34-42	SPBC26H8.01	0.655	87	0.873	368
RS-P09-81	P34-44	SPBC27B12.10c	0.862	319	0.823	198
RS-P09-82	P34-46	SPBC28E12.04	0.740	200	0.749	152
RS-P09-83	P34-58	SPBC32F12.09	0.874	269	0.881	248
RS-P10-14	P34-60	SPBC354.08c	0.885	305	0.869	364
RS-P10-15	P34-67	SPBC36B7.02	NaN	0	0.866	309
RS-P10-16	P34-68	SPBC3B9.06c	NaN	0	0.575	296
RS-P10-17	P34-72	SPBC3H7.07c	NaN	0	0.856	374
RS-P10-18	P34-83	SPBC56F2.12	NaN	0	NaN	0
RS-P10-19	P34-96	SPBC8E4.01c	NaN	0	NaN	0
RS-P10-20	P35-02	SPBCPT2R1.03	0.865	341	0.844	325
RS-P10-21	P35-03	SPBP16F5.04	0.732	300	0.881	265
RS-P10-22	P35-05	SPBP35G2.14	0.607	256	0.880	225
RS-P10-23	P35-06	SPBP4H10.04	0.558	285	0.852	388
RS-P10-26	P35-07	SPBP4H10.07	0.627	274	0.873	394
RS-P10-27	P35-09	SPBP8B7.08c	0.714	252	0.791	249
RS-P10-28	P35-10	SPBP8B7.27	0.856	346	0.866	289
RS-P10-29	P35-16	SPCC1235.06	0.805	182	0.861	268
RS-P10-30	P35-18	SPCC1259.12c	0.808	199	0.881	263
RS-P10-31	P35-21	SPCC1322.15	0.795	225	0.875	321
RS-P10-32	P35-28	SPCC1620.02	NaN	0	0.877	276
RS-P10-33	P35-29	SPCC1620.03	0.896	274	0.880	290
RS-P10-34	P35-30	SPCC1620.12c	0.889	218	0.860	309
RS-P10-35	P35-31	SPCC1672.09	0.893	241	0.862	268
RS-P10-38	P35-32	SPCC1682.07	0.871	187	0.773	168
RS-P10-39	P35-34	SPCC16C4.09	0.868	193	0.819	250
RS-P10-40	P35-39	SPCC1827.03c	NaN	0	0.878	287
RS-P10-41	P35-66	SPCC553.07c	0.886	304	0.845	300
RS-P10-42	P35-79	SPCC777.07	0.877	310	0.854	311
RS-P10-43	P35-90	SPAC1296.06	NaN	0	0.811	222
RS-P10-44	P36-01	SPAC1F8.04c	NaN	0	NaN	0
RS-P10-45	P36-03	SPAC25B8.06c	0.806	183	0.491	218
RS-P10-46	P36-04	SPAC1805.11c	0.786	248	0.777	236
RS-P10-47	P36-06	SPAC27F1.03c	0.745	263	0.721	287
RS-P10-50	P36-07	SPAC29B12.03	0.745	298	0.746	305
RS-P10-51	P36-09	SPAC2E1P3.02c	0.859	277	0.799	256
RS-P10-52	P36-10	SPAC2F3.01	0.891	353	0.875	211
RS-P10-53	P36-12	SPAC30D11.07	0.858	341	0.874	390
RS-P10-54	P36-16	SPAC3A11.08	0.770	82	0.739	127
RS-P10-55	P36-17	SPAC3H5.09c	0.873	222	0.728	272
RS-P10-56	P36-18	SPAC4A8.14	0.823	221	0.741	244
RS-P10-57	P36-19	SPAC4F10.13c	NaN	0	0.597	194
RS-P10-58	P36-20	SPAC4F10.15c	0.710	291	0.715	197
RS-P10-59	P36-21	SPAC56F8.12	0.772	244	0.738	276
RS-P10-62	P36-22	SPAC589.08c	0.838	263	0.800	238
RS-P10-63	P36-28	SPAC6F6.03c	0.894	222	0.709	291
RS-P10-64	P36-29	SPAC7D4.04	0.567	175	0.066	319
RS-P10-65	P36-30	SPAC824.03c	0.749	225	0.412	274
RS-P10-66	P36-31	SPAC977.10	0.868	258	0.755	225
RS-P10-67	P36-32	SPAP14E8.05c	0.880	264	0.798	239
RS-P10-68	P36-33	SPAP8A3.03	0.878	198	0.759	223
RS-P10-69	P36-38	SPBC1198.11c	0.899	130	0.899	225
RS-P10-70	P36-41	SPBC13A2.04c	0.860	339	0.898	324

Rescreen Position	Bioneer Position	Systematic ID	CF index screen 1	Cell number	CF index screen 2	Cell number
RS-P10-71	P36-43	SPBC15C4.01c	0.871	271	0.788	251
RS-P10-74	P36-44	SPBC1652.01	0.862	271	0.777	234
RS-P10-75	P36-45	SPBC16E9.03c	0.850	185	0.875	223
RS-P10-76	P36-47	SPBC16G5.15c	0.791	234	0.857	296
RS-P10-77	P36-53	SPBC17G9.09	0.896	256	0.830	294
RS-P10-78	P36-54	SPBC1921.07c	0.859	191	0.828	270
RS-P10-79	P36-57	SPBC216.06c	0.892	269	0.849	242
RS-P10-80	P36-61	SPBC29A10.02	0.757	299	0.746	475
RS-P10-81	P36-65	SPBC3H7.15	0.831	201	0.829	218
RS-P10-82	P36-70	SPBC713.02c	0.893	329	0.852	334
RS-P10-83	P36-79	SPCC24B10.04	NaN	0	0.835	263
RS-P10-86	P06-04	ste20	0.000	NaN	0.000	0
RS-P10-87	P18-16	SPAC823.12	0.787	1	0.898	78
RS-P10-88	P25-10	SPBC1A4.09	NaN	0	0.838	3
RS-P10-89	P26-40	SPCC1393.03	0.807	262	NaN	0
RS-P10-90	P36-80	SPCC24B10.19c	0.884	285	0.813	254
RS-P10-91	P36-82	SPCC338.05c	0.000	1	NaN	0
RS-P10-92	P36-85	SPCC4B3.02c	0.842	350	0.817	245
RS-P10-93	P36-95	SPCC970.06	0.871	329	0.779	6
RS-P10-94	P22-68	SPAC23C4.11	NaN	0	NaN	0
RS-P10-95	P29-65	SPAC14C4.14	0.874	315	0.847	321